

Nottingham Geospatial Institute

ASSESSMENT OF LONG-TERM DEFORMATION IN JOHOR, MALAYSIA USING GLOBAL POSITIONING SYSTEM (GPS) AND INTERFEROMETRIC SYNTHETIC APERTURE RADAR (INSAR)

By

MUHAMMAD ASYRAN BIN CHE AMAT

Thesis submitted to the University of Nottingham
for the degree of Doctor of Philosophy

October 2017

ABSTRACT

Information about deformation in an area has become vital not only for safety assessment but also for maintenance of geodetic infrastructures. The latter is necessary to support accurate surveying and mapping applications. This research exploits the complementary features of Global Positioning System (GPS) and Interferometric Synthetic Aperture Radar (InSAR) techniques to assess the long-term deformation in Johor, Malaysia, which can be induced by natural and/or anthropogenic activities. Furthermore, modelling and mitigation of tropospheric effects in GPS and InSAR are addressed to achieve the best possible precision from the two techniques. Indeed, their modelling and mitigation improve the quality of the estimation as well as provide valuable resources for atmospheric studies. The assessment of long-term deformation in Johor is firstly made by analysing the five years (2007 - 2011) point-specific profile at eight Malaysia Real-Time Kinematic GNSS Network (MyRTKnet) stations. Two processing strategies, namely Precise Point Positioning (PPP) and Double-Difference (DD), are employed to assess their capability for deformation monitoring. The latter also make used of the GPS data from 27 IGb08 stations and 7 International GNSS Service (IGS) stations. Analysis of the results revealed deformation that can be explained by plate tectonic movement and earthquakes in the surrounding region. While results from the PPP processing showed a higher correlation with the recorded earthquakes, the results from DD have improved correlation coefficients at about 4% in the East-West and 5% in the Up-Down components. These improvements are valuable when the rate of deformation is the primary interest. In addition to the point-specific profile, the surrounding deformation of Johor has been assessed with the line-of-sight (LOS) velocity maps from the InSAR time-series. Two sets of ERS-1/2 data, consisting a total of 67 images acquired at two descending tracks (i.e. track 75 and 347), are utilised for the generation of the maps. Moreover, the feasibility of Sentinel-1 satellites is also tested, which revealed improved coherence owing to their short revisit cycle. Some part of Johor showed subsidence and uplift trends, which also agreed with the literature. This information cannot be perceived by the GPS alone due to its limited coverage; hence, further attests to the benefit of their joint analysis. Numerous developments have been implemented in the in-house software (i.e. Punnet) such as the implementation of tropospheric correction, outlier's rejection scheme, statistical analysis to identify the control point for phase unwrapping, and a new method to retrieve temporal evolution of deformation for a rapidly deforming area.

ACKNOWLEDGEMENTS

Firstly, I would like to express my heartfelt appreciation to my supervisor Associate Professor Dr. Xiaolin Meng for his continuous advice, support, and constructive comments during this long journey in completing my study. This recognition extends to my former second supervisor Dr. Andrew Sowter for introducing me to Interferometric Synthetic Aperture Radar (InSAR) and guide me through the concept, algorithm, and software. Their invaluable advice has shed light to every difficult moment in this journey. I thank them for their time spent during our many discussions and for creating an environment where I could develop my ideas.

I also want to thank my internal examiner Professor Dr. Stuart Marsh for his valuable feedbacks and recommendations during my yearly reviews as well as during the viva examination. My external examiner, Professor Dr. Wu Chen from the Hong Kong Polytechnic University, is also acknowledged for his opinions in making this thesis better.

This research is not possible without the support and trust from my sponsor the Public Service Department of Malaysia (JPA). The Department of Survey and Mapping Malaysia (JUPEM) is highly appreciated for providing the opportunity and resources required for this research.

Special thanks to all members of the Nottingham Geospatial Institute (NGI) especially from the Xiaolin's research group and InSAR teammates for the fruitful conversation and ideas. Your feedbacks during our group meetings are greatly valued.

To my parent, Che Amat and Bidah, thank you for your love, prayers, and constant support. No words can describe my gratitude for all the sacrifices you made thus far. I am also grateful to my parent-in-law, Muhamad and Rokiah, for their understanding and prayers.

As for the utmost appreciation and gratitude, I would like to thank my lovely wife, Diana for her understanding, support, and love during the past few years. To my daughter, Khalisah Humaira, Aisyah Aqilah, and Anna Delisha, you are the main driving force and inspiration for me to complete this study. Your sweet smile and hearty laugh always brought peace to my stressful moment. For that, I am utterly grateful.

TABLE OF CONTENTS

CHAPTER	TITLE	PAGE NUMBER
	ABSTRACT	**i**
	ACKNOWLEDGEMENTS	**ii**
	TABLE OF CONTENTS	**iii**
	LIST OF FIGURES	**viii**
	LIST OF TABLES	**xx**
	LIST OF ABBREVIATIONS	**xxii**
1	**INTRODUCTION**	**1**
	1.1 Preface	1
	1.2 Research Aims and Objectives	4
	1.3 Thesis Overview	5
2.	**LITERATURE REVIEWS ON THE USES OF GPS AND INSAR FOR REGIONAL DEFORMATION MONITORING**	**6**
	2.1 Introduction	6
	2.2 The Importance of Deformation Monitoring	6
	2.3 Techniques for Deformation Monitoring	9
	2.4 GPS for Deformation Monitoring	12
	2.5 InSAR for Deformation Monitoring	15
	2.6 Combining GPS and InSAR for Deformation Monitoring	19
	2.7 Atmospheric Effects on GPS and InSAR	22
	2.7.1 Atmospheric Effects on GPS	22
	2.7.2 Atmospheric Effects on InSAR	24
	2.8 Summary	27
3.	**THE JOHOR SITE**	**28**
	3.1 Introduction	28
	3.2 Geography and Geological Setting	28
	3.3 Surveying and Mapping in Johor, Malaysia	29
	3.4 Deformation in Johor, Malaysia	31

3.4.1 Tectonic Movement 31
3.4.2 Landslide 33
3.4.3 Subsidence in Tropical Peatland 35
3.4.4 Urbanisation 37
3.4.5 Sea Level Rise and Flood 39
3.5 List of Datasets for Processing and Analysis 40
3.5.1 GPS Dataset 41
3.5.2 SAR Dataset 45
3.5.2.1 ERS-1/2 images 45
3.5.2.2 Sentinel-1 images 48
3.6 Summary 52

4. DEFORMATION ANALYSIS USING GPS TIME-SERIES 53
4.1 Introduction 53
4.2 Background 53
4.2.1 Basic GPS Principle 53
4.2.2 Biases and Errors in GPS Observation 58
4.2.2.1 Satellite-related 58
4.2.2.2 Station-related 61
4.2.2.3 Atmospheric-related 65
4.3 Coordinate Reference System for GPS 66
4.3.1 International Terrestrial Reference Frame (ITRF) 66
4.3.2 Geocentric Datum of Malaysia 2000 (GDM2000) 69
4.4 Bernese GNSS Software 71
4.5 GPS Processing Strategy 74
4.5.1 Using Precise Point Positioning (PPP) 75
4.5.2 Using Double Difference (DD) 80
4.5.3 Estimation of the Station Velocity 88
4.6 Summary 89

5. DEFORMATION ANALYSIS USING INSAR TIME-SERIES 91
5.1 Introduction 91
5.2 Background 91
5.2.1 Basic InSAR Principle 91
5.2.2 Noises and Errors in InSAR Measurement 93

5.2.2.1 Ground-related 94
5.2.2.2 Satellite-related 95
5.2.2.3 Atmospheric-related 95
5.3 Coordinate Reference System for InSAR 97
5.4 Punnet Software 98
5.5 Debursting and Merging (for Sentinel-1 Processing) 100
5.6 Images Coregistration and Resampling 101
5.7 Formation of Differential Interferogram 104
5.8 Selection of Coherent Points 110
5.9 Phase Unwrapping and Orbital Ramp Correction 113
5.10 InSAR Time-Series Analysis 117
5.10.1 Estimation of Linear Velocity and DEM Errors 118
5.10.2 Temporal Evolution of the Deformation 123
5.11 Mapping LOS-Velocity to Its Respective 3D Components 126
5.12 Summary 128

6. MODELLING AND MITIGATION OF TROPOSPHERIC EFFECTS IN GPS AND INSAR 130
6.1 Introduction 130
6.2 Atmospheric Effects on Radio Wave Propagation 130
6.3 Mapping Function 132
6.4 Modelling and Mitigation of Tropospheric Effects in GPS 134
6.4.1 Saastamoinen Model and Niell Mapping Function (NMF) 134
6.4.2 Vienna Mapping Function-1 (VMF-1) 138
6.4.3 Precise Point Positioning (PPP) and Double-Difference (DD) 143
6.4.4 Results and Discussion 149
6.5 Modelling and Mitigation of Tropospheric Effects in InSAR 160
6.5.1 Existing Method in Punnet 161
6.5.2 Tropospheric Estimation using Linear Relationship of Phase with Height 165
6.5.3 Tropospheric Estimation using Power-Law Relationship of Phase with Height 165
6.5.4 Results and Discussion 168
6.6 Summary 173

7. ANALYSES OF LONG-TERM DEFORMATION IN JOHOR **175**

7.1 Introduction 175

7.2 Historical Records of Earthquake 175

7.3 Analyses of GPS Time-Series 177

7.3.1 Discussion on the PPP Results 177

7.3.1.1 Analysis of the RMS of Coordinate Estimation 186

7.3.1.2 Analysis of the Velocity Rate 187

7.3.1.3 Analysis of the Horizontal Movement 191

7.3.2 Discussion on the DD Results 194

7.3.2.1 Analysis of the RMS of Coordinate Estimation 203

7.3.2.2 Analysis of the Velocity Rate 206

7.3.2.3 Analysis of the Horizontal Movement 209

7.3.3 Discussion on the Estimated Deformation from GPS Time-Series 211

7.4 Analyses of InSAR Time-Series 214

7.4.1 Results from the ERS-1/2 (Track 347) 215

7.4.2 Results from the ERS-1/2 (Track 75) 223

7.5 Summary 229

8. CONCLUSIONS AND RECOMMENDATIONS **233**

8.1 Conclusions 233

8.1.1 Objective 1: *To investigate and develop a strategy for precise estimation of the long-term deformation in Johor, Malaysia using GPS and InSAR.* 234

8.1.2 Objective 2: *To model and mitigate the tropospheric effects in GPS and InSAR to achieve the most precise and reliable estimation from the measurements*. 235

8.1.3 Objective 3: *To quantify and assess the rate of long-term deformation in Johor, Malaysia, and to analyse the sources of deformation*. 236

8.2 Recommendations 239

8.2.1 GPS Processing 239

8.2.2 SAR Processing 239

8.2.3 Tropospheric Modelling 240

REFERENCES **241**

APPENDICES **273**

A List of Publications and Potential Publications from This Research 273

B Example of Ambiguity Resolution Summary from Bernese Processing using DD 274

C Comparison between the Estimated ZTDs (PPP and DD) and the Published ZTDs from CODE 276

D Extracted Daily Coordinate Time-Series from PPP Processing (1 August 2007 – 31 October 2007) 278

E Extracted Daily Coordinate Time-Series from DD Processing (1 August 2007 – 31 October 2007) 286

LIST OF FIGURES

FIGURE NO.	TITLE	PAGE NUMBER
2.1	Major tectonic plates of the Earth shown in different colour schemes. Arrows indicate the direction of each plate motion. Figure adapted from *http://pubs.usgs.gov/publications/text/slabs.html* (accessed 10.05.2016).	7
2.2	Geographical location of Malaysia (marked in black rectangle) respective to the Pacific Ring of Fire. Figure adapted from http://www.universetoday.com/59341/pacific-ring-of-fire/ (accessed 13.06.2014).	8
3.1	Land cover map of Johor. Figure adapted from the FAO Global Land Cover (GLC-SHARE) Beta-Release 1.0 Database, Land and Water Division, John Latham, Renato Cumani, Ilaria Roasti and Mario Bloise, 2014: *http://www.fao.org/geonetwork/srv/en/main.home* (accessed 18.01.2017), © FAO and NASA.	30
3.2	Elevation map in Johor, Malaysia based on the Shuttle Radar Topography Mission (SRTM) digital elevation model (Farr et al., 2007).	30
3.3	Record of earthquakes in Malaysia (adapted from *www.met.gov.my/*, accessed 30.01.2017).	32
3.4	Landslide hazard map and locations of the historical landslide from 1971 to 2012. Figure adapted from Murakami et al. (2014).	34
3.5	Major peat soil areas in Peninsular Malaysia. Figure adapted from International Wetlands (2010).	35
3.6	Urbanisation process in Johor. (*a*) Rendered image from Google Earth on 31 December 1985, and (*b*) on 31 December 2016.	38
3.7	Tide gauge stations in Malaysia. Figure adapted from Abdul Hadi et al. (2016). The map is not to scale.	39
3.8	The distribution of the GPS stations in this study.	43
3.9	GPS data availability from the year 2007 to 2011.	44
3.10	EOLi-ESA interface for requesting ERS-1/2 images.	46

3.11	Sentinels Scientific Data Hub for acquiring Sentinel-1 images. Accessible on *https://scihub.copernicus.eu/dhus/* (accessed 18.01.2017).	51
4.1	Satellite antenna phase centre offsets in satellite body-fixed reference frame. Figure adapted from Kouba (2009).	61
4.2	ITRF2008 network. Figure adapted from Altamimi et al. (2011).	68
4.3	The distribution of MyRTKnet stations in Peninsular Malaysia (top) and East Malaysia (bottom). Figure adapted from JUPEM (2009a).	70
4.4	Geographical distribution of institutions using the Bernese GPS Software. Figure adapted from Dach et al. (2008).	73
4.5	Workflow for processing GPS data using PPP strategy.	76
4.6	An example of the result from coordinate estimation using ADDNEQ2.	80
4.7	Workflow for processing GPS data using DD strategy.	81
5.1	Geometry of a SAR system. Pulses are emitted at high frequency as the platform moves along the satellite vector $v_{s/c}$. The footprint of each pulse is indicated by successive ellipses in the swath W_a. The entire image is limited in range by the near and far range limits, and in azimuth by the early and late azimuth times. Figure adapted from Hanssen (2001).	97
5.2	Standard processing scheme for Punnet software using (*a*) Sentinel-1 dataset, and (*b*) other standard SLC datasets. Notice that Sentinel-1 requires additional steps of debursting and merging before images coregistration, as well as utilisation of the known deramping function for resampling. Other steps are standard for all dataset, i.e. formation of differential interferograms; identification of coherent points; phase unwrapping; orbital ramp correction; and time-series analysis. Figure adapted from Sowter et al. (2016).	99
5.3	Illustration of debursting and merging in Sentinel-1. (*a*) Arrangement of bursts in an IW sub-swath. (*b*) Sentinel-1 burst structure with small overlaps between bursts and sub-swaths. (*c*) Mosaic for full Sentinel-1 IW swath consisting of 3 sub-swaths with 3 bursts in each. Figure adapted from Sowter et al. (2016).	100
5.4	Differences in SAR geometry between the master and the slave image, which can be represented by six parameters, i.e. shift, stretch and rotation, both in azimuth and range directions.	101

5.5	Selection of the master image to be in the centre of data span. Each vertical gridline corresponds to 1 year different. (*a*) ERS-1/2 descending dataset. The top plot shows data acquisitions in track 347 relative to the master image on 22 August 1997, whereas bottom plot shows data acquisitions in track 75. The image on 10 May 1998 was selected as the master image. (*b*) Sentinel-1 ascending dataset. 22 SAR images were acquired from 22 Mac 2015 to 24 September 2016 with 24 days temporal separation. Images on 20 June 2016 is missing from the Sentinels Scientific Data Hub.	103
5.6	Average amplitude maps of Johor, displayed in range and azimuth directions of the satellites (not orthorectified). Bright pixel corresponds to a field with high signal reflection, whereas dark grey pixel relates to an area with low signal reflection. (*a*) The result from ERS-1/2 (track 347), (*b*) the result from ERS-1/2 (track 75), and (*c*) the result from Sentinel-1 (subset to the area of interest). Waterbody has been masked out and showed as black.	104
5.7	Selection of the temporal and orbital baselines threshold for ERS-1/2 (track 347). (*a*) The number of interferograms from different sets of temporal and orbital thresholds. (*b*) Altitude of ambiguity as a function of normal baseline. Increasing normal baseline will result in low altitude of ambiguity, i.e. phase is more sensitive to the elevation change or DEM errors. (*c*) The number of interferogram as a function of temporal baseline using 350 m for the orbital baseline threshold. (*d*) The network of interferograms using 350 m and 5 years for the baseline and temporal baseline thresholds, respectively.	107
5.8	Selection of the temporal and orbital baselines threshold for ERS-1/2 (track 75). (*a*) The number of interferograms from different sets of temporal and orbital thresholds. (*b*) Altitude of ambiguity as a function of normal baseline. Increasing normal baseline will result in low altitude of ambiguity, i.e. phase is more sensitive to the elevation change or DEM errors. (*c*) The number of interferogram as a function of temporal baseline using 350 m for the orbital baseline threshold. (*d*) The network of interferograms using 350 m and 5 years for the baseline and temporal baseline thresholds, respectively.	108

5.9	Selection of the temporal and orbital baselines threshold for Sentinel-1. (*a*) The number of interferograms from different sets of temporal and orbital thresholds. (*b*) Altitude of ambiguity as a function of normal baseline. Increasing normal baseline will result in low altitude of ambiguity, i.e. phase is more sensitive to the elevation change or DEM errors. (*c*) The number of interferogram as a function of temporal baseline using 350 m for the orbital baseline threshold. (*d*) The network of interferograms using 350 m and 5 years for the baseline and temporal baseline thresholds, respectively.	109
5.10	Average coherence maps, displayed in range and azimuth directions of the satellites (not orthorectified). The urban areas have better coherence than the countryside. Histogram plots next to each map show statistical information for the SBAS points, i.e. candidates for the control point. The criterion used to narrow down the candidates are represented by red arrows, i.e. average coherence value of more than 0.6 and RMS for differential interferograms of less than 1.7. (*a*) Result for the ERS-1/2 (track 347), (*b*) result for the ERS-1/2 (track 75), and (*c*) result for the Sentinel-1 (subset to the area of interest).	111
5.11	Average coherence map of ERS-1/2 (track 347) showing the two subset areas (i.e. blue and red boxes) used to investigate the effects of the water body to the phase unwrapping. Each differential interferograms and its respective coherence maps are subsets to these areas before phase unwrapping using SNAPHU. The green rectangle is the location of the control point, which is common in both areas.	115
5.12	Comparison of the unwrapped differential interferogram (after baseline correction) for five selected image pairs. Figures on the middle and right are from the individual phase unwrapping using SNAPHU. The full scene results are shown in the left figures for comparison. No significant difference is observed among them.	116
5.13	Outliers detection at four points, i.e. PT01 - PT04. (Left) Scatter plot of the unwrapped phase against temporal separation. Red points show linear velocity from the final estimation. Strong subsidence can be observed from the phase, but the estimated rate is affected by outliers in the unwrapped phase. (Middle) Plot of the unwrapped phase against the perpendicular baseline. (Right) Residuals from the LSE. Interferogram with the highest residual value is rejected for the subsequent estimation.	120

5.14	LOS-velocity map from Mexico processing. 18 Sentinel-1 images were acquired between 3 October 2014 and 7 May 2015. (*a*) The result from the original algorithm, i.e. without outlier rejection. (*b*) The result from outlier detection in a single iteration. (*c*) The result from outlier detection in iterative detection.	121
5.15	Standard error for LOS-velocity map of Mexico City. (*a*) The result from the original algorithm, i.e. without outlier rejection. (*b*) The result from outlier detection in a single iteration. (*c*) The result from outlier detection in iterative detection.	122
5.16	Block diagram of the implemented algorithm. Figure adapted from Berardino et al. (2002).	124
5.17	Temporal evolution of deformation for the 10 selected points (represented by different colours) in Mexico City. In general, all points show subsidence trend in relation to the first acquisition.	125
5.18	Relationship between the LOS-velocity (i.e. V_{los}) from InSAR time-series to its 3D components (i.e. V_{north}, V_{east} and V_{height}) considering the right looking ascending satellite geometry.	127
5.19	Comparison between the estimated velocity in LOS and vertical directions. The vertical velocity is more disperse compared to the LOS velocity as resulted from the multiplication of LOS velocity with the inversed cosine of radar incidence angle.	128
6.1	Mapping function to relate the tropospheric delay at zenith and satellite elevation angle. (*a*) Simple mapping function based on the elevation angle of the satellite E. This simple mapping function is not accurate for satellites at low elevation angle due to the bending effects, as illustrated in (*b*).	133
6.2	Structure of the VMF-1 file. The first seven rows are the header of the file (begin with the symbol "!"). The first two columns are the latitudes and longitudes of the grid with 2° and 2.5° resolution, respectively. The next two column provide the coefficient a for the dry and wet delays, whereas the last two column are the zenith delay for dry and wet from the ray tracing.	139
6.3	Bilinear interpolation on the grid for VMF-1 coefficients.	141

6.4	Tropospheric estimation using the Bernese software. A model that represent the dry component is introduced, whereas the wet component and horizontal tropospheric gradients are estimated from the observations. (*a*) Header and the first few lines of a Bernese *.TRP file. The header summarises selected options for the a priori model, mapping function, gradient model, minimum elevation, and the temporal sampling interval. The first eight columns represent the name of the station, a flag marking the estimated coordinates depending on the modifying program, and respective date and time for which the parameters have been computed. The following eight columns give values of the a priori model (i.e. MOD_U) and the site-specific parameters (i.e. CORR_U) in the zenith direction, as well as the horizontal gradients in North (i.e. CORR_N) and East (i.e. CORR_E). The sum of MOD_U and CORR_U is written to the column TOTAL_U. Standard deviations SIGMA_U, SIGMA_N, and SIGMA_E for the respective values of the site-specific troposphere parameters, and the horizontal gradients are also specified. All values are given in metre. (*b*) Representation of the tropospheric components from the Bernese *.TRP file.	148
6.5	Troposphere estimate at PRTS station for DoY 1 - 3 (2007). DD processing strategy is employed using VMF-1 for the tropospheric modelling. Notice the trend of the dry delay changes at 6 hours interval owing to the temporal resolution of the VMF-1 file. Linear interpolation in time is applied to obtain the value at every hour. Following that, the wet component is estimated from the observations.	149
6.6	Comparison between the estimated ZTD from PPP and DD for eight MyRTKnet stations (2007 - 2011).	150
6.7	RINEX data at JHJY station on 3 September 2008. Notice the sparse data recorded on L_2 frequency that limits the number of ionosphere-free linear combination that can be formed.	152
6.8	Tropospheric estimation using NMF. All delays are in zenith direction.	154
6.9	Tropospheric estimation using VMF-1. All delays are in zenith direction.	156
6.10	Different in the ZTD using NMF and VMF-1.	159

6.11	The effects of vertical stratification on unwrapped interferograms. (*a*) Height from the SRTM DEM. (*b*) Unwrapped phases of four selected interferograms (left) and their scatter plot (right) to show correlation with height.	164
6.12	Results of the balloon soundings at Acapulco station, Mexico from 1 October 2014 to 31 October 2014. (*a*) The plot of refractivity with height. (*b*) The plot of LOS phase delay with height. (*c*) The plot of relative LOS phase delay with height. (*d*) The log-log plot of the mean delay with height to estimate the H_0 and α parameters.	167
6.13	Monthly estimation of the parameters H_0 and α at Acapulco station, Mexico. The estimation covers eight months from October 2014 to May 2015. Their weighted average is adopted for the estimation of tropospheric correction in interferograms.	167
6.14	Tropospheric correction using linear relationship of phase with height shown on four selected interferograms from Mexico processing.	169
6.15	Tropospheric correction using power law relationship of phase with height shown on four selected interferograms from Mexico processing.	170
6.16	Comparison of the LOS velocity map for Mexico City: (*a*) without tropospheric correction, (*b*) tropospheric correction by a linear relationship of phase with height, and (*c*) tropospheric correction by power law relationship of phase with height.	171
6.17	Comparison of the standard error map for the LOS-velocity of Mexico City: (*a*) without tropospheric correction, (*b*) tropospheric correction by a linear relationship of phase with height, and (*c*) tropospheric correction by power law relationship of phase with height.	172
6.18	Histogram plot of the standard error for the LOS-velocity of Mexico City. Notice that more points will show small standard error from applying tropospheric corrections (linear or power law corrections) than without correction. No significant difference is observed between linear or power law corrections.	173

7.1	Recorded earthquakes with magnitude Mw4.5 and above in the region bounds by latitude 10° North - 10° South, and longitude 90° East - 110° East, as extracted from the United States Geological Survey (USGS) database: *http://earthquake.usgs.gov/* (accessed 18.01.2017). (*a*) Geographical location of the earthquakes and their magnitude, and (*b*) summary of the earthquakes.	176
7.2	Daily coordinate time-series for station GAJA (2007 - 2011) from PPP processing. (*a*) North-South component, (*b*) East-West component, (*c*) Up-Down component, and (*d*) RMS for the estimation in colour coded, i.e. blue for North-South, green for East-West, and cyan for Up-Down components. The red dotted lines in the y-axis of the figure (*a*), (*b*), and (*c*) represent earthquake that is larger than 6Mw.	178
7.3	Daily coordinate time-series for station JHJY (2007 - 2011) from PPP processing. (*a*) North-South component, (*b*) East-West component, (*c*) Up-Down component, and (*d*) RMS for the estimation in colour coded, i.e. blue for North-South, green for East-West, and cyan for Up-Down components. The red dotted lines in the y-axis of the figure (*a*), (*b*), and (*c*) represent earthquake that is larger than 6Mw.	179
7.4	Daily coordinate time-series for station KLUG (2007 - 2011) from PPP processing. (*a*) North-South component, (*b*) East-West component, (*c*) Up-Down component, and (*d*) RMS for the estimation in colour coded, i.e. blue for North-South, green for East-West, and cyan for Up-Down components. The red dotted lines in the y-axis of the figure (*a*), (*b*), and (*c*) represent earthquake that is larger than 6Mw.	180
7.5	Daily coordinate time-series for station KUKP (2007 - 2011) from PPP processing. (*a*) North-South component, (*b*) East-West component, (*c*) Up-Down component, and (*d*) RMS for the estimation in colour coded, i.e. blue for North-South, green for East-West, and cyan for Up-Down components. The red dotted lines in the y-axis of the figure (*a*), (*b*), and (*c*) represent earthquake that is larger than 6Mw.	181
7.6	Daily coordinate time-series for station PRTS (2007 - 2011) from PPP processing. (*a*) North-South component, (*b*) East-West component, (*c*) Up-Down component, and (*d*) RMS for the estimation in colour coded, i.e. blue for North-South, green for East-West, and cyan for Up-Down components. The red dotted lines in the y-axis of the figure (*a*), (*b*), and (*c*) represent earthquake that is larger than 6Mw.	182

7.7	Daily coordinate time-series for station SPGR (2007 - 2011) from PPP processing. (*a*) North-South component, (*b*) East-West component, (*c*) Up-Down component, and (*d*) RMS for the estimation in colour coded, i.e. blue for North-South, green for East-West, and cyan for Up-Down components. The red dotted lines in the y-axis of the figure (*a*), (*b*), and (*c*) represent earthquake that is larger than 6Mw.	183
7.8	Daily coordinate time-series for station TGPG (2007 - 2011) from PPP processing. (*a*) North-South component, (*b*) East-West component, (*c*) Up-Down component, and (*d*) RMS for the estimation in colour coded, i.e. blue for North-South, green for East-West, and cyan for Up-Down components. The red dotted lines in the y-axis of the figure (*a*), (*b*), and (*c*) represent earthquake that is larger than 6Mw.	184
7.9	Daily coordinate time-series for station TGRH (2007 - 2011) from PPP processing. (*a*) North-South component, (*b*) East-West component, (*c*) Up-Down component, and (*d*) RMS for the estimation in colour coded, i.e. blue for North-South, green for East-West, and cyan for Up-Down components. The red dotted lines in the y-axis of the figure (*a*), (*b*), and (*c*) represent earthquake that is larger than 6Mw.	185
7.10	Histogram plots of the coordinate RMS from PPP processing strategy.	187
7.11	Interpolated stations velocity from PPP processing in (*a*) North-South, and (*b*) East-West components, based on the Natural Neighbour Interpolation within ArcGIS software.	190
7.12	Seismotectonic map of Peninsular Malaysia showing some major and minor fault lines separating the east and the west sectors of Peninsular Malaysia. Figure adapted from JMG (2009).	191
7.13	Scatter plot of the stations movement as estimated from the PPP processing (2007 - 2011).	193
7.14	Vector plot of the horizontal movement of eight MyRTKnet stations as estimated from the PPP processing.	194

7.15	Daily coordinate time-series for station GAJA (2007 - 2011) from DD processing. (*a*) North-South component, (*b*) East-West component, (*c*) Up-Down component, and (*d*) RMS for the estimation in colour coded, i.e. blue for North-South, green for East-West, and cyan for Up-Down components. The red dotted lines in the y-axis of the figure (*a*), (*b*), and (*c*) represent earthquake that is larger than 6Mw.	195
7.16	Daily coordinate time-series for station JHJY (2007 - 2011) from DD processing. (*a*) North-South component, (*b*) East-West component, (*c*) Up-Down component, and (*d*) RMS for the estimation in colour coded, i.e. blue for North-South, green for East-West, and cyan for Up-Down components. The red dotted lines in the y-axis of the figure (*a*), (*b*), and (*c*) represent earthquake that is larger than 6Mw.	196
7.17	Daily coordinate time-series for station KLUG (2007 - 2011) from DD processing. (*a*) North-South component, (*b*) East-West component, (*c*) Up-Down component, and (*d*) RMS for the estimation in colour coded, i.e. blue for North-South, green for East-West, and cyan for Up-Down components. The red dotted lines in the y-axis of the figure (*a*), (*b*), and (*c*) represent earthquake that is larger than 6Mw.	197
7.18	Daily coordinate time-series for station KUKP (2007 - 2011) from DD processing. (*a*) North-South component, (*b*) East-West component, (*c*) Up-Down component, and (*d*) RMS for the estimation in colour coded, i.e. blue for North-South, green for East-West, and cyan for Up-Down components. The red dotted lines in the y-axis of the figure (*a*), (*b*), and (*c*) represent earthquake that is larger than 6Mw.	198
7.19	Daily coordinate time-series for station PRTS (2007 - 2011) from DD processing. (*a*) North-South component, (*b*) East-West component, (*c*) Up-Down component, and (*d*) RMS for the estimation in colour coded, i.e. blue for North-South, green for East-West, and cyan for Up-Down components. The red dotted lines in the y-axis of the figure (*a*), (*b*), and (*c*) represent earthquake that is larger than 6Mw.	199

7.20	Daily coordinate time-series for station SPGR (2007 - 2011) from DD processing. (*a*) North-South component, (*b*) East-West component, (*c*) Up-Down component, and (*d*) RMS for the estimation in colour coded, i.e. blue for North-South, green for East-West, and cyan for Up-Down components. The red dotted lines in the y-axis of the figure (*a*), (*b*), and (*c*) represent earthquake that is larger than 6Mw.	200
7.21	Daily coordinate time-series for station TGPG (2007 - 2011) from DD processing. (*a*) North-South component, (*b*) East-West component, (*c*) Up-Down component, and (*d*) RMS for the estimation in colour coded, i.e. blue for North-South, green for East-West, and cyan for Up-Down components. The red dotted lines in the y-axis of the figure (*a*), (*b*), and (*c*) represent earthquake that is larger than 6Mw.	201
7.22	Daily coordinate time-series for station TGRH (2007 - 2011) from DD processing. (*a*) North-South component, (*b*) East-West component, (*c*) Up-Down component, and (*d*) RMS for the estimation in colour coded, i.e. blue for North-South, green for East-West, and cyan for Up-Down components. The red dotted lines in the y-axis of the figure (*a*), (*b*), and (*c*) represent earthquake that is larger than 6Mw.	202
7.23	Histogram plots of the coordinate RMS from DD processing strategy.	204
7.24	Increment in the RMS of coordinate estimation at four selected MyRTKnet stations. The red dotted line indicates the trend of RMS.	205
7.25	Interpolated stations velocity from DD processing in (*a*) North-South, and (*b*) East-West components, based on the Natural Neighbour Interpolation within ArcGIS software.	208
7.26	Scatter plot of the stations movement as estimated from the DD processing (2007 - 2011).	210
7.27	Vector plot of the horizontal movement of eight MyRTKnet stations as estimated from the DD processing.	211
7.28	Comparison of the coordinates time series at PRTS station between PPP (left) and DD (right). The plot covers the period from 6 October 2009 to 31 December 2009. Note the position shift in the East-West direction as a result of the 6Mw earthquake on 10 November 2009, which is clearly visible in the PPP result.	213

7.29	Coverage comparison between the ISBAS and SBAS techniques from the ERS-1/2 (track 347) results. White points represent coherent points in the image.	215
7.30	LOS-velocity map of Johor from the ERS-1/2 (track 347) processing.	217
7.31	Standard error map for the LOS-velocity of Johor from the ERS-1/2 (track 347) processing.	218
7.32	PS-InSAR results in Johor from 1996 to 2005. (*a*) LOS-velocity estimation in mm/year, and (*b*) standard error of the LOS-velocity. Figure adapted from Ami Hassan (2014).	219
7.33	Spatio-temporal patterns of landscape change in Iskandar Malaysia. Figure adapted from Barau and Qureshi (2015).	220
7.34	Histogram plot of the standard error from the ERS-1/2 (track 347) processing.	223
7.35	Coverage comparison between the ISBAS and SBAS techniques from the ERS-1/2 (track 75) results. White points represent coherent points in the image.	224
7.36	LOS-velocity map of Johor from the ERS-1/2 (track 75) processing.	225
7.37	Standard error map for the LOS-velocity of Johor from the ERS-1/2 (track 75) processing.	226
7.38	Histogram plot of the standard error from the ERS-1/2 (track 75) processing.	229

LIST OF TABLES

TABLE NO.	TITLE	PAGE NUMBER
3.1	List of GPS stations in this study and their locations.	42
3.2	List of proposals submitted to request ERS-1/2 dataset in Johor.	47
3.3	Sentinel satellites and their mission objectives. Table adapted from *http://www.copernicus.eu/main/sentinels* (accessed 18.01.2017).	49
3.4	Properties of Sentinel-1 Interferometric Wide (IW) Single Look Complex (SLC) products (ESA, 2013).	50
3.5	List of the Sentinel-1 dataset used in this research.	51
4.1	GPS satellite ephemerides / satellite and station clocks (see *http://www.igs.org/products*, accessed 13.12.2016).	59
4.2	Errors in baseline components due to orbit errors.	59
4.3	History of reference frames used for IGS products (see *http://acc.igs.org/igs-frames.html*, accessed 13.12.2016).	68
4.4	List of software used by the IGS analysis centres (see *ftp://igs.org/pub/center/analysis/*, accessed 04.01.2017).	72
4.5	External products used in the processing.	74
4.6	List and description of Bernese programs for PPP processing.	77
4.7	List and description of Bernese programs for DD processing.	82
5.1	Different frequency bands used by satellite radar sensors.	92
5.2	Selection of coherent points based on the minimum number of layers used to achieve the average coherence value of 0.25.	112
5.3	SAR coordinate of the selected control point for phase unwrapping.	113
5.4	Range of incidence angle for the coherent points in Johor.	128
6.1	Reference values for height, pressure, temperature and relative humidity used in the Bernese software.	135
6.2	Coefficients of the dry NMF as a function of site latitude φ, according to Boehm (2004).	136

6.3	Coefficients for the height correction of dry NMF, according to Boehm (2004).	136
6.4	Coefficients of the wet NMF as a function of site latitude φ, according to Boehm (2004).	137
6.5	Coefficients for the determination of c_{dry} in VMF-1, according to (Boehm et al. 2006).	140
6.6	Modules in Bernese for the computation of VMF-1.	143
6.7	Comparison between the ZTDs from PPP and DD processing with respect to ZTDs from CODE.	153
6.8	Statistical comparison between NMF and VMF-1.	158
6.9	Standard deviation of coordinate (latitude, longitude and ellipsoid height) from DD processing using NMF and VMF-1.	159
6.10	Summary of the interferograms from Mexico processing that are used to illustrate the correction of tropospheric artefacts due to vertical stratification.	163
7.1	Linear velocity rate for 8 MyRTKnet stations estimated from PPP solution using GPS data from 2007 to 2011.	189
7.2	Linear velocity rate for 8 MyRTKnet stations estimated from DD solution using GPS data from 2007 to 2011.	207
7.3	Comparison between the estimated velocity from DD GPS and ISBAS analysis of ERS-1/2 (track 347) (the nearest point to the GPS station).	221
7.4	Comparison between the estimated velocity from DD GPS and ISBAS analysis of ERS-1/2 (track 347) (average velocity over 2 km radius).	222
7.5	Comparison between the estimated velocity from DD GPS and ISBAS analysis of ERS-1/2 (track 75) (the nearest point to the GPS station).	228
7.6	Comparison between the estimated velocity from DD GPS and ISBAS analysis of ERS-1/2 (track 75) (average velocity over 2 km radius).	228

LIST OF ABBREVIATIONS

1D	-	One-dimensional
2D	-	Two-dimensional
3D	-	Three-dimensional
AIUB	-	Astronomical Institute of the University of Bern
ALOS	-	Advanced Land Observation Satellite
ANTEX	-	Antenna Exchange Format
APS	-	Atmospheric Phase Screen
AVD	-	Absolute Velocity Determination
BIH	-	Bureau International de l'Heure
BPE	-	Bernese Processing Engine
BT68	-	Borneo Triangulation 1968
CDDIS	-	Crustal Dynamics Data Information System
CODE	-	Center for Orbit Determination in Europe
CORS	-	Continuously Operating Reference Station
CPT	-	Coherent Pixels Technique
DD	-	Double-Difference
DEM	-	Digital Elevation Model
DEOS	-	Delft Institute for Earth Oriented Space Research
DePSI	-	Delft Persistent Scatterer Interferometry
DIA	-	Detection Identification Adaptation
DORIS	-	Delft Object-oriented Radar Interferometric Software
DOSM	-	Department of Statistics Malaysia
DoY	-	Day of Year
ECEF	-	Earth-Centered Earth-Fixed
ECMWF	-	European Centre for Medium-Range Weather Forecasts
EMR	-	Natural Resources Canada
ERP	-	Earth Rotation Parameters
ERS	-	European Remote-sensing Satellite
ESA	-	European Space Agency
FAO	-	Food and Agriculture Organisation of the United Nations
FFT	-	Fast Fourier Transform
GDM2000	-	Geocentric Datum of Malaysia 2000

GeoSHM	-	GPS and Earth Observation for Structural Health Monitoring
GFZ	-	GeoForschungsZentrum
GIM	-	Global Ionosphere Map
GIS	-	Geographic Information System
GLC	-	Global Land Cover
GMF	-	Global Mapping Function
GNSS	-	Global Navigation Satellite System
GOP	-	Geodetic Observatory Pecny
GPS	-	Global Positioning System
GPT	-	Global Pressure and Temperature
GUI	-	Graphical User Interface
IAC	-	Information and Analysis Center of Navigation
IAG	-	International Association of Geodesy
IERS	-	International Earth Rotation and Reference Systems Service
IGS	-	International GNSS Service
ILRS	-	International Laser Ranging Service
IMU	-	Inertial Measurement Unit
InSAR	-	Interferometric Synthetic Aperture Radar
IPTA	-	Interferometric Point Target Analysis
ISBAS	-	Intermittent Small Baseline Subset
ITRF	-	International Terrestrial Reference Frame
ITRS	-	International Terrestrial Reference System
IW	-	Interferometric Wide
JPL	-	Jet Propulsion Laboratory
JUPEM	-	Department of Survey and Mapping Malaysia
LIDAR	-	Light Detection and Ranging
LOS	-	Line-of-Sight
LSE	-	Least Square Estimation
MASS	-	Malaysia Active GPS Network
MCC	-	Mission Control Center
MERIS	-	Medium Resolution Imaging Spectrometer
MIT	-	Massachusetts Institute of Technology
MMS	-	Malaysian Meteorological Service
MODIS	-	Moderate Resolution Imaging Spectroradiometer
MRT48	-	Malayan Revised Triangulation 1948

MSL	-	Mean Sea Level
MTG-S	-	Meteosat Third Generation-Sounder
MyRTKnet	-	Malaysia Real-Time Kinematic GNSS Network
NASA	-	National Aeronautics and Space Administration
NMF	-	Niell Mapping Function
NNR	-	No Net Rotation
NOAA	-	National Oceanic and Atmospheric Administration
NWM	-	Numerical Weather Model
PALSAR	-	Phased Array L-band Synthetic Aperture Radar
ppm	-	Parts Per Million
PPP	-	Precise Point Positioning
PSI	-	Persistent Scatterer Interferometry
PSInSAR	-	Permanent Scatterer InSAR
PSP	-	Persistent Scatterer Pairs
PWV	-	Precipitable Water Vapour
QIF	-	Quasi-Ionosphere-Free
QPS	-	Quasi Persistent Scatterers
RCS	-	Radar Cross-Section
RINEX	-	Receiver Independent Exchange Format
RMS	-	Root Mean Square
RSO	-	Rectified Skew Orthomorphic
SAR	-	Synthetic Aperture Radar
SBAS	-	Small Baseline Subset
SCIGN	-	Southern California Integrated GPS Network
SINEX	-	Solution Independent Exchange Format
SIO	-	Scripps Institution of Oceanography
SIR	-	Regional Network for South America
SLC	-	Single Look Complex
SLR	-	Satellite Laser Ranging
SNAPHU	-	Statistical-cost Network-flow Algorithm for Phase Unwrapping
SNR	-	Signal-to-Noise Ratio
SOPAC	-	Scripps Orbit and Permanent Array Center
SPN	-	Stable Points Network
SPOT	-	Landsat and Satellite Pour l'Observation de la Terre
SRTM	-	Shuttle Radar Topography Mission

StaMPS	-	Stanford Method for Persistent Scatterers
SVD	-	Singular Value Decomposition
TEQC	-	Toolkit for GPS / GLONASS / Galileo / SBAS / Beidou / QZSS Data
TOPS	-	Terrain Observation with Progressive Scans
TRAIN	-	Toolbox for Reducing Atmospheric InSAR Noise
UAV	-	Unmanned Aerial Vehicle
USGS	-	United States Geological Survey
USNO	-	United State Naval Observatory
VLBI	-	Very Long Baseline Interferometry
VMF-1	-	Vienna Mapping Functions-1
WHU	-	Wuhan University
WI-MP	-	Wetlands International-Malaysia Programme
WLS	-	Weighted Least Squares
ZHD	-	Zenith Hydrostatic Delay
ZTD	-	Zenith Tropospheric Delay
ZWD	-	Zenith Wet Delay

CHAPTER 1

INTRODUCTION

1.1. Preface

Malaysia is inevitably affected by seismic activities due to its geographical location, which is situated within the buffer zone of the Pacific Ring of Fire. A study by the Department of Survey and Mapping Malaysia (JUPEM) using data from continuous Global Positioning System (GPS) revealed movements up to 25.8 cm, interpreted as the result of co-seismic and post-seismic motions from the 2004, 2005, and 2007 Sumatran earthquakes (JUPEM, 2009a). Similarly, Vigny et al. (2005) detected movements ranging from 2 to 17 cm resulted from the 2004 Sumatra-Andaman earthquake. Larger displacements occurred in the northern peninsula and extended more than 3,000 km from the earthquake epicentre. Interestingly, the direction of these movements was towards the west as opposed to the normal velocity, i.e. towards the east at 1.2 ± 0.3 cm per year with respect to Eurasia plate (Michel et al., 2001).

There are other factors that contribute to the growing demand for deformation monitoring in Malaysia. A number of unfortunate tragedies such as the collapse of Highland Tower on 11 December 1993, the tsunami in West Coast of Peninsular Malaysia on 26 December 2004, and major floods that strike almost every year during monsoon season are among the evidence of the need for this monitoring. The rise of public awareness and concern especially with the increasing number and complexity of engineering structures add onto the list. In general, the primary purpose of deformation monitoring is the detection of spatial deformation to provide information on the stability and extent of any movement or deformation of an object occurring over time (Halim, 1995). It is useful for safety assessment as well as predicting and preventing the possibility of failure or disaster in the future.

Two space-based positioning techniques commonly used for monitoring deformation with high precision and accuracy are Interferometric Synthetic Aperture Radar (InSAR) and GPS. InSAR is suitable for monitoring deformation over large areas owing to its spatial coverage. Since InSAR does not rely on ground observation, it has advantages for remote, dangerous or inaccessible sites. The uses of this technique for deformation monitoring have been reported by various researchers, such as for monitoring earthquakes (e.g. by Massonnet et al., 1993; Stramondo et al., 1999; Wright, 2002), landslides (e.g. by Fruneau et al., 1996; Refice et al., 2000; Rott and Nagler, 2006), volcanoes (e.g. by Massonnet et al., 1995; Lanari et al., 1998; Ara and Luz, 2002), land subsidence (e.g. by Wright and Stow, 1997; Amelung et al., 1999;

Sowter et al., 2013), and engineering structures (e.g. by Wang et al., 2010). Nevertheless, the resultant deformation profile is limited typically to the line-of-sight (LOS) of the satellite.

On the contrary, GPS gives better representation in a three-dimensional view, but this information is limited only to the observed stations (point-specific deformation profile). Other factors such as the cost of setting up GPS stations (monument, equipment and operational cost) and the source of power supply (for continuous monitoring) must also be considered. However, the uses of GPS for monitoring deformation are increasing owing to the rapid increment of permanent GPS network in many countries. In Malaysia, JUPEM has established the Malaysia Real-Time Kinematic GNSS Network (MyRTKnet) since 2002. Currently, it consists of 78 stations, with 50 in Peninsular Malaysia and 28 in East Malaysia. Availability of the permanent GPS network has enabled users, among others, to only use single GPS receivers for deformation monitoring, hence reducing the overall cost. Many researchers have demonstrated the usages of GPS for various applications, such as for monitoring plate tectonics (e.g. by Vernant et al., 2004; Qu et al., 2014), earthquakes (e.g. by Wdowinski et al., 1997; Ergintav et al., 2007; Li et al., 2014), land subsidences (e.g. by Abidin et al., 2001; Baldi et al., 2009), and engineering structures (e.g. by Behr et al., 1993; Meng et al. 2007; Yi et al., 2013).

Integrating InSAR and GPS certainly enable better analysis, covering both surrounding and point-specific deformation profiles. For this reason, various integration techniques were explored and investigated by many researchers. Lagios et al. (2012) utilised results from InSAR and GPS to achieve a better understanding of seismicity patterns in Cephalonia, Greece, thus enabling a prediction of future earthquakes. Similarly, Tang et al. (2012) used InSAR and GPS for monitoring subsidence over a coal mining area and concluded that it is more efficient compared to the conventional method, i.e. using the electronic total station and levelling instrument, especially in the mountainous region. On the other hand, Wang et al. (2012) and Cavalie et al. (2013) incorporated InSAR and GPS results to derived deformation parameters such as the location of the epicentre, the magnitude of the earthquake, and the fault geometry. Another example is the GPS and Earth Observation for Structural Health Monitoring (GeoSHM) project, lead by the Nottingham Geospatial Institute, The University of Nottingham. GeoSHM integrates InSAR and GPS to provide users with real-time measurement of their asset (i.e. bridge) as well as a complete picture of the structure in its changing landscape. It is without a doubt that both of these techniques are complementary to each other, and their integration will enable robust analysis to obtain a complete deformation profile.

Despite the capability of providing good results, one of the challenges for space-based geodetic techniques like InSAR and GPS is atmospheric heterogeneity (Zebker et al., 1997; Hofmann-Wellenhof et al., 2008; Li et al., 2009). As the signal propagates from satellites towards the Earth surface, the wave crosses and interacts with the atmosphere. The primary interaction is atmospheric refraction which causes the signal to change in direction and speed as it passes from one medium to the other. In general, atmospheric heterogeneity can be categorised into troposphere and ionosphere layers. The troposphere layer extends to about 50 km above ground and causes a delay in the signal propagation. It is divided into dry and wet components that account for about 90% and 10% of the delay respectively. Nevertheless, the effect of the dry component can be accurately modelled using surface measurements of temperature and pressure, as opposed to difficulty in modelling the wet part due to high variation in water vapour content (Janssen et al., 2004; Leick et al., 2015).

On the other hand, the ionosphere is the upper part of the atmosphere which extends in a number of distinct layers from 50 to 1,000 km above the Earth's surface (Janssen et al., 2004). A sufficient number of electrons and ions are present in the ionosphere, causing the signal to advance in propagation. The degree of ionisation shows considerable variation, generally correlating with geographic location, solar and geomagnetic activity, season, and local time (SBAS Ionospheric Working Group, 2010; Dach et al., 2015). Malaysia experiences high atmospheric activities and seasonal variations owing to its geographical location, i.e. close to the equator. There is very limited attempt found in the literature to investigate and model the atmospheric effects on space-based geodetic techniques, particularly in Malaysia.

GPS addresses the atmospheric effects in a different way than InSAR. Since GPS satellites broadcast more than one frequency, the ionosphere can be modelled and mitigated considering the refractive index is frequency-dependent. Dach et al. (2007; 2015) suggest that in a first (but excellent) approximation, ionospheric refraction is proportional to the inverse of squared frequency. Therefore, a linear combination such as the Ionosphere-Free Linear Combination can be formed using two frequencies (e.g. L_1 and L_2 for GPS) to minimise or eliminate the ionospheric effects (Hofmann-Wellenhof et al., 2008). Several models based on a standard atmosphere have been developed to account for tropospheric effects in the absence of accurate ground meteorological data such as Hopfield (1969), Saastamoinen (1973), and Vienna Mapping Functions-1 (Boehm et al., 2006). Tesmer et al. (2007) and Urquhart et al. (2013) found that the most accurate model to date is Vienna Mapping Functions-1.

Similarly, the state of atmosphere is never identical when two images are acquired at different times for repeated passes InSAR. Therefore, any difference in the path delays between these two acquisitions will result in additional phase shifts. Unlike GPS, the effects of the troposphere are more prominent in C-band InSAR than that from the ionosphere (Doin et al., 2009; Ferretti, 2014). Methods for mitigating

tropospheric effects are generally divided into two classes, statistical and calibration. The statistical methods rely on the change of the water vapour field with time, or knowledge of the typical spatiotemporal characteristics of the atmospheric signal, whereas the calibration methods depend on some form of a priori information about water vapour fields in a given interferogram.

This study presents an effort to quantify the complete picture of long-term deformation in Johor, Malaysia using a combination of GPS and InSAR techniques. The deformation can be induced by several factors such as plate tectonic movement, landslide, urbanisation processes, development of tropical peatland, sea level rise, as well as flood. The GPS data from 8 MyRTKnet stations in Johor (2007-2011) and SAR images from the European Space Agency (ESA) (1993-2005) are utilised for the investigation. In addition, the potential of the newly available Sentinel-1 satellites is also reported. Mitigation of the tropospheric effects in GPS and InSAR is investigated to achieve high precision results from the two techniques. This study is one of the first systematic assessments of the long-term deformation in Malaysia using these two highly regarded space-based geodetic techniques. The results are expected to be valuable for a wide variety of applications and studies on the environmental issues. The adopted strategy can also be applied for similar investigations in other parts of Malaysia.

1.2. Research Aims and Objectives

The aim of this study is to assess the long-term deformation in Johor, Malaysia using two space-based geodetic techniques, namely GPS and InSAR. It is a comprehensive study that benefits from their complementary features, which enable a better understanding of the deformation from the assessment of both surrounding and point-specific deformation profiles. In pursuit of this goal, this study specifically addresses several objectives as follows:

i. To investigate and develop a strategy for precise estimation of the long-term deformation in Johor, Malaysia using GPS and InSAR.

ii. To model and mitigate the tropospheric effects in GPS and InSAR to achieve the most precise and reliable estimation from the measurements.

iii. To quantify and assess the rate of long-term deformation in Johor, Malaysia, and to analyse the sources of deformation.

1.3. Thesis Overview

The structure of this thesis is arranged into eight chapters as follows.

- **Chapter 1**: *Introduction*. Introduce the research topic, and outline the research aim and objectives.
- **Chapter 2**: *Literature Reviews on the Uses of GPS and InSAR for Regional Deformation Monitoring*. Highlight the importance of deformation studies, provide an overview of various monitoring techniques available to date, review the recent works on GPS and InSAR for regional deformation monitoring, and atmospheric effects on GPS and InSAR.
- **Chapter 3**: *The Johor Site*. Introduce Johor as the study area and the reasons behind its selection. The chapter includes, among others, the potential sources of deformation in Johor, and the data used for the investigation covering data availability, distribution, format, temporal and spatial resolution, source, and requirement.
- **Chapter 4**: *Deformation Analysis using GPS Time-Series*. Discuss the framework and strategy employed to achieve high accuracy requirements for deformation analysis using GPS. It also includes brief theoretical concepts, coordinate reference system, introduction to the software, and the processing strategies.
- **Chapter 5**: *Deformation Analysis using InSAR Time-Series*. Describe the method used for InSAR processing. The chapter encompasses fundamental concepts of InSAR for detecting surface movement, SAR coordinate system, introduction to the software, and the adopted strategies for the processing.
- **Chapter 6**: *Modelling and Mitigation of Tropospheric Effects in GPS and InSAR*. Address the modelling and mitigation of tropospheric effects to achieve the best estimation from GPS and InSAR.
- **Chapter 7**: *Analyses of Long-Term Deformation in Johor*. Present and discuss the final results, i.e. the estimated rates of deformation in Johor as deduced from the GPS and InSAR time-series. They are compared with each other and with the results from the literature.
- **Chapter 8**: *Conclusions and Recommendations*. Summarise the major findings and conclusion of this research, followed by suggestions for possible future investigations

The list of publications and potential publications from this work is given in **Appendix A**.

CHAPTER 2

LITERATURE REVIEWS ON THE USES OF GPS AND INSAR FOR REGIONAL DEFORMATION MONITORING

2.1. Introduction

This chapter primarily aims to summarise some of the recent works on the uses of Global Positioning System (GPS) and Interferometric Synthetic Aperture Radar (InSAR) for regional deformation monitoring. The chapter begins with a brief introduction on the importance of deformation studies particularly in Malaysia, followed by an overview of various monitoring techniques available to date. Their features are briefly described comprising advantages and drawbacks of each method. Advancements in the field of deformation studies using space-based geodetic techniques are discussed regarding GPS and InSAR only, and also the integration of both technologies. The atmosphere has been identified as one of the most challenging error sources in GPS and InSAR; hence, the following discussion addresses some of the works to mitigate the effects. This chapter ends with a summary of the important key points related to the applications of GPS and InSAR for regional deformation monitoring.

2.2. The Importance of Deformation Monitoring

Deformation is commonly known as a change in shape, size or dimensions of a body due to the application of force. This change can vary from a small object to a massive movement of a whole continent. It could be triggered by natural or human factors but most often results from an intricate combination of several natural and human drivers. Understanding this complex system of causes and effects is becoming important in our modern world and is the goal of deformation study. Assessment of spatial deformation provides information on the stability and extent of any movement occurring over time (Halim, 1995). This information is useful for safety assessment as well as predicting and preventing the possibility of failure or disaster in the future.

Various studies have been carried out in the past which eventually led to existing knowledge on the Earth's crustal movement. Today, the movement of large plates can be described by the theory of plate tectonics that divides the lithosphere into a number of plates (**Figure 2.1**) using data from the paleomagnetic studies, seismological studies and many others. The theory of plate tectonics provides clear motion models at the plate boundaries. Regional deformation, however, involves

smaller areas where the movements of small plates are controlled mainly by the forces of large plates but are not clearly delineated. One of the phenomena closely associated with the continuous motion of the Earth's crusts is earthquake, which happens when the energy stored from the locking mechanism of these motions is released in the form of seismic waves. History has recorded countless casualties that could have been prevented or minimised with prior knowledge of those events.

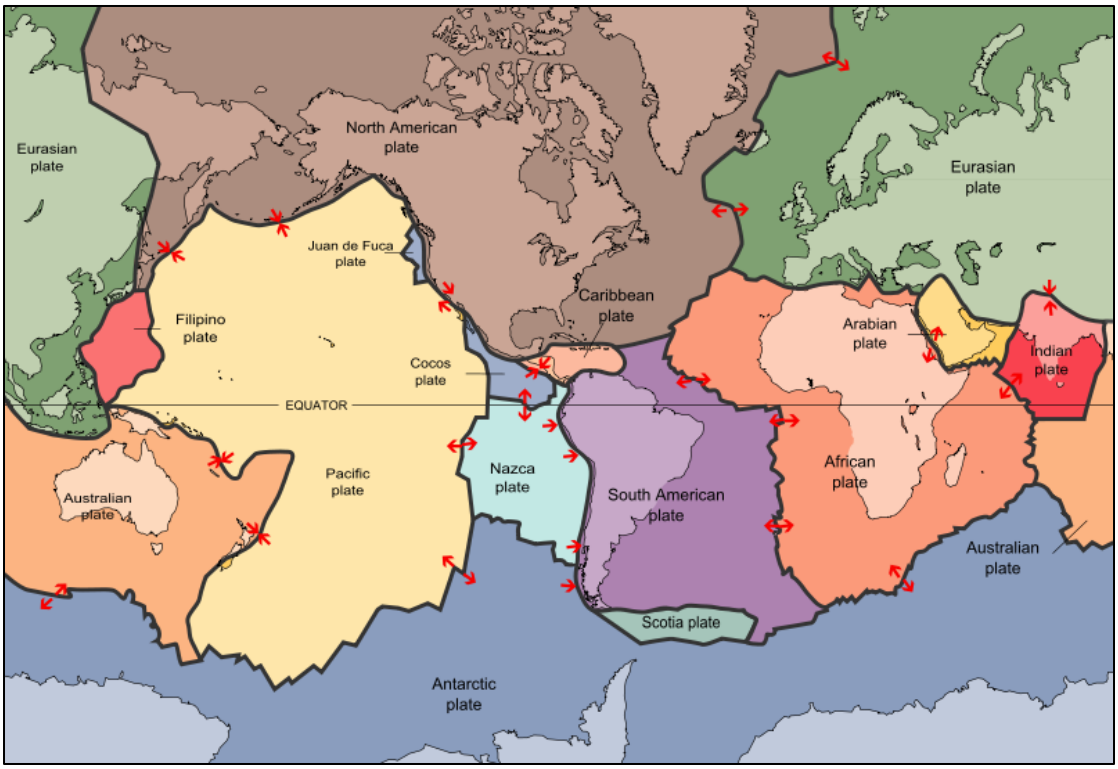


Figure 2.1: Major tectonic plates of the Earth shown in different colour schemes. Arrows indicate the direction of each plate motion. Figure adapted from *http://pubs.usgs.gov/publications/text/slabs.html* (accessed 10.05.2016).

Malaysia, though relatively stable, is no exception from undergoing deformation. It is situated within the buffer zone of the Pacific Ring of Fire (**Figure 2.2**) that has recorded a high number of seismic activities. A study by the Department of Survey and Mapping Malaysia (JUPEM) using data from the continuous Global Navigation Satellite System (GNSS) stations revealed movements up to 25.8 cm, interpreted as the result of co-seismic and post-seismic motions from the 2004, 2005, and 2007 Sumatran earthquakes (JUPEM, 2009a). Likewise, Vigny et al. (2005) detected movements ranging from 2 to 17 cm resulting from the 2004 Sumatra-Andaman earthquake. Larger displacements occurred in the northern peninsula and extended more than 3,000 km from the earthquake epicentre. Interestingly, the direction of these movements was towards the west as opposed to

normal velocity, i.e. towards the east at 1.2 ± 0.3 cm per year with respect to the Eurasian plate (Michel et al., 2001). Complete understanding of this phenomenon, in the past, is greatly hindered by the lack of data available in the region.

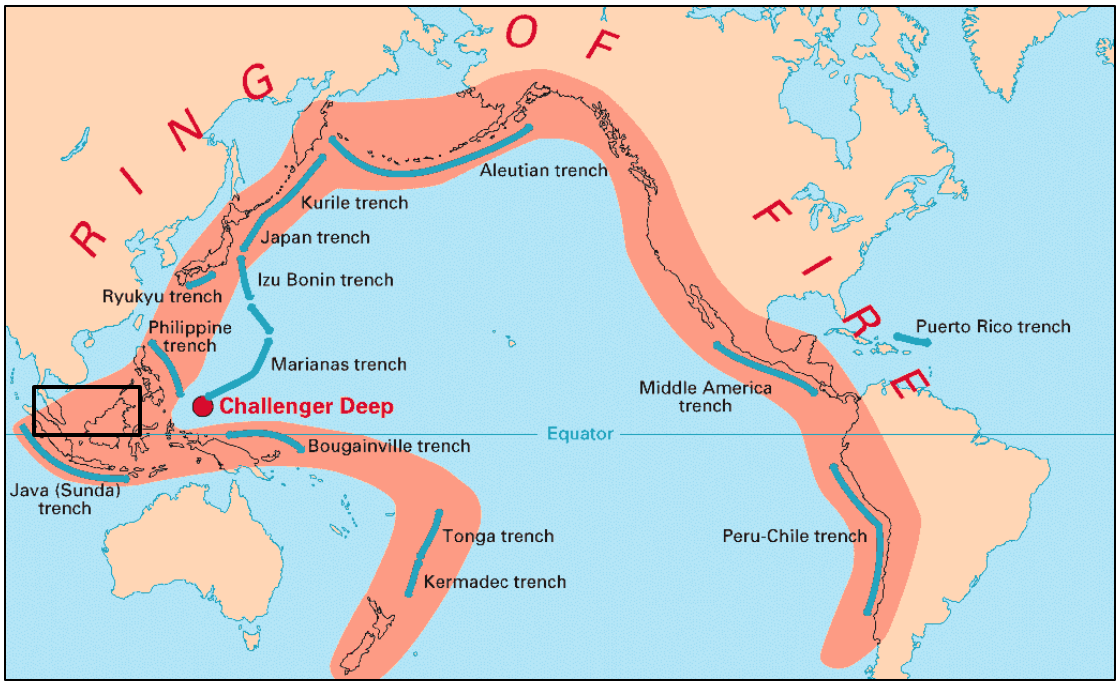


Figure 2.2: Geographical location of Malaysia (marked in black rectangle) respective to the Pacific Ring of Fire. Figure adapted from *http://www.universetoday.com/59341/pacific-ring-of-fire/* (accessed 13.06.2014).

The growing demand for deformation monitoring in Malaysia can also be ascribed to several other factors. Some unfortunate tragedies such as the collapse of Highland Tower on 11 December 1993, the tsunami in West Coast of Peninsular Malaysia on 26 December 2004, and major floods that strike almost every year during monsoon season are among the evidence of the need for this monitoring. The rise of public awareness and concern especially with the increasing number and complexity of engineering structures add onto the list. Ground stability has now become an issue of vital importance. Applications for new developments, for example, have to be submitted with an environmental report (Department of Environment, 2010). Damage to building and infrastructure have led insurance companies to bear a significant cost, which is eventually affecting buyers in term of premiums and policy excess. Authorities require information on ground stability for development planning and decisions making. More than ever before, the public is concerned as to whether existing building specifications, e.g. hospitals, shopping malls, bridges or any other engineering structures, are sufficient to handle deformation from various causes. It is without a doubt that deformation studies have become part and parcel in this modern world, both for understanding the Earth and for safety assessment.

2.3. Techniques for Deformation Monitoring

Determination or detection of deformation requires delicate attention to every step involved in the process, i.e. design, measurement and analysis stages. The magnitude of deformation is typically small, thus could be easily masked by errors from various sources. The monitoring system must be designed to be sensitive, and capable of detecting movements of the object under investigation (Yetkin and Inal, 2015). A complete system that included, for example, proper monumentation, integration of various sensors and state-of-the-art software and telecommunication components, is always desirable and indisputably will deliver the best possible findings. However, the cost involved in setting up such system must also be considered. Very often, a system that offers the best value for money is strived in the design stage.

The measurement techniques are generally categorised into geodetic and geotechnical/structural methods (Shan-Long, 1991). Selection of the appropriate method will determine the sorts of analysis carried out in the later stage. The geotechnical/structural methods are considered as the most accurate for monitoring over short distances of up to few tens of metres (Ogundare, 2015). Specialised equipment is used to directly measure the change in height (settlement gauge), length (extensometer), water pressure (piezometer), tilt (tiltmeter), inclination (inclinometer), displacement (displacement meter), strain (strain meter), and acceleration (accelerometer). However, such methods simply provide information about the local movement and are only suitable to determine changes within the structures, not the overall movement of the object under investigation.

Geodetic methods, on the other hand, often deal with the determination of positions or their changes in a predefined coordinate system (Shan-Long 1991; Erol et al. 2004). Therefore, they not only provide information about movements within the structures (given access is possible), but also overall movements of the object under study. Terrestrial surveys with a total station or levelling equipment are the most commonly used for distance ranging up to 10 km, and one of the economic alternatives. Although their accuracy is affected by refraction, it can be improved by several means, such as adopting proper measurement schemes (Ashkenazi et al., 1980; Secord, 1986) or modifying the functional model (Gruendig and Teskey, 1984). However, data acquisition using a total station and levelling equipment is a relatively labour extensive and time-consuming exercise.

The uses of a laser scanner for monitoring deformations have gained much attention in recent years (e.g. Yang et al., 2017; Jaafar, 2017). Conventional terrestrial techniques such as total station and levelling are significantly hindered by low point density, typically of a few samples located at strategic points. Ground-based laser scanners allow rapid, remote measurement of millions of points, thus providing an unprecedented amount of spatial information. This, in turn, permits more accurate

prediction of the forces acting on a structure. Nevertheless, as an emerging technology, several issues concerning instrument calibration, sensitivity analysis, data processing and filtering techniques still require investigation. The cost of the equipment is also more expensive than the conventional terrestrial options.

Photogrammetry is also a common technique for deformation studies. It can be based on terrestrial, aerial or satellite measurement, whereby the determination of positions is made using triangulation principles. From the photographs taken from at least two different locations, the so-called lines-of-sight (LOS) can be developed from each camera to points on the target. These lines of sight are mathematically intersected to produce the three-dimensional (3D) coordinates of those points (Li et al., 2008). The main advantages of photogrammetry are reduced time of fieldwork, simultaneous 3D coordinates, and in principle, allowing an unlimited number of points to be monitored. Large spatial coverage offered by aerial and satellite photogrammetry made them suitable for large-scale deformation monitoring. However, their broad applications are limited by the high cost induced from expensive equipment, aircraft rental, and price of the satellite images. Uses of aerial and satellite photogrammetry also require clear sky visibility, good weather conditions and in some countries, permission from the authorised agencies.

Recent developments in unmanned aerial vehicles (UAV) provide exciting new opportunities for ultra-high resolution mapping and monitoring of the environment. Some of the applications included monitoring of landslide, deforestation, flood, etc. UAV employs similar principals as in the photogrammetry technique. It is a more flexible platform than the spaceborne or airborne photogrammetry, as the latter requires thorough planning and might be jeopardised by unfavourable weather conditions or other campaigns with higher priorities. UAVs may bridge the gap between terrestrial observations and satellite or full-scale airborne observations. It can be controlled remotely (e.g. flown by a pilot at a ground control station) or can fly autonomously based on pre-programmed flight plans or in more complex dynamic automation systems (*www.theuav.com*, accessed 25.04.2017). The key advantages of this technique include superior spatial resolution, capacity to fly-on-demand at critical times with multiple sensors, as well as ability to collect imagery over terrain that is often difficult to access. As the method mostly uses an optical sensor, it shares similar drawbacks to the common aerial and satellite photogrammetry techniques.

GNSS is a space-based geodetic method that has a broad range of applications in deformation studies. The term GNSS comprises of several systems provided by different countries, namely GPS (United States), GLONASS (Russia), Galileo (European Union) and BeiDou (China). GNSS eliminates the requirement for inter-visibility between stations, allowing greater flexibility in the selection of station locations. Measurements can be made during day or night under varying weather conditions, which makes this technique economical especially when multiple

receivers can be deployed. Continuous researches and advancements have enabled accurate positioning in short observation period. However, it is not feasible for monitoring deformation in dangerous or inaccessible sites, such as volcanoes, since it relies on ground measurements. The spatial coverage is also limited to the observed stations, and high accuracy is only achievable by proper handling of various errors and biases present in the data.

Pseudolite (pseudo-satellite) is a ground-based technique of GNSS-like signals. The quality of GNSS positioning (i.e. availability, accuracy, reliability and integrity) is subject to, among other things, sufficient number of satellites and their geometrical distribution. These requirements are often difficult to meet in some areas such as urban canyons, valleys and deep open-cut mines. Likewise, indoor monitoring is challenging if not impossible without the aid of other sensors. The measurements are not only affected by the atmosphere but also susceptible to severe multipath at low elevation angle (Hofmann-Wellenhof et al., 2008). On the contrary, the quality of pseudolite measurements with less than half-degree elevation angle (from the pseudolite transmitter to the GPS receivers) is still very high. The geometry can be improved by careful selection of the pseudolite locations. Therefore, the positioning quality can be expected to improve significantly by combining GNSS and pseudolite measurements, especially in the height component owing to the inclusion of high-quality measurements at low elevation angles and proper geometrical distribution (Erol et al., 2004). The availability is also increased because a pseudolite provides an additional ranging source to augment the GNSS constellation (Dai et al., 2001).

All techniques discussed thus far require some sort of in-situ observations and are impractical for some dangerous or inaccessible sites. Remote sensing techniques such as InSAR are viewed as useful on this occasion to carry out the task. InSAR provides an accurate deformation map over a wide area without the essential need for ground presence. This feature is handy for obtaining an initial assessment of the deformation. Variations in the phases of radar signal are determined between two epochs, which reveal terrain surface deformations that may have occurred between the two occasions when the images were recorded. It is claimed that height differences as small as one centimetre can be detected (Ferretti, 2014); therefore, InSAR has the potential of being a cost-effective, near-continuous, remote method of measuring terrain subsidence due to mining, and ground movement due to land subsidence, earthquake or volcanic activity, etc. Nevertheless, the resultant deformation profile from InSAR analysis is limited, typically to the LOS of the satellite.

Light Detection and Ranging (LIDAR) is another remote sensing technique that does not require ground presence. It uses light in the form of pulsed laser to measure ranges (variable distances) to the Earth. These light pulses, combined with other data recorded by the airborne system, generate precise, 3D information about the shape of the Earth and its surface characteristics. A LIDAR instrument principally consists of a laser ranging, an Inertial Movement Measurement (IMU), and a

specialised GNSS receiver (Mosaic Mapping System Inc., 2001). Aeroplanes and helicopters are the most commonly used platforms for acquiring LIDAR data over broad areas. Some of the advantages included rapid delivery for monitoring large areas (i.e. capable of surveying hundreds of square kilometres per day and post-acquisition processing is relatively brief compared to the traditional photogrammetrical compilation) and a wealth of detail due to massive point densities. Despite these advantages, LIDAR is not always the optimum solution due to its expensive cost for a smaller project (system mobilisation and acquisition are costly relative to aerial photography), reduced accuracy on steep slopes, and limited cloud penetration. Furthermore, data acquisition is only possible under favourable weather condition and also subject to permission from the authorised agencies in some countries.

For any particular application of deformation monitoring, the most appropriate technique is determined as related to the type of object under study, required accuracy and also economic aspects. Geodetic techniques provide global information on the behaviour of the deformable objects whereas the non-geodetic techniques give localised information. The later, however, are easier to adapt for automatic and continuous monitoring than the former. While the non-geodetic methods are used mainly to identify relative movements within the deformable object and its surroundings, the geodetic methods can determine the absolute displacements of the selected points with respect to some stable reference points (Anonym, 2002). It is evidenced that each measurement technique has their own advantages and drawbacks; hence, their integration will enable better understanding about deformation occurred on the object under study. In this research, two space-based geodetic techniques, i.e. GNSS and InSAR, are utilised for the investigation of deformation.

2.4. GPS for Deformation Monitoring

Although GPS is designed originally for meter-level navigation applications, its potential for millimetre-level positioning to support geodetic and geodynamic applications was recognised from the beginning (Counselman and Gourevitch, 1981). The International GNSS Service (IGS) was established in 1994 by the International Association of Geodesy (IAG) as one of the efforts to realise this goal (Beutler et al., 1994). Since then, many applications have benefited from the GPS analyses such as atmospheric, oceanographic, meteorological and global geodynamic studies. The IGS continuous tracking network has grown to more than 507 globally (*http://www.igs.org/network*, accessed 3.04.2017), and their products include precise GPS orbits, clock corrections, earth rotation parameters, station positions, zenith path delays and ionospheric grid maps. These products have significantly simplified and enhanced numerous applications in a variety of scientific fields (Neilan et al., 1997; Kouba, 2003).

One of the renowned studies on GPS for deformation monitoring is done by Bock et al. (1993) using ten weeks of GPS data at five continuously operating reference stations (CORS). The study aims to investigate the preseismic, coseismic and post-seismic motions of the Landers and Big Bear earthquakes on 28 June 1992. While no significant pre-seismic signature is discernible from the five weeks of daily data before the earthquakes, the study concluded that continuous GPS arrays could provide reliable, precise and rapid determination of the seismically induced deformation. Similarly, Blewitt et al. (1993) estimated the permanent surface displacements in southern California due to the cumulative effect of the earthquakes and proved that geodetic methods provide valuable information on the aspects of rupture mechanism not available with other techniques. Altiner et al. (2013) investigated the changes in coordinate time-series using Precise Point Positioning (PPP) processing before and after the 23 October 2011 Van, Turkey earthquake, but could not detect any pre-seismic horizontal movement at the level more than 5 mm. Although no warning or prediction is possible before the event, they concluded that geodetic results provide a significant contribution for the derivation of occurrence time of an earthquake.

In his work, Kouba (2003) concluded that GPS could observe predominantly the horizontal components of surface seismic waves generated by earthquakes larger than magnitude 7, provided the network spacing and data sampling is sufficient. For large earthquakes such as the Denali Fault earthquake, the effects can be observed by 1-second GPS data nearly a continent-wide (Larson, 2003). As such, GPS can supplement the standard seismic observations owing to its capability to detect seismic waves with periods as short as a few seconds and amplitudes of a few centimetre. Gahalaut et al. (2006) presented an improved estimate of the rupture characteristics using a campaign mode GPS measurements made at 13 sites in Andaman–Nicobar Islands, before and after the 2004 Sumatra-Andaman earthquake. The rupture characteristics of the earthquake are not well resolved from only seismological or far-field geodetic data, particularly in the Andaman-Nicobar region.

Zhang et al. (2005) and Hu et al. (2005) investigated the feasibility of CORS in Victoria, Australia for deformation monitoring and analysis, addressing critical issues associated with the suitability, geological stability, data quality, and stability of the solution. Both of them concluded that CORS is a valuable asset, able to provide a technically advanced and cost-effective geoscientific infrastructure for deformation monitoring. They also found that the precision of GPS network solution is strongly related to the amount of data used in the processing. It consists of two parts, namely the fixed error component not relating to the amount of data used and the proportional error which decreases with the increase of data. The precision of solution improved rapidly with the growth of data but then slowly improved when the data exceeds 6 hours. However, the solution is not precise and stable for deformation study if the amount of data is less than 6 hours. With 24 hours dataset, they are able to achieve 5 mm precision in the 3D coordinates.

Mousavi et al. (2013) described the rigid-body rotation of the South Caspian, which is crucial for the assessment of seismic hazard in North-East Iran, using the velocity field from a network of 27 permanent and 20 campaign GPS stations. Likewise, Aktuğ et al. (2013) obtained a reliable quantification of the ongoing deformation in Azerbaijan by analysing the deformation field from a dense GPS network. Similar research is carried out by Trần et al. (2013) in northern Vietnam to measure the tectonic activity along the few fault systems based on the GPS data collected at 27 stations from 1994 to 2007. Ozener et al. (2013) reported that conventional geodetic measurements are not sufficient for monitoring small movements in the Iznik-Mekece segment of the North Anatolian Fault Zone, and GPS has played an essential role in detecting such deformations. Although similar research is possible with episodic measurements, Mendes et al. (2013) concluded from their study in São Jorge Island, Azores that long time series and dense temporal sampling are vital for a reliable analysis of surface deformation induced by tectonic, volcanic and landslide activities.

There are some works found in the literature on the applicability of GPS in the estimation of the kinematic model for crustal deformation. For example, Qu et al. (2014) utilised GPS data from the China Crustal Movement Observation Network to construct a plate kinematic model of crustal deformation of Fenwei basin. Achievable accuracy of the model is found to be related to the availability of GPS observations. Integration of GPS with InSAR and gravity measurements will likely improve the model. Müller et al. (2013) processed GPS data from the continuous and campaign-type GPS network to analyse the complex kinematic and deformation fields in the North Aegean Sea, Greece and adjacent regions. GPS provides additional constraints on the complex tectonic processes in the area, and the result sheds light on kinematic features previously not known in that detail. Similar research was conducted by Chousianitis et al. (2013) using 30-second GPS data from the continuous GPS stations in central Greece and IGS stations, which provides evidence on the crustal deformation in the area.

Li et al. (2015) introduced a method for real-time earthquake monitoring based on the GPS absolute velocity determination (AVD). Although they only used single-frequency GPS receivers and broadcast orbit, the method can clearly manifest the earthquake displacement signal even when the coseismic displacements at some stations are occasionally not visible in the position time series. The acquired precision is within a few millimetre per second (mm/s), i.e. 1-22 mm/s for horizontal components, which is sufficient for quick assessment of post-earthquake. The estimated magnitude also is in good agreement with that derived from the post-mission kinematic PPP approach. Likewise, Ostini (2012) has developed an automated procedure based on the Detection Identification Adaptation (DIA) specifically to address the increasing number of geodetic networks of tracking stations and the need to reprocess raw data routinely. The procedure replaces the lengthy, inaccurate, subjective and time-consuming manual analysis of time series.

Yigit et al. (2016) compared the efficacy and performance of PPP and relative methods for deformation monitoring considering long to short observation period. Each method is validated against the high accuracy displacement simulator apparatus, which can move accurately over a small distance (up to 0.1 mm precision). The processing for relative and PPP method was made using GAMIT/GLOBK and CSRS-PPP software, respectively. It is concluded that the superiority of relative method over PPP becomes more distinguished when the observation period decreases. The 24 hours PPP results were approximately equivalent to 6 hours relative results in terms of minimum detectable displacement. Depending on displacement rate and amount, PPP method can be used as an efficient alternative to the comparative method to monitor crustal motion and time-varying behaviour of engineering structures.

In a more recent work, Montillet et al. (2016) investigated the precision of continuous GPS in real-time and post-processing mode for measuring structural deformation caused by a variety of environmental stresses. There were four civil infrastructures involved in the study, namely a floating bridge, an elevated highway, and two large dams. Based on the results, they concluded that GPS demonstrate its usefulness for relatively low-cost monitoring. The post-processed daily positions can accurately quantify millimetre-level deformations within heavy civil-engineered structures, which is also of use in long-term structural preservation. As GPS may increasingly be deployed as both a real-time monitoring and long-deformation measurement owing to the reduced costs for deployment, GPS may eventually supplant existing optical systems that have been routinely used for over a century but are prohibitively expensive for continuous and real-time applications.

2.5. InSAR for Deformation Monitoring

Although InSAR can be used for estimation of topography (e.g. Farr et al., 2007), atmospheric modelling (e.g. Hanssen, 1999; Alshawaf et al., 2012; Heublein et al., 2014), or even sub-surface detection (e.g. McCauley et al., 1982; Elachi et al., 1984; Paillou et al., 2006; Morrison et al., 2013), the technique is widely known for surface deformation detection. It has been used to assess ground stability since the late 1980s and has proven invaluable for detecting small ground motions in the order of centimetre with the differential technique, and millimetre with more modern time series approaches. The former achieved prominence when images before and after the Landers earthquake were used to reveal the spatial distribution of ground motion occurring in that event (Massonnet et al., 1993). The latter has come to prominence in recent years and involve the analysis of tens of radar images acquired over the course of several years or even decades to monitor subtle amounts of ground motion (Ferretti et al., 2001; Berardino et al., 2002).

Chaussard et al. (2014) identified land subsidence in 21 areas in central Mexico due to massive groundwater extraction. This task certainly will take an enormous amount of time and cost to be done with conventional methods. They utilised over 600 ALOS PALSAR scenes from 15 ascending tracks, dated from 2007 to 2011, for the analysis. The correlation between subsidence and land use confirms that the leading cause of land subsidence is due to groundwater extraction mainly for agricultural and urban activities. The same area also has been investigated by other researchers using different SAR sensors, such as ENVISAT (e.g. Cabral-Cano et al., 2008; Cigna et al., 2011; Yan et al., 2012; Osmanoğlu et al., 2015), RADARSAT-2 (e.g. Geudtner, 2014; Lanari et al., 2015) and Sentinel-1 (Wegmüller et al., 2015; Sowter et al., 2016). Similar research was conducted by Ge et al. (2014) over Bandung Basin, Indonesia to map the land subsidence between 2002 and 2011. The results from independent analysis of 24 ALOS PALSAR (2002-2008) and 30 ENVISAT ASAR (2007-2011) scenes showed good agreement, suggesting steady subsidence in many areas of the basin. The subsidence was expected mainly as a consequence of excessive groundwater extraction and soil consolidation caused by surficial loading. Good correlation was also observed with GPS data collected between 2002 and 2010, as well as with annual groundwater extraction records.

Sun et al. (2015) utilised 16 scenes of L-band ALOS PALSAR acquired between 28 January 2007 and 23 June 2010 to study the slow-moving landslides in Zhouqu, China before a devastating major mudslide on 8 August 2010. In general, they found good agreement on the locations and extents of the landslides with previous field investigations. It proved that slow-moving slope deformation could be measured adequately in most parts of the area by a multi-temporal InSAR technique and L-band SAR data. Likewise, Schlögel et al. (2015) demonstrated the potential of L-band ALOS PALSAR to analyse deformation patterns of large and rapid landslides in South East France, even with limited available SAR data. They found consistent results with the ground-based measurement (GPS and EDM) and remote estimate from C-band and X-band satellite SAR sensors but expected a better result with more extensive data as it will allow them to investigate the landslides evolution over time and estimate the relationship with the meteorological controlling factors with higher accuracy.

Tang et al. (2016) suggested that multi-temporal InSAR techniques are suitable for monitoring cultural heritage sites as they are not invasive unlike some traditional approaches, where electrical sensors need to be installed in structures for data acquisition. The spatial and temporal coverages provided by InSAR are suitable for monitoring the deformation of structures as well as their surroundings. This can facilitate the early recognition of potential risks and enables effective conservation planning. The techniques are also inexpensive and perform better in detecting subtle deformations due to the high precision (up to mm level). In their work, 20 scenes of COSMO-SkyMed were utilised to assess deformation of the World Heritage Site of Summer Palace in Beijing. InSAR also has been proven useful for investigation of

complex deformation. Yang et al. (2016) analysed cross-correlations among regional ground subsidence, fault activity, and underground water level over Linfen–Yuncheng Basin, China from the 8 Envisat ASAR images acquired from February 2009 to October 2010, and processed using the Stanford Method for Persistent Scatterer Interferometric Synthetic Aperture Radar (StaMPS) technique (Hooper, 2006).

Most InSAR techniques are applicable only in urban areas and rocky terrain due to reliance on the presence of radar scatterers. There are some techniques specifically developed to address this shortcoming such as the SqueeSAR (Ferretti et al., 2011) and the Intermittent Small Baseline Subset (ISBAS) (Sowter et al. 2013; Bateson et al. 2015). The latter is developed in-house at the University of Nottingham and appears particularly well-suited to low-resolution, wide-area deformation monitoring over a broad range of land classes, including grasslands, agricultural and forested cover (Cigna et al., 2014; Sowter et al., 2016). Meanwhile, Milillo et al. (2015) addressed the temporal decorrelation by analysing the potential of X-band COSMO-SkyMed short repeat-pass interferometry over a rural area in the southern part of Italy. They found 180% improvement in usable pixels, which allowed them to extend the spatial coverage and highlight important features related to the landslide areas. The study concluded that short repeat-pass interferometry enables measurement on the dynamics of the seasonal deformation.

The new Sentinel-1 mission offers an exciting new opportunity for InSAR study. The mission comprises two satellites: Sentinel-1A launched on 3 April 2014, and Sentinel-1B launched on 25 April 2016. Their Interferometric Wide (IW) data is gathered using the novel Terrain Observation with Progressive Scans in azimuth (TOPS) SAR imaging technique (Holzner and Bamler, 2002; Torres et al., 2012) that poses several challenges to the interferometric processing, primarily related to the preparation of the individual images and their subsequent coregistration. The coregistration accuracy requirement for Sentinel-1 TOPS InSAR is more stringent than other stripmap products at one thousandth of one pixel (De Zan et al., 2014); thus, it has the highest impact on the processing chain. Nevertheless, the satellites offer many benefits for the monitoring of land motion phenomena and provide continuity to the C-band SAR all-weather and day-and-night imagery of the ERS-1/2 and ENVISAT missions. Rapid deformation can be monitored owing to the short repeat cycle of only 12 days for each satellite (Torres et al., 2012), and reduced to 6 days considering the two satellites now in the constellation. Therefore, a much shorter time is needed to gather a significant stack of images (De Zan et al., 2008; Attema et al., 2010) which will be helpful for routine long-term monitoring applications. Furthermore, the swath width of IW product is around 250 km, allowing the monitoring of large areas with fewer acquisitions. A short revisit time and a large swath width alone mean that Sentinel-1 IW products can provide a very high level of support to operational, routine land monitoring applications (Sowter et al., 2016).

One-dimensional (1D) measurement along the satellite LOS has significantly limited the capability of InSAR in the investigation of surface displacements and their dynamics. When the real deformation vector differs from the LOS, the sensitivity of the technique decreases, and interpretation of the result becomes challenging. Nevertheless, two- or three-dimensional InSAR imaging of the displacement is possible by combining measurements from several directions (Massonnet et al., 1995; Massonnet et al., 1996; Joughin et al., 1998; Fialko and Simons, 2001; Wright, 2004). For example, Gray (2011) exploited three different LOS displacements from the extra-low and extra-high beams of RADARSAT-2 to estimate the full 3D movement of the Henrietta Nesmith Glacier. This situation, however, is a sporadic case, confined only to the regions whose latitudes are greater than around 80°. For most areas, the practical approach is by merging InSAR LOS measurements with other observations which can be from homogenous data (i.e. SAR acquisitions) or heterogeneous data (e.g. GPS data). Hu et al. (2014) reviewed the most recent development in resolving the full 3D displacements from InSAR measurements. On a related note, Eriksen et al. (2017) combined data from the ascending and descending TerraSAR-X acquired in the summer 2009 - 2014 to investigate the surface displacement on unstable slopes in northern Norway. The combination of surface displacement from two geometries (2D InSAR) not only enhanced sensitivity to displacement in the plane spanned by the two LOS vectors (LOS-plane) but allowed them to visualise detailed surface movement in the area. This, in turn, enables them to explain the driving and controlling mechanisms of the deformation.

Despite remarkable features of InSAR, its application is relatively scarce in Malaysia. The technique, however, is gaining more attention in recent years. Din et al. (2015) applied Persistent Scatterer Interferometry (PSI) analysis on 17 ERS-2 descending images to monitor land subsidence in Kelantan catchment due to groundwater extraction. They concluded that land subsidence did occur at the area upon validation with GPS measurements and hydrogeological data. Likewise, Nee et al. (2015) found a similar trend of deformation from the comparison between the InSAR and theodolite surveying. The InSAR analysis is based on the StaMPS method applied to 12 TerraSAR-X data, spanning the period from 9 July 2008 to 4 June 2009. Latip et al. (2015) also utilised StaMPS for monitoring deformation of the offshore platform using 11 high-resolution TerraSAR-X data from 2012 to 2013 and concluded that PSI technique shows potential for such work and the results are comparable to those obtained from GPS. Most studies, however, have reported limited coverage in their areas due to low coherence characteristics, as expected in Malaysian region. Although the result could be improved further with additional SAR dataset, the option is not always possible. This research investigates the feasibility of the ISBAS technique, developed in-house at the University of Nottingham, for deformation monitoring in Malaysia.

2.6. Combining GPS and InSAR for Deformation Monitoring

Integrating GPS and InSAR indeed will enable better analysis as they have complementary features. GPS is sensitive to horizontal movements, whereas InSAR, although somewhat sensitive to East-West motions, is mostly sensitive to those in the vertical direction. GPS has a good temporal resolution when operated in continuous mode, but the density of a regional network is typically composed of a site every 15-30 km due to high operational cost. On the other hand, InSAR provides a spatially dense set of measurements with resolution less than 100 m, but its temporal resolution is in the order of days to months, depending on the return period of the satellite used. InSAR gives 1D profile in the satellite LOS over a wide area, whereas GPS provides a detailed 3D point-specific profile. Joint analysis of GPS and InSAR enables the generation of 3D surface displacement field and allows the characterisation of multiple deformation types including hydrologic and anthropogenic deformation, surface mass movements, volcanic and tectonic processes (Houlié et al., 2016).

In recent years, there have been attempts to integrate GPS and InSAR measurements to exploit the capabilities of both techniques. GPS results are usually interpolated into the same lattice as that of InSAR measurements (Gudmundsson et al., 2002; Samsonov et al., 2008; Qiao et al. 2017). GPS is also used to validate InSAR results, e.g. by projecting GPS observations into radar LOS direction (Feng et al., 2012). Metzger and Jónsson (2014) modelled the plate boundary deformation in North Iceland during 1992-2009 using InSAR time-series and GPS results from their previous studies, i.e. Metzger et al. (2011) and Metzger et al. (2013). The combined GPS-InSAR results not only enabled them to identify various deformation phenomena such as interseismic deformation, transient inflation and deflation at the volcano, and land uplift, but also their changes over that 17 years' time span. They also found that InSAR data alone is not able to constrain the plate-boundary model parameters well despite its broad spatial coverage.

Compared to individual InSAR and GPS measurements, their joint analysis is clearly more suitable to investigate tectonic motions and anthropogenic activities. Hu et al. (2016) successfully resolved the complex ground deformation associated with the tectonic and anthropogenic activities in Los Angeles, California by combining GPS and InSAR measurements acquired from 2003 to 2007. They derived the 3D cumulative displacement velocity field based on the Weighted Least Squares (WLS) InSAR analysis of both ascending and descending ENVISAT data aided by GPS measurements at 54 Southern California Integrated GPS Network (SCIGN) stations. Although they found that the 3D cumulative velocity fields provide more comprehensive information than the InSAR LOS observations and the sparse GPS observations, the GPS-InSAR integrated results are almost blind to the cumulative

horizontal motions associated with anthropogenic activities. They also reported an artefact problem due to interpolation even with dense SCIGN network of 250 continuously observing sites.

Gonzalez-Ortega et al. (2014) were able to explain the early near-field post-seismic deformation of the 2010 Baja California earthquake from the joint inversions of GPS and InSAR data spanning the first five months after the event. Similarly, Cheloni et al. (2014) utilised InSAR, GPS, and high-precision levelling data to investigate the coseismic and post-seismic slip of the 2009 L'Aquila (central Italy) earthquake and its implications on the seismic potential along the Campotosto fault. The combination of the three techniques allowed them to reduce ambiguities associated with each dataset, as well as to constrain the geometrical features of the faults involved and their associated slip distributions. Fuhrmann et al. (2015) developed a database for the Upper Rhine Graben, Southern Germany from the results of joint InSAR, GNSS and precise levelling analyses. Those results are combined by interpolating them onto a common grid along with weighting algorithms and outlier detection. The database allowed them to gain detailed insight into the horizontal and vertical velocity field of the area due to oil extraction. More recently, Feng et al. (2017) presented interseismic, coseismic and post-seismic displacements of the 2015 Illapel earthquake in Chile from a comprehensive analysis of GPS and InSAR. The GPS data were compiled from several studies, whereas the SAR data consist of four RADARSAT-2 (ascending and descending), two ALOS PALSAR (descending) and 20 Sentinel-1A (ascending and descending) images. The massive combination of datasets enabled them to provide in-depth geological analysis and interpretation of the movement before, during, and after the earthquake.

El Gharbawi and Tamura (2014) presented a method for correcting L-band InSAR deformation maps using GPS observable and products. The method involves a sequential procedure to address the troposphere, ionosphere, and baseline errors. The methodology was tested in Tokyo bay which has been affected by the 2011 Tohoku earthquake. The results showed 5.6 and 10.5 mm standard deviation upon comparison with GPS stations and geodetic triangulation network, respectively. In their following work, El Gharbawi and Tamura (2015) identified the proper trend to accurately describe the deformation signature of the 2011 Tohoku earthquake by studying the time series of a single GPS station. This trend is then subtracted from the unwrapped phase maps of InSAR interferogram, followed by a temporal and spatial filtering to extract the un-modelled deformation from the residual phase map. The final deformation map is produced by combining the modelled deformation trend and un-modelled deformation retrieved from the filtering. The methodology was tested using six C-band SAR images, and the result was validated at 13 GPS stations. They obtained 6.9 mm RMS error, which demonstrates the reliability of the proposed methodology.

Doubre et al. (2017) analysed the surface deformation in the whole Central Afar region and concluded that combination of GPS and InSAR is an appropriate way to study the crustal deformation in the area. In addition to the geometric complementarity of the measurements, the GPS technique allows quantification of the relative plate motion while the InSAR technique gives access to deformation across small-scale structures. Similarly, Gahalaut et al. (2017) reported their exciting finding on crustal deformation caused by anthropogenic activities. One GPS station located near the reservoir created by the 260.5 m high Tehri Dam exhibits anomalous variations due to seasonal water loading and unloading. The InSAR analysis of 6 ALOS PALSAR images revealed the spatial pattern of deformation caused by the seasonal filling of the reservoir, which further testified the benefits of their joint studies.

Wan et al. (2017) compiled several GPS and InSAR results and used a nonlinear inversion scheme to solve the fault geometry and slip distribution of the 2008 Wenchuan, China earthquake. Likewise, Guangcai et al. (2015) utilised GPS along with SAR data from the Sentinel 1A and COSMO-SkyMed to identify the sources parameters of the 2014 South Napa earthquake. Each data is weighted according to the uncertainty at the non-deforming region. Donnellan et al. (2017) demonstrated the usefulness of GPS and InSAR to map the spatiotemporal behaviour of the Pacific-North American plate boundary in California. The SAR data was acquired using UAVSAR, i.e. an airborne InSAR instrument mounted onboard Gulfstream-III aircraft. Five areas in California were discussed as examples of different fault behaviour, fault maturity and times within the earthquake cycle: the 2014 South Napa earthquake rupture, the San Jacinto fault, the creeping and locked Carrizo sections of the San Andreas fault, the Landers rupture in the Eastern California Shear Zone, and the convergence of the Eastern California Shear Zone and San Andreas fault in southern California. They indicated that joint InSAR, GNSS, and high-resolution topography could improve understanding of tectonic deformation and rupture characteristics within the broad plate boundary zone.

Joint analysis of GPS and InSAR can also be used for the generation of troposphere maps. Benevides et al. (2016) found the 3D wet refractivity map generated using GPS only performs worse than the corresponding map that included additional constraint from InSAR. The finding is based on their study in the Lisbon area, Portugal. The reconstruction of the atmospheric refractivity is closer to the real atmospheric state as obtained from the meteorological datasets with the additional constraint from InSAR. Despite many benefits of integrating GPS and InSAR, their broad adoption is limited by the availability of both data, which in most cases requires simultaneous observation. In this research, we utilised the corresponding features of GPS and InSAR techniques to investigate the long-term deformation in Johor,

Malaysia. The research profits from the long record of GPS and InSAR measurements available in the region, and is expected to provide valuable information on the local deformation. It is important as earthquakes in the surrounding area also have the potential to trigger nearby faults, e.g. as suggested by Guangcai et al. (2015).

2.7. Atmospheric Effects on GPS and InSAR

One of the challenges in retrieving accurate deformation signals from GPS and InSAR measurements is atmospheric artefacts (Zebker et al., 1997; Hofmann-Wellenhof et al., 2008; Li et al., 2009). The signal from satellites is refracted as it travels through the medium. Two main categories of the atmosphere are troposphere that reaches to approximately 50 km above ground, and ionosphere that extends from 50 to 1,000 km above the Earth's surface (Janssen et al., 2004). In general, the troposphere causes a delay in the signal propagation whereas the ionosphere causes the opposite effect. Malaysia, in particular, experiences high atmospheric activities and seasonal variations as it is located close to the equator. Presently, there is limited attempt found in the literature on the investigation of the atmospheric effects to GPS and InSAR especially in the equatorial region.

2.7.1. Atmospheric Effects on GPS

Ionosphere represents the most significant error source in GPS and can cause loss of lock on several satellites, which is a major issue for navigational applications. However, since it is frequency-dependent, the effects can be mitigated easily by forming the Ionosphere-Free Linear Combination (Hofmann-Wellenhof et al., 2008). On top of that, higher-order effects can be mitigated using Global Ionosphere Maps (GIM), for example, provided by the International GNSS Service (IGS) or Center for Orbit Determination in Europe (CODE). Troposphere, on the contrary, is a non-dispersive medium for frequencies below 15 GHz (Dach et al., 2015). While its dry component accounts for a larger percentage than the wet counterpart, the effect can be modelled accurately using surface measurements of temperature and pressure in contrast to the difficulty in modelling the wet part due to high variation of water vapour content (Janssen et al., 2004; Leick et al., 2015). For this reason, a usual practice in GPS processing is to model for the dry delay and estimate the zenith wet delay from the observations.

Several models based on a standard atmosphere have been developed to account for tropospheric effects in the absence of accurate ground meteorological data such as Hopfield (1969) and Saastamoinen (1973). Alternatively, the Global Pressure and Temperature (GPT) proposed by Boehm et al. (2007) can be used to determine the dry component of the troposphere. It is an empirical tropospheric model based on 3 years (September 1999 to August 2002) of 15° × 15° global grids of monthly mean profiles for pressure and temperature from the European Center for Medium-range Weather Forecasts (ECMWF) 40 years reanalysis data. GPT model allows determination of pressure and temperature at any site around the world using spherical harmonic, which subsequently can be used to calculate the dry troposphere. Input parameters for the GPT are the station coordinates and the day of the year; thus, the model also accounts for the annual variations of the parameters.

Kouba (2009a) reported that GPT shows a maximum of 5.7 hPa bias and 12.9 hPa RMS for the estimated pressure and a 2.3 °C bias and 7.2 °C RMS for the estimated temperature. Lagler et al. (2013) improved the GPT model by adding semi-annual meteorological variation effects, i.e. rainy or dry seasons. The improved model is known as GPT2. Moreover, replacing the constant temperature rate with semi-annual variations and mean values significantly increases the accuracy of estimating temperature (Munekane and Boehm, 2010; Fund et al., 2011). Boehm et al. (2015) further developed the GPT2 model and introduced GPT2 wet (GPT2w) model based on a new set of reanalysed data known as ERA-Interim from ECMWF. GPT2w can be performed on two gridded input data with 1° and 5° horizontal resolutions that are also suitable for applications requiring a prediction model. Yao et al. (2015) developed a new global tropospheric model based on the GPT2w model by adding the daily variation effect to the GPT2w model, which offers slightly improved results. More recently, Rahimi et al. (2017) developed a new regional model called Malaysian Pressure Temperature (MPT), which is designed particularly for Peninsula Malaysia. Based on the comparison with the GPT2w model at one IGS station in the south of Peninsula Malaysia, the MPT model indicated a better performance in producing the Precipitable Water Vapour (PWV) during monsoon season. The accuracy of the estimated pressure and temperature improved by 30% and 10%, respectively, in comparison with GPT2w model.

The Vienna Mapping Function-1 (VMF-1) (Boehm et al., 2006) is arguably the most accurate troposphere model available to date (Tesmer et al., 2007; Urquhart et al., 2013) as it is a result of a direct ray-tracing through Numerical Weather Model (NWM). Therefore, it should represent tropospheric delays more accurately than any empirical models and is recommended for precise applications (Kouba, 2008). The hydrostatic and wet

zenith delays together with the coefficients of the VMF-1, necessary to map the zenith delays to lower elevation angles, are provided on a global grid (2.0° resolution in latitude and 2.5° resolution in longitude) every six hours. On the other hand, the Global Mapping Function (GMF) (Boehm et al., 2007) is an empirical representation of the VMF1 that is designed to be more easily implemented into existing software packages to capture the first-order variations of the VMF-1.

2.7.2. Atmospheric Effects on InSAR

The state of the atmosphere is never identical for two SAR images acquired at different times in repeat-pass InSAR. Any difference in the path delays between these two acquisitions will result in additional phase shifts in the interferogram. The first indication of the atmospheric effects on InSAR has been reported by Massonnet et al. (1994). Since then, much research has been carried out to better understand and mitigate the effects. Although ionosphere can be quite crucial for low-frequency radar sensors in regional mapping (Meyer, 2010), it has limited impact on local InSAR analyses, particularly at mid-latitudes. The impact of the ionosphere on SAR systems is increasing with decreasing carrier frequency and directly proportional to the total electron content (TEC) (Meyer and Nicoll, 2008). Therefore, L-band spaceborne radar systems such as the ALOS PALSAR suffer more severe ionospheric artefacts than many presently operating C-band spaceborne radar systems (Chen and Zebker, 2012). Some of the most significant effects to be considered are relative range shifts, internal image deformations, range and azimuth blurring, and interferometric phase errors.

Chen and Zebker (2012) presented L-band InSAR analysis over three areas located at different latitude, i.e. a high-latitude Iceland region, a mid-latitude California region, and a low-latitude Hawaii region to directly relate the misregistration of azimuth pixels seen in radar interferograms to simultaneous independent GPS measurements of the ionospheric TEC gradient. While California and Hawaii show no significant ionospheric artefacts, they found that the Iceland interferograms show a maximum misregistration of three pixels in the azimuth direction, which are due to dispersive ionospheric propagation. They concluded that the spatial gradient of TEC estimated by GPS carrier-phase data could predict the misregistration of complex pixels seen in the nearby InSAR observation over Iceland. Significant spatial variations in the GPS vertical TEC occurred as azimuth streaks in the interferograms. The ionospheric effects can be corrected if the SAR sensor can measure the change in TEC along the radar swath. However, in their previous work, Chen and Zebker (2009) have developed an accurate

image coregistration method that compensates for ionospheric spatial variations and significantly improves the interferometric coherence in the high-latitude InSAR observations.

Unlike GPS, the effects of the troposphere are more prominent in C-band InSAR than that from the ionosphere (Doin et al., 2009; Ferretti, 2014). Zebker et al. (1997) reported that spatial and temporal changes of 20% in the relative humidity of the troposphere could lead up to 10 to 14 cm errors in the measured ground deformations and 80 to 290 m errors in derived topographic maps for baselines ranging from 100 m to 400 m. The Atmospheric Phase Screen (APS) in the troposphere can be categorised into two components: stratified APS and turbulent APS. The stratified APS results from the different vertical refractivity profiles during the two SAR acquisitions and affects mountainous terrain; therefore, it is strongly correlated with topography. The turbulent APS is the result of the turbulent processes in the atmosphere. It causes 3D heterogeneity in the refractivity during the SAR acquisitions and affects flat terrain as well as mountainous terrain (Hanssen, 2001). Although the long wavelength atmospheric phase delays relating to topography can be removed relatively easily with the assistance of a DEM, the delays caused by the turbulent mixing of tropospheric water vapour are difficult to correct when there are no external data (Li et al., 2012).

The challenges faced in InSAR processing due to the tropospheric delays have been described, for example, in Guangcai et al. (2015). Phase artefacts in InSAR images degrade the interpretability of the phase and correlation signatures of terrain. While InSAR showed potential for studying a large amplitude displacements, the measurement of small amplitude displacement is complex due to the turbulent tropospheric signal, except in the case of large number SAR images (Doubre et al., 2017). Numerous correction methods have been developed to minimise the tropospheric effects. Ding et al. (2008) reviewed the mitigation strategies. In general, they can be divided into four types, as follows (Ding et al. 2008; Holley, 2009; Leighton, 2010):

i. Stacking SAR interferogram

Stacking is a statistical method that minimises the atmospheric effects by calculating its average, thus reducing the errors by $\sqrt{n}$, where n denotes the number of independent pairs. It assumes that troposphere is uncorrelated in time and non-stationary in space. This method provides average deformation rates, making it suitable for monitoring areas with relatively constant deformation rates. Nevertheless, it may be affected

by seasonal variations if the stacked interferograms are not evenly distributed throughout the year. Implementation of this method has been reported, for examples, in Williams et al. (1998) and Ferretti et al. (1999).

ii. Correlation analysis between interferograms or between interferometric phases and elevations

The correlation analysis allows tropospheric artefacts to be determined from the high-resolution interferometric phase itself. However, it can only reduce the tropospheric noise that strongly correlates within different interferograms or with elevation. One type of approach is assuming a linear relationship between height and interferometric phase (e.g. Cavalié et al., 2007). Unfortunately, if the expected deformation signal correlates with elevation, the deformation and the atmospheric phases are difficult to discriminate. Bekaert et al. (2015a) introduce a spatially variable power law tropospheric correction for InSAR that also accounts for the spatial variability of the tropospheric properties. Likewise, Zhu et al. (2016) used a robust and multi-weighted approach to estimate the topography correlated tropospheric delays in radar interferograms with a successful application to the Southern California area.

iii. InSAR time-series analysis

Times-series analysis can be thought as an extension of stacking. It uses statistical analysis over a large number of SAR images to model the troposphere. The method for isolating the troposphere from the deformation signal relies on the assumption that the troposphere is random in time, whereas the deformation signal correlates with time (Ferretti et al., 2001; Berardino et al., 2002; Hooper et al., 2004). This assumption allows mitigation of the troposphere using temporal filtering of large time series SAR images. Typically, a minimum number of 15-20 images are required with more than 30 images being ideal to obtain good results (Holley, 2009). However, the assumption is not always valid for the stratified APS component because the seasonal oscillation of the atmospheric condition is not well sampled in time by temporal filtering. The remaining residuals would bias the velocity fields estimated by those conventional time series analysis methods. Examples of time series method for tropospheric estimation are PSI (Ferretti et al., 2000; Ferretti et al., 2001) and SBAS (Berardino et al., 2002).

iv. Calibration with external data

The tropospheric effects in InSAR also can be mitigated using external data. The uses of radiometric PWV data from the MERIS onboard Envisat, and MODIS onboard Terra and Aqua platforms have been proven useful (e.g. Li et al., 2012) but subjected to the daytime acquisition and the cloud-free environment. The tropospheric delay from the GNSS processing can also be employed as demonstrated by Janssen et al. (2004) and Li et al. (2006a) but it is only useful when a dense network exists. Alternatively, meteorological data such as from ground station and radiosonde profile can be utilised but this method is typically subjected to high error budget due to sparse data acquisition.

2.8. Summary

This chapter provides a general perspective on the significance of deformation studies particularly in Malaysia. It is important to acquire information about local deformation not only for safety assessment but also to support development planning and decision making as well as maintenance of geodetic infrastructures. Various monitoring techniques are briefly reviewed highlighting their advantages and drawbacks. Evidently, a combination of several sensors and methods allows one to retrieve extra information about deformation in the study area. Following that, advancements in the field of two renowned space-based geodetic techniques, i.e. GPS and InSAR, are discussed regarding GPS and InSAR only and also their integration. Numerous publications have testified to the superiority of their integration as opposed to their individual analysis. Many researchers have also reported degradation of quality in the GPS and InSAR estimations owing to atmospheric artefacts. Therefore, this chapter has also addressed recent works pertaining to the atmospheric correction in GPS and InSAR.

CHAPTER 3

THE JOHOR SITE

3.1. Introduction

Johor has been selected in this research as the study area to investigate the feasibility of using Global Positioning System (GPS) and Interferometric Synthetic Aperture Radar (InSAR) for the assessment of long-term deformation in Malaysia. The selection is based on various reasons including public interest in the Iskandar Malaysia as one of the leading development corridors in Malaysia as well as the availability of sufficiently large datasets (at least five years) which is paramount for the study. This chapter aims to describe the selected area along with the data used to achieve the research objectives. It covers a brief description of the geography and geological setting of Johor, followed by the surveying and mapping activities in the area as the implications of deformation are not only limited to socio-economic, but also in term of sciences such as surveying and mapping. The discussion continues with the potential sources of deformation, which also covers previous and current researches made on the topic. Subsequently, the lists of the dataset (i.e. GPS and InSAR) are highlighted covering data availability, distribution, format, temporal and spatial resolution, source, and requirement. This chapter ends with a summary of the area and data, in particular, related to the causes of deformation, previous works, and the choice of data adopted for the research.

3.2. Geography and Geological Setting

Malaysia consists of 13 states and 3 federal territories with Johor being one of the states. Johor is located in the southern part of Peninsular Malaysia, which is also the most southern point of the Asian continental mainland. It is the fifth largest state in Malaysia by land area (~19,209 square kilometres) and the third most populous state in Malaysia (DOSM, 2016). In term of economy, Johor is one of the most developed states. Iskandar Malaysia, formerly known as Iskandar Development Region and South Johor Economic Region, is a government initiative to develop a dynamic and world-class metropolis in southern Johor to be a major development corridor in Malaysia. It is intended to draw investment and business to Johor as a hub for development projects (*http://iskandarmalaysia.com.my*, accessed 18.01.2017).

In general, Johor is dominated by cropland and tree covered areas with some regions covered with mangroves and artificial surfaces (**Figure 3.1**). The topography is mostly coastal plain (elevation below 100 m) with hills and mountains in the interior (**Figure 3.2**). The lowest elevation is sea level along the coasts and the highest point is Gunung Ledang (also known as Mount Ophir) at 1,276 m. Johor also has 400 km of coastline on both the East and the West coasts. The characteristic features of climate in Johor, or Malaysia in general, are uniform temperature (maximum 33°C and minimum 23°C), high humidity (the mean monthly relative humidity is between 70% to 90%) and copious rainfall. The average annual rainfall is around 2,400 mm. Situated in the equatorial doldrums area, it is extremely rare to have a full day with completely clear sky even during periods of severe drought. Likewise, it is also rare to have a stretch of a few days with completely no sunshine except during the northeast monsoon seasons.

3.3. Surveying and Mapping in Johor, Malaysia

The implications of deformation, are not only related to socio-economic factors but also in term of sciences such as surveying and mapping. For example, deformation can alter the position of reference points used in surveying and mapping works, thus, affecting the achievable accuracy. Surveying and mapping in Johor can be grouped into two categories, namely cadastral and engineering. The cadastral survey deals with land entitlement or property boundaries, whereas engineering survey usually involves monitoring work or producing engineering plans such as hydrography, construction, bridge and structural monitoring, etc. In Peninsular Malaysia, there are two distinct projected coordinate systems used for cadastral and mapping applications. The former uses Cassini Geocentric, whereas the latter uses Rectified Skew Orthomorphic (RSO) Geocentric projections.

Cassini Geocentric is based on a transverse cylindrical projection that maintains scale along the central meridian and all lines parallel to it. There are nine state origins used in the cadastral system of Peninsular Malaysia. The origin in Johor is located at Gunung Belumut (latitude 2° 02’ 33” North and longitude 103° 33’ 40” East). On the other hand, RSO Geocentric is an oblique Mercator projection developed by Hotine in 1947 (Snyder, 1984). The properties of this projection have made it suitable for countries such as Switzerland, Italy, New Zealand, Madagascar and Malaysia. The origin of RSO Geocentric for Peninsular Malaysia is approximately at the centre of Peninsular Malaysia, i.e. latitude 4° 00’ 00” North and longitude 102° 15’ 00” East. Interested readers are referred to JUPEM (2009a) and JUPEM (2009b) for a more detailed description of the topic.

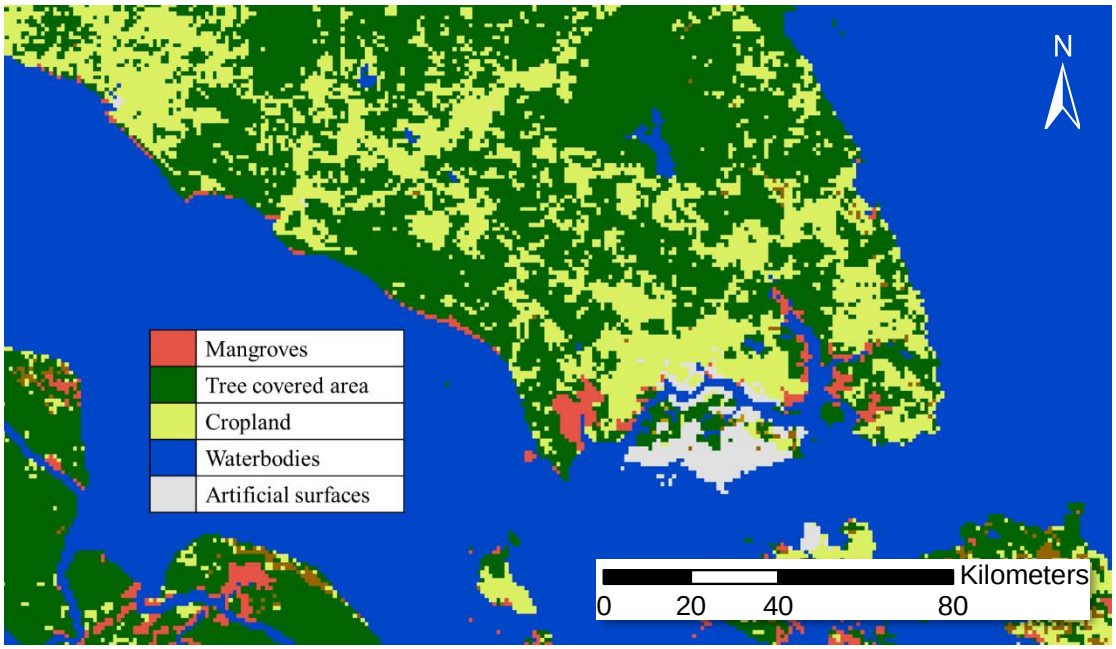


Figure 3.1: Land cover map of Johor. Figure adapted from the FAO Global Land Cover (GLC-SHARE) Beta-Release 1.0 Database, Land and Water Division, John Latham, Renato Cumani, Ilaria Roasti and Mario Bloise, 2014: *http://www.fao.org/geonetwork/srv/en/main.home* (accessed 18.01.2017), © FAO and NASA.

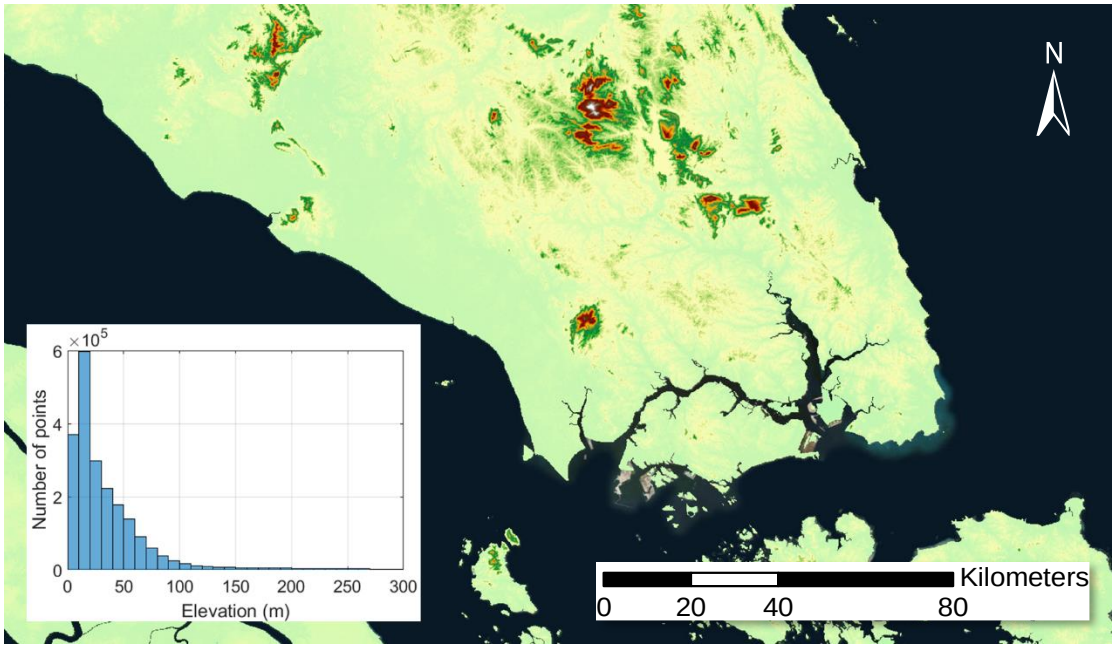


Figure 3.2: Elevation map in Johor, Malaysia based on the Shuttle Radar Topography Mission (SRTM) digital elevation model (Farr et al., 2007).

3.4. Deformation in Johor, Malaysia

Deformation of a place can be caused by various reasons, either from the natural or human-induced factors. Although Malaysia is fortunate to be spared from the threats of severe natural disasters and calamities such as major earthquakes and volcanoes, it is nonetheless affected by other disasters such as flood, human-made disaster, landslide and severe haze (Hashim, 2010). Research on deformation is a relatively new topic in Malaysia, but it is rapidly increasing. Some unfortunate tragedies such as the collapse of Highland Tower on 11 December 1993, the tsunami in West Coast of Peninsular Malaysia on 26 December 2004, and major floods that strike almost every year during monsoon season have triggered the need for this monitoring. The following points are considered worthy of note when considering potential areas of ground motion that may be visible in deformation study.

3.4.1. Tectonic Movement

One of the major drivers for deformation study in Malaysia is tectonic activities in the surrounding regions. Malaysia is situated close to the two most seismically active plate boundaries (Hesse et al., 2009): (1) the inter-plate boundary between the Indo-Australian and Eurasian plates on the west, and (2) the inter-plate boundary between Eurasian and Philippine plates on the east. Indo-Australian plate moves north-eastward and subducts under Sumatra with an estimated velocity of the order of 7 cm/year. The force generated by the movement of this plate has yielded the great Sumatran fault which divides Sumatra Island into two blocks, i.e. west and east. In the East Malaysia, the Philippine plate moves westward with an estimated velocity of the order of 8 cm/year. Several micro faults in Sabah could be generated by the movement of this plate (Che Abas, 2001).

In the past, Malaysia was considered to be on a relatively stable continent. No earthquake has originated from the area, although the flooding of the Kenyir Dam in Terengganu during 1984 - 1987 did create some seismic activity with maximum magnitude at 4.6 Richter scale (Che Abas, 2001). This fact, however, had changed when the 9.2 Mw Sumatra-Andaman mega earthquake struck on 26 December 2004. The earthquake has caused large co-seismic displacements: 27 cm in Phuket, Thailand, 17 cm in Langkawi, Malaysia, and 15 cm in Sampali, Indonesia (Vigny et al., 2005). Moreover, the post-seismic relaxation processes have been continuing for years in Andaman (Paul et al., 2012).

Large earthquakes in and around the Pacific Ring of Fire could extend and have extended to Malaysia. Occasionally, Peninsular Malaysia is affected by tremors originating from large earthquakes in the Sumatran plate margin. Although the intensity is not significant, it is important to note that the degree of damage not only depends on the physical size of an earthquake but also on other factors such as location and time, population density in the area concerned and secondary events such as fire (Che Abas, 2001). The epicentre of the 7.8 Mw Bengkulu earthquake on 4 June 2000 was about 650 km from Johore Baharu. Nevertheless, the earthquake shook several buildings in the area. Hundreds of people rushed out of their high-rise building down to the ground level. A minor crack in the building wall was also reported. A similar event was testified during the earthquake in 1995 (magnitude 7 Richter scale) with epicentre at about 450 km from Johor.

The task for monitoring earthquake activities in Malaysia falls under the jurisdiction of the Malaysian Meteorological Service (MMS). The agency is operating twelve seismic stations, while the MMS Head Quarter in Petaling Jaya, Selangor functions as a national seismic centre. **Figure 3.3** summarised the earthquakes record by MMS from the year 2013 to 2016. Hetland and Hager (2006) suggests four cycles of earthquake that need continuous monitoring: (1) pre-seismic, i.e. tectonic motion before an earthquake occurs; (2) co-seismic, i.e. tectonic motion or instantaneous displacement during an earthquake at the time of fault rupture; (3) post-seismic, i.e. tectonic motion that lasts weeks to decades following a fault rupture; and (4) inter-seismic, i.e. the relatively steady tectonic movement that occurs after the post-seismic deformation has decayed. Continuous monitoring of the earthquake cycle can contribute to the understanding of tectonic movement for a given area.

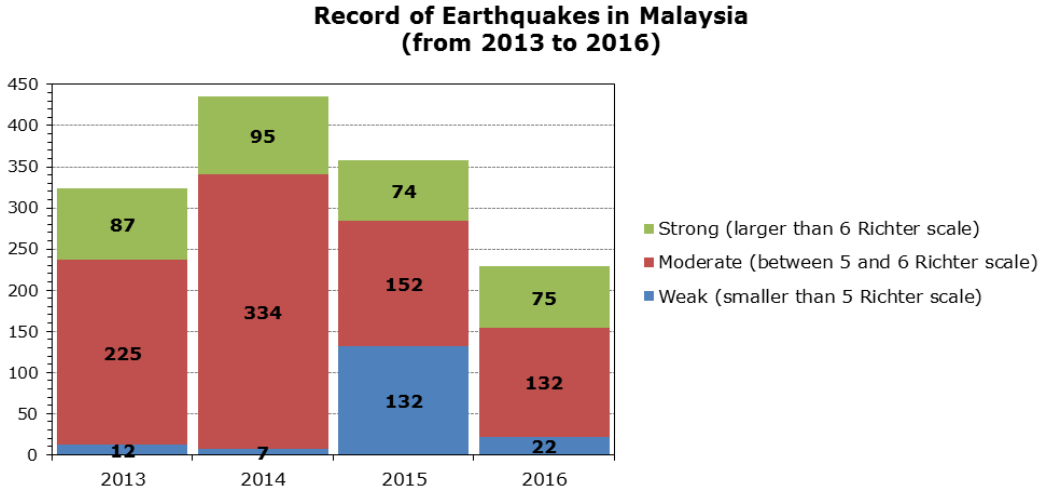


Figure 3.3: Record of earthquakes in Malaysia (adapted from *www.met.gov.my/*, accessed 30.01.2017).

3.4.2. Landslide

Landslides are considered as the second most disastrous natural hazard in Malaysia after flash floods (Matori et al., 2012). Most of these landslides occur on cut slopes and embankments of roads and highways in hilly areas (Murakami et al., 2014), and a few of them involved residential areas leading to disastrous loss of lives (Pradhan, 2010; Pradhan et al., 2010; Pradhan and Youssef, 2010; Althuwaynee et al., 2012). On 6 December 2008, Malaysia was shocked by a landslide in Bukit Antarabangsa, Kuala Lumpur. The landslide claimed 4 lives and 15 casualties, destroyed 14 houses, and cut off the access road to the residential area, leaving hundreds of people trapped in the location. In Johor, a local newspaper has reported a few landslide occurrences. For example, a landslide in Johor Bahru on 17 September 2016 has resulted in a mound of a loose soil of about 30 metres high (Astro Awani, 2016). Similarly, six squatter houses were buried in Johor following a landslide on 29 June 2015 (The Star, 2015).

Landslides in Malaysia are mainly attributed to frequent and prolonged rainfall, in many cases associated with monsoon rainfalls (Lee et al., 2014). As a consequence, it was considered as the primary triggering factor in hazard analysis (Abdulwahid and Pradhan, 2016). Likewise, Elmahdy et al. (2014) suggested that urban development in the mountainous areas with heavy rainfall, steep slopes, and wrong slope designs to be the essential factors that cause the landslides occurrence. Over the decades, the topic of landslide susceptibility mapping has been discussed and investigated by many researchers (e.g. Akgun and Erkan, 2016; Raja et al., 2016; Martins et al., 2016; Kornejady et al., 2017).

The monitoring process can be done, for example, using precise survey or geotechnical instruments (Othman et al., 2011). Precise surveys such as traverse or triangulation (e.g. using levelling and total station instruments) can provide information on the extent of movement on the ground surface. On the other hand, geotechnical instruments such as inclinometer can be used to assess the rate of landslide movement. They give reasonable accuracy but result in a heavy workload, high personnel risk and low efficiency. For a complex area such in mountainous terrain, the use of remote sensing techniques is preferable. Aerial photo interpretation is the most widely used technique for landslide mapping in many countries and regions (Althuwaynee et al., 2012). For example, Jaw et al. (2015) utilised two sets of medium resolution Landsat 8 OLI to create an inventory of major landslides in Kelantan river basin due to a massive flood in December 2014 and January 2015. Changes in the vegetation index value were used to identify the landslide occurrences on the satellite image. Integration of remote sensing and Geographic Information System (GIS) has also been proven successful

(Pradhan and Youssef, 2010; Pradhan, 2010; Elmahdy et al., 2014; Kornejady et al., 2017; Akgun and Erkan, 2016). Nevertheless, annual landslide inventories are rarely done; instead, maps are generated after major landslide events, sometimes years later.

There are some works found in the literature focussing on landslides in Malaysia. For example, in Cameron Highland, Pahang (Matori et al., 2012), Kuala Lumpur and Selangor (Othman et al., 2011; Latif et al., 2012; Althuwaynee et al., 2012; Hassaballa et al., 2014; Lee et al., 2014), Kelantan (Pour and Hashim, 2016), and Penang (Elmahdy et al., 2014). Some researchers aim to develop landslide hazards map for Peninsular Malaysia such as found in Murakami et al. (2014) and Murakmi et al. (2014). **Figure 3.4** shows the landslide hazard map and the locations of historical landslide events from 1971 to 2012, as extracted from Murakami et al. (2014). Nevertheless, there are no publications apart from the newspaper reports on the landslides in Johor. This research can contribute to the development of improved landslide susceptibility maps by providing results from GPS and InSAR.

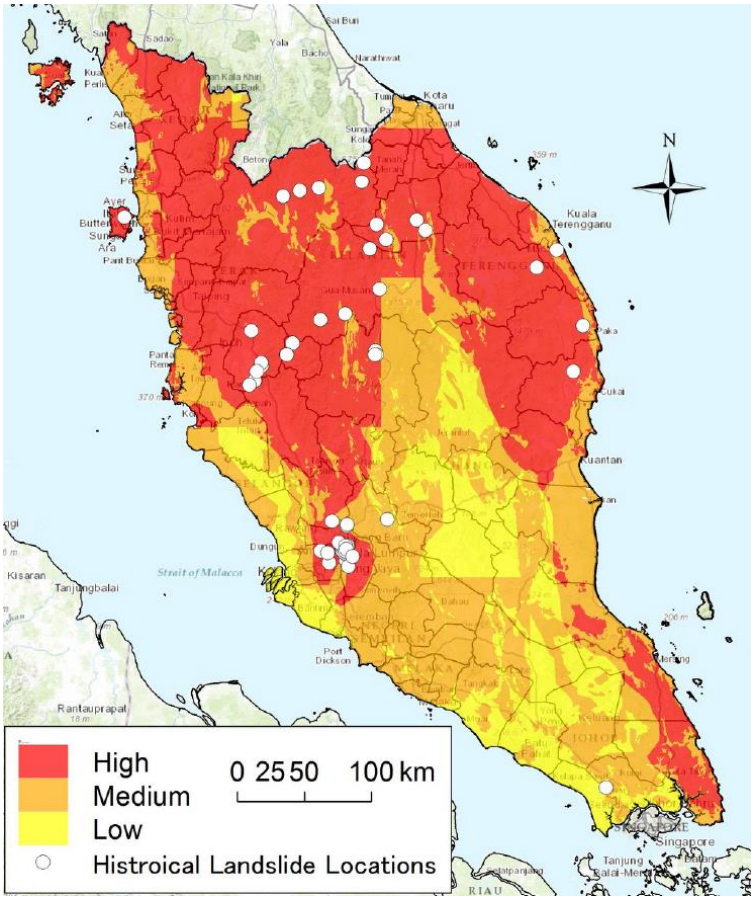


Figure 3.4: Landslide hazard map and locations of the historical landslide from 1971 to 2012. Figure adapted from Murakami et al. (2014).

3.4.3. Subsidence in Tropical Peatland

Peatlands encompass 7.45% of Malaysia's total land area with Sarawak supporting the largest area of peat soils in Malaysia (69.08% of the total peatland area), followed by Peninsular Malaysia (26.16%) (**Figure 3.5**), and Sabah (4.76%). Malaysia supports some of the most extensive tropical peatlands in the world. They consist of peat swamp forest - a critically endangered category of forested wetland, characterised by thick layers of peat soil and waters so acidic that many of the plants and animals found in them do not occur in the other tropical forests of Asia (International Wetlands, 2010). Johor has the greatest extent of oil palm on peat soils, accounting for about one-third of all oil palm plantations on peat in Peninsular Malaysia. Peat deposits cover a large area of West Johore especially Pontian, Batu Pahat, and Muar (Wösten et al., 1997). Peatlands in Malaysia play a critical role in preserving water supply, regulating and reducing flood damage, providing fish, timber, and other resources for local communities, and regulating the release of greenhouse gases by storing large amounts of carbon within peat. They also support a host of globally threatened and restricted-ranged plants and animals (Morrogh-Bernard et al., 2003; Giesen, 2004; Meijaard et al., 2012).

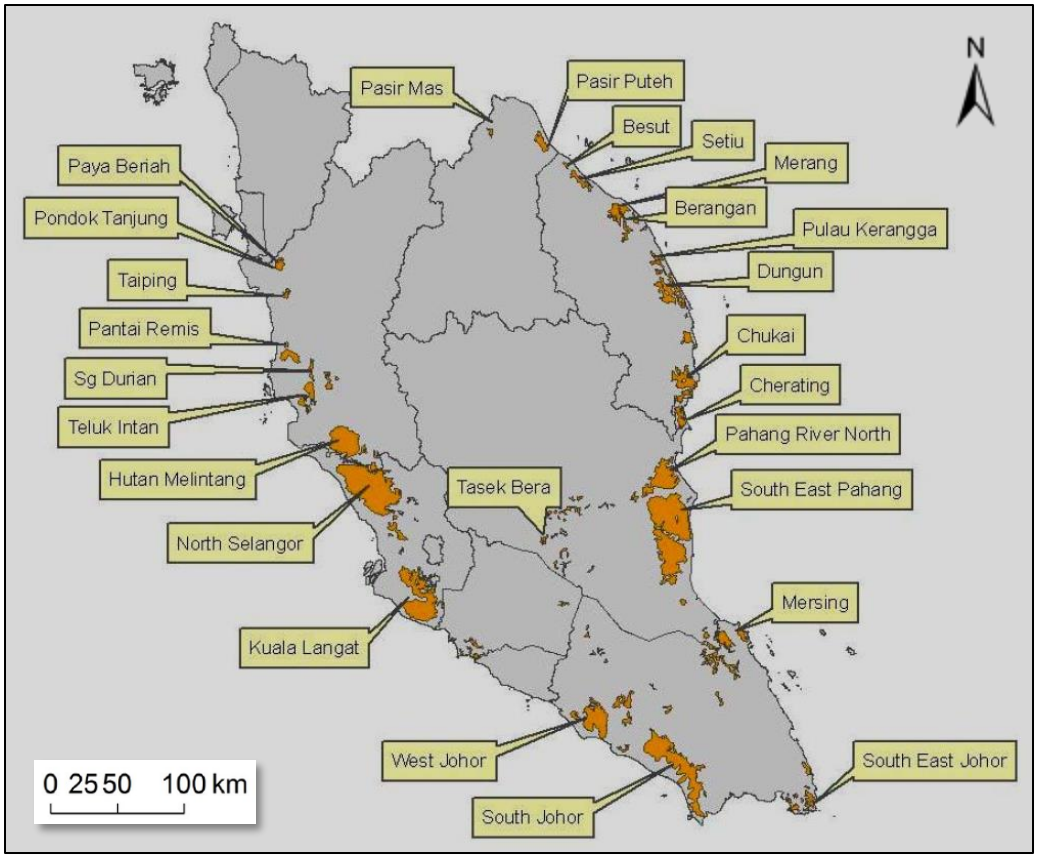


Figure 3.5: Major peat soil areas in Peninsular Malaysia. Figure adapted from International Wetlands (2010).

Conversion of tropical peatlands to agriculture can lead to a release of carbon from previously stable, long-term storage. This, in turn, can result in land subsidence, which can be measured by CO_2 emissions to the atmosphere (Wösten et al., 1997). Vast areas of peat swamp forest have been developed to meet domestic and international demand particularly for palm oil and other agricultural products (Miettinen et al., 2016). While this development is growing, scientists and conservation organisations have raised concern that the clearing and conversion of peatlands might affect the rate of emission of greenhouse gases and lead to biodiversity loss (e.g. Joosten et al., 2012; Miettinen et al., 2012; Miettinen et al., 2016; Padfield et al., 2014; Kumaran, 2014; Gaveau et al., 2014). It also contributes to recurrent annual haze, which has had grave consequences on the people's health and the economy of the region (Gaveau et al., 2014). International consumers are also implementing more stringent requirements for eco-friendly products (International Wetlands, 2010). This new development triggered the need for better management policies and strategies to achieve economic targets without compromising biodiversity of the peatlands. Development of management strategies, in the past, is hindered by limited data availability on the extent and status of Malaysia's peatlands as well as the lack of a national strategy for peatland management (International Wetlands, 2010).

Wetlands International-Malaysia Programme (WI-MP) conducted an assessment in 2007 - 2009 and produced a report on the status, extent, distribution, and conservation needs for peatlands in Malaysia (International Wetlands, 2010). Policy and practise on peat management in Peninsular Malaysia are discussed in detail in Kumaran (2014), whereas changes of peatland land cover in some parts of Malaysia (including Johor) and Indonesia are reported, among others, in Miettinen and Liew (2010) and Miettinen et al. (2016). Analysis of optical satellite images, e.g. Landsat and Satellite Pour l'Observation de la Terre (SPOT), enables them to reveal continued deforestation and conversion of peatlands into managed land cover types since 2007. A similar finding is reported by Koh et al. (2011) using images from Moderate Resolution Imaging Spectroradiometer (MODIS) and Daichi-Advanced Land Observing Satellite (ALOS). On the other hand, Wösten et al. (1997) found the average subsidence rate for the peatland area in Johor to be 2 cm per year, based on 17 subsidence markers planted in the area. This research will enable quantitative measure on the subsidence rate of peatlands in Johor using GPS and InSAR to support previous and existing research.

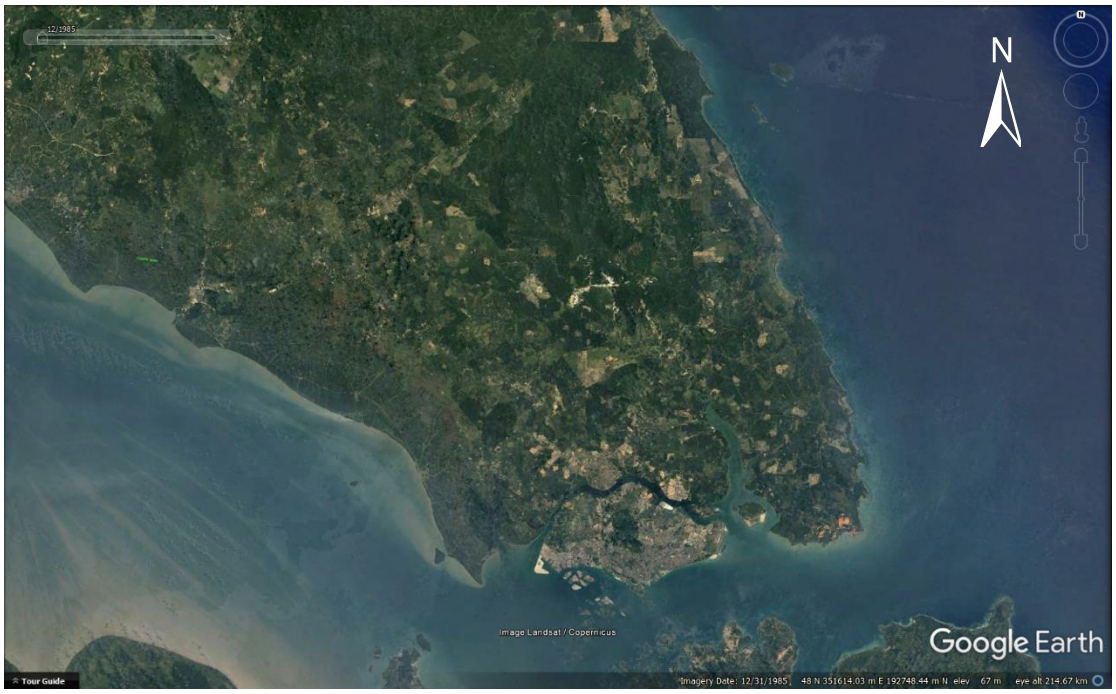
3.4.4. Urbanisation

Urbanisation impacts the environment by creating air, water and noise pollution as well as deteriorating the geological environment by inducing geohazards, for example, groundwater contamination and land subsidence (Xu et al., 2012). The risk of land subsidence increases with population and urban development activities. Population growth demands a variety of public utilities such as water or energy and other essential needs such as housing, education or healthcare. These eventually lead to increase in built-up areas and artificial landforms that create additional tension to the ground. Compaction may occur if the fill is composed of little strength or highly compressible material. Furthermore, exploitation of aquifers may introduce subsidence due to pore pressure reduction. The impact of land subsidence due to urbanisation could be seen in several forms, for example, cracking of permanent constructions and roads, changes in river canal and drain flow systems, wider expansion of flooding areas, malfunction of a drainage system, and increased inland sea water (Abidin et al., 2011).

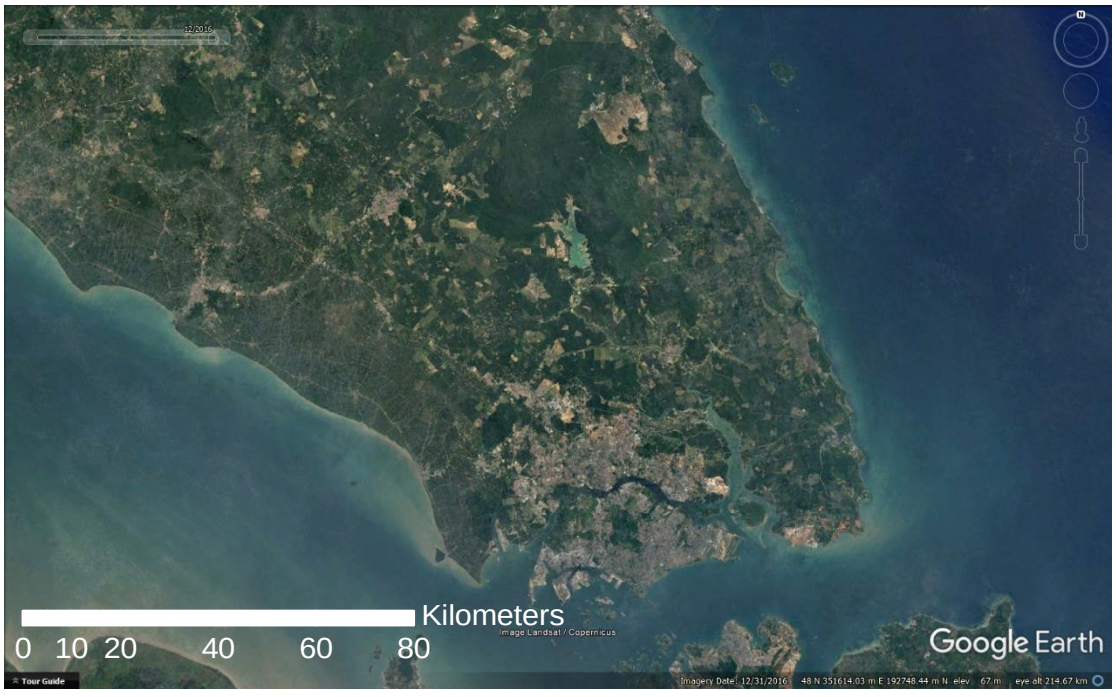
Studies on the land subsidence due to urbanisation have been reported by many researchers around the world. For instance, parts of the city in Bangkok have sunk by more than 160 cm since the 1930s, resulting in widespread floods at high river levels or after substantial downpours (Phien-wej et al., 2006). Likewise, Abidin et al. (2011) summarised their finding on land subsidence in Jakarta, Indonesia detected from geodetic measurements, namely levelling, GPS, and InSAR (over the period between 1982 and 2010). They concluded that land subsidence in Jakarta has spatial and temporal variations, reaching up to about 20 - 28 cm/year with high correlation with urban development activities. Similar research on the side effects of urban development also have been reported in several cities such as Calcutta (Chatterjee et al., 2006), Taipei (Chen et al., 2007), Shanghai (Xu et al., 2016), Semarang (Marfai and King, 2007; Abidin et al., 2010), Hanoi (Dang et al., 2014), and Bandung (Abidin et al., 2008).

As one of the most developed states in Malaysia, Johor has undergone significant urbanisation processes. Two images rendered from Google Earth on 31 December 1985 and 31 December 2016 (**Figure 3.6**) provide a glance of the urbanisation process that has taken place in Johor. In their work, Hatta and Rashid (1998) had compiled more than 220 wells drilled in Johor by the government bodies and private sector to support development activities. The number is expected to increase exponentially considering the urbanisation process in the area. On top of that, Johor also supplies water to Singapore as part of the Johore Water Agreements (Luan, 2010). Despite continuous urbanisation processes in Johor, there is only sparse research available on the

deformation in the area. Monitoring and studying the characteristics of subsidence phenomena have become necessary considering the importance of land subsidence information for supporting the development activities.



(*a*)



(*b*)

Figure 3.6: Urbanisation process in Johor. (*a*) Rendered image from Google Earth on 31 December 1985, and (*b*) on 31 December 2016.

3.4.5. Sea Level Rise and Flood

Sea level rise is one of the indications of climate change as a consequence of thermal expansion caused by warming of the ocean (since water expands as it warms) and increased melting of land-based ice such as glaciers and ice sheets (Church et al., 2013). As a country surrounded mostly by sea, Malaysia is inevitably affected by sea level rise. The impacts of sea level rise in Malaysia, concerning physical, economic and social aspects, has been discussed in Sarkar et al. (2014). Several studies have tried to quantify the impacts through several issues such as increased risk of flooding, wetland loss, loss of rice production, cost of protection and loss of dry land, and the number of people who would be forced to migrate (e.g. Tol, 2002a; Tol, 2002b; Nicholls, 2004; Nicholls and Tol, 2006). Human health is another sector where the indirect effects of sea-level rise could be significant (Sarkar et al., 2014).

Although technology such as satellite altimeters have already been used in studying the related sea level, the conventional methods of obtaining data related to the sea are still in use today. There is a total of 21 tide gauge stations used to record tidal measurement in Malaysia; 12 are located in Peninsular Malaysia, and 9 are in Sabah and Sarawak (**Figure 3.7**). Port Klang has the longest tidal record, dated back to 1984. Johor, in particular, has four tide gauge stations, located in Kukup, Tanjung Sedili, Tanjung Keling, and Johor Bahru.



Figure 3.7: Tide gauge stations in Malaysia. Figure adapted from Abdul Hadi et al. (2016). The map is not to scale.

A newspaper article on 23 July 2010 has reported that the sea level on the west coast of Peninsular Malaysia will rise in a century by up to 10 cm in Pulau Langkawi and 13 cm in Tanjung Piai, Johor, as quoted from the Deputy Minister of Natural Resources and Environment (New Straits Times, 2010). The results were drawn from a study by the Drainage and Irrigation Department in 2006. Shaaban (2008) found that sea level in Malaysia has risen at an average rate of 1.25 mm/year from 1986 to 2006. Similarly, Radzi and Ismail (2013) analysed the sea level rise at Kukup, Johor from 1986 to 2005, and found the rate to be between 0.829 mm/year and 2.021 mm/year. More recently, Abdul Hadi et al. (2016) reported their findings on the sea level rise observed at 21 tide gauge stations in Malaysia from 1986 to 2013. Four stations in Johor showed the positive rate at 3.51 ± 0.32 mm/year in Kukup, 2.97 ± 0.30 mm/year in Tanjung Sedili, 2.85 ± 0.34 mm/year in Tanjung Keling, and 3.32 ± 0.24 mm/year in Johor Bahru. The differences in rates might be due to the tidal complexities at this region as an interchange between the semi-diurnal regime in the west and the diurnal regime in the east (Din, 2014).

On top of that, Malaysia also experiences monsoonal floods annually with variations in terms of severity, place, and time of occurrences (Abdul Hadi et al., 2016; Ami Hassan Md Din, 2012). The flood in the late 2006 and lasted until February 2007 was among the worst floods ever experienced since hundred years ago. The most affected state was Johor, where more than 65,000 families had to be evacuated. 19 casualties were reported with the total economic loss estimated at RM1.2 billion (Hashim, 2010). Research on land deformation provides helpful resources for sea level rise and flood management. Land subsidence will decrease the elevation of dikes and drainage system, hence, reducing their functionality in the subsidence affected areas and may introduce flooding during the rainy season (Abidin et al., 2011). Similarly, tidal measurements can be contaminated by the land deformation (Ami Hassan, 2014). Therefore, information on land movement is necessary to allow separation between the actual sea level rise and land deformation. Research on land deformation also will be beneficial to support marine researchers, oceanography and coastal management.

3.5. List of Datasets for Processing and Analysis

In the past, long-term deformation studies in Malaysia were hindered by the lack of data owing to the significant cost involved to carry out a continuous measurement. Establishment of Continuously Operating Reference Station (CORS) opens up new possibilities for such kind of monitoring. A denser CORS network allows improved understanding of the local deformation phenomena. Similarly,

InSAR technique has benefited from the long record of SAR images acquired over the past years through various platforms. Assessment of the long-term deformation in Johor is made possible as a consequence of these data availability. GPS and SAR are selected due to their complementary features. While GPS can be used to investigate the precise movement of a station in three-dimensions (3D), InSAR is beneficial to inspect deformation in the surrounding area. It has made them ideal for the assessment of deformation in Johor.

3.5.1. GPS Dataset

The GPS data used in this study cover a five year period spanning from the year 2007 to 2011. At first, a total of 42 stations has been selected which can be categorised into three groups. The first group consists of 27 IGb08 stations, which represent the core-site of the IGb08 reference frame. They are used as the reference stations in the double-difference (DD) processing strategy, necessary for the datum definition. The second group consists of 7 International GNSS Service (IGS) stations, used to bridge and shorten the baselines length in DD, whereas the third group is 8 Malaysia Real-Time Kinematic GNSS Network (MyRTKnet) stations which are located in the study area and serve as the target stations. The list of the stations as well as their coordinates are given in **Table 3.1**. The corresponding **Figure 3.8** shows their geographical distribution.

The GPS data for 27 IGb08 stations and 7 IGS stations are provided by the Crustal Dynamics Data Information System (CDDIS), National Aeronautics and Space Administration (NASA). They are accessible through the following link:

ftp://cddis.gsfc.nasa.gov/gnss/data/daily/ (accessed 18.01.2017)

The data are resampled at 30 seconds intervals and stored in their respective year and day of observation. Meanwhile, GPS data for the 8 MyRTKnet stations are available courtesy of the Department of Survey and Mapping Malaysia (JUPEM). The stations are part of the total 78 stations established nationwide by JUPEM to support local GNSS applications. The original data are recorded at the 1-second interval but are subsequently resampled to 30 seconds using the Toolkit for GPS / GLONASS / Galileo / SBAS / Beidou / QZSS Data (TEQC) software. It not only reduces the computational burden but also synchronises the sampling rate of the data with other datasets.

Table 3.1: List of GPS stations in this study and their locations.

No.	Station	Latitude			Longitude			
1.	AIRA	31°	49’	27”	130°	35’	59”	IGb08 stations
2.	ALIC	-23°	40’	12”	133°	53’	08”	
3.	BAN2	13°	02’	04”	77°	30’	42”	
4.	COCO	-12°	11’	18”	96°	50’	02”	
5.	DARR	-12°	50’	37”	131°	07’	58”	
6.	DARW	-12°	50’	37”	131°	07’	58”	
7.	DGAR	-7°	16’	11”	72°	22’	13”	
8.	DGAV	-7°	16’	11”	72°	22’	13”	
9.	GMSD	30°	33’	23”	131°	00’	56”	
10.	GUAM	13°	35’	22”	144°	52’	06”	
11.	GUUG	13°	25’	60”	144°	48’	10”	
12.	HYDE	17°	25’	02”	78°	33’	03”	
13.	IISC	13°	01’	16”	77°	34’	13”	
14.	JAB1	-12°	39’	32”	132°	53’	38”	
15.	KARR	-20°	58’	53”	117°	05’	50”	
16.	KUNM	25°	01’	46”	102°	47’	50”	
17.	LHAS	29°	39’	26”	91°	06’	14”	
18.	LHAZ	29°	39’	26”	91°	06’	14”	
19.	NNOR	-31°	02’	55”	116°	11’	34”	
20.	PERT	-31°	48’	07”	115°	53’	07”	
21.	PIMO	14°	38’	09”	121°	04’	40”	
22.	SHAO	31°	05’	59”	121°	12’	02”	
23.	TCMS	24°	47’	53”	120°	59’	15”	
24.	TNML	24°	47’	53”	120°	59’	14”	
25.	TWTF	24°	57’	13”	121°	09’	52”	
26.	WUHN	30°	31’	54”	114°	21’	26”	
27.	YAR2	-29°	02’	48”	115°	20’	49”	
28.	BAKO	-6°	29’	28”	106°	50’	56”	IGS stations
29.	CUSV	13°	44’	09”	100°	32’	02”	
30.	KAT1	-14°	22’	34”	132°	09’	12”	
31.	NTUS	1°	20’	45”	103°	40’	48”	
32.	PBR2	11°	38’	16”	92°	42’	44”	
33.	PTAG	14°	32’	07”	121°	02’	27”	
34.	XMIS	-10°	27’	00”	105°	41’	19”	
35.	GAJA	2°	07’	20”	103°	25’	22”	MyRTKnet stations
36.	JHJY	1°	32’	13”	103°	47’	48”	
37.	KLUG	2°	01’	31”	103°	19’	01”	
38.	KUKP	1°	20’	00”	103°	27’	12”	
39.	PRTS	1°	58’	53”	102°	52’	23”	
40.	SPGR	1°	48’	38”	103°	19’	16”	
41.	TGPG	1°	22’	03”	104°	06’	30”	
42.	TGRH	2°	04’	47”	103°	56’	49”	

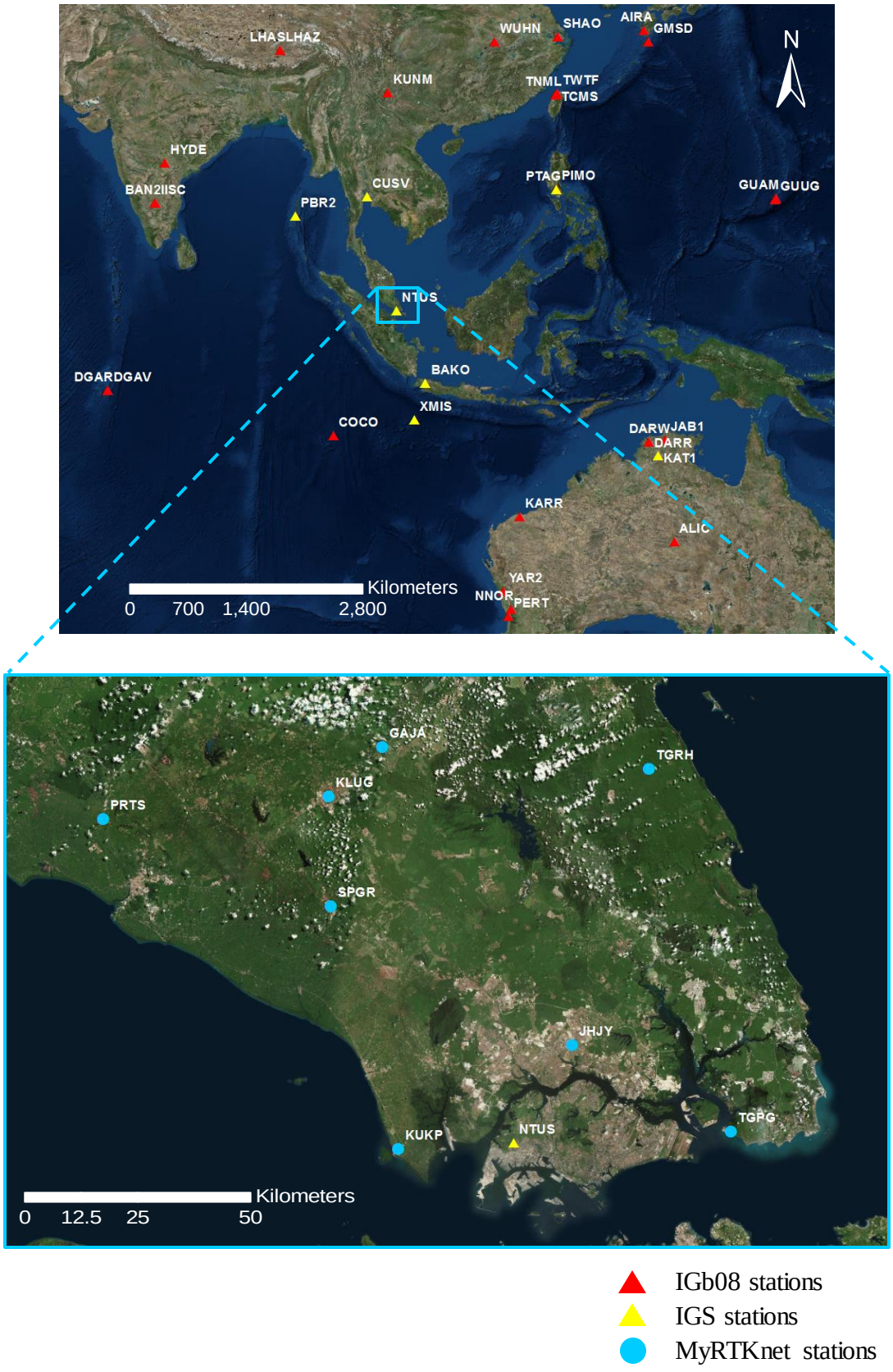


Figure 3.8: The distribution of the GPS stations in this study.

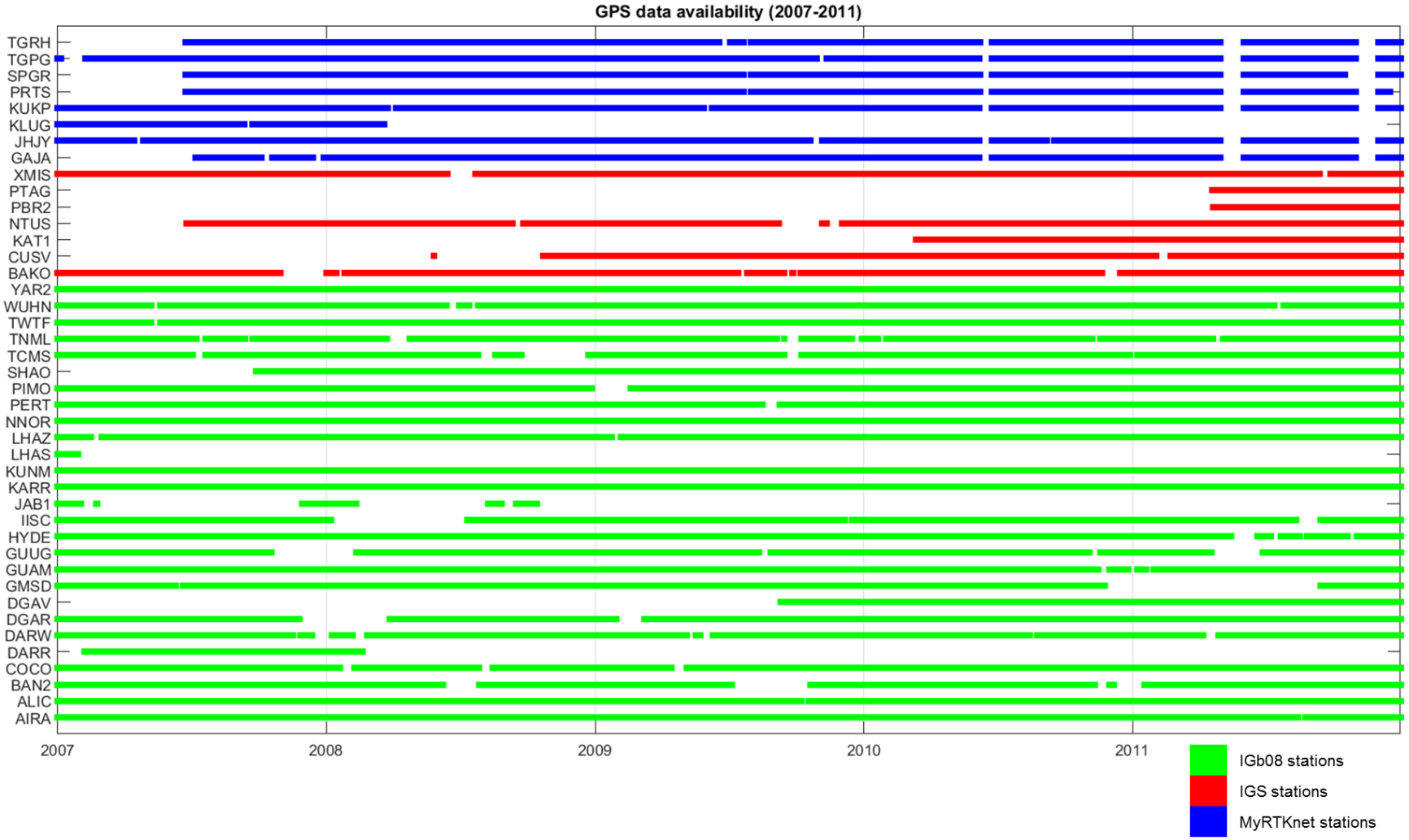


Figure 3.9: GPS data availability from the year 2007 to 2011.

Figure 3.9 shows the summary of data availability from 2007 to 2011. Some stations such as PTAG, PBR2, LHAS, JAB1 and DARR suffer from less data coverage. Therefore, they were excluded from the processing. Similarly, KLUG also has less data coverage but is kept as it serves as one of the monitoring stations. The station is part of the original Malaysia Active GPS Network (MASS), which was later decommissioned in 2008 and replaced by MyRTKnet. Although some gaps are present in the data, this is as expected and could be due to maintenance works such as receiver and antenna replacements or firmware updates. It is worth mentioning that all target stations are suitable for long-term deformation study as they are properly monumented (mounted to bedrock). Since the process of data download, decimation as well as data screening are considerably cumbersome owing to massive data volumes, the author has developed a program using Microsoft Visual Basic 2013 to automate the processes. Discussion on the GPS processing adopted in this research is made in **Chapter 4**.

3.5.2. SAR Dataset

The SAR images used in this study were acquired from two satellite missions, namely European Remote-sensing Satellite (ERS)-1/2 and Sentinel-1A/B. Those satellites operate in C-band frequency and have approximately 5.6 cm wavelength. The L-band datasets from TerraSAR-X and COSMO-SkyMed missions are excluded despite their high resolution as they are more susceptible to complex ionospheric effects in the equatorial region. The ionosphere is harder to handle with a single frequency data in SAR as opposed to more than one frequency data in GPS. On the other hand, the Envisat datasets are not utilised since there are only 7 images available and they are insufficient for ISBAS analysis.

3.5.2.1. ERS-1/2 images

ERS is the first European Space Agency (ESA) program in Earth observation to provide environmental monitoring in the microwave spectrum. Two ERS satellites, i.e. ERS-1 and ERS-2, were launched into the same orbit at altitude ~785 km in 1991 and 1995, respectively. Their payloads included synthetic aperture imaging radar, radar altimeter and instruments to measure ocean surface temperature and wind fields. In addition, ERS-2 also has additional sensors for ozone and atmospheric monitoring. Their standard operational mode provided a 35-day repeat orbit. The ERS-1 mission ended on

10 March 2000 due to the failure of the onboard attitude control system, whereas ERS-2 mission ended on 5 September 2011 after the satellite altitude had been lowered to altitude ~573 km. More information on the ERS-1/2 satellites is available at the ESA website:

https://earth.esa.int/web/sppa/mission-performance/esa-missions (accessed 19.01.2017).

ERS-1/2 data availability over a particular area of interest can be identified using Eoli-sa software (**Figure 3.10**). The software is a catalogue for users to browse metadata and preview Earth Observation data acquired by various satellites such as Envisat, ERS, Landsat, IKONOS, DMC, ALOS, SPOT, Kompsat, Proba, IRS, and SCISAT. Scientific users with a registered account can order or download products at various processing levels, subjected to submission of a proposal.

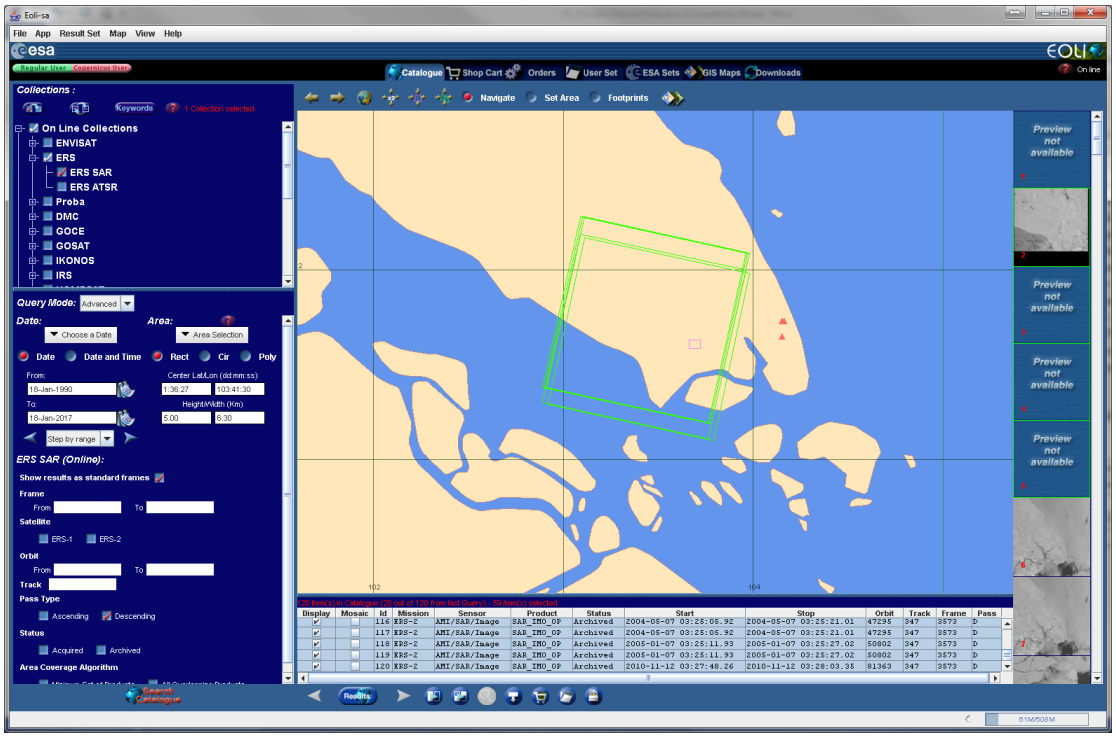


Figure 3.10: EOLi-ESA interface for requesting ERS-1/2 images.

Table 3.2 showed the proposals submitted to ESA for ERS-1/2 data acquisition in Johor. Furthermore, it also highlights the status of data. Two proposals were presented to acquire 34 ERS-1/2 images in track 75, and 33 ERS-1/2 images in track 347. All images are from descending orbit and located in frame 3573. From the two proposals, four out of the total images are from the ERS-1 mission while the rest

are from the ERS-2 mission. Data in the first proposal (track 75) cover from 5 August 1993 to 23 February 2003, whereas the second proposal (track 347) covers the period from 4 May 1995 to 12 November 2010. Some images were rejected, i.e. on 9 December 1999 and 12 November 2010, due to unavailability of their precise orbit. The precise orbits in this research are obtained from the Delft Institute for Earth Oriented Space Research (DEOS). They are accessible through the following link:

http://www.deos.tudelft.nl/ers/precorbs/ (accessed 19.01.2017)

The same case happened to image on 11 October 1997 from the first proposal. Likewise, the image on 26 December 1999 from the first proposal as well as the image on 1 October 1999 from the second proposal are not available from the links provided by ESA. It leaves a total of 32 images for data in track 75 and 30 images from track 347 to be used in the processing. Discussion on the adopted InSAR processing strategy is made in **Chapter 5**.

Table 3.2: List of proposals submitted to request ERS-1/2 dataset in Johor.

Project ID 33195: Application of InSAR Time-Series using ISBAS Algorithm for Deformation Analysis in Johor, Malaysia

No.	Mission	Acq. Date	Status
1.	ERS-1	05/08/1993	Accepted
2.	ERS-1	07/10/1995	Accepted
3.	ERS-1	30/03/1996	Accepted
4.	ERS-1	11/10/1997	Rejected
5.	ERS-2	31/03/1996	Accepted
6.	ERS-2	05/05/1996	Accepted
7.	ERS-2	09/06/1996	Accepted
8.	ERS-2	18/08/1996	Accepted
9.	ERS-2	22/09/1996	Accepted
10.	ERS-2	27/10/1996	Accepted
11.	ERS-2	01/12/1996	Accepted
12.	ERS-2	03/08/1997	Accepted
13.	ERS-2	07/09/1997	Accepted
14.	ERS-2	12/10/1997	Accepted
15.	ERS-2	16/11/1997	Accepted
16.	ERS-2	01/03/1998	Accepted
17.	ERS-2	10/05/1998	Accepted

Project ID 29656: Application of Numerical Weather Model for Tropospheric Correction in Interferometric Synthetic Aperture Radar (InSAR) - A Case Study in Peninsular Malaysia

No.	Mission	Acq. Date	Status
1.	ERS-1	04/05/1995	Accepted
2.	ERS-1	08/06/1995	Accepted
3.	ERS-1	13/07/1995	Accepted
4.	ERS-1	09/12/1999	Rejected
5.	ERS-2	19/04/1996	Accepted
6.	ERS-2	24/05/1996	Accepted
7.	ERS-2	28/06/1996	Accepted
8.	ERS-2	02/08/1996	Accepted
9.	ERS-2	06/09/1996	Accepted
10.	ERS-2	11/10/1996	Accepted
11.	ERS-2	15/11/1996	Accepted
12.	ERS-2	20/12/1996	Accepted
13.	ERS-2	28/02/1997	Accepted
14.	ERS-2	04/04/1997	Accepted
15.	ERS-2	18/07/1997	Accepted
16.	ERS-2	22/08/1997	Accepted
17.	ERS-2	31/10/1997	Accepted

Table 3.2: (continue).

Project ID 33195: Application of InSAR Time-Series using ISBAS Algorithm for Deformation Analysis in Johor, Malaysia			
No.	**Mission**	**Acq. Date**	**Status**
18.	ERS-2	23/08/1998	Accepted
19.	ERS-2	27/09/1998	Accepted
20.	ERS-2	01/11/1998	Accepted
21.	ERS-2	06/12/1998	Accepted
22.	ERS-2	10/01/1999	Accepted
23.	ERS-2	21/03/1999	Accepted
24.	ERS-2	30/05/1999	Accepted
25.	ERS-2	08/08/1999	Accepted
26.	ERS-2	12/09/1999	Accepted
27.	ERS-2	17/10/1999	Accepted
28.	ERS-2	26/12/1999	NA
29.	ERS-2	30/01/2000	Accepted
30.	ERS-2	18/06/2000	Accepted
31.	ERS-2	10/12/2000	Accepted
32.	ERS-2	03/06/2001	Accepted
33.	ERS-2	15/12/2002	Accepted
34.	ERS-2	23/02/2003	Accepted
Images acquired in descending orbit (track 75 and frame 3573)			

Project ID 29656: Application of Numerical Weather Model for Tropospheric Correction in Interferometric Synthetic Aperture Radar (InSAR) - A Case Study in Peninsular Malaysia			
No.	**Mission**	**Acq. Date**	**Status**
18.	ERS-2	05/12/1997	Accepted
19.	ERS-2	09/01/1998	Accepted
20.	ERS-2	13/02/1998	Accepted
21.	ERS-2	20/03/1998	Accepted
22.	ERS-2	24/04/1998	Accepted
23.	ERS-2	29/05/1998	Accepted
24.	ERS-2	16/10/1998	Accepted
25.	ERS-2	20/11/1998	Accepted
26.	ERS-2	01/10/1999	NA
27.	ERS-2	05/11/1999	Accepted
28.	ERS-2	10/12/1999	Accepted
29.	ERS-2	09/11/2001	Accepted
30.	ERS-2	29/11/2002	Accepted
31.	ERS-2	07/05/2004	Accepted
32.	ERS-2	07/01/2005	Accepted
33.	ERS-2	12/11/2010	Rejected
Images acquired in descending orbit (track 347 and frame 3573)			

3.5.2.2. Sentinel-1 images

Sentinel-1 belongs to one of the six different families of Sentinel satellites (**Table 3.3**), developed to cater the specific needs of the Copernicus programme. The programme is headed by the European Commission, which aims to provide information to improve environmental management, climate change and civil security. The Sentinel-1 mission comprises of two satellites: Sentinel-1A launched on 3 April 2014, and Sentinel-1B launched on 25 April 2016. Both satellites are placed in a near-polar, Sun-synchronous orbit at an altitude of approximately 693 km. The repeat period is 12 days with one satellite in the constellation and reduced to 6 days with the second satellite. The lifespan expectancy of the satellites is 7 years with consumables for 12 years.

Table 3.3: Sentinel satellites and their mission objectives. Table adapted from *http://www.copernicus.eu/main/sentinels* (accessed 18.01.2017).

No.	Satellite	Brief description
1.	Sentinel-1	A polar-orbiting, all-weather, day-and-night radar imaging mission for land and ocean services.
2.	Sentinel-2	A polar-orbiting, multispectral high-resolution imaging mission for land monitoring to provide, for example, the imagery of vegetation, soil and water cover, inland waterways and coastal areas. Sentinel-2 can also deliver information for emergency services.
3.	Sentinel-3	A multi-instrument mission to measure sea-surface topography, sea- and land-surface temperature, ocean colour and land colour with high-end accuracy and reliability. The mission will support ocean forecasting systems, as well as environmental and climate monitoring.
4.	Sentinel-4	A payload devoted to atmospheric monitoring that will be embarked upon a Meteosat Third Generation-Sounder (MTG-S) satellite in geostationary orbit.
5.	Sentinel-5	A payload that will monitor the atmosphere from polar orbit aboard a MetOp Second Generation satellite.
	Sentinel-5 Precursor	Developed to reduce data gaps between Envisat, in particular, the Sciamachy instrument, and the launch of Sentinel-5. This mission will be dedicated to atmospheric monitoring.
6.	Sentinel-6	Provide high accuracy altimetry for measuring global sea-surface height, primarily for operational oceanography and for climate studies.

The Sentinel-1 satellites provide a continuity of C-band SAR imagery after the ERS-1/2 and ENVISAT missions and offer many benefits for deformation monitoring. Rapid deformation rates can be monitored owing to the short revisit cycle of the satellites (Torres et al., 2012). As a consequence, a shorter time is required to gather a sufficient stack of images (De Zan et al. 2008, Attema et al. 2010) which will be helpful for routine long-term monitoring applications. Furthermore, the swath width of the Interferometric Wide (IW) product is around 250 km, allowing the monitoring of large areas using fewer acquisitions. IW is the primary mode for Sentinel-1 over land. Some basic specifications for IW products are shown in **Table 3.4**. A short revisit time and a large swath width mean that Sentinel-1 IW products can provide a very high level of support to operational, routine land

monitoring applications. This research provides the first assessment on the feasibilities of Sentinel-1 for deformation monitoring in a tropical region such as Malaysia. More information about Sentinel-1 satellites can be found on the ESA website, as follows:

https://sentinels.copernicus.eu/web/sentinel/missions/sentinel-1 (accessed 19.01.2017)

Table 3.4: Properties of Sentinel-1 Interferometric Wide (IW) Single Look Complex (SLC) products (ESA, 2013).

Spatial Resolution	5 m (range) x 20 m (azimuth)
Pixel Spacing	2.3 m (range) x 14.1 m (azimuth)
Incidence Angle	29° - 46°
Polarisations	HH + HV, VH + VV, HH, VV
Total Swath Width	250 km

Unlike the ERS-1/2 data acquisition, Sentinel-1 data can be acquired freely without any requirement for proposal submission. The data can be achieved through Sentinel Scientific Data Hub (**Figure 3.11**). In this research, there are 22 Sentinel-1 images used for the processing. The data cover the period from 22 March 2015 to 24 September 2016. This study provides the first assessment of the feasibility of using Sentinel-1 for deformation analysis in Malaysia. All images are separated by 24 days interval, although the image on 20 June 2016 is missing from the Sentinel Scientific Data Hub. The list and availability of the Sentinel-1 data are summarised in **Table 3.5**.

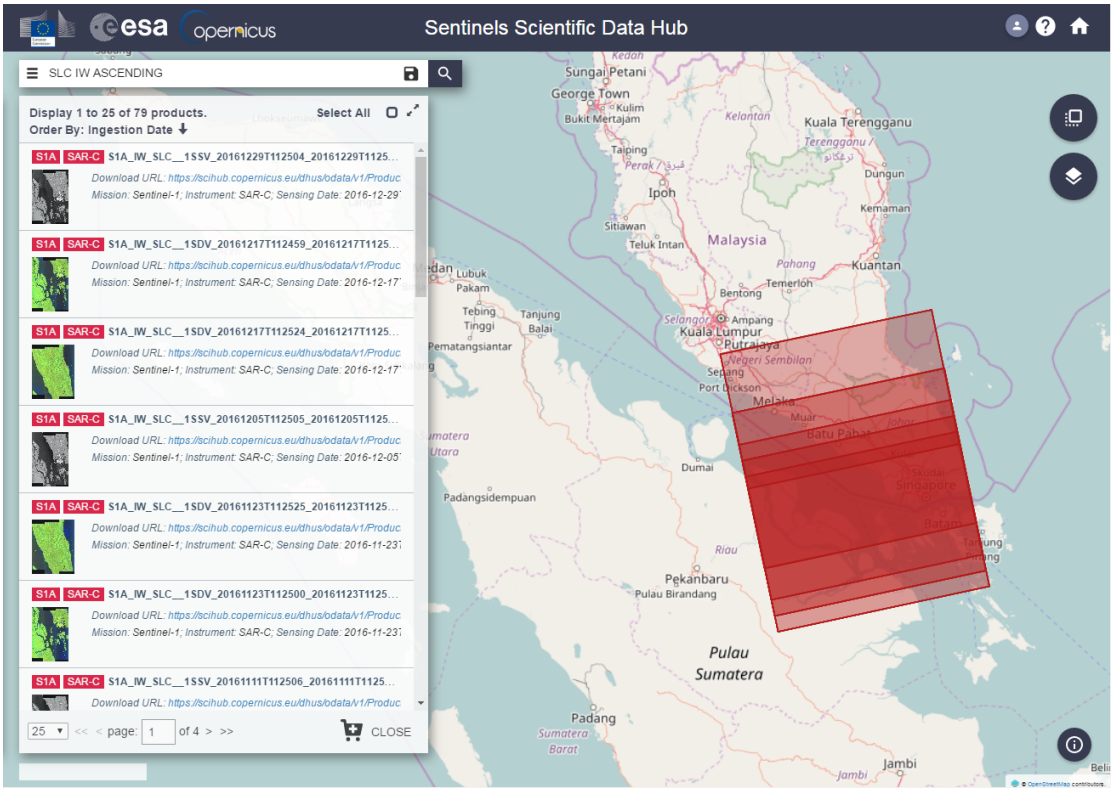


Figure 3.11: Sentinels Scientific Data Hub for acquiring Sentinel-1 images. Accessible on *https://scihub.copernicus.eu/dhus/* (accessed 18.01.2017).

Table 3.5: List of the Sentinel-1 dataset used in this research.

No.	Acq. Date	Status
1.	22/03/2015	Available
2.	15/04/2015	Available
3.	09/05/2015	Available
4.	02/06/2015	Available
5.	26/06/2015	Available
6.	20/07/2015	Available
7.	13/08/2015	Available
8.	06/09/2015	Available
9.	30/09/2015	Available
10.	24/10/2015	Available
11.	17/11/2015	Available
12	04/01/2016	Available

No.	Acq. Date	Status
13.	28/01/2016	Available
14.	21/02/2016	Available
15.	16/03/2016	Available
16.	09/04/2016	Available
17.	03/05/2016	Available
18.	27/05/2016	Available
19.	20/06/2016	NA
20.	14/07/2016	Available
21.	07/08/2016	Available
22.	31/08/2016	Available
23	24/09/2016	Available

3.6. Summary

This chapter has briefly introduced the geography and geological setting of Johor as the area of interest. It is selected for a few reasons, mainly due to the availability of sufficiently large datasets which is paramount for this study, and public interest in the Iskandar Malaysia as one of the leading development corridors in Malaysia. Surveying and mapping activities in the selected area are briefly discussed as they are also affected by the deformation. Previous and existing works on deformation, particularly in Johor, are deliberated and some of the benefits of this research are highlighted. These included deformation induced by tectonic movement, landslide, development of tropical peatland, urbanisation, as well as sea level rise and flood. It is without a doubt that the output of this research can contribute in many ways to the development of Johor as well as research on deformation. Following that, the lists of the dataset for this investigation are highlighted covering data availability, distribution, format, temporal and spatial resolution, source, and requirement. Two primary datasets are GPS and SAR, observed over a long time span of at least five years. They are selected owing to their complementary features - GPS to investigate the detailed movement of a station in 3D, and InSAR to study surrounding deformation. Together, they will enable better assessment of long-term deformation in Johor.

CHAPTER 4

DEFORMATION ANALYSIS USING GPS TIME-SERIES

4.1. Introduction

Global Positioning System (GPS) is one of the many techniques available today for deformation analysis. It has a wide spread of applications, from monitoring large-scale structures such as plate tectonics to small-scale structures such as buildings and bridges. Some of the uses have been discussed previously in **Section 2.4**. This chapter primary aims to discuss the framework and strategy employed to achieve high accuracy requirements for deformation analysis using GPS. Firstly, some theoretical concepts are recalled to better understand the development of this research. Biases and errors affecting the GPS observations are briefly introduced as they require proper mitigation strategy, especially for precise applications. Following that, coordinate reference systems used in GPS are explained in terms of global and local contexts. This is followed by the introduction to software used to process the GPS data in this research, i.e. Bernese GNSS Software version 5.2. The processing strategies employed to obtain a daily solution using Precise Point Positioning (PPP) and Double-Difference (DD) are highlighted. The discussion then continues with the time-series analysis of the daily results based on long-term observations. This chapter finally ends with a summary to highlight important key-notes of the research concerning deformation analysis using GPS time-series.

4.2. Background

4.2.1. Basic GPS Principle

GPS is one of the Global Navigation Satellite Systems (GNSS) in use today, which was developed by the United States Department of Defence for military purposes and is now operated by the United States Air Force. It is capable of providing users operating suitably equipped receivers on or close to the Earth' surface with timing, position and velocity. The basic GPS measurement is time for the signal to travel from satellite to receiver that is then converted to distance observation. The position of the receiver can be derived from the distance measurements of at least four satellites with known coordinates. There are two observables in GPS to measure this distance, namely pseudo-range and carrier-phase. Pseudo-range uses cross-correlation

analysis from the measured signal and replica signal generated by the receiver to determine the distance. On the other hand, carrier-phase measures cycle of phases received since the measurement began. The following Equations (4.1) and (4.2) show the observation equation for pseudo-range and carrier-phase, respectively, made from a satellite s to a receiver k at frequency j. For dual-frequency GPS receiver, frequency f_1 corresponds to 1575.42 MHz, whereas frequency f_2 is 1227.60 MHz.

$$P_{j,k}^s = \rho_k^s + c \cdot \delta_k^s + T_k^s + \alpha \cdot I_k^s + b_{j,k}^s + e_{j,k}^s \quad \cdots\cdots (4.1)$$

$$L_{j,k}^s = \rho_k^s + c \cdot \delta_k^s + T_k^s - \alpha \cdot I_k^s + B_{j,k}^s + N_{j,k}^s \cdot \lambda_j + \varepsilon_{j,k}^s \quad \cdots\cdots (4.2)$$

where:

- $P_{j,k}^s$ and $L_{j,k}^s$ are the pseudo-range and carrier-phase measurements in metre, respectively.
- ρ_k^s is the geometric range between satellite and receiver antenna phase centres, i.e. $\rho_k^s = \sqrt{(X_s - X_k)^2 + (Y_s - Y_k)^2 + (Z_s - Z_k)^2}$, where (X_s, Y_s, Z_s) is the Cartesian coordinate of the satellite and (X_k, Y_k, Z_k) is the Cartesian coordinate of the receiver.
- c is the vacuum speed of light, corresponds to 299,792,458 metres per second (m/s).
- $\delta_k^s = \delta t_k - \delta t^s$, where δt_k and δt^s are the receiver and satellite clock offsets, respectively.
- T_k^s is the tropospheric delay between satellite s and receiver k.
- I_k^s is the ionospheric effect between satellite s and receiver k, scaled by $\alpha = f_1^2/f_2^2$ on P_2 and L_2 to obtain their corresponding value with respect to P_1 and L_1.
- $b_{j,k}^s = b_{j,k} - b_j^s$, where $b_{j,k}$ and b_j^s are the receiver and satellite code hardware biases, respectively.
- $B_{j,k}^s = B_{j,k} - B_j^s$, where $B_{j,k}$ and B_j^s are the receiver and satellite carrier-phase fractional cycle biases, respectively.
- $N_{j,k}^s$ is the carrier-phase integer ambiguity (number of cycle) between satellite s and receiver k.
- λ_j is the carrier-phase wavelength, corresponds to 19.0 cm on L_1 and 24.4 cm on L_2.
- $e_{j,k}^s$ and $\varepsilon_{j,k}^s$ are the remaining errors including multipath, observation noise, etc., in the pseudo-range and carrier phase measurements, respectively.

As can be seen from the above equations, ionosphere I_k^s affects the pseudo-range and carrier-phase measurements differently. It delays the pseudo-range while advances the carrier-phase. Since the medium is dispersive to a radio signal, the first order effects account for approximately 99% of the total delay and can be mitigated using the ionosphere-free linear combination (Hofmann-Wellenhof et al., 2008). Equation (4.3) and (4.4) show the ionosphere-free linear combination for pseudo-range P_3 and carrier-phase L_3.

$$P_3 = \frac{f_1^2}{f_1^2 - f_2^2} \cdot P_1 - \frac{f_2^2}{f_1^2 - f_2^2} \cdot P_2 \quad \cdots\cdots (4.3)$$

$$L_3 = \frac{f_1^2}{f_1^2 - f_2^2} \cdot L_1 - \frac{f_2^2}{f_1^2 - f_2^2} \cdot L_2 \quad \cdots\cdots (4.4)$$

Upon formation of the ionosphere-free linear combination, the ionospheric term $\alpha \cdot I_k^s$ in Equation (4.1) and (4.2) can be neglected, and those equations can be rewritten as follows:

$$P_{3,k}^s = \rho_k^s + c \cdot \delta_k^s + T_k^s + b_{3,k}^s + e_{3,k}^s \quad \cdots\cdots (4.5)$$

$$L_{3,k}^s = \rho_k^s + c \cdot \delta_k^s + T_k^s + \left(N_{3,k}^s + B_{3,k}^s\right) \cdot \lambda_3 + \varepsilon_{3,k}^s \quad \cdots\cdots (4.6)$$

where:

- $P_{3,k}^s$ is the ionosphere-free linear combination formed using P_1 and P_2 pseudo-ranges, i.e. Equation (4.3), between receiver k satellite s.
- $L_{3,k}^s$ is the ionosphere-free linear combination formed using L_1 and L_2 carrier-phases, i.e. Equation (4.4), between receiver k satellite s.
- λ_3 is the wavelength of the ionosphere-free linear combination.
- $e_{3,k}^s$ and $\varepsilon_{3,k}^s$ are the remaining errors including multipath, observation noise, etc in the $P_{3,k}^s$ and $L_{3,k}^s$, respectively.
- $b_{3,k}^s = b_{3,k} - b_3^s$, where $b_{3,k}$ and b_3^s are the receiver and satellite code hardware biases in the ionosphere-free linear combination. They can be computed using Equation (4.7) and (4.8).

$$b_{3,k} = \frac{f_1^2}{f_1^2 - f_2^2} \cdot b_{1,k} - \frac{f_2^2}{f_1^2 - f_2^2} \cdot b_{2,k} \quad \cdots\cdots (4.7)$$

$$b_3^s = \frac{f_1^2}{f_1^2 - f_2^2} \cdot b_1^s - \frac{f_2^2}{f_1^2 - f_2^2} \cdot b_2^s \quad \cdots\cdots (4.8)$$

- $B_{3,k}^s = B_{3,k} - B_3^s$, where $B_{3,k}$ and B_3^s are the receiver and satellite carrier-phase fractional cycle biases in the ionosphere-free linear combination. They can be computed using Equation (4.9) and (4.10).

$$B_{3,k} = \frac{f_1^2}{f_1^2 - f_2^2} \cdot B_{1,k} - \frac{f_2^2}{f_1^2 - f_2^2} \cdot B_{2,k} \quad \text{..... (4.9)}$$

$$B_3^s = \frac{f_1^2}{f_1^2 - f_2^2} \cdot B_1^s - \frac{f_2^2}{f_1^2 - f_2^2} \cdot B_2^s \quad \text{..... (4.10)}$$

- $N_{3,k}^s$ is the integer ambiguity (number of cycle) of ionosphere-free linear combination between satellite s and receiver k. It can be computed using Equation (4.11).

$$N_{3,k}^s = \frac{f_1^2}{f_1^2 - f_2^2} \cdot N_{1,k}^s - \frac{f_2^2}{f_1^2 - f_2^2} \cdot N_{2,k}^s \quad \text{..... (4.11)}$$

It is worth noting that the integer nature of ionosphere-free linear combination ambiguity $N_{3,k}^s$ is affected by the presence of $B_{3,k}^s$. Furthermore, based on the error propagation law (Charles D. Ghilani and Wolf, 2006), the noise of measurements upon formation of ionosphere-free linear combination (i.e. $e_{3,k}^s$ and $\varepsilon_{3,k}^s$) are about three times larger than the original measurements (i.e. $e_{j,k}^s$ and $\varepsilon_{j,k}^s$). Determination of receiver's position can be made from a straightforward relationship between satellites and receiver using Equation (4.5) and (4.6). This method is known as zero-difference processing. Alternatively, relative positioning between receivers and satellites can be exploited to eliminate their common errors. Considering two stations k and l that track a similar satellite s, single-difference between two receivers will eliminate errors and biases related to the satellite (i.e. δt^s, b_3^s and B_3^s) simply by subtracting the corresponding equation made from the two stations as follows, where $\Delta(\cdot)_{kl}^s$ denotes the single-difference:

$$P_{3,kl}^s = \Delta\rho_{kl}^s + c \cdot \Delta\delta_{kl} + \Delta T_{kl}^s + \Delta b_{3,kl} + \Delta e_{3,kl}^s \quad \text{..... (4.12)}$$

$$L_{3,kl}^s = \Delta\rho_{kl}^s + c \cdot \Delta\delta_{kl} + \Delta T_{kl}^s + \left(N_{3,k}^s + B_{3,kl}\right) \cdot \lambda_3 + \Delta\varepsilon_{3,kl}^s \quad \text{..... (4.13)}$$

Furthermore, DD can be formed by subtracting Equation (4.12) and (4.13) made on satellite s with respect to satellite t, as follows:

$$P_{3,kl}^{st} = \Delta\rho_{kl}^{st} + \Delta T_{kl}^{st} + \Delta e_{3,kl}^{st} \quad \cdots\cdots (4.14)$$

$$L_{3,kl}^{st} = \Delta\rho_{kl}^{st} + \Delta T_{kl}^{st} + N_{3,kl}^{st} \cdot \lambda_3 + \Delta\varepsilon_{3,kl}^{st} \quad \cdots\cdots (4.15)$$

$\Delta(\cdot)_{kl}^{st}$ represents the respective DD for the station k and l, and satellite s and t. Notice that all common errors in the station k and l and satellite s and t (namely clock offsets, code hardware biases, and carrier-phase fractional cycle biases) are eliminated assuming that all channels within the receiver, tracking different satellites, share exactly the same clock offsets. This is generally true for GPS where all the satellites use common carrier frequencies but is not usually the case for GLONASS where satellites broadcast on different carrier frequencies.

It is important to note that $N_{3,kl}^{st}$ has become integer since the fractional cycle biases are eliminated by the differencing scheme. Consequently, once the L_1 and L_2 ambiguities are resolved, the ionospheric-free ambiguities $N_{3,kl}^{st}$ become known and can thus be removed from the Equation (4.15), which then becomes equivalent to the pseudorange Equation (4.14). Fixed ambiguity solutions yield relative positioning of the highest possible precision, typically at or below the millimetre precision level (e.g. Hofmann-Wellenhof et al., 2008). It is also important to note that Equation (4.14) and (4.15) have a different number of unknowns and different magnitudes of the individual terms as compared to the respective Equation (4.5) and (4.6). For example, the DD tropospheric delay ΔT_{kl}^{st} is much smaller than the un-differenced T_k^s, whereas the noise $\Delta e_{3,kl}^{st}$ and $\Delta\varepsilon_{3,kl}^{st}$ are significantly larger than the original, un-differenced noise $e_{3,k}^s$ and $\varepsilon_{3,k}^s$, etc. To solve for the unknowns, several methods are possible such as sequential least-square adjustment and (extended) Kalman filtering. A detailed discussion about positioning solutions using GPS is beyond the scope of this research. Interested readers are referred to various publications available, such as Hofmann-Wellenhof et al. (2008), Leick et al. (2015) and Dach et al. (2015) for a more detail discussion on the topic.

4.2.2. Biases and Errors in GPS Observation

Like any other techniques, GPS measurements are contaminated with errors and biases. The term bias refers to physical phenomena, while error relates to the quantity remaining after the bias has been mitigated (Bingley, 2004). The presence of biases and errors limits the achievable accuracy in positioning, thus, they should be mitigated in precise applications. Relative positioning with short baselines, e.g. less than 100 km, may benefit from the cancellation of some common biases and errors. However, they can be significant for all precise global analyses (relative or un-differenced approaches). Their classification can be made into three groups, namely satellite, station, and atmospheric related.

4.2.2.1. Satellite-related

Estimation of a receiver's coordinates relies on the known properties (i.e. coordinate and clock) of at least four satellites. These properties, however, are only accurate to a certain degree depending on the types of product as listed in **Table 4.1**. Any errors in the satellites properties will propagate to the estimated receiver's coordinates. The error propagation is less prominent in relative positioning between receivers. A crude, but handy rule of thumb suggested in Dach et al. (2015), giving the error ΔBL in a component of a baseline of length l as a function of an orbit error of size ΔOrb is shown in Equation (4.16):

$$\Delta BL(m) \approx \frac{1}{d} \cdot \Delta Orb(m) \approx \frac{l(km)}{25{,}000(km)} \cdot \Delta Orb(m) \quad \cdots\cdots\cdots\cdots\cdots \quad (4.16)$$

where $d \approx 25{,}000$ km is the approximate distance between satellite and survey area. This equation gives a satisfactory result for sessions of about 1 - 2 hours (and shorter) (Beutler, 1992). However, the formula given by Zielinski (1988) is preferable for permanent site occupations, which were derived using statistical methods. **Table 4.2** gives the actual baseline errors in meters and parts per million (ppm) for different baseline lengths and different orbit qualities as computed using Equation (4.16).

Table 4.1: GPS satellite ephemerides / satellite and station clocks (see *http://www.igs.org/products*, accessed 13.12.2016).

Type		Accuracy	Latency	Sample Interval
Broadcast	orbits	~100 cm	real time	daily
	Sat. clocks	~5 ns RMS ~2.5 ns SDev		
Ultra-Rapid (predicted half)	orbits	~5 cm	real time	15 min
	Sat. clocks	~3 ns RMS ~1.5 ns SDev		
Ultra-Rapid (observed half)	orbits	~3 cm	3 - 9 hours	15 min
	Sat. clocks	~150 ps RMS ~50 ps SDev		
Rapid	orbits	~2.5 cm	17 - 41 hours	15 min
	Sat. clocks	~75 ps RMS ~25 ps SDev		5 min
Final	orbits	~2.5 cm	12 - 18 days	15 min
	Sat. clocks	~75 ps RMS ~20 ps SDev		Sat.: 30s Stn.: 5 min

Table 4.2: Errors in baseline components due to orbit errors.

Orbit Error	Baseline Length	Baseline Error	Baseline Error
0.1 m	1 km	0.004 ppm	- mm
0.1 m	10 km	0.004 ppm	- mm
0.1 m	100 km	0.004 ppm	0.4 mm
0.1 m	1000 km	0.004 ppm	4.0 mm
0.05 m	1 km	0.002 ppm	- mm
0.05 m	10 km	0.002 ppm	- mm
0.05 m	100 km	0.002 ppm	0.2 mm
0.05 m	1000 km	0.002 ppm	2.0 mm
0.03 m	1 km	0.001 ppm	- mm
0.03 m	10 km	0.001 ppm	- mm
0.03 m	100 km	0.001 ppm	0.1 mm
0.03 m	1000 km	0.001 ppm	1.2 mm
0.025 m	1 km	0.001 ppm	- mm
0.025 m	10 km	0.001 ppm	- mm
0.025 m	100 km	0.001 ppm	0.1 mm
0.025 m	1000 km	0.001 ppm	1.0 mm

Satellite antenna offset is another bias that should be addressed in GPS for precise applications. It accounts for the separation between the satellite centre of mass and the phase centre of its antenna. The pseudo-range and carrier-phase measurements shown in Equation (4.1) and (4.2) are referred to the satellite antenna phase centre. The same reference is used for the satellite coordinates and clocks in broadcast ephemerides. On the contrary, the force models used for satellite orbit as well as the satellite coordinates and clocks in precise ephemerides are referred to the satellite centre of mass. For that reason, one must know the offset between the two and its orientation as the satellite orbits the Earth to correct for this bias. **Figure 4.1** illustrates the satellite antenna offset between the centre of mass and centre of phase. The Z-axis is pointing towards the Earth, while the X-axis is pointing towards the Sun. The Y-axis is perpendicular to those two axes. Prior to 5 November 2006 (GPS Week 1400), the zero value was adopted with zero phase centre variations for the Block IIR satellites, but then the so-called "absolute" phase centre offsets and non-zero PCVs are utilised for the satellite (Schmid et al., 2005; Schmid et al., 2007). Satellite antenna offset is continuously being monitored by International GNSS Service (IGS) analysis centres, and the corrections are given in the ANTenna EXchange format (ANTEX) file. Its format description is available at:

ftp://igs.org/pub/station/general/antex14.txt (accessed 13.12.2016)

The observed carrier-phase shown in Equation (4.2) depends on the mutual orientation of the satellite and receiver antennas. Wu et al. (1991) suggested that any rotation of either receiver or satellite antenna around its vertical axis could change the carrier-phase up to one cycle (one wavelength), which is termed phase wind-up effects. For a static measurement, the receiver antenna does not rotate and is typically oriented towards north direction. Satellite antennas, however, undergo slow rotations as their solar panels are being oriented towards the Sun and the station-satellite geometry changes. A similar scenario happens in the event of solar eclipses, where satellites are subjected to rapid rotations (within less than half an hour) in order to reorient their solar panels towards the Sun. The phase wind-up correction has generally been neglected even in the most precise differential positioning software as it is quite negligible for DD positioning on baselines/networks spanning up to a few hundred kilometres. However, Wu et al. (1992) indicated that the effects could reach up to 4 cm for a baseline of 4,000 km which is significant for global processing. For zero-difference processing such as PPP, the effect is significant (could

cause position and clock errors at decimetre level) when fixing the precise satellites coordinate and clock. In the case of kinematic positioning, the phase wind-up due to receiver antenna rotation is fully absorbed into station clock solutions or eliminated by DD.

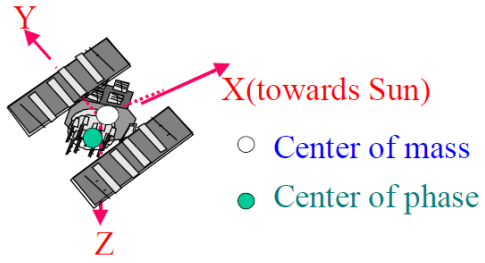


Figure 4.1: Satellite antenna phase centre offsets in satellite body-fixed reference frame. Figure adapted from Kouba (2009b).

4.2.2.2. Station-related

Station coordinates are changing in time owing to the steady motion of tectonic plates. The rates of movements are given by the station velocity which varies on location. It can reach up to few decimetres per year, thus should be accounted for in precise GPS analyses. The coordinate of reference stations in relative positioning should always be propagated from the reference epoch to the observation epoch using its respective stations' velocity. It is to ensure consistency with the satellite orbits and prevents network deformations induced by moving plates. Alternatively, the velocity derived from a model such as NNR-NUVEL-1A (DeMets et al., 1994) may be used if it is not known. Relative positioning over short baselines (< 100 km) might benefit from the differencing process as the rate of movement is nearly the same between stations, resulting in their cancellation during DD. However, zero-difference or relative positioning over long baselines (> 500 km) must account for the tectonic plates motion as recommended in the International Earth Rotation and Reference Systems Service (IERS) Conventions (Petit and Luzum, 2010).

Changes in the station's coordinates also can be induced by solid earth tides, which refer to the elastic deformation of the earth due to the gravitational attraction of the sun and the moon (and other bodies in the solar system). Solid earth tides consist of a latitude dependent permanent displacement and a periodic part with predominantly semi-diurnal and diurnal periods of changing amplitudes. The periodic part is mostly averaged out for static positioning over a 24-hour period, but the permanent part remains in such a 24-hour average position. Since the effects are two orders of magnitude larger than the accuracies currently achieved for GPS- and SLR-derived coordinates (Dach et al., 2015), they have to be taken into account in precise GPS analyses. Detailed technical discussion about solid earth tides can be found in Petit and Luzum (2010). A corresponding FORTRAN subroutine, i.e. *dehanttideinel.f*, also can be found for a straightforward implementation in Chapter 7 of the following link:

http://maia.usno.navy.mil/conv2010/conventions.html
(accessed 13.12.2016)

For relative positioning over short baselines (< 100 km), both stations have similar tidal displacements, thus are unaffected by the solid earth tides. On the contrary, point or relative positioning over long baselines should account for these effects. Kouba (2009b) suggested that systematic position errors of up to 12 and 5 cm can be observed in radial and north directions, respectively, from neglecting the correction in point positioning.

Another important site displacement effect is the crustal deformation caused by the changing mass distribution due to ocean tides (ocean tidal loading). The movements due to ocean tidal loading rely on time and location, and comprise a combination of semidiurnal, diurnal and long-period tides (Baker et al., 1995). It occurs in both horizontal and vertical directions, and is more localise compared to solid earth tides. The magnitude is typically small, within few millimetres, but can increase to more than 1 cm in certain locations. Ocean tidal loading can be explained by a complex interaction of eleven tidal harmonics. The detailed discussion can be found in Petit and Luzum (2010), and a FORTRAN subroutine for their implementation, i.e. *hardisp.f*, can also be found in the same link given previously. A station-specific amplitude and phase of the eleven largest tidal harmonics for the vertical and horizontal components can be obtained using a web-service at:

http://holt.oso.chalmers.se/loading/ (accessed 13.12.2016)

According to Kouba (2009b), the effects can be safely neglected for single epoch positioning at the 5 cm precision level or mm static positioning over 24 hours period and/or for stations that are far from the oceans. Nevertheless, it has to be considered for cm precise kinematic point positioning or precise static positioning along coastal regions over observation intervals significantly shorter than 24 hours. Ocean tidal loading is also important to be modelled when the troposphere and clock solution is required as the effects will map into the solutions, unless the station is far (> 1,000 km) from the nearest coastline (Kouba, 2009b).

Pole tides result from the changes of the Earth's spin axis with respect to the Earth's crust, which causes deformations due to minute changes in the Earth's centrifugal potential (Kouba, 2009b). They are marginally periodic and resulting from a major 434 days constituent known as the Chandler period (Leick et al., 2015). The pole position may vary and can reach 0.8 arcseconds, corresponding to a maximum horizontal displacement of about 7 mm and a maximum radial displacement of about 25 mm (McCarthy, 1996). The correction for the point movement due to pole tide can be derived from the expressions given in Petit and Luzum (2010). The tides correction needs to be applied to obtain an apparent station position, free from the effects. The correction is also necessary to ensure consistency when using precise orbit and clock since most of IGS analysis centres utilise this correction when generating their product. Information about pole tides is also important to perform the transformation between the terrestrial and the celestial (inertial) reference frame.

The geometric distance, described previously in Equation (4.1) and (4.2), is referred to antenna phase centre. The position of the antenna phase centre depends on the various directions of GPS signals from individual satellites arrived at the receiver antenna. This direction-dependence is called antenna phase centre variations. Furthermore, the fact that the antenna phase centre offsets (with respect to the antenna reference point) and the antenna phase centre variations (with respect to the mean antenna phase centre) are not identical for different carrier frequencies also needs to be considered. Radomes that are used to protect the antennas from multipath and environmental effects have an impact on the antenna phase centre variations. Although it is preferable to calibrate each individual antenna to obtain its phase centre corrections, the task is not practical for most GPS applications. Usually, antenna phase centre

variations are assumed to be dependent only on antenna and radome type. Nevertheless, it is important to model the effects especially when different antenna/radome combinations with individual characteristics are used simultaneously. Ignoring the antenna phase centre corrections may cause relative station height errors reaching values of up to 10 cm, independent of the baseline length. If only antennas of the same type are used, the main effect is a scale factor in the network of up to about 0.015 ppm. Correction for each individual antenna and radome can be obtained from the similar ANTEX file used for satellite antenna offset.

Multipath is another potential error source affecting the GPS measurements. It is caused by reflecting surfaces, causing the emitted signal from the satellite to arrive at the receiver in multiple paths. The effects are time- and location-dependent, thus cannot be mitigated using a general model. However, it can be estimated from the residual of ionosphere-free linear combination, made on pseudo-range and carrier-phase measurements. It is because multipath is frequency dependent, similar to ionospheric effects; therefore it can be separated from the others with an appropriate differencing technique. Measurements at low elevation angle are more susceptible to multipath than the ones made at high elevation angle. Similarly, pseudo-range measurements are more affected by multipath than carrier-phase. Wells et al. (1986) suggested that the effect may amount to 10 - 20 m for pseudo-range and under certain circumstances, the error from multipath may grow to about 100 m in the vicinity of buildings (Nee, 1992). On the contrary, multipath effects on carrier-phases for relative positioning with short baselines should not be greater than 1 cm with good geometry and a reasonably long observation interval. Nevertheless, it is sensitive to the change of receiver height. Ray et al. (1999) classified various methods to reduce or estimate multipath into (1) antenna-based mitigation, (2) improved receiver tracking technology, and (3) signal and data processing. Employing choke ring antenna is a very efficient way to minimise multipath effects. New receivers also apply rigorous multipath detection and correction algorithm during data acquisition. Similarly, various algorithms have been developed to detect and correct the multipath effects in the post-processing.

4.2.2.3. Atmospheric-related

The GPS signal crosses and interacts with the atmosphere as it propagates from the satellite towards the Earth's surface. The main interaction is refraction which causes the signal to change in direction and speed as it passes from one medium to the other. Atmospheric layers can be categorised into troposphere and ionosphere. The former extends to about 50 km above ground and causes a delay in the signal propagation. It can be divided into dry and wet components which contributes to approximately 90% of the total delay. Nevertheless, it can be modelled accurately using surface measurements of temperature and pressure. Ionosphere, however, is highly variable and difficult to model although it only accounts for 10% of the total delay (Janssen et al., 2004; Hofmann-Wellenhof et al., 2008). Troposphere remains as one of the most challenging error sources in GPS. A more detailed discussion about modelling and mitigation of tropospheric effects in GPS is made in **Chapter 6**.

Ionosphere, on the other hand, is the upper part of the atmosphere which extends in many distinct layers from 50 to 1,000 km above the Earth's surface (Janssen et al., 2004). A sufficient number of electrons and ions are present in the ionosphere, causing the signal to advance in propagation. The degree of ionisation shows considerable variation, generally correlating with geographic location, solar and geomagnetic activity, season, and local time (SBAS Ionospheric Working Group, 2010; Dach et al., 2015). As mentioned previously, the first order ionosphere accounts for about 99% of the total effects, and can be mitigated using dual-frequency GPS receiver. Furthermore, higher-order effects can also be reduced using Global Ionosphere Maps (GIM) from the International GNSS Service (IGS).

Similar to the effects of solid earth tide and ocean tide loading, time-varying atmospheric pressure also can induce surface deformation. The diurnal heating of the atmosphere causes surface pressure oscillations at diurnal, semidiurnal, and higher harmonics (Petrov and Boy, 2004). Vandam et al. (1994) found improvement in the vertical and baseline repeatability by incorporating correction for the atmospheric pressure loading. Numerical analyses (e.g. Tregoning and Vandam, 2005) have suggested that pressure loading can cause peak radial displacements of the Earth's surface as large as 10 to 25 mm with associated horizontal movements of one-third to one-tenth this magnitude. To a first-order, it suffices to correct the GPS height time series for the loading effect by applying a daily-averaged correction. However, a greater reduction in the variance of heights can

be achieved when non-tidal atmospheric pressure loading is applied at the observation level. Correction for the three-dimensional displacements can be made, for example, using an atmospheric tides model from Ray and Ponte (2003) as suggested in Petit and Luzum (2010). The model is derived from the European Centre for Medium-Range Weather Forecasts (ECMWF) operational global surface pressure fields, using a procedure outlined by van den Dool et al. (1997).

4.3. Coordinate Reference System for GPS

The definition of a reference system plays a crucial role in geodetic positioning. A reference system is realised by a reference frame, which is a catalogue of Cartesian station positions at an arbitrary and fundamental epoch (Bock, 1998). The fundamental properties of a reference system are origin, scale and orientation that define the axes. The International Terrestrial Reference System (ITRS) is a very accurate geodetic reference system, comprising a set of right-handed orthogonal axes, whose origin is defined at the centre of mass, whose axes are orientated to be consistent with those of the Bureau International de l'Heure (BIH) at epoch 1984.0, and whose unit of length is the metre. The axes are fixed to the Earth's crust such that there is no residual global rotation of the system with respect to the crust (Petit and Luzum, 2010). The ITRS is maintained by the International Earth Rotation Service (IERS). Realisations of ITRS are produced by the IERS under the name International Terrestrial Reference Frame (ITRF). Once the station positions have been defined, it must be maintained by associating the rotated, translated and deformed positions at a later epoch back to the fundamental epoch. In other words, when observing the motion of the Earth's crust, it must be referenced. The usefulness of the reference frame for the computation of highly accurate station velocities from GPS coordinate time series depends on its ability to describe changes in coordinates over time. In time, station coordinates are degraded by spurious movement of the station relative to the reference frame, internal deformations of the reference frame and during updates of the reference frame (Teferle, 2003).

4.3.1. International Terrestrial Reference Frame (ITRF)

The ITRF is realized through the Cartesian coordinates and linear velocities of a global set of monitoring stations, obtained from various space geodetic techniques such as very long baseline interferometry (VLBI), satellite laser ranging (SLR), Doppler orbit determination and radio positioning integrated on satellites (DORIS), and GNSS (Altamimi et al., 2011; Altamimi

et al., 2016). As none of the four space geodetic techniques can provide the full reference frame defining parameters, the ITRF is demonstrated to be the most accurate reference frame available today, gathering the strengths of the four space geodesy techniques contributing to its construction and compensating for their weaknesses and systematic errors. The ITRF combination fundamentally depends on the availability of colocation sites where (1) two or more geodetic instruments of different techniques are operated and (2) local surveys between instrument measuring points are available (Altamimi et al., 2011; Altamimi et al., 2016). Local surveys are usually conducted using terrestrial measurements (direction angles, distances, and spirit levelling) or the GPS technique.

The first realisation of the ITRS was ITRF88 (Boucher et al., 1996). Since then, IERS has published ITRS realisations on a regular basis sustaining continuous improvements and enhancements. The most recent realisation is ITRF2014 (Altamimi et al., 2016), which is adopted on 26 February 2015. IGS also has its own realisation of the ITRF since ITRF97 (**Table 4.3**). Though not necessarily more accurate, it is more consistent (Dach et al., 2015). In this work, IGS realisation of ITRF2008, i.e. IGb08, has been selected as the reference frame for the GPS processing owing to the availability of consistent products (i.e. satellite precise orbits and clocks) via second reprocessing campaign (Rebischung et al., 2016; Altamimi et al., 2016). The ITRF2008 network (Altamimi et al., 2011) comprises of 934 stations located at 580 sites, with 463 sites in the northern hemisphere and 117 in the southern hemisphere. Its combination involves 84 co-location sites where two or more technique instruments were or are currently operating and for which local ties are available. **Figure 4.2** illustrates the distribution of VLBI, SLR, DORIS and GPS station within ITRF2008. The ITRF2008 is specified by the following datum parameters (Altamimi et al., 2011).

i. Origin: The ITRF2008 origin is defined in such a way that there are null translation parameters at epoch 2005.0 and null translation rates with respect to the International Laser Ranging Service (ILRS) SLR time series.
ii. Scale: The scale of the ITRF2008 is defined in such a way that there is null scale factor at epoch 2005.0 and null scale rate with respect to the mean scale and scale rate of VLBI and SLR time series.
iii. Orientation: The ITRF2008 orientation is defined in such a way that there are null rotation parameters at epoch 2005.0 and null rotation rates between ITRF2008 and ITRF2005. These two conditions are applied over a set of 179 reference stations located at 161 reference sites. The reference sites include 107 GPS, 27 VLBI, 15 SLR and 12 DORIS.

Table 4.3: History of reference frames used for IGS products (see *http://acc.igs.org/igs-frames.html*, accessed 13.12.2016).

Frame	Used for IGS products	
	GPS week	Date
ITRF92	0730 – 0781	02 Jan. 1994 – 31 Dec. 1994
ITRF93	0782 – 0859	02 Jan. 1995 – 29 June 1996
ITRF94	0860 – 0947	30 June 1996 – 07 Mar. 1998
ITRF96	0948 – 1020	08 Mar. 1998 – 31 July 1999
ITRF97	1021 – 1064	01 Aug. 1999 – 03 June 2000
IGS97	1065 – 1142	04 June 2000 – 01 Dec. 2001
IGS00	1143 – 1252	02 Dec. 2001 – 10 Jan. 2004
IGS00b	1253 – 1398	11 Jan. 2004 – 04 Nov. 2006
IGS05	1400 – 1631	05 Nov. 2006 – 16 Apr. 2011
IGS08	1632 – 1708	17 Apr. 2011 – 06 Oct. 2012
IGb08	1709 – 1933	07 Oct. 2012 – 28 Jan. 2017
IGS14	1934 – present	29 Jan. 2017 – present

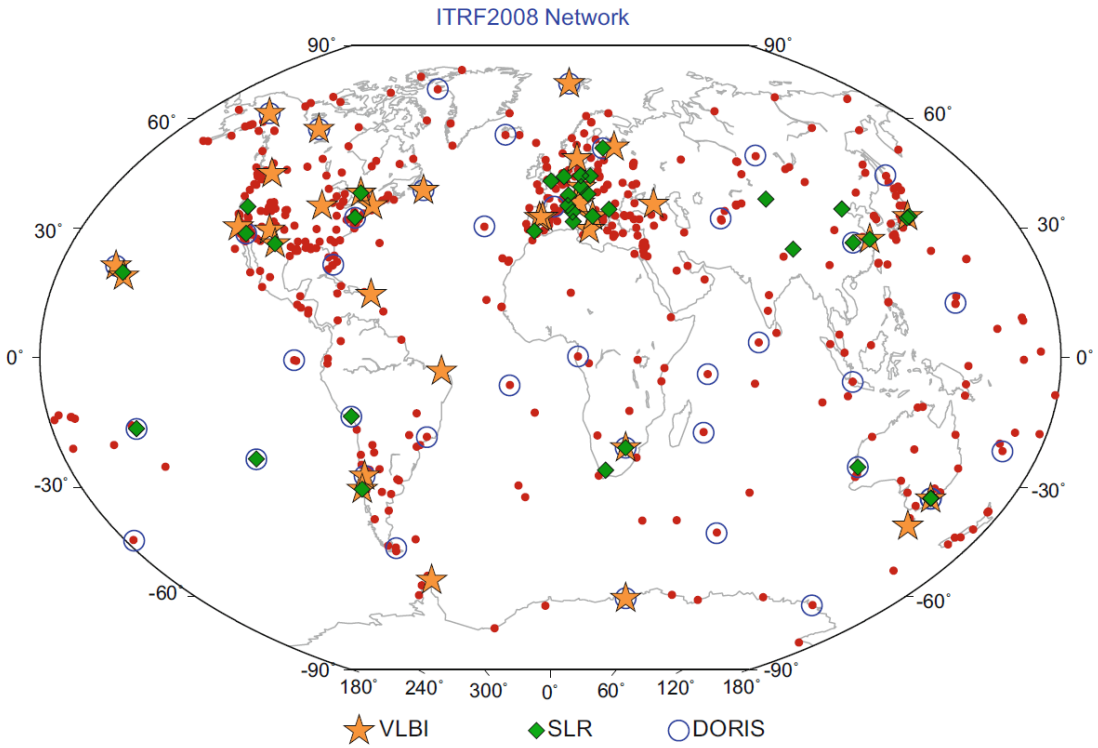


Figure 4.2: ITRF2008 network. Figure adapted from Altamimi et al. (2011).

Interested readers are referred to Dermanis (2001; 2004); Sillard and Boucher (2001); Altamimi et al. (2002a; 2004) or to Chapter 4 of the IERS Conventions (Petit and Luzum, 2010) for a more detailed description regarding the type of constraints applied by the techniques, and the minimum constraints concept in general, which were used to derive ITRF2008.

4.3.2. Geocentric Datum of Malaysia 2000 (GDM2000)

Geocentric Datum of Malaysia 2000 or GDM2000 is the new national geodetic datum for Malaysia that replaces the old datum, i.e. Malayan Revised Triangulation 1948 (MRT48) and Borneo Triangulation 1968 (BT68) (JUPEM, 2009a). It can be regarded as an extension of ITRF2000 (Altamimi et al. 2002b), developed by the Department of Survey and Mapping Malaysia (JUPEM) based upon the dire needs for the accurate coordinate system to support local GPS applications. GDM2000 was officially launched nationwide on 26 August 2003.

Realisation of GDM2000, among others, is made through Malaysia Real-Time Kinematic GNSS Network (MyRTKnet), which is the permanent GNSS network setup by JUPEM since 2002. The coordinate of the stations is referred to epoch 1 January 2000. GDM2000 also had undergone a revision in 2009 owing to few earthquakes in Sumatra. JUPEM (2009a) has reported the accumulative stations' displacement due to three major earthquakes, i.e. in 2004, 2005 and 2007, ranges from 1.0 to 25.8 cm. Consequently, the displaced stations are not suitable for high accuracy applications. A multiple-regression parameter has been derived to relate the coordinate from the previous to the latest realisation of GDM2000 (JUPEM, 2009b). **Figure 4.3** shows the location of 78 MyRTKnet stations, whereby 50 stations are located in Peninsular Malaysia and the remaining 28 stations are in East Malaysia. The current spacing of these stations is ranging between 30 and 100 km, with longer distances observed in East Malaysia. MyRTKnet allows users to obtain a real-time position using single GNSS receiver with accuracy better than 3 cm in horizontal and 6 cm in vertical (JUPEM, 2008).

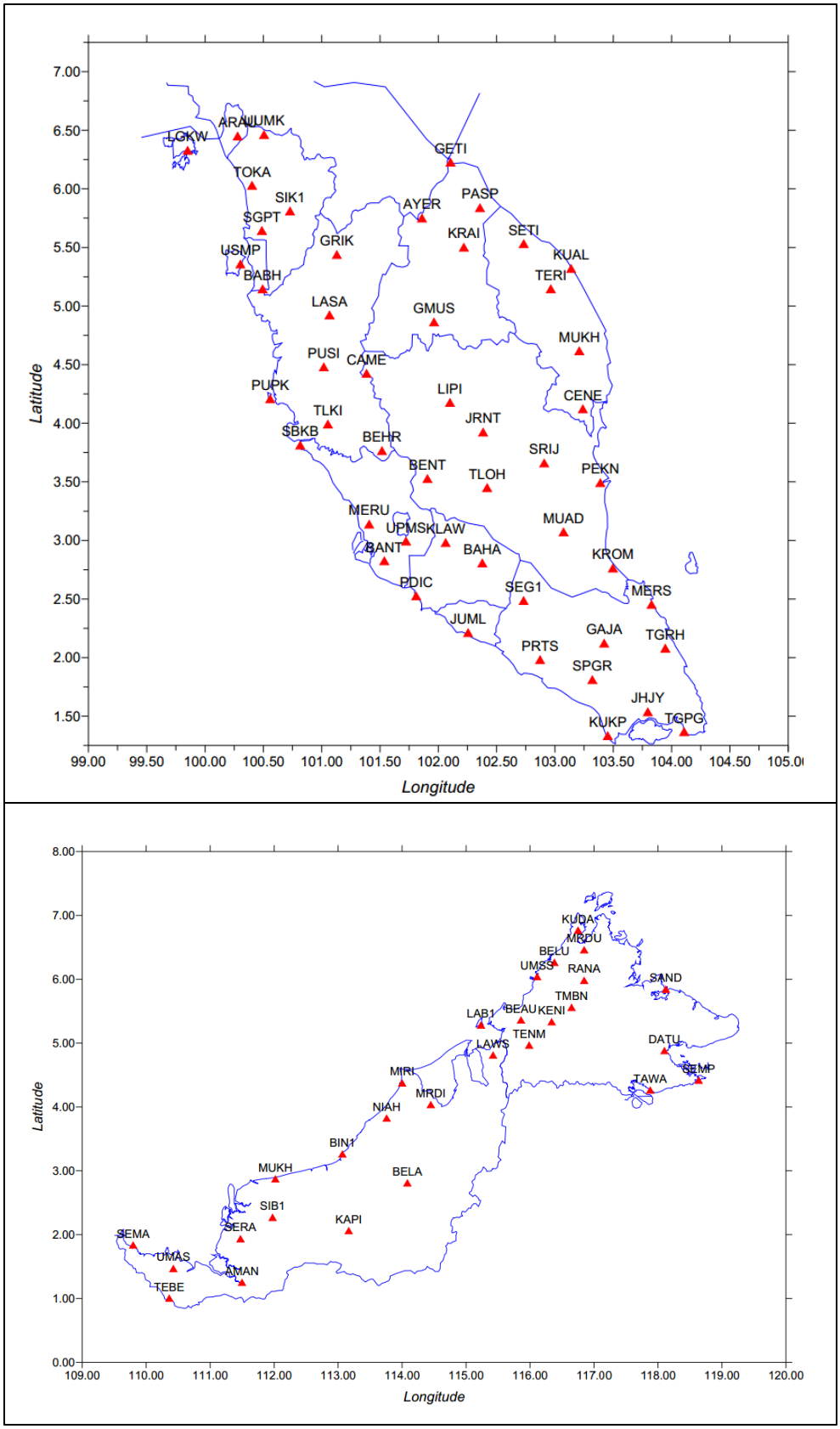


Figure 4.3: The distribution of MyRTKnet stations in Peninsular Malaysia (top) and East Malaysia (bottom). Figure adapted from JUPEM (2009a).

4.4. Bernese GNSS Software

There are three high-precision GNSS software package highly regarded for data processing especially for scientific studies requiring accurate geodetic positioning. They are the Bernese software developed by the Astronomical Institute of University of Berne (AIUB), the GIPSY software developed by the Jet Propulsion Laboratory (JPL) and the GAMIT software developed by the Massachusetts Institute of Technology (MIT) and Scripps Institution of Oceanography (SIO) (Kouba, 2009b). Some other renowned software used by the IGS Analysis Centres are listed in **Table 4.4**. In this study, Bernese GNSS software version 5.2, hereafter termed as Bernese, is utilised for GNSS data processing. The software is widely used by researchers around the world. The geographical distribution of institutions using the software is shown in **Figure 4.4**.

The software was originally developed for geodetic monitoring and GNSS satellite orbit determination (Dach et al., 2015). However, it has been adopted for other applications such as monitoring ionosphere and troposphere, estimating clock, time transfer and earth orientation parameters. Bernese achieves high performance, high accuracy, and high flexibility for GPS/GLONASS post-processing. Typical users include scientists for research and education, national survey agencies responsible for high-accuracy GNSS surveys (e.g. first-order networks), agencies responsible for the maintenance of CORS networks and commercial users with complex applications demanding high accuracy, reliability, and high productivity (Dach et al., 2015).

One of the benefits of using Bernese is the ability to do batch processing for multi-session GNSS data via Bernese Processing Engine (BPE). It covers processing using PPP or DD (small or large network) even with a combination of different receiver types. Nevertheless, the main advantage lies in its ability to perform ambiguity resolution over long baselines (greater than 1000 km), combine processing of GPS and GLONASS observations and generate minimally constrained network solutions. Furthermore, Bernese employs complex modelling for biases and errors presented in GPS observations (Dach et al., 2015).

Table 4.4: List of software used by the IGS analysis centres (see *ftp://igs.org/pub/center/analysis/*, accessed 04.01.2017).

IGS Analysis Centre	Software
Center for Orbit Determination in Europe (CODE)	• Bernese GNSS Software version 5.3
Natural Resources Canada (EMR)	• GIPSY OASIS II version 6.3 • Bernese GNSS Software version 5.2
European Space Agency (ESA)	• NAPEOS version 3.9
Helmholtz Centre Potsdam	• EPOS.P8
Geodetic Observatory Pecny (GOP)	• Bernese GPS software version 5.0
GRGS-CNES/CLS	• GINS software • DYNAMO software
Information and Analysis Center of Navigation (IAC) / Mission Control Center (MCC)	• STARK software • POLAR software
Jet Propulsion Laboratory (JPL)	• GIPSY OASIS II version 6.3
Massachusetts Institute of Technology (MIT)	• GAMIT version 10.32 • GLOBK version 5.12
National Oceanic and Atmospheric Administration (NOAA)	• arc software • orb software (replaced arc on 28 July 2009) • pages software • gpscom software
GeoForschungsZentrum (GFZ) Potsdam	• Bernese GPS Software version 5.1
Scripps Orbit and Permanent Array Center (SOPAC)	• GAMIT version 10.20 • GLOBK version 5.08
Regional Network for South America (SIR)	• Bernese GPS Software version 4.2
French Consortium of University of La Rochelle	• GAMIT • GLOBK • CATREF
U.S. Naval Observatory (USNO)	• Bernese GPS Software version 5.0
Wuhan University (WHU)	• PANDA Software

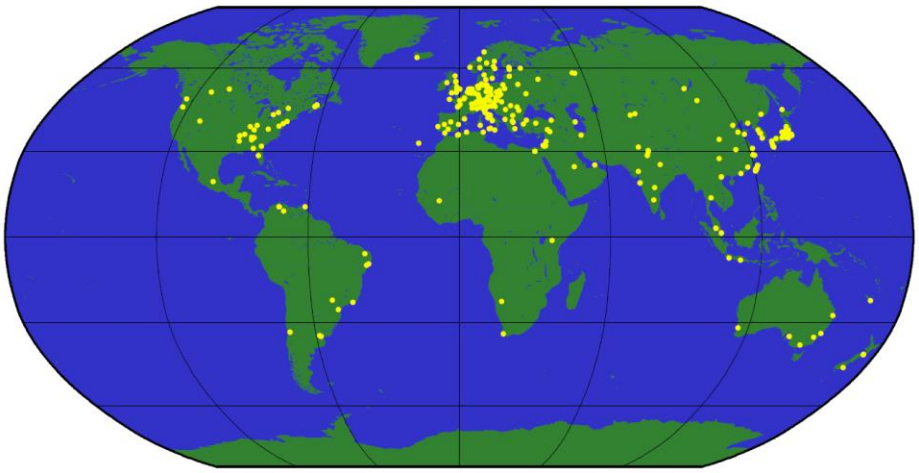


Figure 4.4: Geographical distribution of institutions using the Bernese GPS Software. Figure adapted from Dach et al. (2008).

The Graphical User Interface (GUI) of the software utilises PERL script for data input manipulation and scripts. There are four major areas in the software, namely program, user, data, and temporary. The "Program area" consists of the core of the program system, source code and executables, master options, BPE scripts, as well as general data files that provide basic information necessary for processing GNSS data. This area is independent of specific users and from any project. The "User area" stores user-specific configuration files including the BPE-related files, allowing multiple users to use the software with their unique configurations. The "Data area", on the other hand, is divided into a few directories, namely datapool, campaign, and savedisk. The datapool contains local copies of external files, such as from IGS analysis centres that can be shared between users. These include global ionospheric models, differential code biases, precise orbits, precise clocks, and earth orientation parameters. It eliminates the need to download the data each time when starting the processing. This directory also contains an archive of Receiver Independent Exchange Format (RINEX) files that can then be copied into the campaign directory. As the name implies, the campaign directory holds campaign specific files, whereas the savedisk areas store the main results from the processing. This area serves as a backup for the main results from the campaign directory, allowing users to clean up the campaign area without losing important files. It is also intended for long-term archive of the result files. The structure of folder can be organised freely according to the user's needs. Last but not least, "Temporary area" is allocated for temporary files during BPE run (Dach et al., 2015).

4.5. GPS Processing Strategy

There is a massive amount of GPS data involved in this study; thus it can benefit from using BPE for automated processing. The author has developed two BPEs, namely the PPP.PCF and the DD.PCF for GPS processing using PPP and DD strategies, respectively. The developed BPEs address all biases and errors discussed previously in **Section 4.2.2**. In order to obtain the highest possible precision as well as the consistency of the products with the models used in the software (e.g. for orbital modelling), the BPEs is customised to utilise GNSS products from CODE - the developer of Bernese and also one of the IGS analyses centres. Other external products, namely ocean tidal loading parameters are retrieved from the web service provided by the Onsala Space Observatory, Chalmers University of Technology, whereas parameters necessary for the estimation of the troposphere is attained from the Global Geodetic Observing System, Vienna University of Technology. The list of products used in this study is summarised in **Table 4.5**. There are four Vienna Mapping Function-1 (VMF-1) files each day, which need to be merged with the first file of the following day to produce a single file. An independent GPS tool has been developed by the author using Visual Basic 2013 to facilitate this process. It eliminates the tasks of navigating through the websites and downloading the products manually as well as merging the VMF-1 files, which would be cumbersome when working with extensive data.

Table 4.5: External products used in the processing.

Product	File Format	Website
Precise satellites orbit	COD*wwwwd*.EPH	*ftp://ftp.unibe.ch/aiub/REPRO_yyyy/*
Precise satellites clock	COD*wwwwd*.CLK	
Global ionosphere model	COD*wwwwd*.ION	
Earth Rotation Parameters (ERP) information from an IERS formatted pole	COD*wwww*7.ERP	
Differential code biases	P1P2*yymm*.DCB P1C1*yymm*.DCB	
Ocean tidal loading parameters	*.BLQ	*http://holt.oso.chalmers.se/loading/*
Vienna Mapping Function-1 (VMF-1) coefficients	VMFG_*yyyymmdd*.H*ss*	*http://ggosatm.hg.tuwien.ac.at/DELAY/GRID/VMFG*

* *wwww* stands for the GPS week and *d* is the respective day of the data in that week (i.e. from 0 to 6).

* *yy* and *mm* are the two digits year and month of the data respectively.

* *yyyy* is the year and *ss* is the session of the data. VMF-1 file is produced at six hours interval, thus *ss* corresponds to 00, 06, 12, or 18.

4.5.1. Using Precise Point Positioning (PPP)

Figure 4.5 shows the workflow of PPP.PCF developed in this work. In general, it can be divided into four stages: (1) data preparation, (2) pre-processing, (3) main processing, and (4) extracting and saving the results. The list and description of Bernese programs involved in each stage are summarised in **Table 4.6**. The whole process is controlled by the actions of Perl scripts. GPS daily data is processed in a continuous run, from and to a user specified dates. The data preparation stage mainly deals with files transfer from the datapool area to the specific directories in the campaign area (**Section 4.4**), defining the geodetic datum and coordinate reference epoch, as well as converting external files to Bernese formatted files (i.e. ERP, and precise satellites orbit and clock). Program CRDMERGE defines the geodetic datum and coordinate reference epoch for all stations involved in the processing to a common value, i.e. IGb08 at observation epoch, to be consistent with the epoch of precise satellites orbit and clock. Program RNXCLK converts a precise satellites clock file to Bernese format, program POLUPD extracts the Earth Rotation Parameters (ERP) from an IERS formatted pole file into a Bernese formatted pole file, whereas program PRETAB converts a precise satellite's orbit in Earth-fixed frame into a tabular position in the inertial frame. Subsequently, program ORBGEN integrates the equations of motions using the positions given in the tabular orbit file to produce a Bernese standard orbit file. This file will be utilised in all processing programs needing orbit information.

The pre-processing step aims to synchronise the receiver clocks with GPS time, clean the RINEX observations data, identify and repair cycle slips, and to update the list of ambiguities for phase measurements. The receiver clocks synchronisation is achieved using CODSPP program. Program CODXTR allows inspection of the station/receiver related problems based on the results of CODSPP. It should be mentioned that Bernese offers two possibilities for pre-processing the RINEX file, particularly for the phase measurements. If high-rate satellite clocks (equivalent to the sampling rate of the data) are available, as in the case of this work, the pre-processing can be made using MAUPRP program to detect and correct cycle slips, identify outliers, and to update the list of ambiguities for phase measurement. Alternatively, program RNXSMT can be utilised which is only based on the consistency between code and phase data of the two frequencies. The code measurements are smoothed using RNXSMT prior to their conversion to Bernese zero-difference format using RNXOBV3. At this stage, no change is made on the phase observations.

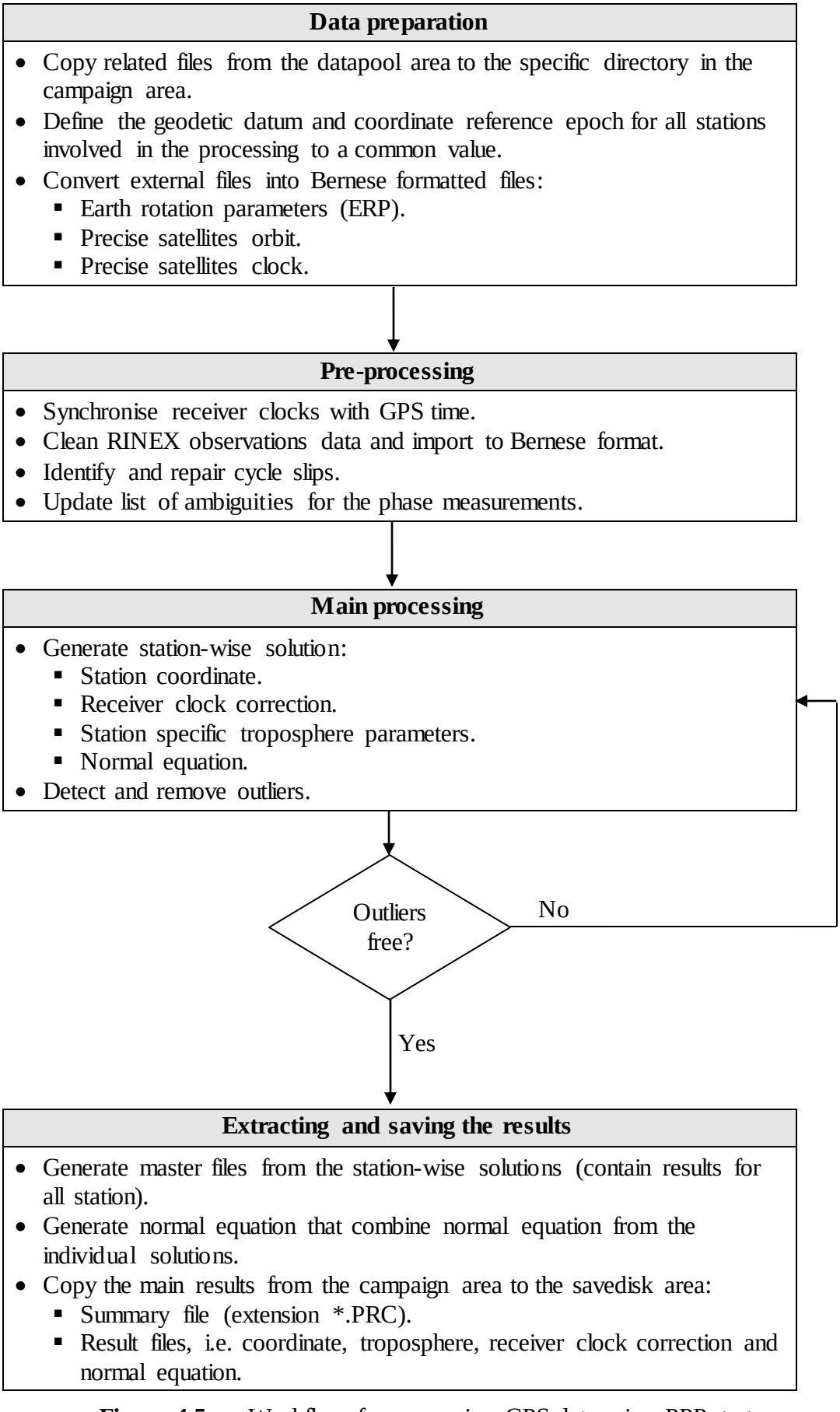


Figure 4.5: Workflow for processing GPS data using PPP strategy.

Table 4.6: List and description of Bernese programs for PPP processing.

Step	Bernese Program	Description	
1.	CRDMERGE	Define the geodetic datum and coordinate reference epoch for all stations involved in the processing to a common value, i.e. IGb08 at observation epoch. The program is configured to run in parallel to speed up the processing time.	Data preparation
2.	POLUPD	Extract the ERP information from an IERS formatted pole file into a Bernese formatted pole file.	
3.	PRETAB	Convert the orbit information from a precise orbit file in SP3c format (Earth-fixed frame) into tabular position in an inertial frame for subsequent numerical integration by ORBGEN.	
4.	ORBGEN	Integrate the equations of motion using the positions given in the tabular orbit file to produce a Bernese standard orbit file. The resulting standard orbit file will be used in all processing programs needing orbit information.	
5.	RNXCLK	Convert a precise clock file into a Bernese satellite clock file.	
6.	CODSPP	Synchronise the receiver clocks with GPS time. The outliers detected on code measurements are marked for further processing.	Pre-processing
7.	CODXTR	Create a summary for the CODSPP to facilitate in identifying problematic stations.	
8.	RNXSMT	Clean and smooth the code measurements. No change is made on the phase observations. Processing is done in parallel to speed up the processing time, i.e. the program receives a list of RINEX files to be cleaned in one run.	
9.	RNXGRA	Produce a summary of the smoothed code measurements, giving a complete overview of observed satellites, involved stations and their performance.	
10.	RNXOBV3	Create Bernese observation files from the code and phase measurements. The results are zero-difference code and phase observation files for each station.	
11.	MAUPRP	Pre-processing of phase measurements to detect and correct cycle slips, identify outliers, and to update the list of ambiguities for the phase measurements. The process requires well-established satellite clock corrections with the same sampling rate as the data files (i.e. 30 seconds). The higher sampling for screening the phase observations is necessary to improve the capability to distinguish between potential cycle slips and the change of ionosphere from one epoch to the next. The program is configured to run in parallel to speed up the processing time.	
12.	MPRXTR	Extract essential information from the MAUPRP program output files into a summary table.	

Table 4.6: (continue).

Step	Bernese Program	Description	
13.	GPSEST	Run the first solution and generate a residual file for data screening based on the ionosphere-free linear combination. Normalised residuals are written as an elevation-dependent weighting of observations is applied.	Main processing
14.	RESRMS	Screen the residual file for outliers exceeding a certain threshold.	
15.	SATMRK	Mark the identified outliers in observation files (flagged as bad data).	
16.	GPSEST	Run the final solution based on the cleaned observations. The results are stored in station-wise result files. • Station coordinate. • Receiver clock corrections. • Station-specific troposphere parameters. • Normal equation.	
17.	ADDNEQ2	Generate the PPP results for each station in Bernese and Solution INdependent EXchange (SINEX) format.	
18.	GPSXTR	Extract the outputs from GPSEST program, producing an overview of the PPP solution and the data cleaning.	Extracting and saving the results
19.	RESRMS	Produce the residual statistics based on the files generated in the first solution (before outliers' rejection).	
20.	RESRMS	Produce the residual statistics based on the files generated in the final solution (after outliers' rejection).	
21.	RESCHK	Create residual screening statistics.	
22.	CRDMERGE	Merge station-specific coordinate files into a single coordinate file.	
23.	ADDNEQ2	Collect the normal equations and troposphere estimates (from step 16), and produces a single Bernese formatted file and troposphere SINEX file.	
24.	CCRNXC	Combine the station-specific clock RINEX files (from step 16), and produces a single RINEX clock file.	
25.	ADDNEQ2	Write a single SINEX file and a combined normal equation file containing all stations based on the normal equation files generated for each station in the final solution (step 16).	

* Main processing is performed based on the station by station data.

* Step (13) - (15) run iteratively with different (decreasing) limits for outlier detection in program RESRMS. There are 6 iterations in total with the threshold reduces from 600 m to 0.006 m.

The main processing for PPP solution is conducted in a station wise manner and is customised to run in parallel to speed up the processing time. Estimation of parameters, including modelling of errors and biases as described in **Section 4.2.2**, is made using program GPSEST. The basic observables are ionosphere-free linear combination formed between frequency f_1 and f_2. Program RESRMS screens the residual for outliers exceeding a predefined threshold, which is configured as 0.006 m. Program SATMRK then marks the identified outliers to be excluded in the next solution. The final estimation is based on the outliers-free solution, and the results are saved as an independent file for each station, i.e. coordinate, receiver clock corrections, station-specific troposphere parameters and normal equation. It should be noted that tropospheric modelling and estimation is accomplished using VMF-1. This topic requires particular attention as it provides one of the most challenging error sources in GPS measurement. Modelling and mitigation of tropospheric effects are discussed further in **Section 6.4**. It is worth noting that the final estimation is based on float ambiguities resolution, no attempt is made to fix the ambiguities to their integer value. Program ADDNEQ2 then generates the PPP result files for each station in Bernese, and Solution INdependent EXchange (SINEX) formats.

Following completion of processing for all stations, program GPSXTR is called to extract the outputs from the final GPSEST. Likewise, program RESRMS is called twice to produce residual statistics for the first and the final solutions. This step is followed by program RESCHK to create residual screening statistics, which allow inspection of the number of rejected observations. Problematic stations or satellites can be identified by a high percentage of deleted data. The individual station's solution is compiled to a single file using program CRDMERGE for coordinate, program CCRNXC for receiver clocks offset, and program ADDNEQ2 for normal equation and troposphere. The resultant files are then copied to savedisk area for backup. An example of the coordinate estimation from the program ADDNEQ2 is shown in **Figure 4.6**. The results of data processing from the year 2007 to 2011 are reported in **Chapter 7** along with their analysis.

Station coordinates and velocities:

Reference epoch: 2011-01-01 12:00:00

Station name	Typ	A priori value	Estimated value	Correction	RMS error	3-D ellipsoid		2-D ellipse	
ALIC	X	-4052052.37340	-4052052.37340	0.00000	0.00223				
	Y	4212836.02594	4212836.02594	0.00000	0.00230				
	Z	-2545105.07578	-2545105.07578	0.00000	0.00130				
	U	603.23640	603.23640	0.00000	0.00320	0.00320	2.0		
	N	-23.6701150	-23.6701150	0.00000	0.00059	0.00058	178.7	0.00059	178.8
	E	133.8855188	133.8855188	0.00000	0.00118	0.00118	0.1	0.00118	
BAKO	X	-1836969.26771	-1836969.26771	0.00000	0.00109				
	Y	6065617.01759	6065617.01759	0.00000	0.00191				
	Z	-716257.86692	-716257.86692	0.00000	0.00041				
	U	158.12274	158.12275	0.00000	0.00193	0.00193	6.5		
	N	-6.4910550	-6.4910550	0.00000	0.00038	0.00038	178.1	0.00038	178.7
	E	106.8489119	106.8489119	0.00000	0.00106	0.00105	-1.9	0.00106	
COCO	X	-741950.67386	-741950.67386	0.00000	0.00098				
	Y	6190961.68694	6190961.68694	0.00000	0.00156				
	Z	-1337767.87368	-1337767.87368	0.00000	0.00050				
	U	-35.28238	-35.28238	0.00000	0.00160	0.00160	2.9		
	N	-12.1883446	-12.1883446	0.00000	0.00036	0.00036	0.2	0.00036	0.2
	E	96.8339717	96.8339717	0.00000	0.00098	0.00098	1.0	0.00098	
CUSV	X	-1132914.77517	-1132914.77517	0.00000	0.00095				
	Y	6092528.58465	6092528.58465	0.00000	0.00129				
	Z	1504633.24539	1504633.24539	0.00000	0.00043				
	U	74.28189	74.28189	0.00000	0.00135	0.00135	5.3		
	N	13.7359144	13.7359144	0.00000	0.00032	0.00031	178.4	0.00032	178.5
	E	100.5339215	100.5339215	0.00001	0.00092	0.00092	1.0	0.00092	

Figure 4.6: An example of the result from coordinate estimation using ADDNEQ2.

4.5.2. Using Double-Difference (DD)

The BPE, developed in this work, for processing using DD strategy (i.e. DD.PCF) is customised for the regional network. Similar to the BPE for PPP processing, the whole processes are controlled by the actions of Perl scripts. GPS daily data is handled in a continuous run, from and to a user specified dates. **Figure 4.7** shows the overall workflow of the BPE, whereas the corresponding **Table 4.7** describes the Bernese programs used to execute the tasks. In general, the processing consists of seven stages: (1) data preparation, (2) pre-processing code measurements, (3) forming single-difference and pre-processing phase measurements, (4) computation of float network solution, (5) ambiguity resolution, (6) computation of fixed network solution, and (7) extraction and saving the results.

In the first stage, all required files are copied from the datapool area to the specific directories in the campaign area. The coordinates of reference stations as well as target stations are propagated to the observation epoch using program COOVEL, and subsequently merged into a single coordinate file using program CRDMERGE. Program POLUPD is called to extract the ERP information from an IERS formatted pole into a Bernese formatted pole file. Similarly, program PRETAB converts a satellite precise orbit from SP3c format into tabular position in an inertial frame, which is then used by ORBGEN for the derivation of satellites orbits in Bernese standard format. The resulting standard orbit file will be used in all processing programs needing orbit information.

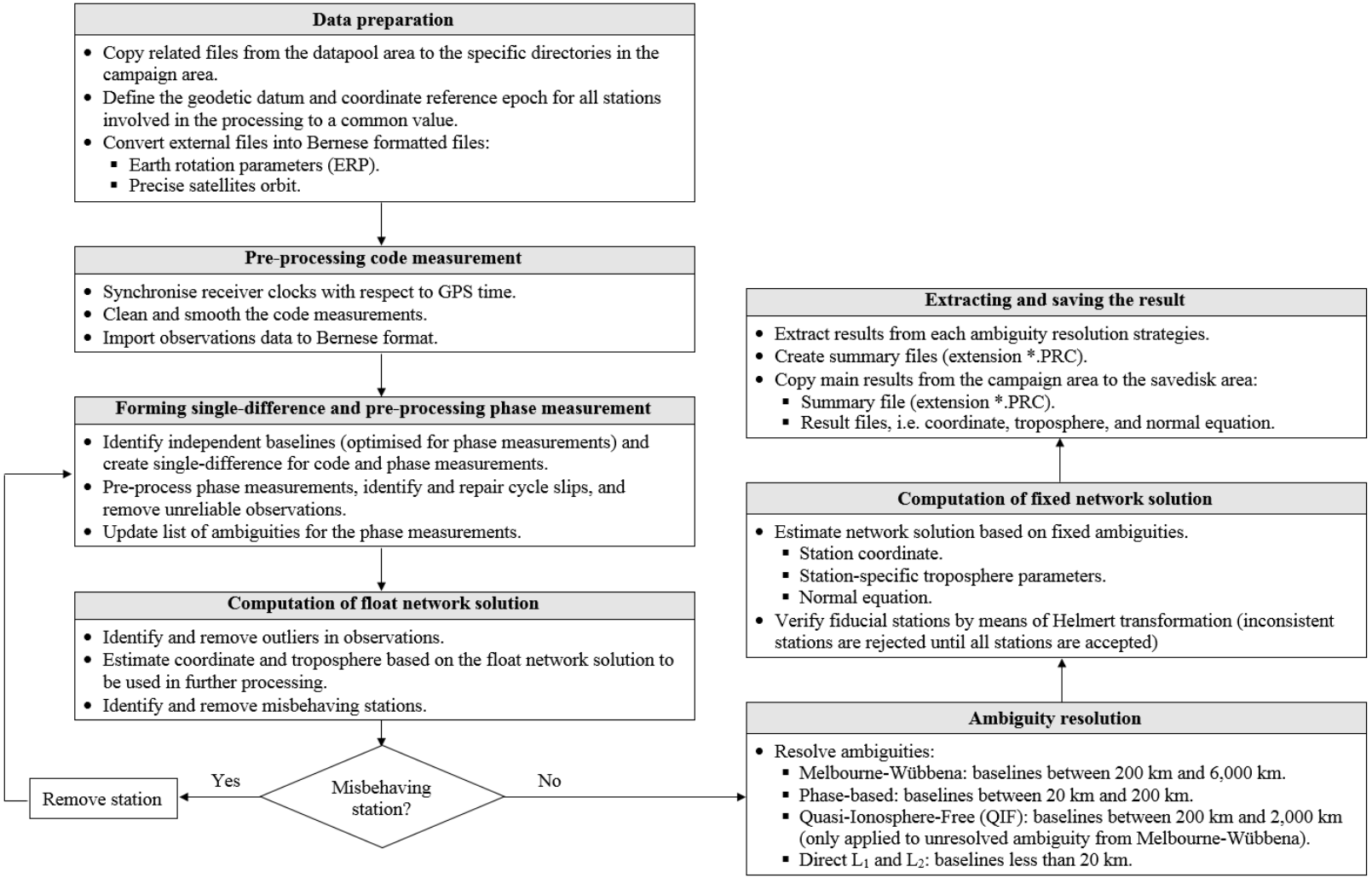


Figure 4.7: Workflow for processing GPS data using DD strategy.

Table 4.7: List and description of Bernese programs for DD processing.

Step	Bernese Program	Description	
1.	COOVEL	Propagate the coordinate of IGS reference stations from the reference epoch (i.e. 1 January 2005) to the date of observation using velocity.	Data preparation
2.	COOVEL	Propagate the coordinate of target stations to the date of observation using velocity.	
3.	CRDMERGE	Merge the coordinate of IGS reference stations and target stations into a single coordinate file.	
4.	POLUPD	Extract the ERP information from an IERS formatted pole file into a Bernese formatted pole file.	
5.	PRETAB	Convert the orbit information from a precise orbit file in SP3c format (Earth-fixed frame) into tabular position in an inertial frame for subsequent numerical integration by ORBGEN.	
6.	ORBGEN	Integrate the equations of motion using the positions given in the tabular orbit file to produce a Bernese standard orbit file. The resulting standard orbit file will be used in all processing programs needing orbit information.	
7.	CODSPP	Synchronise the receiver clocks with GPS time. The outliers detected on code measurements are marked for further processing.	Pre-processing code measurement
8.	CODXTR	Create a summary for the CODSPP to facilitate in identifying problematic stations.	
9.	RNXSMT	Clean and smooth the code measurements. No change is made on the phase observations. Processing is done in parallel to speed up the processing time.	
10.	RNXGRA	Produce a summary of the smoothed code measurements, giving a complete overview of observed satellites, involved stations and their performance.	
11.	RNXOBV3	Create Bernese observation files from the code and phase measurements. The results are zero-difference code and phase observation files for each station.	
12.	SNGDIF	Select a complete set of independent baselines and create phase single-difference observation files (optimal network configuration for the phase measurements).	Forming single-difference and pre-processing phase measurement
13.	SNGDIF	Create code single-difference observation files for the same baselines as in step 12.	
14.	MAUPRP	Pre-process the phase single-difference files. Cycle slips are detected and corrected. If the size of the cycle slips cannot be reliably determined, a new ambiguity is set up. Unpaired observations (i.e. only L_1 or L_2 at an epoch) and observations gathered at very low elevation angles are flagged as unusable. Processing is done in parallel.	
15.	MPRXTR	Extract essential information from the MAUPRP program output files into a summary table.	

Table 4.7: (continue).

Step	Bernese Program	Description	
16.	GPSEST	Run the first DD float solution using the ionosphere-free linear combination. All coordinate are loosely constrained to their a priori values.	Computation of float network solution
17.	RESRMS	Screen the residual file for outliers exceeding a certain threshold.	
18.	SATMRK	Mark the identified outliers in observation files (flagged as bad data).	
19.	GPSEST	Run the final DD float solution using the cleaned ionosphere-free linear combination. Store the normal equation files.	
20.	ADDNEQ2	Use normal equation files from the GPSEST to perform a network solution with real-valued ambiguities. Save the results for further use in the ambiguity resolution step: • Station coordinate. • Station-specific troposphere parameters.	
21.	GPSXTR	Extract outputs from the GPSEST after removal of outliers (overview of the float solution).	
22.	RESRMS	Produce the residual statistics based on the files generated in the first solution (before outliers' rejection).	
23.	RESRMS	Produce the residual statistics based on the files generated in the final solution (after outliers' rejection).	
24.	RESCHK	Create residual screening statistics.	
	Ambiguity resolution based on Melbourne-Wübbena linear combination.		Ambiguity Resolution
25.	BASLST	Select all baselines between 200 km to 6,000 km.	
26.	GPSEST	Compute solution using only code measurements, where coordinate and troposphere estimates from the float solution (step 20) are introduced as known.	
27.	RESRMS	Screen the residual file for outliers.	
28.	SATMRK	Mark the identified outliers in observation files (flagged as bad data) for subsequent processing.	
29.	GPSEST	Perform wide-lane ambiguity resolution based on the Melbourne-Wübbena linear combination.	
30.	GPSEST	Introduce the resolved wide-lane ambiguities and perform narrow-lane ambiguity resolution.	
	Phase-based ambiguity resolution.		
31.	BASLST	Select all baselines between 20 km to 200 km.	
32.	GPSEST	Perform phase-based wide-lane ambiguity resolution for the selected baseline using sigma-dependent strategy.	
33.	GPSEST	Introduce the resolved phase-based wide-lane ambiguities and perform phase-based narrow-lane ambiguity resolution.	

Table 4.7: (continue).

Step	Bernese Program	Description	
	Ambiguity resolution based on Quasi-Ionosphere-Free (QIF)		Ambiguity Resolution
34.	BASLST	Select all baselines between 200 km to 2,000 km.	
35.	GPSEST	Perform ambiguity resolution using QIF strategy (only applied to the remaining ambiguities).	
	Ambiguity resolution based on a direct L_1 and L_2 observations		
36.	BASLST	Select all baselines shorter than 20 km.	
37.	GPSEST	Perform ambiguity resolution from a direct L_1 and L_2 observations using sigma-dependent strategy.	
38.	GPSEST	Compute ambiguity-fixed network solution. The resolved ambiguities are introduced. All station are loosely constraint to their a priori value. Save normal equation.	Computation of fixed network solution
39.	ADDNEQ2	Compute network solution based on the normal equation from the GPSEST. The datum is realised by three no-net-translation conditions imposed on a set of reference frame sites (IGb 08 reference coordinates) included in the processing. • Station coordinate. • Station-specific troposphere parameters. • Normal equation.	
40.	HELMCHK	Verify the estimated coordinates of all involved reference station by means of a Helmert transformation. If discrepancies are detected, the solution is recomputed with a reduced set of fiducial stations.	
41.	GPSXTR	Extract result from the ambiguity resolution using code-based wide-lane (step 29).	Extracting and saving the results
42.	GPSXTR	Extract result from the ambiguity resolution using code-based narrow-lane (step 30).	
43.	GPSXTR	Extract result from the ambiguity resolution using phase-based wide-lane (step 32).	
44.	GPSXTR	Extract result from the ambiguity resolution using phase-based narrow-lane (step 33).	
45.	GPSXTR	Extract the result from the ambiguity resolution using QIF strategy (step 35).	
46.	GPSXTR	Extract result from the ambiguity resolution using direct L_1 / L_2 observations (step 37).	
47.	GPSXTR	Extract result from the final ADDNEQ2, producing an overview of the ambiguity-fixed network solution.	

* Step (16) - (18) run iteratively with different (decreasing) limits for outlier detection in program RESRMS. There are 6 iterations in total with the threshold reduces from 400 m to 0.004 m.

* Step (39) - (40) run iteratively until all reference stations are accepted.

The second stage, i.e. pre-processing code measurements, consists of receiver clocks synchronisation with GPS time, clean and smooth the code measurements, as well as converting the observation files to Bernese format. Program CODSPP synchronises the receiver clocks to GPS time on a sub-microsecond level by performing a code-based zero-difference point positioning. A basic outlier detection is also performed. Program CODXTR creates a summary from the output files written in the CODSPP step. High RMS value or significant outliers indicate a site with bad code tracking performance. Code measurements are cleaned using program RNXSMT based on the consistency between code and phase data of the two frequencies. Program RNXGRA produces a summary of the smoothed code measurements, giving an overview of the observed satellites, involved stations, and their performance. Bernese zero-difference code and phase observation files for each station are created from the observations data using program RNXOBV3.

The third step mainly deals with the formation of single-difference observation files and pre-processing the phase measurements. A complete set of independent baselines is identified using program SNGDIF, which is optimised for the phase measurements. The adopted strategy for the selection is OBS-MAX that takes into account the number of common observations for the associated stations. From all possible combinations, a set of baselines with maximum common observations is chosen, which will be beneficial for DD processing. Alternatively, users can define the baselines manually (option DEFINED), based on the shortest distance (option SHORTEST), or simply from a common reference station (option STAR). Single-difference files are created both for the phase and code measurements, which are essential for ambiguity resolution using Melbourne-Wübbena linear combination (combination of code and phase measurements). Following that, program MAUPRP pre-processes the single-difference phase observation files. Cycle slips are detected and repaired, and a new ambiguity is set up if the size of the cycle slips cannot be determined reliably. Measurements made at low elevation angle, and any unpaired observations (i.e. only L_1 or L_2 at an epoch) are flagged as unusable. A summary file for the process is created using program MPRXTR.

The first network solution is computed in the fourth step based on the float ambiguities. Several GPSEST runs are made iteratively to detect outliers (using program RESRMS) that are subsequently flagged by program SATMRK to be excluded in the next run. In this step, all stations are fixed to their a priori coordinates. Normal equation files are generated once the observations are cleaned from the outliers (defined as bigger than 4 mm). Estimation of the coordinate and troposphere is made using program ADDNEQ2, based on the normal equation files from the final GPSEST. Program GPSXTR extracts result from the GPSEST. Following that, program

RESRMS is called twice to produce residual statistics, i.e. for the first and the final GPSEST runs. Program RESCHK create residual screening statistics from the results, which can then be used to detect bad stations or satellites. Problematic stations or satellites are indicated by large residuals and a high percentage of deleted data. Any misbehaving stations are rejected by program RESCHK to ensure reliable result from the processing. Since problematic stations may influence other stations through errors propagation, only one station is rejected per iteration, which has the highest RMS. In this case, the process of baseline creation is repeated to create a network of baselines without the deficient station (step 12 in **Table 4.7**). The whole processes continues until all stations are accepted.

Ambiguity resolution can be carried out independently for each baseline; thus, the fifth step is configured to run in parallel to speed up the required processing time. In this step, the coordinate and troposphere estimates from the float network solution are introduced as known. For each baseline, the coordinate of the second station is estimated with respect to the first one. Technical discussion about ambiguity resolution is beyond the scope of this work. Interested readers are referred to various publications on the topic, such as from Hofmann-Wellenhof et al. (2008) and Leick et al. (2015). The following ambiguity resolution strategies are adopted, depending on the baselines length (Dach et al., 2015):

i. Melbourne-Wübbena linear combination: for baseline length between 200 km and 6,000 km
ii. Phase-based: for baseline length between 20 km to 200 km.
iii. Quasi-Ionosphere-Free (QIF) strategy: for baseline length between 200 km and 2,000 km (only applied to unresolved ambiguities from the Melbourne-Wübbena linear combination).
iv. Direct L1 and L2: for baseline length shorter than 20 km.

In each strategy, selection of baselines is made using program BASLST, whereas the actual task is performed using program GPSEST. Melbourne-Wübbena linear combination depends on both code and phase measurements (Hofmann-Wellenhof et al., 2008). To ensure the reliability of code measurements, the first GPSEST run aims to obtain the code-only solution. Residuals are screen using program RESRMS and outliers are excluded for the next run using program SATMRK. Subsequent runs of program GPSEST aim to fix the wide-lane and narrow-lane ambiguities. The resolved ambiguities are stored in the related observations files. Other adopted strategies for the ambiguity resolution are also carried out in the same manner, i.e. using program BASLST to select relevant baselines, followed by the resolution itself using program GPSEST. It is worth noting that QIF strategy is

only applied to unresolved ambiguity from the Melbourne-Wübbena linear combination. Stochastic ionosphere parameters are estimated in QIF to absorb the impact of the ionosphere (Dach et al., 2015). Meanwhile, sigma-dependent strategy, which is applied in phased-based, and direct L_1 and L_2 ambiguity resolutions, utilises the full variance-covariance information (Dach et al., 2015).

Following completion of the ambiguity resolution step, the observation files can be considered as cleaned and most of the ambiguities are resolved to their integer value. This allows computation of a network solution based on the fixed ambiguity. The resolved ambiguities from the previous step are introduced to the equation and baselines are processed considering their correct correlation using program GPSEST. The resulting normal equation files are stored for the subsequent run using program ADDNEQ2. Although GPSEST is also able to compute the final solution, ADDNEQ2 is preferable owing to its more sophisticated datum definition capabilities. The datum is realised by three-no-net translation conditions imposed on a set of reference frame stations (IGb 08 reference coordinates). Program HELMCHK is called to verify the estimated coordinates through assessment of the reference stations by means of Helmert transformation. The solution is recomputed with a reduced set of reference stations if discrepancies are detected. The output from the HELMCHK program can be used to identify problems concerning the reference sites.

The last stage deals with extracting and saving the results from the processing. A file with extension *.PRC is created for each daily processing to summarise important aspects of the results. Six GPSXTR program are called to extract the result from each ambiguity resolution steps, i.e. code-based wide-lane and narrow-lane (Melbourne-Wübbena linear combination), phase-based wide-lane and narrow-lane, QIF, and direct L_1 / L_2 observations. Additional GPSXTR program is called to extract the result from the final estimation using ADDNEQ2, which provides an overview of the ambiguity-fixed network solution. Important files are then copied from the campaign area to the savedisk area, to facilitate further processing such as estimation of velocities from the saved normal equations. Coordinate estimation from the DD.PCF is similar the one produced from the PPP.PCF, as shown previously in **Figure 4.7**. An example of summary from the ambiguity resolution step is shown in **Appendix B**.

4.5.3. Estimation of the Station Velocity

Accurate station velocity is needed for many investigations on geodynamic processes including plate tectonics, strain rates, sea level rise with respect to vertical land motion, glacial isostatic adjustment, mountain uplift, subsidence, secular unloading/loading of water reservoirs, and ice sheets (Blewitt et al., 2016). There is an increasing demand on detecting millimetre to sub-millimetre level of ground displacement signals in order to further understand regional scale geodetic phenomena, hence, requiring further improvements in the sensitivity of the GPS solutions (He et al., 2017).

Nevertheless, velocity estimation is often made complicated by a variety of errors with different timescales. The presence of seasonal signals can significantly bias velocity estimates, particularly for short time-series (Blewitt and Lavallée, 2002). Equipment changes could introduce data discontinuities or jumps in the coordinate time-series. Other common problems include outliers, time-dependent noises, and un-modelled errors. The noise level in GPS time-series tends to be worse for earlier data when there were fewer satellites and reference frame stations. It also tends to be noisier in summer than in winter owing to the increased variation in atmospheric refractivity, although some stations that are subject to sustained snow cover may experience the opposite seasonal effect (Blewitt et al., 2013).

The errors in GPS time-series are normally characterised by time-correlated noises (also term as coloured noises) and time un-correlated noises (also term as white noises). Some other terms that are normally used to differentiate noises in time-series were described in Zhang et al. (1997) and Mao et al. (1999). Characterisation of these noise terms are made considering their behaviours using spectral analysis (see, e.g. Zhang et al., 1997 and Mao et al., 1999). While the effect of white noises can be reduced significantly through frequent measurement and averaging, this is less useful for time-correlated noises. In particular, it has no benefit at all for one type of time-correlated noises, i.e. the random walk. Examples of the time-correlated noise include the spurious motion of the mark unrelated to Earth's crust motion and miss-modelled parameters such as satellite orbits, Earth orientation, atmosphere, and antenna phase centre.

There are various attempts to retrieve valuable signals from the GPS time-series. For example, Mao et al. (1999) used two methods, namely spectral analysis and Maximum Likelihood Estimation (MLE) to assess time correlated noises in the time-series. They found that a combination of white and flicker noises appears to be the best model for the noise characteristics of all three components, i.e. north, east, and vertical. Both white and flicker noise amplitudes are smallest in the north component and largest in the vertical

components. The white noise part of the vertical component is higher for tropical stations (± 23° latitude) compared to mid-latitude stations. These conclusions were based on daily estimates of 3 years of data for 23 globally distributed GPS stations. Ostini (2012) conducted analysis and quality assessment of GNSS-derived parameter time-series and developed an automated tool to analyse long time-series based on Detection Identification Adaptation (DIA) procedure. Similarly, Blewitt et al. (2016) developed a method, called Median Inter-annual Difference Adjusted for Skewness (MIDAS) to determine accurate GPS station velocities. Yet to date, blind tests conducted on detecting step discontinuities in GPS data prove that the best expert eyeball performs better than the world's best automatic methods (Gazeaux et al., 2013).

The topic of time-series analysis deserves special attention on its own and is beyond the scope of this research. Interested readers are referred to He et al. (2017), which provides a review of current GPS methodologies for producing accurate time-series and their error sources. In this work, time-series analysis is made to estimate the station velocities using weighted linear regression. The analysis is based on daily GPS positions. Weighted linear regression yields estimates of slope and abscissa intercept. The former is the important quality for the investigation of inter-seismic deformation, whereas the latter is the dominant parameter for coseismic deformation (Zhang et al. 1997). A measured station coordinate component x at day number t can be modelled by an initial value of the component x_0 (abscissa intercept) and velocity r (assuming a linear accumulation of deformation) as depicted by Equation (4.1):

$$x(t) = x_0 + r \cdot t + \varepsilon_x(t) \quad \cdots\cdots (4.1)$$

where $\varepsilon_x(t)$ is the un-modelled errors which is assumed to be normally distributed. Implementation of Equation (4.1) to estimate slope and abscissa intercept in this research is realised using a function developed by the author in Matlab software.

4.6. Summary

This chapter has covered, among others, the fundamental principles of GPS, which are paramount to better understand the development of this research. In addition, biases and errors in the GPS observations have been discussed as they may obscure the deformation signals and lead to a wrong interpretation of the results. The discussion also covered coordinate reference system, which forms the basis of coordinate determination using GPS. In particular, IGb08 which is the latest IGS

realisation of ITRF2008 is adopted as the reference frame for the coordinate determination. The said frame can be considered as one of the most accurate reference system available today, thus suited for the purpose of regional deformation study. Likewise, GDM2000, i.e. the local coordinate reference system in Malaysia for GPS-related applications has also been introduced. GDM2000 is based on the ITRF2000. In this research, processing of the GPS data was carried out using Bernese GNSS Software version 5.2. The software framework as well as the processing strategy to achieve high accuracy requirements for deformation analysis are also presented in this chapter. The reasoning behind every decision made by the author is explained at length. It covers processing using both PPP and DD, which were performed using two BPEs developed by the author, namely PPP.PFC and DD.PCF. The latter is customised for processing regional network and benefits from fixed-ambiguity resolution as compared to the former, which is based on float-ambiguity resolution.

CHAPTER 5

DEFORMATION ANALYSIS USING INSAR TIME-SERIES

5.1. Introduction

The primary purpose of this chapter is to discuss the method employed in this research to process the Synthetic Aperture Radar (SAR) dataset, described in **Section 3.5.2**, as one of the components to assess deformation in Johor, Malaysia. The chapter begins with a brief introduction to Interferometric SAR (InSAR) as a unique tool for detecting deformation; discussion on SAR coordinate system to ease interpretation of the result with respect to different coordinate system used in Global Positioning System (GPS) (**Section 4.3**); introduction to Punnet – the software used to process the data; and continue with the approach taken in this work, from image coregistration and resampling to producing the final line-of-sight (LOS)-velocity maps. The discussion also covers improvements made to existing method during the implementation stage. Following that, a method for projecting LOS-velocity to its respective 3-dimensional (3D) components, i.e. northing, easting, and height, is reviewed to allow comparison with the result from other techniques. This chapter finally ends with a summary to highlight essential key-notes of the research with regard to deformation analysis using InSAR time-series.

5.2. Background

5.2.1. Basic InSAR Principle

SAR is an active radar sensor that operates in the microwave domain of the electromagnetic spectrum. Different radar sensors operate at different frequencies, but typically of a few centimetres long (**Table 5.1**). In general, longer wavelength increases the ability to penetrate a dielectric material. As an active sensor, SAR image is created by illuminating the area of interest with electromagnetic pulses, independent of solar illumination, and recording the echoes backscattered from natural and human-made objects to the radar antenna. Therefore, SAR satellite can operate any time of the day compared to optical sensors which typically work only in broad daylight.

Table 5.1: Different frequency bands used by satellite radar sensors.

Band	Frequencies	Wavelengths	Sensors
L	1 – 2 GHz	30 – 15 cm	SEASAT, JERS-1, ALOS-PALSAR
S	2 – 4 GHz	15 – 7.5 cm	HJ-1
C	4 – 8 GHz	7.5 – 3.75 cm	ERS-1, ERS-2, RADARSAT-1, ENVISAT, Sentinel-1
X	8 – 12 GHz	3.75 – 2.5 cm	COSMO-SkyMed, TerraSAR-X, Tandem-X

Radar sensors can record both amplitude and phase for each ground target. Amplitude represents the radar backscatter which is brighter for a pixel with stronger backscatter. On the other hand, the phase is related to the sensor-to-target distance as well as the interaction of electromagnetic signal with the radar targets. The sensor-to-target distance can be expressed as an integer number of wavelengths plus a segment equal to a fraction of that wavelength. The phase associated with a sample of the radar signal is just this fraction of a cycle, typically known as modulo-2π, and has a value ranging from 0 to 2π. Since the radar pulse travels a two-way path, the effective range sensitivity is essentially half of the wavelength (Ferretti, 2014). This means that selecting an appropriate SAR system in relation to its respective wavelength is essential as the chosen system will be less effective for measuring any phase changes exceeding half of the wavelength.

A phase map of an individual SAR image is not as useful for the simple fact that only modulo-2π information is recorded in each pixel. However, valuable information could be retrieved upon successful formation of an interferogram, which corresponds to the phase difference between two SAR images acquired at different times (also known as repeat-pass InSAR), particularly in relation to the change of phase (or distance) between the two acquisitions. More precisely, an interferogram is computed by multiplying the complex values of the first SAR image, called the master image, by the complex conjugate of the second acquisition, called the slave image (Ferretti, 2014). The property of the phase difference $\Delta\emptyset$ between epoch i and j of a pixel P can be attributed from several factors as represented by Equation (5.1) (Hanssen, 2001):

$$\Delta\emptyset_{P(i,j)} = \Delta\emptyset_{P(i,j)}^{defo} + \Delta\emptyset_{P(i,j)}^{topo} + \Delta\emptyset_{P(i,j)}^{atmo} + \Delta\emptyset_{P(i,j)}^{orb} + \Delta\emptyset_{P(i,j)}^{noise} \quad \cdots\cdots\cdots\cdots\cdots (5.1)$$

where:

- $\Delta\emptyset^{defo}_{P(i,j)}$ is the phase contribution from deformation that occurred between the two SAR acquisition dates, i.e. at epoch i and j.
- $\Delta\emptyset^{topo}_{P(i,j)}$ is the phase contribution from topography due to different satellite position in each acquisition.
- $\Delta\emptyset^{atmo}_{P(i,j)}$ is the phase contribution due to different atmospheric effects between the two acquisitions.
- $\Delta\emptyset^{orb}_{P(i,j)}$ is the phase contribution from orbital error of the satellite.
- $\Delta\emptyset^{noise}_{P(i,j)}$ is the phase contribution related to any noise source, the most important being thermal noise. It depends on the signal-to-noise ratio (SNR) and is related to the level of thermal noise of the radar system as well as the power of the received signal. The contribution is stronger on a weaker radar echo and a lower radar cross-section (RCS) of the target.

It is clear from Equation (5.1) that valuable information can be retrieved from the phase difference of two SAR images, for example, surface deformation (i.e. using $\Delta\emptyset^{defo}_{P(i,j)}$), topography or Digital Elevation Model (DEM) (i.e. using $\Delta\emptyset^{topo}_{P(i,j)}$), and atmospheric change (i.e. using $\Delta\emptyset^{atmo}_{P(i,j)}$). Separating individual components from the others is the main task in InSAR processing (Hanssen, 2001), and the process has evolved tremendously since its first introduction. This research only focuses on extracting precise information about surface deformation by mitigating all other contributions.

5.2.2. Noises and Errors in InSAR Measurement

Although surface deformation can be estimated from the repeat-pass InSAR, the quality of estimation can be degraded by several factors. Those factors can be summarised into three groups, namely ground, satellite, and atmospheric related. Detailed explanation about noises and errors in InSAR as well as their mitigation strategies is well documented. Interested readers are referred to, for example, Rodriguez and Martin (1992), Bamler and Hartl (1998), Bürgmann et al. (2000), Hanssen (2001), Ferretti et al. (2007) and Ferretti (2014) for a more in-depth review. For completeness, they are briefly described in this thesis.

5.2.2.1. Ground-related

One of the assumptions made in Equation (5.1) is that the number, nature and locations of all scatterer within each resolution cell did not change between the two acquisitions. Following this assumption, the reflectivity phase due to those factors is expected to cancel out upon formation of interferogram. However, this is often not the case in real interferograms, especially in a rural area where the scatterers undergo several changes over time. For example, radar signature of a tree will not be the same after a certain period: leaves can fall, canopy can change, small branches can grow, etc. This phenomenon will lead to signal decorrelation. The amount of change varies among objects but usually more subtle on a man-made feature such as road and building than a natural feature such as tree and grass. Therefore, higher correlation is often observed in urban as compared to rural areas. Since signal decorrelation is related to, among other things, temporal separation between SAR images, some InSAR techniques such as Small Baseline Subset (SBAS) (Berardino et al., 2002) employ a maximum threshold for the formation of interferograms.

Likewise, change in the satellite position during each acquisition will affect the phase difference owing to the topography of the area. Fortunately, it can be minimised by subtracting the simulated phase, formulated using satellite orbital geometry and DEM, from the original interferogram. This process creates a differential interferogram, which is essentially an interferogram that has been corrected for topography or baseline-related components. However, any inaccuracies in the DEM will be propagated to the result. The SBAS technique in particular, only forms interferograms for satellite pairs that have small orbital baselines to minimise errors due to topography.

SAR acquires data in a side-looking geometry; therefore, the recorded signals are subjected to geometric distortion especially in the mountainous or urban areas (in the presence of tall buildings). The effects can be manifested in several ways, i.e. foreshortening, layover and shadowing. Slopes facing the sensor are prone to foreshortening which correspond to bright pixels due to larger resolution cell and more power backscattered towards the radar as compared to the flat terrain. On the contrary, slope facing the opposite direction appears dark, local incidence angles are high, and spatial sampling is better than that over flat terrain as the resolution cell shrinks (Ferretti, 2014).

Layover is a more extreme version of foreshortening, which happens when the reflected radar beam from the top of the mountain or a high feature reached the radar sensor before the signal from the bottom. As a result, those features are displaced toward the radar from their actual position on the ground. The effect is most prominent for radar acquisition at small incidence angles as it will occur whenever the local slope exceeds those angles (Hanssen, 2001). On the other hand, shadowing corresponds to the effects caused by the areas in shadow, which has not been reached by the radar signal and does not contain any radar return. Areas exhibiting foreshortening, layover and shadowing effects can be identified using satellite orbital geometry and DEM, and can be masked out in the final deformation map.

5.2.2.2. Satellite-related

Another potential error described in Equation (5.1) is due to different satellite positions during SAR acquisitions, termed the geometrical baseline. In the presence of geometrical baseline, the interferogram shows linear phase components, especially in the range direction. These effects are proportional to the normal baseline and presence even on a flat terrain with no surface deformation. Large baselines will also create geometrical decorrelation and should be avoided to obtain a reliable estimation of deformation. The face ramp effects, however, can be modelled and removed simply using, for example, low order polynomial function (Ferretti et al., 2007).

5.2.2.3. Atmospheric-related

The radar pulses are also affected by atmosphere during transmit and receive. For single-pass interferometry, where the measurements are made simultaneously for the master and the slave images, this effect is not present as the atmospheric state is identical for both images. Single-pass interferometry is applied for generating DEM in Shuttle Radar Topography Mission (SRTM) (Farr et al., 2007). On the contrary, atmospheric artefacts are always present in repeat-pass InSAR. It is often the greatest obstacle in conventional InSAR analyses and may compromise the detection of surface deformation signals.

The primary concern is not the absolute effects on each image, but phase differences due to inhomogeneity of the atmosphere between images. The inhomogeneity of atmosphere can be caused by several factors: variation of temperature, pressure and water content in the troposphere as well as variation of electron density in the ionosphere. Although ionosphere can be quite crucial for low-frequency radar sensors (Meyer and Nicoll, 2008), especially for regional mapping, it has limited impact on local InSAR analyses especially at mid-latitudes (Doin et al., 2009). Ionospheric activities are generally more dominant at high latitude regions (Hofmann-Wellenhof et al., 2008). Ionosphere produces long wavelength signals in differential interferograms, quite similar to baseline errors over flat areas. Therefore, it is often assumed to be removed along with baseline errors.

Tropospheric effects, on the other hand, are a more challenging noise source than the ionosphere. Phase values due to troposphere are correlated in space and often resemble cloud patterns. It is important to note that although clouds are usually transparent to radar in term of amplitude images, their impact can be significant on the phase values (Ferretti, 2014). As the troposphere changes quickly with time, two SAR images acquired a few hours or minutes apart can have entirely different value. Thus, it can be considered as uncorrelated in time given the typical temporal baseline of SAR measurements. The tropospheric effects can be divided into two components: vertical stratification and turbulence phenomena (Li et al., 2005; Bekaert et al., 2015a).

In summary, atmospheric stratification behaves similarly to the dry component of the troposphere in GPS observation, apart from the two-way as opposed to the one-way travel in GPS. Meanwhile, turbulence phenomena correspond to the wet part of the delay. Vertical stratification is related to the index of refraction at different elevations, which can be modelled using temperature and pressure (Li et al., 2005; Bekaert et al., 2015a). It is strongly correlated with local topography and is likely apparent in mountainous regions. Turbulence phenomena, on the other hand, are related to variations in water vapour density that can be considered as random in each SAR acquisition. The phenomena are typically less intense in the absence of sun illumination (Ferretti, 2014), therefore, are less apparent in night acquisitions compared to daytime images.

5.3. Coordinate Reference System for InSAR

It is important to note the differences between the coordinate reference systems used in SAR and GPS to ease interpretation from both results. **Figure 5.1** illustrates the basic geometry of a SAR system. A radar image is a matrix of complex numbers. Each element is identified by two SAR coordinates, i.e. in azimuth and range, which are related to the acquisition geometry: azimuth being the direction of the satellite path, whereas range corresponds to the direction of satellite look angle, perpendicular to the azimuth direction. The complex number in each resolution cell corresponds to an amplitude that tells the strength of the reflected signal, and a phase in modulo-2π, which is related to sensor-to-target distance.

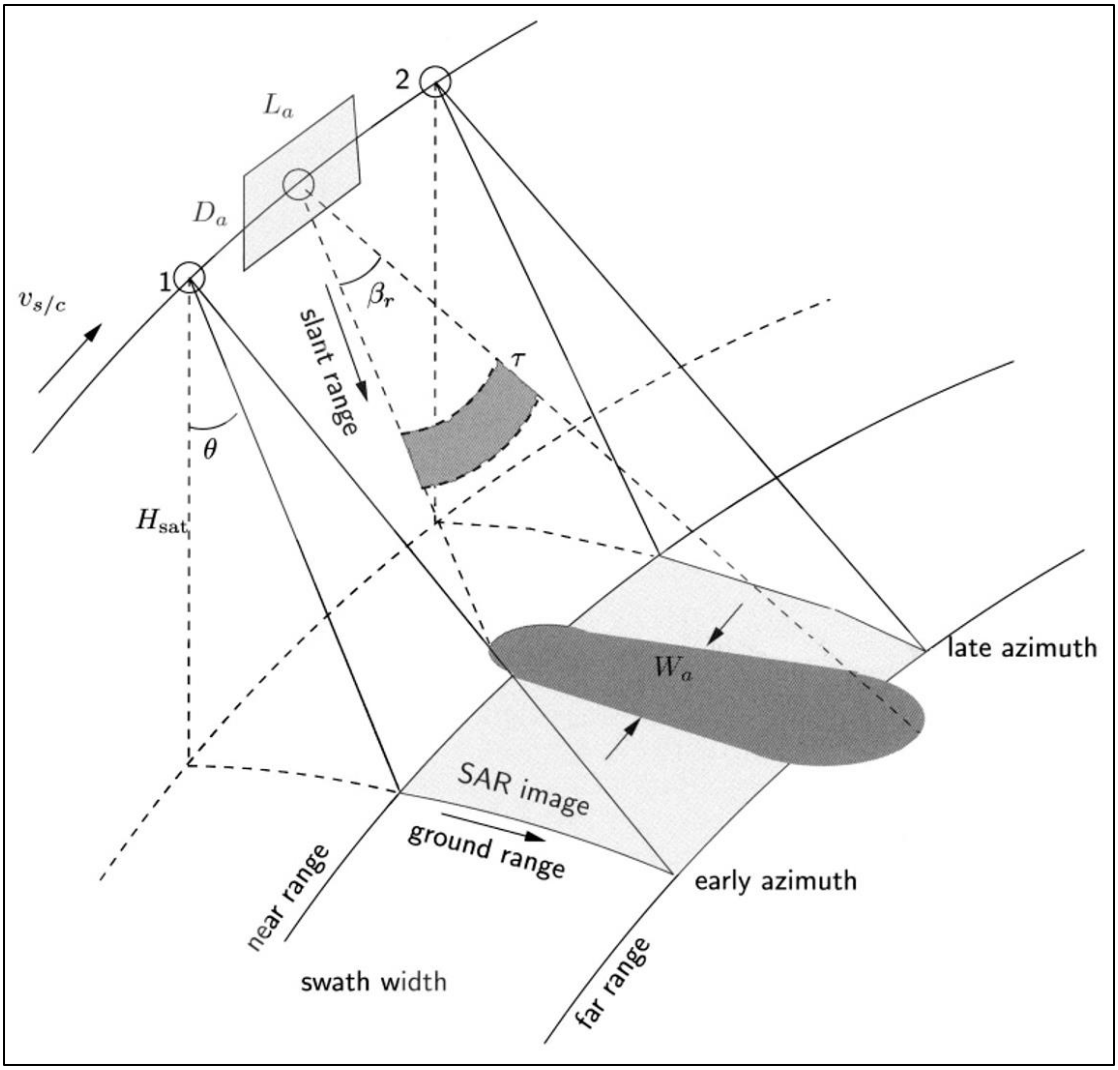


Figure 5.1: Geometry of a SAR system. Pulses are emitted at high frequency as the platform moves along the satellite vector $v_{s/c}$. The footprint of each pulse is indicated by successive ellipses in the swath W_a. The entire image is limited in range by the near and far range limits, and in azimuth by the early and late azimuth times. Figure adapted from Hanssen (2001).

The value of the radar return in each element is given by the superposition of many scatterers, which is bound by the spatial resolution in range and azimuth. Spatial resolution is the shortest distance between two points such that they can be discerned as separate objects in the image (Hanssen, 2001). Therefore, any echoes within the same resolution cell will be superimposed together. For range resolution, two targets must be separated by a distance (in slant range) greater than half the physical length of the pulse (Curlander and McDonough, 1992). The side-looking configuration eliminates this ambiguity as echoes from the far range will take longer to return than those from the near range (Woodhouse, 2005). For two objects to be resolved in the azimuth direction, they must be separated by a distance greater than the focused beamwidth on the ground. Azimuth resolution is dependent on the synthetic aperture of the system. Interested readers are referred to, for example, Hanssen (2001) and Ferretti (2014) for a more thorough description of the range and azimuth resolution.

Most of the satellites equipped with SAR sensors orbit the Earth in a near-polar orbit at an altitude ranging from 500 to 800 km above the Earth's surface, depending on the satellite platform hosting the SAR sensor. The angle between the true north-south and the satellite orbit varies slightly depending on the satellite, but in general, lies in the range of ten degrees. For most satellite SAR systems available today, the incidence angle can be selected from a set of values ranging from about 20 to 50 degrees, which is useful for hilly or mountainous terrain as it allows the possibility to achieve better geometry (Ferretti et al., 2007; Ferretti, 2014). The portion of the image closest to the satellite's nadir is known as the near range, while the portion furthest from nadir is the far range. The incidence angle increases as the beam moves from near to far range. As the recorded phase in each resolution cell of SAR images is referring to the satellite's viewpoint, deformation derived from the InSAR processing also corresponds to the same direction as they represent the phase difference between the satellite acquisitions.

5.4. Punnet Software

The processing of SAR data in this work is carried out by the author using Punnet - software developed in-house at the Nottingham Geospatial Institute, the University of Nottingham using Matlab. Punnet employs Intermittent SBAS (ISBAS) algorithm (Sowter et al. 2013; Bateson et al. 2015) that is well-suited to low-resolution, wide-area deformation monitoring over a broad range of land classes, including grasslands, agricultural and forested cover (Cigna et al., 2014; Sowter et al., 2016). In general, ISBAS follows similar principles as the standard SBAS method (Berardino et al., 2002), but relax the threshold that the pixel must display consistently high coherence, i.e. the degree of similarity between the two images, over all interferograms. The software supports Single Look Complex (SLC) data from the majority of the SAR sensors shown previously in **Table 5.1**.

Figure 5.2 shows the standard processing scheme for Punnet software. The scheme can be categorised into two, owing to the differences in data acquisition modes, i.e. for processing Sentinel-1 and other standard SLC datasets. It can be seen from the figure that the main differences between the two categories lie on the additional requirements for processing Sentinel-1 dataset: (1) debursting and merging prior to image coregistration and resampling, and (2) utilisation of the known de-ramping function for image coregistration and resampling.

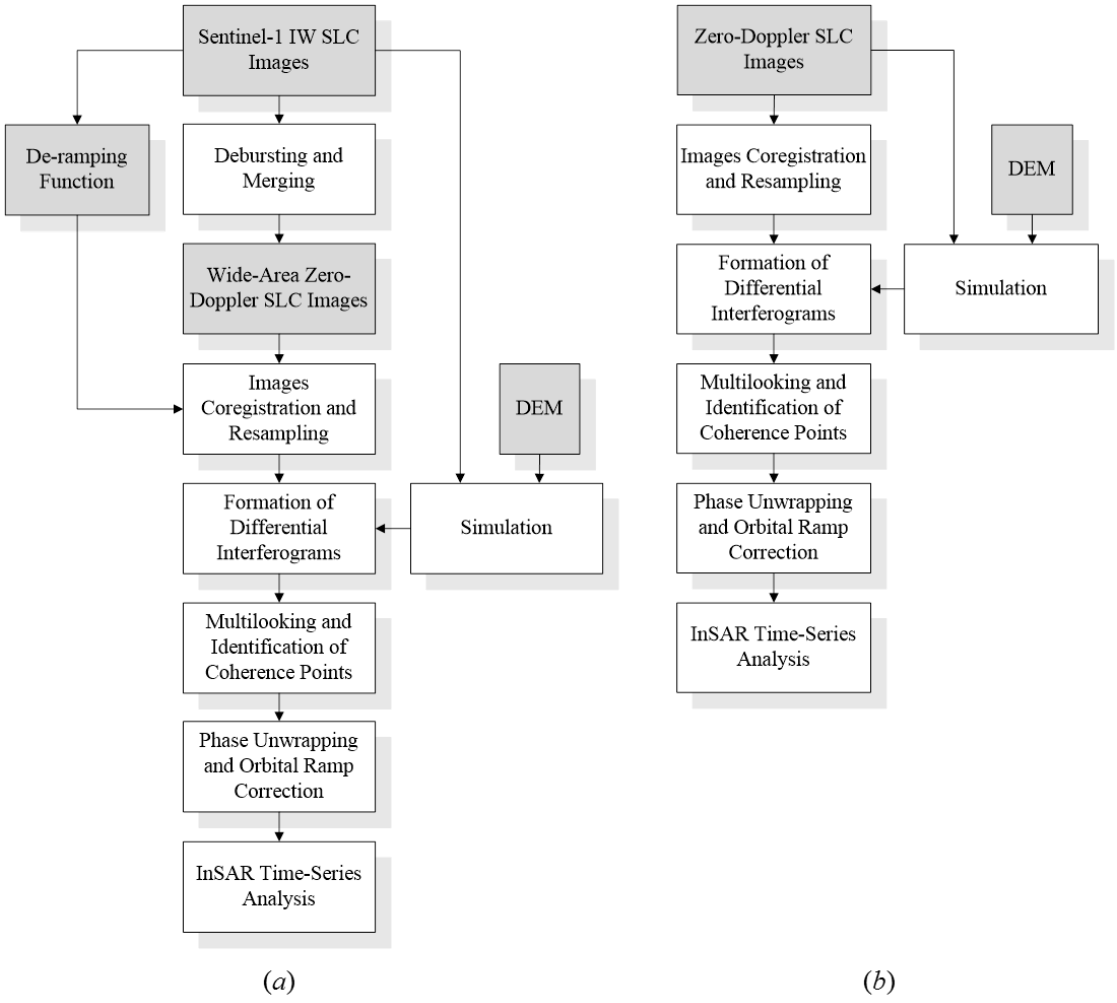


Figure 5.2: Standard processing scheme for Punnet software using (*a*) Sentinel-1 dataset, and (*b*) other standard SLC datasets. Notice that Sentinel-1 requires additional steps of debursting and merging before images coregistration, as well as utilisation of the known deramping function for resampling. Other steps are standard for all dataset, i.e. formation of differential interferograms; identification of coherent points; phase unwrapping; orbital ramp correction; and time-series analysis. Figure adapted from Sowter et al. (2016).

5.5. Debursting and Merging (for Sentinel-1 Processing)

The Sentinel-1 Interferometric Wide (IW) swath SLC products used in this study were acquired using the Terrain Observation with Progressive Scans in azimuth (TOPS) imaging technique (Holzner and Bamler, 2002; Torres et al., 2012). The product is provided as three separate sub-swaths, whereby each sub-swath consists of a series of bursts (**Figure 5.3**). Each burst has been processed as a separate SLC image and included into the sub-swath, in azimuth time order, with black-fill demarcation in between. To create a wide-area IW product from the three sub-swaths supplied, two separate processes need to be applied in order (ESA, 2013):

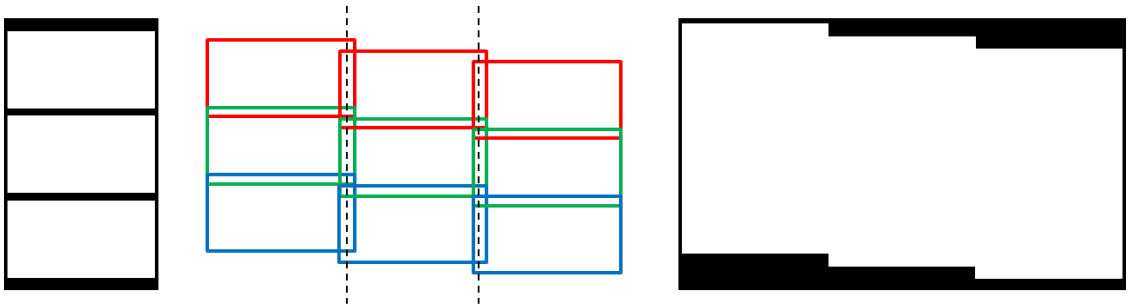
i. Debursting

This process concatenates the individual bursts from one sub-swath into a single deburst sub-swath where the azimuth line spacing is constant from start to end, and there is no black line demarcation between subsequent bursts.

ii. Merging

After debursting has been applied to each of the three sub-swaths (i.e. IW1, IW2 and IW3), the sub-swaths are mosaicked into a single wide-swath product where range column spacing is constant from near to the far end, and the sub-swaths are aligned in azimuth.

Considering the lines and columns of the bursts and sub-swaths have been resampled to a common pixel spacing grid, no resampling of the original pixel values is needed and wide area product can be obtained by only shifting sub-images around integer numbers of rows and columns based on orbit information (Sowter et al., 2016).



(a) (*b*) (*c*)

Figure 5.3: Illustration of debursting and merging in Sentinel-1. (*a*) Arrangement of bursts in an IW sub-swath. (*b*) Sentinel-1 burst structure with small overlaps between bursts and sub-swaths. (*c*) Mosaic for full Sentinel-1 IW swath consisting of 3 sub-swaths with 3 bursts in each. Figure adapted from Sowter et al. (2016).

5.6. Images Coregistration and Resampling

The first common step to process interferometric SAR is coregistration, which aims to map all SAR images onto a common master so that each pixel in the slave images equates to the same pixel in the master image (**Figure 5.4**). Ferretti et al. (2007) suggested that coregistration should account for orbit crossing/skewing, differences in sensor altitudes, different sampling rates (e.g. due to different pulse repetition frequency, sensor velocities, etc.) and shifts in the azimuth and range direction. The master image can be selected from the set of available images, preferably in the centre of the timespan covered by the dataset to minimise temporal decorrelation. For *n* number of dataset, there are *n - 1* images to be coregistered. The master image chosen for each dataset in this research is summarised in **Figure 5.5**.

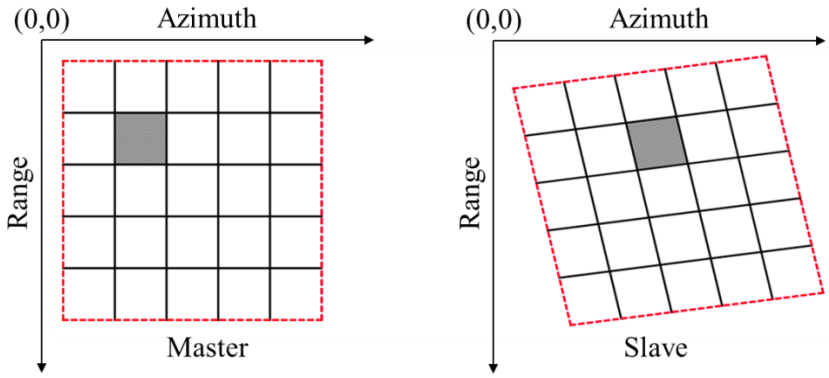


Figure 5.4: Differences in SAR geometry between the master and the slave image, which can be represented by six parameters, i.e. shift, stretch and rotation, both in azimuth and range directions.

For most SAR images, coregistration and resampling should be performed on a pixel by pixel basis, with accuracy on the order of one-tenth of the resolution, or better. This is not a difficult task to perform and interested readers can refer to Ferretti et al. (2007) and references therein for a more in-depth explanation. For Sentinel-1 TOPS data, any imprecision of less than one thousandth of one pixel in co-registration may result in noticeable phase ramps on individual bursts (De Zan et al., 2014). Although difficult to achieve through typical convolution methods, higher levels of accuracy may be achieved through, for example, a spectral diversity technique (Scheiber and Moreira, 2000) as implemented by some authors (e.g. Lanari et al., 2015; Wegmüller et al., 2015). Nevertheless, spectral diversity is not applied in this research, and the task is subjected to future work. The images coregistration and resampling technique employed in this research is summarised as follows:

i. Coarse coregistration

The process begins with a coarse coregistration based on the known acquisition geometry of the master and the slave images. A list of candidates on the master image is identified at a regular 50×50 grid, and any points with no elevation information (e.g. water body) are rejected. The location of those points in the corresponding slave image can be identified from the known acquisition geometry, i.e. from DEM and precise orbits. Polynomial coefficients are estimated from the offset of those points to approximate the pixel-to-pixel relationship between the two images.

ii. Fine coregistration

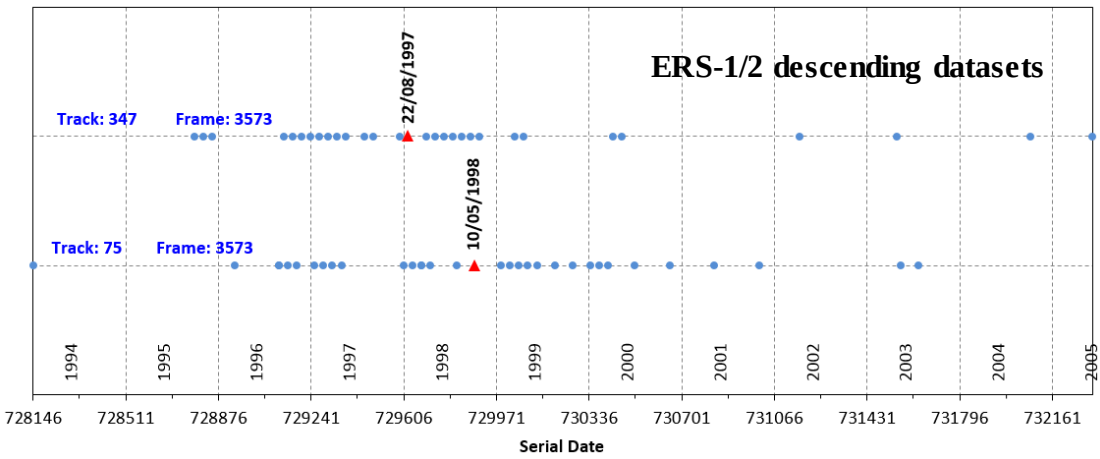
Coarse coregistration is accurate to within a few pixels accuracy. The coregistration is further refined to sub-pixel accuracy using fine coregistration. It can be done either using amplitude cross-correlation or fringe contrast techniques. The former is implemented in the software. First, amplitude data from the master and the slave images is extracted from a small region surrounding the point candidates. The initial location of those points in the respective slave image can be determined from the derived polynomial. Subpixel image registration is then conducted using cross-correlation technique described in Guizar-Sicairos et al. (2008), i.e. using a fast Fourier transform (FFT) algorithm.

It is worth mentioning that amplitude cross-correlation and fringe contrast techniques have complementary features and drawbacks. The latter has superior performance when the topography is flat, or the baseline is moderate, but they require high computational cost and perform badly in the presence of image contrasts. On the other hand, amplitude-based techniques could work very well with wide baseline spans and image contrasts, the computational cost is moderate, but they have a coarser accuracy. According to Li and Goldsten (1990), conventional correlation of amplitude image patches can achieve accuracy near 0.03 pixels, which is sufficient for this work.

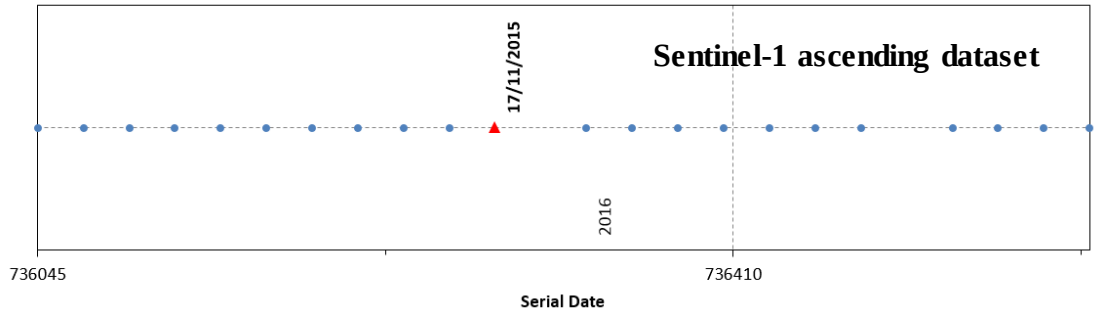
iii. Resampling

The final step is to resample data in the slave images onto the master coordinate system using the refined polynomial. Implementation of the slave image resampling is quite efficient, since it can be approximated by two one-dimensional (1D) resampling steps: along range and then along azimuth. Resampling is usually done using bilinear (Lin et al., 1992) or bicubic (Kwoh et al., 1994) methods. The latter is

adopted by Punnet software. For Sentinel-1 TOPS data, the phase of a product changes rapidly in azimuth and may not easily be resampled as the phase difference between adjacent pixels can be ambiguous. It is a well-known effect and may be solved by first subtracting a simulation of the rapidly-varying azimuth phase (deramping), resampling the remainder and finally adding back the simulated phase (re-ramping). The deramping function for Sentinel-1 data is known, and interested readers are referred to Miranda (2015) for a more in-depth discussion.



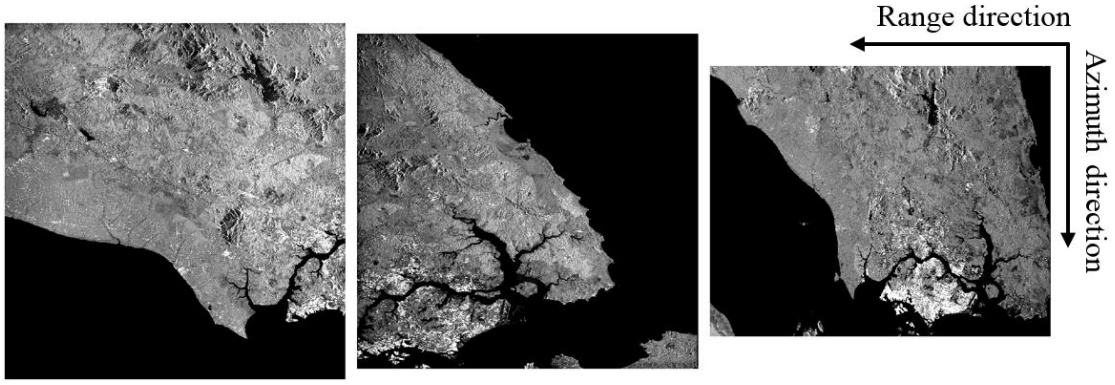
(*a*)



(*b*)

Figure 5.5: Selection of the master image to be in the centre of data span. Each vertical gridline corresponds to 1 year different. (*a*) ERS-1/2 descending dataset. The top plot shows data acquisitions in track 347 relative to the master image on 22 August 1997, whereas bottom plot shows data acquisitions in track 75. The image on 10 May 1998 was selected as the master image. (*b*) Sentinel-1 ascending dataset. 22 SAR images were acquired from 22 Mac 2015 to 24 September 2016 with 24 days temporal separation. Images on 20 June 2016 is missing from the Sentinels Scientific Data Hub.

Following the completion of image coregistration and resampling, an average amplitude map is generated for each dataset, based on all individual amplitude data. The results are shown in **Figure 5.6**. Bright pixels in the maps correspond to an area with high signal reflection, typically associated with urban area, whereas dark grey colour corresponds to an area with low signal reflection (rural area).



(*a*) (*b*) (*c*)

Figure 5.6: Average amplitude maps of Johor, displayed in range and azimuth directions of the satellites (not orthorectified). Bright pixel corresponds to a field with high signal reflection, whereas dark grey pixel relates to an area with low signal reflection. (*a*) The result from ERS-1/2 (track 347), (*b*) the result from ERS-1/2 (track 75), and (*c*) the result from Sentinel-1 (subset to the area of interest). Waterbody has been masked out and showed as black.

5.7. Formation of Differential Interferogram

A complex value z of a master image m and a slave image s can be represented by amplitude A and phase $\emptyset$ information as follows (Hanssen, 2001), where $j = \sqrt{-1}$:

$$z_m = A_m \cdot e^{j\emptyset_m}$$
$$z_s = A_s \cdot e^{j\emptyset_s} \quad \text{..... (5.2)}$$

An interferogram I is computed by multiplying the complex value of the master image with the complex conjugate of the slave image. This would result in multiplying the amplitudes and differencing the phases.

$$I = z_m z_s^* = A_m A_s e^{j(\emptyset_m - \emptyset_s)} \quad \text{..... (5.3)}$$

Differential interferogram can then be formulated by subtracting the simulated phase due to topography from the real interferogram - a process that is also known as interferogram flattening. The simulated phase can be derived from the precise orbit of the satellite and DEM. Although Persistent Scatterer Interferometry (PSI) and SBAS

share similar principles in the formation of the differential interferogram, selection of image pairs differs between the two techniques. The former only form interferograms to a single master (Ferretti et al., 2001), ensuring that any errors associated with the master image remain constant. For n number of image, there will be $n - 1$ interferograms. Although the technique could achieve high accuracy results on a full-resolution scale, it requires a sufficient number of images for a reliable analysis (Ferretti et al., 2007). On the other hand, SBAS (Berardino et al., 2002) is a multi-master technique, which forms interferograms for all possible combinations that meet certain criteria, the most common of which is short orbital baseline between image pairs. Unlike PSI, this technique utilises phase information from a large number of interferograms to model the errors.

ISBAS algorithm is developed based on the multi-master technique. For n number of image, the maximum possible combination N_{max} can be identified from Equation (5.4).

$$N_{max} = n \cdot \left(\frac{n-1}{2}\right) \quad \text{(if } n \text{ is an odd number)}$$
$$N_{max} = (n-1) \cdot \left(\frac{n}{2}\right) \quad \text{(if } n \text{ is an even number)} \qquad \text{(5.4)}$$

Two parameters that need to be considered in the formation of differential interferogram are (1) orbital baseline and (2) temporal baseline between image pairs. Increasing the threshold for orbital and temporal baselines will result in an increment in the number of interferograms (**Figure 5.7a**, **Figure 5.8a** and **Figure 5.9a**). However, careful thought should be taken upon selecting the appropriate thresholds. Short orbital baseline will minimise phase sensitivity to topography error but will limit the number of interferograms produced. The phase sensitivity to topography can be represented by the altitude of ambiguity $h_{2\pi}$, which is defined as the elevation change that will generate a 2π phase variation in a multi-pass SAR interferogram (Hanssen, 2001). It can be calculated using Equation (5.5).

$$h_{2\pi} = \frac{\lambda}{2} \cdot \frac{r_{m0} \sin\theta}{B_n} \qquad \text{(5.5)}$$

This equation shows that significant normal baseline B_n will result in small altitude of ambiguity, i.e. phase is more sensitive to elevation change. Similarly, the sensitivity will decrease with long wavelength λ, high incidence angle θ, or increased distance between satellite and target r_{m0}. Average distance from the satellite to the master image and average incidence angle, determined from the dataset, are used to simulate variation in the altitude of ambiguity with respect to the normal baseline (**Figure 5.7b**, **Figure 5.8b** and **Figure 5.9b**). Ferretti et al. (2007) suggested that the optimum baseline for ERS case is approximately 300 - 400 m considering signal to noise ratio. For this processing, the orbital baseline threshold is configured to be 350 m.

Selection of the appropriate temporal threshold, among others, depends on the rate of deformation (i.e. a small threshold for rapid deformation to avoid phase ambiguity) and characteristics of the scatterers in the area of interest (short temporal baseline for fast changing scatterers). Long temporal baseline will increase decorrelation between images and subsequently will produce a noisy differential interferogram. The maximum temporal baseline is configured to be five years (1,825 days). Furthermore, no significant increment in the number of interferogram is expected from using larger threshold, as shown in **Figure 5.7c**, **Figure 5.8c** and **Figure 5.9c**. The rate of deformation is also projected to be slow.

The network of interferograms from using these configurations are shown as **Figure 5.7d**, **Figure 5.8d** and **Figure 5.9d**. For ERS-1/2 processing, the total interferograms produced are 172 and 149 for data acquired in track 347 and 75, respectively. As for the Sentinel-1 dataset, a total of 231 interferograms have been produced, owing to the short revisiting cycle and a small orbital tube of the satellite. As can be seen from the **Figure 5.7d**, all image pairs with respect to 31 October 1997 and 9 November 2001 do not meet the specified conditions (i.e. assigned thresholds); thus, no interferogram is produced. Similarly, the image acquired on 19 April 1996 and 15 November 1996 only forms interferogram to each other, and not with other images. On the contrary, the network of interferogram for Sentinel-1 and ERS-1/2 (track 75) are well connected.

The final differential interferograms from ERS processing are multi-looked by a factor of 4×24 pixels in range and azimuth resolution respectively, corresponding to approximately 100 m in ground resolution. For Sentinel-1, the multi-looked setting is configured to be 30×6 pixels, resulting to about 90 m in ground resolution. The phase value in the differential interferograms, at this stage, should be attributed to deformation, atmosphere and residual from baseline related components, while other contributions are expected to be minimal. For significant magnitude deformation such as from the Lander's earthquake (Massonnet et al. 1993), the deformation can be observed as fringes across the resulting differential interferogram. However, slow deformation could be masked out by other contributions; the most frequent is atmospheric effects. Further analysis using time series is required to extract the deformation trend. Although the multi-looked differential interferograms can be filtered, for example, using modified Goldstein filter before phase unwrapping, no significant improvement is found in the final LOS-velocity map from using the filtered interferograms. Therefore, no filtering is applied in this work.

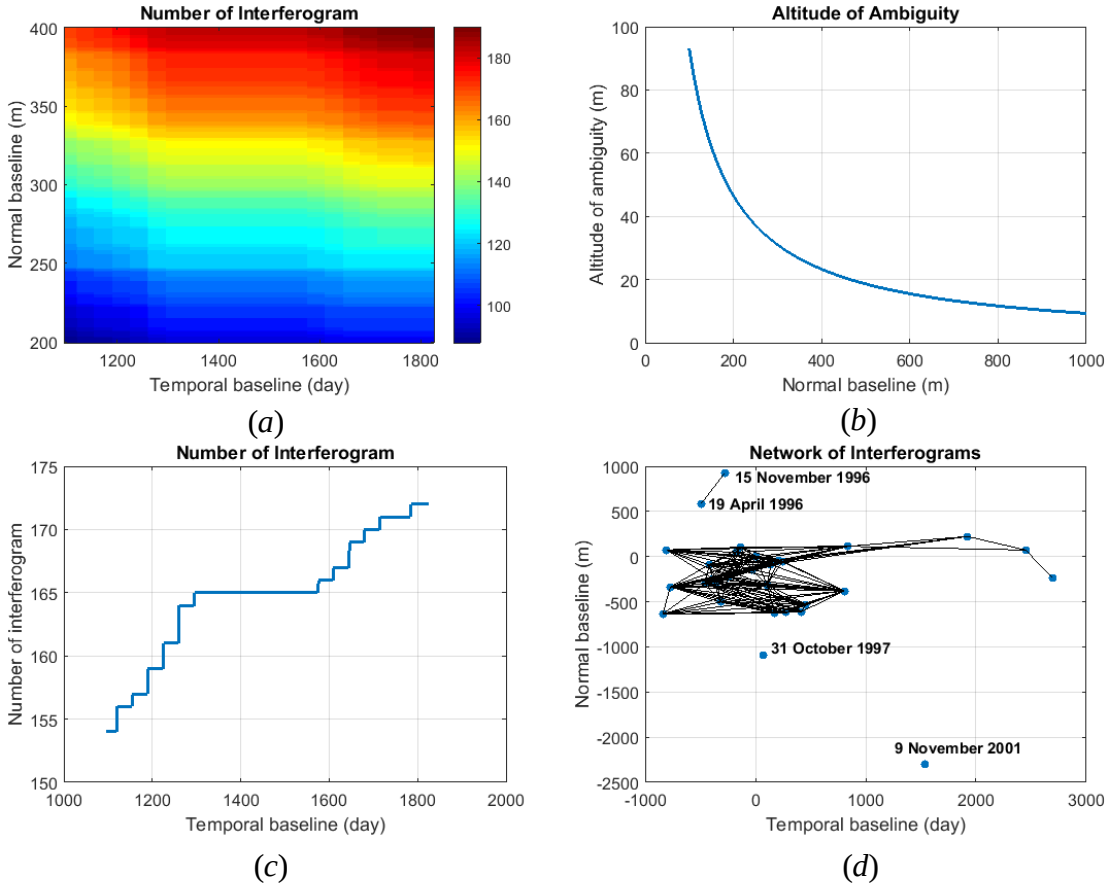


Figure 5.7: Selection of the temporal and orbital baselines threshold for ERS-1/2 (track 347). (*a*) The number of interferograms from different sets of temporal and orbital thresholds. (*b*) Altitude of ambiguity as a function of normal baseline. Increasing normal baseline will result in low altitude of ambiguity, i.e. phase is more sensitive to the elevation change or DEM errors. (*c*) The number of interferogram as a function of temporal baseline using 350 m for the orbital baseline threshold. (*d*) The network of interferograms using 350 m and 5 years for the baseline and temporal baseline thresholds, respectively.

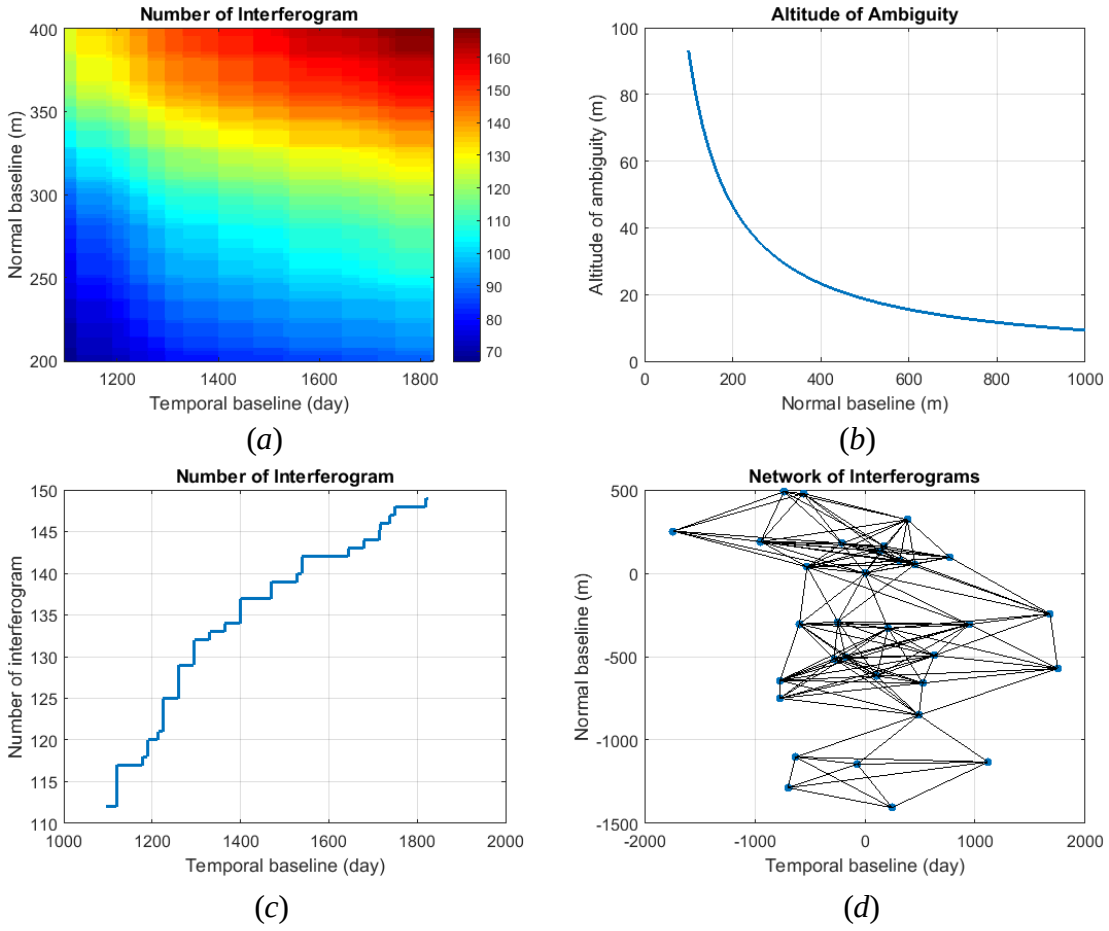


Figure 5.8: Selection of the temporal and orbital baselines threshold for ERS-1/2 (track 75). (*a*) The number of interferograms from different sets of temporal and orbital thresholds. (*b*) Altitude of ambiguity as a function of normal baseline. Increasing normal baseline will result in low altitude of ambiguity, i.e. phase is more sensitive to the elevation change or DEM errors. (*c*) The number of interferogram as a function of temporal baseline using 350 m for the orbital baseline threshold. (*d*) The network of interferograms using 350 m and 5 years for the baseline and temporal baseline thresholds, respectively.

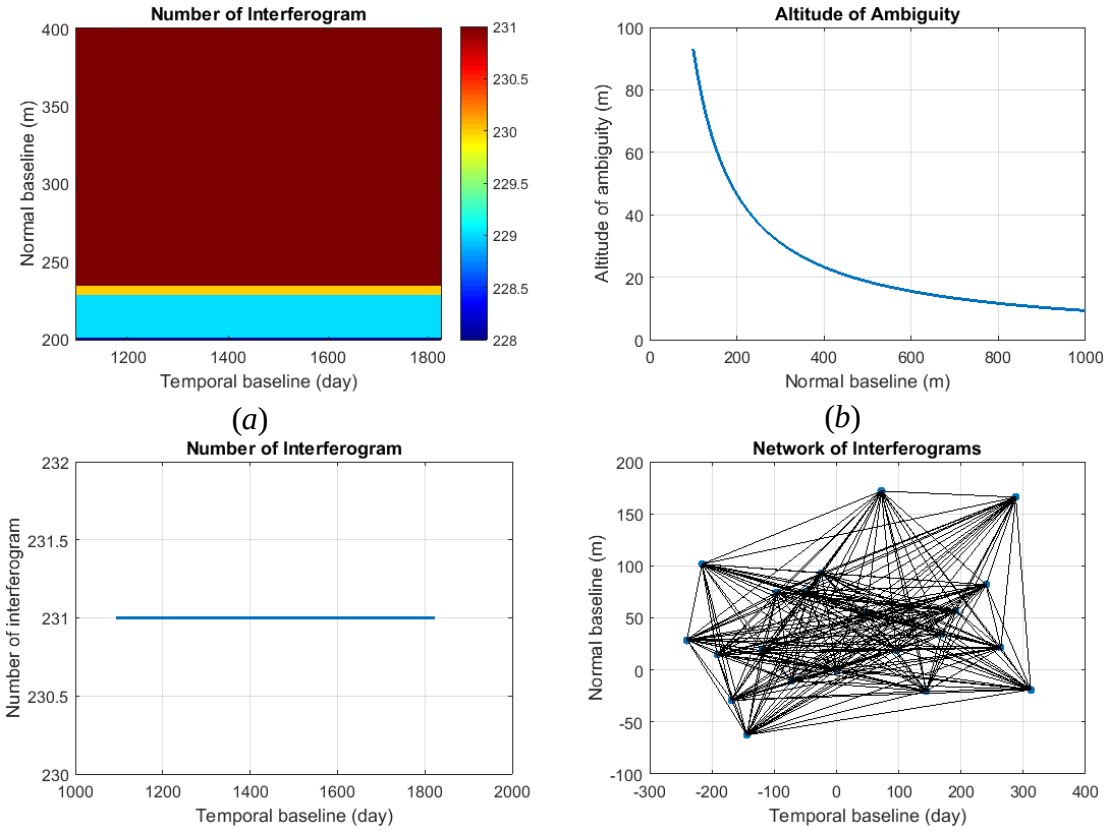


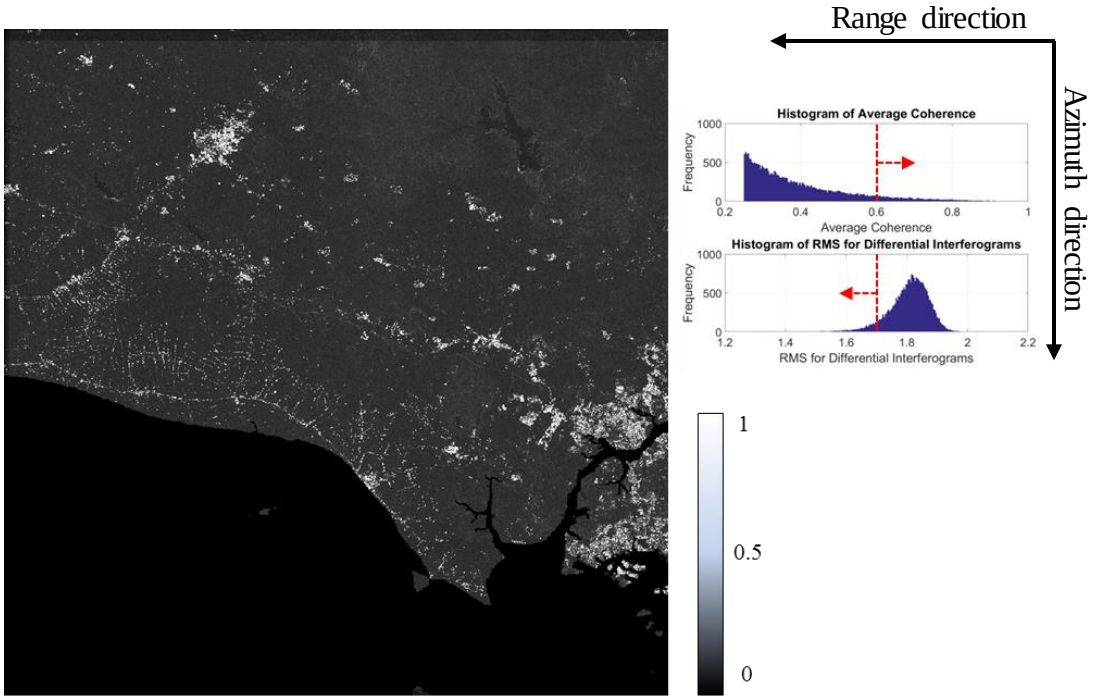
Figure 5.9: Selection of the temporal and orbital baselines threshold for Sentinel-1. (*a*) The number of interferograms from different sets of temporal and orbital thresholds. (*b*) Altitude of ambiguity as a function of normal baseline. Increasing normal baseline will result in low altitude of ambiguity, i.e. phase is more sensitive to the elevation change or DEM errors. (*c*) The number of interferogram as a function of temporal baseline using 350 m for the orbital baseline threshold. (*d*) The network of interferograms using 350 m and 5 years for the baseline and temporal baseline thresholds, respectively.

5.8. Selection of Coherent Points

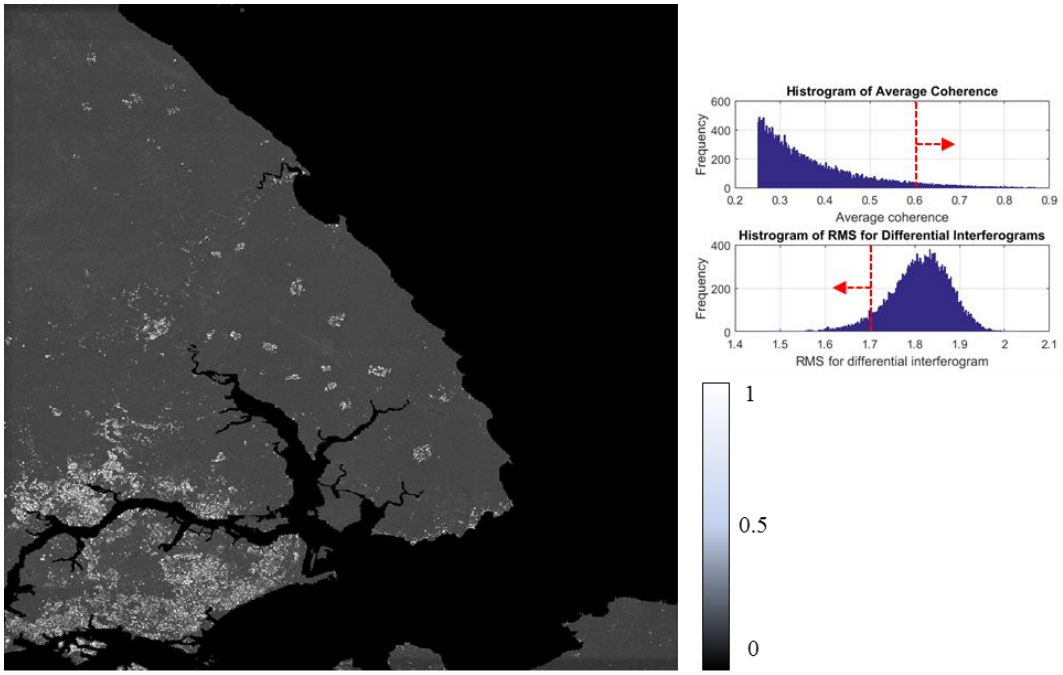
The level of noise in each differential interferogram depends on SNR, which can be expressed in term of similarity between the master and the slave images. Higher SNR is achieved for higher similarity between the reflectivity values. The degree of similarity, in this work, is measured using coherence, i.e. normalised cross-correlation coefficient estimated in a multi-looked window. For two random variables z_m and z_s, coherence γ_c can be expressed as (Ferretti et al., 2007):

$$\gamma_c = \frac{E(z_m z_s^*)}{\sqrt{E(|z_m|^2) \cdot E(|z_s|^2)}} = \gamma \cdot e^{j\emptyset f} \quad \text{..... (5.6)}$$

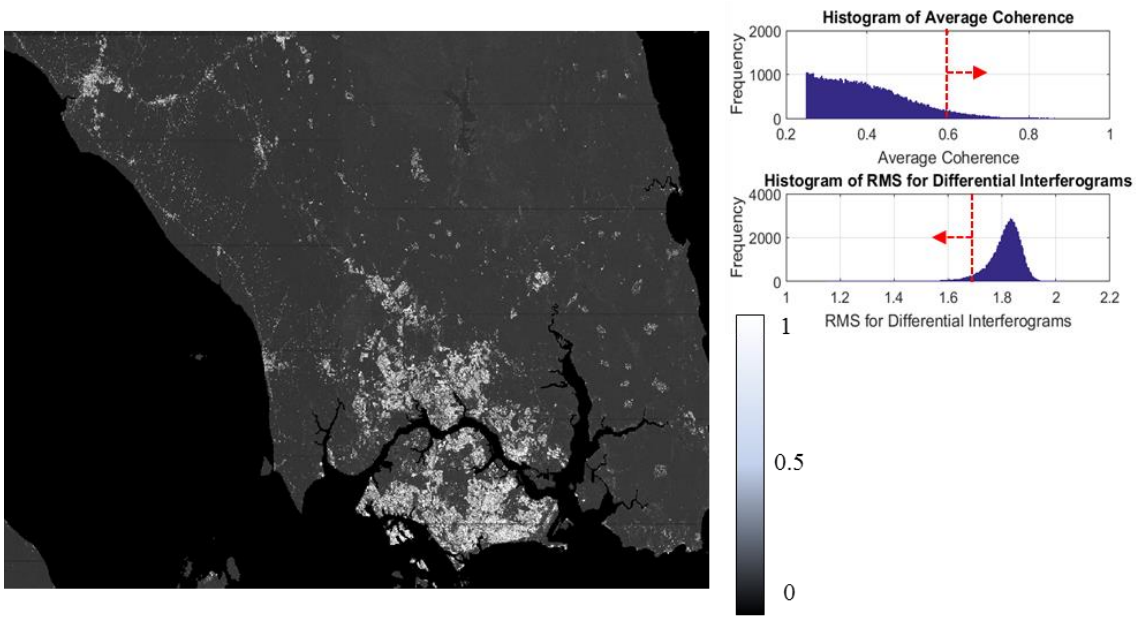
where γ_c is a complex variable with amplitude ranging from 0 to 1. $E(\cdot)$ is the expectation operator, which is defined as a spatial average in a multi-looked window. The multi-looked settings are similar to those used for differential interferograms, i.e. 4 × 24 pixels in range and azimuth resolution for ERS-1/2, and 30 × 6 pixels for Sentinel-1 processing. Coherence is computed for every multi-looked pixel in each differential interferogram, and subsequently average coherence map from all image pairs is generated as shown in **Figure 5.10**. As expected, urban areas exhibit higher coherence value than the rural areas.



(*a*)



(*b*)



(*c*)

Figure 5.10: Average coherence maps, displayed in range and azimuth directions of the satellites (not orthorectified). The urban areas have better coherence than the countryside. Histogram plots next to each map show statistical information for the SBAS points, i.e. candidates for the control point. The criterion used to narrow down the candidates are represented by red arrows, i.e. average coherence value of more than 0.6 and RMS for differential interferograms of less than 1.7. (*a*) Result for the ERS-1/2 (track 347), (*b*) result for the ERS-1/2 (track 75), and (*c*) result for the Sentinel-1 (subset to the area of interest).

Selection of points for the final LOS-velocity map is made based on the number of layers used to achieve the average coherence value of better than 0.25. Since urban areas typically have high coherence value in each layer, fewer layers will be rejected compared to rural areas. The threshold for the minimum number of layers used in the computation of coherence as well as the resulting number of points for the estimation of velocity are summarised in **Table 5.2**.

Table 5.2: Selection of coherent points based on the minimum number of layers used to achieve the average coherence value of 0.25.

Dataset	Total Interferogram	Minimum Layer Threshold	Number of Coherent Points above Minimum Layer	Number of Coherent Points in All Layer	Coverage Improvement *
ERS-1/2 (track 347)	172	45	293,339 (31.34%)	26,955 (2.88%)	28.46%
ERS-1/2 (track 75)	149	45	178,877 (28.08%)	19,244 (3.02%)	25.06%
Sentinel-1	231	45	173,929 (15.68%)	73,901 (6.66%)	9.02%

* Based on the number of points excluding the water body.

Selection of control points for phase unwrapping is usually made in a geologically stable area, which would be problematic for a field without geological information. Furthermore, the selected point is not necessarily coherent in all interferograms, which is necessary for phase unwrapping. Wrong selection of a control point not only will result in an offset in the estimated deformation but also contributes to the phase unwrapping error. In the event of no prior knowledge about the stability of the area, a statistical method is introduced by the author for the selection of control point candidates. The method is based on the assumption that a right candidate should exhibit stable phase behaviour across selected differential interferograms, where the normal baseline is considerably small to minimise baseline related errors. Furthermore, a good candidate should be situated close to the area of interest (preferably in the middle of the scene) and have a high average coherence value to minimise error propagation from phase unwrapping. The author has implemented this method as an additional module to Punnet software. Based on the histogram plots of average coherence values and RMS for differential interferograms (**Figure 5.10**), the candidates for control point are narrowed down by extracting points that only have the average coherence of better than 0.6 and RMS of differential interferograms of lower than 1.7. The best point is manually selected from those candidates considering their geographical location (i.e. close to the area of interest), as well as their statistical result. The chosen control point for each dataset is summarised in **Table 5.3**.

Table 5.3: SAR coordinate of the selected control point for phase unwrapping.

Dataset	Reference Azimuth	Reference Range	Average Coherence Value	RMS for Differential Interferogram
ERS-1/2 (track 347)	567	405	0.78	1.62
ERS-1/2 (track 75)	773	974	0.69	1.61
Sentinel-1	384	1040	0.69	1.43

5.9. Phase Unwrapping and Orbital Ramp Correction

Since the principal observation of InSAR is relative phase signal in modulo-2π of the (unknown) absolute phase signal, phase unwrapping is necessary to obtain the phase value for each coherent point with respect to a chosen control point. The selected control point will be common across all interferograms. Usually, phase unwrapping is based on the assumption that the phase gradient between adjacent pixels varies smoothly within 2π interval, i.e. from $-\pi$ to $+\pi$. More precisely, neighbouring phase values are expected to be within one-half cycle of one another (Ferretti, 2014). Although this hypothesis is valid for most of the image pixels, the presence of phase discontinuities prevents one from using the most straightforward procedure - a simple integration of the phase differences starting from a reference point as of levelling survey. Discontinuities can result from two factors (Hanssen, 2001): (1) phase noises, and (2) fast phase variations of the signal due to local topography or surface deformation.

Many phase unwrapping algorithms have been developed since InSAR became an active field of research. For example, residue-cut method (Goldstein et al., 1988; Ching et al., 1992), least-square method (Hunt, 1979; Ghiglia and Romero, 1994; Ghiglia and Romero, 1996; Pritt, 1996; Fornaro et al., 1996a; Fornaro et al., 1996b; Bamler and Hartl, 1998) and minimal cost flow methods (Costantini and Esrin, 1996; Costantini, 1998; Chen and Zebker, 2000; Chen and Zebker, 2001). Detailed discussion on phase unwrapping is beyond the scopes of this work. Interested readers are referred to the references provided for a more in-depth review. Despite numerous developments, phase unwrapping remains as one of the most challenging tasks in obtaining accurate InSAR result, along with atmospheric effects.

The Punnet software benefits from the Statistical-cost Network-flow Algorithm for Phase Unwrapping (SNAPHU) program by Chen and Zebker (2002) to individually unwrap coherent pixels within each differential interferogram. Two files are provided for the program, i.e. differential interferogram as well as its respective coherence map. The latter is used as a weight to identify noisy areas that will discredit the underlying hypothesis of smooth phase gradient. For similar reasons, nearest neighbour interpolation is applied to the coherent points in differential interferograms prior to the process. It is worth mentioning that assessment of the reliability of phase unwrapping is difficult without additional information and will always be based on strong assumptions about the data behaviour. Long radar wavelengths, high SNR values and slow variation of phase values will have a positive impact, making it more robust and reliable (Hanssen, 2001). The probability of phase unwrapping errors would rely on the statistics of the signal (Monti Guarnieri, 2003) as well as a thorough analysis of the algorithm used to unwrap the interferogram. More often than not, phase unwrapping is addressed as an adjustment and filtering problem based on the availability of more than one interferogram for the area under study.

One of the challenges encountered in the phase unwrapping using SNAPHU is related to waterbody that creates isolated patches of coherent points. Although phase unwrapping can be done independently for each patch, this will create an offset between them. The author has investigated the effects of waterbody using ERS-1/2 data from track 347. Firstly, the area is divided into two (**Figure 5.11**), ensuring that they will share similar control points for the phase unwrapping. The area covered by the water body is minimised without scarifying too much on the coverage. The coherence for the remaining area of the water body is assigned to zero to down-weight their contribution. It is worth noting that no differences regarding coregistration and resampling are expected between the two areas as the subdivision is made of the full differential interferograms and coherence maps. The result from the individual phase unwrapping is compared to each other as well as with the result from the full scene. **Figure 5.12** shows the unwrapped interferograms after orbital correction for five selected pairs. Although small discrepancies are observed in a few unwrapped interferograms (e.g. **Figure 5.12a**), there are no significant differences attained in the final LOS-velocity map, most probably due to the nearest neighbour interpolation applied before the process and the relatively large number of interferograms used to compute the velocity.

The unwrapped phase also contains a linear phase component due to different geometry of the satellite during acquisition. These effects, however, can be easily modelled and mitigated as they are proportional to the normal baseline. Punnet applies least square estimation (LSE) based on the phase of coherent points using the bilinear model to estimate and remove the baseline related components. The corrected unwrapped phases for every coherent point are then stored for the subsequent time-series analysis.

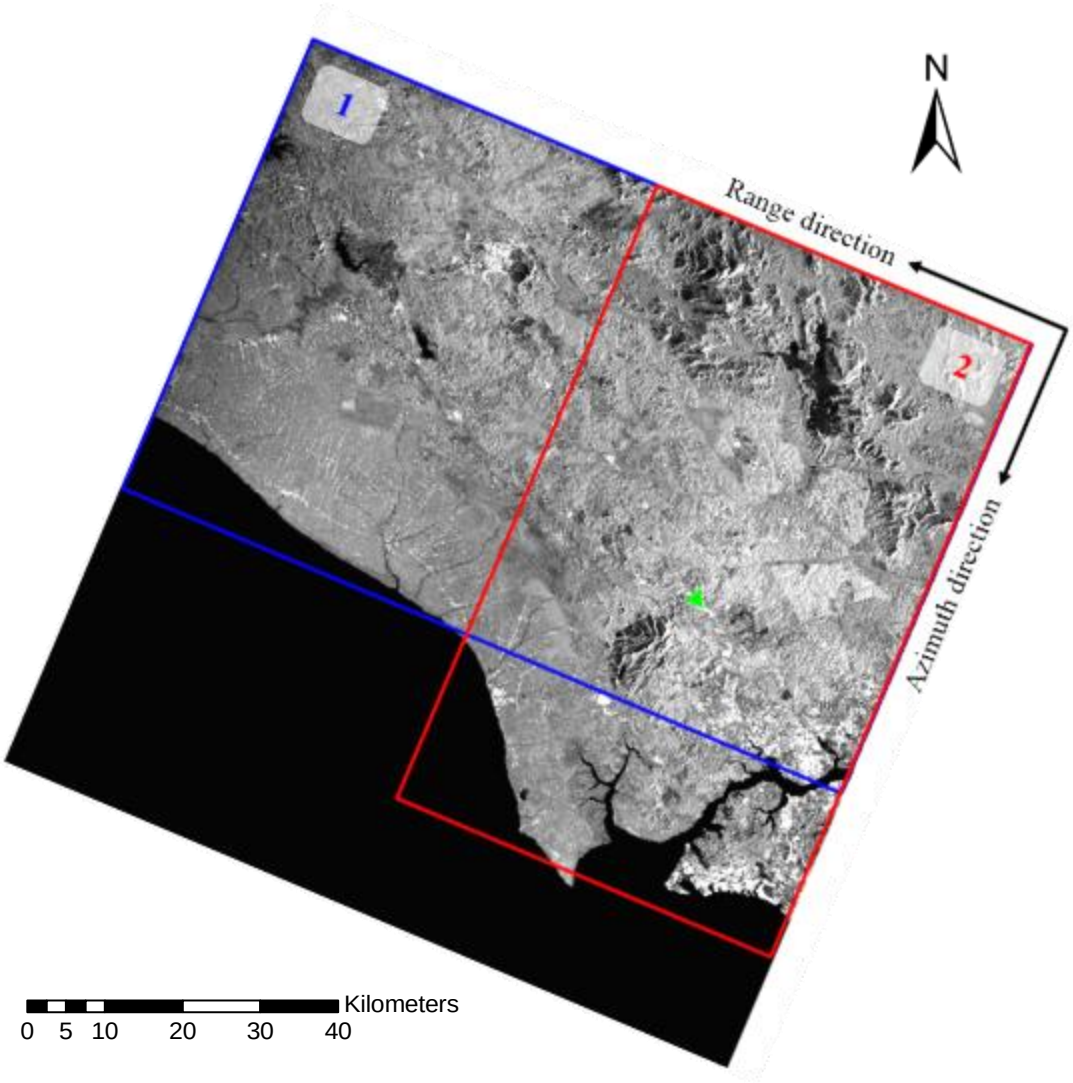


Figure 5.11: Average coherence map of ERS-1/2 (track 347) showing the two subset areas (i.e. blue and red boxes) used to investigate the effects of the water body to the phase unwrapping. Each differential interferograms and its respective coherence maps are subsets to these areas before phase unwrapping using SNAPHU. The green rectangle is the location of the control point, which is common in both areas.

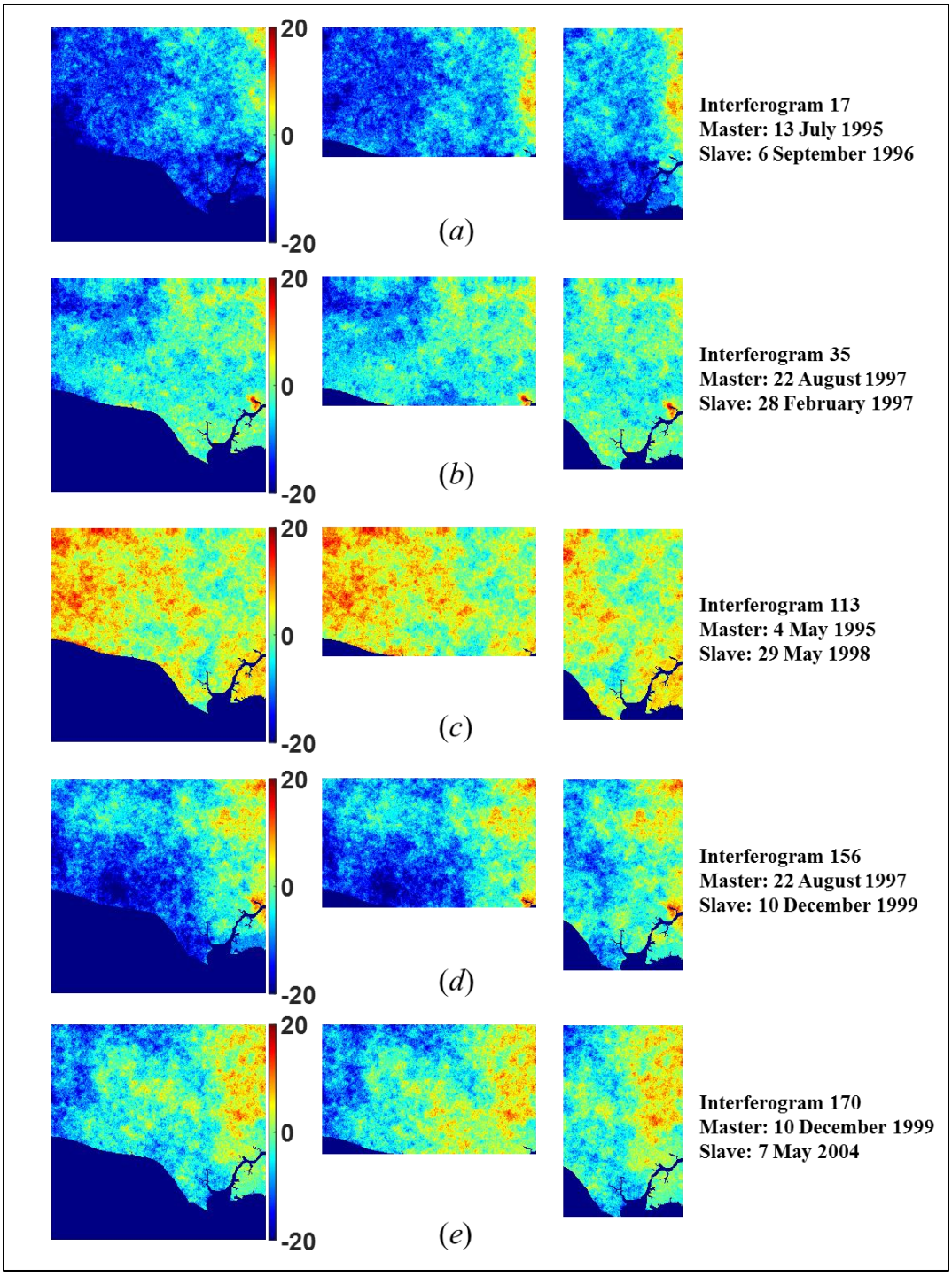


Figure 5.12: Comparison of the unwrapped differential interferogram (after baseline correction) for five selected image pairs. Figures on the middle and right are from the individual phase unwrapping using SNAPHU. The full scene results are shown in the left figures for comparison. No significant difference is observed among them.

5.10. InSAR Time-Series Analysis

In a single unwrapped differential interferogram, the phase of a coherent point represents deformation relating to a chosen control point. The phase, however, is also affected by several factors that will obscure more subtle changes in position such as DEM errors, atmospheric delays and decorrelation due to the presence of temporal and orbital baselines between satellite passes. Several techniques have been developed based upon the analysis of a stack of unwrapped differential interferograms to overcome these limitations and produce a long time series of ground motion. Some of those techniques are Coherent Pixels Technique (CPT) (Blanco-Sánchez et al., 2008); Delft Persistent Scatterer Interferometry (DePSI) (Kampes, 2005; Kampes, 2006); Interferometric Point Target Analysis (IPTA) (Werner et al., 2003); Permanent Scatterer InSAR (PSInSAR) (Ferretti et al., 2000; Ferretti et al., 2001); Persistent Scatterer Pairs (PSP) (Costantini et al., 2008; Costantini et al., 2012); Quasi Persistent Scatterers (QPS) (Perissin and Wang, 2012); SqueeSAR (Ferretti et al., 2011); Stable Points Network (SPN) (Crosetto et al., 2008; Kuehn et al., 2010); and Stanford Method for Persistent Scatterers (StaMPS) (Hooper et al., 2004; Hooper, 2008). Each technique possesses inherently unique strengths and weaknesses. Interested readers can refer to Osmanoğlu et al. (2016) for a review of those techniques.

The efficiency of InSAR time-series analysis has been proven in numerous applications. Examples include for monitoring earthquakes (e.g. by Lanari et al., 2010; Sansosti et al., 2010; Wen et al., 2012; Shao et al., 2016), landslides (e.g. by Liu et al., 2012; Bovenga et al., 2012; Tong and Schmidt, 2016), volcanoes (e.g. by Hooper et al., 2004; Ofeigsson et al., 2011; Samsonov and d'Oreye, 2012; Sato et al., 2016), land subsidence (e.g. by Osmanoğlu et al., 2011; Sowter et al., 2013; Chaussard et al., 2014; Bai et al., 2016; Wanwan Zhang et al., 2016; Yin et al., 2016), and engineering structures (e.g. by Wang et al., 2008; Wang et al., 2010; Du et al., 2016).

The software used in this research utilises the ISBAS algorithm (Sowter et al., 2013; Bateson et al., 2015) for the time-series analysis. The algorithm follows similar principles as the standard SBAS algorithm (Berardino et al., 2002; Lanari et al., 2004), but is further refined to also include intermittent points in the time-series analysis. Some of the essential characteristics of the technique are listed below:

i. Selection of interferograms only includes image pairs separated by small temporal and orbital baselines to maximise coherence.

ii. The interferograms form a redundant network linking between images in the temporal and spatial baseline space.

iii. Decorrelation noise in the interferograms is partly removed by range filtering of the non-overlapping part of the spectrum and by applying a spatial filter, thus reducing the interferogram spatial resolution.

iv. Selection of coherent points takes into account the speckle properties of most targets in SAR images.

v. Interferograms are spatially unwrapped, and inversion of the whole set of interferograms is made using Singular Value Decomposition (SVD) to provide phase delay time series.

5.10.1. Estimation of Linear Velocity and DEM Errors

The time-series analysis within Punnet begins with the estimation of linear velocity and DEM errors. The unwrapped phase for each coherent point $\Delta\emptyset_{i,j}$ is assumed to contain contributions from the monotonic deformation V which is linear with time, and the DEM errors δh which is proportional to the normal (or perpendicular) baseline. Meanwhile, atmospheric effect is considered as random across the whole unwrapped interferograms, thus has mean zero.

$$\Delta\emptyset_{i,j} = \frac{4\pi}{\lambda} \cdot \left(t_i - t_j\right) \cdot V + \frac{4\pi}{\lambda} \cdot \frac{B_{perp}^{i,j}}{R \cdot \sin\theta} \cdot \delta h + \varepsilon \quad \cdots\cdots\cdots\cdots\cdots\cdots\cdots\cdots\cdots\cdots\cdots\cdots \quad (5.7)$$

where:

- $4\pi/\lambda$ represents conversion of unit from cycle to metre considering two ways signal travel (transmit and receive).
- $\left(t_i - t_j\right)$ is the temporal separation between the master image t_i and the slave image t_j.
- $\left(B_{perp}^{i,j}/R \cdot \sin\theta\right)$ is a coefficient to map the relationship between DEM error and perpendicular baseline $B_{perp}^{i,j}$ using satellite-to-target distance R and incidence angle θ.
- ε represents noises from other factor (e.g. thermal noise) and un-modelled errors.

From Equation (5.7), it is possible to estimate the linear velocity and DEM errors for each coherent point using LSE on a series of unwrapped phases. Nevertheless, it is worth mentioning that the quality of estimation can be degraded by the presence of outliers (e.g. from the phase unwrapping errors), which is previously overlooked. In this research, the author has improved the previous algorithms by incorporating an outlier rejection scheme. The parameters for detection of outliers are customisable, but for robust processing,

the maximum rejection number is configured to be 10% of the available observations and the threshold for the acceptable observations to be three times the standard deviation of residuals.

The algorithm is tested using Mexico processing made on 18 Sentinel-1 images (Sowter et al., 2016), considering the known velocity rates and available ground truth in the area. The dataset was acquired between 3 October 2014 and 7 May 2015. **Figure 5.13** shows the time-series analysis of four individual points, i.e. PT01 - PT04. PT01 to PT03 are located in an area that undergoes rapid subsidence, whereas PT04 is located in a relatively stable area. The red-dotted points represent the estimated velocity (left figures) and DEM error (middle figures). The right figures show the residuals from the LSE estimation. The subsidence at PT01 - PT03 is clearly visible, but the estimated values are affected by outliers, observed at the top-right region of the left figures. The same outliers correspond to high residual values on the bottom-right side of the right figures. The presence of residuals from this processing has caused underestimation of the real subsidence rates.

The LOS-velocity maps from the processing are shown in **Figure 5.14**. The result from the original algorithm (without outlier removal) is presented as **Figure 5.14a**. The detection of outliers can be made in a single or multiple iterations, and the results are shown as **Figure 5.14b** and **Figure 5.14c**, respectively. It is evident that the original algorithm failed to address the outliers, thus underestimate the subsidence rates. Although detection of outliers through multiple sequences can yield a slightly better result, the required time for processing also increased considerably. For comparison, the original algorithm took approximately 5.5 hours for the LSE (consisting of ~2.77 million coherent points), whereas single and iterative method took about 6.0 and 8.3 hours, respectively. The required time will vary upon data, depending on the number of coherent points and outliers detected in the process. The corresponding standard error for the LOS-velocity map is shown in **Figure 5.15**. It is worth noting that significant improvement is achieved by adopting the new algorithm that incorporated outlier rejection scheme as compared to the previous algorithm.

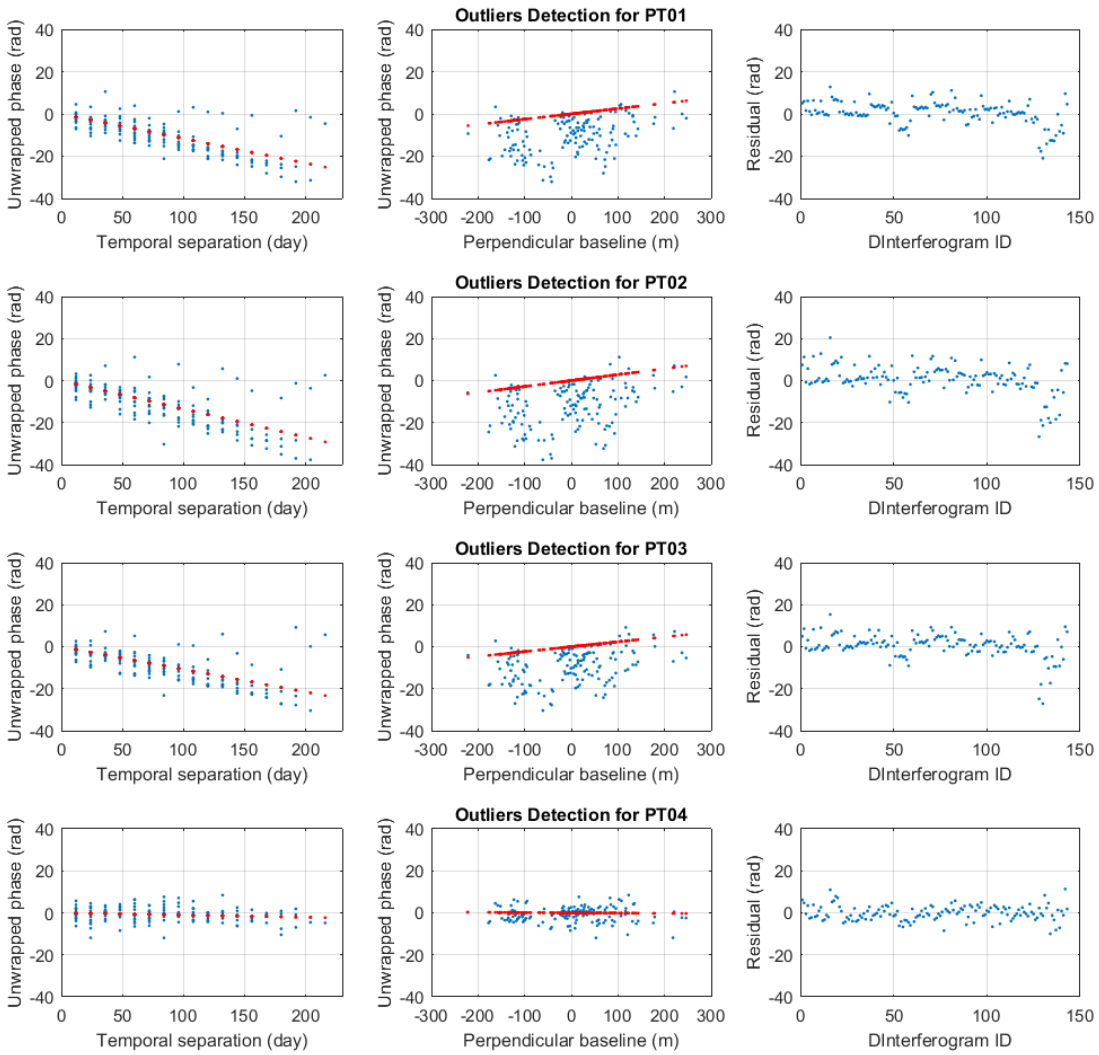


Figure 5.13: Outliers detection at four points, i.e. PT01 - PT04. (Left) Scatter plot of the unwrapped phase against temporal separation. Red points show linear velocity from the final estimation. Strong subsidence can be observed from the phase, but the estimated rate is affected by outliers in the unwrapped phase. (Middle) Plot of the unwrapped phase against the perpendicular baseline. (Right) Residuals from the LSE. Interferogram with the highest residual value is rejected for the subsequent estimation.

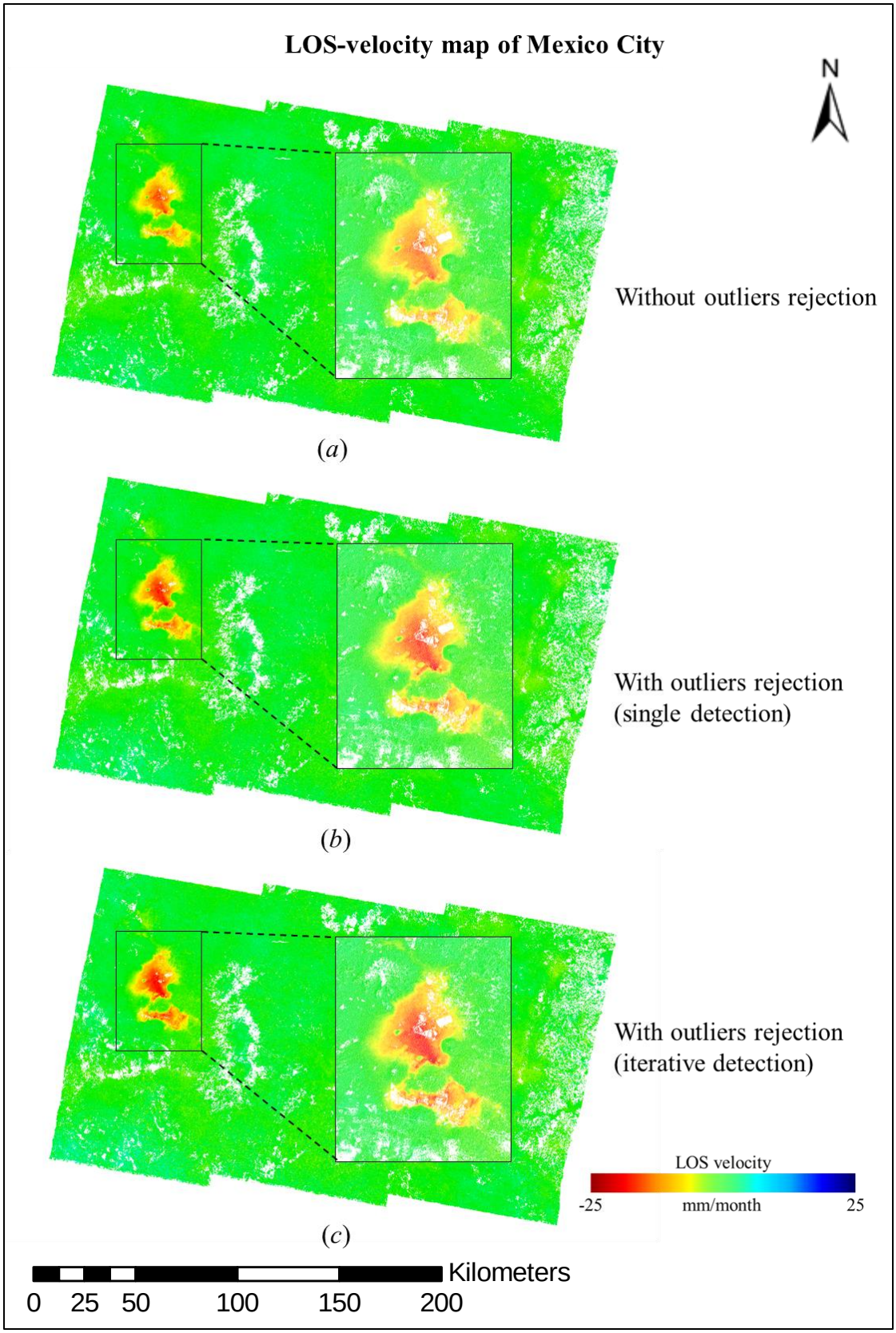


Figure 5.14: LOS-velocity map from Mexico processing. 18 Sentinel-1 images were acquired between 3 October 2014 and 7 May 2015. (*a*) The result from the original algorithm, i.e. without outlier rejection. (*b*) The result from outlier detection in a single iteration. (*c*) The results from outlier detection in iterative detection.

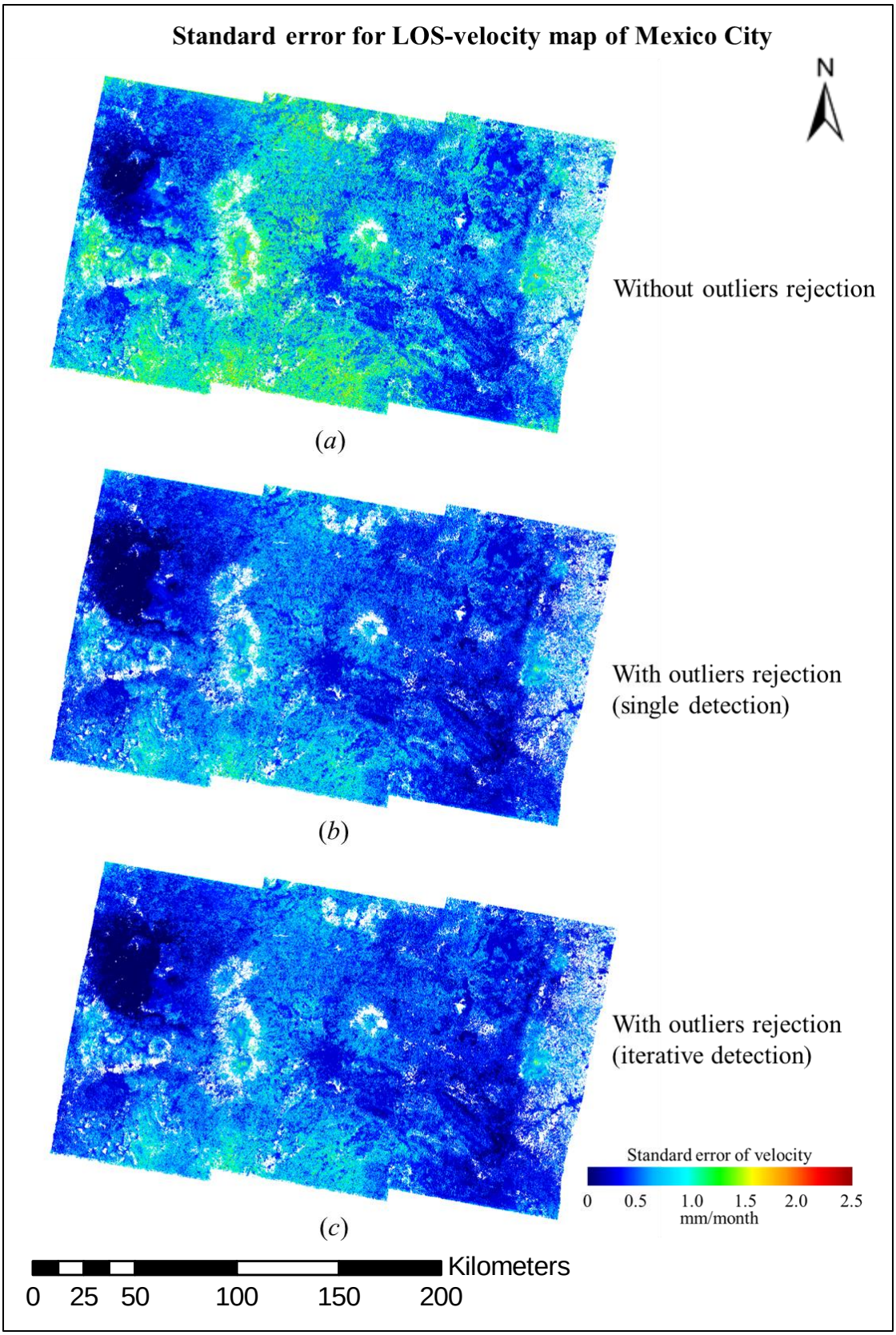


Figure 5.15: Standard error for LOS-velocity map of Mexico City. (*a*) The result from the original algorithm, i.e. without outlier rejection. (*b*) The result from outlier detection in a single iteration. (*c*) The results from outlier detection in iterative detection.

5.10.2. Temporal Evolution of the Deformation

Although linear velocities estimated from the previous step provide meaningful information about deformation in the study area, the interest of the scientific community is now progressively moving toward the study of the temporal evolution of the detected deformation. Punnet is also capable of retrieving such information by adopting SVD to link independent SAR acquisition datasets, separated by large baselines. The same algorithm is described in Berardino et al. (2002). The whole process is summarised in **Figure 5.16**. SVD becomes handy in this situation to solve singular systems that can be caused by several factors as follows:

i. Implementation of maximum threshold for orbital and temporal baselines in the formation of differential interferograms

   As has been highlighted, the ISBAS algorithm only forms interferograms between image pairs that have orbital and temporal baselines below predefined thresholds, i.e. 350 m for the perpendicular baseline and 5 years for the temporal baseline. Although in doing so, phase information from interferograms that suffer decorrelation phenomena is excluded, this could also create isolated networks of interferograms characterised by small baseline subsets, but separated by the large baseline.

ii. Implementation of minimum interferograms threshold for the identification of coherent points

   ISBAS algorithm identifies coherent points to represent deformation in an area based on the number of layers required to achieve average coherence value of better than 0.25. For intermittent points, some interferograms that exhibit low coherence value are rejected and thus could contribute to the aforesaid isolated networks of interferograms.

iii. Implementation of outliers rejection

   Although improved results can be achieved by incorporating an outlier rejection scheme as seen in the Mexico processing, the process of filtering out interferograms that exhibit high residual values can contribute to disconnection of the interferograms network. Since the detection is made independently for each coherent point, different points may exclude different interferograms for the final estimation of velocity and DEM error.

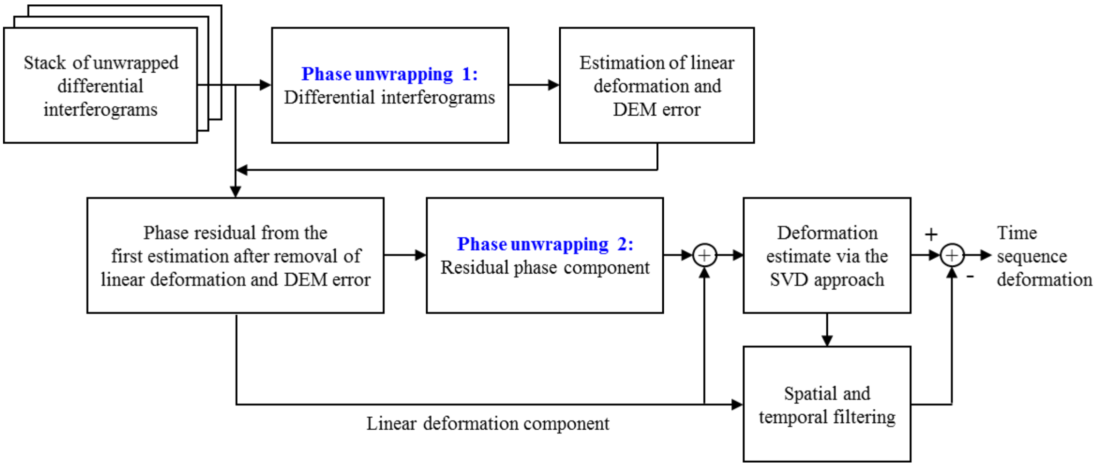


Figure 5.16: Block diagram of the implemented algorithm. Figure adapted from Berardino et al. (2002).

Apart from that, the ISBAS algorithm also requires two phase unwrapping procedures for the retrieval of deformation at SAR acquisition dates. The first is described previously in **Section 5.9**, made on the differential interferograms to estimate the linear component of the deformation and possible topographic artefacts. The second phase unwrapping is performed on the residual from the first analysis to determine non-linear elements of the deformation along with atmospheric phase screen (APS). There are two potential errors from implementing this procedure: (1) additional phase unwrapping errors, and (2) dubious quality of the estimation from using SVD to solve a singular system.

For areas that undergo significant deformation such as in Mexico City, a method is introduced by the author to estimate the temporal evolution of deformation without the requirement for a second phase unwrapping procedure. The proposed method has two main benefits: (1) minimise the errors contribution from phase unwrapping, and (2) reduce the processing time as phase unwrapping accounts to a large sum of the time required in the processing chain. From Equation (5.7), it can be seen that the phases of unwrapped differential interferograms (after baseline correction) contain three main contributions, namely from deformation (linear and non-linear), DEM error, and noise. It is possible to remove the contribution from DEM error using the estimated value and rearranging the Equation (5.7) as follows:

$$\Delta\emptyset_{i,j} - \frac{4\pi}{\lambda} \cdot \frac{B_{perp}^{i,j}}{R \cdot \sin\theta} \cdot \delta h = \frac{4\pi}{\lambda} \cdot \left(t_i - t_j\right) \cdot V + \varepsilon \quad (5.8)$$

Assuming the APS is random (thus, has mean zero) across the entire set of interferograms, deformation (linear and non-linear) at SAR acquisition dates can be retrieved by inverting the phase from Equation (5.8) with respect to the earliest image. As expected, a single phase inversion cannot be performed in the case of isolated networks. This problem is rectified by introducing a new reference, i.e. the earliest image in that network and carrying out independent estimation. The author has implemented this strategy as an additional module to Punnet. The algorithm is tested over Mexico City considering the large deformation magnitud, as well as the availability of numerous references from the literature. **Figure 5.17** shows the result of ten selected points from the processing. It can be seen that all points show a subsidence trend in relation to the first image. The amount of deformation varies between points as they are all located in different parts of the city, but range from about 6 to 13 cm over 3 months period. The estimated magnitude agreed reasonably well with the literature, such as found in Cabral-Cano et al. (2010), Cigna et al. (2011), López-Quiroz et al. (2009), Yan et al. (2012) and Osmanoğlu et al. (2011) using ENVISAT images, as well as Chaussard et al. (2014) using ALOS-PALSAR. A similar agreement is also observed with other Sentinel-1 processing found in Geudtner (2014), Lanari et al. (2015), Prats-Iraola et al. (2015) and Wegmüller et al. (2015).

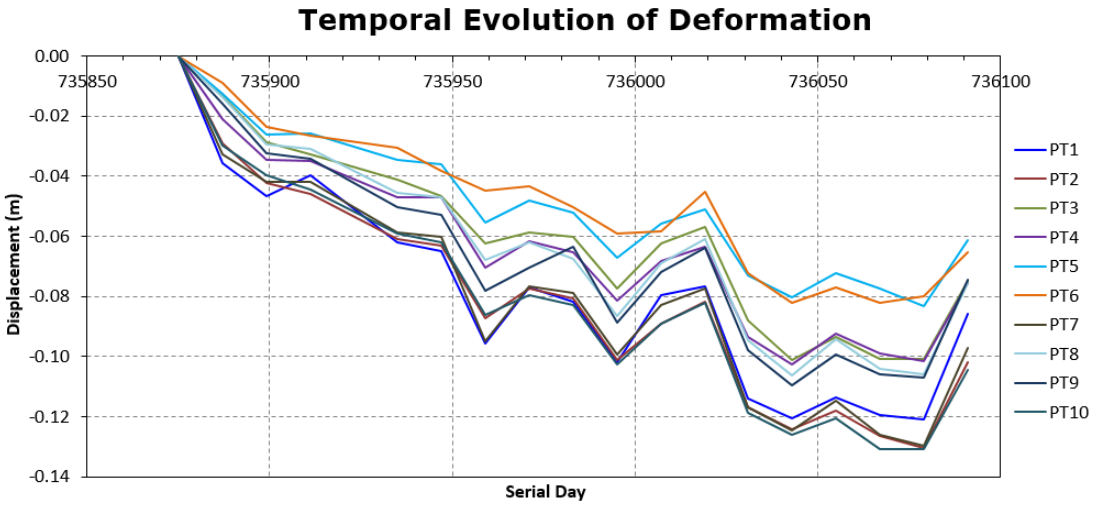


Figure 5.17: Temporal evolution of deformation for the 10 selected points (represented by different colours) in Mexico City. In general, all points show subsidence trend in relation to the first acquisition.

5.11. Mapping LOS-Velocity to Its Respective 3D Components

1-dimensional (1D) measurement along the LOS direction has greatly limited the capability of InSAR to investigate surface displacements and their dynamics. Unless the deformation occurs parallel to the satellite viewing angle, the rate of deformation from InSAR time-series can only capture part of the real movement on the ground. Although resolving the complete 3D displacements, i.e. in northing, easting, and height (or vertical), from InSAR measurements is of great importance and highly beneficial (for example, allowing comparison with other techniques), this is impossible to achieve without additional information (e.g. on other SAR dataset from a different geometry/system or GPS data) or assumption made to the deformation in the area (e.g. the deformation is mainly dominant in the vertical direction). Considerable efforts have been made in recent years and interested readers are referred to Hu et al. (2014) for a complete review of the methods available to resolve 3D surface displacements from InSAR measurements.

According to Fialko and Simons (2001), the LOS-velocity estimated from InSAR time-series (i.e. in satellite LOS) corresponds to the summation of its respective 3D components as shown in the Equation (5.9).

$$V_{los} = \sin\theta \cdot \sin Az \cdot V_{north} - \sin\theta \cdot \cos Az \cdot V_{east} + \cos\theta \cdot V_{height} + \varepsilon \cdots\cdots\cdots (5.9)$$

where V_{los} is the velocity estimated from InSAR time-series, V_{north}, V_{east} and V_{height} are the respective 3D components, θ is the radar incidence angle at the reflection point, Az is the azimuth of the satellite heading vector (positive clockwise from the North) and ε is the measurement error (e.g. due to imprecise knowledge of satellite orbits, atmospheric delays, poor phase coherence, incorrect DEM, etc). **Figure 5.18** illustrates the relationship between them.

From Equation (5.9), it can be seen that complete 3D displacements can be resolved from the combination of multiple InSAR LOS measurements from different geometries. For instance, Gray (2011) exploited three different LOS displacements from the extra-low and extra-high beams of RADARSAT-2 to estimate a full 3D movement of the Henrietta Nesmith Glacier. Ansari et al. (2015) used different statistical measures to assess and compare the influence of different image acquisition strategies as well as data fusion on the performance of InSAR in 3D deformation retrieval. They observed a strong correlation between the retrieved 3D parameters in the local vertical-north plane from integrating nominal InSAR acquisitions, i.e. a set of measurements from ascending and descending tracks acquired from right-looking geometry. However, the correlation is thought to be decreased by non-nominal acquisitions, i.e. left-looking or squinted observations.

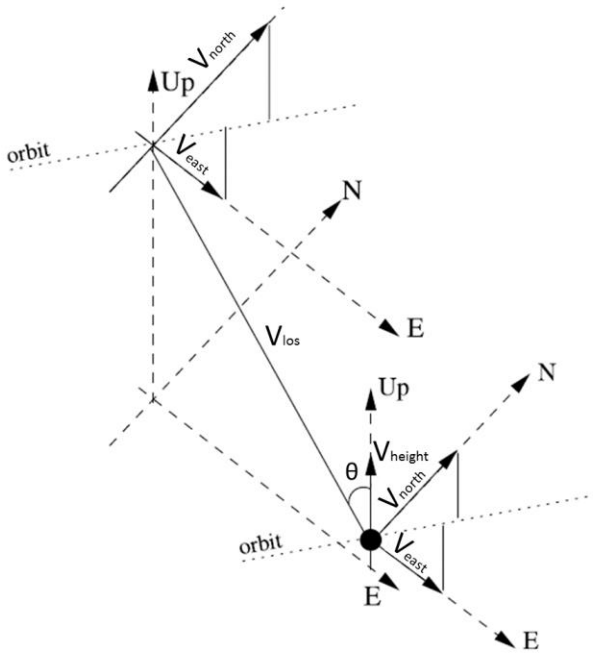


Figure 5.18: Relationship between the LOS-velocity (i.e. V_{los}) from InSAR time-series to its 3D components (i.e. V_{north}, V_{east} and V_{height}) considering the right looking ascending satellite geometry.

In practice, it is often difficult to obtain a sufficient number of SAR images for an area in more than one geometry, primarily covering the same period. Although results from different geometries can be retrieved from this work, i.e. ERS-1/2 dataset in descending mode and Sentinel-1 in ascending mode, they were acquired over a different time span. Therefore, each point could have different velocity rate between the two periods. This difference will introduce errors in the estimated 3D displacement. Furthermore, Sentinel-1 datasets only cover an 18 month period which is considered insufficient for a reliable estimation of the long-term deformation rate. It is worth noting that most SAR satellites orbit the Earth in a near-polar orbit. Therefore, they are less sensitive to the movement in a North-South direction. When both left-looking and right-looking interferograms are available, the errors of this course will decrease significantly (Wright et al., 2004). The side-looking geometry of SAR sensors along with relatively small incidence angle has caused the InSAR measurements to be sensitive mostly to height (or vertical) movements. The usual case to estimate the vertical ground deformation is to divide the InSAR LOS measurement by the cosine of the incidence angle assuming no horizontal ground motion occurred (Galloway et al., 1998; Amelung et al., 1999; Hung et al., 2011).

Based on this argument, vertical deformation is computed for comparison with the GPS result assuming contributions from the first two terms of Equation (5.9) are marginal. The radar incidence angle increases from near to far end (**Table 5.4**), thus each point exhibits their unique value. For Mexico City, although the resulting

deformation map is somewhat similar to that seen in LOS direction (**Figure 5.16)**, the calculated vertical deformations are more dispersed, and the rates are higher than those in the LOS direction (**Figure 5.19**). For the Johor dataset, the result is discussed in **Chapter 7**.

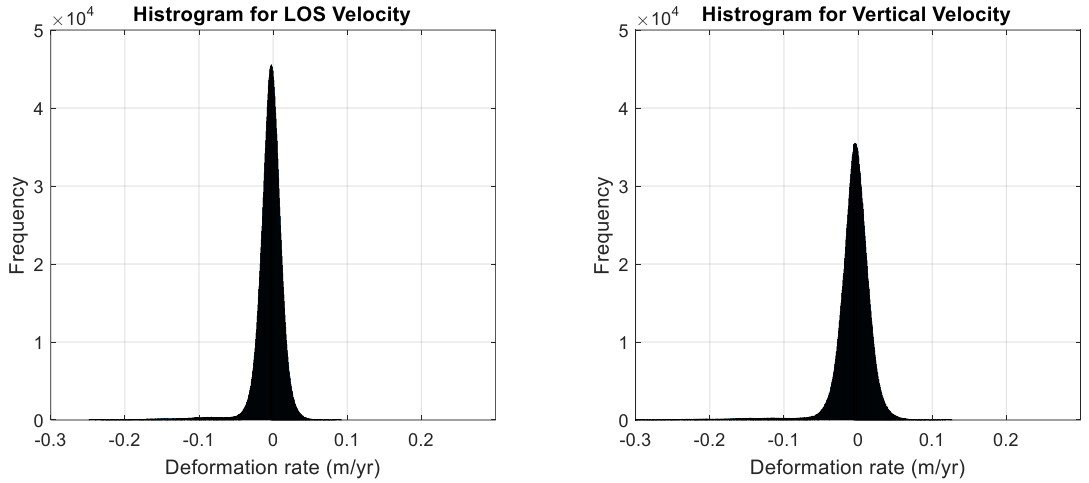


Figure 5.19: Comparison between the estimated velocity in LOS and vertical directions. The vertical velocity is more disperse compared to the LOS velocity as resulted from the multiplication of LOS velocity with the inversed cosine of radar incidence angle.

Table 5.4: Range of incidence angle for the coherent points in Johor.

Dataset	Minimum Incidence Angle	Maximum Incidence Angle	Average Incidence Angle
ERS-1/2 (track 347)	19.65°	26.42°	23.13°
ERS-1/2 (track 75)	19.62°	26.48°	24.45°
Sentinel-1	30.99°	42.28°	39.76°

5.12. Summary

In this chapter, the fundamental concepts of deformation analysis using InSAR time-series have been discussed, which is based on the analysis of a series of phase differences obtained from the repeat-pass InSAR measurements. Although in theory, InSAR time-series are capable of detecting surface changes with the precision of centimetres or even millimetres, the achievable precision in practice is subject to various error sources affecting the measurements. Indeed, the main challenges usually come from the phase decorrelation, atmospheric effects and difficulties related to phase unwrapping.

Throughout this research, the processing of SAR datasets is made using Punnet - an in-house software developed based on the ISBAS algorithm. The algorithm, in general, follows the standard SBAS algorithm described in Berardino et al. (2002) but is further customised to achieve better coverage over rural or vegetated areas. Detailed processing strategies, from the formation of differential interferograms to the derivation of final deformation maps (both in LOS and vertical directions), have been highlighted encompassing the rationale behind every decision made by the author. Some important aspects that deserve attention are discussed and investigated. The existing algorithm also has been improved from the works carried out in this research. Those investigations and improvements have been implemented by the author as additional modules to Punnet software, and they are summarised as follows:

i. Application of statistical measures to identify the appropriate thresholds for the orbital and spatial baselines to maximise the number of acquired interferograms.

ii. Present one of the earliest Sentinel-1 results over Malaysia, following targeted changes made to the in-house software. The changes consist of (1) additional module for debursting and merging prior to images coregistration and resampling, and (2) utilisation of the known de-ramping function from Miranda (2015) for the images coregistration and resampling.

iii. Application of statistical analysis to assist in identifying candidates of the control point for phase unwrapping. This is based on the assumption that the candidates should exhibit high coherence values with minimum RMS across selected differential interferograms (i.e. with low orbital separation).

iv. Investigation on the effects of the water body to phase unwrapping using SNAPHU. They are found to be nominal, most probably due to nearest neighbour interpolation applied prior to the phase unwrapping.

v. Implementation of outliers' rejection for the estimation of linear velocity. The algorithm showed promising result upon testing on the Mexico processing.

vi. Implementation of a new method to investigate temporal evolution of deformation for areas that undergo significant deformation magnitude such as Mexico City. The method eliminates the need for second phase unwrapping procedure and SVD, which would cause additional errors to the results.

CHAPTER 6

MODELLING AND MITIGATION OF TROPOSPHERIC EFFECTS IN GPS AND INSAR

6.1. Introduction

Despite numerous advancements that have been achieved in the field of GPS and InSAR, the troposphere remains one of the most challenging error sources that requires delicate attention to obtain precise information about surface deformation. This chapter aims to investigate and mitigate the effects of the troposphere in GPS and InSAR processing. It begins with a brief introduction to atmospheric effects on radio wave propagation and mapping function to map the troposphere from zenith to satellites direction and vice versa. It is followed by a discussion on the strategies and parameters used in the GPS processing. After that, the benefits of using a troposphere model based on real weather data as opposed to empirical models based on the standard atmosphere are discussed. Two processing techniques, namely Precise Point Positioning (PPP) and Double-Difference (DD), are compared in terms of tropospheric modelling. The discussion then continues with the strategy adopted for InSAR processing. Attempts made to improve InSAR results are reported, i.e. using linear and power law correlations with height. Improvements made to the in-house software are also highlighted. This chapter finally ends with a summary of the essential aspects of tropospheric modelling and mitigation in GPS and InSAR.

6.2. Atmospheric Effects on Radio Wave Propagation

The radio signals transmitted from GPS and SAR satellites are affected by the atmosphere as they travel through the medium. Apart from two-way travel in SAR as opposed to one-way travel in GPS, the effects are common on both systems. There are several ways of categorising atmosphere found in the literature. For example, in meteorology, different layers of the atmosphere are characterised by variation of temperature with height. Low tropospheric layers start from negative temperature, up to about 10 - 12 km, where an absolute temperature of about -57°C is reached. The temperature initially stays constant beyond the so-called tropopause, which represents the upper limit of the troposphere (Lydolph, 1985). Characterisation of atmosphere with respect to temperature even varies in the meteorological literature, for example, found in Lydolph (1985) and Mohanakumar (2008).

A more simplistic way to distinguish these layers is based on the occurring density of free electrons, which is used in this research. Next to the Earth's surface up to a height of about 20 km, the ionisation is virtually absent (Dach et al., 2015). This layer is defined as the troposphere. Above this layer, a significant density of free electrons is observed that extends up to about 1000 km, which is termed the ionosphere. The ionospheric layer is not of interest in this research. In GPS, the first-order ionospheric delay accounts for about 99% of the total delay but can be eliminated by using an ionosphere-free linear combination (Hofmann-Wellenhof et al., 2008) as the medium is dispersive to a radio signal. On top of that, higher-order effects can also be mitigated using Global Ionosphere Maps (GIM), for example, provided by the International GNSS Service (IGS) or Center for Orbit Determination in Europe (CODE). Likewise, SAR acquisitions using C-band, as utilised in this research, are much less affected by ionosphere than the L-band observations (Doin et al., 2009). Ionosphere causes a long wavelength signal on SAR interferograms, quite similar to baseline related errors (Ferretti, 2014). Thus, it can be assumed to be negligible after orbital correction.

On the contrary, the troposphere is a non-dispersive medium for frequencies below 15 GHz (Dach et al., 2015). The signal propagation delay depends mainly on temperature, pressure, and water vapour content of the atmosphere. For a one-way travel signal, the tropospheric path delay T is defined by Equation (6.1).

$$T = \int (n-1)\, ds = 10^{-6} \int N^{trop}\ ds \quad \cdots\cdots (6.1)$$

where n is the refractive index and N^{trop} the so-called refractivity. The refractivity can be subdivided into two parts: (1) dry component (N_{dry}^{trop}) which contribute to approximately 90% of the total delay (Janes et al., 1989) and (2) wet component (N_{wet}^{trop}). The latter, although it accounts for a smaller contribution at 10%, shows much higher variability than the former (Hofmann-Wellenhof et al., 2008). Therefore, their precise computation is a big challenge. Separating tropospheric path delay T to its respective dry and wet components can be represented by Equation (6.2).

$$T = T_{dry} + T_{wet} = 10^{-6} \int N_{dry}^{trop}\ ds + 10^{-6} \int N_{wet}^{trop}\ ds \quad \cdots\cdots (6.2)$$

Although it is preferable to directly solve the integral of refractivity using a ray tracing technique based on global numerical models, for example, using European Centre for Medium-Range Weather Forecasts (ECMWF), this task requires high computational load considering the nature of GPS and InSAR observations. For example, in GPS, the number of tracked satellites could reach up to ~12 satellites at a time in various directions. Therefore, a more practical alternative is necessary. Essen

and Froome (1951) have suggested an empirical value for modelling the dry and the wet refractivity at zenith direction using surface meteorological data. Equation (6.3) shows the approximation of these components using pressure P, temperature τ, and partial pressure of water vapour e.

$$N_{dry}^{trop} = 77.64 \cdot \frac{P}{\tau}$$
$$N_{wet}^{trop} = -12.96 \cdot \frac{e}{\tau} + 3.718 \cdot 10^5 \cdot \frac{e}{\tau^2} \quad \cdots\cdots (6.3)$$

where the measurement of pressure and water vapour is in millibars, and the temperature is in Kelvin.

6.3. Mapping Function

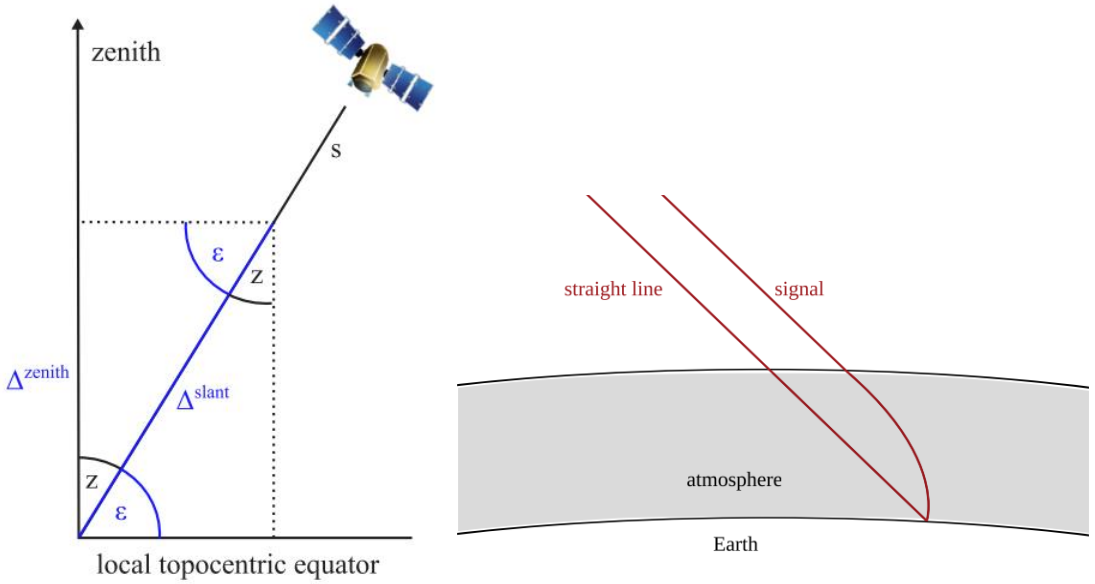
The measurements of meteorological data, for example, using radiosonde (also known as balloon sounding), are made in zenith direction as the balloon travels through different levels of the troposphere. Similarly, most of the tropospheric models for GPS are given in zenith direction as shown in Equation (6.3). The effect of troposphere on satellite signals, on the other hand, increases with deviation from the zenith and reaches its maximum value at the horizon as the signal travels through a thicker layer of the troposphere. The first order approximation for mapping the tropospheric delay from zenith to satellite elevation angle E, and vice versa, is given by Equation (6.4).

$$MF = \frac{1}{\sin E} = \frac{1}{\cos z} \quad \cdots\cdots (6.4)$$

where z is the zenith angle (also equivalent to SAR incident angle). **Figure 6.1a** illustrates this relationship.

The mapping function, as shown in Equation (6.4), however, is not sufficient to model the delay accurately, particularly at the low elevation angles, owing to the bending effects of the signals caused by the troposphere (**Figure 6.1b**). A more precise mapping function, described by a continued fraction of $\sin E$ (Marini, 1972), as shown in Equation (6.5), is more preferable. The value for coefficient a, b, and c in the equation varies between various mapping functions, such as used in Niell (1996), Marini (1972) and Boehm (2004).

$$MF = \frac{1 + \dfrac{a}{1 + \dfrac{b}{1 + c}}}{\sin E + \dfrac{a}{\sin E + \dfrac{b}{\sin E + c}}} \quad \text{..... (6.5)}$$



(*a*) (*b*)

Figure 6.1: Mapping function to relate the tropospheric delay at zenith and satellite elevation angle. (*a*) Simple mapping function based on the elevation angle of the satellite E. This simple mapping function is not accurate for satellites at low elevation angle due to the bending effects, as illustrated in (*b*).

According to Rothacer (1992), it is better to use different mapping functions for the dry and wet parts of the delay. Therefore, Equation (6.3) can be rewritten as follows.

$$T = MF_{dry} \cdot T_{dry}^{zenith} + MF_{wet} \cdot T_{wet}^{zenith} \quad \text{..... (6.6)}$$

where:

- MF_{dry} is the mapping function to map the zenith dry delay T_{dry}^{zenith} to satellite elevation angle, or vice versa.
- MF_{wet} is the mapping function to map the zenith wet delay T_{wet}^{zenith} to satellite elevation angle, or vice versa.

On the contrary, Equation (6.4) is sufficient and usually applied for InSAR applications owing to the incidence angle of the satellites, which range from about 20 to 50 degrees (Li, 2005). At these incidence angles, no significant difference is observed between the two mapping functions.

6.4. Modelling and Mitigation of Tropospheric Effects in GPS

Similar to the GPS processing for coordinates estimation discussed in **Chapter 4**, the estimation of the troposphere is carried out using Bernese GNSS Software version 5.2, hereafter termed Bernese. There are a few strategies for tropospheric modelling and estimation available within Bernese, but the most common practice is to model for the dry delay and estimate the zenith wet delay from the observations. The latter is also known as site-specific troposphere parameters. Although the software offers a broad range of selections for the dry model, only Saastamoinen and VMF-1 are investigated in this research. The former, as well as the rest of the options, are based on the empirical models, whereas the latter benefits from using real weather measurements. As such, VMF-1 is recommended for tropospheric modelling in high accuracy applications (Kouba, 2008), and provides improved result especially in the height component (Heublein et al., 2014).

6.4.1. Saastamoinen Model and Niell Mapping Function (NMF)

One of the most popular models that has been used for a long time to compute tropospheric refraction was the model by Saastamoinen (1973) based on the laws associated with an ideal gas. Saastamoinen relies on the station's height, latitude, zenith angle, surface temperature, surface pressure, and partial pressure of water vapour to model the tropospheric path delay T. In this model, Equation (6.2) has been rewritten as:

$$T = \frac{0.002277}{\cos z}\left[P + \left(\frac{1255}{\tau} + 0.05\right) \cdot e - \tan^2 z\right] \quad \cdots\cdots\cdots\cdots\cdots\cdots\cdots\cdots \quad (6.6)$$

where the pressure P and the partial water vapour e are given in millibars, the temperature τ in Kelvin, and the result is in meters. This model implicitly contains a mapping function to map zenith tropospheric delay (ZTD) to satellite at zenith angle z. Baueršíma (1983) proposed special correction terms B as a function of height at the observing site, and δR which depends on the station height and elevation of the satellite. Their value can be obtained from a lookup table. Equation (6.7) shows the modified equation.

$$T = \frac{0.002277}{\cos z}\left[P + \left(\frac{1255}{\tau} + 0.05\right) \cdot e - B \cdot \tan^2 z\right] + \delta R \quad \cdots\cdots\cdots\cdots\cdots\cdots \quad (6.7)$$

Within Bernese, only B-term correction is applied when using the Saastamoinen model. For any site where the meteorological data is available, tropospheric delay can be calculated directly using Equation (6.7). Unfortunately, no such information is observed at our sites. This is also true

for most of the other GNSS sites. For that reason, Dach et al. (2015) deduce the input value for pressure, temperature and partial water vapour from a standard atmosphere. The following height-dependent values, shown in Equation (6.8), are assumed.

$$P = p_{H0} \cdot \left(1 - 0.0000226 \cdot (H - H_0)\right)^{5.225}$$
$$\tau = \tau_{H0} - 0.0065 \cdot (H - H_0) \quad \cdots\cdots (6.8)$$
$$rh = rh_{H0} \cdot \exp\left(-0.0006396 \cdot (H - H_0)\right)$$

where P, τ and rh are pressure (millibar), temperature (Celsius), and humidity (%) at station height H, whereas p_{H0}, τ_{H0} and rh_{H0} are the corresponding values at the reference height H_0. Those reference parameters have been assigned to the value shown in **Table 6.1**. Following that, partial water vapour e can be derived from the humidity using Equation (6.9), where the temperature τ is given in Kelvin.

$$e = \frac{rh}{100} \cdot \exp(-37.2465 + 0.213166 \cdot \tau - 0.000256908 \cdot \tau^2) \quad \cdots\cdots (6.9)$$

Table 6.1: Reference values for height, pressure, temperature and relative humidity used in the Bernese software.

Parameter	Value
Reference height H_0	0 m
Reference pressure p_{H0}	1013.25 mb
Reference temperature τ_{H0}	18°C
Reference humidity rh_{H0}	50%

On the other hand, Niell Mapping Functions (NMF) use the zenith delays computed following the Saastamoinen model (similar as assigning the zenith distance z in Equation (6.6) to zero), but applies a different mapping function. The coefficients for the mapping function are derived from the radiosonde observations in 1987 and 1988 at four different sites and three representative heights (Boehm, 2004). Therefore, they do not represent actual and highly variable weather patterns. In the case of dry part of the delay, the coefficients a, b, and c in Equation (6.5) are determined as follows:

$$a_{dry}(\varphi, DoY) = a_{avg}(\varphi) + a_{amp}(\varphi) \cdot \sin\left(2\pi \cdot \frac{DoY - DoY_0}{365.25}\right)$$
$$b_{dry}(\varphi, DoY) = b_{avg}(\varphi) + b_{amp}(\varphi) \cdot \sin\left(2\pi \cdot \frac{DoY - DoY_0}{365.25}\right) \quad \cdots\cdots\cdots\cdots \quad (6.10)$$
$$c_{dry}(\varphi, DoY) = c_{avg}(\varphi) + c_{amp}(\varphi) \cdot \sin\left(2\pi \cdot \frac{DoY - DoY_0}{365.25}\right)$$

where the value for a_{avg}, b_{avg}, c_{avg}, a_{amp}, b_{amp} and c_{amp} at a site latitude φ are linearly interpolated from **Table 6.2**, whereas DoY being the analysed day-of-year and DOY_0 equalling to either 28 in the case of northern hemisphere, or 211 for the southern hemisphere. In addition, a correction term Δmf_{dry} to account for height at the observing site, for which the delay is calculated, has to be added within the modelled dry delay. This correction term is calculated using Equation (6.11).

$$\Delta mf_{dry} = H \cdot \left(\frac{1}{\sin \varepsilon} - f(\varepsilon, a_H, b_H, c_H)\right) \quad \cdots\cdots\cdots\cdots\cdots\cdots\cdots\cdots\cdots\cdots \quad (6.11)$$

where a_H, b_H, and c_H are given in **Table 6.3**, H is the site height in kilometres, and ε is the elevation angle of the satellite. These computations are made within the module s_NMFDRY.f of Bernese software.

Table 6.2: Coefficients of the dry NMF as a function of site latitude φ, according to Boehm (2004).

	φ = 15°	φ = 30°	φ = 45°	φ = 60°	φ = 75°
a_{avg}	$1.2769934 \cdot 10^{-3}$	$1.2683230 \cdot 10^{-3}$	$1.2465397 \cdot 10^{-3}$	$1.2196049 \cdot 10^{-3}$	$1.2045996 \cdot 10^{-3}$
b_{avg}	$2.9153695 \cdot 10^{-3}$	$2.9152299 \cdot 10^{-3}$	$2.9288445 \cdot 10^{-3}$	$2.9022565 \cdot 10^{-3}$	$2.9024912 \cdot 10^{-3}$
c_{avg}	$62.610505 \cdot 10^{-3}$	$62.837393 \cdot 10^{-3}$	$63.721774 \cdot 10^{-3}$	$63.824265 \cdot 10^{-3}$	$64.258455 \cdot 10^{-3}$
a_{amp}	0.0	$1.2709626 \cdot 10^{-5}$	$2.6523662 \cdot 10^{-5}$	$3.4000452 \cdot 10^{-5}$	$4.1202191 \cdot 10^{-5}$
b_{amp}	0.0	$2.1414979 \cdot 10^{-5}$	$3.0160779 \cdot 10^{-5}$	$7.2562722 \cdot 10^{-5}$	$11.723375 \cdot 10^{-5}$
c_{amp}	0.0	$9.0128400 \cdot 10^{-5}$	$4.3497037 \cdot 10^{-5}$	$84.795348 \cdot 10^{-5}$	$170.37206 \cdot 10^{-5}$

Table 6.3: Coefficients for the height correction of dry NMF, according to Boehm (2004).

a_H	b_H	c_H
$2.53 \cdot 10^{-5}$	$5.49 \cdot 10^{-3}$	$1.14 \cdot 10^{-3}$

Likewise, the wet NMF is also based on the Marini continued fraction form shown in Equation (6.5). A height correction is not necessary in this case, and the coefficients a, b, and c can be interpolated linearly from **Table 6.4**.

Table 6.4: Coefficients of the wet NMF as a function of site latitude φ, according to Boehm (2004).

	φ = 15°	φ = 30°	φ = 45°	φ = 60°	φ = 75°
a	$5.8021897 \cdot 10^{-4}$	$5.6794847 \cdot 10^{-4}$	$5.8118019 \cdot 10^{-4}$	$5.9727542 \cdot 10^{-4}$	$6.1641693 \cdot 10^{-4}$
b	$1.4275268 \cdot 10^{-3}$	$1.5138625 \cdot 10^{-3}$	$1.4572752 \cdot 10^{-3}$	$1.5007428 \cdot 10^{-3}$	$1.7599082 \cdot 10^{-3}$
c	$4.3472961 \cdot 10^{-2}$	$4.6729510 \cdot 10^{-2}$	$4.3908931 \cdot 10^{-2}$	$4.4626982 \cdot 10^{-2}$	$5.4736038 \cdot 10^{-2}$

Regardless of any mapping function or model selected, the tropospheric delay is usually addressed in GPS by introducing a model to represent the dry delay and estimating the wet component using least square estimation (LSE) of the observations data (Boehm et al., 2006). This strategy is employed owing to the difficulty in the precise modelling of partial water vapour. Separating tropospheric delay to its respective dry and wet components is achieved by setting the relative humidity to zero, which yields a partial pressure of water vapour e = 0. According to Saastamoinen model shown in Equation (6.7), the respective dry and wet component of the delay can be represented by Equation (6.12).

$$T_{dry} = \frac{0.002277}{\cos z} \cdot (P - B \cdot \tan^2 z)$$
$$T_{wet} = \frac{0.002277}{\cos z} \cdot \left[\left(\frac{1255}{\tau} + 0.05\right) \cdot e\right] \quad \text{..... (6.12)}$$

where:

- T_{dry} is the dry component of the tropospheric path delay.
- T_{wet} is the wet component of the tropospheric path delay.
- z is the satellite's zenith distance.
- P is the pressure in millibar.
- τ is the temperature in Celsius.
- e is the partial water vapour in millibar.
- B is the correction term as a function of height at the observing site from a lookup table.

6.4.2. Vienna Mapping Function-1 (VMF-1)

In the previous section, Saastamoinen model and NMF have been introduced for tropospheric modelling in GPS. The former relies on the assumption of standard atmosphere to deduce the input value for pressure, temperature, and partial water vapour, following height-dependent values as described in Equation (6.8). The latter, although it takes into account variations of the troposphere with respect to latitude and DoY (see Equation (6.10)), was derived from limited radiosonde observations. Indeed, other models are available within the Bernese software, such as Hopfield (Hopfield, 1969) and Global Mapping Function (GMF) (Boehm et al., 2007). Nevertheless, they are also based on empirical values, thus, not truly representing the real state of the troposphere. On the contrary, VMF-1 described in Boehm et al. (2006) refers to the tropospheric delays from a direct ray-tracing through Numerical Weather Models (NWMs). Therefore, it should represent tropospheric delays more accurately and is recommended for precise applications (Kouba, 2008).

Implementation of VMF-1 within Bernese requires an additional file containing all necessary parameters from the ray-tracing to be provided. This file is produced at every six hours interval, which is the usual time resolution for the ECMWF data. Therefore, four files are produced each day. These files are provided by the Vienna University of Technology and are accessible through the following link.

http://ggosatm.hg.tuwien.ac.at/DELAY/GRID/VMFG (accessed 25.10.2016)

For any observation dates and times, the corresponding VMF-1 files can be retrieved based on the following naming convention: *VMFG_yyyymmdd.Hss*, where:

yyyy	year
mm	month
dd	day
ss	00, 06, 12, or 18 for each of the four six-hours files

Processing the daily data using Bernese requires merging five of these six-hour files to obtain a single file, i.e. *VMF_yyyyDoY.GRD*, for a particular DoY. This means that four files of the day itself are merged with the first file (*ss* = 00) of the following day. The author has developed an in-house tool as part of this research to automate the processes of data download and files merging. Bernese does not require the headers to be removed during file concatenation. The structure of the VMF-1 file is given in **Figure 6.2**. In the first two columns, the grid points are defined by their respective latitude and

longitude, with a resolution of 2° and 2.5°, respectively. The next two columns provide the dry coefficients a and the wet coefficients a for the Marini continued fraction (refer to Equation (6.5)). Finally, in the last two columns, the value for zenith dry (T_{dry}^{zenith}) and zenith wet delays (T_{wet}^{zenith}) at the grid points are given.

```
! Version:            1.0
! Source:             J. Boehm, TU Vienna (created: 2011-01-02)
! Data_types:         VMF1 (lat lon ah aw zhd zwd)
! Epoch:              2011 01 01 00 00  0.0
! Scale_factor:       1.e+00
! Range/resolution:   -90 90 0 360 2 2.5
! Comment:            http://ggosatm.hg.tuwien.ac.at/DELAY/GRID/VMFG/
 90.0   0.0 0.00114714  0.00065385  2.3334  0.0089
 90.0   2.5 0.00114714  0.00065385  2.3334  0.0089
 90.0   5.0 0.00114714  0.00065385  2.3334  0.0089
 90.0   7.5 0.00114714  0.00065385  2.3334  0.0089
 90.0  10.0 0.00114714  0.00065385  2.3334  0.0089
 90.0  12.5 0.00114714  0.00065385  2.3334  0.0089
 90.0  15.0 0.00114714  0.00065385  2.3334  0.0089
   ⋮     ⋮       ⋮           ⋮         ⋮       ⋮
-90.0 330.0 0.00118903  0.00042736  1.5444  0.0042
-90.0 332.5 0.00118903  0.00042736  1.5444  0.0042
-90.0 335.0 0.00118903  0.00042736  1.5444  0.0042
-90.0 337.5 0.00118903  0.00042736  1.5444  0.0042
-90.0 340.0 0.00118903  0.00042736  1.5444  0.0042
-90.0 342.5 0.00118903  0.00042736  1.5444  0.0042
-90.0 345.0 0.00118903  0.00042736  1.5444  0.0042
-90.0 347.5 0.00118903  0.00042736  1.5444  0.0042
-90.0 350.0 0.00118903  0.00042736  1.5444  0.0042
-90.0 352.5 0.00118903  0.00042736  1.5444  0.0042
-90.0 355.0 0.00118903  0.00042736  1.5444  0.0042
-90.0 357.5 0.00118903  0.00042736  1.5444  0.0042
```

Figure 6.2: Structure of the VMF-1 file. The first seven rows are the header of the file (begin with the symbol "!"). The first two columns are the latitudes and longitudes of the grid with 2° and 2.5° resolution, respectively. The next two column provide the coefficient a for the dry and wet delays, whereas the last two column are the zenith delay for dry and wet from the ray tracing.

Notice that only coefficient a for dry and wet are given in the file. This is because the coefficient b for dry (b_{dry}) is kept constant at 0.0029, whereas the coefficient c for dry (c_{dry}) can be computed using the following formula (Boehm et al., 2006).

$$c_{dry} = c_0 + \left[\left(\cos\left(\frac{DoY - 28}{365} \cdot 2\pi + \psi\right) + 1\right) \cdot \frac{c_{10}}{2} + c_{10}\right] \cdot (1 - \cos\varphi) \quad \cdots\cdots (6.13)$$

The value for c_0, c_{10}, c_{10} and ψ in the equation are taken from the **Table 6.5**. Likewise, the value for coefficient b and c for wet mapping function are fixed at 0.00146 and 0.04391, respectively. Boehm et al. (2006) suggested that their values are not significant as the zenith wet delays are smaller by a factor of ~10 than the zenith dry delays. Those adopted values are the same as the coefficients used in NMF at 45° latitude.

Table 6.5: Coefficients for the determination of c_{dry} in VMF-1, according to (Boehm et al. 2006).

	Northern Hemisphere	Southern Hemisphere
c_0	0.062	0.062
c_{10}	0.001	0.002
c_{11}	0.005	0.007
ψ	0	π

Since the parameters from the VMF-1 files are given in gridded coordinates, spatial interpolation is required to obtain the respective value at station's position. Bernese uses bilinear interpolation as shown in **Figure 6.3** based on the value at four grid corners. Following the same notation used in the figure, Equation (6.14) describes the interpolation steps. Likewise, linear interpolation in time is made to acquire the value at the observation epoch based on the value of six hours interval as shown in Equation (6.15).

$$a_{13} = \frac{\delta\varphi \cdot (a_3 - a_1)}{\Delta\varphi} + a_1$$

$$a_{24} = \frac{\delta\varphi \cdot (a_4 - a_2)}{\Delta\varphi} + a_2$$

$$a_{site} = \frac{(\Delta\lambda - \delta\lambda) \cdot (a_{13} - a_{24})}{\Delta\lambda} + a_{13} \quad \cdots\cdots (6.14)$$

$$a_{site,t_{obs}} = a_{site,t1} + \frac{t_{obs} - t_1}{t_2 - t_1} \cdot \left(a_{site,t2} - a_{site,t1}\right) \quad \cdots\cdots (6.15)$$

where:

- λ_{site} and φ_{site} are the site latitude and longitude.
- a_1, a_2, a_3 and a_4 are the value at four corners of the grid.
- $\Delta\lambda$ and $\Delta\varphi$ are the grid spacing in latitude and longitude, correspond to 2° and 2.5°, respectively.
- $\delta\varphi$ is the different in latitude between site and top-left corner of the grid.
- $\delta\lambda$ is the different in longitude between the site and top-left corner of the grid.
- a_{site} is the value at site coordinate after spatial interpolation.
- $a_{site,t1}$ is the value at site coordinate after spatial interpolation at time t_1, correspond to the first epoch of the VMF-1 file. Similarly, $a_{site,t2}$ is the value at time t_2 in the subsequent epoch, separated by six hours interval.
- $a_{site,obs}$ is the value at site coordinate at observation time t_{obs} after spatial and temporal interpolations.

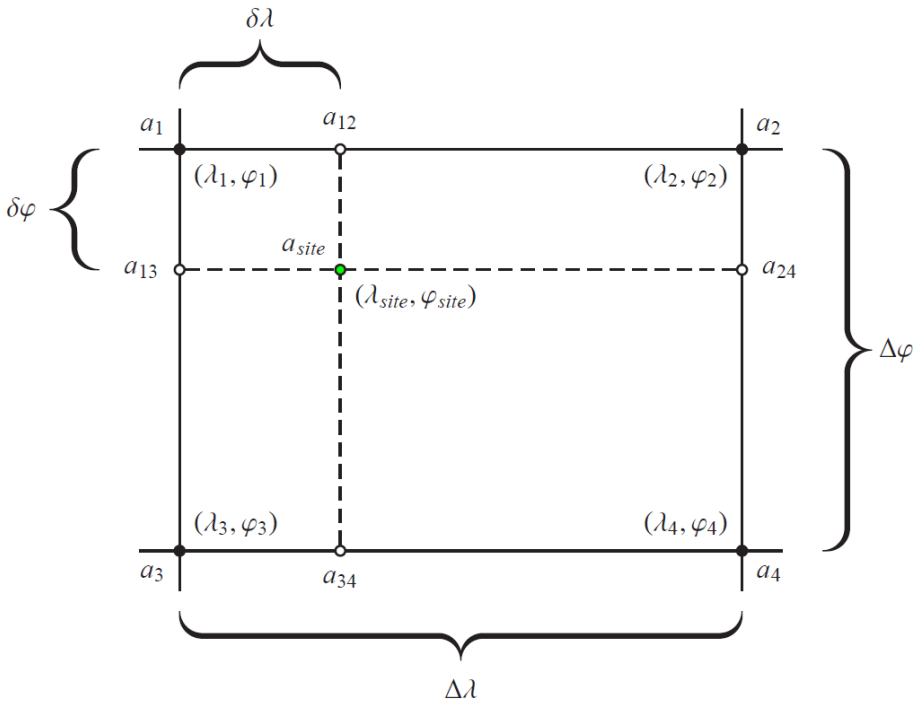


Figure 6.3: Bilinear interpolation on the grid for VMF-1 coefficients.

Following these interpolations, the complete form of dry and wet mapping functions can be retrieved by applying the coefficients a, b, and c to Equation (6.5). It should be noted that these values are referred to grid height, which is given in a file accessible from the following link:

http://ggosatm.hg.tuwien.ac.at/DELAY/GRID/orography_ell
(accessed 25.10.2016)

Therefore, an adjustment is necessary to acquire the corrected value at the station height, i.e. above ellipsoid. While this change can be neglected for the wet mapping function (Boehm et al., 2006), it should be applied to the dry mapping function as well as to the interpolated zenith dry and zenith wet delays. Correction for the dry mapping function is made after Niell (1996), and the final dry mapping function $MF_{dry,ell}$ can be calculated using Equation (6.16).

$$MF_{dry,ell} = \left(\frac{1}{\sin E} - \frac{1 + \dfrac{a}{1 + \dfrac{b}{1+c}}}{\sin E + \dfrac{a}{\sin E + \dfrac{b}{\sin E + c}}} \right) \cdot H_{site,ell} \quad \cdots\cdots\cdots\cdots\cdots\cdots \quad (6.16)$$

where E is the elevation angle of satellite, coefficients a, b, and c are defined as constant at 0.0000253, 0.00549 and 0.00114, and $H_{site,ell}$ is the station's height above ellipsoid in kilometre. Meanwhile, the final zenith dry $T_{dry,ell}^{zenith}$ and zenith wet $T_{wet,ell}^{zenith}$ delays can be estimated using Equation (6.17) and Equation (6.18), respectively.

$$T_{dry,ell}^{zenith} = T_{dry,\mathrm{grid}}^{zenith} \cdot \frac{\left(1 - 2.26 \cdot 10^{-5} \cdot H_{site,ell}\right)^{5.225}}{\left(1 - 2.26 \cdot 10^{-5} \cdot H_{site,grid}\right)^{5.225}} \cdot \frac{1 - 0.00266 \cdot \cos 2\varphi - 0.28 \cdot 10^{-6} \cdot H_{site,grid}}{1 - 0.00266 \cdot \cos 2\varphi - 0.28 \cdot 10^{-6} \cdot H_{site,ell}} \quad \cdots\cdots\cdots (6.17)$$

$$T_{wet,ell}^{zenith} = T_{wet,grid}^{zenith} \cdot e^{-\frac{\left(H_{site,ell} - H_{site,grid}\right)}{2000}} \quad \cdots\cdots\cdots (6.18)$$

where:

- $T_{dry,\mathrm{grid}}^{zenith}$ is the interpolated zenith dry delay on grid height, obtained from Equations (6.14) and (6.15).
- $T_{wet,grid}^{zenith}$ is the is the interpolated zenith wet delay on grid height, obtained from Equations (6.14) and (6.15).
- $H_{site,ell}$ is the site height above ellipsoid.
- $H_{site,grid}$ is the interpolated grid height, obtained from Equation (6.14).
- φ is the latitude of the station.
- $T_{dry,ell}^{zenith}$ is the zenith dry delay at the station height, above ellipsoid.
- $T_{wet,ell}^{zenith}$ is the zenith wet delay at the station height, above ellipsoid.

Since no comparable approach exists for the conversion of wet delays at different heights, Kouba (2008) deduces Equation (6.18) from the average differences between the zenith wet delay at an observing site (about 1100 m above the mean grid height) and the values of the zenith wet delay at the mean grid heights, assuming an exponential decay. Alternatively to the gridded VMF-1, site-dependent VMF-1 are also available for selected IGS stations. Although the gridded coefficients are interpolated within sparse grids (i.e. 2° in latitude and 2.5° in longitude), their comparison with the site-dependent VMF-1 shows an excellent agreement. Kouba (2008) found the RMS of their difference is at the level of 1×10^{-6} and 2×10^{-5} in term of coefficients a_{dry} and a_{wet}, respectively. **Table 6.6** below listed all modules within Bernese involved in the VMF-1 computations.

Table 6.6: Modules in Bernese for the computation of VMF-1.

Module	Description
d_grid	• Bilinear interpolation to obtain the value at the station coordinate based on the value at four grid corners. • Linear interpolation in time to obtain the value at the observation epoch.
s_vmf1_ht	• Compute the complete mapping function for dry and wet delays at grid height, based on the interpolated value of coefficient a from the VMF-1 file. • Height correction for the dry mapping function.
f_vmf1ell	• Correct the zenith delays provided by the VMF-1, from the grid to station's heights.

6.4.3. Precise Point Positioning (PPP) and Double-Difference (DD)

Two processing strategies in GPS for accurate positioning are PPP and DD. When dealing with troposphere, both strategies share a common practice which is to model for the dry delay and estimate the wet delay through LSE. Going down to satellites at low elevation angles, azimuthal asymmetry of the local troposphere at an observation site becomes more and more important and must be accounted for. Estimating horizontal tropospheric gradients along with the wet component of the delays is a common way to cope with these asymmetries. Rothacher et al. (1998) and Meindl et al. (2004) found considerable improvements in the coordinate repeatability by adopting this method. Interested readers are referred to Meindl et al. (2004) for a more detailed description about horizontal tropospheric gradients.

In **Chapter 4**, it has been shown that troposphere is one of the components that affect GPS signals, both in code and phase measurements. The tropospheric refraction term T_k^i, discussed previously, can be expanded further into four components, shown in Equation (6.19) (Dach et al., 2015). The first term represents the a priori model used in the processing, normally associated with the dry component of the delay. The second term is the estimated value, corresponding to the wet component of the delay, whereas the third and fourth terms are horizontal gradient in north and east components, respectively.

$$T_k^i\left(t, A_k^i, z_k^i\right) = MF_{dry}\left(t, z_k^i\right) \cdot T_{dry,k}^{zenith} + MF_{wet}\left(t, z_k^i\right) \cdot T_{wet,k}^{zenith} + \frac{\partial MF}{\partial z} \cdot \cos A_k^i \cdot T_k^{north} + \frac{\partial MF}{\partial z} \cdot \sin A_k^i \cdot T_k^{east} \quad \text{..... (6.19)}$$

where:

- T_k^i is the total tropospheric path delay between station k and satellite i.
- t is the observation time.
- z_k^i and A_k^i are the zenith and azimuth of satellite i observed from station k.
- MF_{dry} is the mapping function to map the zenith dry delay $T_{dry,k}^{zenith}$ to satellite direction. Together, these two terms represent dry component of the delay.
- MF_{wet} is the mapping function for wet delay.
- $\frac{\partial MF}{\partial z}$ is the partial derivative of the mapping function with respect to zenith distance.
- $T_{wet,k}^{zenith}$ is the zenith wet delay at station k, estimated in LSE.
- T_k^{north} is the tropospheric gradient in north, estimated in LSE.
- T_k^{east} is the tropospheric gradient in east, estimated in LSE.

When dealing with the troposphere in PPP, Equation (6.19) is applied directly to each satellite tracked in the observation. For n number of satellites, there will be $2 \times n$ equations at a certain epoch, which are the ionosphere-free linear combination (formed between L_1 and L_2 frequencies) for code and phase measurements (Hofmann-Wellenhof et al., 2008). For zero difference processing between a receiver and a satellite i, usually eight parameters are estimated in total, i.e. satellite position X, Y and Z in the Earth-centered Earth-fixed (ECEF) coordinate system, receiver clock offset, wet component of the troposphere, horizontal tropospheric gradients in north and east, and phase ambiguity between the receiver and satellite i (assuming no cycle slip in the data). With additional satellite j in view, another parameter is added to the list, which is the phase ambiguity between the receiver and satellite j. Estimation of troposphere (represents wet component of the delay) using PPP in this research is made at one hour interval. Likewise, the tropospheric gradient parameters are determined twice per day (beginning and end) using the model described in Chen and Herring (1997). Their value at every hour is estimated linearly. Although the receiver clock offset is estimated at every epoch, their value is not of particular interest in this research. The presence of fractional cycle bias for satellite and receiver prevents a straight forward approach for ambiguity resolution. No attempt is made to fix the ambiguities to their integer value, and the estimation of troposphere is based on float solutions.

On the other hand, DD strategy uses differencing between observations to solve for the parameters. Considering two receivers k and l, that track two satellites i and j, it is not difficult to prove that Equation (6.19) can be rewritten as follows, neglecting the third and fourth terms for simplicity:

$$\begin{aligned}\Delta T_{k,l}^{i,j}\left(t, z_{k,l}^{i,j}\right) = &\left[MF_{dry}\left(t, z_l^j\right) - MF_{dry}\left(t, z_l^i\right)\right] \cdot T_{dry,l}^{zenith} \\ &- \left[MF_{dry}\left(t, z_k^j\right) + MF_{dry}\left(t, z_k^i\right)\right] \cdot T_{dry,k}^{zenith} \\ &+ \left[MF_{wet}\left(t, z_l^j\right) - MF_{wet}\left(t, z_l^i\right)\right] \cdot T_{wet,l}^{zenith} \\ &- \left[MF_{wet}\left(t, z_l^j\right) + MF_{wet}\left(t, z_l^i\right)\right] \cdot T_{wet,k}^{zenith} \quad \cdots\cdots\cdots\cdots\cdots\cdots \quad (6.20)\end{aligned}$$

where:

- $\Delta T_{k,l}^{i,j}$ is the DD total tropospheric path delay between satellite i and j, and receiver k and l.
- t is the observation time.
- z_k^i is the zenith distance of satellite i observed from station k. The same notation is used to represent zenith distance for station l and receiver j.
- MF_{dry} is the dry mapping function to map the zenith dry delay T_{dry}^{zenith} to satellite elevation angle. Together, these two terms represent the dry component of the delay.
- MF_{wet} is the mapping function to map the wet delay from satellites to zenith directions.
- T_{wet}^{zenith} is the zenith wet delay, estimated in LSE.

The first two terms of Equation (6.20) can be computed directly from the chosen model, whereas the zenith wet delay is estimated for station k and l, based on the difference in their mapping functions. The equation can be simplified further as shown in Equation (6.21).

$$\begin{aligned}\Delta T_{k,l}^{i,j}\left(t, z_{k,l}^{i,j}\right) = &\Delta T_{k,l}^{i,j}\left(t, z_{k,l}^{i,j}\right)_{dry} + \left[MF_{wet}\left(t, z_l^j\right) - MF_{wet}\left(t, z_l^i\right)\right] \cdot T_{wet,l}^{zenith} \\ &- \left[MF_{wet}\left(t, z_l^j\right) + MF_{wet}\left(t, z_l^i\right)\right] \cdot T_{wet,k}^{zenith} \quad \cdots\cdots\cdots\cdots\cdots\cdots \quad (6.21)\end{aligned}$$

where $\Delta T_{k,l}^{i,j}\left(t, z_{k,l}^{i,j}\right)_{dry}$ represents the DD dry tropospheric delay taken from a model. For two stations that track n number of satellites simultaneously, there will be $(n-1) \times 2$ independent observations, which are the DD made on the ionosphere-free linear combination for all satellites with respect to a reference satellite (1 for code and 1 for phase measurements). Normally, the satellite at the highest elevation angle is selected as the reference (Hofmann-Wellenhof et al., 2008). Although the number of observation is less than one could achieve

using PPP, DD has some other benefits that are difficult to accomplish otherwise, the first being the cancelation of fractional cycle biases for the satellite and receiver during the differencing process. Furthermore, receiver clock offsets are also neutralised, ensuing a higher chance of ambiguities resolution. As a result, only six parameters are estimated in total (as opposed to eight in PPP) if the first station is held fixed as a reference, namely position of the second station X, Y and Z in ECEF, wet component of the troposphere, and tropospheric gradients in north and east. With more satellites in view, no additional parameter is introduced.

The scripts developed by the author in Bernese employed a more sophisticated approach for modelling the troposphere, which is based on network processing rather than a simple baseline processing described above. The normal equation for each baseline is saved without introducing any reference station. The final estimation is carried out using a minimum constraint condition, imposed on the geometry of a set of reference frame sites. These sites, which are included in the DD processing, are continuously being monitored and represent the core sites in the realisation of International Terrestrial Reference Frame (ITRF). Furthermore, their coordinate from the LSE is checked against their derived coordinates, after applying velocity, using Helmert transformation. Any reference station with high residual value is excluded in the next run until all stations are accepted. This strategy ensures that no errors result from the wrong selection of reference station(s), as could be the case for conventional DD processing. The geometry of the network can be constrained by the following parameters (Dach et al., 2015):

i. Translation in X, Y and Z.
ii. Rotation in X, Y and Z.
iii. Scale.

The troposphere in DD processing is estimated at the one-hour interval, whereas the tropospheric gradients are estimated twice per day, as is the case for PPP. The estimation is made by three no-net-translation conditions imposed on a set of reference sites.

It is worth noting the differences between PPP and DD in terms of their tropospheric estimation. The former is based on a straightforward relationship between the satellites and the receiver. Therefore, precise modelling of satellites orbits and clocks, as well as all other models such as antennas phase centre, ocean tide loading, solid earth tide, and atmospheric pressure, play a significant role in the determination of troposphere. Furthermore, the quality of the estimation could be degraded by the presence of ambiguity, if not correctly solved. In contrast, DD benefits from the differencing made between observations to cancel common errors in the

satellites and receivers, thus attaining higher possibility for ambiguity resolution. The tropospheric estimation, however, is based on a constraint imposed on the geometry of the network. Usually, the troposphere is regarded as a by-product of coordinates. Therefore, any imprecision in the coordinate estimation will also reflect on the quality of the estimated troposphere. Both troposphere estimations using PPP and DD techniques are tested in this research, and their results are in discussed in the next section.

Bernese produces a troposphere file with extension *.TRP upon successful processing of each session (i.e. daily result as in this research). This file contains, among others, the a priori model used for the processing, site-specific troposphere parameters (associated with the wet component of the delay), and horizontal tropospheric gradients. An example is given in **Figure 6.4a**, along with the definition of each element in the file, as shown in **Figure 6.4b**. The header summarises selected options for the a priori model, mapping function, gradient model, minimum elevation, and the temporal sampling interval. The first eight columns represent the name of the observing site, a flag marking the estimated coordinates depending on the modifying program, and the respective date and time for which the parameters have been computed. The following eight columns give values of the a priori model (i.e. MOD_U) and the site-specific parameters (i.e. CORR_U) in the zenith direction, as well as horizontal gradients in North (i.e. CORR_N) and East (i.e. CORR_E). The sum of MOD_U and CORR_U is written to the column TOTAL_U. Standard deviations SIGMA_U, SIGMA_N, and SIGMA_E for the respective values of the site-specific troposphere parameters, and the horizontal gradients are also specified. All values are given in metres. The a priori model is introduced as exact into the computations and therefore does not contribute to the standard deviation given in the troposphere files.

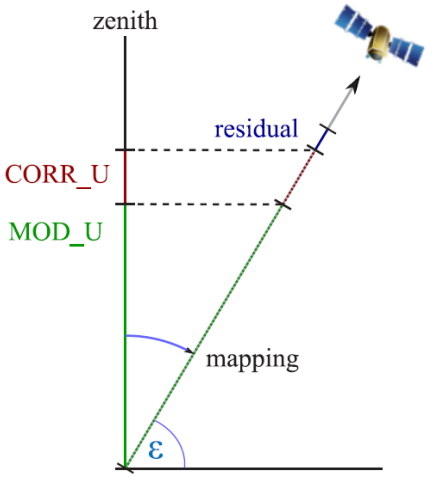
An in-house tool has been developed by the author to extract and plot the data from Bernese *.TRP files. **Figure 6.5** shows the variation of the troposphere at PRTS station from DoY 1 to DoY 3 in 2007. The data is processed using DD and VMF-1 for the tropospheric modelling. Notice the trend of the dry delay changes at 6 hours interval, as it is computed based on the parameters in the VMF-1 files. The files are produced at 6 hours interval. Linear interpolation in time is made according to the sampling configured in the processing, i.e. every one hour. The value is then introduced into Equation (6.21), and the wet component, as well as the horizontal tropospheric gradients, are estimated from the observations. The wet component can be regarded as a correction to the selected model. Nevertheless, some errors from the model inaccuracy could be propagated to the estimated coordinate, most notably in the height component (Kouba, 2008). Heublein et al. (2014) suggested that some part of the troposphere remains in the observations residual. However, that aspect is not investigated in this research.

DD_JOHOR_110010: Final coordinate/troposphere results 23-SEP-15 16:38

A PRIORI MODEL: -17 MAPPING FUNCTION: 8 GRADIENT MODEL: 4 MIN. ELEVATION: 3 TABULAR INTERVAL: 3600 / 86400

STATION NAME	FLG	YYYY MM DD HH MM SS	YYYY MM DD HH MM SS	MOD_U	CORR_U	SIGMA_U	TOTAL_U	CORR_N	SIGMA_N	CORR_E	SIGMA_E
JHJY	A	2011 01 01 00 00 00		2.2897	0.33183	0.00164	2.62153	-0.00094	0.00008	0.00039	0.00009
JHJY	A	2011 01 01 01 00 00		2.2894	0.33713	0.00128	2.62654	-0.00089	0.00008	0.00039	0.00008
JHJY	A	2011 01 01 02 00 00		2.2891	0.33927	0.00116	2.62840	-0.00083	0.00008	0.00039	0.00008
JHJY	A	2011 01 01 03 00 00		2.2888	0.33400	0.00113	2.62284	-0.00078	0.00007	0.00039	0.00007
JHJY	A	2011 01 01 04 00 00		2.2886	0.34076	0.00106	2.62932	-0.00073	0.00007	0.00039	0.00007
JHJY	A	2011 01 01 05 00 00		2.2883	0.33887	0.00113	2.62715	-0.00067	0.00006	0.00039	0.00006
JHJY	A	2011 01 01 06 00 00		2.2880	0.34978	0.00113	2.63777	-0.00062	0.00006	0.00039	0.00006
JHJY	A	2011 01 01 07 00 00		2.2883	0.34636	0.00118	2.63471	-0.00056	0.00006	0.00039	0.00006
JHJY	A	2011 01 01 08 00 00		2.2887	0.34938	0.00123	2.63808	-0.00051	0.00006	0.00039	0.00005
JHJY	A	2011 01 01 09 00 00		2.2891	0.34978	0.00115	2.63884	-0.00046	0.00005	0.00039	0.00005
JHJY	A	2011 01 01 10 00 00		2.2894	0.36429	0.00125	2.65371	-0.00040	0.00005	0.00039	0.00005
JHJY	A	2011 01 01 11 00 00		2.2898	0.34919	0.00134	2.63896	-0.00035	0.00005	0.00040	0.00005
JHJY	A	2011 01 01 12 00 00		2.2901	0.36758	0.00144	2.65772	-0.00029	0.00005	0.00040	0.00005
JHJY	A	2011 01 01 13 00 00		2.2904	0.36374	0.00144	2.65419	-0.00024	0.00005	0.00040	0.00005
JHJY	A	2011 01 01 14 00 00		2.2908	0.33976	0.00117	2.63052	-0.00019	0.00005	0.00040	0.00005
JHJY	A	2011 01 01 15 00 00		2.2911	0.35110	0.00107	2.64218	-0.00013	0.00005	0.00040	0.00006
JHJY	A	2011 01 01 16 00 00		2.2914	0.35306	0.00112	2.64444	-0.00008	0.00006	0.00040	0.00006
JHJY	A	2011 01 01 17 00 00		2.2917	0.34277	0.00122	2.63447	-0.00003	0.00006	0.00040	0.00006
JHJY	A	2011 01 01 18 00 00		2.2920	0.33811	0.00113	2.63012	0.00003	0.00006	0.00040	0.00007
JHJY	A	2011 01 01 19 00 00		2.2920	0.33995	0.00114	2.63197	0.00008	0.00006	0.00040	0.00007
JHJY	A	2011 01 01 20 00 00		2.2920	0.34289	0.00131	2.63492	0.00014	0.00007	0.00040	0.00008
JHJY	A	2011 01 01 21 00 00		2.2920	0.33344	0.00111	2.62549	0.00019	0.00007	0.00040	0.00008
JHJY	A	2011 01 01 22 00 00		2.2921	0.33137	0.00113	2.62343	0.00024	0.00008	0.00040	0.00009
JHJY	A	2011 01 01 23 00 00		2.2921	0.33027	0.00125	2.62234	0.00030	0.00008	0.00040	0.00009
JHJY	A	2011 01 02 00 00 00		2.2921	0.33085	0.00178	2.62293	0.00035	0.00008	0.00040	0.00010

(*a*)



(*b*)

Figure 6.4: Tropospheric estimation using the Bernese software. A model that represent the dry component is introduced, whereas the wet component and horizontal tropospheric gradients are estimated from the observations. (*a*) Header and the first few lines of a Bernese *.TRP file. The header summarises selected options for the a priori model, mapping function, gradient model, minimum elevation, and the temporal sampling interval. The first eight columns represent the name of the station, a flag marking the estimated coordinates depending on the modifying program, and respective date and time for which the parameters have been computed. The following eight columns give values of the a priori model (i.e. MOD_U) and the site-specific parameters (i.e. CORR_U) in the zenith direction, as well as the horizontal gradients in North (i.e. CORR_N) and East (i.e. CORR_E). The sum of MOD_U and CORR_U is written to the column TOTAL_U. Standard deviations SIGMA_U, SIGMA_N, and SIGMA_E for the respective values of the site-specific troposphere parameters, and the horizontal gradients are also specified. All values are given in metre. (*b*) Representation of the tropospheric components from the Bernese *.TRP file.

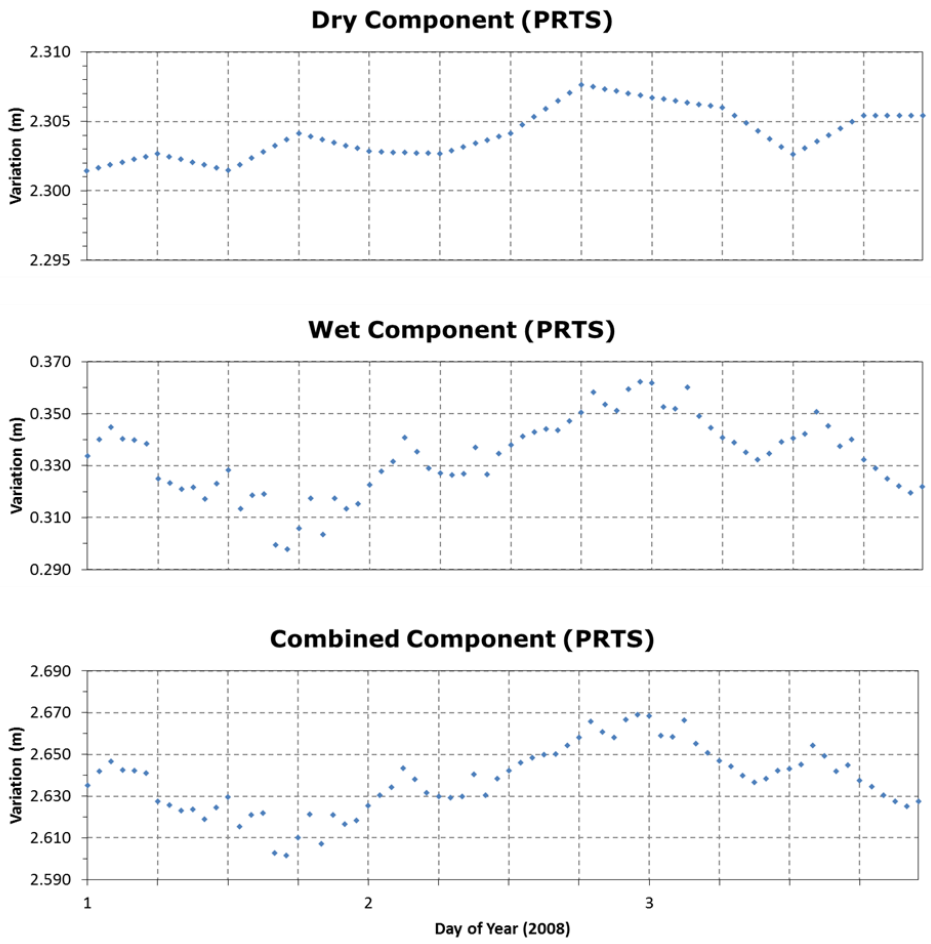


Figure 6.5: Troposphere estimate at PRTS station for DoY 1 - 3 (2007). DD processing strategy is employed using VMF-1 for the tropospheric modelling. Notice the trend of the dry delay changes at 6 hours interval owing to the temporal resolution of the VMF-1 file. Linear interpolation in time is applied to obtain the value at every hour. Following that, the wet component is estimated from the observations.

6.4.4. Results and Discussion

Discussion on the results of tropospheric estimations will begin by comparing the estimated troposphere between PPP and DD. For simplicity, only VMF-1 is utilised for the tropospheric modelling as in theory, it should represent real states of troposphere better than any empirical models (Kouba, 2008; Heublein et al., 2014). Comparisons are made in terms of ZTD since the two techniques differ in their estimated wet delays, which also represents a correction to the model introduced in the processing (refer to **Section 6.4.3** for the discussion). **Figure 6.6** shows the plots of the comparison made on eight MyRTKnet stations between the year 2007 and 2011.

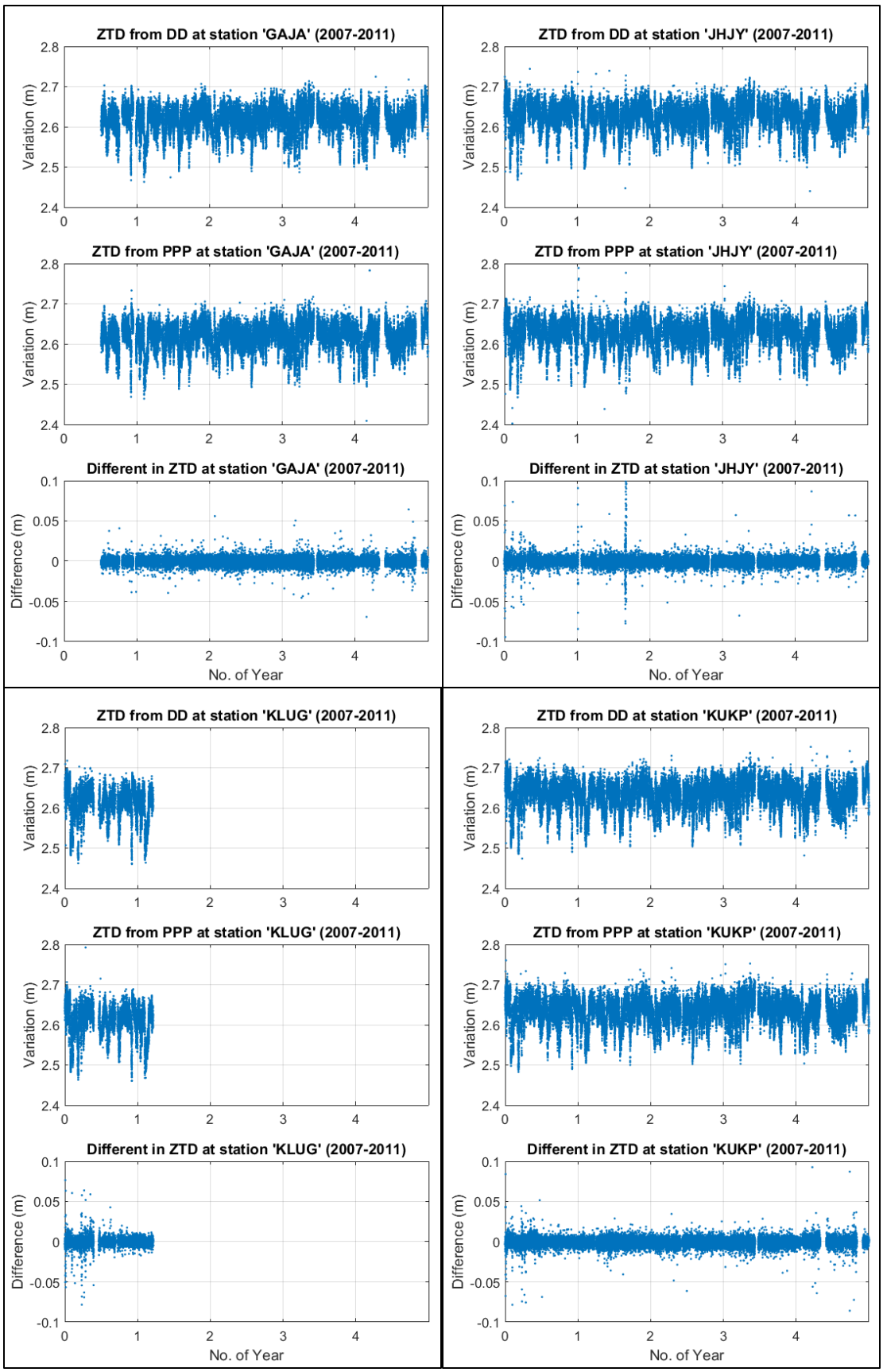


Figure 6.6: Comparison between the estimated ZTD from PPP and DD for eight MyRTKnet stations (2007 - 2011).

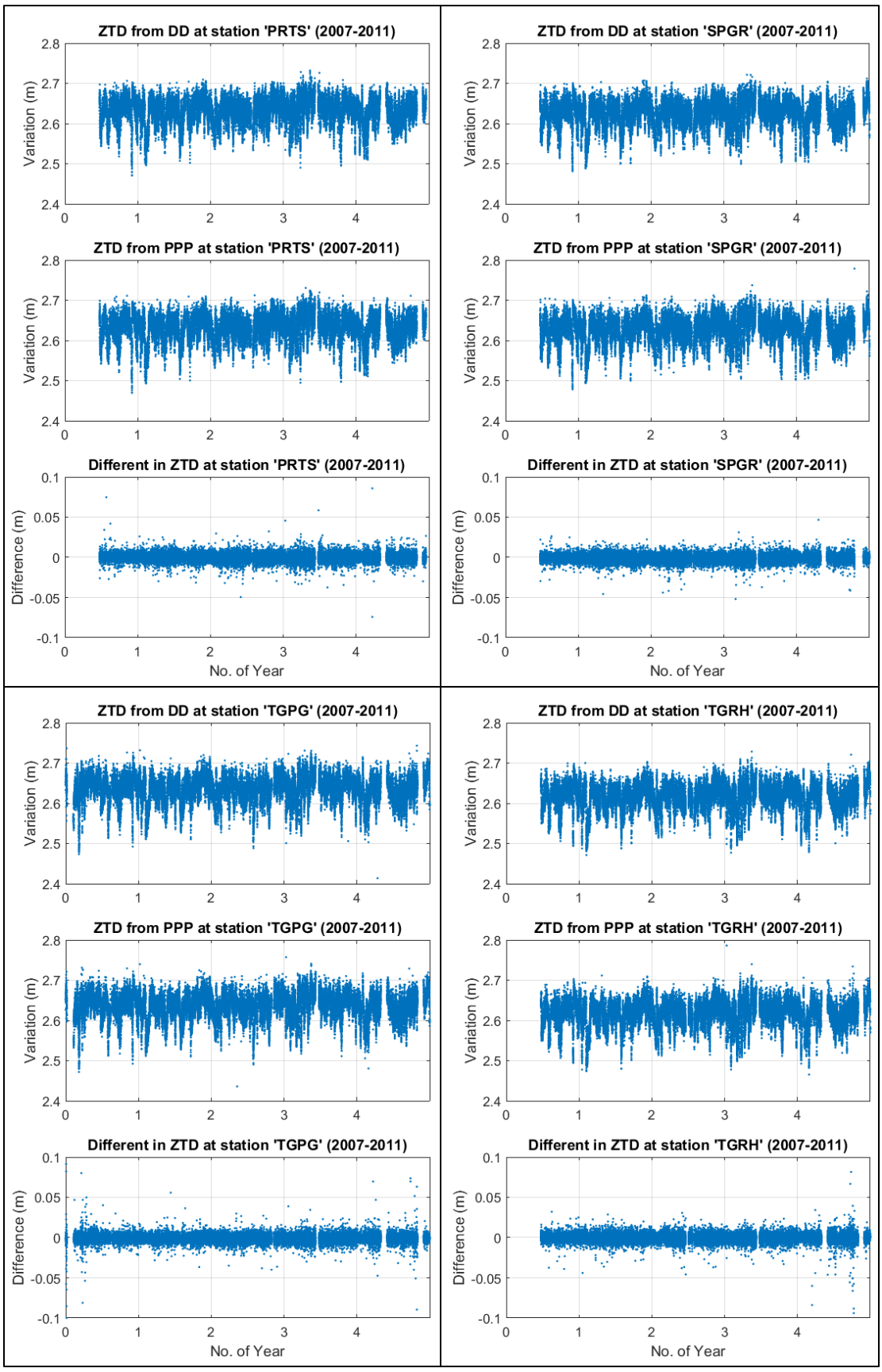


Figure 6.6: Comparison between the estimated ZTD from PPP and DD for eight MyRTKnet stations (2007 - 2011) (continue).

It can be seen that both ZTDs from PPP and DD, in general, agreed reasonably well with each other. Some outliers are present in the results, for example, seen at JHJY station in the year 2008. Upon investigation, it is found that those outliers are attributed from bad data quality on that day as shown in **Figure 6.7**. There were sparse data recorded on L_2 frequency, thus limiting the number of ionosphere-free linear combinations that can be formed. This in turn, substantially affected the estimated troposphere. After removing outliers exceeding three times the standard deviation, the two estimations agreed within 4 mm standard deviation for all eight stations.

```
     2.11           OBSERVATION DATA    G (GPS)             RINEX VERSION / TYPE
teqc  2007Jun25                         20080925 07:52:00UTCPGM / RUN BY / DATE
MSXP|IAx86-PII|bcc32 5.0|MSWin95->XP|486/DX+                COMMENT
teqc  2007Jun25                         20080925 07:51:58UTCCOMMENT
GPSNet 2.60 3062                        02-Sep-08 23:59:45  COMMENT
JHJY                                                        MARKER NAME
JHJY                                                        MARKER NUMBER
                                                            OBSERVER / AGENCY
20228               TRIMBLE 5700        Nav  2.21 / Boot  1 REC # / TYPE / VERS
75166               TRM41249.00                             ANT # / TYPE
 -1520489.8997  6191944.5444   169912.8269                  APPROX POSITION XYZ
        0.0500         0.0000         0.0000                ANTENNA: DELTA H/E/N
     1     1                                                WAVELENGTH FACT L1/2
     4    L1    C1    L2    P2                             # / TYPES OF OBSERV
    15.0000                                                 INTERVAL
Forced Modulo Decimation to 15 seconds                      COMMENT
teqc windowed: start @ 2008 Sep  3 00:00:00.000             COMMENT
teqc windowed: delta = 86370.000 sec                        COMMENT
  2008     9     3     0     0    0.0000000     GPS         TIME OF FIRST OBS
                                                            END OF HEADER
 08  9  3  0  0  0.0000000  0  9G 6G22G21G31G30G14G16G29G18
  -7101323.896 3  24790936.716
 -23671183.015 7  20789848.519   -18439485.52146  20789841.337
 -15120564.476 6  22565094.687
 -19148063.313 7  21373905.241   -14910174.72245  21373898.464
 -20817201.938 7  21548621.486   -16213343.91045  21548616.231
  -9322540.294 5  23686626.617
  -9768769.557 5  23423869.947
  -3602040.936 5  24684951.651
 -22495161.628 7  21026159.854   -17521621.42745  21026154.261
 08  9  3  0  0 15.0000000  0  9G 6G22G21G31G30G14G16G29G18
  -7112930.878 3  24788727.223
 -23696251.177 7  20785078.404   -18459019.15146  20785071.383
 -15074545.591 6  22573851.655
 -19142515.189 7  21374961.052   -14905851.50145  21374955.220
 -20798202.154 7  21552237.236   -16198538.88945  21552231.886
  -9328284.238 5  23685534.385
  -9819124.659 6  23414287.443
  -3600943.374 6  24685160.258
 -22485736.931 7  21027953.398   -17514277.51545  21027947.474
  ...
 08  9  3 22 59 15.0000000  0  9G21G30G22G24G14G31G12G29G18
 -24017694.914 7  20762149.852    11960615.61645  20762143.748
 -21092117.807 7  21344367.348    45801950.63945  21344363.102
 -15743207.386 6  22192156.671
  -5787264.595 6  23914176.247
  -8835914.458 4  23673233.253
 -16879802.927 7  21701203.952     8263072.65145  21701198.100
  -8742795.044 6  23879332.597
  -4074417.394 5  24472626.001
 -20859310.965 7  21215235.430    43673840.39745  21215230.540
 08  9  3 22 59 30.0000000  0  9G21G30G22G24G14G31G12G29G18
 -23983365.748 7  20768682.595    11987365.60845  20768676.608
 -21100614.855 7  21342750.428    45795329.56445  21342746.304
 -15780204.044 6  22185116.296
  -5738546.097 6  23923447.379
  -8830224.032 5  23674316.915
 -16901323.260 7  21697109.002     8246303.56045  21697103.256
  -8717794.674 6  23884090.414
  -4064376.212 6  24474537.036
 -20875625.337 7  21212130.870    43661127.87045  21212125.759
 08  9  3 22 59 45.0000000  0  9G21G30G22G24G14G31G12G29G18
 -23948941.256 7  20775233.616    12014189.88645  20775227.309
 -21109008.114 7  21341153.344    45788789.35045  21341149.459
 -15817185.839 6  22178079.114
  -5689822.247 6  23932719.589
  -8824572.052 5  23675391.768
 -16922719.386 7  21693037.393     8229631.23145  21693032.074
  -8692697.503 6  23888865.893
  -4054388.387 6  24476437.936
 -20891854.003 7  21209042.667    43648482.15745  21209036.893
```

Figure 6.7: RINEX data at JHJY station on 3 September 2008. Notice the sparse data recorded on L_2 frequency that limits the number of ionosphere-free linear combination that can be formed.

ZTDs from CODE are used as the reference to determine the most precise technique for troposphere estimation. CODE is one of the IGS analysis centres that contribute to the realisation of ITRF. Their final troposphere is estimated from the three-day long-arc solutions (Dach et al., 2016). Since their troposphere is estimated at two-hour intervals, the ZTDs from the PPP and DD estimations have been resampled to that resolution. The comparison is made on 14 IGS stations, which are included in the processing. The results are summarised in **Table 6.7**, and the corresponding plots are attached as **Appendix C**.

Table 6.7: Comparison between the ZTDs from PPP and DD processing with respect to ZTDs from CODE.

Station	DD		PPP	
	Average (mm)	Std. Deviation (mm)	Average (mm)	Std. Deviation (mm)
ALIC	2	5	1	5
BAKO	1	6	0	7
COCO	0	5	0	7
DARW	0	5	0	7
HYDE	1	4	1	5
KARR	0	5	1	7
LHAZ	1	4	0	6
NTUS	0	4	1	6
PERT	-1	7	1	9
PIMO	1	8	4	10
SHAO	1	5	2	6
TWTF	0	5	1	6
WUHN	1	7	1	9
YAR2	0	6	0	8

It can be concluded from the table that ZTDs from DD attained smaller deviation than PPP. Lower standard deviations observed in DD, as compared to PPP, indicate a better agreement with CODE. Next, one-year data in 2008 is used to investigate the improvement from using a model based on a direct ray-tracing through NWM (i.e. VMF-1) as opposed to an empirical model (i.e. Saastamoinen model and NMF). **Figure 6.8** shows the variations of the troposphere in dry, wet and combined components, made using DD processing strategy and NMF for the tropospheric modelling. The corresponding results using VMF-1 are shown in **Figure 6.9**. Their statistical results are summarised in **Table 6.8**.

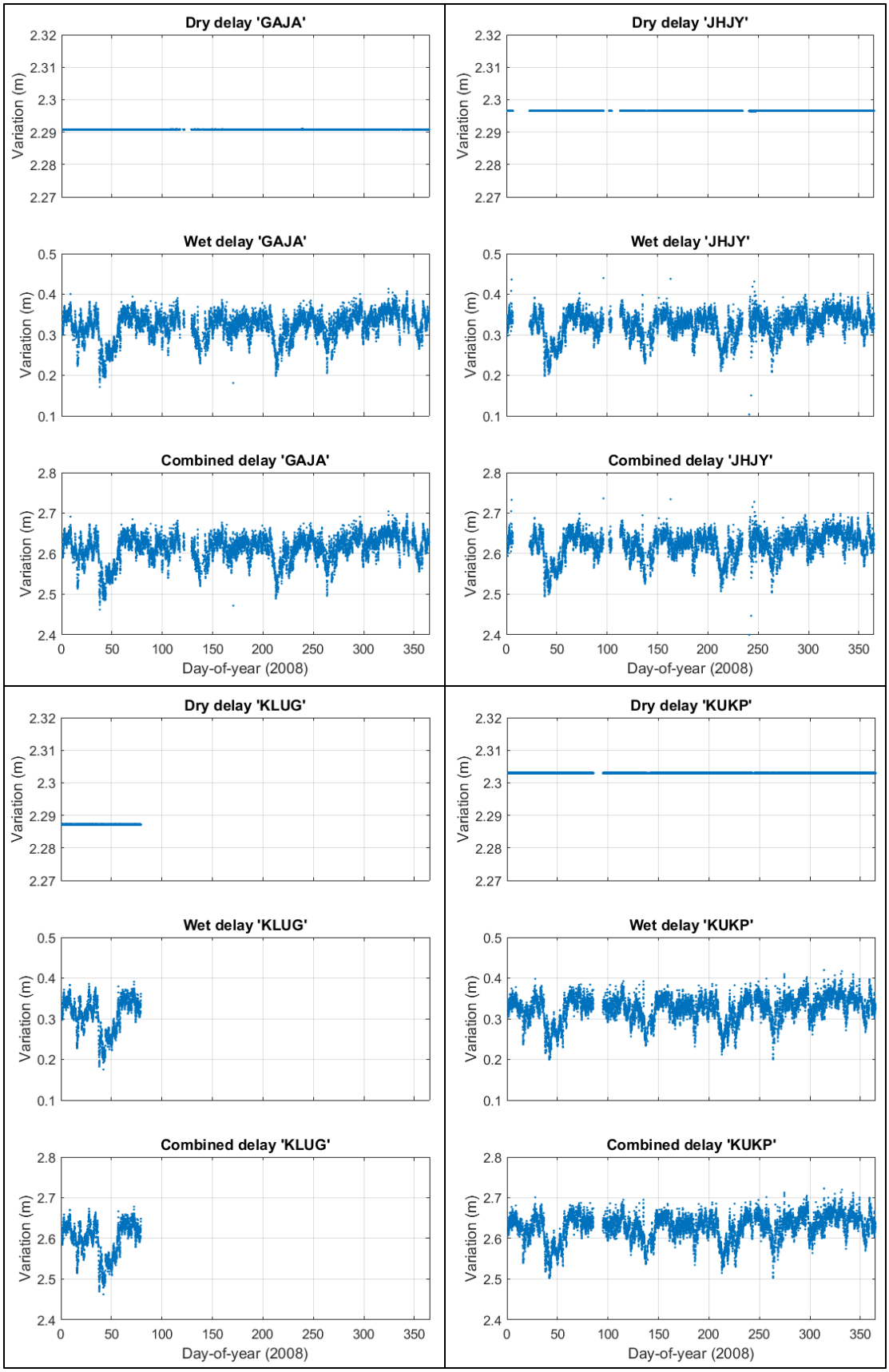


Figure 6.8: Tropospheric estimation using NMF. All delays are in zenith direction.

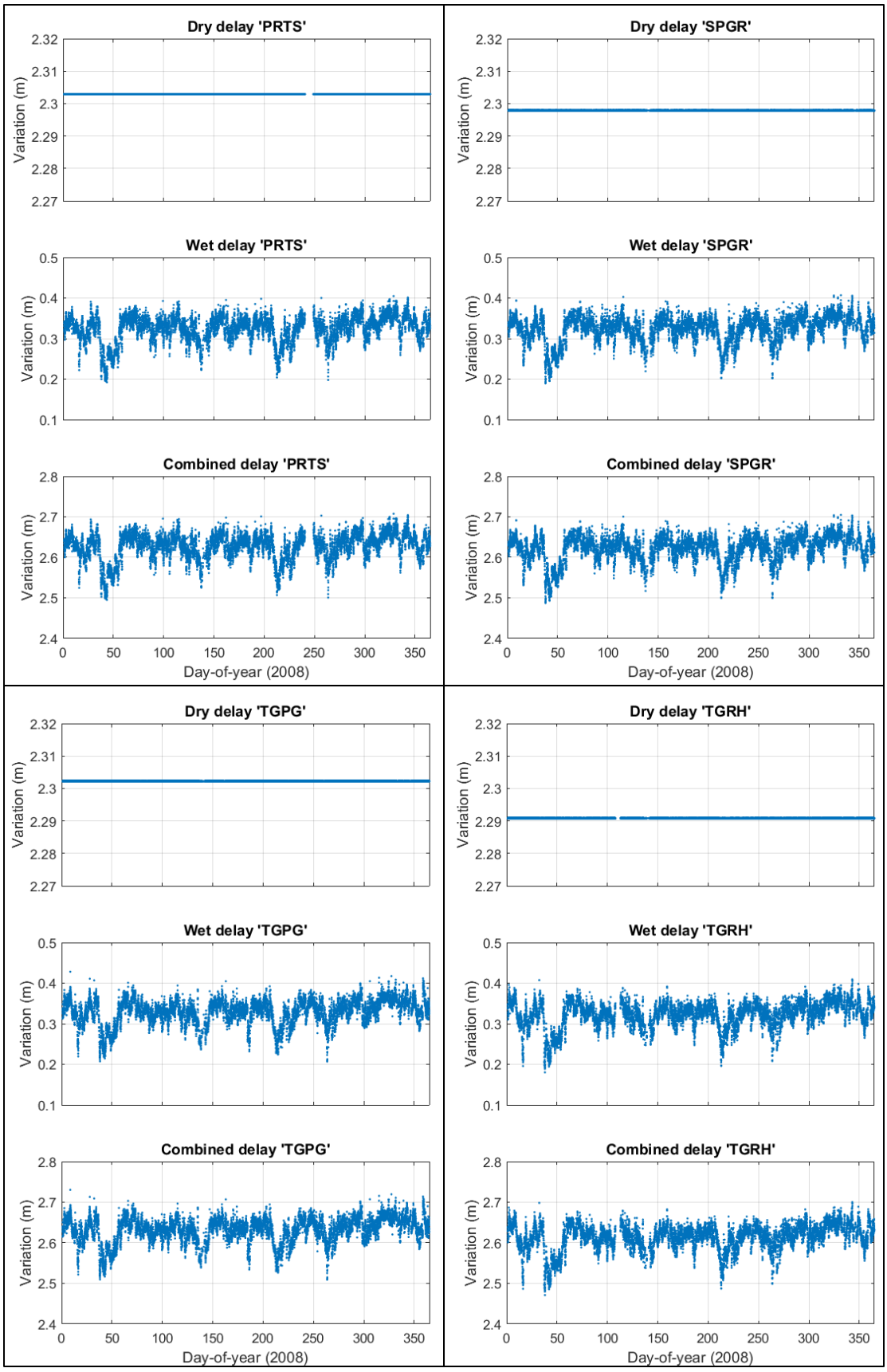


Figure 6.8: Tropospheric estimation using NMF. All delays are in zenith direction (continue).

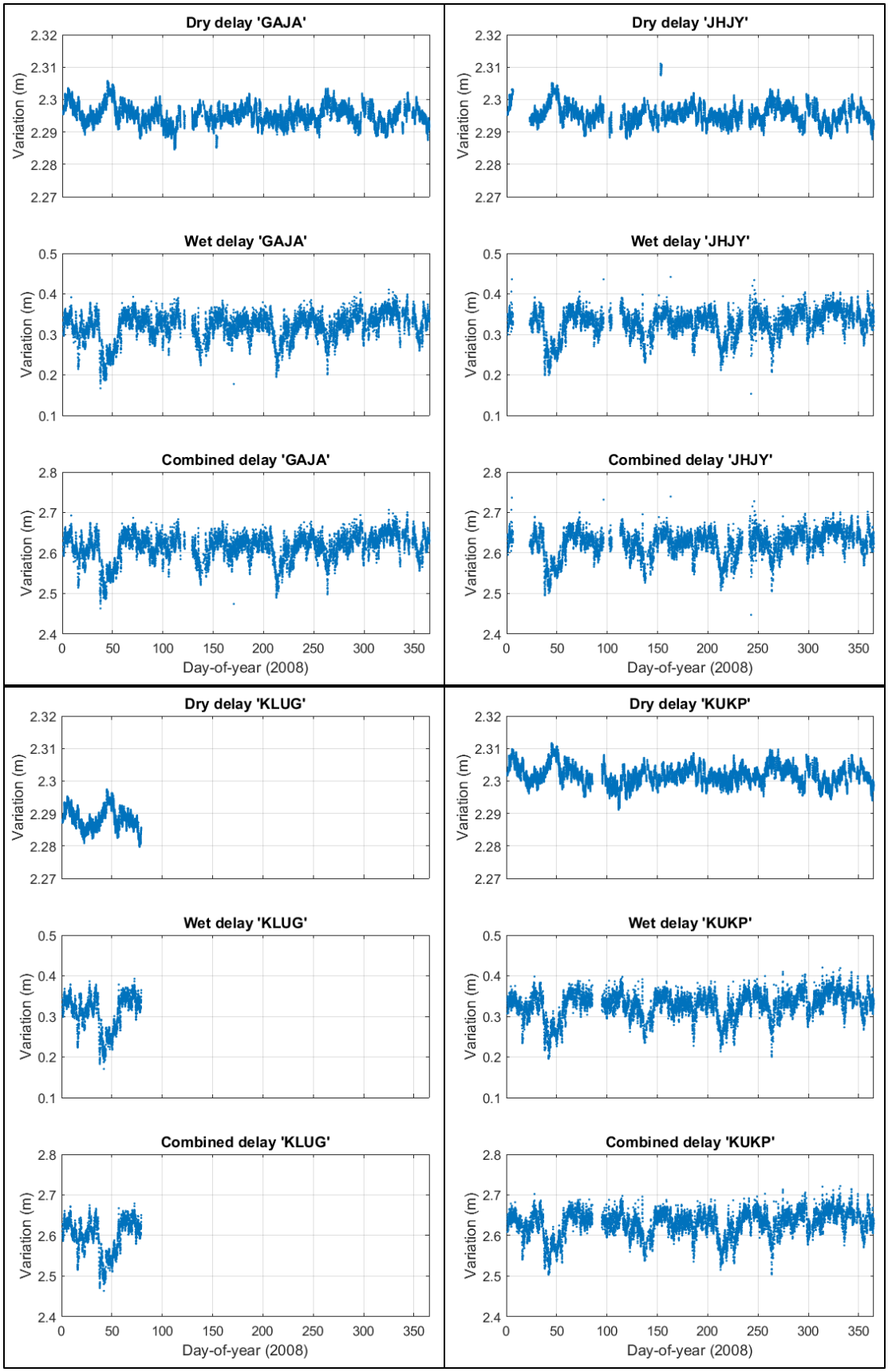


Figure 6.9: Tropospheric estimation using VMF-1. All delays are in zenith direction.

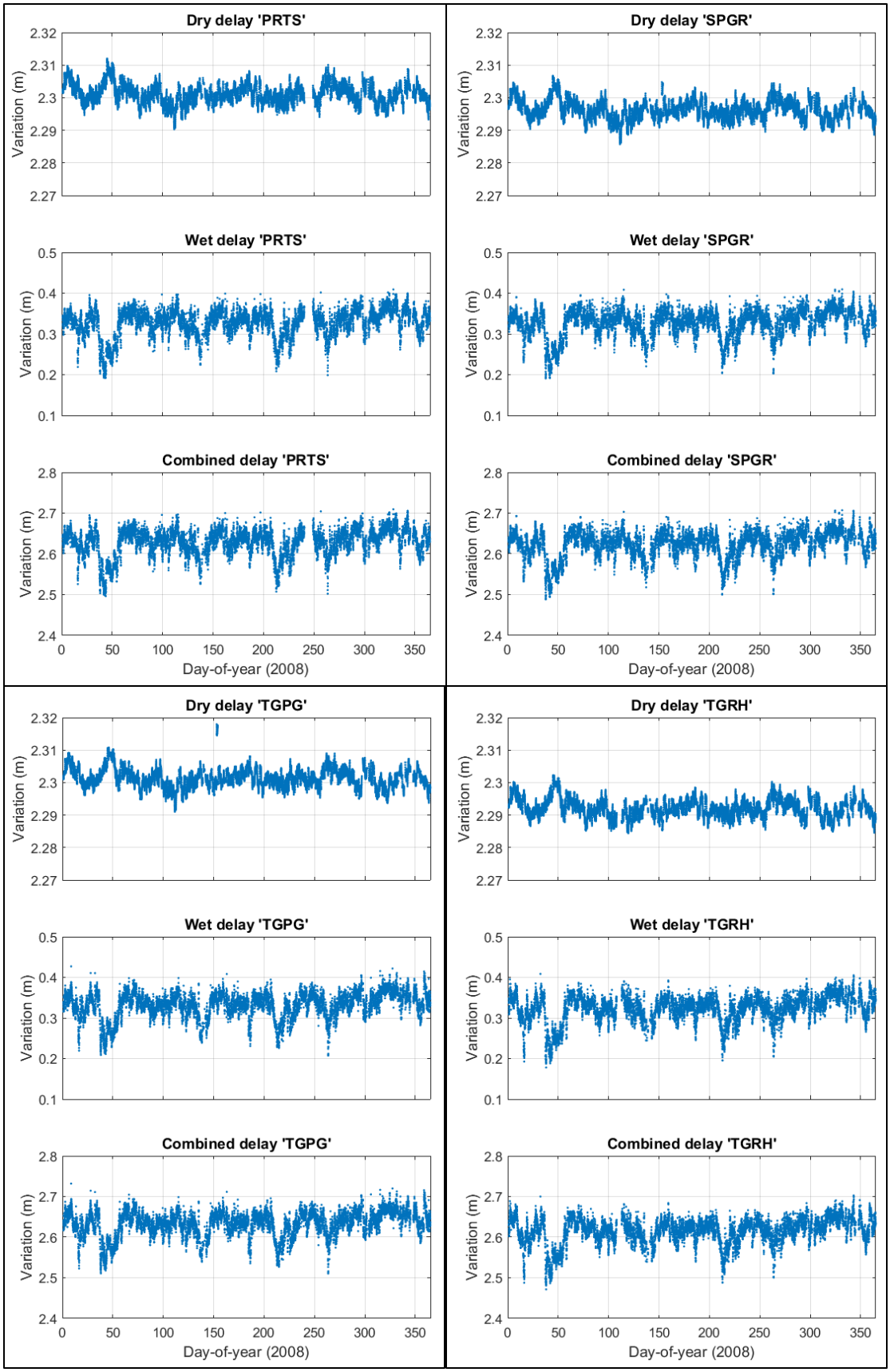


Figure 6.9: Tropospheric estimation using VMF-1. All delays are in zenith direction (continue).

Table 6.8: Statistical comparison between NMF and VMF-1.

Station	Ell. Height (m)	NMF				VMF-1			
		Average Dry (m)	Std. Dry (m)	Average Wet (m)	Std. Wet (m)	Average Dry (m)	Std. Dry (m)	Average Wet (m)	Std. Wet (m)
GAJA	60.244	2.291	0.000	0.323	0.033	2.295	0.003	0.320	0.034
JHJY	39.206	2.297	0.000	0.326	0.033	2.295	0.003	0.328	0.033
KLUG	73.778	2.287	0.000	0.310	0.042	2.288	0.003	0.310	0.043
KUKP	15.429	2.303	0.000	0.326	0.031	2.302	0.003	0.328	0.032
PRTS	15.676	2.303	0.000	0.324	0.033	2.301	0.003	0.327	0.033
SPGR	34.208	2.298	0.000	0.324	0.032	2.296	0.003	0.327	0.033
TGPG	18.107	2.302	0.000	0.329	0.031	2.301	0.003	0.332	0.032
TGRH	60.146	2.291	0.000	0.323	0.032	2.292	0.003	0.323	0.033

It is worth noting that the dry delay is always correlated with the station's height, regardless of any model selected. The higher the station is, the lesser the value of average dry delay as the signals travelled a shorter path. Plots of the zenith dry delay using NMF only showed a constant value as they are based on Saastamoinen model (see **Section 6.4.1**). Their daily variations, however, are addressed in terms of the mapping function to each satellite. On the other hand, VMF-1 not only showed changes in the zenith dry delay but also in its respective mapping function (see **Section 6.4.2**). This is owing to the availability of VMF-1 file, which is at six-hour intervals. The results also revealed that although the dry delay has a higher magnitude than wet, the latter shows much greater variability than the former. As such, the combined delay (i.e. ZTD), in general, follows the same pattern seen in the wet component, but offset based on the dry part. This is particularly true in the case of NMF since the value is constant for the zenith dry delay.

A comparison of the resulting heights is of great interest when aiming at modelling the tropospheric delays, for example, seen in Kouba (2008) and Heublein et al. (2014). The relationship between the mapping function, zenith delay and site height is discussed in detail in Boehm and Schuh (2013). **Table 6.9** summarised the coordinate repeatability in latitude, longitude and ellipsoidal height for each station in the study area following the tropospheric modelling made using NMF and VMF-1. Interestingly, no significant improvement is found when using VMF-1 as opposed to NMF. It might be due to DD processing strategy and network adjustment mode applied in Bernese. A further test is required to verify if VMF-1 will only be beneficial when used in PPP, as found in Kouba (2008). Comparison between the ZTDs obtained from NMF, and VMF (**Figure 6.10**) revealed that they are in order of 1 mm agreement between each other. Interestingly, the ZTDs from VMF-1 seems to be higher in order 1 - 2 mm compared to those from NMF. This

finding suggests that although VMF-1 does not give significant improvements in term of coordinate's repeatability, it should provide a better representation of troposphere when the precise value of ZTDs is the primary concern. Applications such as weather modelling or atmospheric correction in InSAR can benefit from using this new model as opposed to the conventional Saastamoinen model.

Table 6.9: Standard deviation of coordinate (latitude, longitude and ellipsoid height) from DD processing using NMF and VMF-1.

Station	NMF			VMF-1		
	Std. Lat. (mm)	Std. Lon. (mm)	Std. Height (mm)	Lat. (mm)	Lon. (mm)	Ell. Height (mm)
GAJA	4	5	6	4	5	7
JHJY	4	6	10	4	6	10
KLUG	2	2	6	2	1	6
KUKP	4	5	7	4	5	7
PRTS	4	5	6	4	5	6
SPGR	4	5	7	4	5	7
TGPG	4	5	7	4	5	7
TGRH	4	5	7	4	5	7

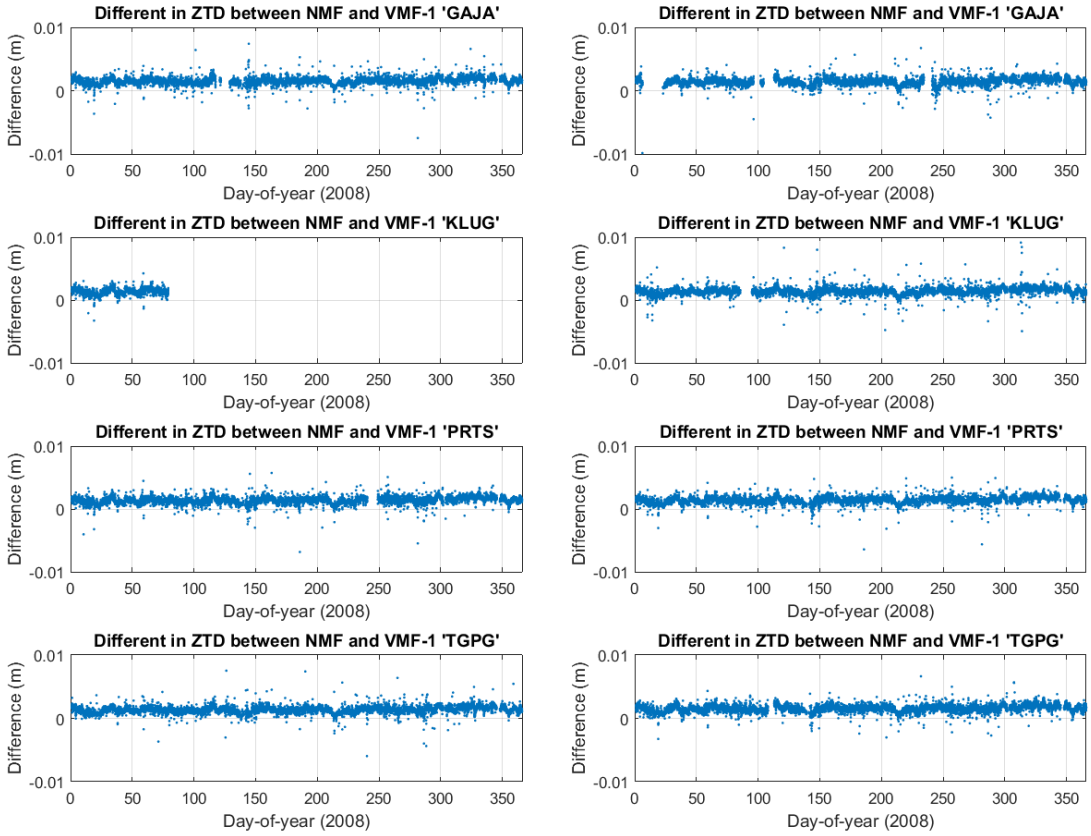


Figure 6.10: Different in the ZTD using NMF and VMF-1.

6.5. Modelling and Mitigation of Tropospheric Effects in InSAR

As has been discussed previously in **Chapter 5**, repeat-pass (i.e. multi-temporal) InSAR is affected by the inhomogeneity of troposphere. In single-pass interferometry, where the measurements are made simultaneously for the master and the slave images, these effects are not present since they are identical, and thus cancel out during interferogram formation. Although they may look similar, they are never the same in repeat-pass interferometry. Their effects on radio wave propagation have been discussed in **Section 6.2**. Equation (6.1) described the signal propagation delay for a one-way travel signal. According to Hanssen (2001), the tropospheric phase delay for a two-way travel signal in InSAR can be described as follows:

$$T = \frac{-4\pi}{\lambda} \cdot \frac{1}{\cos z} \cdot 10^{-6} \int N^{trop} \; ds \quad \cdots\cdots (6.22)$$

where $-4\pi/\lambda$ is a conversion factor to convert from pseudorange increase to phase delay, $1/\cos z$ is the mapping function to map the troposphere at zenith to SAR incidence angle z and N^{trop} the so-called refractivity.

The constants used for the computation of dry and wet refractivity, found in the InSAR literature, differ slightly from the one suggested by Essen and Froome (1951) as shown previously in Equation (6.3). According to Smith and Weintraub (1953) as well as Thayer (1974), the refractivity N for the dry and wet can be computed using the following equation:

$$N_{dry}^{trop} = 77.6 \cdot \frac{P}{\tau}$$
$$N_{wet}^{trop} = 23.3 \cdot \frac{e}{\tau} + 3.75 \cdot 10^{5} \cdot \frac{e}{\tau^{2}} \quad \cdots\cdots (6.23)$$

where the measurement of pressure P and water vapour e is in millibars, and the temperature τ is in Kelvin. Resch (1984) indicated that Equation (6.23) is accurate to within 0.5 percent. Although the refractivity is dependent on temperature, pressure, and water vapour, it is the water vapour that dominantly causes the phase artefacts within SAR images (Ding et al., 2008).

ZTDs estimation from the GPS processing has revealed that the total tropospheric delay in the Johor region can reach up to several metres. This full range can never be captured by interferometric data, which were originally wrapped to half of the radar wavelength (i.e. 2.8 cm for ERS-1/2 and Sentinel-1), unless some sort of independent absolute calibration is possible. Therefore, every integral in Equation (6.22) can be regarded as the sum of two contributions. First, a fixed contribution (bias) which is constant for the whole scene, and can be subtracted from

the data. Second, a variable contribution dependent on the position of the image. As a result of this relative representation, the influence of refractivity is dependent on their lateral variability within the scene (Hanssen, 2001).

The characterisation of tropospheric effects in InSAR is usually made in term of vertical stratification and turbulence mixing (Ferretti, 2014). Vertical stratification is the result of different vertical refractivity between SAR acquisitions, assuming no heterogeneities within the horizontal layers. It is correlated with topography and most visible in a mountainous terrain (Massonnet and Feigl, 1998). For an infinite number of thin atmospheric layers, each will have their constant value. No difference in the horizontal delay is expected over a flat terrain. For hilly or mountainous terrain, differences in the vertical refractivity during SAR acquisitions will affect the phase difference between two arbitrary resolution cells with different topographic height (Ferretti, 2014). This may cause erroneous interpretation of the deformation. On the other hand, turbulent mixing is a result of turbulent processes in the atmosphere due to solar heating of the earth's surface (causing convection), differences in wind direction or velocity at different layers, frictional drag, and large-scale weather systems (Hanssen, 2001). It creates spatial (3D) heterogeneity in the refractivity during SAR acquisitions and affects flat as well as mountainous terrains.

Different methods have been documented to estimate the tropospheric signal in InSAR data, such as using weather models (Wadge et al., 2002; Pinel et al., 2011; Walters et al., 2014), GNSS data (Williams et al., 1998; Onn and Zebker, 2006), spectrometer measurements (Li et al., 2006b), or by combining weather models and spectrometer data (Walters et al., 2013), or GNSS and spectrometer measurements (Puysségur et al., 2007; Li et al., 2009). While all of these techniques can, under certain conditions, reduce the tropospheric signal, they are often limited by the lower spatial resolution of the auxiliary data. Alternatively, tropospheric signals can be estimated by filtering the InSAR data in space and time (Hooper et al., 2012), or from the correlation between the interferometric phase and the topography (Wicks, 2002; Cavalié et al., 2007; Bekaert et al., 2015b; Zhu et al., 2016). The correlation between the interferometric phase and the topography can be represented either by linear or power law relationships, and both of them are implemented and tested in this research. The author also has developed several Matlab scripts as two additional modules in Punnet (i.e. linear and power law) to address the tropospheric effects.

6.5.1. Existing Method in Punnet

It is important to note that the troposphere is very well correlated in space and its statistical behaviour can be described using well-known statistical figures (Ferretti, 2014). As for its temporal behaviour, two SAR images acquired a few hours or minutes apart can have two completely

different troposphere values as they change quickly with time. Given a typical temporal baseline of satellite InSAR measurements, it can be considered as uncorrelated in time. This is an important feature exploited by multi-interferogram InSAR techniques, such as PSI and SBAS. To separate tropospheric artefacts from the deformation, most of the techniques implement a spatiotemporal filtering in time series analysis, e.g. Ferretti et al. (2001), Berardino et al. (2002) and Ferretti et al. (2009). Usually, it is achieved using a spatial low-pass filter followed by a temporal high-pass filter which takes into account the different characteristics between the surface deformations and atmospheric artefacts. The former has high temporal correlation and moderate spatial correlation, whereas the latter has low temporal correlation but high spatial correlation (Ferretti, 2014). A similar principle is applied within the ISBAS algorithm and Punnet software.

In general, tropospheric modelling and mitigation within Punnet is achieved in two sequences: (1) linear analysis, and (2) non-linear analysis. In linear analysis, estimation of LOS-velocity and DEM error for each coherent point is made assuming that troposphere is random over time, thus has mean zero. This assumption can be considered as valid for a large stack of interferograms that are properly distributed over the long observation period. Following that, phase contribution from the linear deformation is subtracted from the original unwrapped phases and the residuals are assumed to contain a non-linear component of the deformation, relative troposphere (also termed the Atmospheric Phase Screen or APS), and noise (thermal noise, remaining residual from orbital error, etc). The non-linear deformation and APS can then be separated from each other using custom filters based on the assumption that troposphere is correlated in space, whereas deformation is correlated in time. The effectiveness of the filter depends on the validity of assumptions (e.g. atmosphere is correlated within 5 km radius), as well as the number and distribution of the interferograms. Separating individual contributions, i.e. non-linear deformation and APS, is more challenging for an area with slow deformation rate as it can be masked out by noise from various sources. The final deformation is the result of addition between linear and non-linear deformation. Interested readers are referred to Berardino et al. (2002) for a complete description about tropospheric modelling in Small Baseline Subset (SBAS) algorithm, as applied in Punnet.

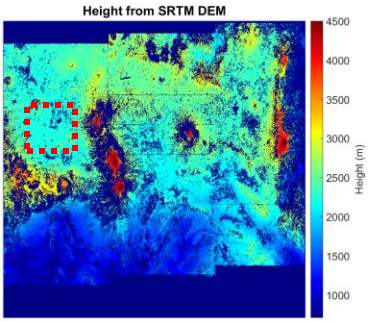
Mexico processing is used by the author for the illustration of tropospheric modelling and mitigation carried out in this research considering the known velocity rate and visible tropospheric artefacts due to vertical stratification. The effects of vertical stratification are more visible in Mexico than in Johor owing to the large range of height in the area. For comparison, the height range in Mexico based on the Shuttle Radar Topography Mission (SRTM) DEM is between ~702 m and ~5,568 m above mean sea level (MSL),

whereas the corresponding range for Johor is from 0 m to ~971 m above MSL. **Figure 6.11a** shows the height for each coherent point in Mexico. Their respective unwrapped phase after baseline correction on four selected image pairs is shown in **Figure 6.11b** along with the plot of correlation between the phase and the height. These pairs are individually selected from the total 143 interferograms as they clearly showed high correlation value between the phase and the height. Summary of the selected image pairs is made in **Table 6.10**.

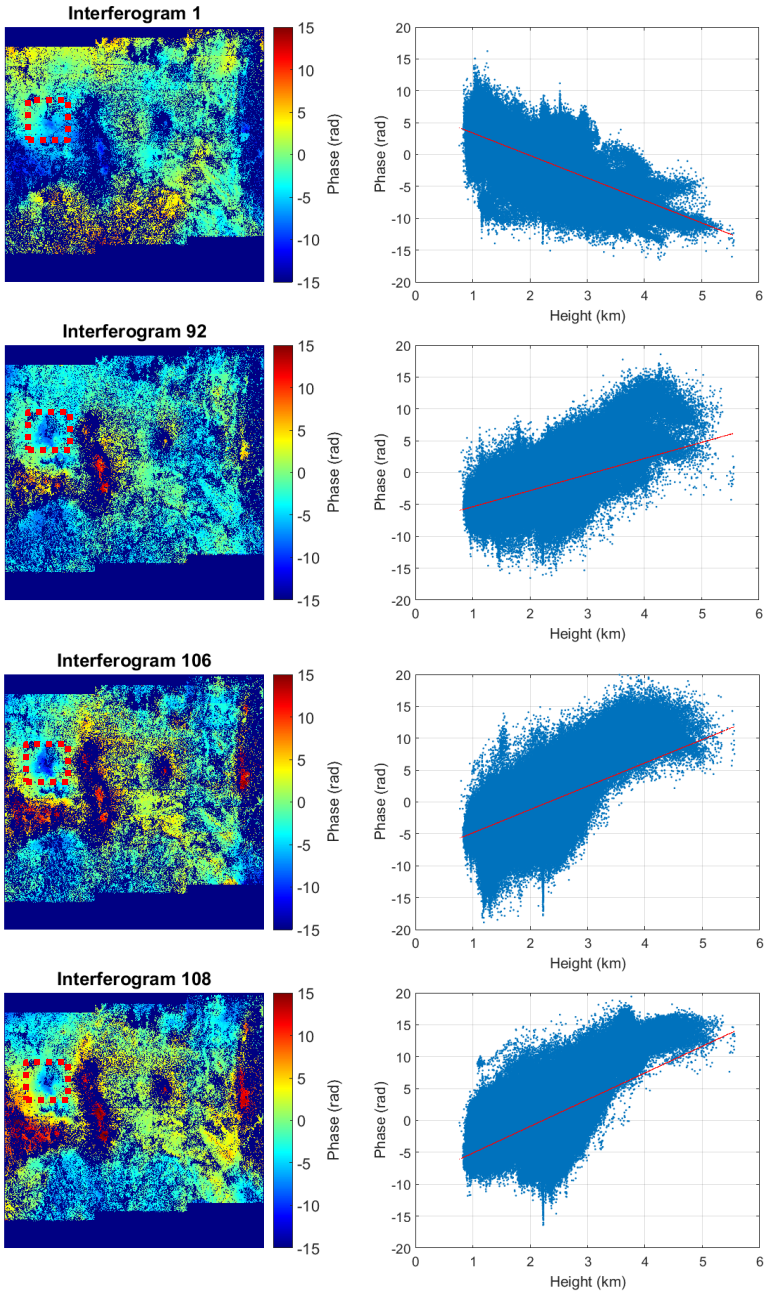
It is evident from the figure that vertical stratifications exist in the interferograms, thus they should be accounted for to achieve a precise estimation of the deformation. The correlation between phase and height can be either negative (as in Interferogram 1) or positive (as in the other three interferograms). The Pearson correlation coefficient for the total 143 interferograms ranges between - 0.60 to + 0.59. As for the Johor area, no apparent correlation is observed between the phase and the height. The Pearson correlation coefficient in Johor ranges from - 0.23 to + 0.28. The deforming area in the interferograms, shown in **Figure 6.11**, is marked by a red dotted rectangle. In Interferogram 1, no significant deformation signal is observed owing to its short temporal baseline, i.e. 12 days. Meanwhile, deformation signal is clearly visible in the other three interferograms due to their relatively long temporal baselines. Mitigation of the vertical stratification effects should be made without affecting the original deformation signal. This aim forms the basis of the tropospheric modelling and mitigation discussed in the following sections.

Table 6.10: Summary of the interferograms from Mexico processing that are used to illustrate the correction of tropospheric artefacts due to vertical stratification.

Interferogram	Master	Slave	Perpendicular Baseline (m)	Temporal Baseline (day)	Corr. Coeff.
1	3 October 2014	15 October 2014	-4.9	12	-0.55
92	31 January 2015	1 April 2015	-140.3	60	0.48
106	31 January 2015	13 April 215	-135.5	72	0.52
108	24 February 2015	13 April 215	30.8	48	0.59



(*a*)



(*b*)

Figure 6.11: The effects of vertical stratification on unwrapped interferograms. (*a*) Height from the SRTM DEM. (*b*) Unwrapped phases of four selected interferograms (left) and their scatter plot (right) to show correlation with height.

6.5.2. Tropospheric Estimation using Linear Relationship of Phase with Height

The first attempt made to address vertical stratification effects in interferograms is by using a linear relationship between phase and height, as represented by Equation (6.24).

$$\Delta\emptyset_{tropo} = K_{\Delta\emptyset} \cdot H + \Delta\emptyset_0 \quad \cdots\cdots (6.24)$$

where $\Delta\emptyset_{tropo}$ is the unwrapped phase after baseline correction, H is the height from DEM, whereas $K_{\Delta\emptyset}$ and $\Delta\emptyset_0$ are the coefficients estimated from the LSE: $K_{\Delta\emptyset}$ being the slope of the linear line and $\Delta\emptyset_0$ is the offset in phase when H is equal to zero. Estimation of these coefficients is made independently for each interferograms. Only phase of the coherent points is utilised for a reliable estimation. Similarly, the phase of points in the deformation area is masked out to avoid bias in the estimation.

Although coefficient $K_{\Delta\emptyset}$ and $\Delta\emptyset_0$ can be estimated in a number of window patches within an interferogram, as seen in Bekaert et al. (2015a) and Zhu et al. (2016), this requires some sort of interpolation or weighting technique to acquire a seamless value across the whole interferogram. It can be done, for example, using a combination of distance between the points and the centre of windows as well as standard deviation of the estimated coefficients (for each windows), as applied in the Toolbox for Reducing Atmospheric InSAR Noise (TRAIN) software (Bekaert et al., 2015a). In this work, only one set of coefficient is estimated for each interferograms. Following that, a correction map is generated using Equation (6.24). Considering that InSAR is a relative measurement from a control point, an offset is applied so that the correction at the selected control point is zero. Previous processing workflow is adapted to include tropospheric correction due to vertical stratification prior to the time series analysis. The results are discussed in **Section 6.5.4**.

6.5.3. Tropospheric Estimation using Power-Law Relationship of Phase with Height

Sounding measurements made during ascents of large inflated hydrogen or helium balloons provide a detailed vertical profile of atmospheric properties such as pressure, temperature, relative humidity, and wind speed. The properties of these measurements, such as their frequency, measurement accuracy and sampling, as well as their maximum height, vary strongly

depending on the location and operator (Parker et al., 2008). Based on these sounding measurements, Bekaert et al. (2015a) suggested that troposphere can be represented by a power law relationship of phase with height, as shown in Equation (6.25).

$$\Delta\emptyset_{tropo} = K_{\Delta\emptyset} \cdot (H_0 - H)^{\alpha} + \Delta\emptyset_0 \quad \cdots\cdots (6.25)$$

where $\Delta\emptyset_{tropo}$ is the unwrapped phase after baseline correction, H is the height from DEM, H_0 is the maximum height where the relative delay is small and not significant, α is a the constant describing the power law decay, $K_{\Delta\emptyset}$ is a coefficient that relates phase to topography, and $\Delta\emptyset_0$ is the phase delay when H is equal H_0. Parameters H_0 and α can be estimated from the sounding measurements, whereas coefficients $K_{\Delta\emptyset}$ and $\Delta\emptyset_0$ are estimated from the LSE. The second attempt made to address the vertical stratification effects in this work is by using this power-law relationship between phase and height.

Sounding data at Acapulco station, Mexico from October 2014 to May 2015 (corresponds to SAR acquisitions period) is used to estimate the parameters H_0 and α. The sounding files are provided by the University of Wyoming, and can be accessed through the following link:

http://weather.uwyo.edu (accessed 25.10.2016)

The sounding file for the station is available twice per day, i.e. at UTC 00 and UTC 12. A Matlab script is created to simplify the process of data download. The parameters H_0 and α are estimated on a monthly basis, and their weighted average is adopted for the computation. **Figure 6.12a** shows the scatter plot of refractivity and height computed using Equation (6.23), whereas the scatter plot of phase delay in LOS direction and height is shown in **Figure 6.12b**. The phase delay is computed using Equation (6.22), described previously. Both of the figures are based on one month sounding data in October 2014. It is evident that the phase delay shows a power law relationship with height. The delay increases at low altitude as the signal needs to travel farther through the troposphere. Since the phase in interferogram is the difference between two SAR acquisitions, the tropospheric delay depends on the change in refractivity rather than the total refractivity. **Figure 6.12c** shows the relative tropospheric delays for that month. It can be seen that the relative delay is negligible (i.e. less than 0.5 cm) after a certain height. Meanwhile, the variation of H_0 and α over an eight month period is shown in **Figure 6.13**. The average values for H_0 and α, i.e. 14.6183 km and 1.2863, are adopted for the next computation. The results from using a power law relationship between phase and height are discussed in the following section.

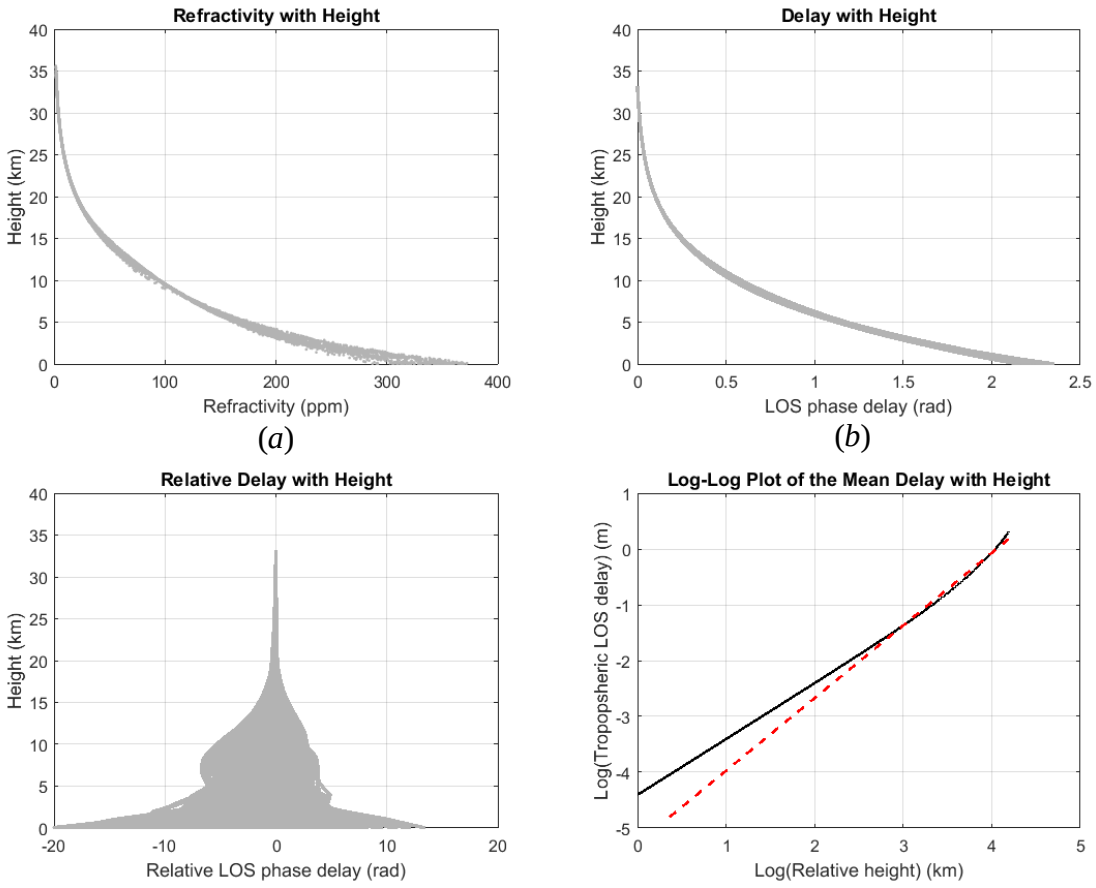


Figure 6.12: Results of the balloon soundings at Acapulco station, Mexico from 1 October 2014 to 31 October 2014. (*a*) The plot of refractivity with height. (*b*) The plot of LOS phase delay with height. (*c*) The plot of relative LOS phase delay with height. (*d*) The log-log plot of the mean delay with height to estimate the H_0 and α parameters.

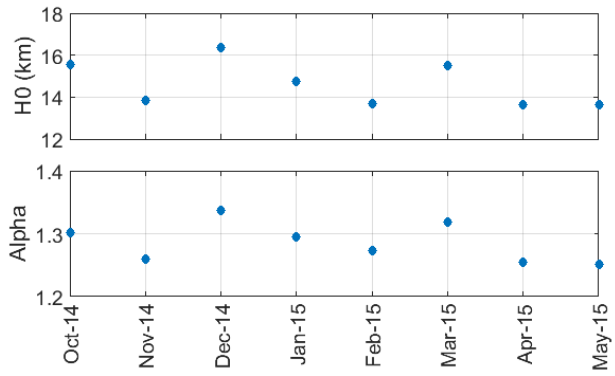


Figure 6.13: Monthly estimation of the parameters H_0 and α at Acapulco station, Mexico. The estimation covers eight months from October 2014 to May 2015. Their weighted average is adopted for the estimation of tropospheric correction in interferograms.

6.5.4. Results and Discussion

The first investigation is made to observe the improvement in the unwrapped differential interferograms from using tropospheric correction based on linear and power law relationships between phase and height. Four interferograms, shown previously in **Figure 6.11** and **Table 6.10**, are selected for the illustration. The results are shown in **Figure 6.14** for the linear correction, and **Figure 6.15** for the power-law correction. The correction map (middle figures), is added to the original interferogram to obtain the corrected interferogram (right figures). It is clear that both methods can reduce tropospheric artefacts due to vertical stratification significantly. No noticeable difference is observed in terms of the corrected interferograms between the two approaches. Although some residuals are still present in the corrected interferograms as highlighted in the red dotted rectangles, they can be removed further by refining the coefficients estimated from a certain height range, where the correlation is more prominent. For example, the correlations are seen higher at heights above 2.5 km in most of the unwrapped interferograms (see also **Figure 6.11**). Furthermore, only one set of coefficients is estimated for each interferogram; thus, they failed to address local correlation in a smaller region. A better result is expected from using multiple window patches, but this task is subject to future work.

Considering that phase is correlated with topography, this will also affect the estimated deformation. Though not as apparent as in the unwrapped interferograms, some degree of correlation is observed between the estimated LOS-velocity and the height. The correlation value is much lower owing to the LSE used for the estimation as well as the neutralisation of negative and positive correlations from all interferograms. No significant improvement is observed in the LOS-velocity map with or without tropospheric correction as can be seen in **Figure 6.16**. The Pearson correlation coefficient between the estimated deformation and height is at - 0.111 in the original result, and slightly improved to - 0.010 and - 0.009 upon correction of troposphere using linear and power law, respectively. Nevertheless, substantial improvement is observed in the standard error for the LOS-velocity as shown in **Figure 6.17** and **Figure 6.18**. This means that a more trustable result can be expected from the estimation with tropospheric correction than without one. It also suggests that non-linear analysis will benefits from this tropospheric correction as it is based on the residuals from the linear analysis. It is worth mentioning that tropospheric mitigation implemented in this work relies on the correlation with height; thus, it is not applicable to the area where the deformation is correlated with height.

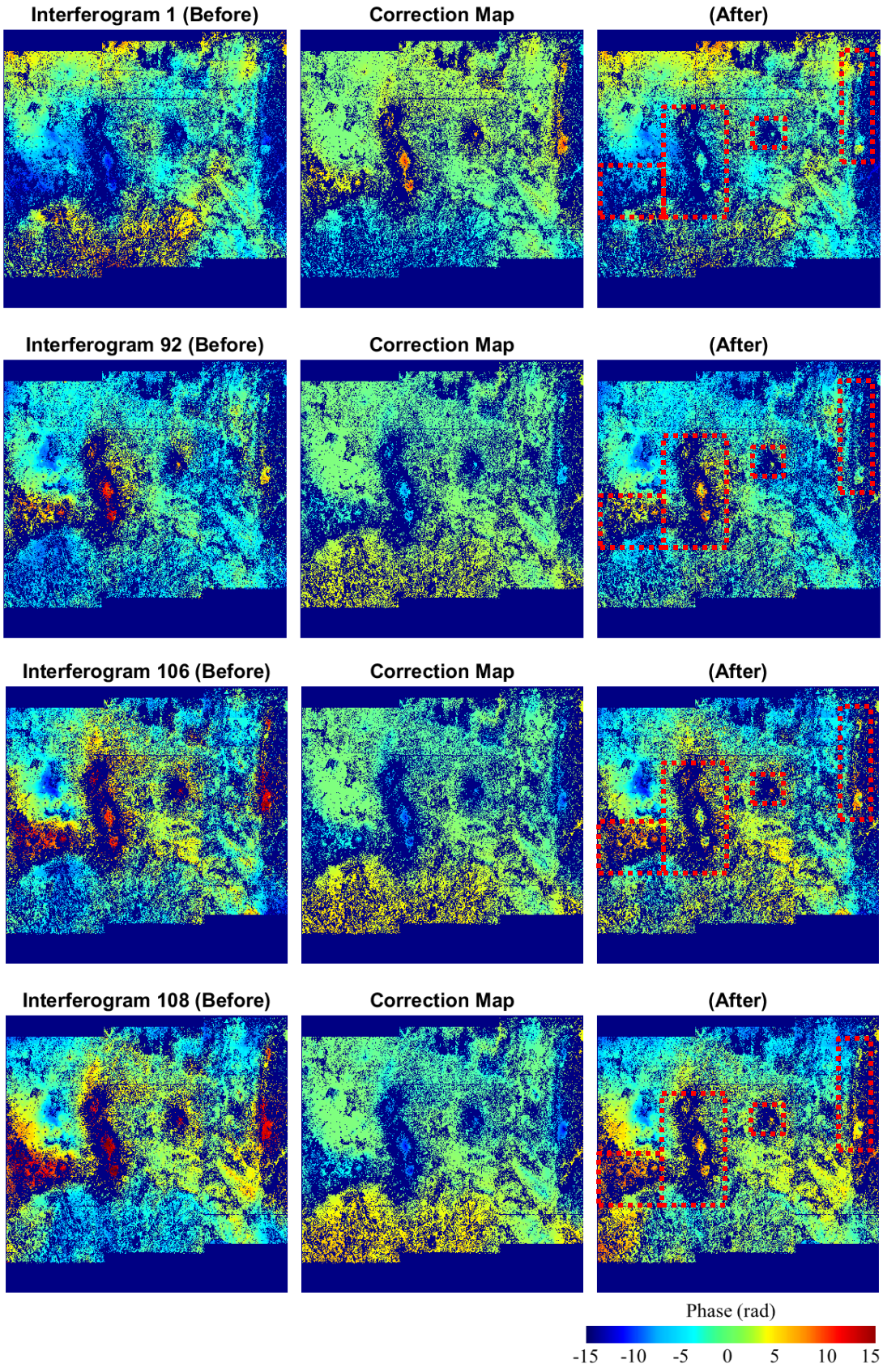


Figure 6.14: Tropospheric correction using linear relationship of phase with height shown on four selected interferograms from Mexico processing.

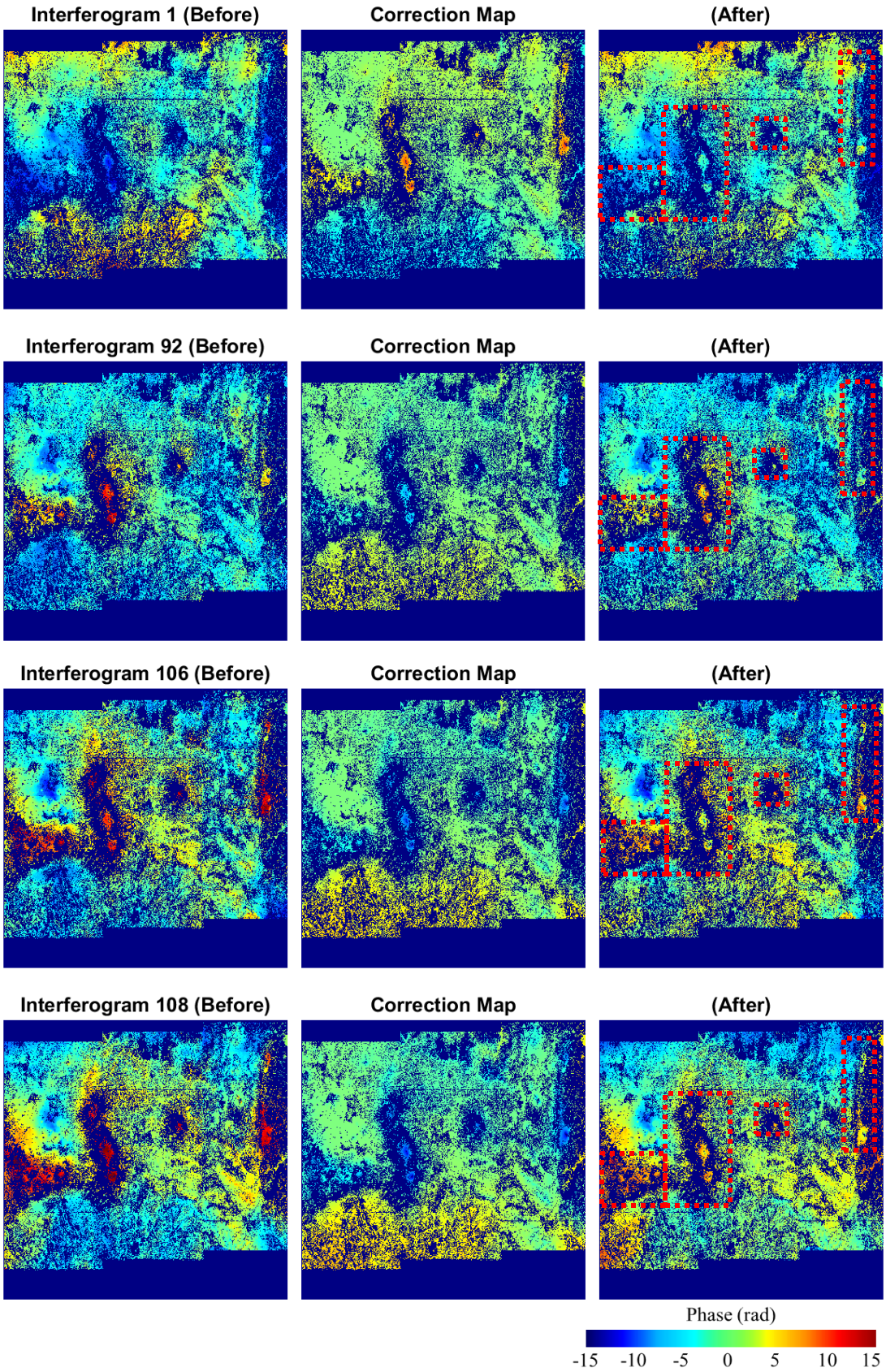
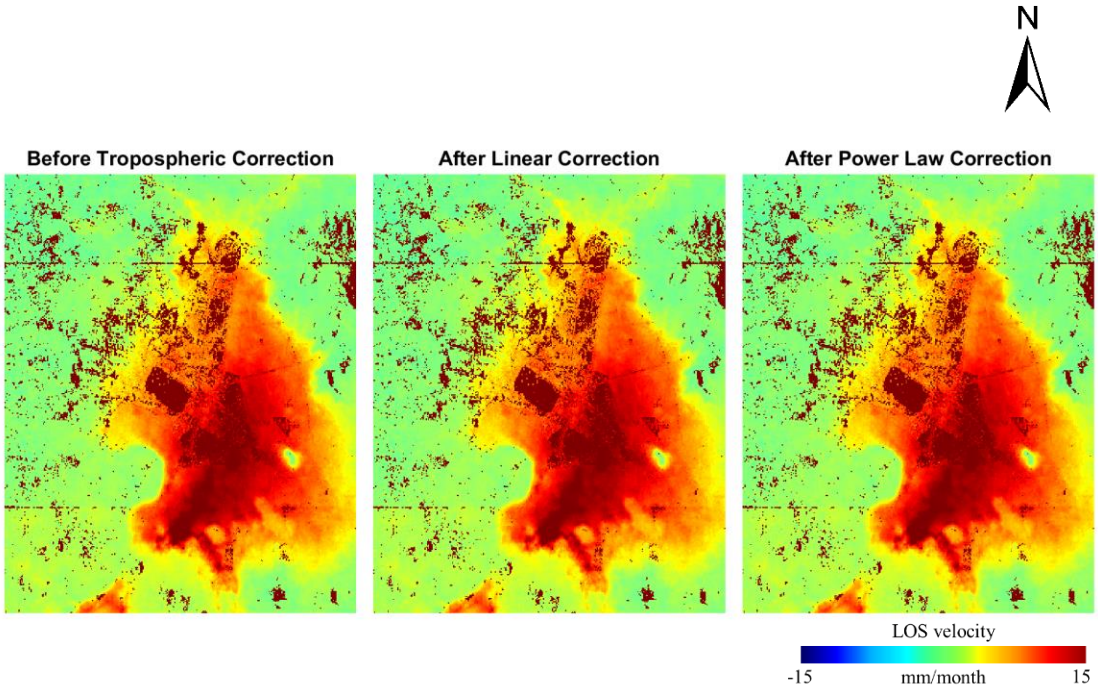


Figure 6.15: Tropospheric correction using power law relationship of phase with height shown on four selected interferograms from Mexico processing.



(*a*) (*b*) (*c*)

Figure 6.16: Comparison of the LOS velocity map for Mexico City: (*a*) without tropospheric correction, (*b*) tropospheric correction by a linear relationship of phase with height, and (*c*) tropospheric correction by power law relationship of phase with height.

It is evident from these results that tropospheric modelling and mitigation implemented in this work can reduce tropospheric artefacts due to vertical stratification successfully without affecting the original deformation signals. The Pearson correlation coefficient for the original 143 interferograms in Mexico ranges between - 0.60 to + 0.59. These values are reduced to zeros after linear correlation, and between - 0.006 and + 0.009 after power law correction. Unfortunately, there are no apparent vertical stratification effects from the SAR processing in Johor, which prevents successful utilisation of these techniques. One of the reasons is due to smaller height range in Johor (i.e. from 0 m to ~971 m above MSL) as opposed to Mexico (i.e. from ~702 m and ~5,568 m above MSL). Furthermore, results from the GPS processing also reveal that the area is dominated by turbulence mixing effects.

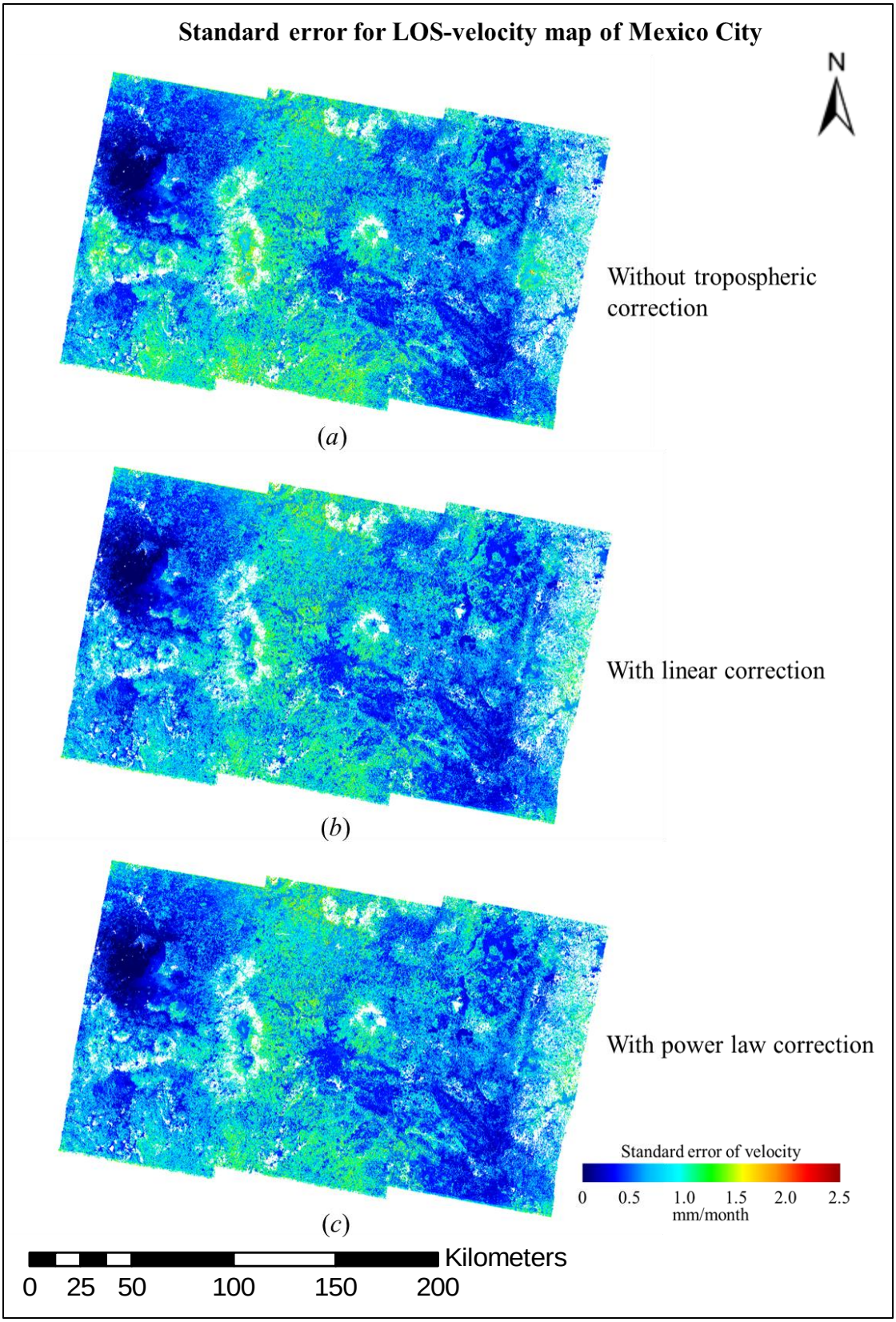


Figure 6.17: Comparison of the standard error map for the LOS-velocity of Mexico City: (*a*) without tropospheric correction, (*b*) tropospheric correction by a linear relationship of phase with height, and (*c*) tropospheric correction by power law relationship of phase with height.

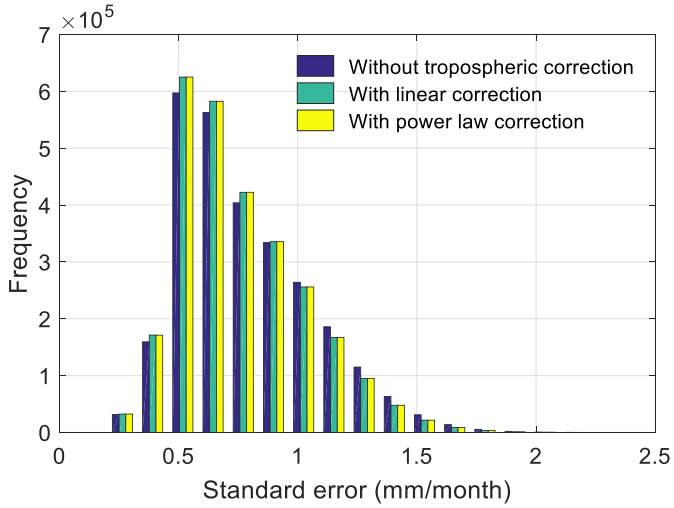


Figure 6.18: Histogram plot of the standard error for the LOS-velocity of Mexico City. Notice that more points will show small standard error from applying tropospheric corrections (linear or power law corrections) than without correction. No significant difference is observed between linear or power law corrections.

6.6. Summary

This chapter focusses on the works carried out in this research to address tropospheric effects in GPS and InSAR. In GPS, a usual practice is to introduce a dry component from a model and estimate the wet part from the LSE based on the observations data. The dry component can be taken from an empirical model based on the standard atmosphere (e.g. Saastamoinen) or from a model based on real weather measurements (e.g. VMF-1). Although no significant improvement is found in term of coordinate repeatability, their small deviation suggests that VMF-1 is more suitable than NMF when precise ZTD is the primary concern. Despite different approaches in the estimation, comparison of the estimated troposphere from PPP and DD indicates that they agreed reasonably well with each other to within 4 mm standard deviation. However, in the event where data problems occurred as also encountered in this research (i.e. missing L_2 observation, thus limiting the number of ionosphere-free linear combination formed), DD can benefit from the good data quality at nearby stations and not solely rely on the ionosphere-free linear combinations. Upon comparison with ZTDs from CODE, which is treated as the truth, it is found that DD yields better agreement than PPP. In general, the tropospheric delays in the study area range between 2.5 m and 2.7 m, thus they must be accounted for in precise applications such as deformation monitoring. The trends are dominated by the wet delay as it has higher variability than the dry, but the overall value is offset owing to the greater magnitude of the dry delay.

On the other hand, modelling and mitigation of tropospheric effects in InSAR are addressed by the author considering the correlation of phase in the unwrapped interferograms with height. The correlation can be represented either in linear or power-law relationships. In this research, both methods are implemented into Punnet – an in-house software used for the SAR processing. Significant reduction in the correlation between phase and height is observed after applying the correction. Although no noticeable difference is found in the corrected interferograms between the linear and power-law corrections, a slight improvement is achieved using power law as opposed to linear correction in the estimated deformation. The benefits of tropospheric correction in InSAR become more noticeable in the quality of the estimation, which is represented by the standard error map for the LOS-velocity. The results show a more trustable estimation after tropospheric correction than without one. This also suggests that non-linear analysis will benefits from this tropospheric correction as it relies on the residuals from the linear analysis.

CHAPTER 7

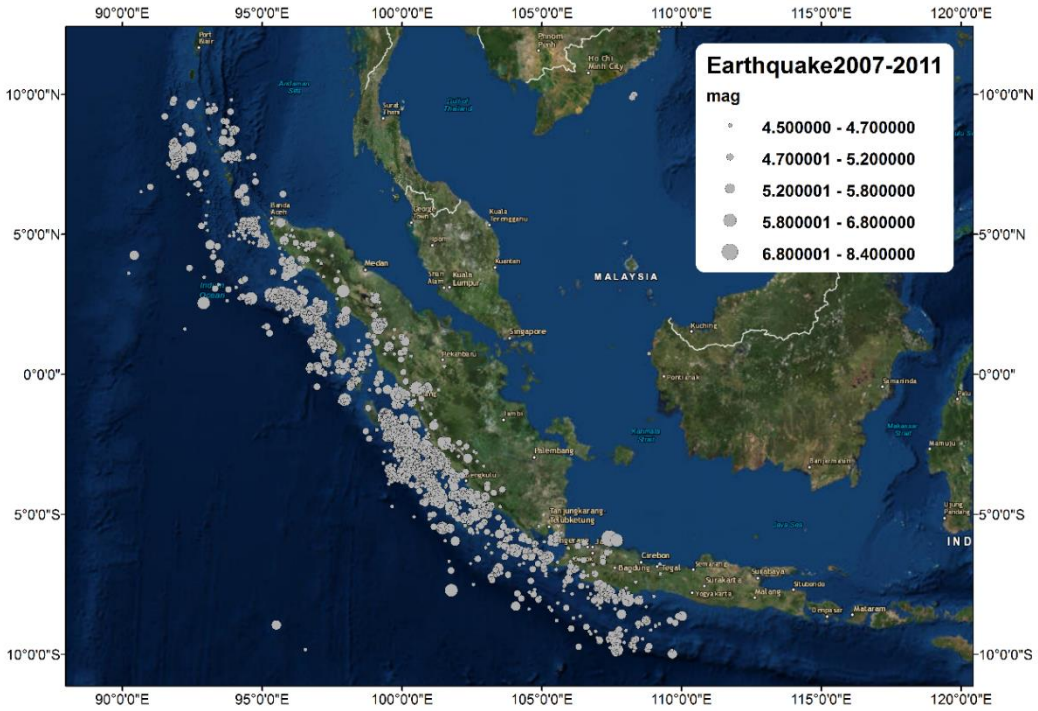
ANALYSES OF LONG-TERM DEFORMATION IN JOHOR

7.1. Introduction

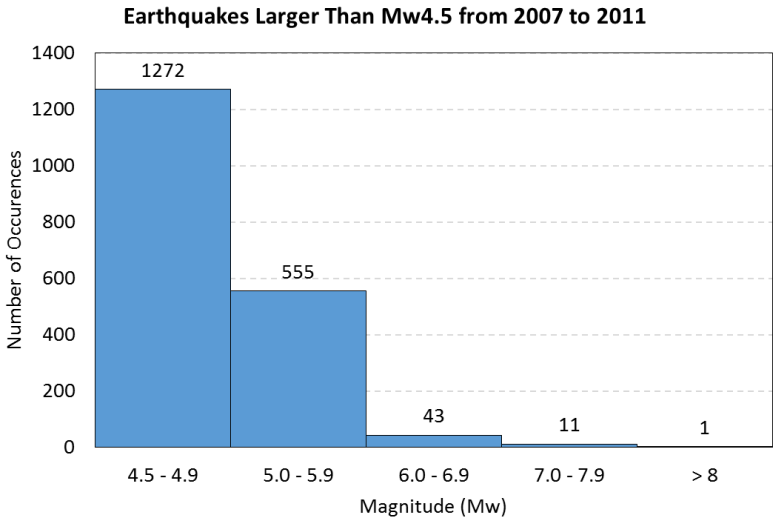
This chapter presents the final results and interpretation of the long-term deformation in Johor as quantified from the Global Positioning System (GPS) and Synthetic Aperture Radar (SAR) measurements. Firstly, historical records of the earthquakes from 2007 to 2011 are reported to correlate their effects with the GPS time-series. This is followed by a quantification and interpretation of the results from GPS, covering both the Precise Point Positioning (PPP) and Double-Difference (DD) processing. Analyses of the results are carried out regarding their root mean square (RMS) errors for the coordinate estimation, velocity estimation, as well as detected horizontal movements. Subsequently, the results from PPP and DD are compared to each other followed by a quantitative measure of the stations' movement considering their current coordinates. After that, the results from Interferometric SAR (InSAR) are presented and analysed. These include independent processing made on the SAR dataset listed in **Section 3.5.2**. The results are analysed in relation to previous studies and known deformation in the area. Comparison between the GPS and InSAR time-series is also made. This chapter ends with a summary of the significant findings of the long-term deformation in Johor as measured by GPS and InSAR techniques. The idea to quantify the long-term deformation from GPS and InSAR is also summarised.

7.2. Historical Records of Earthquake

The Pacific Ring of Fire is very well known for its active seismicity. It is a direct result of plate tectonics, i.e. the movement and collisions of lithospheric plates. About 90% of the world's earthquakes (USGS, 2016a) and 81% of the world's largest earthquakes occurred along the Pacific Ring of Fire (USGS, 2016b). **Figure 7.1a** shows the plot of earthquakes from 2007 to 2011 that took place within a region bounds by latitude 10° North - 10° South and longitude 90° East - 110° East, as extracted from the United States Geological Survey (USGS) database. Summary of those earthquakes is available in the corresponding **Figure 7.1b**. There is a total of 1,882 earthquakes with magnitude larger than Mw4.5. In general, the number of occurrences reduces with the magnitude as can be seen from the **Figure 7.1b**. Most of these earthquakes are smaller than 5Mw with a sum of 1,106. There are 555 earthquakes occurred between 5.0Mw and 5.9Mw, 43 earthquakes between 6.0Mw and 6.9Mw, 11 earthquakes between 7.0Mw and 7.9Mw, and 1 earthquake larger than 8Mw.



(*a*)



(*b*)

Figure 7.1: Recorded earthquakes with magnitude Mw4.5 and above in the region bounds by latitude 10° North - 10° South, and longitude 90° East - 110° East, as extracted from the United States Geological Survey (USGS) database: *http://earthquake.usgs.gov/* (accessed 18.01.2017). (*a*) Geographical location of the earthquakes and their magnitude, and (*b*) summary of the earthquakes.

7.3. Analyses of GPS Time-Series

This section presents and analyses the daily coordinate time series from GPS processing. They are used as the input to estimate the rate of long-term deformation in Johor. The time frame for GPS data covers from the year 2007 to 2011, processed with high precision Bernese GNSS Software version 5.2. Two processing strategies were employed, i.e. PPP and DD. Detailed strategies along with the method to estimate station velocity are discussed in **Section 4.5**. 8 Continuously Operating Reference Stations (CORS) stations served as the monitoring stations in the area. On top on that, 27 IGb08 stations are used as the reference points, and 7 International GNSS Service (IGS) stations are used to bridge and shorten the baselines length in DD processing mode. Geographical distribution of the stations is given in **Figure 3.8**. All station positions are determined in the International Terrestrial Reference Frame 2008 (ITRF2008).

7.3.1. Discussion on the PPP Results

PPP technique is attractive as it is computationally efficient, does not rely on reference stations, and is able to provide homogeneous positioning quality within a consistent global frame with a single GPS receiver. Nevertheless, long convergence time and difficulties in the ambiguity resolution limit its merits and widespread adoption. The PPP results from this work are based on float ambiguities resolution. The daily coordinate time-series of 8 Malaysia Real-Time Kinematic GNSS Network (MyRTKnet) stations in Johor are given in **Figure 7.2** to **Figure 7.9**. The coordinates are plotted in their own North-South, East-West, and Up-Down components. The red dotted lines in the y-axis represent earthquakes with magnitude larger than 6Mw. Additionally, the RMS of the coordinate estimation is also plotted. They are colour coded to show the RMS in North-South (dark blue), East-West (green), and Up-Down (cyan) components.

In general, all stations undergo constant movements. The North-South component shows declining trends, whereas the East-West part shows increasing trends. The Up-Down component is rather stable, but some stations such as KUKP and TGPG seem to show slightly declining trends. There are some noticeable data gaps in the time series owing to missing data as indicated previously in **Figure 3.9**. Nevertheless, this is as expected and could be due to maintenance works such as receiver and antenna replacements, or firmware updates. The following discussion is categorised in term of the RMS of coordinate estimation, velocity estimation, as well as analyses of the detected horizontal movements.

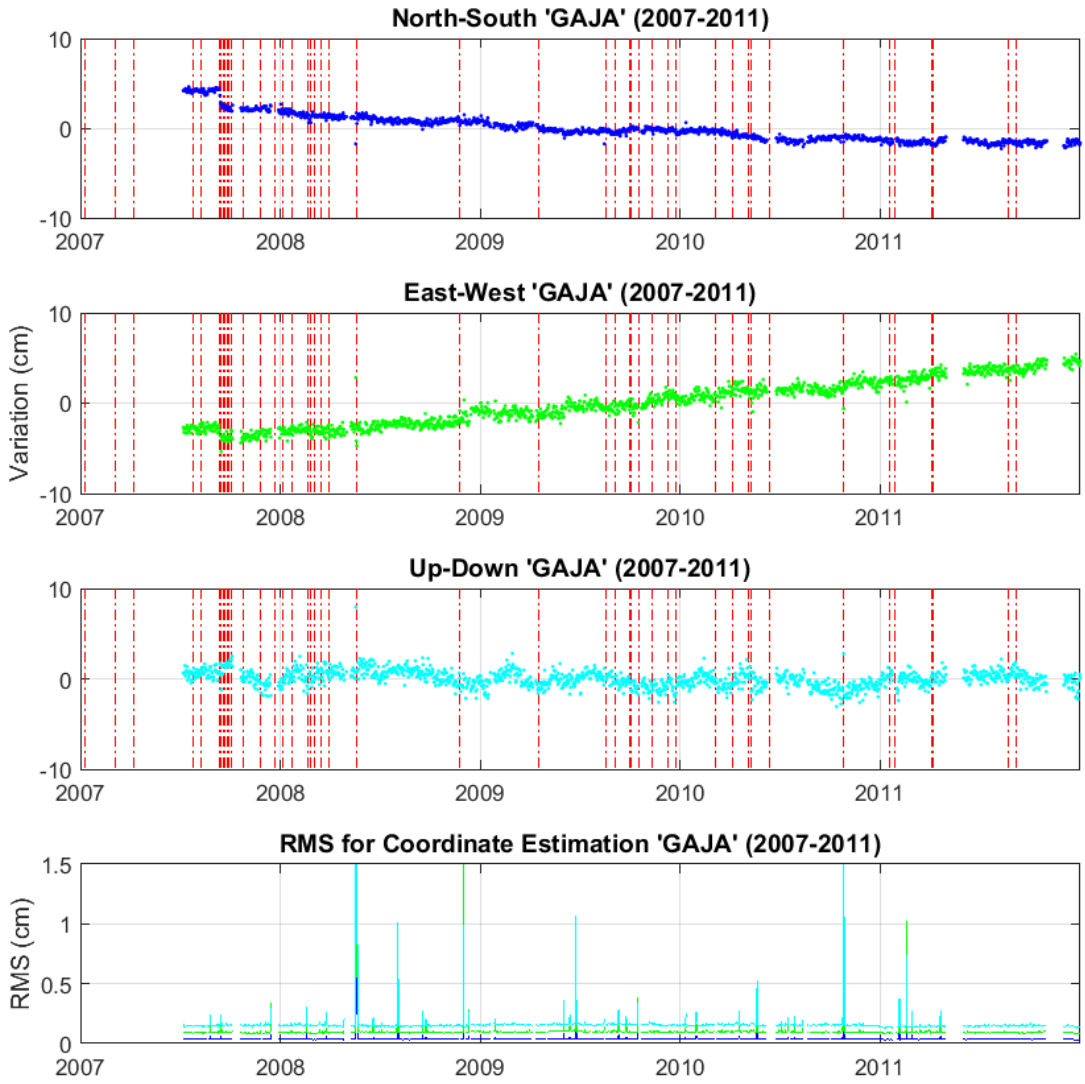


Figure 7.2: Daily coordinate time-series for station GAJA (2007 - 2011) from PPP processing. (*a*) North-South component, (*b*) East-West component, (*c*) Up-Down component, and (*d*) RMS for the estimation in colour coded, i.e. blue for North-South, green for East-West, and cyan for Up-Down components. The red dotted lines in the y-axis of the figure (*a*), (*b*), and (*c*) represent earthquake that is larger than 6Mw.

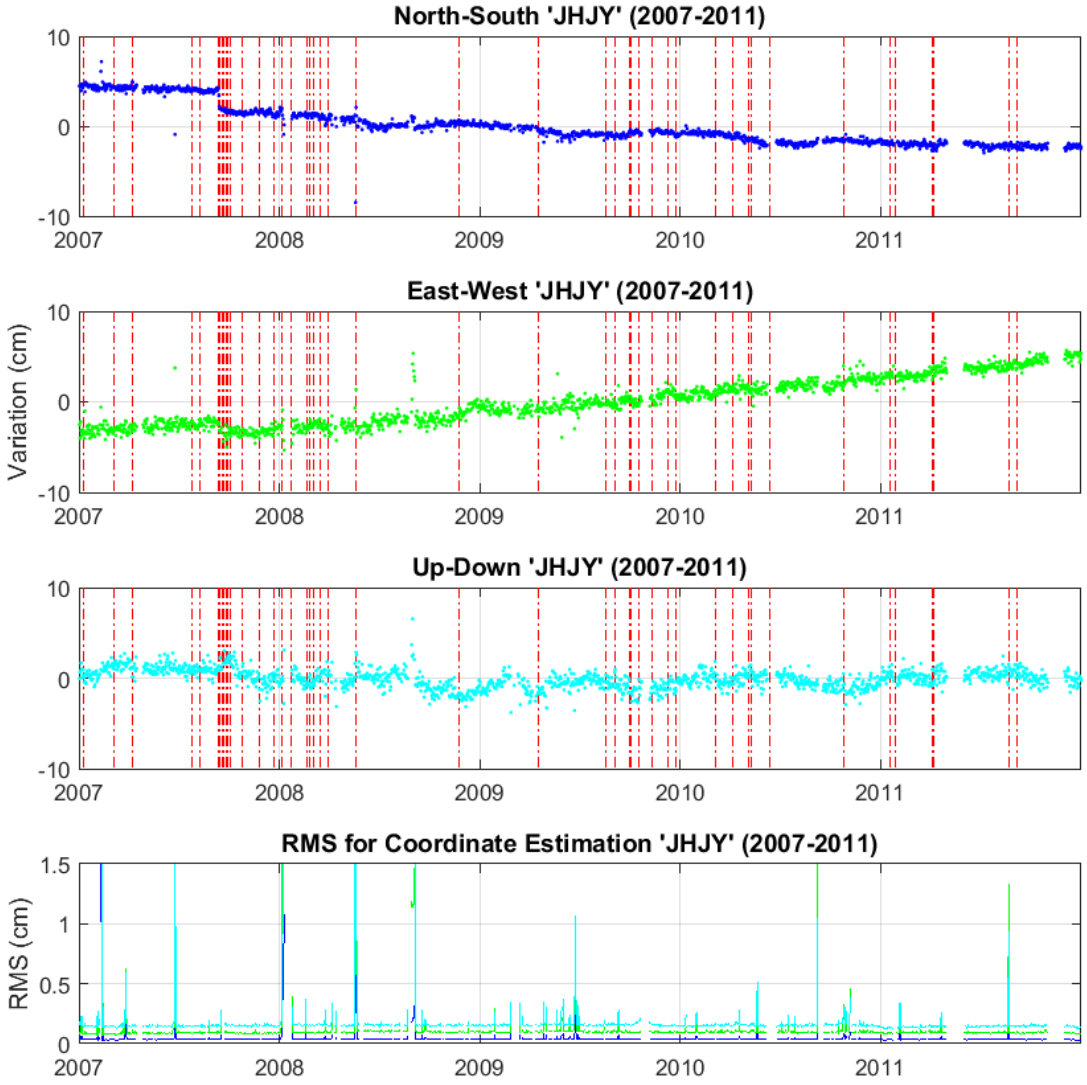


Figure 7.3: Daily coordinate time-series for station JHJY (2007 - 2011) from PPP processing. (*a*) North-South component, (*b*) East-West component, (*c*) Up-Down component, and (*d*) RMS for the estimation in colour coded, i.e. blue for North-South, green for East-West, and cyan for Up-Down components. The red dotted lines in the y-axis of the figure (*a*), (*b*), and (*c*) represent earthquake that is larger than 6Mw.

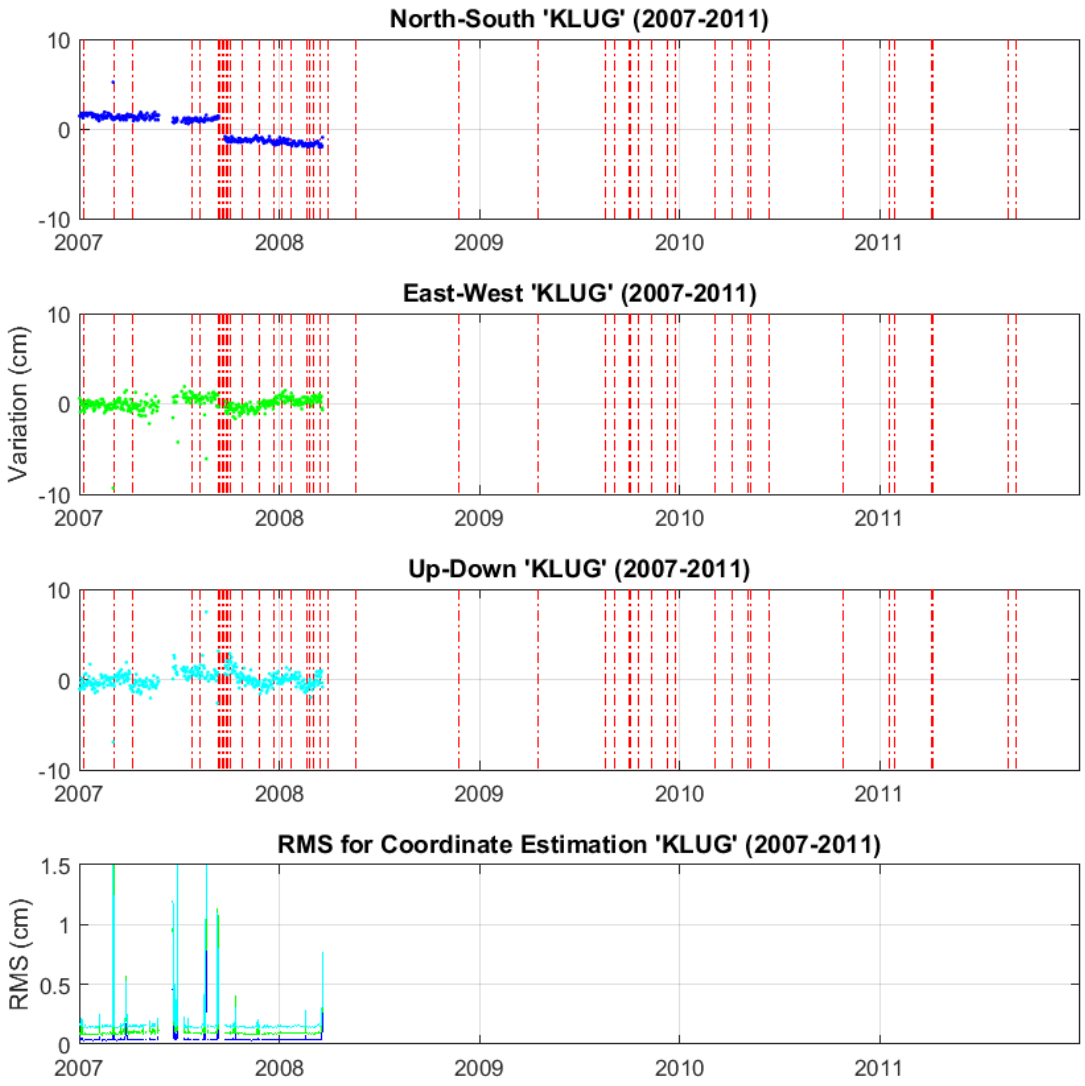


Figure 7.4: Daily coordinate time-series for station KLUG (2007 - 2011) from PPP processing. (*a*) North-South component, (*b*) East-West component, (*c*) Up-Down component, and (*d*) RMS for the estimation in colour coded, i.e. blue for North-South, green for East-West, and cyan for Up-Down components. The red dotted lines in the y-axis of the figure (*a*), (*b*), and (*c*) represent earthquake that is larger than 6Mw.

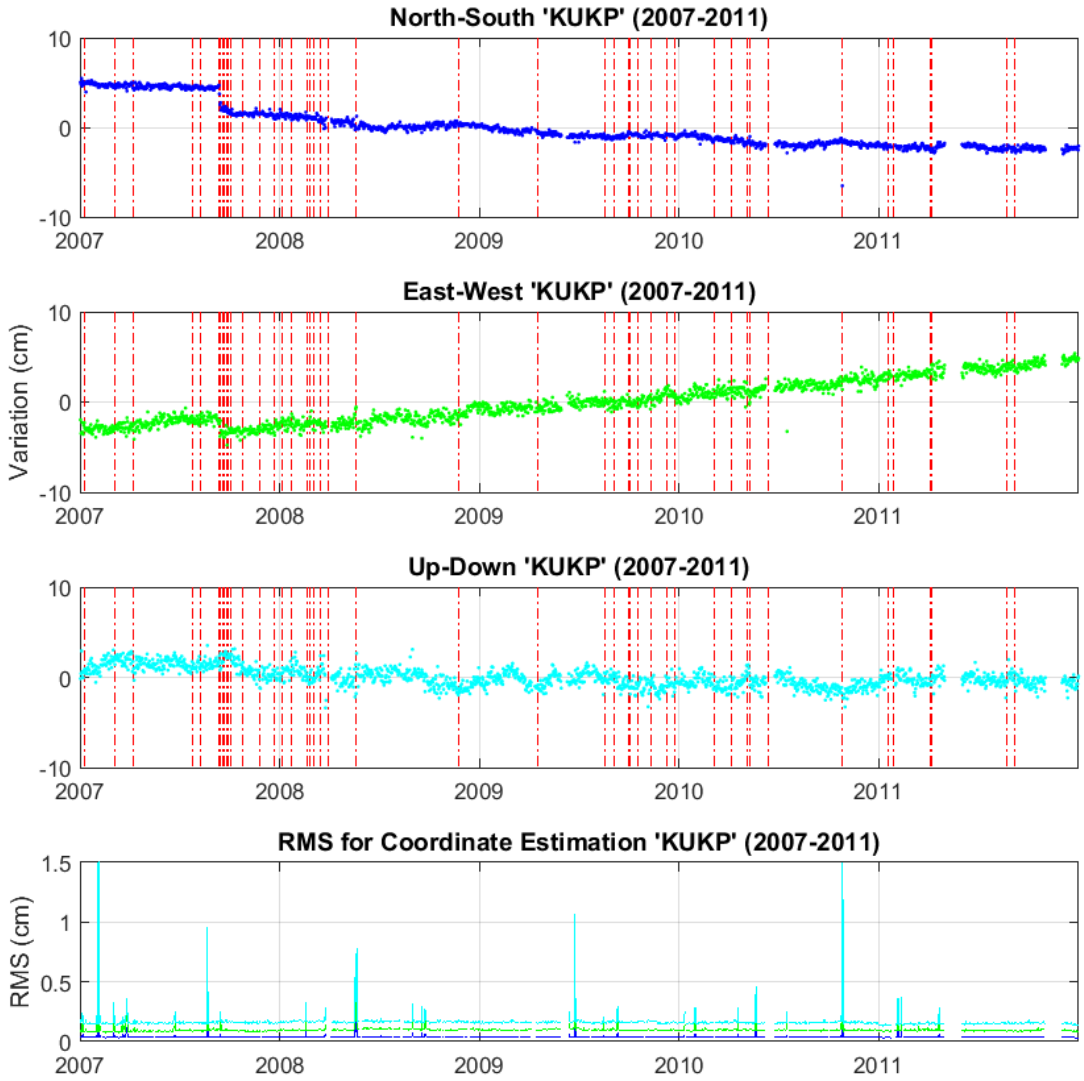


Figure 7.5: Daily coordinate time-series for station KUKP (2007 - 2011) from PPP processing. (*a*) North-South component, (*b*) East-West component, (*c*) Up-Down component, and (*d*) RMS for the estimation in colour coded, i.e. blue for North-South, green for East-West, and cyan for Up-Down components. The red dotted lines in the y-axis of the figure (*a*), (*b*), and (*c*) represent earthquake that is larger than 6Mw.

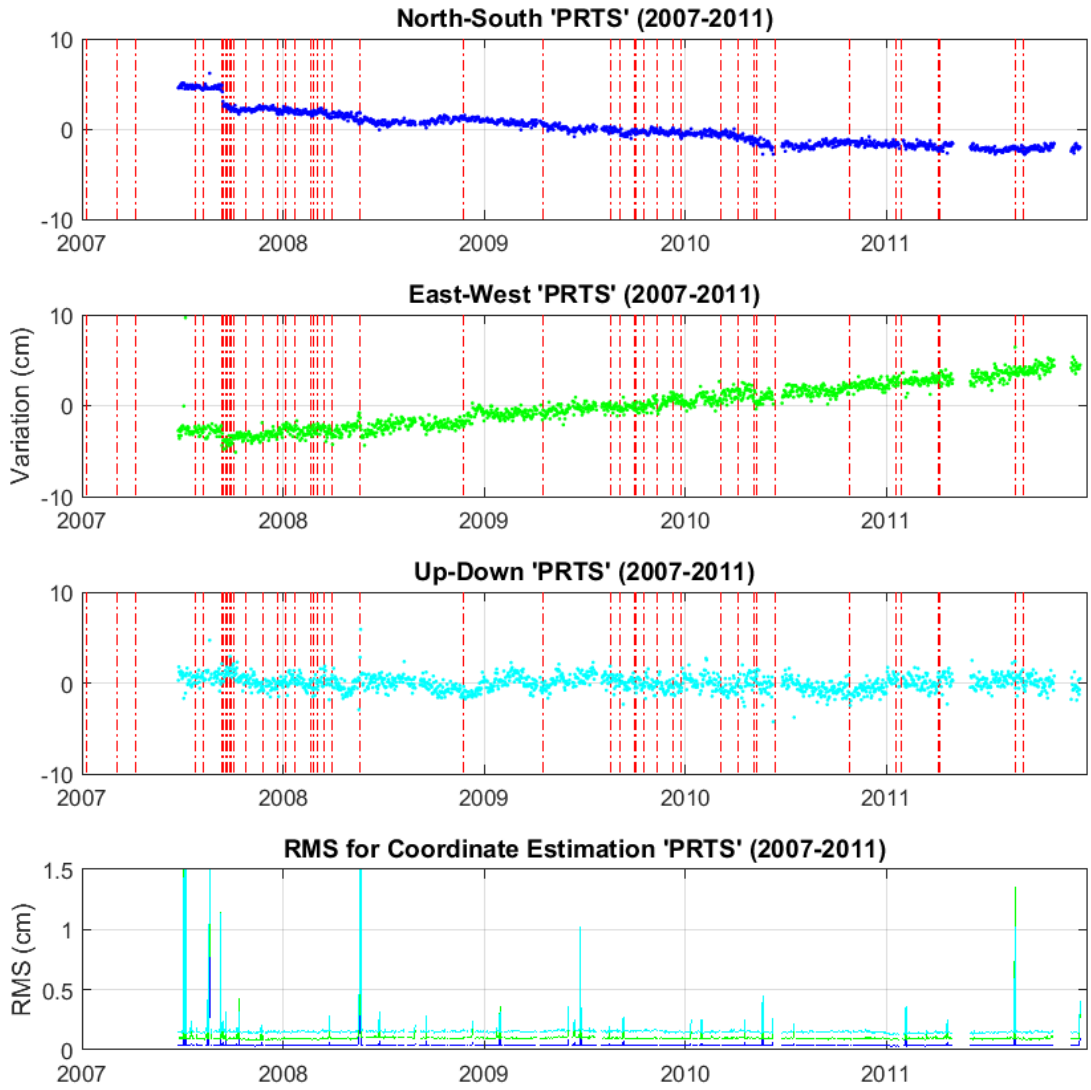


Figure 7.6: Daily coordinate time-series for station PRTS (2007 - 2011) from PPP processing. (*a*) North-South component, (*b*) East-West component, (*c*) Up-Down component, and (*d*) RMS for the estimation in colour coded, i.e. blue for North-South, green for East-West, and cyan for Up-Down components. The red dotted lines in the y-axis of the figure (*a*), (*b*), and (*c*) represent earthquake that is larger than 6Mw.

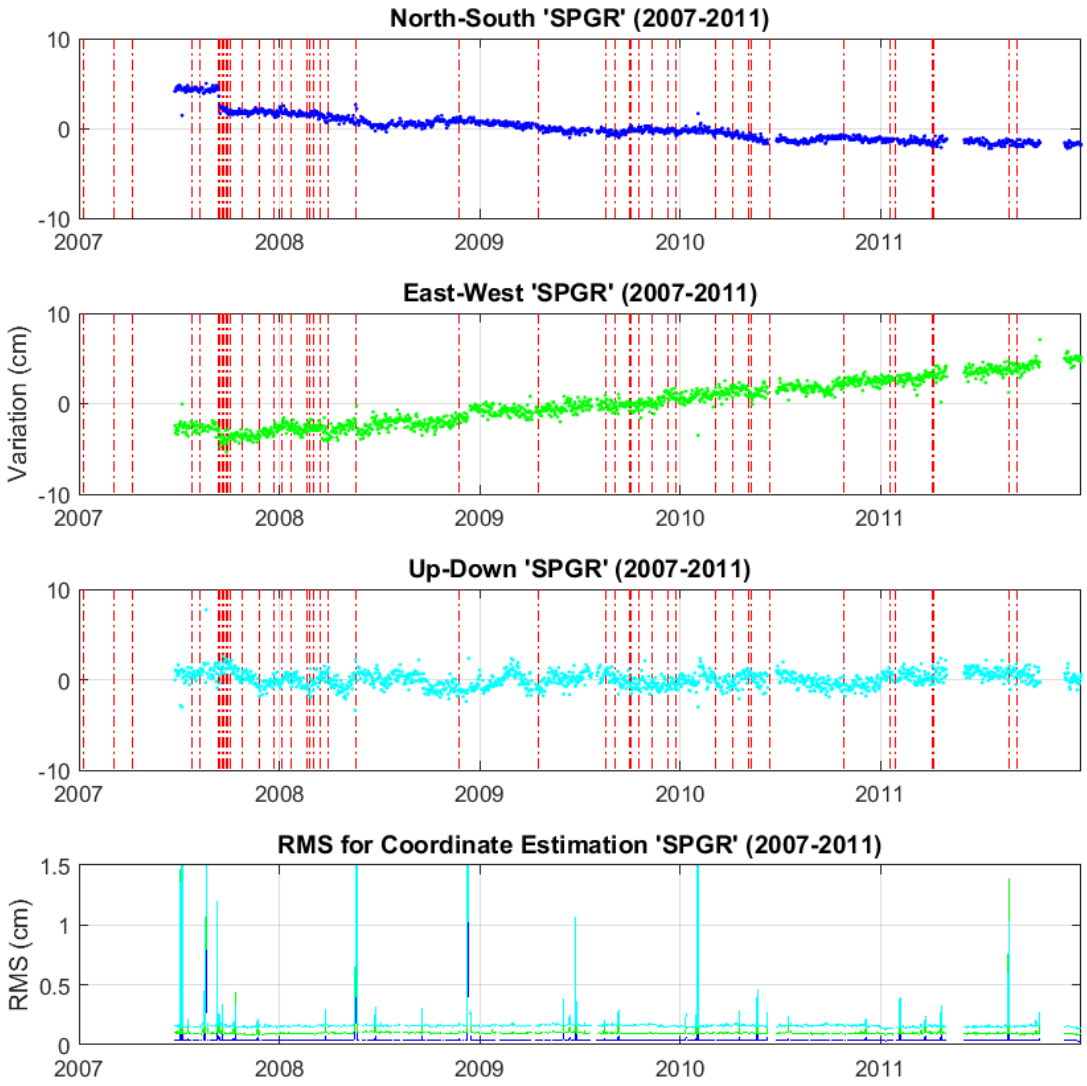


Figure 7.7: Daily coordinate time-series for station SPGR (2007 - 2011) from PPP processing. (*a*) North-South component, (*b*) East-West component, (*c*) Up-Down component, and (*d*) RMS for the estimation in colour coded, i.e. blue for North-South, green for East-West, and cyan for Up-Down components. The red dotted lines in the y-axis of the figure (*a*), (*b*), and (*c*) represent earthquake that is larger than 6Mw.

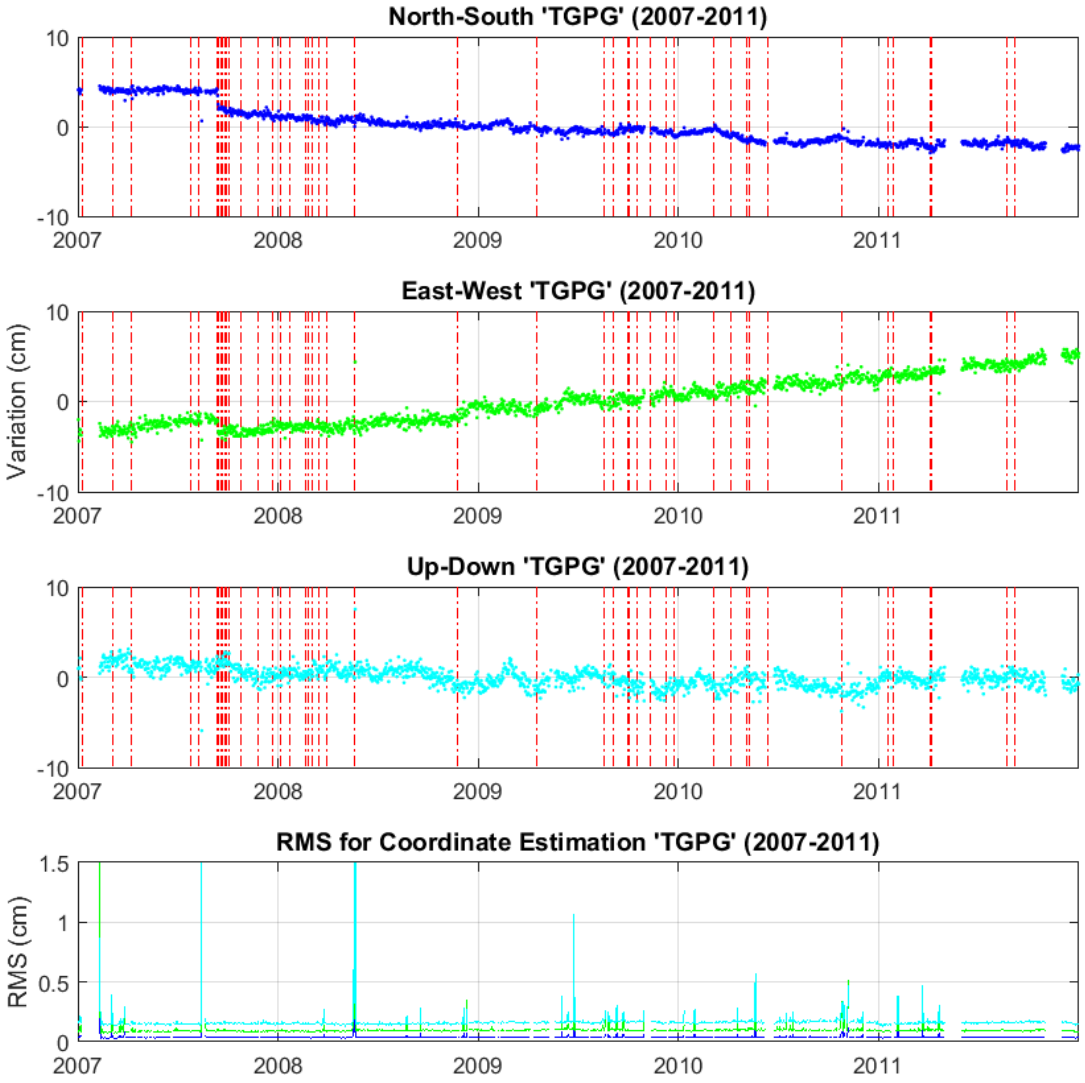


Figure 7.8: Daily coordinate time-series for station TGPG (2007 - 2011) from PPP processing. (*a*) North-South component, (*b*) East-West component, (*c*) Up-Down component, and (*d*) RMS for the estimation in colour coded, i.e. blue for North-South, green for East-West, and cyan for Up-Down components. The red dotted lines in the y-axis of the figure (*a*), (*b*), and (*c*) represent earthquake that is larger than 6Mw.

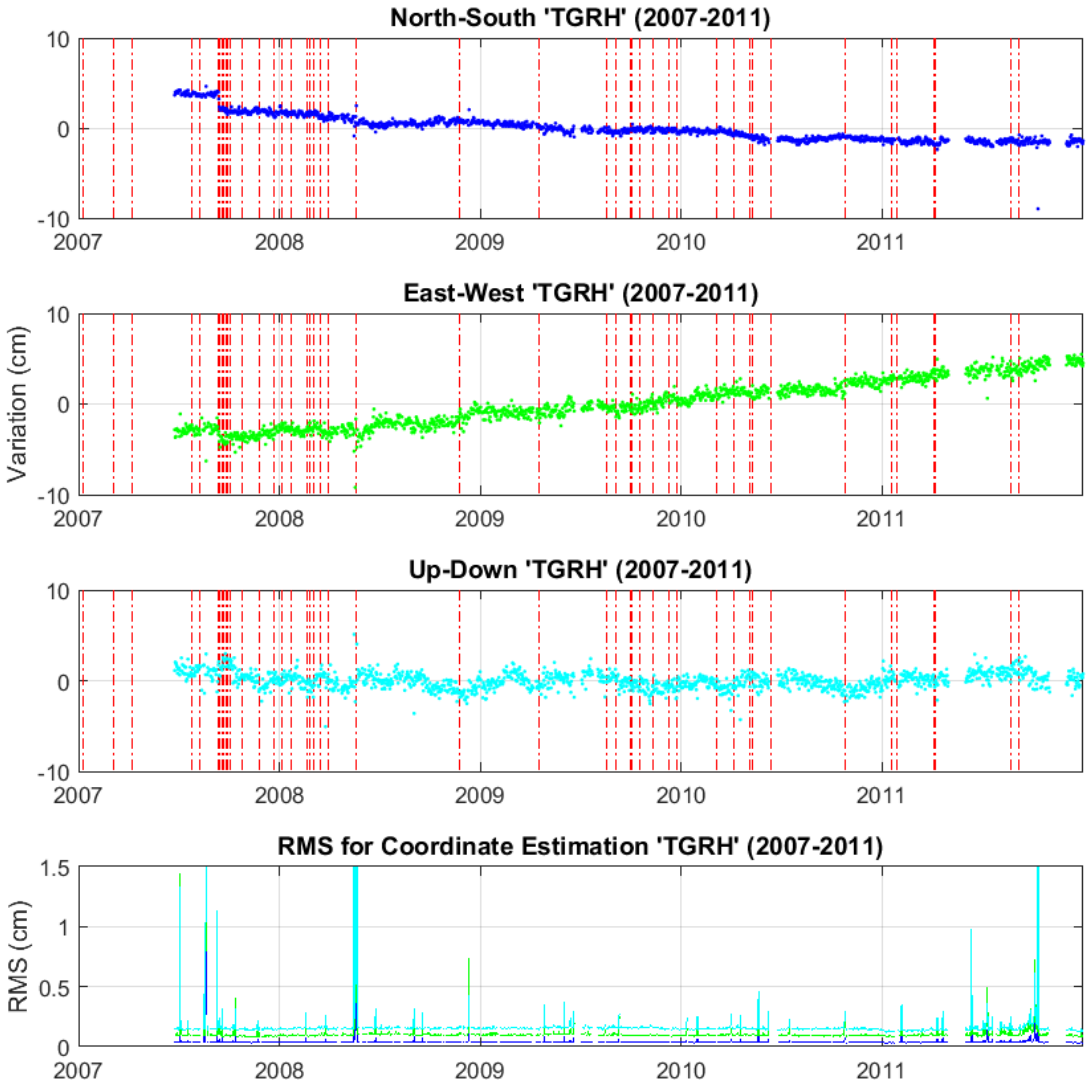


Figure 7.9: Daily coordinate time-series for station TGRH (2007 - 2011) from PPP processing. (*a*) North-South component, (*b*) East-West component, (*c*) Up-Down component, and (*d*) RMS for the estimation in colour coded, i.e. blue for North-South, green for East-West, and cyan for Up-Down components. The red dotted lines in the y-axis of the figure (*a*), (*b*), and (*c*) represent earthquake that is larger than 6Mw.

7.3.1.1. Analysis of the RMS of Coordinate Estimation

It is of paramount importance, especially in GPS measurements, to distinguish between accuracy and precision to understand the ability and quality of GPS for deformation detection. Accuracy is a measure of the difference between the true value and the best-estimated value. The accuracy indicator accounts for all types of errors, but it is particularly useful for describing systematic errors (Langley, 2010). Various sources of systematic errors in GPS has been discussed in **Section 4.2.2**. Those errors must be properly analysed and mitigated to extract the highest quality of information from the measurements. In this research, they have been reduced by applying the best available processing strategy via Bernese software.

On the other hand, precision is the degree of repeatability of the measurements. It is, therefore, a means of describing the quality of data with respect to random errors (Langley, 2010). The precision demonstrates the margin of detectable displacement, which means any deformation magnitude under this tolerance is hardly detectable. The precision of a point is defined as the formal standard error associated with the individual determination and is normally calculated as the RMS (Hofton, 1995; Williams, 1995). In general, the RMS errors for all 8 MyRTKnet stations are relatively good as shown in **Figure 7.2** to **Figure 7.9** despite some spikes that reach up to 1.5 cm. Any spikes that are larger than three sigmas are considered as outliers and are removed in the subsequent analyses. Upon investigation, it is found that they are attributable to bad data quality as reported previously in **Figure 6.7**. There were sparse data recorded on L_2 frequency, thus limiting the number of ionosphere-free linear combination. The reason for such a problem to occur is not known, but it could be due to receivers tracking performance or connection problems.

Figure 7.2 to **Figure 7.9** also reveal that the smallest RMS is achieved in North-South components, followed by East-West and Up-Down components. The average RMS for 8 MyRTKnet stations after the rejection of outliers is 0.4 mm in North-South, 1.0 mm in East-West, and 1.5 mm in Up-Down components. These values represent the minimum magnitude of position shift that can be detected using the PPP strategy presented in this work. **Figure 7.10** shows the histogram plots of the RMS, which further illustrates their deviation in all three components. The slightly large difference between the value in North-South and East-West components can be ascribed to the float ambiguity resolution employed in this work as also suggested in Choy et al. (2016). A better RMS is expected in the East-West component with fixed

ambiguity resolution, but this work is subject to future research. Nevertheless, it can be concluded that PPP solution within Bernese software with float ambiguity resolution can provide a precise estimation of coordinates.

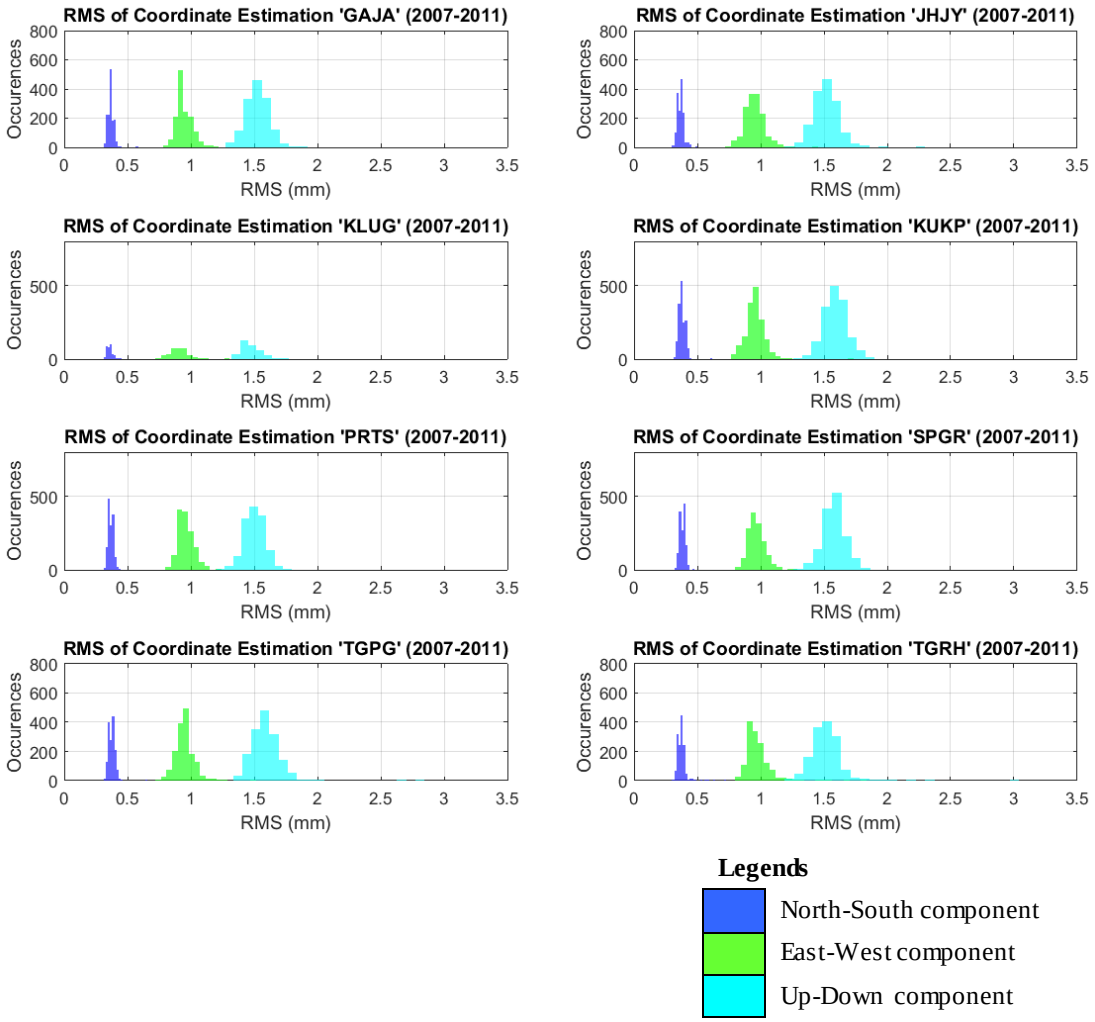


Figure 7.10: Histogram plots of the coordinate RMS from PPP processing.

7.3.1.2. Analysis of the Velocity Rate

Analysis on the coordinate RMS is necessary to identify and remove outliers from the time-series. It ensures that only reliable coordinates are used to estimate the velocity as well as provides an indication of the sensitivity of PPP technique to the position movement. It is worth noting from **Figure 7.2 - Figure 7.9** that the stations are non-stationary, i.e. the statistical or random noise remains relatively constant, while the mean varies with time. Their linear movement seems

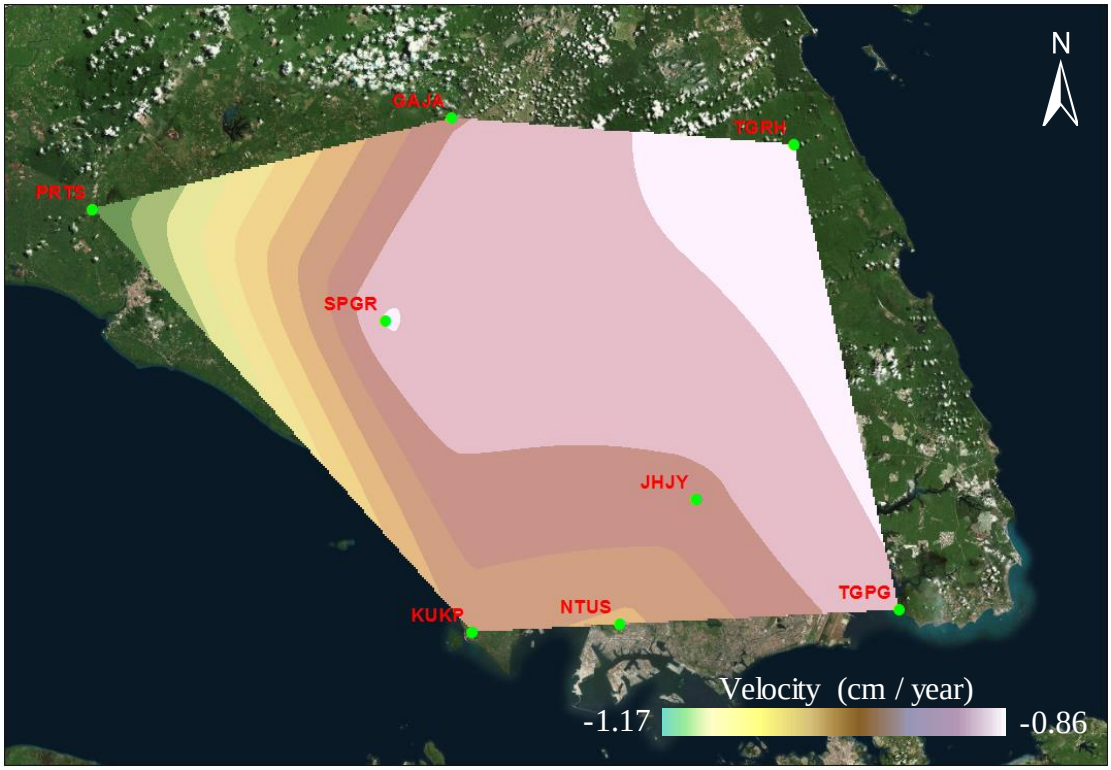
to be affected by earthquakes. The most notable one is Sumatra earthquake on 12 September 2007, which was also followed by a series of aftershocks. Those have resulted in an apparent shift in the coordinate time-series. Extracted time-series for the 8 MyRTKnet stations from 1 August 2007 to 31 October 2007 are given in the **Appendix D**. Although movement from some other earthquakes is also detectable, they are not as significant. More discussion on this is made in **Section 7.3.3** along with the results from DD. For simplicity, the rate of linear velocity is estimated using data after the earthquakes, i.e. from 18 September 2007 (DoY 261) onward. This is also supported by the time-series shown in **Appendix D**, whereby the coordinate of the stations did not vary by much after that date.

Table 7.1 presents the summary of GPS-derived time-series and their uncertainties (standard errors) in centimetre per year (cm/year). From the table, the trend for all station are similar in North-South (i.e. negative) and East-West (i.e. positive) components, whereas the Up-Down has both uplift and subsidence patterns. The standard errors of the velocities are good, apart from KLUG station. In lateral components, they are at ± 0.01 cm/year, whereas in vertical components, they are below ± 0.03 cm/year. High standard errors at KLUG can be explained by less data availability as compared to the others. The most significant movement in North-South direction occurred at station PRTS at -1.17 ± 0.01 cm/year, whereas the smallest movement is observed at station TGRH at -0.86 ± 0.01 cm/year. On the contrary, the largest movement in East-West direction is seen at TGPG at 2.00 ± 0.01 cm/year, and the smallest movement is at KUKP station at 1.85 ± 0.01 cm/year. Three out of seven stations (excluding KLUG) show an uplift trend, i.e. JHJY, SPGR, and TGRH, while the others show subsidence trend. The most substantial movement is found at station TGPG at -0.30 ± 0.02 cm/year and the smallest change is at station JHJY at 0.02 ± 0.03 cm/year.

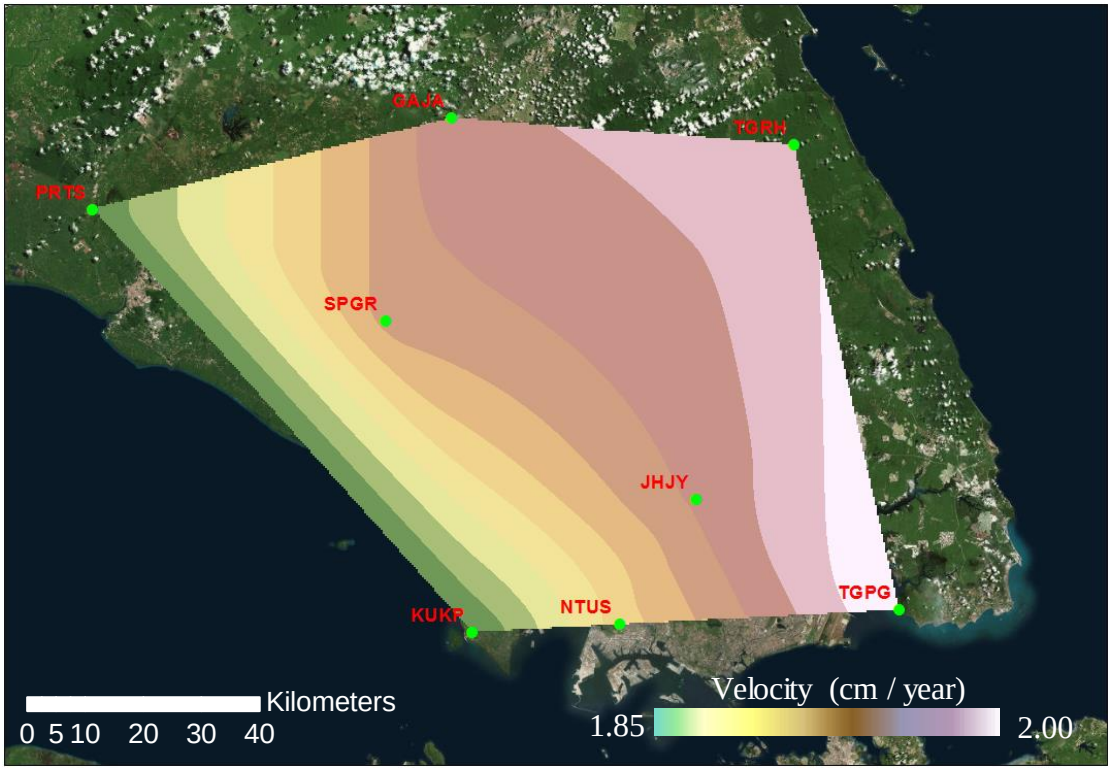
Table 7.1: Linear velocity rate for 8 MyRTKnet stations estimated from PPP solution using GPS data from 2007 to 2011.

Station	PPP solution		
	North-South (cm/year)	East-West (cm/year)	Up-Down (cm/year)
GAJA	-0.93 ± 0.01	1.97 ± 0.01	-0.19 ± 0.02
JHJY	-0.93 ± 0.01	1.96 ± 0.01	0.02 ± 0.03
KLUG	-1.32 ± 0.11	2.84 ± 0.24	-2.46 ± 0.39
KUKP	-0.97 ± 0.01	1.85 ± 0.01	-0.29 ± 0.02
PRTS	-1.17 ± 0.01	1.86 ± 0.01	-0.05 ± 0.02
SPGR	-0.89 ± 0.01	1.95 ± 0.01	0.09 ± 0.02
TGPG	-0.90 ± 0.01	2.00 ± 0.01	-0.30 ± 0.02
TGRH	-0.86 ± 0.01	1.98 ± 0.01	0.04 ± 0.02

On a closer inspection, the stations in the West seem to be moving at a different rate than the stations in the East in term of their individual lateral components, i.e. higher in the North-South and lower in the East-West directions. **Figure 7.11** shows the interpolated stations velocity in the North-South and East-West from the Natural Neighbour Interpolation made using a toolbox within ArcGIS software. An IGS station in Singapore, namely NTUS, is also included in the interpolation. However, KLUG station is excluded due to significant uncertainties in the estimated velocity which can affect the result. The figure clearly reveals the different rate of individual lateral movements between the two parts of Peninsular Malaysia. Nevertheless, no apparent trend is observed in the vertical direction. This finding seems to suggest a presence of geological separation between the two areas. This assumption is further supported by the seismotectonic map from the Department of Mineral and Geoscience Malaysia (JMG) (**Figure 7.12**). The map shows several major and minor fault lines that might separate the east and west sectors of Peninsular Malaysia. It is possible that these fault lines have influenced the tectonic movements from the subduction of the Indo-Australian plate under the Eurasian plates. These influences are observed as the different rate between the two areas. Future research would benefit from an in-depth geological analysis pertaining to the properties, mechanisms, and influences of these fault lines to fully understand the driving forces behind this deformation.



(*a*)



(*b*)

Figure 7.11: Interpolated stations velocity from PPP processing in (*a*) North-South, and (*b*) East-West components, based on the Natural Neighbour Interpolation within ArcGIS software.

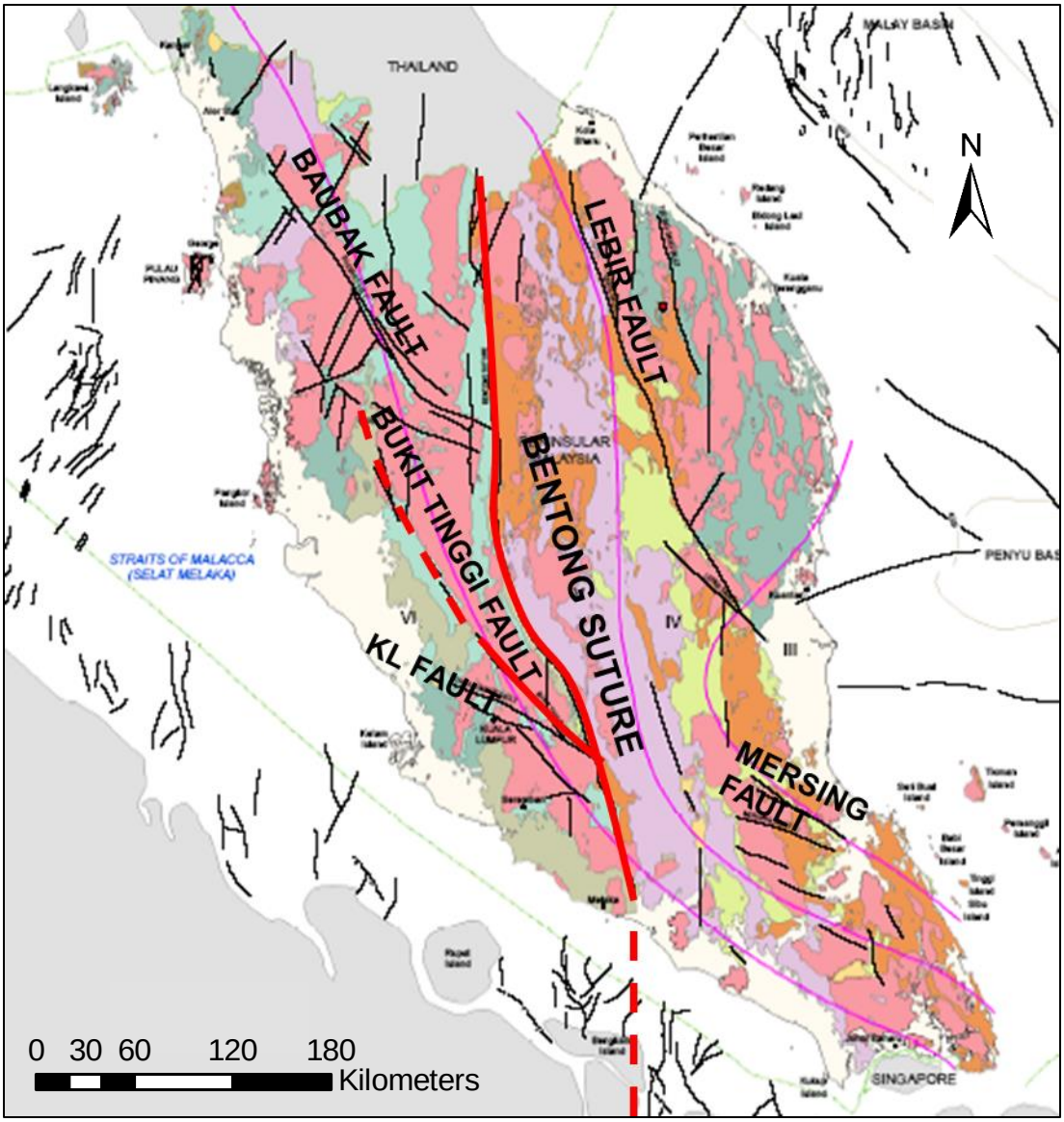


Figure 7.12: Seismotectonic map of Peninsular Malaysia showing some major and minor fault lines separating the east and the west sectors of Peninsular Malaysia. Figure adapted from JMG (2009).

7.3.1.3. Analysis of the Horizontal Movement

Following the individual analysis made previously, the stations' movement is also analysed in term of their plane movement. This process enables assessment not only of the horizontal magnitude but also of the direction of motion. **Figure 7.13** shows the plot of horizontal coordinates for 8 MyRTKnet stations, colour coded by years, i.e. cyan for 2007, dark blue for 2008, green for 2009, black for 2010, and magenta for 2011. On top of that, earthquakes larger than 6.5Mw

are also plotted to investigate their potential implications. All stations, in general, moved towards the South-East direction. There is no apparent shift in the position apart from the one induced by the Sumatra earthquake on 12 September 2007, which was also followed by a series of aftershocks.

Estimation of horizontal magnitude H_{Vel} and direction A_{Vel} of movement in this research are made through a simple relationship between change in the North-South NS_{Vel} and the East-West EW_{Vel}, as shown in Equation (7.1) and (7.2).

$$H_{Vel} = \sqrt{{NS_{Vel}}^2 + {EW_{Vel}}^2} \quad \cdots\cdots (7.1)$$

$$A_{Vel} = \tan^{-1}\left(\frac{EW_{Vel}}{NS_{Vel}}\right) \quad \cdots\cdots (7.2)$$

Figure 7.14 shows the vector plot of the horizontal stations' movement. The largest change occurred at station KLUG (i.e. 3.14 cm/year), but the result is of dubious quality considering the large standard deviation, i.e. ± 0.27 cm/year. It is followed by station PRTS at 2.20 ± 0.01 cm/year and TGPG at 2.19 ± 0.01 cm/year. Station GAJA and JHJY show similar horizontal movement at 2.17 cm/year, although the standard deviation varies slightly at ± 0.01 cm/year and ± 0.02 cm/year, respectively. Station KUKP recorded the lowest movement at 2.09 ± 0.01 cm/year, next to SPGR at 2.14 ± 0.02 cm/year. The direction of movement ranges between 113.579° to 122.209°.

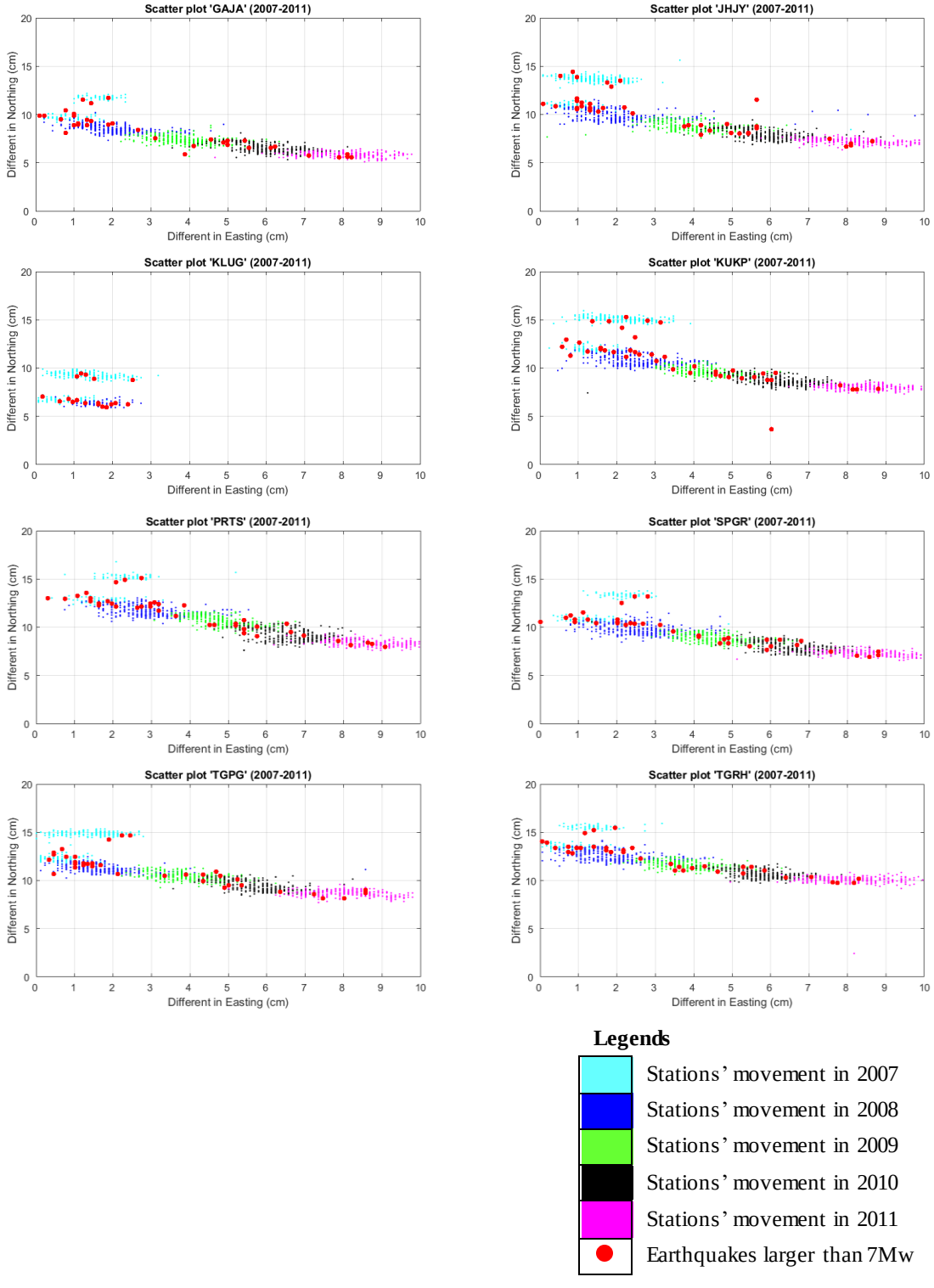


Figure 7.13: Scatter plot of the stations movement as estimated from the PPP processing (2007 - 2011).

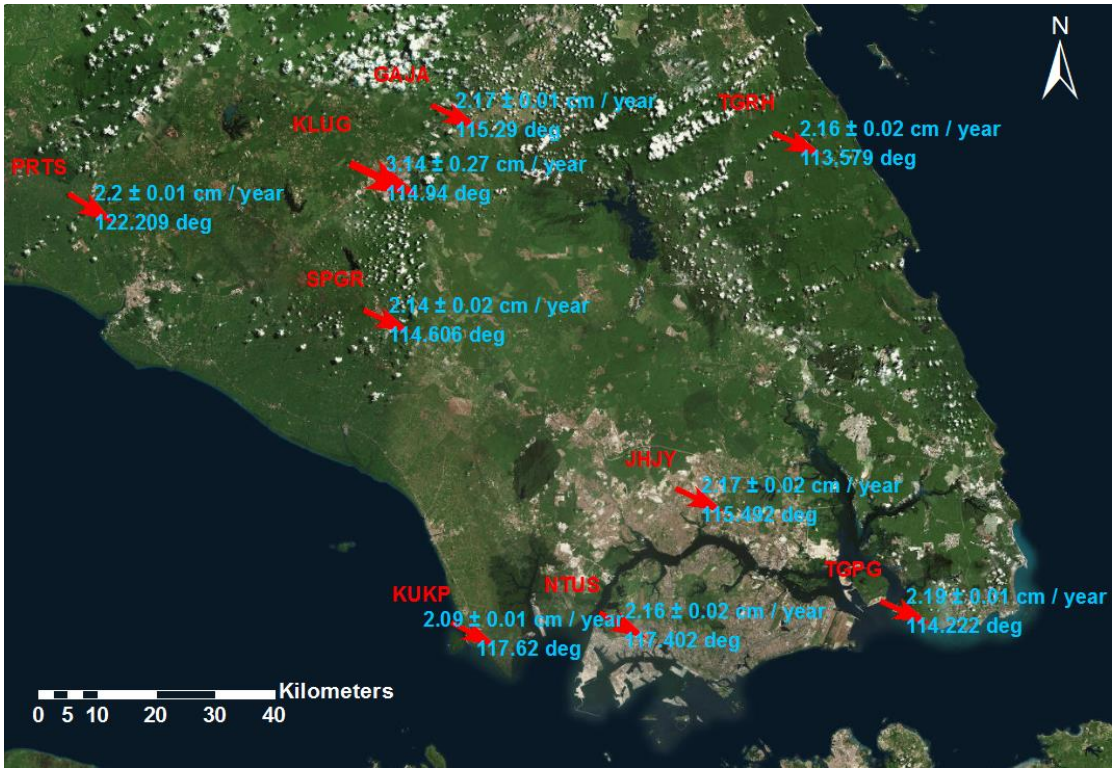


Figure 7.14: Vector plot of the horizontal movement of eight MyRTKnet stations as estimated from the PPP processing.

7.3.2. Discussion on the DD Results

In DD processing, the coordinate of a point is determined based on the reference point(s) with known coordinates. It eliminates or reduces most GNSS observation errors that are spatially correlated at both points, thus providing high accuracy positioning solutions. DD is the dominant precise positioning and data processing method for the last three decades (Choy et al., 2016). One of its major advantages is that the double-differenced ambiguity term, between two receivers and two satellites, has an integer nature (hardware dependent biases have cancelled) and consequently can be fixed to the correct integer value. In this work, DD is expected to give better results than PPP as it is based on fixed ambiguity resolution, whereas the latter is based on float ambiguity resolution.

Figure 7.15 to **Figure 7.22** show the coordinate time-series for 8 MyRTKnet stations in Johor. The North-South, East-West, and Up-Down components are plotted individually. On top of that, the RMS for coordinate estimation is also plotted, colour coded to show the value in North-South (dark blue), East-West (green), and Up-Down (cyan). The red dotted lines in the y-axes indicate earthquakes larger than 6Mw. Discussion on the results follows

similar principle as in the PPP. First, the RMS of coordinate estimation is analysed, followed by the estimation of the velocity rate. Subsequently, analysis of the movement in the horizontal component is carried out.

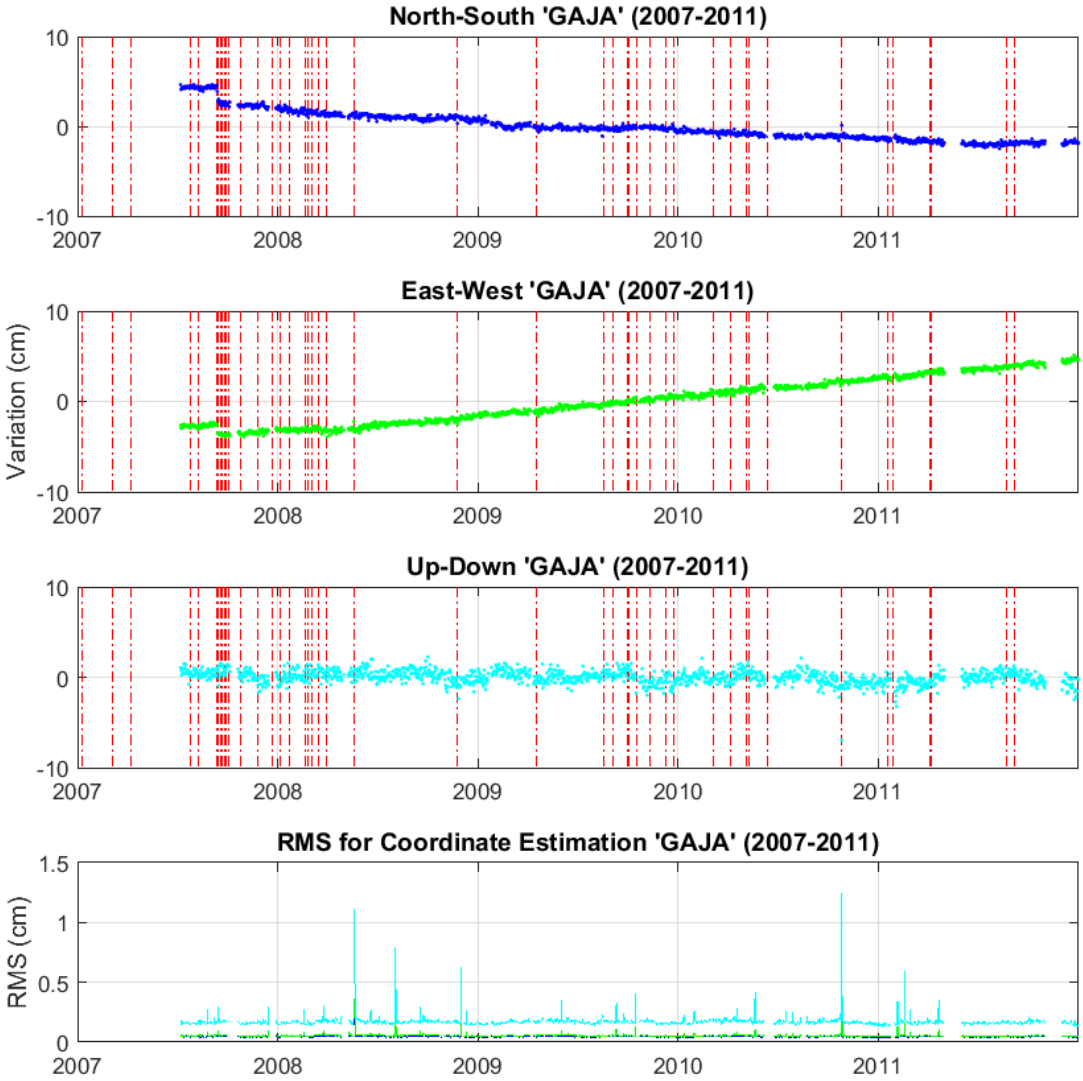


Figure 7.15: Daily coordinate time-series for station GAJA (2007 - 2011) from DD processing. (*a*) North-South component, (*b*) East-West component, (*c*) Up-Down component, and (*d*) RMS for the estimation in colour coded, i.e. blue for North-South, green for East-West, and cyan for Up-Down components. The red dotted lines in the y-axis of the figure (*a*), (*b*), and (*c*) represent earthquake that is larger than 6Mw.

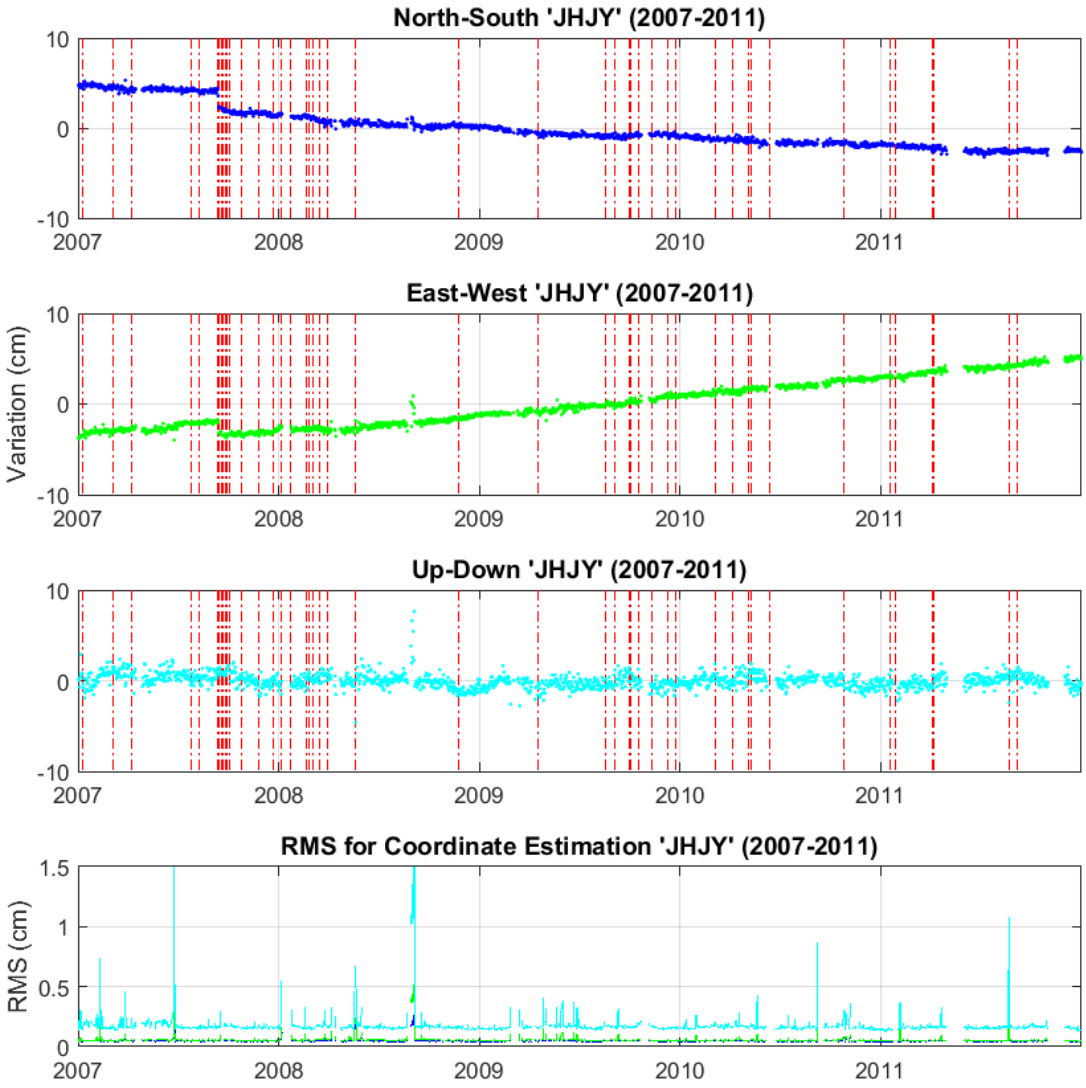


Figure 7.16: Daily coordinate time-series for station JHJY (2007 - 2011) from DD processing. (*a*) North-South component, (*b*) East-West component, (*c*) Up-Down component, and (*d*) RMS for the estimation in colour coded, i.e. blue for North-South, green for East-West, and cyan for Up-Down components. The red dotted lines in the y-axis of the figure (*a*), (*b*), and (*c*) represent earthquake that is larger than 6Mw.

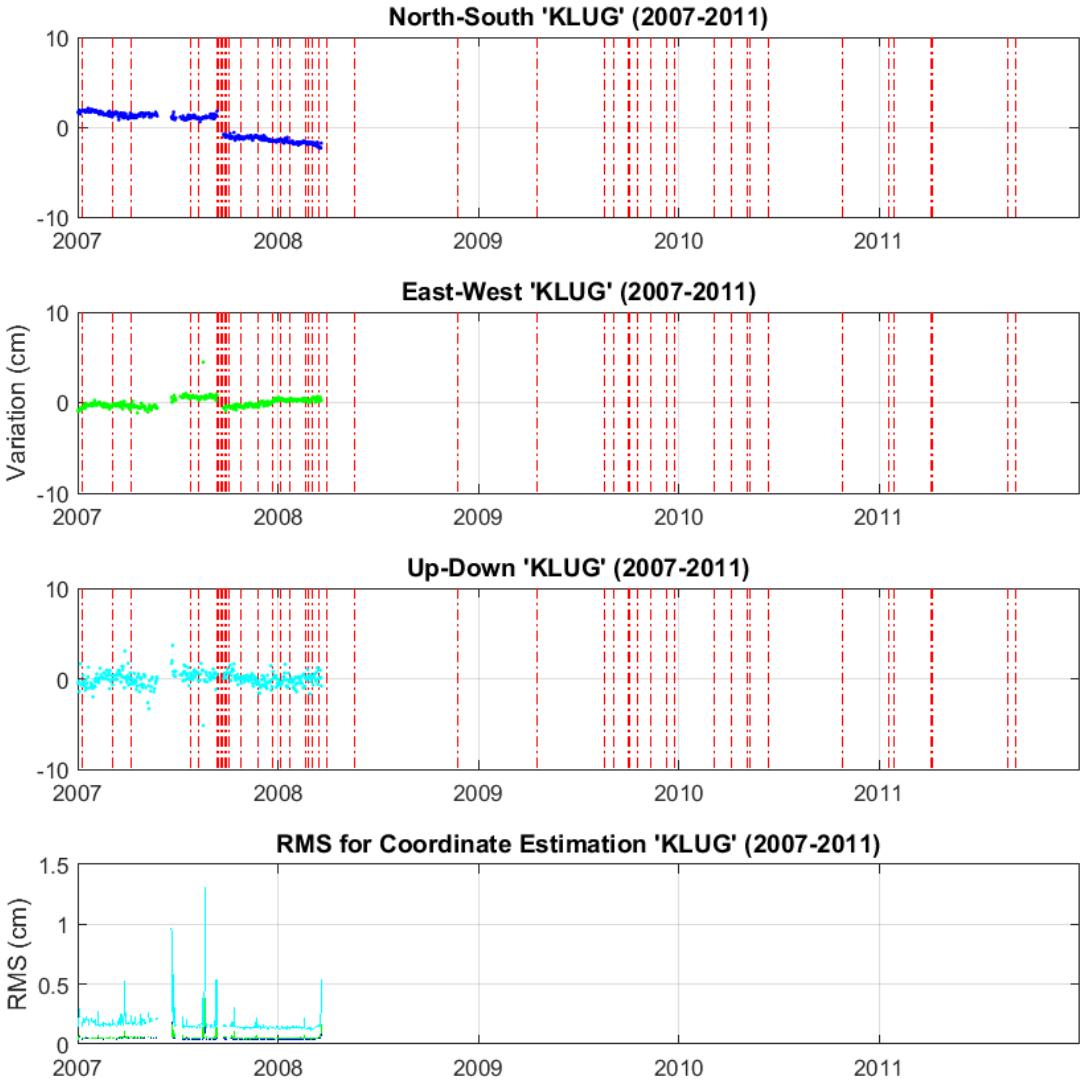


Figure 7.17: Daily coordinate time-series for station KLUG (2007 - 2011) from DD processing. (*a*) North-South component, (*b*) East-West component, (*c*) Up-Down component, and (*d*) RMS for the estimation in colour coded, i.e. blue for North-South, green for East-West, and cyan for Up-Down components. The red dotted lines in the y-axis of the figure (*a*), (*b*), and (*c*) represent earthquake that is larger than 6Mw.

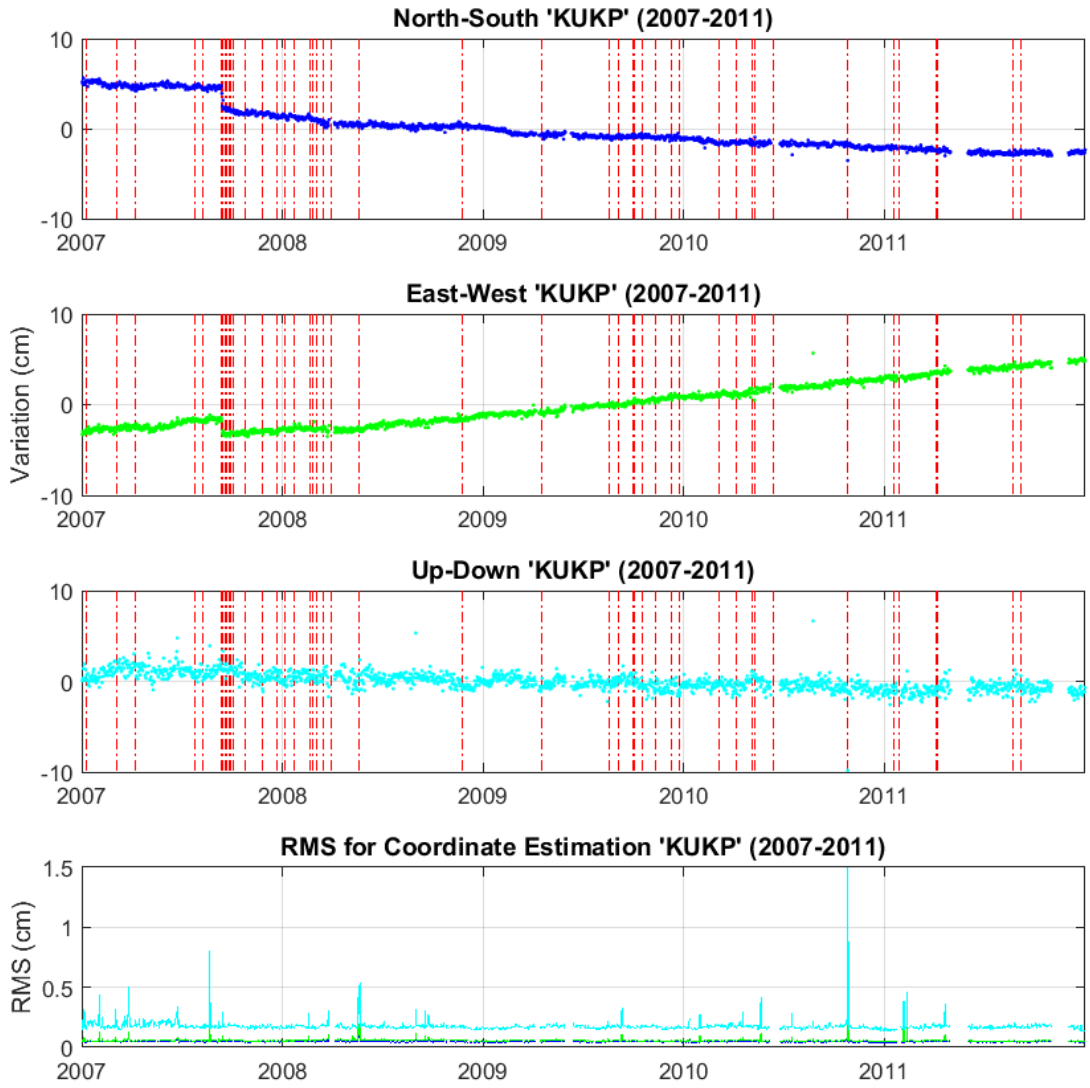


Figure 7.18: Daily coordinate time-series for station KUKP (2007 - 2011) from DD processing. (*a*) North-South component, (*b*) East-West component, (*c*) Up-Down component, and (*d*) RMS for the estimation in colour coded, i.e. blue for North-South, green for East-West, and cyan for Up-Down components. The red dotted lines in the y-axis of the figure (*a*), (*b*), and (*c*) represent earthquake that is larger than 6Mw.

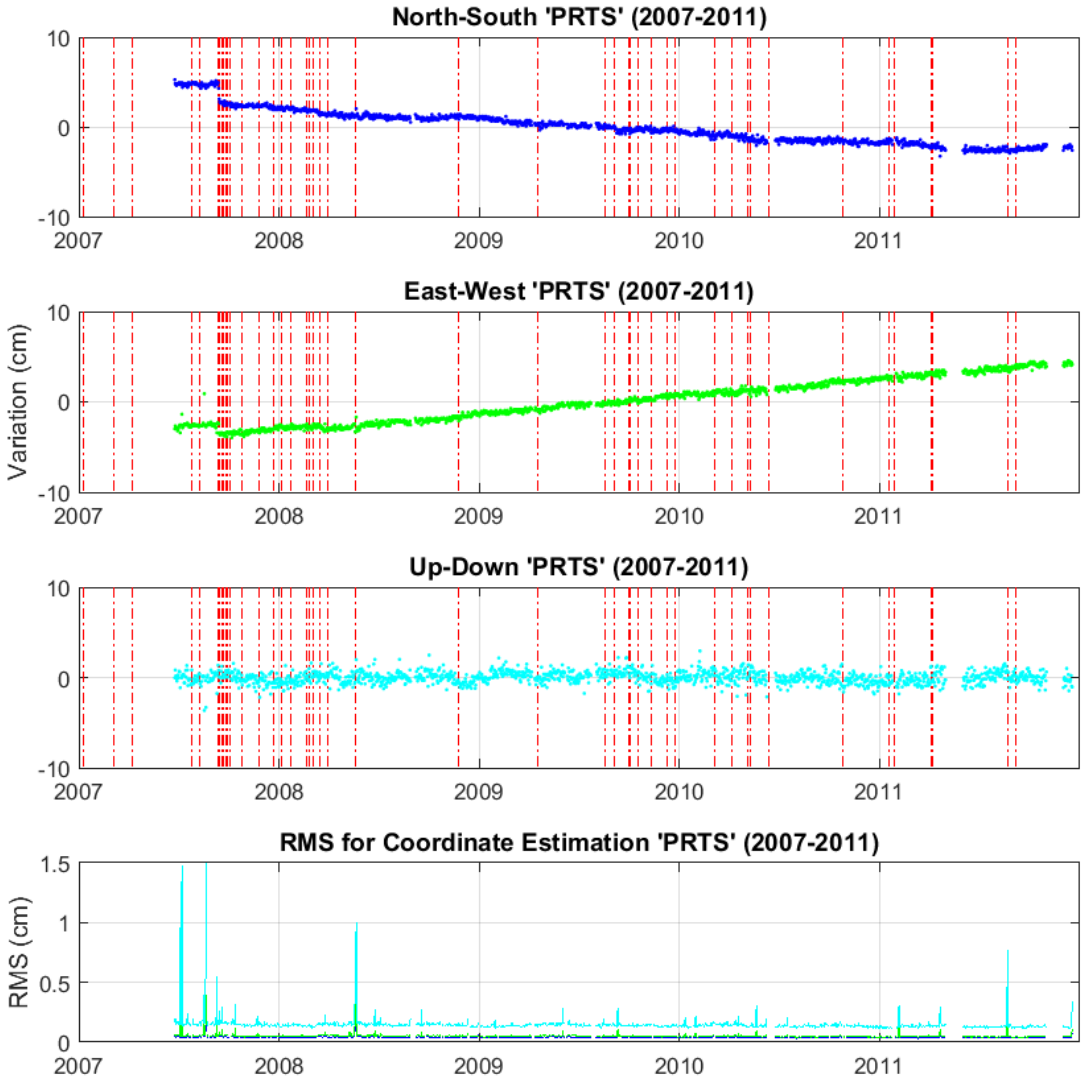


Figure 7.19: Daily coordinate time-series for station PRTS (2007 - 2011) from DD processing. (*a*) North-South component, (*b*) East-West component, (*c*) Up-Down component, and (*d*) RMS for the estimation in colour coded, i.e. blue for North-South, green for East-West, and cyan for Up-Down components. The red dotted lines in the y-axis of the figure (*a*), (*b*), and (*c*) represent earthquake that is larger than 6Mw.

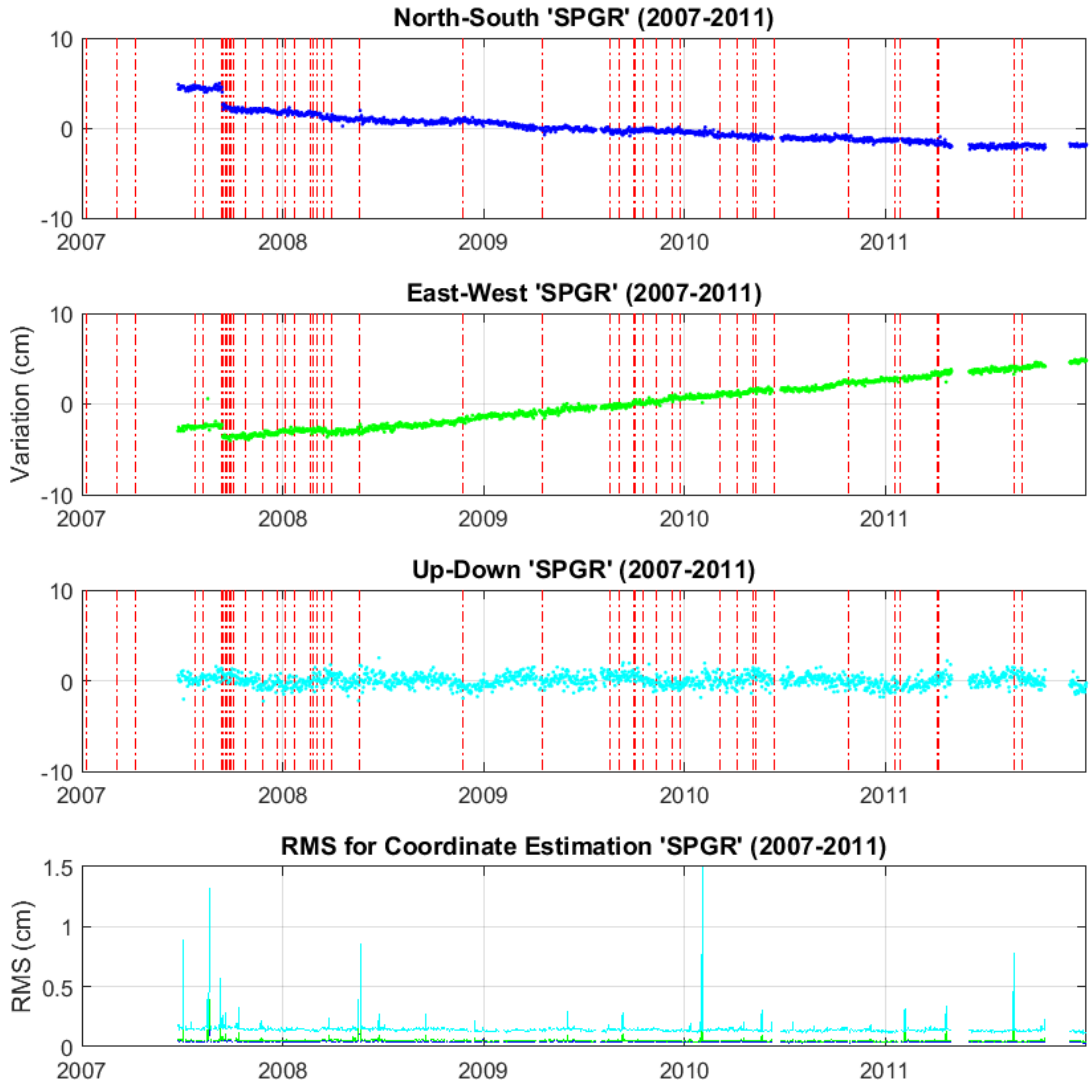


Figure 7.20: Daily coordinate time-series for station SPGR (2007 - 2011) from DD processing. (*a*) North-South component, (*b*) East-West component, (*c*) Up-Down component, and (*d*) RMS for the estimation in colour coded, i.e. blue for North-South, green for East-West, and cyan for Up-Down components. The red dotted lines in the y-axis of the figure (*a*), (*b*), and (*c*) represent earthquake that is larger than 6Mw.

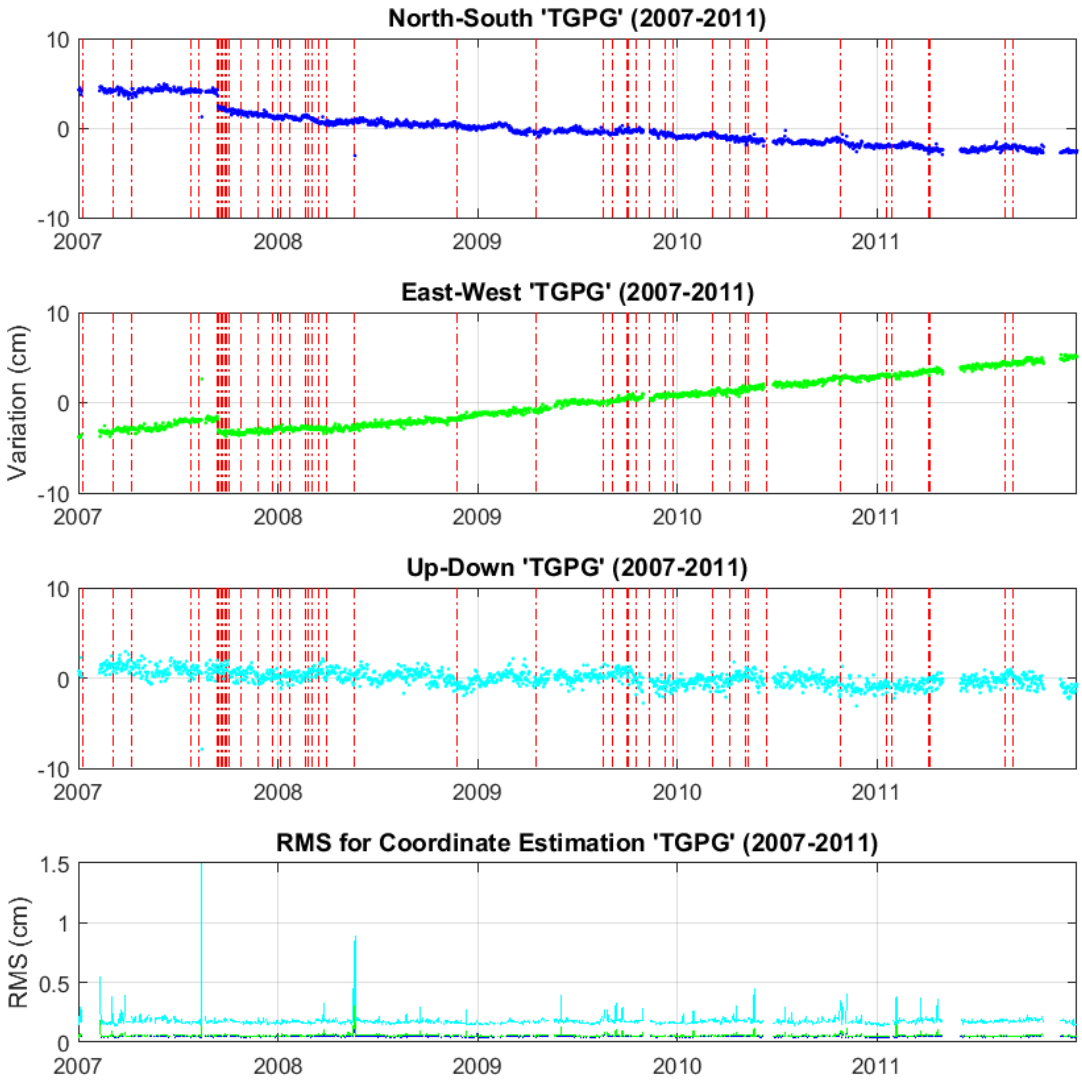


Figure 7.21: Daily coordinate time-series for station TGPG (2007 - 2011) from DD processing. (*a*) North-South component, (*b*) East-West component, (*c*) Up-Down component, and (*d*) RMS for the estimation in colour coded, i.e. blue for North-South, green for East-West, and cyan for Up-Down components. The red dotted lines in the y-axis of the figure (*a*), (*b*), and (*c*) represent earthquake that is larger than 6Mw.

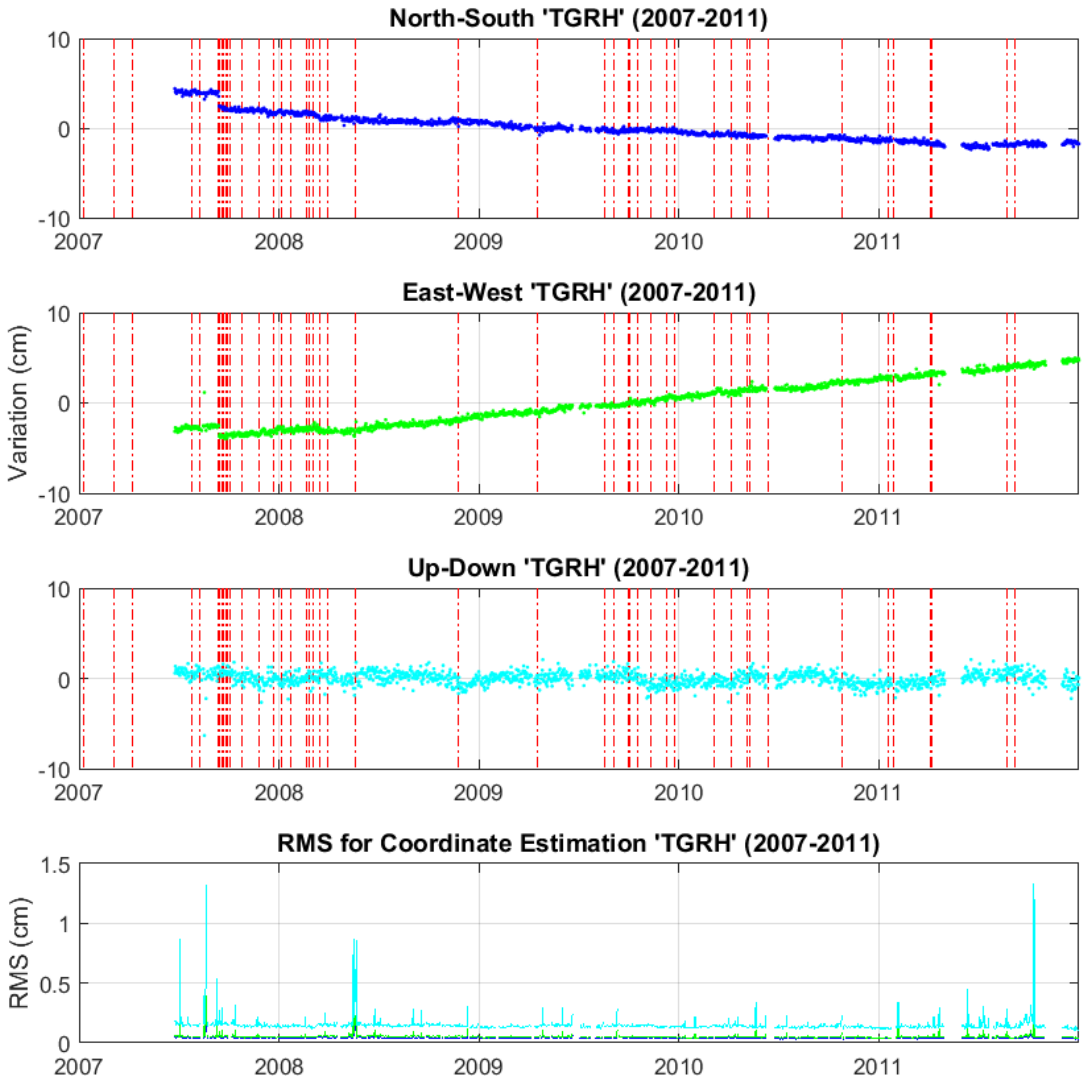


Figure 7.22: Daily coordinate time-series for station TGRH (2007 - 2011) from DD processing. (*a*) North-South component, (*b*) East-West component, (*c*) Up-Down component, and (*d*) RMS for the estimation in colour coded, i.e. blue for North-South, green for East-West, and cyan for Up-Down components. The red dotted lines in the y-axis of the figure (*a*), (*b*), and (*c*) represent earthquake that is larger than 6Mw.

7.3.2.1. Analysis of the RMS of Coordinate Estimation

There are two noticeable improvements from using DD (**Figure 7.15 - Figure 7.22**) with fixed ambiguities resolution as opposed to PPP (**Figure 7.2 - Figure 7.9)** with float ambiguities resolution. The first improvement is better repeatability in the East-West component, and the second one is a more accurate estimation of the East-West component as indicated by the coordinate RMS. Similar to PPP, any coordinates with RMS larger than three sigmas are considered as outliers, and are removed in the subsequent analysis. The RMS of coordinates throughout the complete GPS data set range from 0.3 to 0.9 mm for North-South component, with an average of 0.4 mm. It is similar to what is observed from PPP solution. On the contrary, the RMS in the East-West component improved about 50% from average 1.0 mm in PPP to 0.5 mm in DD. The improvement is attributed from the fixed ambiguity resolution employed in DD. Meanwhile, the RMS in vertical component remains relatively the same at 1.6 mm in DD as opposed to 1.5 mm in PPP. It is as expected considering the RMS of horizontal component is typically three times better than the RMS of the vertical component. Deviation of RMS in the three elements, i.e. North-South, East-West, and Up-Down, is better seen in **Figure 7.23**.

It is also worth mentioning that the quality of the estimation seems to increase from year to year. This increment can be associated with the increase in the quality of GPS products such as satellite ephemerides (orbits and clocks), antenna phase centres, ionospheric and tropospheric modelling, etc., as well as the quality of the recorded measurements. They are subtle but noticeable in all 8 MyRTKnet stations. The rate varies, ranging from - 0.02 to - 0.47 mm / year. **Figure 7.24** shows the plot of RMS for four selected stations, i.e. JHJY, PRTS, SPGR, and TGRH, which clearly showed this improvement. In summary, the RMS of daily repeatability for all GPS stations are considered excellent and also proof that GPS data processing via Bernese software performed well in this study in deriving horizontal and vertical time-series coordinates.

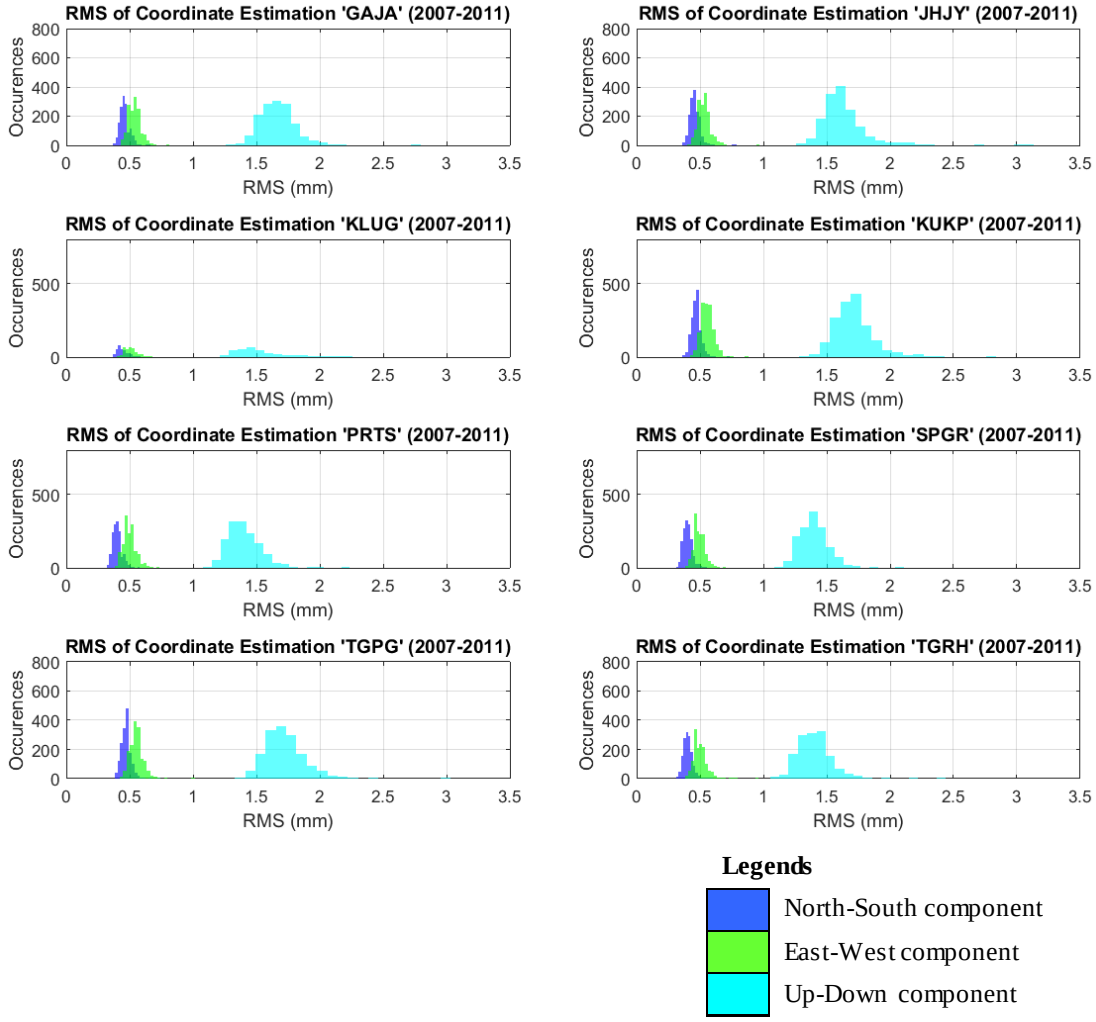


Figure 7.23: Histogram plots of the coordinate RMS from DD processing.

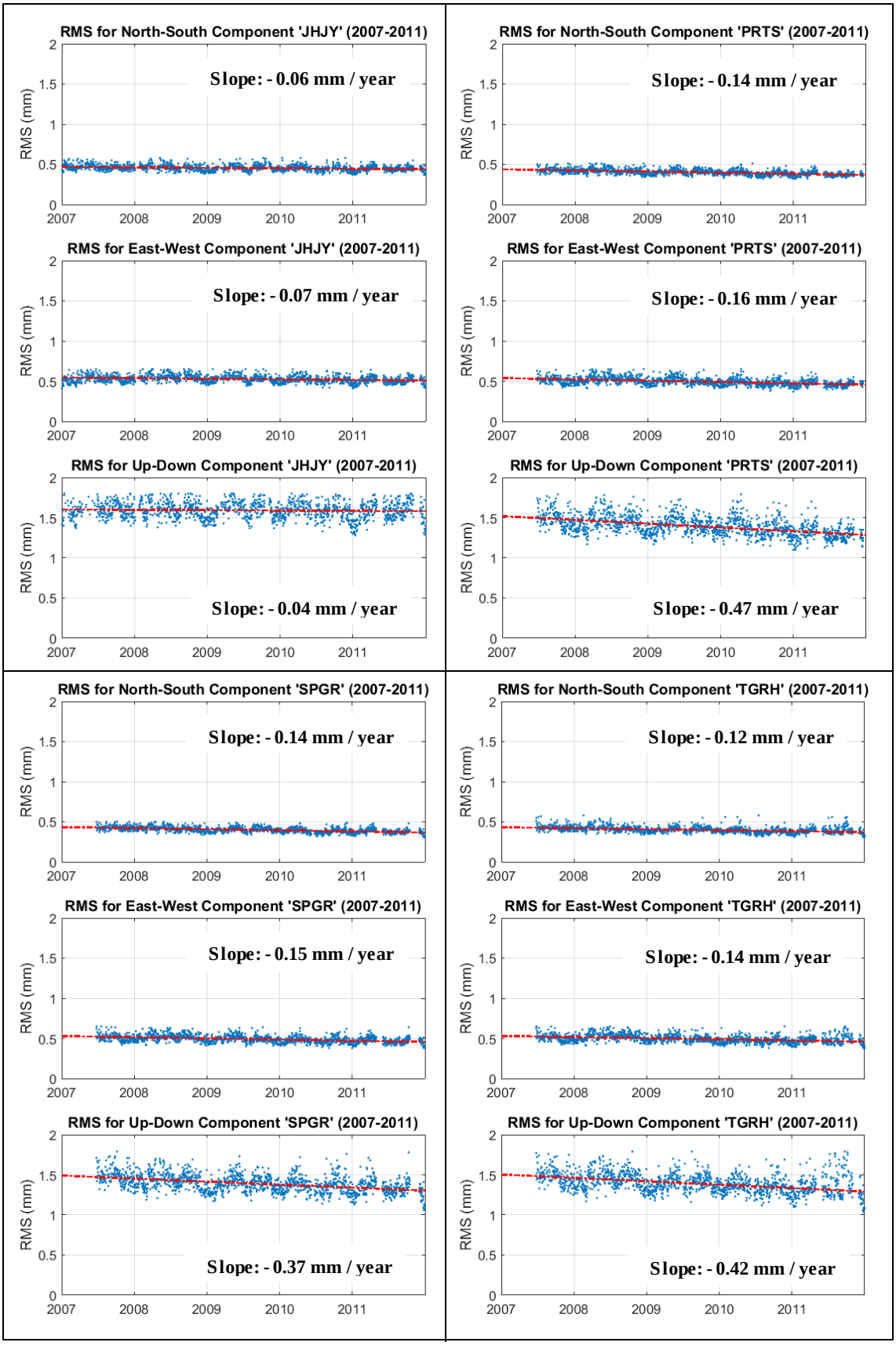


Figure 7.24: Increment in the RMS of coordinate estimation at four selected MyRTKnet stations. The red dotted line indicates the trend of RMS.

7.3.2.2. Analysis of the Velocity Rate

Analysis of the coordinate time-series from DD processing (**Figure 7.15 - Figure 7.22**) confirms the findings from PPP analysis. The stations' movement can partly be explained by earthquakes in the surrounding region, apart from the linear velocity due to plate tectonic motion. The most notable one is Sumatra earthquake on 12 September 2007 which has triggered an apparent shift in the stations' position. Other earthquakes have caused more subtle changes in the velocity. In general, the stations' movement can be represented by a linear trend. Therefore, it is estimated using the similar approach described previously in PPP, i.e. using daily coordinates starting from 18 September 2007 (DoY 261) onward. Extracted time-series from 1 August 2007 to 31 October 2007 for all 8 MyRTKnet stations, as attached in **Appendix E**, also confirmed that the position remains stable after that date. The velocity rate estimated from DD solution is expected to be more reliable than PPP considering the more precise results, particularly in the East-West direction.

Comparison between the DD and PPP results has revealed some exciting features of the two techniques. While the former can give a more reliable estimation of the velocity rate, the latter seems to be more favourable for earthquake analysis owing to its sensitivity to the movements caused by them. These results can be explained by the fundamental principle of the two techniques. Estimation of coordinates using PPP is primarily based on the satellites' position and clock as well as the complete modelling of errors in the measurements. Therefore, it can provide actual stations' movement. On the contrary, DD relies on the control stations and mitigation of errors via differencing to estimate the coordinate. If the selected control stations are situated within the earthquakes region and being affected by the same movement, the sensitivity of the technique is reduced. In this case, an inclusion of reference stations outside the earthquake region will be advantageous. The underestimation of the velocity rates from the DD, as found in this research, could be due to the same reason.

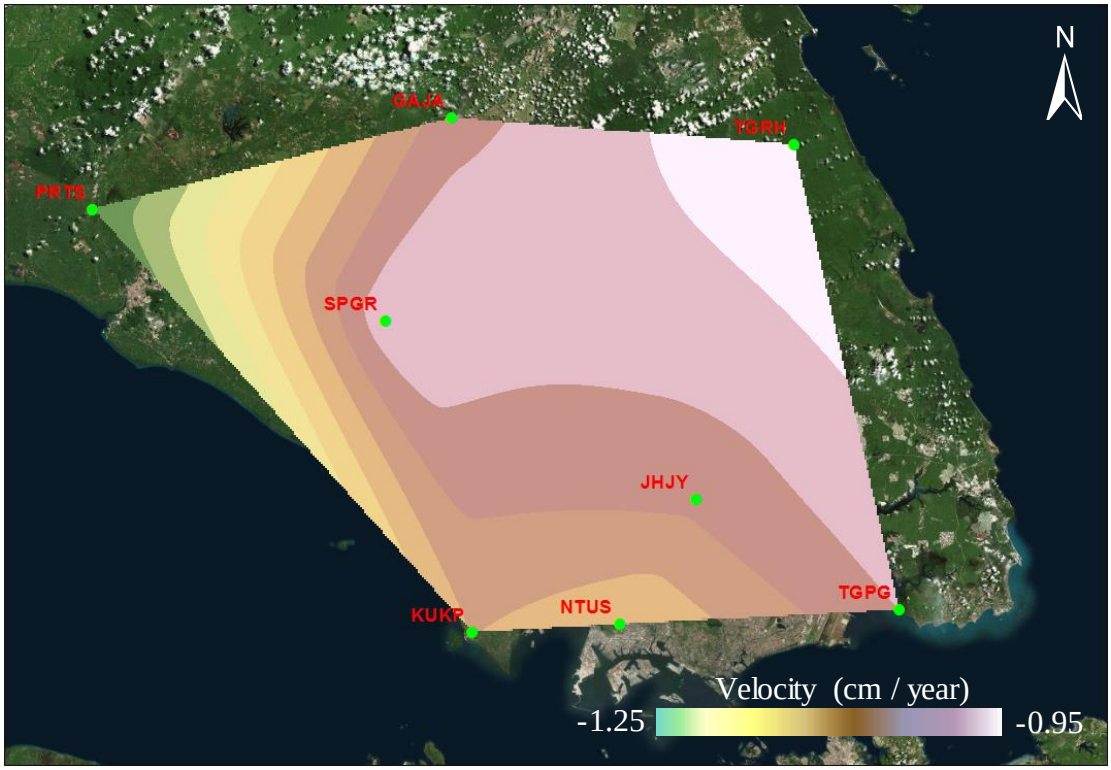
Table 7.2 summarised the linear velocity and their uncertainties in cm/year, as estimated from the DD solution. The general trend is almost similar to PPP results, i.e. negative in the North-South and positive in the East-West directions. However, it differs in the Up-Down component. While some stations, namely JHJY, SPGR, and TGRH, showed uplift movements in the PPP, all stations seem to undergo subsidence in DD results. Since the velocity estimation for station KLUG is of dubious quality owing to significantly less data, it is

excluded from the analysis. Similar to PPP, the most significant velocity in the North-South is observed at station PRTS (-1.25 ± 0.01 cm/year), and the smallest is found at station TGRH (-0.95 ± 0.01 cm/year). This result is expected considering the precision of the two techniques is quite similar in that direction. Nevertheless, it is not the case for the East-West and Up-Down components owing to their improved precision as compared to PPP. On average, the Pearson correlation coefficients improved at about 4% in the East-West component, and about 5% in the Up-Down component. The largest movements in the East-West component is found at station TGPG (2.06 ± 0.01 cm/year), and the smallest is at station PRTS (1.91 ± 0.01 cm/year). On the contrary, the largest movement in the Up-Down is observed at station KUKP (-0.41 ± 0.01 cm/year), and the smallest is found at station SPGR (-0.01 ± 0.01 cm/year).

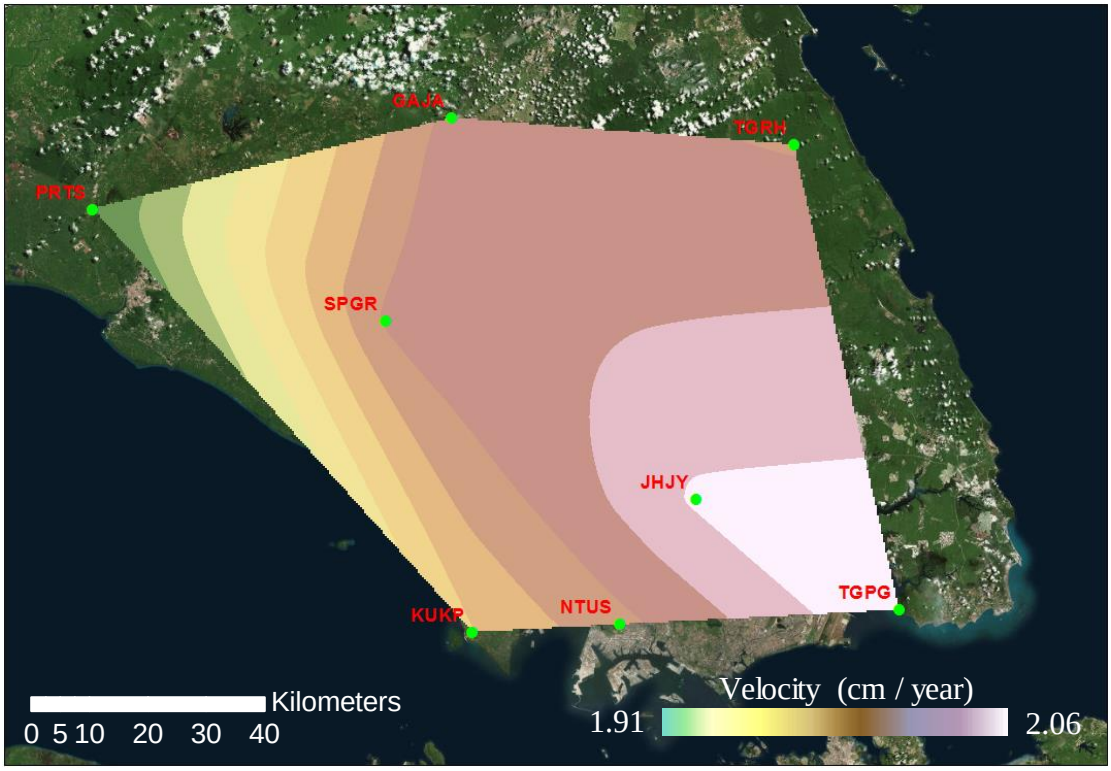
It is worth noting that the stations in the West moved at a different rate than the stations in the East, as reported previously in the PPP analysis. **Figure 7.25** shows the interpolated stations velocity from DD processing in North-South and East-West components based on Natural Neighbour Interpolation. Comparing with the result from PPP analysis (**Figure 7.11**), the improvement in the velocity estimation can be appreciated, whereby SPGR station confirms with the rest of the pattern. The differences could be due to several fault lines separating the east and west sectors of Peninsular Malaysia as described before. Nevertheless, further investigation needs to be carried out to explain the in-depth geological process of the phenomena.

Table 7.2: Linear velocity rate for 8 MyRTKnet stations estimated from DD solution using GPS data from 2007 to 2011.

Station	DD solution		
	North-South (cm/year)	East-West (cm/year)	Up-Down (cm/year)
GAJA	-1.02 ± 0.01	2.02 ± 0.01	-0.17 ± 0.01
JHJY	-1.03 ± 0.01	2.05 ± 0.01	-0.03 ± 0.02
KLUG	-2.16 ± 0.08	2.20 ± 0.10	-0.77 ± 0.32
KUKP	-1.07 ± 0.01	1.99 ± 0.01	-0.41 ± 0.01
PRTS	-1.25 ± 0.01	1.91 ± 0.01	-0.02 ± 0.01
SPGR	-0.99 ± 0.01	2.02 ± 0.01	-0.01 ± 0.01
TGPG	-1.01 ± 0.01	2.06 ± 0.01	-0.27 ± 0.01
TGRH	-0.95 ± 0.01	2.02 ± 0.01	-0.06 ± 0.01



(*a*)



(*b*)

Figure 7.25: Interpolated stations velocity from DD processing in (*a*) North-South, and (*b*) East-West components, based on the Natural Neighbour Interpolation within ArcGIS software.

7.3.2.3. Analysis of the Horizontal Movement

Analysis of the horizontal movement is carried out in a similar manner as in **Section 7.3.1.3**. **Figure 7.26** shows the stations' position, colour coded to show movement in 2007 (cyan), 2008 (dark blue), 2009 (green), 2010 (black), and 2011 (magenta). Earthquakes larger than 6.0Mw are plotted as red dots to examine their implication. No significant shift is visible in the horizontal position apart from the one induced by the Sumatra earthquake on 12 September 2007. The earthquake was also followed by a series of aftershocks. In general, all stations moved toward South-East, although they seem to change toward East direction after 2011. The subtle change can also be observed upon careful inspection of **Figure 7.15** - **Figure 7.22** in North-South component. The 6.7Mw earthquake that occurred on 3 April 2011, followed by another 6.0Mw earthquake on 6 April 2011, could have triggered the change. However, further data is required to verify this finding as they only occurred at the end of the dataset.

Equation (7.1) and (7.2) are used to estimate the horizontal magnitude and direction. **Figure 7.27** shows the vector plot of the horizontal movement. The results suggest that the calculated rate from PPP are lower by as much as 1.6 mm/year as compared to DD. A similar finding is attained in the estimated direction, i.e. the value is less in PPP than DD. The difference reaches up to 1.822°, discarding the ambiguous estimation for KLUG station. The magnitudes range from 2.23 to 2.30 cm/year, whereas angle range between 115.165° and 123.184° (not considering the KLUG station). Again, the underestimation can be explained by the fundamental principle of the two techniques as discussed in the previous section. Meanwhile, the standard deviation is good at ± 0.01 cm/year. The most substantial horizontal movement is found at station TGPG, and the smallest change is at station TGRH.

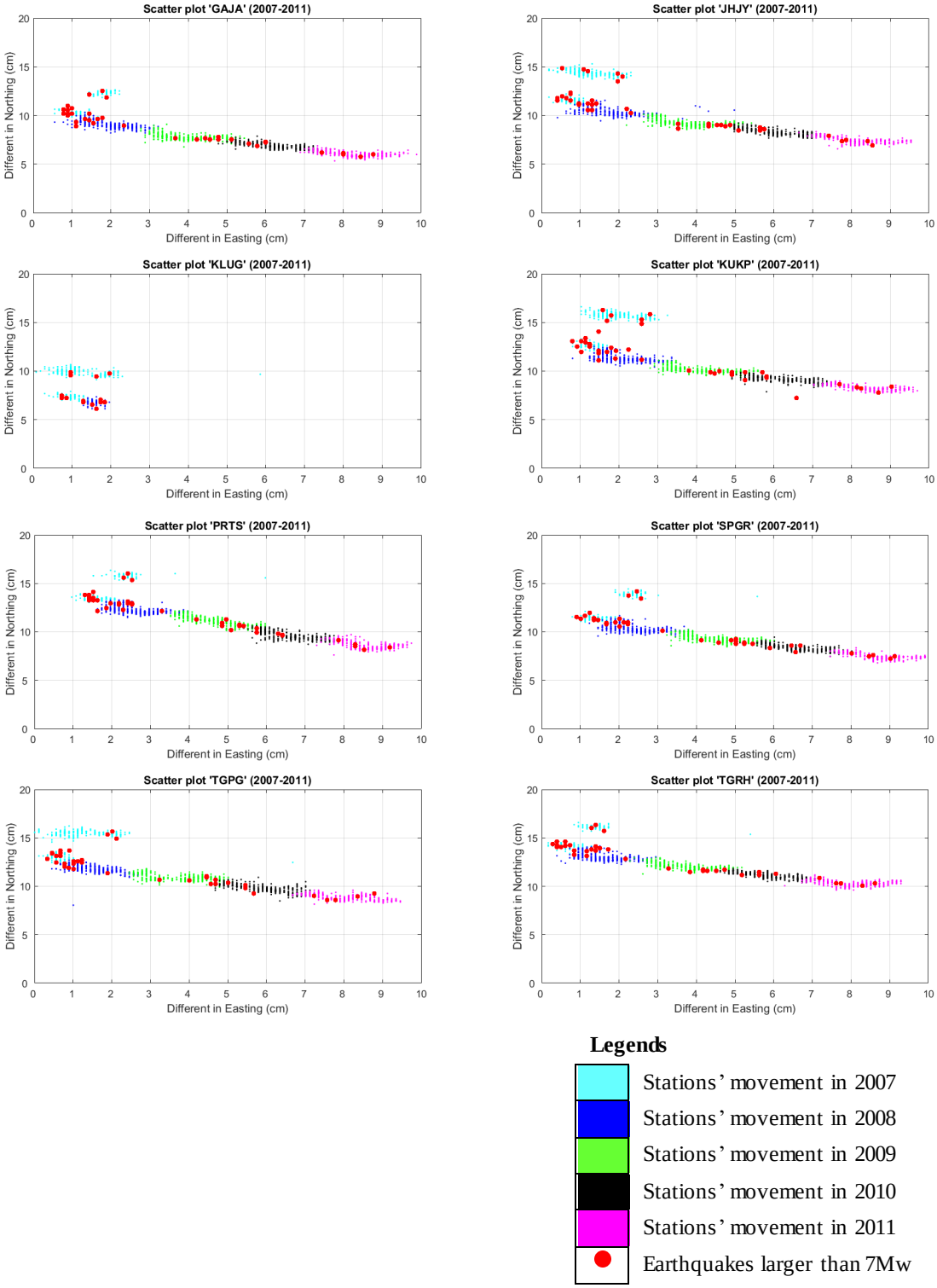


Figure 7.26: Scatter plot of the stations movement as estimated from the DD processing (2007 - 2011).

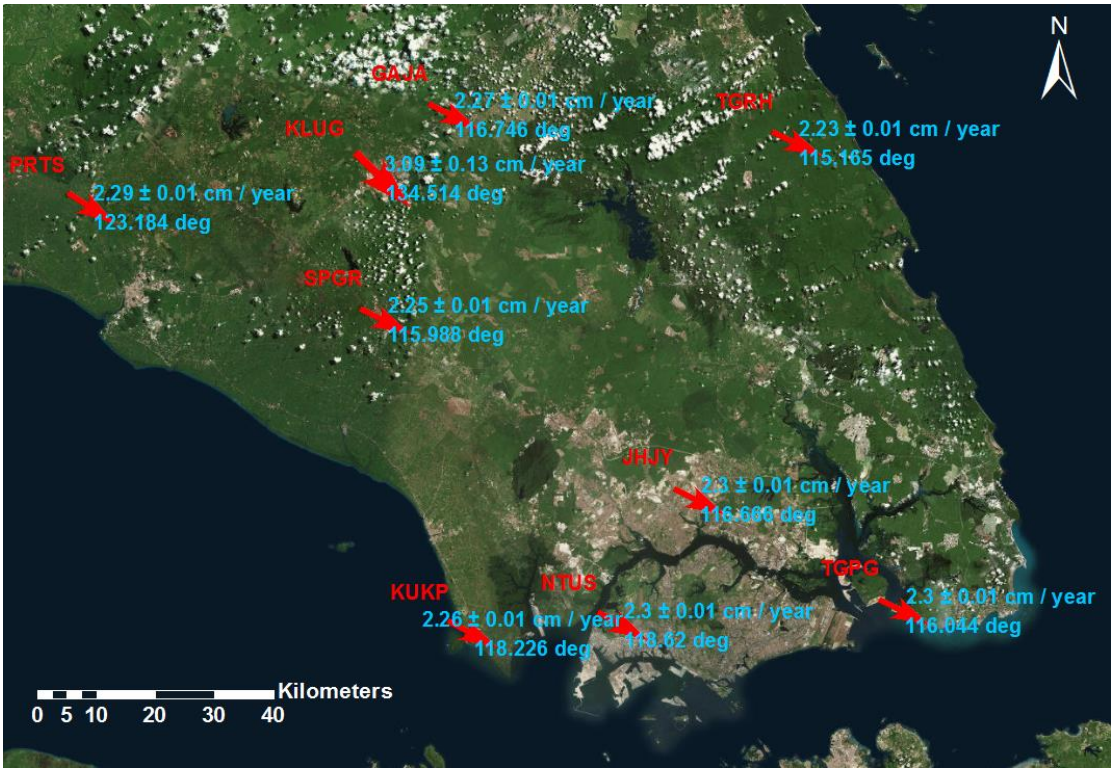


Figure 7.27: Vector plot of the horizontal movement of eight MyRTKnet stations as estimated from the DD processing.

7.3.3. Discussion on the Estimated Deformation from GPS Time-Series

It can be concluded from the individual analysis of PPP and DD that both techniques have corresponding features. The results confirmed with the literature on the advantages of PPP for earthquakes study owing to its sensitivity to the movements induced by them. For example, the effect of the 6Mw earthquake on 10 November 2009 is better seen in the PPP result as compared to the DD (**Figure 7.28**). It is because the estimation of coordinates in PPP is independent of reference stations, but relies on the precise satellite orbits and clocks as well as accurate modelling of the biases and errors affecting the measurements. However, ambiguity resolution is somewhat challenging in PPP. Fixed ambiguity resolution requires that modelling and processing be standardised at both the service provider and the user-end (Teunissen and Khodabandeh, 2015). It is only possible if the service providers also deliver their estimates of the hardware biases in addition to the satellite orbits and clocks, which are consistent and compatible for ambiguity fixing. Furthermore, ambiguity resolution technique may not be able to resolve the ambiguities correctly and consistently, or to maintain fixed solutions throughout the processing given the inherently weaker model of PPP (Bisnath and Collins, 2012). The problem is not only limited to the initial ambiguities resolution but

also in the case of signal interruption. Some standard ambiguity search and validation methods, e.g. the ratio test and their empirical thresholds, do not work well especially when the satellite geometry is poor (Collins et al., 2009; Shi, 2012). Rigorous integer ambiguity validation methods for PPP remain an issue to be investigated (Choy et al., 2016).

On the other hand, DD requires the reference stations to be in the area free from the earthquakes' movement. Therefore, it is usually involved with long baseline processing. However, DD benefits from the fixed ambiguities; ensuring improvement in the horizontal component estimates and to a lesser extent, the vertical component. The results revealed improvements primarily in the East-West component by up to 50% from an average RMS of 1.0 mm in PPP to 0.5 mm in DD. This increment can also be discerned in **Figure 7.28**, where the deviation in the East-West coordinates from the DD is significantly less than PPP. On the other hand, no significant change is perceived in the North-South and Up-Down components. More interestingly, the RMS in DD in all three elements seems to improve over time as shown previously in **Figure 7.24**. It could be ascribed by the relative improvement of the products, models, as well as the quality of data. Increase in the coordinate precision also means a better estimation of velocity, which is useful for long-term deformation analysis. It is noticeable that the rates estimated from PPP undervalue the rates from DD in both North-South and East-West components, which again could be due to the location of reference stations and ambiguity resolution.

It is worth reporting that no clear correlation is seen between the detected deformation and the individual properties of earthquakes such as magnitude, depth, and location of the epicentre. It is because deformation at a GPS station is induced by a complex combination of several factors, and not only on the earthquake scale. Those factors included depth, location, magnitude, and distance of the earthquake epicentre with respect to GPS stations, as well as the geometry and mechanism (e.g. strike-slip, dip-slip, oblique-slip, etc.) of the fault lines. For example, a small earthquake with shallow hypocentre and located close to the GPS stations will likely cause a more significant deformation than a massive earthquake with deep hypocentre and situated far from the station. Seismic waves from deep quakes have to travel farther to the surface, losing energy along the way. This process is further complicated by the geometry and mechanism of the fault lines. It is evident that earthquakes can affect the station movements as seen from the Sumatra earthquake on 12 September 2007. However, considering the primary interest of this research is related to the rate of long-term deformation as opposed to the short-term displacement from earthquakes, only linear velocities are estimated from the GPS results. It is also supported by the results from PPP (**Figure 7.2 - Figure 7.9**) and DD (**Figure 7.15 - Figure 7.22**), whereby a linear trend can mostly represent the stations' movement.

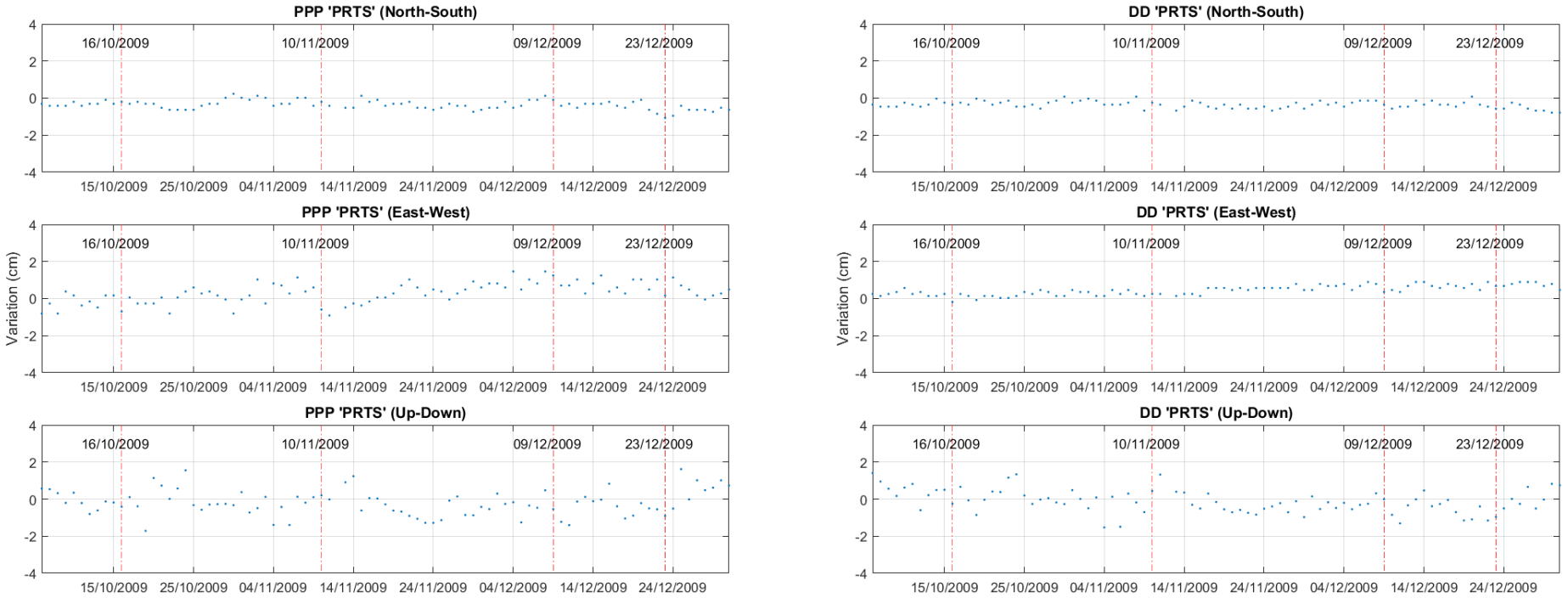


Figure 7.28: Comparison of the coordinates time series at PRTS station between PPP (left) and DD (right). The plot covers the period from 6 October 2009 to 31 December 2009. Note the position shift in the East-West direction as a result of the 6Mw earthquake on 10 November 2009, which is clearly visible in the PPP result.

MyRTKnet serves as the backbone for surveying and mapping activities in Malaysia; therefore, it requires continuous monitoring to ensure the coordinate remains accurate and reliable. Any imprecision in the coordinate will directly influence the positioning works tied to them. Examples of such works included setting up the control points for a cadastral survey and aerial mapping. It is evident from the results that the stations undergo continuous movement due to plate tectonics. The velocity rates, as estimated from the DD processing, reach up to -1.25 ± 0.01 cm/year in the North-South, 2.06 ± 0.01 cm/year in the East-West, and -0.41 ± 0.01 in the Up-Down components if KLUG station is not considered (due to its ambiguous estimation). The current MyRTKnet coordinate is based on ITRF2000 at epoch 2000.0. It implies that the stations in Johor have moved by as much as -21.25 cm in North-South, 35.02 cm in East-West, and -6.97 in Up-Down components, as of 1 January 2017. The movement corresponds to approximately 40.96 cm in the horizontal plane. Thence, the coordinates are due revision to ensure that they are in line with the latest realisation of ITRF, as well as to ensure that they provide an accurate and reliable solution for relative positioning.

7.4. Analyses of InSAR Time-Series

The GPS velocity estimation, discussed in **Section 7.3**, can provide a precise rate of the stations' movement. However, the technique is limited only to the observed stations. It is hard to obtain conclusive results on the deformation in Johor considering the relatively sparse distribution of the 8 MyRTKnet stations (distances range between 16 km and 153 km). Although interpolation can be useful to some extent, the quality of interpolation becomes poor for areas far from the GPS stations. Interpolation also relies on the minimum and maximum values used in the input. Therefore, the results from InSAR time-series analysis enable quantification of the surface movement, particularly in the vertical direction, for the area not covered by GPS. As has been mentioned previously, the SAR data were processed using an in-house software developed at the University of Nottingham, known as Punnet. The software utilises the Intermittent Small Baseline Subset (ISBAS) algorithm, which is suitable for various types of land classes. Details regarding the InSAR concept and processing strategy have been discussed extensively in **Chapter 5**. This section presents and analyses the results from the processing. The following discussion is divided into the analysis of the ERS-1/2 (track 347), and ERS-1/2 (track 75) results. Both data were acquired in descending mode. No interpretation on the deformation is made on the Sentinel-1 processing as it only covers an 18 months period, which is insufficient for long-term deformation analysis, considering the slow deformation rate expected in the study area.

7.4.1. Results from the ERS-1/2 (Track 347)

The processing of ERS-1/2 (track 347) involved 30 SAR images acquired between 4 May 1995 and 7 January 2005. The image on 22 August 1997 has been selected as the master image since the acquisition date is approximately in the middle of the data span. The selection, among others, ensures that coherence remains high between images pairs. A total of 172 differential interferograms were generated from the processing using 350 m for the orbital baseline and 5 years as the temporal baseline thresholds. The interferograms are multi-looked by a factor of 4 × 24 pixels in range and azimuth resolution, respectively, corresponding to approximately 100 m in ground resolution. Selection of the coherent point is made using 0.25 as the minimum coherence threshold. Furthermore, a condition is introduced so that the minimum number of layers used to achieve the average coherence value of 0.25 is equal to 45. There are 293,339 points identified with these settings; an improvement of approximately 28.46% compared to the standard Small Baseline Subset (SBAS) algorithm (**Figure 7.29**). The percentage is calculated by excluding the water body, which also dominates the image (32.66%). It is noticeable that the standard SBAS points are very sparse, typically concentrated in the urban areas such as Johor Bahru, Kluang, Skudai, Senai, Kulai, and Pontian. The areas have dense man-made structures, which are convenient targets for the coherent pixels. On the other hand, ISBAS coverage is more distributed across the entire image; thus, allowing better representation of the deformation. It is worth noting, however, that inclusion of more ISBAS points also increases the risk of noisy results. A lower interferogram threshold implies that fewer interferograms are required to achieve an average coherence value of 0.25.

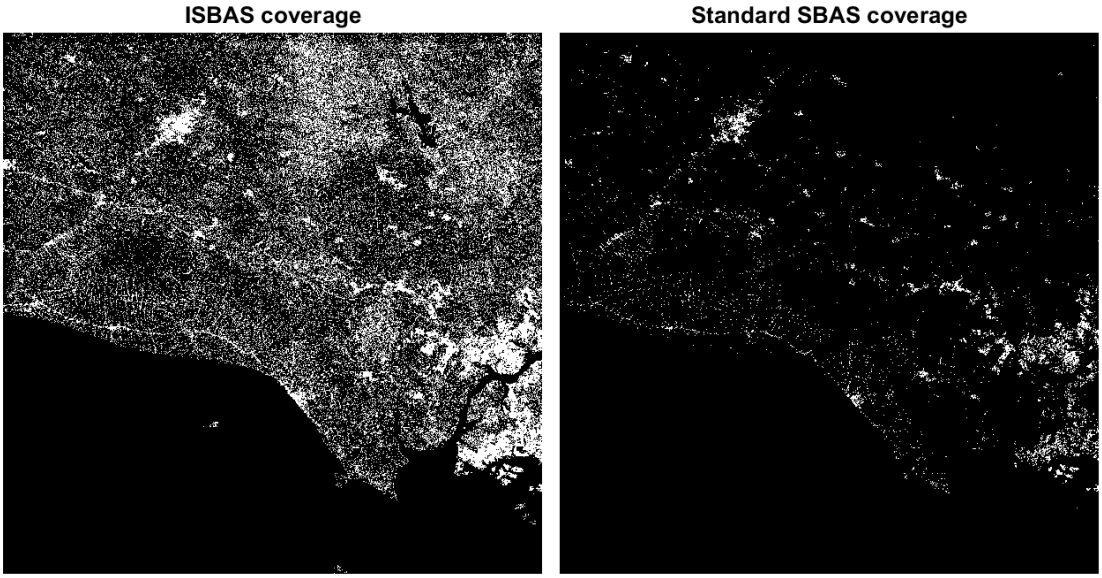


Figure 7.29: Coverage comparison between the ISBAS and SBAS techniques from the ERS-1/2 (track 347) results. White points represent coherent points in the image.

The velocity of coherent points is derived to produce a vertical land motion map. **Figure 7.30** shows the LOS-velocity map of Johor as estimated from the ISBAS linear analysis. Location of the 8 MyRTKnet stations is shown as red points. Additionally, the peatland area, as extracted from the International Wetlands (2010), is shown in the black polygon. The map is somewhat noisy as low coherent targets dominate the area. Errors from the phase unwrapping also could propagate to the estimated velocities. The rates range from -1.16 cm/year (subsidence) to 1.03 cm/year (uplift), with the average value of -0.13 cm/year. The standard error map for the velocities is given in **Figure 7.31**. They are relatively good in the urban areas but deteriorate in the remote/rural regions. The values vary between 0.03 and 0.53 cm/year. Approximately 91.8% of the coherent points have the standard error of less than 0.25 cm/year, but the percentage dropped to about 57.2% for points with a standard error of lower than 0.20 cm/year.

It is interesting to note that the peatland area, marked by the black polygon in **Figure 7.30**, generally shows a subsidence trend. Wösten et al. (1997) have reported a similar pattern, with an average subsidence rate of 2 cm/year. The rate was derived from 17 markers planted in the area. They also reported that the subsidence rate decreases gradually with time and may be divided into an initial, very rapid consolidation component, and a slow oxidation and shrinkage component. Based on the recorded measurement over 21 years, the estimated rate in the earlier period was 4.6 cm/year but reduced to 2.0 ± 1.5 cm/year after 1988. For comparison, the estimated rates from the ISBAS analysis, using data spanning from 4 May 1995 to 7 January 2005, reach up to -1.6 cm/year (subsidence) for the peatland area. On the other hand, the standard errors range from 0.03 to 0.40 cm/year. Therefore, it can be concluded that the rates from the two results are comparable considering their standard errors.

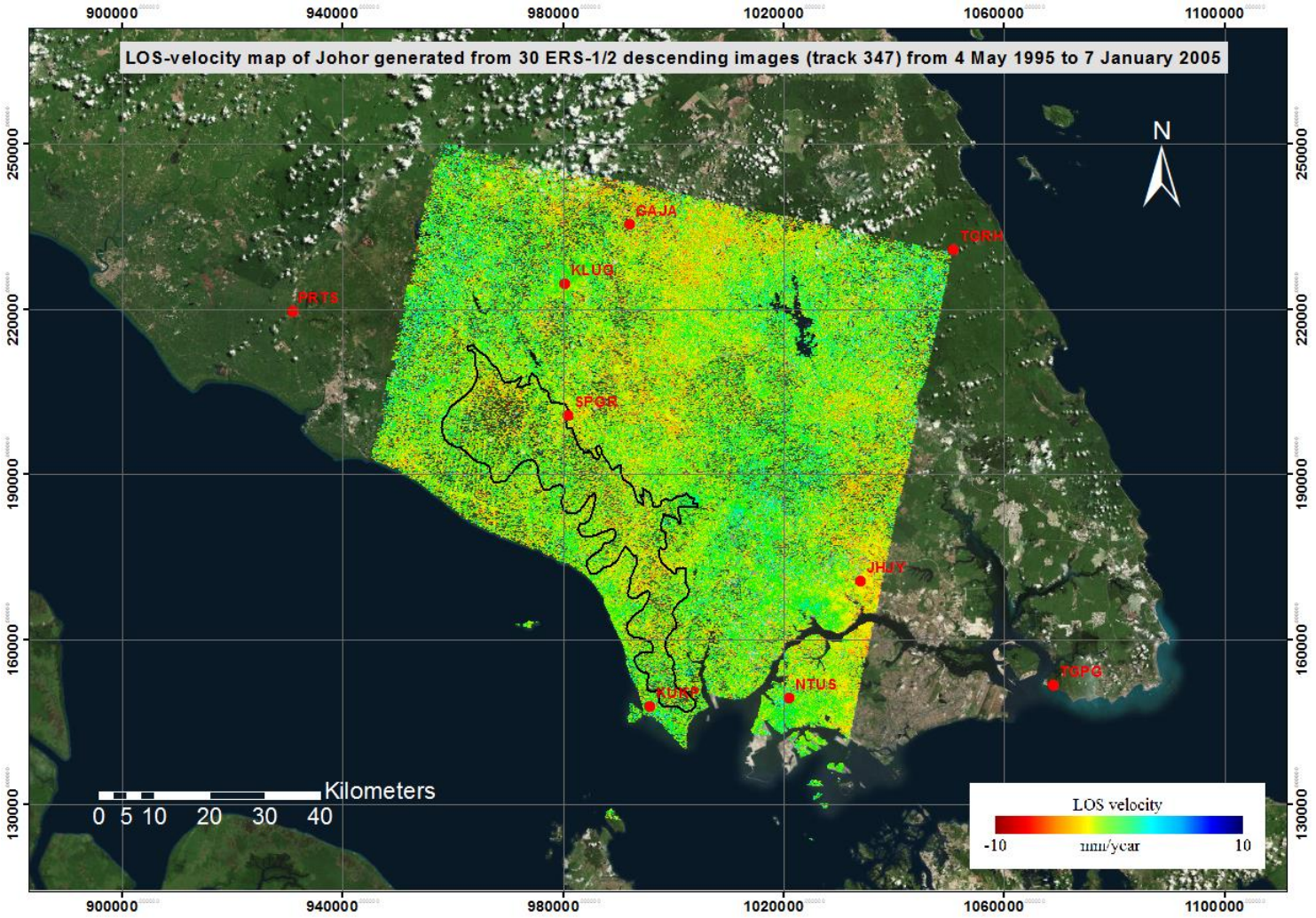


Figure 7.30: LOS-velocity map of Johor from the ERS-1/2 (track 347) processing.

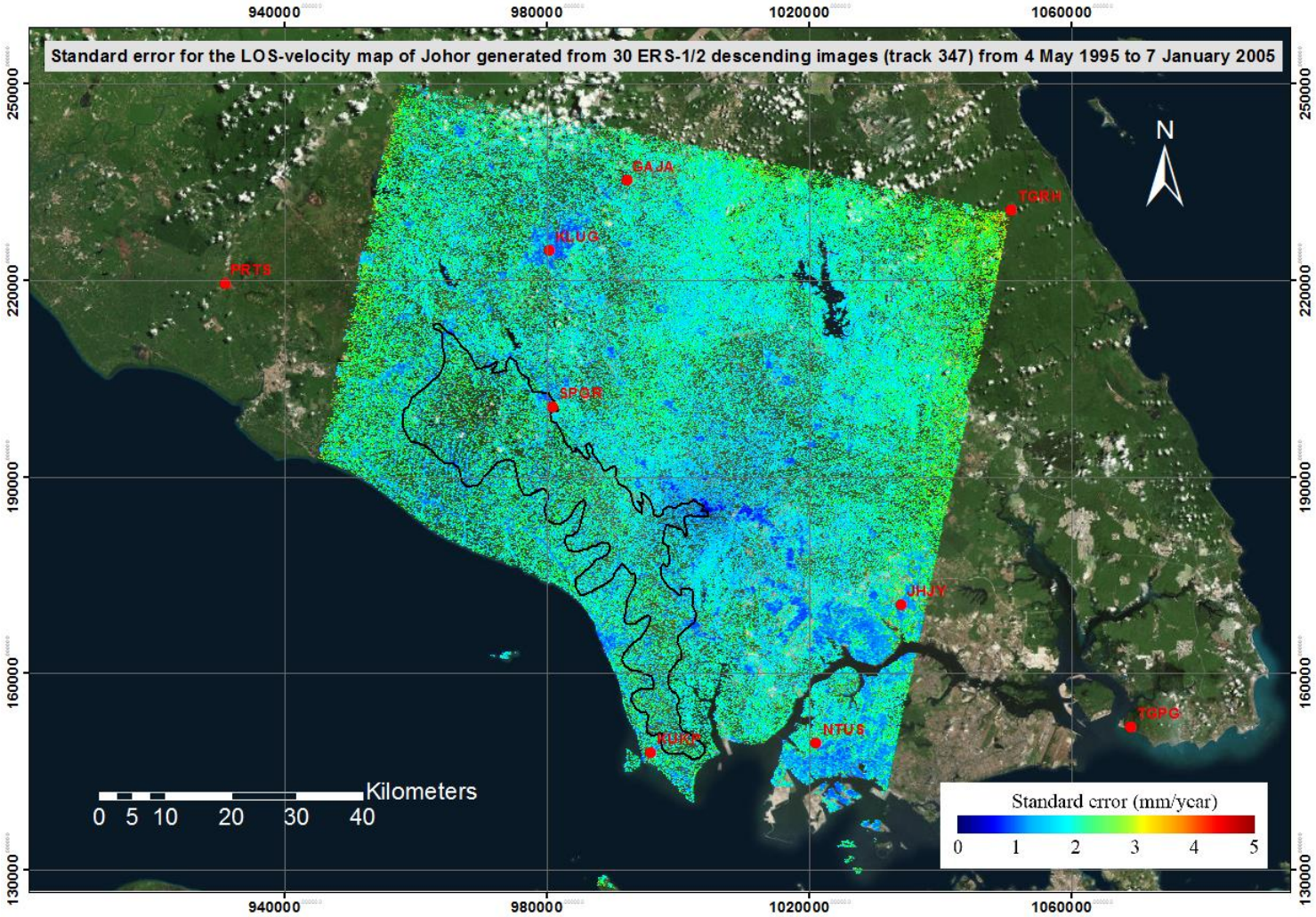


Figure 7.31: Standard error map for the LOS-velocity of Johor from the ERS-1/2 (track 347) processing.

The LOS-velocity map is also compared with the Persistent Scatterer (PS)-InSAR results from Ami Hassan (2014). In his work, 21 ERS-2 SAR images have been used to derive the LOS-velocity map with data spanning from May 1996 to January 2005. Formation of differential interferograms was implemented using Delft Object-oriented Radar Interferometric Software (DORIS) (Kampes and Usai, 1999), whereas the selection of PS pixels and time-series analysis were made using the Stanford Method for Persistent Scatterer (StaMPS) (Hooper, 2006). **Figure 7.32** shows the LOS-velocity map and the standard error map for the estimation in mm/year from the PS-InSAR processing. It can be seen that the coverage is significantly less than ISBAS result, and consequently limiting the interpretation on the extent of deformation. For example, the subsidence in the peatland area is not clearly visible. PS-InSAR is mainly suitable for urban settings where the phases stability can be assured. The standard errors are relatively similar, which are higher in urban than in remote/rural areas.

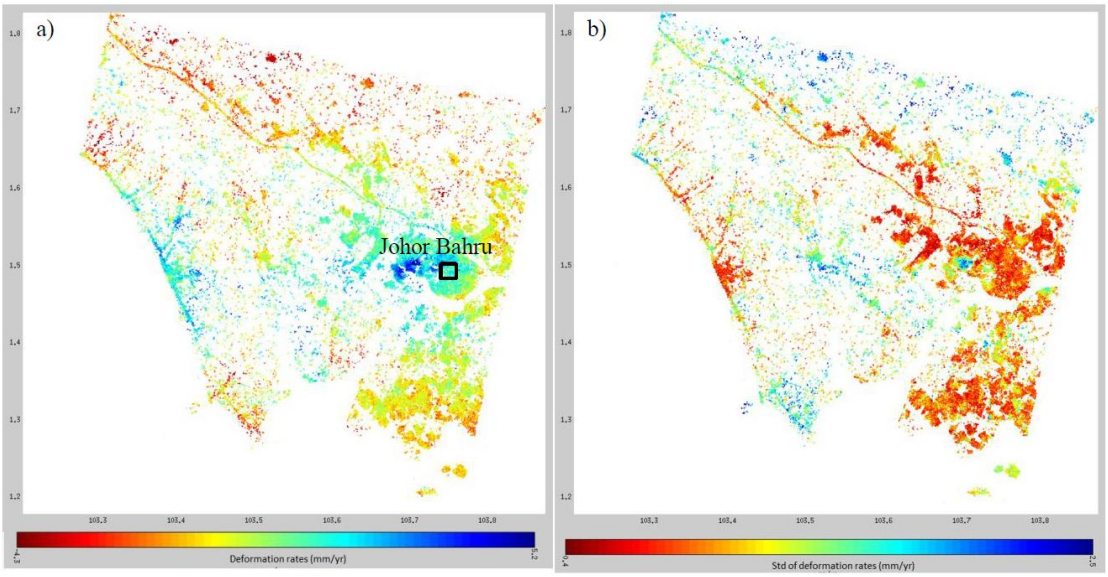


Figure 7.32: PS-InSAR results in Johor from 1996 to 2005. (*a*) LOS-velocity estimation in mm/year, and (*b*) standard error of the LOS-velocity. Figure adapted from Ami Hassan (2014).

Visual inspection on the PS-InSAR result seems to suggest that some part of the Johor Bahru City had undergone uplifting, which could be due to construction processes. The uplift trend could be speculated as a result from the steady increment in the height of buildings (i.e. new human-made structures). It should be noted that most of the InSAR time-series assume a slow monotonic motion in producing the LOS-velocity map, which is also the case for the PS-InSAR in Ami Hassan (2014) and the ISBAS analysis in this work. It is suspected that the uplift signals from the steady increment of the buildings'

height are captured in the estimation of linear velocity as they are more prominent than the subsidence from the urbanisation processes. Unfortunately, there is no ground data available concerning the rate of growth in the area to support this assumption. Although not directly related, the spatio-temporal patterns of landscape change from Barau and Qureshi (2015), as shown in **Figure 7.33**, provides an indication of the development in Johor as the results of Iskandar Malaysia initiative. Despite the author's attempts to correlate the deformation with groundwater extractions data, regrettably, it does not show any correlation between them. However, a similar finding is also perceived in the ISBAS result but differs in the measured rates. Ami Hassan (2014) found the rates to be between -0.43 and 0.52 cm/year with standard errors range from 0.04 to 0.25 cm/year. On the other hand, the estimated rates from the ISBAS analysis are between -0.98 and 0.71 cm/year with standard errors from 0.09 to 0.46 cm/year. The dissimilarities can be due to, among other things, the difference in the temporal resolution of the data, and/or the spatial resolution of the results (PS-InSAR works on full resolution pixels, whereas ISBAS technique applies multi-looking). Assessment of the accuracy of the two techniques is hindered by the absence of ground truth in the area.

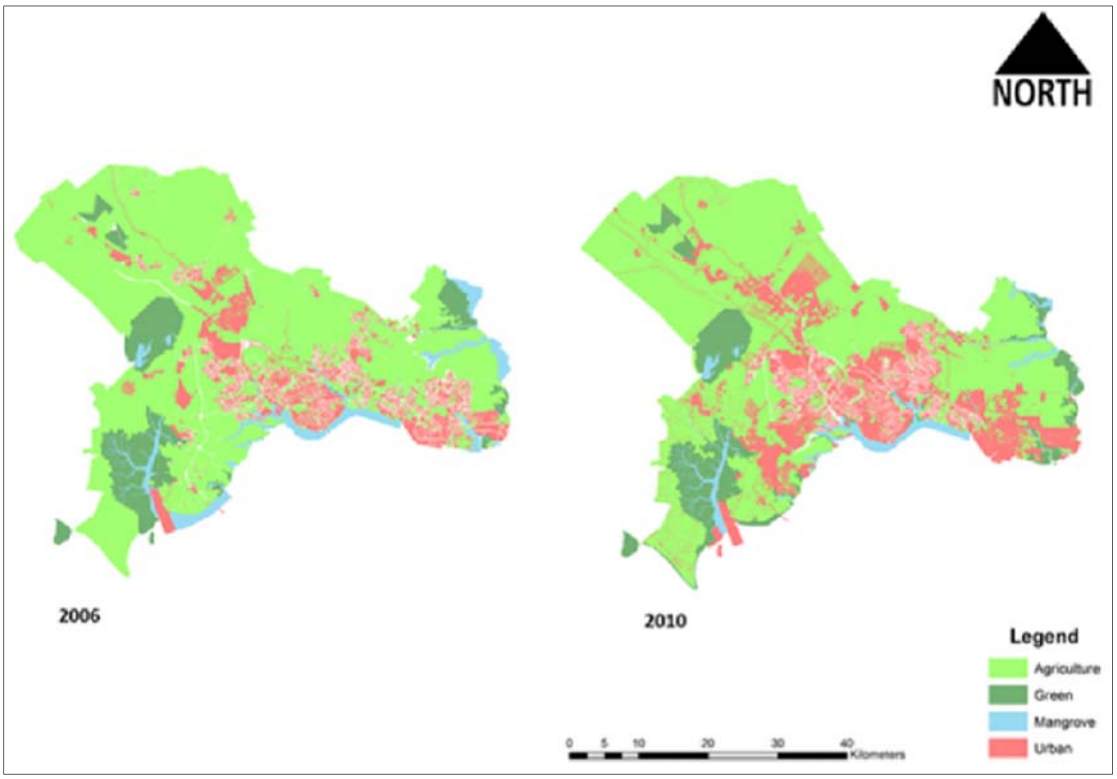


Figure 7.33: Spatio-temporal patterns of landscape change in Iskandar Malaysia. Figure adapted from Barau and Qureshi (2015).

Table 7.3 summarised the comparison between the velocity rates estimated from the GPS DD processing in the vertical direction and the ISBAS analysis at the nearest coherent point. The rates from the DD are selected as opposed to the PPP, as it gives slightly better precision. The LOS-velocities are converted to the vertical direction for the comparison (refer to **Section 5.11** of **Chapter 5**). There are 7 GPS points, namely 6 MyRTKnet stations and 1 IGS station, situated within the SAR coverage (refer to **Figure 7.30** and **Figure 7.31**). Approximate distance between the two points is also given in the table. The precision of the velocity rates from GPS is better than InSAR, apart from the KLUG station. The lower precision at KLUG is due to limited data used for the estimation. The velocities between GPS and InSAR, in general, agreed in their trend (considering the precision) but differ in the estimated value. The following **Table 7.4**, on the other hand, compares the same rates from GPS with the average rates from ISBAS, computed from all coherent points within a 2 km radius. The number of points used to calculate the average rate is also listed. TGRH station has significantly fewer points as it is located at the edge of the SAR frame. Again, the same pattern is observed at all locations, suggesting that the areas had undergone subsidence. The differences can be explained, among others, by the spatial resolution of the results. While GPS observed the trend at a particular point measured by the receiver, the velocity of an ISBAS point represents the movement of an area covered by the multi-looked windows, i.e. approximately 100 m x 100 m on the ground resolution.

Table 7.3: Comparison between the estimated velocity from DD GPS and ISBAS analysis of ERS-1/2 (track 347) (the nearest point to the GPS station).

Station	Vertical velocity from DD GPS (cm/year)	Velocity from InSAR	
		Rate (cm/year)	Distance (m)
GAJA	-0.17 ± 0.01	-0.43 ± 0.17	11
JHJY	-0.03 ± 0.02	-0.21 ± 0.19	33
KLUG	-0.77 ± 0.32	-0.27 ± 0.21	81
KUKP	-0.41 ± 0.01	-0.11 ± 0.17	38
SPGR	-0.01 ± 0.01	-0.21 ± 0.12	129
TGRH	-0.06 ± 0.01	0.09 ± 0.35	545
NTUS	-0.15 ± 0.01	-0.35 ± 0.15	38

Table 7.4: Comparison between the estimated velocity from DD GPS and ISBAS analysis of ERS-1/2 (track 347) (average velocity over 2 km radius).

Station	Vertical velocity from DD GPS (cm/year)	Average velocity from InSAR (2 km radius)	
		Rate (cm/year)	Number of coherent points
GAJA	-0.17 ± 0.01	-0.29	343
JHJY	-0.03 ± 0.02	-0.26	1092
KLUG	-0.77 ± 0.32	-0.08	1419
KUKP	-0.41 ± 0.01	-0.03	436
SPGR	-0.01 ± 0.01	-0.24	662
TGRH	-0.06 ± 0.01	-0.03	48
NTUS	-0.15 ± 0.01	-0.04	904

The histogram plot of the standard errors for LOS-velocities, as shown in **Figure 7.34**, revealed an interesting feature of the ISBAS analysis as compared to the standard SBAS analysis. There is a two bell shape found in the ISBAS histogram. The first one mostly corresponds to the SBAS points, which has low standard errors, and the second one represents the standard errors for the intermittent points. The inclusion of ISBAS points increases the number of coherent points, which will improve understanding of the extent of the deformation. Nevertheless, careful consideration should be taken so as not to introduce noisy observations that could lead to wrong interpretation of the result. For comparison, the SBAS points in Johor have standard errors between 0.03 and 0.15 cm/year with the average value of 0.11 cm/year. Meanwhile, the standard errors for the ISBAS points are slightly larger, ranging from 0.03 to 0.49 cm/year with the average value of 0.19 cm/year. Therefore, only points that have reliable estimation (i.e. small standard errors) are considered for the analysis. The task, however, is easily implemented with the aid of ArcGIS software to visualise the result, as applied in this research.

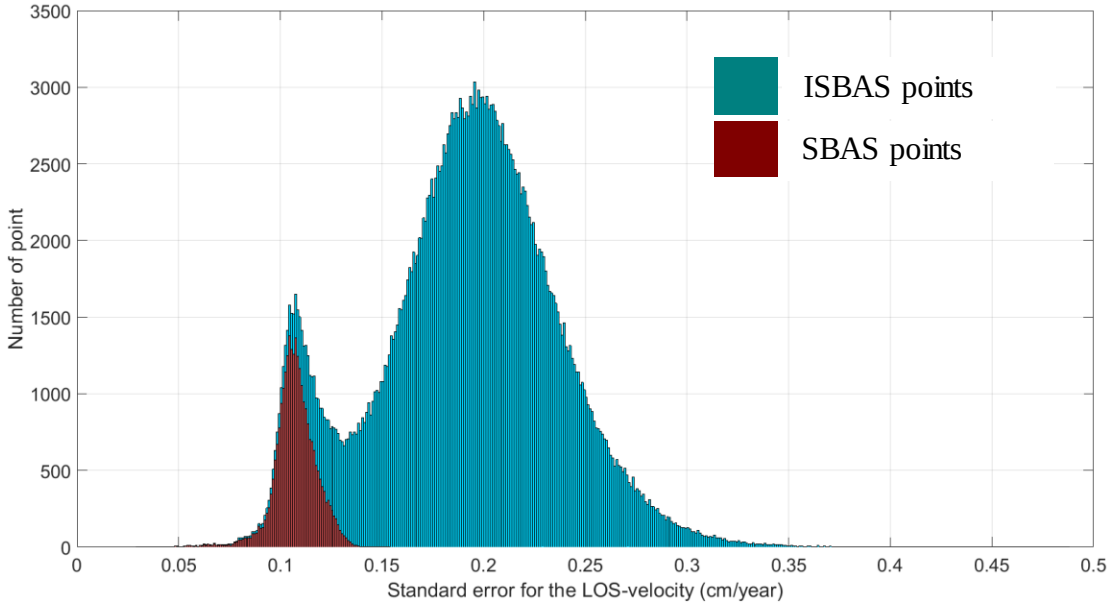


Figure 7.34: Histogram plot of the standard error from the ERS-1/2 (track 347) processing.

7.4.2. Results from the ERS-1/2 (Track 75)

The processing of the ERS-1/2 (track 75) involved 32 SAR images acquired from 5 August 1993 to 23 February 2003. The image on 10 May 1998 has been selected as the master image as it was attained approximately in the middle of the data span. The water body covers approximately 54.17% of the scene. Formation of differential interferograms is based on 350 m as the orbital baseline threshold, and 5 years as the temporal baseline threshold, resulting in 149 differential interferograms. The multi-looked setting is configured as 4×24 pixels in range and azimuth resolution, respectively. Coherence threshold is set as 0.25 with 45 as the minimum number of interferograms for the computation of average coherence. There are 178,877 identified points, an improvement of 25.06% from the standard SBAS analysis (**Figure 7.35**). As expected, the SBAS points are distributed in urban areas such as Pasir Gudang, Kota Tinggi, and Johor Bahru, whereas the ISBAS points are widely distributed over various land classes. The increase of coverage permits better representation of the deformation in the area.

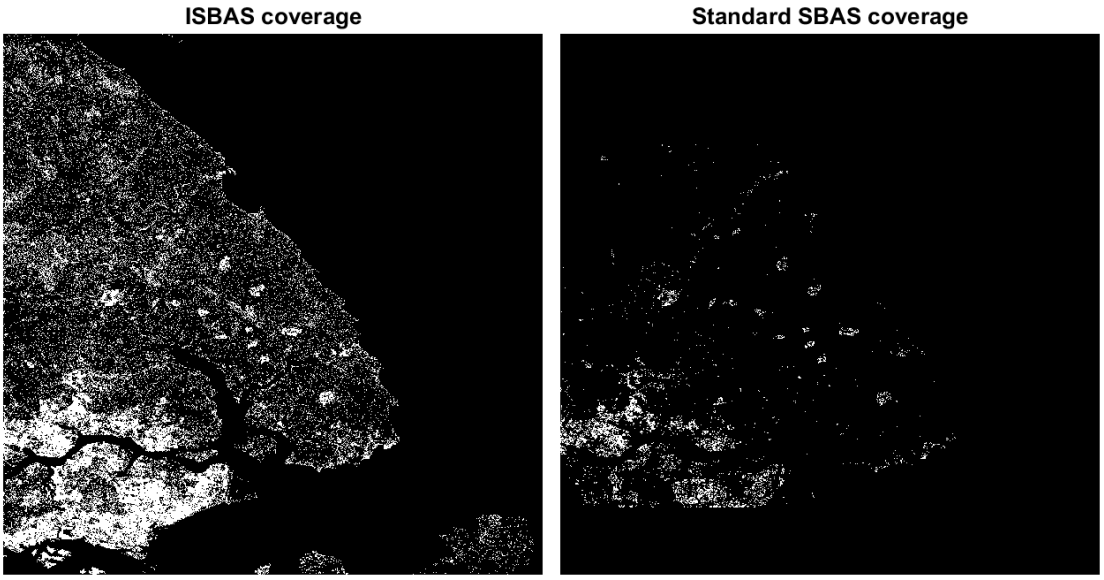


Figure 7.35: Coverage comparison between the ISBAS and SBAS techniques from the ERS-1/2 (track 75) results. White points represent coherent points in the image.

The LOS-velocity map, generated from the processing of 32 ERS-1/2 (track 75) images, is given in **Figure 7.36**. As suggested from the comparison between SBAS and ISBAS, the area is dominated with low coherent targets (tree covered area and cropland); hence, the map is somewhat noisy. Errors from the phase unwrapping due to sparse coherent points also could propagate into the results. The estimation of velocity is done assuming monotonic motion. Therefore, one must also consider if this assumption is not valid. The estimated velocity rates range between -1.11 cm/year (subsidence) and 0.64 cm/year (uplift) with the average value of -0.18 cm/year. The following **Figure 7.37** gives the standard error map for the LOS-velocity. The standard error map is relatively good in the urban areas due to a large number of interferograms used to estimate the velocity, but the value reduces in the remote/rural areas as the number of interferograms decreases. The values range from 0.03 to 0.40 cm/year. Approximately 99.4% of the coherent pixels have a standard error of less than 0.25 cm/year. The percentage dropped to about 88.6% and 43.8% for coherent pixels with a standard error less than 0.20 cm/year and 0.15 cm/year, respectively. Low standard error value implies that atmospheric phase, orbital and DEM errors are well reduced in the time-series processing.

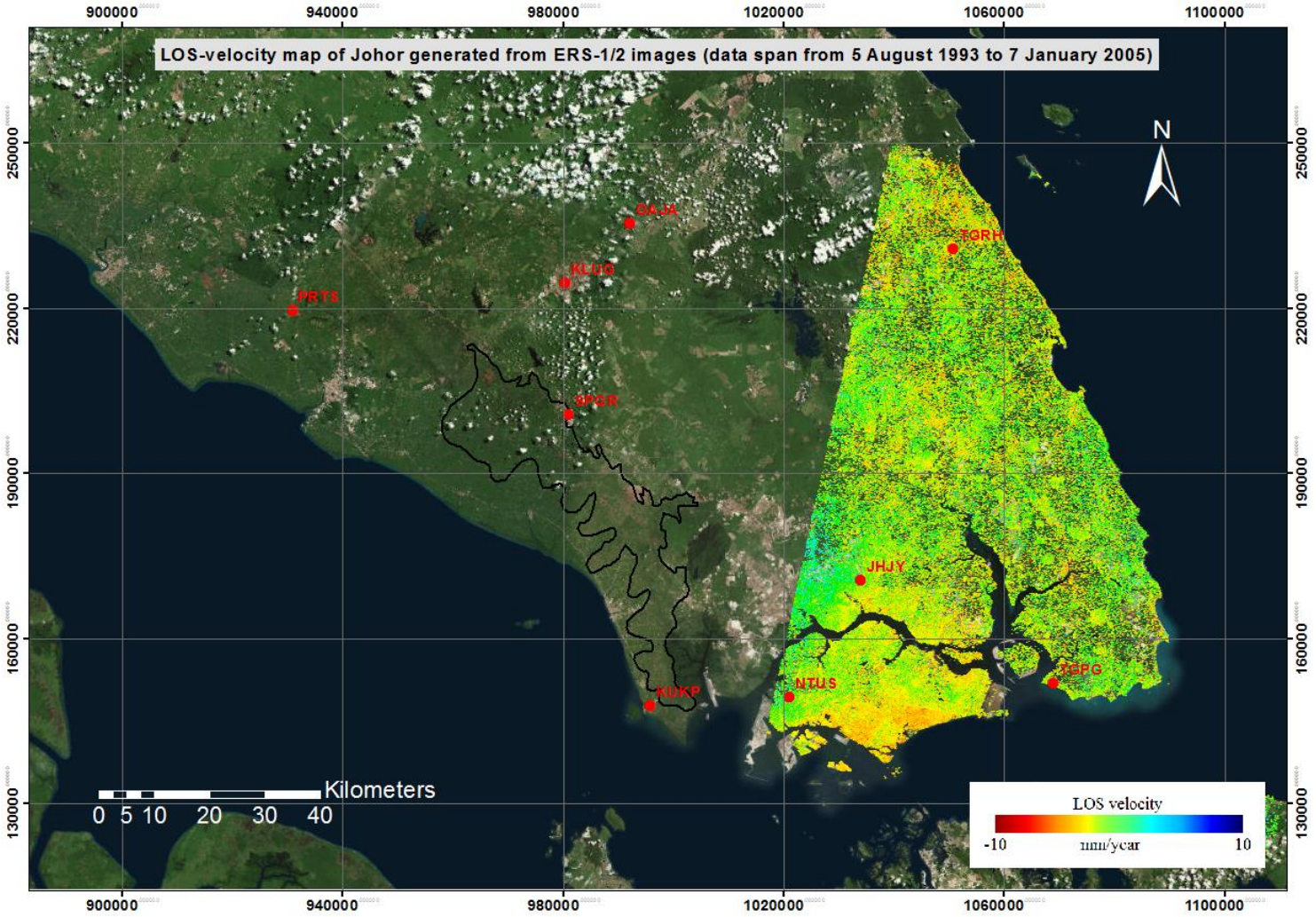


Figure 7.36: LOS-velocity map of Johor from the ERS-1/2 (track 75) processing.

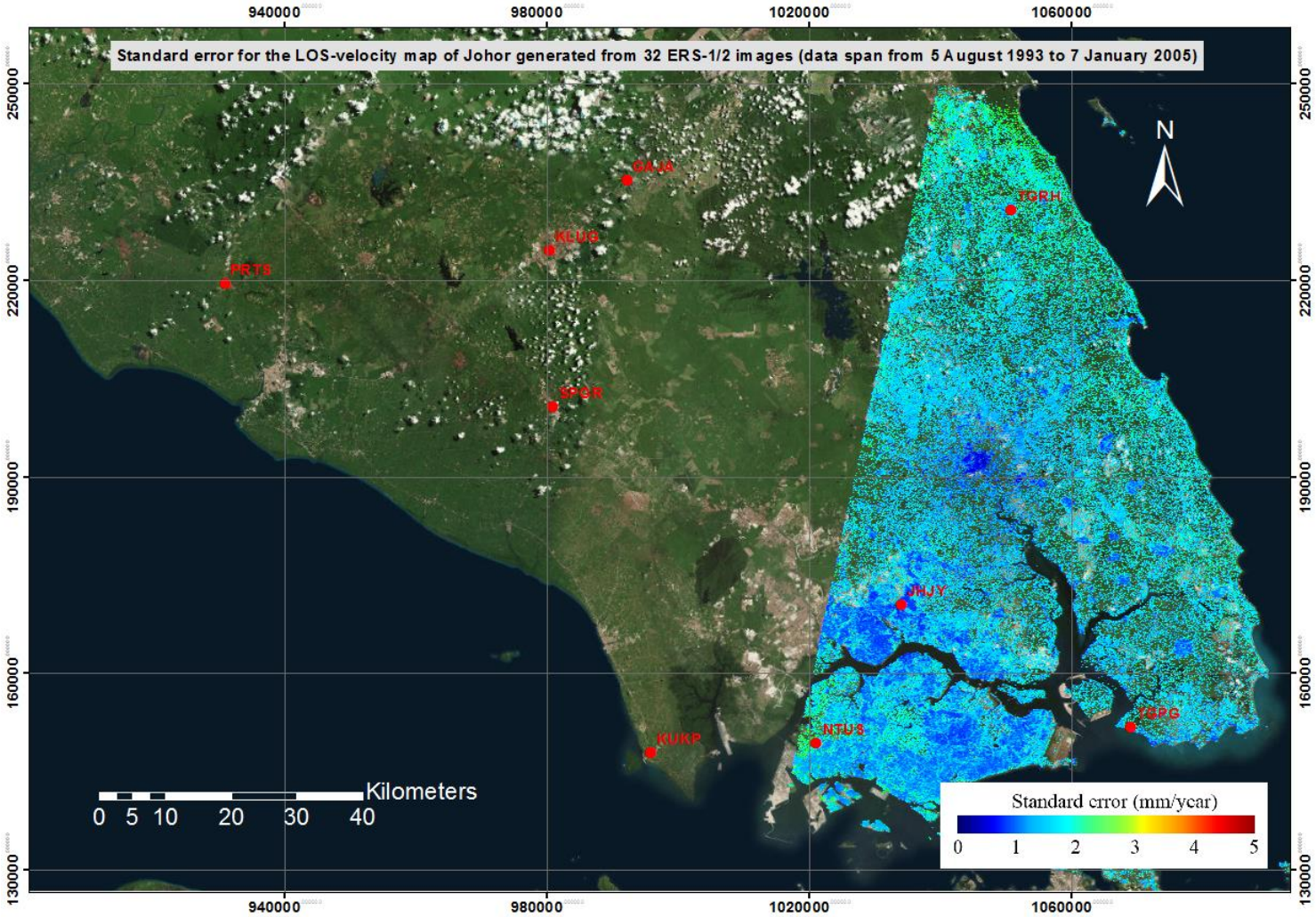


Figure 7.37: Standard error map for the LOS-velocity of Johor from the ERS-1/2 (track 75) processing.

In general, the LOS-velocity map from the ERS-1/2 (track 75) and ERS-1/2 (track 347) processing agreed in their overlapping area, considering the standard error, difference in data span, as well as satellite's viewing angle. It is interesting to note that the map from ERS-1/2 (track 75) processing also showed an uplift trend in some part of the Johor Bahru City, as found in the PS-InSAR and ERS-1/2 (track 347) results. The uplift could be due to construction processes as discussed before. This assumption is further supported by the Google rendered images shown before in **Figure 3.6**. The velocity rates range between -0.86 and 0.76 cm/year with the standard errors from 0.08 to 0.38 cm/year. For comparison, the rates stated in Ami Hassan (2014) are between -0.43 and 0.52 cm/year with the standard errors from 0.04 to 0.25 cm/year. Meanwhile, the rates from ERS-1/2 (track 347) are between -0.98 and 0.71 cm/year with the standard errors from 0.09 to 0.46 cm/year. They agree reasonably well with expected variations due to the difference in temporal resolution of the data, the spatial resolution of the results (PS-InSAR works on full resolution pixels, whereas ISBAS technique applies multi-looking), and the satellite's viewing angle. Assessment of their accuracy is hindered by the absence of ground truth in the area. Other areas in Johor are relatively stable.

Table 7.5 shows the comparison between the estimated velocity from DD GPS in the vertical direction and ISBAS analysis of ERS-1/2 (track 75) at the nearest coherent point. The LOS-velocities are converted to vertical direction for the comparison. It is noticeable that the precision of the velocities estimation from GPS is better than InSAR. Similarly, **Table 7.6** shows the same comparison but with the average rate computed from all coherent points within 2 km radius. It is noticeable that their trend is similar, suggesting the areas had undergone subsidence. Although they differ in their estimated rates, it can be explained by the difference in the spatial resolution. GPS observes the trend at a particular point measured by the receiver, whereas an ISBAS point gives the movement of an area covered by the multi-looked windows, i.e. approximately 100 m x 100 m on the ground resolution. It is also important to note that the horizontal movement (i.e. in North-South and East-West direction) is neglected when converting the LOS-velocities to the vertical direction (refer to **Section 5.11** of **Chapter 5**). This poor assumption may cause misinterpretation of the actual ground motion that occurs in both vertical and horizontal directions. Moreover, if the surface displacement were in the azimuth direction, which is perpendicular to the LOS direction, it may be entirely missed from the InSAR LOS measurement.

Table 7.5: Comparison between the estimated velocity from DD GPS and ISBAS analysis of ERS-1/2 (track 75) (the nearest point to the GPS station).

Station	Vertical velocity from DD GPS (cm/year)	Velocity from InSAR	
		Rate (cm/year)	Distance (m)
JHJY	-0.03 ± 0.02	-0.16 ± 0.09	27
TGPG	-0.27 ± 0.01	-0.15 ± 0.09	88
TGRH	-0.06 ± 0.01	-0.15 ± 0.10	50
NTUS	-0.15 ± 0.01	-0.09 ± 0.01	65

Table 7.6: Comparison between the estimated velocity from DD GPS and ISBAS analysis of ERS-1/2 (track 75) (average velocity over 2 km radius).

Station	Vertical velocity from DD GPS (cm/year)	Average velocity from InSAR (2 km radius)	
		Rate (cm/year)	Number of coherent points
JHJY	-0.03 ± 0.02	-0.01	1383
TGPG	-0.27 ± 0.01	-0.17	266
TGRH	-0.06 ± 0.01	-0.25	515
NTUS	-0.15 ± 0.01	-0.08	883

The histogram plot of the standard errors for the LOS-velocities (**Figure 7.38**) also shows similar features to the ISBAS analysis as reported previously in the ERS-1/2 (track 347) result; though, the two bells shape is not as prominent. The first curve mostly corresponds to the SBAS points. ISBAS increases the number of coherent points, which will be beneficial for the representation of deformation. However, they are noisier than the corresponding SBAS points. The SBAS points from the ERS-1/2 (track 75) processing have standard errors between 0.03 to 0.12 cm/year with the average value of 0.09 cm/year. Meanwhile, the maximum standard errors for the ISBAS points increases to 0.27 cm/year with the average value of 0.12 cm/year. In this work, only points that have reliable estimation (i.e. small standard errors as compared to the estimated LOS-velocities) are considered for the analysis. Visualisation of those points is made using ArcGIS software.

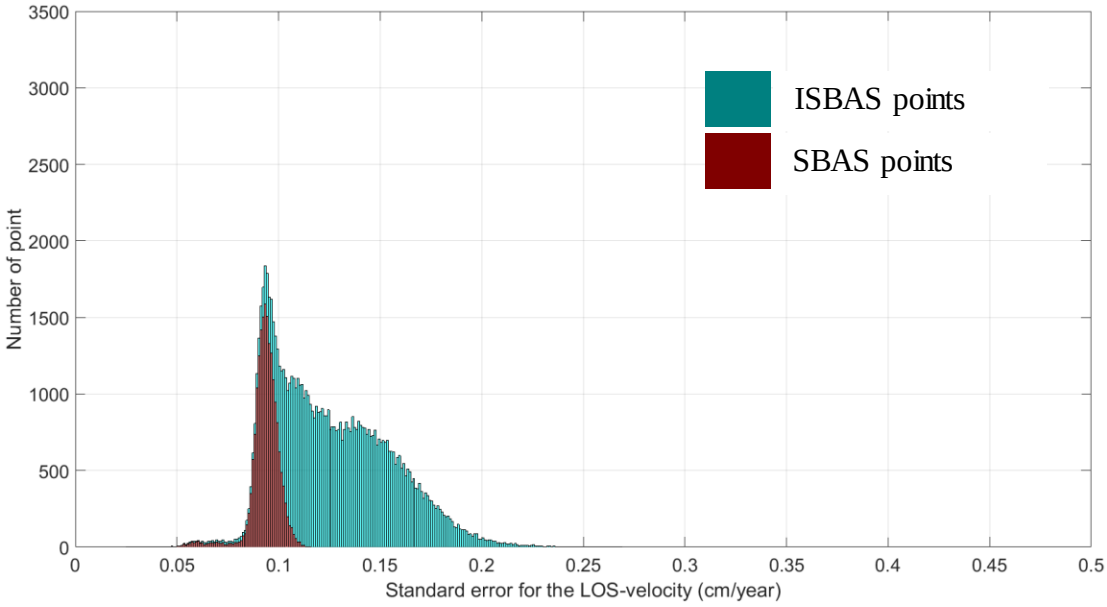


Figure 7.38: Histogram plot of the standard error from the ERS-1/2 (track 75) processing.

7.5. Summary

This chapter presents the main results from the processing of GPS and SAR datasets to quantify the rate of long-term deformation in Johor. From the GPS time-series analyses, it is evident that all stations are non-stationary. The mean of position varies with time, but the statistical or random noise remains fairly constant. The movement can be explained by a linear velocity of the plate tectonic motion and earthquakes in the surrounding region. Comparison between the DD and PPP results suggests that the latter is more sensitive to the movement induced by earthquakes as it only relies on the satellites information (position and clock) and the complete modelling of errors and biases affecting the measurements. In contrast, if the reference stations in DD are within the earthquake region, the sensitivity of the technique to the movement is reduced. Hence, the inclusion of reference stations outside the earthquake area will be advantageous. In this study, the results from DD processing is favourable for the assessment of long-term deformation as it benefits from the fixed ambiguities resolution as compared to float ambiguity resolution in PPP.

There are two tangible improvements from using DD with fixed ambiguities resolution as opposed to PPP with float ambiguities resolution, i.e. a more reliable estimation and a better coordinate repeatability especially in the East-West component. The latter is beneficial for velocity estimation. After removal of outliers larger than three sigmas, the average RMS for all 8 MyRTKnet stations from PPP estimate is 0.4 mm in the North-South, 1.0 mm in the East-West, and 1.5 mm in the Up-Down components. The value improves by 50% in the East-West component as a consequent

of the fixed ambiguities resolution DD. The RMS in the Up-Down component is slightly high as it is usually three times worse than the horizontal counterpart. Interestingly, the RMS from DD estimation also decreases with time, which could be attributed to the relative improvement of the GPS products, models, as well as the quality of the data. The rates are subtle (between -0.02 to - 0.47 mm/year) but visible on all 8 MyRTKnet stations. In summary, the GPS data processing via Bernese software performed well in this study in deriving horizontal and vertical time-series coordinates.

The linear velocity rate for 8 MyRTKnet stations is estimated using data from 18 September 2007 onward as the stations' movement is stable after that date. The standard errors of the velocity are good, apart from KLUG station, which can be explained by less data availability as compared to the others. Both the PPP and DD results showed declining trend in the North-South and increasing trend the East-West components. However, they differ in the vertical direction. While some stations, i.e. JHJY, SPGR, and TGRH, showed uplift movements in the PPP, all stations indicated subsidence pattern in the DD results. Since the Pearson correlation coefficient is higher in DD than PPP by 4% in the East-West and 5% in the Up-Down element, the rates from DD are accepted. The largest movement in the North-South, East-West, and Up-Down components is found at PRTS (-1.25 ± 0.01 cm/year), TGPG (2.06 ± 0.01 cm/year), and KUKP (-0.41 ± 0.01 cm/year), respectively. It implies that the current MyRTKnet stations in Johor have moved by as much as -21.25 cm in North-South, 35.02 cm in East-West, and -6.97 in Up-Down components, as of 1 January 2017, considering their reference epoch (i.e. ITRF2000 at epoch 2000.0).

The results also suggest that MyRTKnet stations in the West moved at different rates than the stations in the East, which is larger in North-South but smaller in East-West. No clear trend is perceived in the vertical direction. There could be a geological separation between the two areas as supported by the seismotectonic map from JMG, but the in-depth geological interpretation concerning the properties, mechanisms, and influences of the fault lines is subject to future work. Analysis of the horizontal movement showed that all stations moved towards a South-East direction, although they seem to change toward East direction after 2011. The 6.7Mw earthquake on 3 April 2011, which also followed by another 6.0Mw earthquake on 6 April 2011, could have triggered the change, but further data is required to verify this finding as it is only present at the end of the dataset. The calculated rates from PPP are found to be lower than DD by as much as 1.6 mm/year. A similar pattern is attained in the estimated direction. The difference reaches up to 1.822°, discarding the ambiguous estimation for KLUG station. The magnitudes range from 2.23 to 2.30 cm/year, whereas angle range between 115.165° and 123.184° (not considering the KLUG station). Reviewing these movements, the coordinates of MyRTKnet stations are due to revision to ensure that they are in line with the latest realisation of ITRF, and to ensure they provide an accurate and reliable solution for relative positioning.

The results from InSAR time-series enable quantification of the vertical deformation for areas not covered by MyRTKnet stations. ISBAS produced 293,339 points for the ERS-1/2 (track 347) processing and 178,877 points from the ERS-1/2 (track 75) processing, an improvement of 28.46% and 25.06%, respectively, when comparing to the standard SBAS analysis. This increment allows better representation of the deformation in the area. For example, the Peatland area in Johor showed a clear subsidence trend which also agreed with the reported rate. This finding cannot be achieved from the GPS, standard SBAS and PS-InSAR analysis due to their limited coverage. The LOS-velocity maps from ISBAS are somewhat noisy owing to the low coherent targets, error in the phase unwrapping, and assumption on the monotonic motion. The standard errors are relatively good in urban but deteriorate in remote/rural areas. About 91.8% points in the ERS-1/2 (track 347) results have a standard error less than 0.25 cm/year. The corresponding percentage for ERS-1/2 (track 75) points is 99.4%. Small standard error value suggests that atmospheric phase, orbital and DEM errors are well reduced in the time-series processing.

The LOS-velocity map from ERS-1/2 (track 75) and ERS-1/2 (track 347) processing matched in their overlapping area. Some part of Johor Bahru City showed an uplift trend, which is perceived in both results and the PS-InSAR result from Ami Hassan (2014). It could be due to constructions that had taken place, which also supported by the Google rendered images. Although the estimated rate from the three analyses is not similar, it can be ascribed to the difference in data span and spatial resolution of the results (PS-InSAR works on full resolution pixels, whereas ISBAS technique applies multi-looking). Assessment of their accuracy is hindered by the absence of ground truth in the area. Comparison of the vertical rate from GPS and InSAR showed agreement in the direction, but differ in the magnitude. While GPS observed the trend at a particular point measured by the receiver, the velocity of an ISBAS point represents the movement of an area covered by the multi-looked windows. As the conversion of LOS-velocities to the vertical direction is based on the assumption of no deformation in horizontal, it may cause misinterpretation of the actual ground motion that happens in both horizontal and vertical directions. If the surface displacement were in the SAR azimuth direction, it might be entirely missed from the InSAR LOS measurement. The properties of the ISBAS analysis is best seen in the histogram plot of the standard errors. The inclusion of ISBAS points increases the coverage but decreases the average standard error. For ERS-1/2 (track 347) processing, the SBAS points have an average error value of 0.11 cm/year as compared to 0.19 cm/year for the ISBAS points. The mean value in ERS-1/2 (track 75) is 0.09 cm/year for the SBAS points but increases to 0.12 cm/year for the ISBAS points. In this study, only points that have small standard errors in comparison with the estimated LOS-velocities are considered.

It is evident that the combination of GPS and InSAR has enabled comprehensive representation of the long-term deformation in Johor. GPS has successfully quantified the movements from the tectonic motion and earthquakes in the surrounding region, whereas InSAR has identified local subsidence due to the development of tropical peatland and urbanisation in the Johor Bahru City. It is expected that their combination for the assessment of deformation will continue to be exploited in light of the newly available Sentinel-1 satellites. The satellites have a short revisit cycle and small orbital separation, which will improve the coherence for areas such as Malaysia. Moreover, the Sentinel-1 data is accessible for free, which definitely adds to its interest.

CHAPTER 8

CONCLUSIONS AND RECOMMENDATIONS

8.1. Conclusions

Research on deformation is gaining much attention in Malaysia following the rising of public concern and awareness as the lesson learnt from unfortunate tragedies in the past. Some of those tragedies are the collapse of Highland Tower on 11 December 1993, the tsunami in West Coast of Peninsular Malaysia on 26 December 2004, and major floods that strikes almost every year during monsoon season. This awareness has demanded government and other responsible agencies to take preventative and continuous measures to ensure public safety. Deformation can be induced by various factors such as tectonic activities in the surrounding region, mining, landslide, development of tropical peatland, flood, and sea level rise. Deformation study provides information deemed necessary not only in the context of safety assessment but also for the maintenance of geodetic infrastructures. The latter is essential for accurate positioning in surveying and mapping applications. There are many methods available for the investigation of deformation; each with their own unique characteristics. Global Positioning System (GPS) and Interferometric Synthetic Aperture Radar (InSAR) are two of the most commonly used space-based geodetic techniques for deformation analysis. They are complementary in their features; InSAR for the investigation of surface movement over a wide area particularly in the vertical direction, and GPS for a detailed point-specific analysis.

This study presents an effort to quantify the rate of long-term deformation in Johor, Malaysia using a combination of GPS and InSAR. It is made possible with the availability of large recorded datasets, which has been a major limitation in the past. In general, the data included five years GPS data at 8 Malaysia Real-Time Kinematic GNSS Network (MyRTKnet) stations (2007 - 2011), and a total of 62 ERS-1/2 SAR images (1993 - 2005) from two satellite tracks. On top of that, 27 IGb08 stations are used as the reference stations, and 7 International GNSS Service (IGS) stations are utilised to bridge and shorten the baselines length in the double-difference (DD) processing. The feasibility of the newly available Sentinel-1 satellite is also investigated using 23 datasets from March 2015 to September 2016. In pursuit of this goal, three objectives have been addressed with the following conclusion.

8.1.1. Objective 1: *To investigate and develop a strategy for precise estimation of the long-term deformation in Johor, Malaysia using GPS and InSAR.*

The first objective is achieved through a detailed investigation of the biases and errors affecting the measurements and subsequently addressing them to extract the real deformation signal. For GPS, high accuracy daily coordinates are computed using Bernese GNSS Software that allows complete modelling and mitigation of those errors term. There are two processing methods tested in this study, namely Precise Point Positioning (PPP) and DD. The latter is customised for processing a regional network and benefits from the fixed ambiguity resolution. The former, on the other hand, is based on the float ambiguity resolution. The coordinate in both methods is determined on the International Terrestrial Reference Frame 2008 (ITRF2008). For PPP, it is done by fixing the satellites coordinate and clock, as well as a full modelling of errors and biases in the measurements. On the other hand, DD cancels the common errors and biases at the satellites and receiver during differencing processes. The final coordinate is realised by three-no-net translation conditions imposed on a set of reference frame stations (IGb 08 reference coordinates). Two Bernese Processing Engines (BPEs) have been customised to process the extensive data, i.e. PPP.PCF and DD.PCF. The detailed of each strategy is discussed in **Chapter 4**.

Similarly, the SAR processing employed in this research is discussed in **Chapter 5**. It is carried out using Punnet; a software developed in-house at the University of Nottingham. Punnet utilises the Intermittent Small Baseline Subset (ISBAS) algorithm, which appears particularly well-suited for an area like Malaysia. The coverage improvement when compared to the standard Small Baseline Subset (SBAS) processing reaches up to 28.46% in the study area. There are also improvements made to the existing algorithm, namely (1) statistical analysis to identify the appropriate thresholds for orbital and spatial baselines, (2) a new method to determine the control point for phase unwrapping, (3) implementation of outliers' rejection algorithm, and (4) a new method for the non-linear analysis in areas with significant deformation. The results from the improvements seem promising and give added values to the software.

The effects of the water body to phase unwrapping using SNAPHU are investigated and found to be nominal owing to the utilisation of nearest neighbour interpolation and the use of the coherence map as the weight. This research also presents one of the earliest Sentinel-1 results in Malaysia following targeted changes made to the existing workflow. Those changes consist of (1) additional module for debursting and merging prior to image coregistration and resampling, and (2) utilisation of the known de-ramping

function for the image's coregistration and resampling. The results suggest that Sentinel-1 will likely improve the coherence owing to the short revisiting cycle and small orbital separation. The network of the interferogram is also well connected; hence, producing a maximum number of interferograms given the data span.

8.1.2. Objective 2: *To model and mitigate the tropospheric effects in GPS and InSAR to achieve the most precise and reliable estimation from the measurements.*

The troposphere is one of the most challenging errors sources in GPS and InSAR and deserves special attention. The second objective is to minimise the tropospheric effects in order to achieve the best possible estimation from the measurements. In GPS, it is accomplished by introducing the dry component of the delay from a model and subsequently, estimating the wet part from the observation data. There were two models tested in this research, i.e. Saastamoinen model with Niell Mapping Function (NMF), and Vienna Mapping Function-1 (VMF-1). The former is an empirical model based on the standard atmosphere and the latter is a model based on the real weather measurements. Although no significant improvement is found in terms of coordinate repeatability, their small deviation suggests that VMF-1 is more suitable than NMF when precise zenith tropospheric delay (ZTD) is the primary concern. Comparison between the estimated troposphere from PPP and DD showed that they are within 4 mm standard deviation. However, DD can benefit from the good data quality at the nearby stations in the event of data problems. It is found that DD yields better agreement with ZTDs from the Center for Orbit Determination in Europe (CODE) than PPP. In general, the tropospheric delays in the study area range between 2.5 and 2.7 m, thus they must be accounted for in the precise applications such as deformation monitoring. The trends are dominated by the wet delay as it has high variability, but the overall value is offset owing to the greater magnitude of the dry delay.

The modelling and mitigation of tropospheric effects in InSAR are addressed considering their correlation with height. This method, however, only addresses the vertical stratification effects but not the turbulence mixing phenomena. The correlation can either be in linear or power-law relationships. Both approaches are implemented into Punnet, which significantly reduces the correlation. The Mexico processing is utilised for the illustration since the effects are more visible than in Johor, owing to the large range of height. The height range in Mexico based on the Shuttle Radar Topography Mission (SRTM) DEM is between ~702 and ~5,568 m above mean sea level (MSL),

whereas the corresponding range for Johor is from 0 to ~971 m above MSL. Although no noticeable difference is observed in the corrected interferograms between the linear and the power-law corrections, a slight improvement is achieved using power law as opposed to the linear correction in the estimated deformation. The benefits of tropospheric correction in InSAR become more noticeable in the quality of the estimation, which is represented by the standard error map. This finding also suggests that the non-linear analysis will benefit from this tropospheric correction as it relies on the residuals from the linear analysis. The in-depth discussion on the modelling and mitigation of tropospheric effects in GPS and InSAR is addressed in **Chapter 6**.

8.1.3. Objective 3: *To quantify and assess the rate of long-term deformation in Johor, Malaysia, and to analyse the sources of deformation.*

The derived velocities from GPS and InSAR time-series enable quantification and assessment of the long-term deformation in Johor, Malaysia. It is evident from the GPS time-series that all stations are non-stationary. Their movement can be explained by a linear velocity of the plates tectonic motion and earthquakes in the surrounding region. Firstly, the reliability of the coordinate estimation is assessed by analysing the root mean square (RMS) errors. Any outliers larger than three sigmas are rejected. Two improvements are noticeable from using DD with fixed ambiguities resolution as opposed to PPP with float ambiguities resolution: (1) a lower RMS value, and (2) a better coordinate repeatability especially in the East-West component, which will be beneficial for velocity estimation. The average RMS for all 8 MyRTKnet stations from PPP is 0.4 mm in the North-South, 1.0 mm in the East-West, and 1.5 mm in the Up-Down components. The value improved by 50% in the East-West as a consequence of the fixed ambiguities resolution in DD. The RMS from DD estimation also decreases with time, which could be attributed to the relative improvement of the GPS products, models, as well as the quality of the data. The rates are subtle (between -0.02 to - 0.47 mm/year) but visible on all 8 MyRTKnet stations. In summary, the GPS data processing via Bernese software performed well in deriving the coordinates.

It is worth mentioning that PPP is preferable for earthquakes study owing to its sensitivity to the movements induced by earthquakes. DD requires the reference stations to be outside the region to ensure they are not affected by the same movement. Nevertheless, the results from DD is favourable for the assessment of long-term deformation in this study as it benefits from the fixed ambiguities resolution. The linear velocity rate from PPP and DD

showed declining trend in the North-South and increasing trend the East-West components. However, they differ in the vertical direction. While some stations, i.e. JHJY, SPGR, and TGRH, showed uplift movements in the PPP, all stations indicated subsidence pattern in the DD results. The rates from DD are accepted considering the Pearson correlation coefficient is higher by 4% in the East-West and 5% in the Up-Down element. The largest movement in the North-South, East-West, and Up-Down components is found at PRTS (-1.25 ± 0.01 cm/year), TGPG (2.06 ± 0.01 cm/year), and KUKP (-0.41 ± 0.01 cm/year), respectively. It implies that the current MyRTKnet stations in Johor have moved by as much as -21.25 cm in North-South, 35.02 cm in East-West, and -6.97 in Up-Down components, as of 1 January 2017, considering their reference epoch (i.e. ITRF2000 at epoch 2000.0). The results also suggest that MyRTKnet stations in the West moved at different rates than the stations in the East. In-depth geological interpretation of these results is subject to future work.

Analysis of the horizontal movement showed that all stations moved towards a South-East direction, although they seem to change toward East direction after 2011. The 6.7Mw earthquake on 3 April 2011, which was also followed by another 6.0Mw earthquake on 6 April 2011, could have triggered the change, but further data is required to verify this finding as it only occurred at the end of the dataset. The calculated rates from PPP are found to be lower than DD by as much as 1.6 mm/year. A similar pattern is perceived in the estimated direction. The difference reaches up to 1.822°. The magnitudes range from 2.23 to 2.30 cm/year, whereas angle range between 115.165° and 123.184°. Reviewing these movements, the coordinates of MyRTKnet stations are due revision to ensure that they are in line with the latest realisation of ITRF, and to ensure that they provide an accurate and reliable solution for relative positioning.

The LOS-velocity map from the InSAR time-series allows assessment on the vertical deformation for areas not covered by MyRTKnet. ISBAS analysis produced 293,339 points for the ERS-1/2 (track 347) processing and 178,877 points for the ERS-1/2 (track 75) processing. Improvement in coverage means better representation of the deformation in the area. The Peatland area in Johor showed a clear subsidence trend, which is similar to the reported rates in the literature. This finding cannot be retrieved from the GPS, standard SBAS or PS-InSAR analysis due to their limited coverage. The standard errors are relatively small in urban areas but deteriorate in remote/rural areas. About 91.8% points in the ERS-1/2 (track 347) results have a standard error less than 0.25 cm/year, and the corresponding percentage for ERS-1/2 (track 75) points is 99.4%. The small standard errors suggest that the atmospheric phase, orbital and DEM errors are well reduced in the time-series processing.

The LOS-velocity map for ERS-1/2 (track 347) and ERS-1/2 (track 75) also matched in their overlapping area. Some part of the Johor Bahru City showed an uplift trend, which is observed in both results and the PS-InSAR result from Ami Hassan (2014). It could be due to urbanisation process, which is also supported by the Google rendered images. Although their estimated rate is slightly different, it can be caused by the difference in the data span, the spatial resolution of the results (PS-InSAR works on full resolution pixels, whereas ISBAS technique applies multi-looking), and the satellite viewing angles. Assessment of their accuracy is hindered by the absence of ground truth in the area.

Comparison of the vertical rate from GPS and InSAR showed agreement in the direction, but difference in the magnitude. While GPS observed a trend at a particular point measured by the receiver, the velocity of an ISBAS point represents the movement of an area covered by the multi-looked windows. As the conversion of LOS-velocities to the vertical direction also based on the assumption that there is no horizontal movement, it may cause misinterpretation of the actual ground motion that happens in both horizontal and vertical directions. If the surface displacement were in the SAR azimuth direction, it might be entirely missed from the InSAR LOS measurement.

The properties of the ISBAS analysis is best seen in the histogram plot of the standard errors. The inclusion of ISBAS points increases the coverage but decreases the average standard error. For ERS-1/2 (track 347) processing, the SBAS points have an average value of 0.11 cm/year as compared to 0.19 cm/year for the ISBAS points. The mean value for the ERS-1/2 (track 75) is 0.09 cm/year for the SBAS points but reduces to 0.12 cm/year for the ISBAS points. In this study, only points that have small standard errors in comparison with the estimated LOS-velocities are considered to ensure reliable results.

It is evident that the combination of GPS and InSAR has enabled comprehensive representation of the long-term deformation in Johor. GPS has successfully quantified the movements from the tectonic motion and earthquakes in the surrounding region, whereas InSAR has identified local subsidence due to the development of tropical peatland and urbanisation in the Johor Bahru City. It is expected that their combination for the assessment of deformation will continue to develop in light of the newly available Sentinel-1 satellites. The satellites have short revisit cycle, and small orbital separation, which is expected to improve the coherence in the area. Moreover, the Sentinel-1 data is accessible for free, which definitely adds to its interest.

8.2. Recommendations

The following items are drawn from the discussion points which indicate that further research may be useful and perhaps lead to significant results.

8.2.1. GPS Processing

The PPP processing in this research is based on the float ambiguity resolution. The results can be improved further, especially in the East-West direction, with the fixed ambiguities resolution. A few well-known software are available for the PPP processing with fixed ambiguity resolution such as the GIPSY OASIS II by the Jet Propulsion Laboratory (JPL). The DD processing, on the other hand, is customised for a regional network. The final solution relies on the 27 IGb08 stations for the reference stations. The inclusion of more stations, scattered in all continents, will produce a result that better fit the global network. It is because a better geometry is constrained for the coordinate estimation. Future work also can benefit from the geological interpretation of the results, which will give knowledge on the driving forces behind the deformation. The individual contribution of each driving factors can also be investigated. The results of this study indicate a change in the direction of movement at a later date, i.e. toward the East direction. However, a conclusive result is hindered by limited data as the change only occurred at the end of the dataset. It is recommended to include recent data, which will enable a better conclusion. The longer dataset also allow verification on the RMS improvement in DD as observed in this research.

8.2.2. SAR Processing

Although this research also investigates the feasibility of Sentinel-1 for deformation monitoring in Malaysia, no LOS-velocity map is produced from the processing as the data is insufficient for long-term deformation monitoring (only covers 18 months period). The Sentinel-1 processing is made following targeted changes to the existing workflow as described in **Section 5.5** of **Chapter 5**. The coherence is likely to improve owing to the short revisiting cycle of the satellite and the small orbital tube. Hence, it is expected to give a better result. There are several challenges faced in the Sentinel-1 processing as the data is gathered using the novel Terrain Observation with Progressive Scans in azimuth (TOPS) (Holzner and Bamler, 2002; Torres et al., 2012). The coregistration accuracy requirement is much more stringent than other stripmap products at one thousandth of one pixel (De Zan et al., 2014). Any

imprecision in the coregistration may result in noticeable phase ramps on the individual bursts as found in this research. A higher level of accuracy can be achieved through, for example, a spectral diversity technique (Scheiber and Moreira, 2000), as implemented by some authors (e.g. Lanari et al., 2015; Wegmüller et al., 2015).

The number of interferograms generated from the SBAS or ISBAS analysis is larger than the independent interferograms (i.e. the number of images minus one). Some image may have influenced the derived velocities more than the others as a result of more interferogram pairs. The predefined threshold used for the temporal and spatial baselines determine the number of pairs for each image. Further research may look into this aspect to see if appropriate weighting to interferogram could improve the result. It is also interesting to compare the ISBAS result in Johor with other InSAR time-series techniques such as the SqueeSAR (Ferretti et al. 2011). Furthermore, three-dimensional (3D) InSAR analysis can be implemented if multiple SAR acquisitions are available from different geometries or SAR systems.

8.2.3. Tropospheric Modelling

In this research, the tropospheric modelling in InSAR is addressed considering their correlation with height. This method, however, only addresses the vertical stratification effects but not the turbulence mixing phenomena. It will be desirable to consider both effects for the tropospheric correction. This can be achieved, for example, using external numerical weather model, the National Aeronautics and Space Administration (NASA) Moderate Resolution Imaging Spectroradiometer (MODIS), the European Space Agency (ESA) Medium Resolution Imaging Spectrometer (MERIS) measurements, or their combination. The power law correction applied in this research can also be improved by splitting the study area into multiple small windows and estimating the power law coefficients locally, as implemented in Bekaert et al. (2015a). This procedure will account for the spatial variability of the tropospheric properties over larger regions.

REFERENCES

Abdul Hadi, K., Ami Hassan, M.D., Muhammad Faiz, P. and Kamaludin, M.O., 2016. "Long-Term Sea Level Trend from Tidal Data in Malaysia." In *2016 7th IEEE Control and System Graduate Research Colloquium (ICSGRC)*. IEEE, pp. 187–192.

Abdulwahid, W.M. and Pradhan, B., 2016. "Landslide Vulnerability and Risk Assessment for Multi-Hazard Scenarios using Airborne Laser Scanning Data (LiDAR)." *Landslides*, (February), pp.1–20.

Abidin, H.Z., Andreas, H., Gamal, M., Wirakusumah, A.D., Darmawan, D., Deguchi, T. and Maruyama, Y., 2008. "Land Subsidence Characteristics of the Bandung Basin, Indonesia, as Estimated from GPS and InSAR." *Journal of Applied Geodesy*, 2(3).

Abidin, H.Z., Andreas, H., Gumilar, I., Fukuda, Y., Pohan, Y.E. and Deguchi, T., 2011. "Land Subsidence of Jakarta (Indonesia) and Its Relation with Urban Development." *Natural Hazards*, 59(3), pp.1753–1771.

Abidin, H.Z., Andreas, H., Gumilar, I., Sidiq, T.P., Gamal, M. and Murdohardono, D., 2010. "Studying Land Subsidence in Semarang (Indonesia) using Geodetic Methods." *FIG Congress*, (April 2010), pp.11–16.

Abidin, H.Z., Djaja, R., Darmawan, D., Hadi, S., Akbar, A., Rajiyowiryono, H., Sudibyo, Y., Meilano, I., Kasuma, M.A., Kahar, J. and Subarya, C., 2001. "Land Subsidence of Jakarta (Indonesia) and Its Geodetic Monitoring System." *Natural Hazards*, pp.365–387.

Akgun, A. and Erkan, O., 2016. "Landslide Susceptibility Mapping by Geographical Information System-Based Multivariate Statistical and Deterministic Models: In an Artificial Reservoir Area at Northern Turkey." *Arabian Journal of Geosciences*, 9(2), pp.1–15.

Aktuğ, B., Meherremov, E., Kurt, M., Özdemir, S., Esedov, N. and Lenk, O., 2013. "GPS Constraints on the Deformation of Azerbaijan and Surrounding Regions." *Journal of Geodynamics*, 67, pp.40–45.

Alshawaf, F., Fuhrmann, T., Heck, B., Hinz, S., Knoepfler, A., Luo, X., Mayer, M., Schenk, A., Thiele, A. and Westerhaus, M., 2012. "Atmospheric Water Vapour Determination by the Integration of InSAR and GNSS Observation." In *Fringe 2011 Workshop*. Frascati, Italy, pp. 19–23.

Altamimi, Z., Boucher, C. and Sillard, P., 2002a. "New Trends for the Realization of the International Terrestrial Reference System." *Advances in Space Research*, 30(2), pp.175–184.

Altamimi, Z., Collilieux, X. and Métivier, L., 2011. "ITRF2008: An Improved Solution of the International Terrestrial Reference Frame." *Journal of Geodesy*, 85(8), pp.457–473.

Altamimi, Z., Rebischung, P., Métivier, L. and Collilieux, X., 2016. "ITRF2014: A New Release of the International Terrestrial Reference Frame Modeling Nonlinear Station Motions." *Journal of Geophysical Research: Solid Earth*, 121(8), pp.6109–6131.

Altamimi, Z., Sillard, P. and Boucher, C., 2002b. "ITRF2000: A New Release of the International Terrestrial Reference Frame for Earth Science Applications." *Journal of Geophysical Research: Solid Earth*, 107(B10), p.ETG 2-1-ETG 2-19.

Altamimi, Z., Sillard, P. and Boucher, C., 2004. "ITRF2000: From Theory to Implementation." In *V Hotine-Marussi Symposium on Mathematical Geodesy*. Springer Berlin Heidelberg, pp. 157–163.

Althuwaynee, O.F., Pradhan, B. and Lee, S., 2012. "Application of an Evidential Belief Function Model in Landslide Susceptibility Mapping." *Computers and Geosciences*, 44, pp.120–135.

Altiner, Y., Söhne, W., Güney, C., Perlt, J., Wang, R. and Muzli, M., 2013. "A Geodetic Study of the 23 October 2011 Van, Turkey Earthquake." *Tectonophysics*, 588(October 2011), pp.118–134.

Amelung, F., Galloway, D.L., Bell, J.W., Zebker, H.A. and Laczniak, R.J., 1999. "Sensing the Ups and Downs of Las Vegas: InSAR Reveals Structural Control of Land Subsidence and Aquifer-System Deformation." *Geology*, 27(6), p.483.

Ami Hassan, M.D., 2012. "Long-Term Sea Level Change in the Malaysian Seas from Multi-Mission Altimetry Data." *International Journal of Physical Sciences*, 7(10), pp.1694–1712.

Ami Hassan, M.D., 2014. *Sea Level Rise Estimation and Interpretation in Malaysian Region Using Multi-Sensor Techniques*. PhD Thesis, Universiti Teknologi Malaysia.

Astro Awani, 2016. "Landslide in Bandar Putra Near Kulai." Available at: http://english.astroawani.com/malaysia-news/landslide-bandar-putra-near-kulai-117017 [Accessed January 25, 2017].

Attema, E., Cafforio, C., Gottwald, M., Guccione, P., Monti Guarnieri, A., Rocca, F. and Snoeij, P., 2010. "Flexible Dynamic Block Adaptive Quantization for Sentinel-1 SAR Missions." *IEEE Geoscience and Remote Sensing Letters*, 7(October), pp.766–770.

Bai, L., Jiang, L., Wang, H. and Sun, Q., 2016. "Spatiotemporal Characterization of Land Subsidence and Uplift (2009–2010) over Wuhan in Central China Revealed by TerraSAR-X InSAR Analysis." *Remote Sensing*, 8(4), p.350.

Baker, T.F., Curtis, D.J. and Dobson, A.H., 1995. "Ocean Tide Loading and GPS." *GPS World*, 6(3), pp.54–59.

Baldi, P., Casula, G., Cenni, N., Loddo, F. and Pesci, A., 2009. "GPS-Based Monitoring of Land Subsidence in the Po Plain (Northern Italy)." *Earth and Planetary Science Letters*, 288(1–2), pp.204–212.

Bamler, R. and Hartl, P., 1998. "Synthetic Aperture Radar Interferometry." *Inverse Problems*, 14(4), pp.R1–R54.

Barau, A. S., and Qureshi, S. (2015). "Using Agent-Based Modelling and Landscape Metrics to Assess Landscape Fragmentation in Iskandar Malaysia." *Ecological Processes*, *4*(1), 8.

Bateson, L., Cigna, F., Boon, D. and Sowter, A., 2015. "The Application of the Intermittent SBAS (ISBAS) InSAR Method to the South Wales Coalfield, UK." *International Journal of Applied Earth Observation and Geoinformation*, 34(2015), pp.249–257.

Baueršíma, I., 1983. *NAVSTAR/Global Positioning System (GPS), II*, Astronomical Institute, University of Bern.

Behr, J.A., Hudnut, K.W. and King, N.E., 1998. "Monitoring Structural Deformation at Pacoima Dam, California Using Continuous GPS." In *Proceeding of ION GPS Vol. 11*. Institute of Navigation, pp. 59–68.

Bekaert, D.P.S., Hooper, A. and Wright, T.J., 2015a. "A Spatially Variable Power Law Tropospheric Correction Technique for InSAR Data." *Journal of Geophysical Research: Solid Earth*, 120(2), pp.1345–1356.

Bekaert, D.P.S., Walters, R.J., Wright, T.J., Hooper, A.J. and Parker, D.J., 2015b. "Statistical Comparison of InSAR Tropospheric Correction Techniques." *Remote Sensing of Environment*, 170, pp.40–47.

Benevides, P., Nico, G., Catalao, J. and Miranda, P.M.A., 2016. "Bridging InSAR and GPS Tomography: A New Differential Geometrical Constraint." *IEEE Transactions on Geoscience and Remote Sensing*, 54(2), pp.697–702.

Berardino, P., Fornaro, G., Lanari, R. and Sansosti, E., 2002. "A New Algorithm for Surface Deformation Monitoring based on Small Baseline Differential SAR Interferograms." *IEEE Transactions on Geoscience and Remote Sensing*, 40(11), pp.2375–2383.

Bingley, R.M., 2004. *GNSS Principles and Observables*, Nottingham, IESSG, University of Nottingham UK, M.Sc. Lecture Monograph.

Bisnath, S. and Collins, P., 2012. "Recent Developments in Precise Point Positioning." *GEOMATICA*, 66(2), pp.103–111.

Blanco-Sánchez, P., Mallorquí, J.J., Duque, S. and Monells, D., 2008. "The Coherent Pixels Technique (CPT): An Advanced DInSAR Technique for Nonlinear Deformation Monitoring." *Pure and Applied Geophysics*, 165(6), pp.1167–1193.

Blewitt, G. and Lavallée, D., 2002. "Effect of Annual Signals on Geodetic Velocity." *Journal of Geophysical Research: Solid Earth*, 107(B7), p.ETG 9-1-ETG 9-11.

Blewitt, G., Heflin, M.B., Hurst, K.J., Jefferson, D.C., Webb, F.H. and Zumberge, J.F., 1993. "Absolute Far-Field Displacements from the 28 June 1992 Landers Earthquake Sequence." *Nature*, 361(6410), pp.340–342.

Blewitt, G., Kreemer, C., Hammond, W.C. and Gazeaux, J., 2016. "MIDAS Robust Trend Estimator for Accurate GPS Station Velocities without Step Detection." *Journal of Geophysical Research: Solid Earth*, 121(3), pp.2054–2068.

Blewitt, G., Kreemer, C., Hammond, W.C. and Goldfarb, J.M., 2013. "Terrestrial Reference Frame NA12 for Crustal Deformation Studies in North America." *Journal of Geodynamics*, 72, pp.11–24.

Bock, Y., 1998. "Reference Systems." In *GPS for Geodesy*. Berlin, Heidelberg: Springer Berlin Heidelberg, pp. 1–41.

Bock, Y., Agnew, D.C., Fang, P., Genrich, J.F., Hager, B.H., Herring, T.A., Hudnut, K.W., King, R.W., Larsen, S., Minster, J.-B., Stark, K., Wdowinski, S. and Wyatt, F.K., 1993. "Detection of Crustal Deformation from the Landers Earthquake Sequence using Continuous Geodetic Measurements." *Nature*, 361(6410), pp.337–340.

Boehm, J., 2004. "Vienna Mapping Functions in VLBI Analyses." *Geophysical Research Letters*, 31(1), pp.4–9.

Boehm, J. and Schuh, H., 2013. *Atmospheric Effects in Space Geodesy* J. Böhm & H. Schuh, eds., Berlin, Heidelberg: Springer Berlin Heidelberg.

Boehm, J., Heinkelmann, R. and Schuh, H., 2007. "Short Note: A Global Model of Pressure and Temperature for Geodetic Applications." *Journal of Geodesy*, 81(2007), pp.679–683.

Boehm, J., Möller, G., Schindelegger, M., Pain, G. and Weber, R., 2015. "Development of an Improved Empirical Model for Slant Delays in the Troposphere (GPT2w)." *GPS Solutions*, 19(3), pp.433–441.

Boehm, J., Werl, B. and Schuh, H., 2006. "Troposphere Mapping Functions for GPS and Very Long Baseline Interferometry from European Centre for Medium-Range Weather Forecasts Operational Analysis Data." *Journal of Geophysical Research*, 111(B2), p.B02406.

Boucher, C., Altamimi, Z., Feissel, M. and Sillard, P., 1996. *Results and Analysis of the ITRF94*, Obs. de Paris: IERS Tech. Note 20.

Bovenga, F., Wasowski, J., Nitti, D.O., Nutricato, R. and Chiaradia, M.T., 2012. "Using COSMO/SkyMed X-Band and ENVISAT C-Band SAR Interferometry for Landslides Analysis." *Remote Sensing of Environment*, 119, pp.272–285.

Bürgmann, R., Rosen, P.A. and Fielding, E.J., 2000. "Synthetic Aperture Radar Interferometry to Measure Earth's Surface Topography and Its Deformation." *Annual Review of Earth and Planetary Sciences*, 28(1), pp.169–209.

Cabral-Cano, E., Dixon, T.H., Miralles-Wilhelm, F., Díaz-Molina, O., Sánchez-Zamora, O. and Carande, R.E., 2008. "Space Geodetic Imaging of Rapid Ground Subsidence in Mexico City." *Bulletin of the Geological Society of America*, 120(December), pp.1556–1566.

Cabral-Cano, E., Osmanoglu, B., Dixon, T., Wdowinski, S., Demets, C., Cigna, F. and Díaz-Molina, O., 2010. "Subsidence and Fault Hazard Maps Using PSI and Permanent GPS Networks in Central Mexico." *IAHS-AISH Publication*, 339(January 2004), pp.255–259.

Catita, C., Feigl, K.L., Catalão, J., Miranda, J.M. and Victor, L.M., 2005. "InSAR Time Series Analysis of the 9 July 1998 Azores Earthquake." *International Journal of Remote Sensing*, 26(13), pp.2715–2729.

Cavalié, O., Doin, M.P., Lasserre, C. and Briole, P., 2007. "Ground Motion Measurement in the Lake Mead Area, Nevada, by Differential Synthetic Aperture Radar Interferometry Time Series Analysis: Probing the Lithosphere Rheological Structure." *Journal of Geophysical Research: Solid Earth*, 112(3), pp.1–18.

Cavalie, O., Pathier, E., Radiguet, M., Vergnolle, M., Cotte, N., Walpersdorf, A., Kostoglodov, V. and Cotton, F., 2013. "Slow Slip Event in the Mexican Subduction Zone: Evidence of Shallower Slip in the Guerrero Seismic Gap for the 2006 Event Revealed by the Joint Inversion of InSAR and GPS Data." *Earth and Planetary Science Letters*, 367, pp.52–60.

Charles D. Ghilani and Wolf, P.R., 2006. *Adjustment Computations: Spatial Data Analysis* Fourth Edi., John Wiley and Sons, Inc.

Chatterjee, R.S., Fruneau, B., Rudant, J.P., Roy, P.S., Frison, P.L., Lakhera, R.C., Dadhwal, V.K. and Saha, R., 2006. "Subsidence of Kolkata (Calcutta) City, India During the 1990s as Observed from Space by Differential Synthetic Aperture Radar Interferometry (D-InSAR) Technique." *Remote Sensing of Environment*, 102(1–2), pp.176–185.

Chaussard, E., Wdowinski, S., Cabral-Cano, E. and Amelung, F., 2014. "Land Subsidence in Central Mexico Detected by ALOS InSAR Time-Series." *Remote Sensing of Environment*, 140, pp.94–106.

Che Abas, M.R., 2001. "Earthquake Monitoring in Malaysia." In *Seismic Risk Seminar, Malaysia*. Malaysian Meteorological Department.

Cheloni, D., Giuliani, R., D'Anastasio, E., Atzori, S., Walters, R.J., Bonci, L., D'Agostino, N., Mattone, M., Calcaterra, S., Gambino, P., Deninno, F., Maseroli, R. and Stefanelli, G., 2014. "Coseismic and Post-Seismic Slip of the 2009 L'Aquila (Central Italy) Mw 6.3 Earthquake and Implications for Seismic Potential Along the Campotosto Fault from Joint Inversion of High-Precision Levelling, InSAR and GPS Data." *Tectonophysics*, 622, pp.168–185.

Chen, A.C. and Zebker, H.A., 2009. "Modeling Greenland Ice Sheets Using ALOS Polarimetric InSAR Data." *AGU Fall Meeting Abstracts*.

Chen, C.W. and Zebker, H.A, 2000. "Network Approaches to Two-Dimensional Phase Unwrapping: Intractability and Two New Algorithms." *Journal of the Optical Society of America A*, 18(5), p.1192.

Chen, C.W. and Zebker, H.A., 2001. "Two-Dimensional Phase Unwrapping with use of Statistical Models for Cost Functions in Nonlinear Optimization." *Journal of the Optical Society of America A*, 18(2), p.338.

Chen, C.W. and Zebker, H.A., 2002. "Phase Unwrapping for Large SAR Interferograms: Statistical Segmentation and Generalized Network Models." *IEEE Transactions on Geoscience and Remote Sensing*, 40, pp.1709–1719.

Chen, G. and Herring, T. A., 1997. "Effects of Atmospheric Azimuthal Asymmetry on the Analysis of Space Geodetic Data." *Journal of Geophysical Research: Solid Earth*, 102(B9), pp.20489–20502.

Chen, J. and Zebker, H.A., 2012. "Ionospheric Artifacts in Simultaneous L-Band InSAR and GPS Observations." *IEEE Transactions on Geoscience and Remote Sensing*, 50(4), pp.1227–1239.

Chen, T.C., Wang, S.Y. and Yen, M.C., 2007. "Enhancement of Afternoon Thunderstorm Activity by Urbanization in a Valley: Taipei." *Journal of Applied Meteorology and Climatology*, 46(9), pp.1324–1340.

Ching, N.H., Rosenfeld, D. and Braun, M., 1992. "Two-Dimensional Phase Unwrapping Using A Minimum Spanning Tree Algorithm." *IEEE Transactions on Image Processing*, 1(3), pp.355–365.

Chousianitis, K., Ganas, A. and Gianniou, M., 2013. "Kinematic Interpretation of Present-Day Crustal Deformation in Central Greece from Continuous GPS Measurements." *Journal of Geodynamics*, 71, pp.1–13.

Choy, S., Bisnath, S. and Rizos, C., 2016. "Uncovering Common Misconceptions in GNSS Precise Point Positioning and Its Future Prospect." *GPS Solutions*, (September 2016), pp.1–10.

Church, J.A., Clark, P.U., Cazenave, A., Gregory, J.M., Jevrejeva, S., Levermann, A., Merrifield, M.A., Milne, G.A., Nerem, R.., Nunn, P.D., Payne, A.J., Pfeffer, W.T., Stammer, D. and Unnikrishnan, A.S., 2013. "Sea Level Change." *Climate Change 2013: The Physical Science Basis. Contribution of Working Group I to the Fifth Assessment Report of the Intergovernmental Panel on Climate Change*, pp.1137–1216.

Cigna, F., Cabral-Cano, E., Osmanoglu, B., Dixon, T.H. and Wdowinski, S., 2011. "Detecting Subsidence-Induced Faulting in Mexican Urban Areas by Means of Persistent Scatterer Interferometry and Subsidence Horizontal Gradient Mapping." In *2011 IEEE International Geoscience and Remote Sensing Symposium*. IEEE, pp. 2125–2128.

Cigna, F., Sowter, A., Jordan, C.J. and Rawlins, B.G., 2014. "Intermittent Small Baseline Subset (ISBAS) Monitoring of Land Covers Unfavourable for Conventional C-Band InSAR: Proof-of-Concept for Peatland Environments in North Wales, UK." In C. Notarnicola, S. Paloscia, & N. Pierdicca, eds. *SAR Image Analysis, Modeling, and Techniques XIV*. Amsterdam, The Netherlands, p. 924305.

Collins, P., Henton, J., Mireault, Y., Héroux, P., Schmidt, M., Dragert, H. and Bisnath, S., 2009. "Precise Point Positioning for Real-Time Determination of Co-Seismic Crustal Motion." In *Proceedings of the 22nd International Technical Meeting of The Satellite Division of the Institute of Navigation (ION GNSS 2009)*. Savannah, GA, pp. 2479–2488.

Costantini, M., 1998. "A Novel Phase Unwrapping Method Based on Network Programming." *IEEE Transactions on Geoscience and Remote Sensing*, 36(3), pp.813–821.

Costantini, M. and Esrin, E.S.A., 1996. "A Phase Unwrapping Method Based on Network Programming." In *FRINGE 96 Workshop on ERS SAR Interferometry*. Zurich, Switzerland.

Costantini, M., Falco, S., Malvarosa, F. and Minati, F., 2008. "A New Method for Identification and Analysis of Persistent Scatterers in Series of SAR Images." In *IGARSS 2008 - 2008 IEEE International Geoscience and Remote Sensing Symposium*. IEEE, p. II-449-II-452.

Costantini, M., Malvarosa, F. and Minati, F., 2012. "A General Formulation for Redundant Integration of Finite Differences and Phase Unwrapping on a Sparse Multidimensional Domain." *IEEE Transactions on Geoscience and Remote Sensing*, 50(3), pp.758–768.

Counselman, C.C. and Gourevitch, S. A., 1981. "Miniature Interferometer Terminals for Earth Surveying: Ambiguity and Multipath with Global Positioning System." *IEEE Transactions on Geoscience and Remote Sensing*, GE-19(4), pp.244–252.

Crosetto, M., Biescas, E., Duro, J., Closa, J. and Arnaud, A., 2008. "Generation of Advanced ERS and Envisat Interferometric SAR Products Using the Stable Point Network Technique." *Photogrammetric Engineering and Remote Sensing*, 74(4), pp.443–450.

Curlander, J.C. and McDonough, R.N., 1992. *Synthetic Aperture Radar: Systems and Signal Processing*, John Wiley & Sons, Inc, New York.

Dach, R., Bock, H., Lutz, S., Meindl, M., Ostini, L., Prange, L., Schaer, S., Steinbach, A., Thaller, D., Walser, P. and Beutler, 2008. "Bernese GPS Software: Recent Developments and Plans." In *EUREF-LAC-Workshop*. Frankfurt, 22/23 October 2008: EUREF–LAC–Workshop.

Dach, R., Hugentobler, U., Fridez, P. and Meindl, M., 2007. *Bernese GPS Software Version 5.0*, Astronomical Institute, University of Bern.

Dach, R., Lutz, S., Walser, P. and Fridez, P., 2015. *Bernese GNSS Software, Version 5.2*, Astronomical Institute, University of Bern.

Dach, R., Schaer, S., Arnold, D., Orliac, E., Prange, L., Susnik, A., Villiger, A. and Jaeggi, A., 2016. *CODE Final Product Series for the IGS*, Available at: http://www.aiub.unibe.ch/download/CODE.

Dang, V.K., Doubre, C., Weber, C., Gourmelen, N. and Masson, F., 2014. "Recent Land Subsidence Caused by the Rapid Urban Development in the Hanoi Region (Vietnam) using ALOS InSAR Data." *Natural Hazards and Earth System Sciences*, 14(3), pp.657–674.

De Zan, F., Guarnieri, a. M. and Rocca, F., 2008. "Advances in SAR Interferometry for Sentinel-1 with TOPS." In *2008 IEEE Radar Conference, RADAR 2008*. pp. 1–6.

De Zan, F., Prats-Iraola, P., Scheiber, R. and Rucci, A., 2014. "Interferometry with TOPS: Coregistration and Azimuth Shifts." In *EUSAR 2014; 10th European Conference on Synthetic Aperture Radar*. pp. 1–4.

DeMets, C., Gordon, R.G., Argus, D.F. and Stein, S., 1994. "Effect of Recent Revisions to the Geomagnetic Reversal Time Scale on Estimate of Current Plate Motions." *Geophysical Research Letters*, 21(20), pp.2191–2194.

Department of Environment, 2010. "Environmental Requirements: A Guide For Investors." *Ministry of Natural Resources and Environment*, (October), pp.1–78.

Dermanis, A., 2001. "Establishing Global Reference Frames. Nonlinear, Temporal, Geophysical and Stochastic Aspects." In *Gravity, Geoid and Geodynamics 2000*. Springer Berlin Heidelberg, pp. 35–42.

Dermanis, A., 2004. "The Rank Deficiency in Estimation Theory and the Definition of Reference Systems." In *V Hotine-Marussi Symposium on Mathematical Geodesy*. Springer Berlin Heidelberg, pp. 145–156.

Din, A.H., Reba, M.N., Omar, K.M. and Rashidi, M., 2015. "Land Subsidence Monitoring using Persistent Scatterer InSAR (PSInSAR) in Kelantan Catchment." In *The 36th Asian Conference on Remote Sensing (ACRS 2015)*. Quezon City, Metro Manila Philippines.

Ding, X., Li, Z., Zhu, J., Feng, G. and Long, J., 2008. "Atmospheric Effects on InSAR Measurements and Their Mitigation." *Sensors*, 8(9), pp.5426–5448.

Doin, M.-P., Lasserre, C., Peltzer, G., Cavalié, O. and Doubre, C., 2009. "Corrections of Stratified Tropospheric Delays in SAR Interferometry: Validation with Global Atmospheric Models." *Journal of Applied Geophysics*, 69(1), pp.35–50.

Donnellan, A., Arrowsmith, R. and DeLong, S., 2017. "Spatio-Temporal Mapping of Plate Boundary Faults in California Using Geodetic Imaging." *Geosciences*, 7(1), p.15.

DOSM, 2016. "Current Population Estimates, Malaysia, 2014 - 2016." *Department of Statistics Malaysia*. Available at: https://www.dosm.gov.my [Accessed January 25, 2017].

Doubre, C., Déprez, A., Masson, F., Socquet, A., Lewi, E., Grandin, R., Nercessian, A., Ulrich, P., De Chabalier, J.-B., Saad, I., Abayazid, A., Peltzer, G., Delorme, A., Calais, E. and Wright, T., 2017. "Current Deformation in Central Afar and Triple Junction Kinematics Deduced from GPS and InSAR Measurements." *Geophysical Journal International*, 208(2), pp.936–953.

Du, Z., Ge, L., Li, X. and Ng, A., 2016. "Subsidence Monitoring Over the Southern Coalfield, Australia Using both L-Band and C-Band SAR Time Series Analysis." *Remote Sensing*, 8(7), p.543.

Elachi, C., Roth, L.E. and Schaber, G.G., 1984. "Spaceborne Radar Subsurface Imaging in Hyperarid Regions." *IEEE Transactions on Geoscience and Remote Sensing*, GE-22(4), pp.383–388.

El Gharbawi, T. and Tamura, M., 2014. "Measuring Deformations using SAR Interferometry and GPS Observables with Geodetic Accuracy: Application to Tokyo, Japan." *ISPRS Journal of Photogrammetry and Remote Sensing*, 88, pp.156–165.

El Gharbawi, T. and Tamura, M., 2015. "Coseismic and Postseismic Deformation Estimation of the 2011 Tohoku Earthquake in Kanto Region, Japan, using InSAR Time Series Analysis and GPS." *Remote Sensing of Environment*, 168, pp.374–387.

Elmahdy, S.I., Marghany, M.M. and Mohamed, M.M., 2016. "Application of A Weighted Spatial Probability Model in GIS to Analyse Landslides in Penang Island, Malaysia." *Geomatics, Natural Hazards and Risk*, 7(1), pp.345–359.

Ergintav, S., Doğan, U., Gerstenecker, C., Çakmak, R., Belgen, A., Demirel, H., Aydın, C. and Reilinger, R., 2007. "A Snapshot (2003–2005) of the 3D Postseismic Deformation for the 1999, Mw=7.4 İzmit Earthquake in the Marmara Region, Turkey, by First Results of Joint Gravity and GPS Monitoring." *Journal of Geodynamics*, 44(1–2), pp.1–18.

Eriksen, H.Ø., Lauknes, T.R., Larsen, Y., Corner, G.D., Bergh, S.G., Dehls, J. and Kierulf, H.P., 2017. "Visualizing and Interpreting Surface Displacement Patterns on Unstable Slopes using Multi-Geometry Satellite SAR Interferometry (2D InSAR)." *Remote Sensing of Environment*, 191, pp.297–312.

Erol, S., Erol, B. and Ayan, T., 2004. "A General Review of the Deformation Monitoring Techniques and A Case Study: Analysing Deformations using GPS/Levelling." In *XXth ISPRS Congress" Geo-Imagery Bridging Continents*. Istanbul, Turkey, pp. 12–23.

ESA, 2013. *Sentinel-1 User Handbook*, Ref: GMES-OP-EOPG-TN-13-0001, 1st September 2013.

Essen, L. and Froome, K.D., 1951. "The Refractive Indices and Dielectric Constants of Air and its Principal Constituents at 24,000 Mc/s." *Proceedings of the Physical Society. Section B*, 64(10), p.862.

Farr, T.G., Rosen, P.A., Caro, E., Crippen, R., Duren, R., Hensley, S., Kobrick, M., Paller, M., Rodriguez, E., Roth, L., Seal, D., Shaffer, S., Shimada, J., Umland, J., Werner, M., Oskin, M., Burbank, D. and Alsdorf, D.E., 2007. "The Shuttle Radar Topography Mission." *Reviews of Geophysics*, 45, pp.1–43.

Feng, G., Ding, X., Li, Z., Mi, J., Zhang, L. and Omura, M., 2012. "Calibration of an InSAR-Derived Coseimic Deformation Map Associated with the 2011 Mw-9.0 Tohoku-Oki Earthquake." *IEEE Geoscience and Remote Sensing Letters*, 9(2), pp.302–306.

Feng, W., Samsonov, S., Tian, Y., Qiu, Q., Li, P., Zhang, Y., Deng, Z. and Omari, K., 2017. "Surface Deformation Associated with the 2015 Mw 8.3 Illapel Earthquake Revealed by Satellite-Based Geodetic Observations and Its Implications for the Seismic Cycle." *Earth and Planetary Science Letters*, 460, pp.222–233.

Fernandez, J., Romero, R., Carrasco, D., Luzon, F. and Arana, V., 2002. "InSAR Volcano and Seismic Monitoring in Spain. Results for the Period 1992–2000 and Possible Interpretations." *Optics and Lasers in Engineering*, 37, pp.285–297.

Ferretti, A., 2014. *Satellite InSAR Data: Reservoir Monitoring from Space*, EAGE Publications.

Ferretti, A., Fumagalli, A., Novali, F. and Prati, C., 2009. "The Second Generation PSInSAR Approach: SqueeSAR." *Fringe 2009*, 2(1).

Ferretti, A., Fumagalli, A., Novali, F., Prati, C., Rocca, F. and Rucci, A., 2011. "A New Algorithm for Processing Interferometric Data-Stacks: SqueeSAR." *IEEE Transactions on Geoscience and Remote Sensing*, 49(9), pp.3460–3470.

Ferretti, A., Monti-guarnieri, A., Prati, C. and Rocca, F., 2007. *InSAR Principles: Guidelines for SAR Interferometry Processing and Interpretation*, ESA Publications.

Ferretti, A., Prati, C. and Rocca, F., 1999. "Multibaseline InSAR DEM Reconstruction: The Wavelet Approach." *IEEE Transactions on Geoscience and Remote Sensing*, 37(2), pp.705–715.

Ferretti, A., Prati, C. and Rocca, F., 2000. "Nonlinear Subsidence Rate Estimation using Permanent Scatterers in Differential SAR Interferometry." *IEEE Transactions on Geoscience and Remote Sensing*, 38(5), pp.2202–2212.

Ferretti, A., Prati, C. and Rocca, F., 2001. "Permanent Scatterers in SAR Interferometry." *IEEE Transactions on Geoscience and Remote Sensing*, 39(1), pp.8–20.

Fialko, Y. and Simons, M., 2001. "The Complete (3-D) Surface Displacement Field in the Epicentral Area of the 1999 Mw 7.1 Hector Mine Earthquake, California, from Space Geodetic Observations." *Geophysical Journal International*, 28(16), pp.3063–3066.

Flynn, T.J., 1997. "Two-Dimensional Phase Unwrapping with Minimum Weighted Discontinuity." *Journal of the Optical Society of America A*, 14(10), p.2692.

Fornaro, G., Franceschetti, G. and Lanari, R., 1996a. "Interferometric SAR Phase Unwrapping Using Green's Formulation." *IEEE Transactions on Geoscience and Remote Sensing*, 34(3), pp.720–727.

Fornaro, G., Franceschetti, G., Lanari, R. and Sansosti, E., 1996b. "Robust Phase-Unwrapping Techniques: A Comparison." *Journal of the Optical Society of America A*, 13(12), p.2355.

Fruneau, B., Achache, J. and Delacourt, C., 1996. "Observation and Modelling of the Saint-Etienne-de-Tinee Landslide using SAR Interferometry." *Tectonophysics*, 265, pp.181–190.

Fuhrmann, T., Knöpfler, A., Mayer, M., Schenk, A., Westerhaus, M., Zippelt, K. and Heck, B., 2015. "An Inventory of Surface Movements in the Upper Rhine Graben Area, Southwest Germany, from SAR-Interferometry, GNSS and Precise Levelling." In *ESA Living Planet Symposium 2013*. Edinburgh, UK, pp. 1–7.

Fund, F., Morel, L., Mocquet, A. and Boehm, J., 2011. "Assessment of ECMWF-Derived Tropospheric Delay Models within the EUREF Permanent Network." *GPS Solutions*, 15(1), pp.39–48.

Gahalaut, V.K., Nagarajan, B., Catherine, J. and Kumar, S., 2006. "Constraints on 2004 Sumatra–Andaman Earthquake Rupture from GPS Measurements in Andaman–Nicobar Islands." *Earth and Planetary Science Letters*, 242(3–4), pp.365–374.

Gahalaut, V.K., Yadav, R.K., Sreejith, K.M., Gahalaut, K., Bürgmann, R., Agrawal, R., Sati, S.. and Kumar, A., 2017. "InSAR and GPS Measurements of Crustal Deformation due to Seasonal Loading of Tehri Reservoir in Garhwal Himalaya, India." *Geophysical Journal International*, p.ggx015.

Galloway, D.L., Hudnut, K.W., Ingebritsen, S.E., Phillips, S.P., Peltzer, G., Rogez, F. and Rosen, P. a, 1998. "Detection of Aquifer System Compaction and Land Subsidence using Interferometric Synthetic Aperture Radar, Antelope Valley, Mojave Desert, California." *Water Resources Research*, 34(10), pp.2573–2585.

Gaveau, D.L.A., Salim, M.A., Hergoualc'h, K., Locatelli, B., Sloan, S., Wooster, M., Marlier, M.E., Molidena, E., Yaen, H., DeFries, R., Verchot, L., Murdiyarso, D., Nasi, R., Holmgren, P. and Sheil, D., 2014. "Major Atmospheric Emissions from Peat Fires in Southeast Asia During Non-Drought Years: Evidence from the 2013 Sumatran Fires." *Scientific Reports*, 4, p.6112.

Gazeaux, J., Williams, S., King, M., Bos, M., Dach, R., Deo, M., Moore, A.W., Ostini, L., Petrie, E., Roggero, M., Teferle, F.N., Olivares, G. and Webb, F.H., 2013. "Detecting Offsets in GPS Time Series: First Results from the Detection of Offsets in GPS Experiment." *Journal of Geophysical Research: Solid Earth*, 118(5), pp.2397–2407.

Ge, L., Ng, A.H.M., Li, X., Abidin, H.Z. and Gumilar, I., 2014. "Land Subsidence Characteristics of Bandung Basin as Revealed by ENVISAT ASAR and ALOS PALSAR Interferometry." *Remote Sensing of Environment*, 154, pp.46–60.

Gérard, P. and Luzum, B., 2010. *IERS Conventions (2010)*, IERS Technical Note No. 36, IERS Conventions (2010).

Geudtner, D., 2014. *Implementation of the TOPS Mode on RADARSAT-2 in Support of the Copernicus Sentinel-1 Mission. RADARSAT-2 TOPS SAR Interferometry (InSAR) Scene Pair Data Acquisitions.* ESA Technical Note.

Ghiglia, D.C. and Romero, L.A., 1994. "Robust Two-Dimensional Weighted and Unweighted Phase Unwrapping That Uses Fast Transforms and Iterative Methods." *Journal of the Optical Society of America A*, 11(1), p.107.

Ghiglia, D.C. and Romero, L.A., 1996. "Minimum L^p-Norm Two-Dimensional Phase Unwrapping." *Journal of the Optical Society of America A*, 13(10), p.1999.

Giesen, W., 2004. *Causes of Peat Swamp Forest Degradation in Berbak NP, Indonesia, and Recommendations for Restoration*. Water for Food and Ecosystems Programme - Arcadis Euroconsult.

Goldstein, R.M., Zebker, H.A. and Werner, C.L., 1988. "Satellite Radar Interferometry: Two-Dimensional Phase Unwrapping." *Radio Science*, 23(4), pp.713–720.

Gonzalez-Ortega, A., Fialko, Y., Sandwell, D., Alejandro Nava-Pichardo, F., Fletcher, J., Gonzalez-Garcia, J., Lipovsky, B., Floyd, M. and Funning, G., 2014. "El Mayor-Cucapah (Mw 7.2) Earthquake: Early Near-Field Postseismic Deformation from InSAR and GPS Observations." *Journal of Geophysical Research: Solid Earth*, 119(2), pp.1482–1497.

Gray, L., 2011. "Using Multiple RADARSAT InSAR Pairs to Estimate a Full Three-Dimensional Solution for Glacial Ice Movement." *Geophysical Research Letters*, 38(5).

Guangcai, F., Zhiwei, L., Xinjian, S., Bing, X. and Yanan, D., 2015. "Source Parameters of the 2014 Mw 6.1 South Napa Earthquake Estimated from the Sentinel 1A, COSMO-SkyMed and GPS Data." *Tectonophysics*, 655, pp.139–146.

Gudmundsson, S., Sigmundsson, F. and Carstensen, J.M., 2002. "Three-Dimensional Surface Motion Maps Estimated from Combined Interferometric Synthetic Aperture Radar and GPS Data." *Journal of Geophysical Research: Solid Earth*, 107(B10), p.ETG 13-1-ETG 13-14.

Guizar-Sicairos, M., Thurman, S.T. and Fienup, J.R., 2008. "Efficient Subpixel Image Registration Algorithms." *Optics Letters*, 33(2), p.156.

Halim, S., 1995. *Functional and Stocastic Models for Geometrical Detection of Deformation in Engineering: A Practical Approach*. PhD thesis. City University.

Hanssen, R.F., 1999. "High-Resolution Water Vapor Mapping from Interferometric Radar Measurements." *Science*, 283(5406), pp.1297–1299.

Hanssen, R.F., 2001. *Radar Interferometry - Data Interpretation and Error Analysis*, Dordrecht: Kluwer Academic Publishers.

Hashim, A., 2010. *Malaysia Country Profile*, Malaysian Meteorological Department.

Hassaballa, A.A., Althuwaynee, O.F. and Pradhan, B., 2014. "Extraction of Soil Moisture from RADARSAT-1 and Its Role in the Formation of the 6 December 2008 Landslide at Bukit Antarabangsa, Kuala Lumpur." *Arabian Journal of Geosciences*, 7(7), pp.2831–2840.

Hatta, A.M. and Rashid, B.A., 1998. "Groundwater Resources in Johor, Malaysia: Resource Potential and Information Management." *GEOSEA'98, Ninth Regional Congress on Geology, Mineral and Energy Resources of Southeast Asia, Geological Society of Malaysia*, pp.367–373.

He, X., Montillet, J.-P., Fernandes, R., Bos, M., Yu, K., Hua, X. and Jiang, W., 2017. "Review of Current GPS Methodologies for Producing Accurate Time Series and Their Error Sources." *Journal of Geodynamics*, 106, pp.12–29.

Hesse, S., Back, S. and Franke, D., 2009. "The Deep-Water Fold-and-Thrust Belt Offshore NW Borneo: Gravity-Driven Versus Basement-Driven Shortening." *Bulletin of the Geological Society of America*, 121(5–6), pp.939–953.

Hetland, E.A. and Hager, B.H., 2006. "Interseismic Strain Accumulation: Spin-Up, Cycle Invariance, and Irregular Rupture Sequences." *Geochemistry, Geophysics, Geosystems*, 7(5).

Heublein, M., Alshawaf, F., Mayer, M., Hinz, S. and Heck, B., 2014. *Towards a Rigorous Fusion of GNSS and InSAR Observations for the Purpose of Water Vapor Retrieval*, KIT Scientific Publishing.

Hilley, G.E., 2004. "Dynamics of Slow-Moving Landslides from Permanent Scatterer Analysis." *Science*, 304(5679), pp.1952–1955.

Hofmann-Wellenhof, Bernhard, L. and Herbert, Wasle, E., 2008. *GNSS — Global Navigation Satellite Systems*, Vienna: Springer Vienna.

Hofton, M.A., 1995. *Anelastic Deformation in Iceland Studied using GPS: With Special Reference to Post-Tectonic Motion Following the 1975-1985 Krafla Rifting Episode, and Isostatic Rebound*. PhD Thesis, Durham University.

Holley, R., 2009. *Mitigating Atmospheric Path Delays In Radar Interferometry Over Volcanoes - Atmospheric Modelling And Persistent Scatterer Techniques*. PhD Thesis, University of Reading.

Holzner, J. and Bamler, R., 2002. "Burst-Mode and ScanSAR Interferometry." *IEEE Transactions on Geoscience and Remote Sensing*, 40(September), pp.1917–1934.

Hooper, A., 2008. "A Multi-Temporal InSAR Method Incorporating Both Persistent Scatterer and Small Baseline Approaches." *Geophysical Research Letters*, 35(16), p.L16302.

Hooper, A., Bekaert, D., Spaans, K. and Arıkan, M., 2012. "Recent Advances in SAR Interferometry Time Series Analysis for Measuring Crustal Deformation." *Tectonophysics*, 514–517, pp.1–13.

Hooper, A., Zebker, H., Segall, P. and Kampes, B., 2004. "A New Method for Measuring Deformation on Volcanoes and Other Natural Terrains Using InSAR Persistent Scatterers." *Geophysical Research Letters*, 31(23), pp.1–5.

Hooper, A.J., 2006. *Persistent Scatterer Radar Interferometry for Crustal Deformation Studies and Modeling of Volcanic Deformation*. PhD Thesis, Stanford University.

Hopfield, H.S., 1969. "Two-Quartic Tropospheric Refractivity Profile for Correcting Satellite Data." *Journal of Geophysical Research*, 74(18).

Houlié, N., Funning, G. and Bürgmann, R., 2016. "Use of a GPS-derived troposphere model to improve InSAR deformation estimates in the San Gabriel Valley, California." *Geophys. J. Int.*, (22).

Hu, J., Ding, X.L., Li, Z.W., Zhang, L., Zhu, J.J., Sun, Q. and Gao, G.J., 2016. "Vertical and Horizontal Displacements of Los Angeles from InSAR and GPS Time Series Analysis: Resolving Tectonic and Anthropogenic Motions." *Journal of Geodynamics*, 99, pp.27–38.

Hu, J., Li, Z.W., Ding, X.L., Zhu, J.J., Zhang, L. and Sun, Q., 2014. "Resolving Three-Dimensional Surface Displacements from InSAR Measurements: A Review." *Earth-Science Reviews*, 133, pp.1–17.

Hu, Y., Hu, Y., Zhang, K., Zhang, K., Liu, G. and Liu, G., 2005. "Deformation Monitoring and Analysis Using Regional GPS Permanent Tracking Station Networks." In *FIG Working Week 2005 and GSDI-8*. Cairo, Egypt, pp. 1–15.

Hung, W.-C., Hwang, C., Chen, Y.-A., Chang, C.-P., Yen, J.-Y., Hooper, A. and Yang, C.-Y., 2011. "Surface Deformation from Persistent Scatterers SAR Interferometry and Fusion with Leveling Data: A Case Study Over the Choushui River Alluvial Fan, Taiwan." *Remote Sensing of Environment*, 115(4), pp.957–967.

Hunt, B.R., 1979. "Matrix Formulation of the Reconstruction of Phase Values from Phase Differences." *Journal of the Optical Society of America*, 69(3), p.393.

International Wetlands, 2010. *A Quick Scan of Peatlands in Malaysia*. Petaling Jaya, Malaysia: Wetlands International – Malaysia.

Jaafar, H., 2017. *Detection and Localisation of Structural Deformations using Terrestrial Laser Scanning and Generalised Procrustes Analysis*. PhD Thesis, The University of Nottingham.

Janes, H.W., Langley, R.B. and Newby, S.P., 1989. "A Comparison of Several Models for the Prediction of Tropospheric Propagation Delay." In *Proceedings 5th International Geodetic Symposium on Satellite Positioning*. Las Cruces, New Mexico, USA, pp. 777–788.

Janssen, V., Ge, L. and Rizos, C., 2004. "Tropospheric Corrections to SAR Interferometry from GPS Observations." *GPS Solutions*, 8(3), pp.140–151.

Jaw, S.W., Zafirah, N., Lah, A., Khairul, M. and Halim, A., 2015. "Satellite-Based Inventorying Major Landslides in Kelantan River Basin due to Massive December 2014 Flood Episode." In *ACRS 2015 - 36th Asian Conference on Remote Sensing: Fostering Resilient Growth in Asia*. pp. 1–5.

JMG, 2009. "Assessment of the Seismic Threats to Malaysia from Major Earthquakes in the Southeast Asian Region and Seismotectonic Map of Malaysia and Fault Line / Zone Study." In *Forum on Seismic and Tsunami Hazards and Risks Study in Malaysia*. Putrajaya, Malaysia (29 September 2009).

Joosten, H., Tapio-Biström, M.-L. and Tol, S., 2012. *Peatlands - Guidance for Climate Change Mitigation Through Conservation, Rehabilitation and Sustainable Use*. The Food and Agriculture Organisation of the United Nations and Wetlands International.

Joughin, I.R., Kwok, R. and Fahnestock, M., 1998. "Interferometric Estimation of Three-Dimensional Ice-Flow using Ascending and Descending Passes." *IEEE Transactions on Geoscience and Remote Sensing*, 36(1), pp.25–37.

JUPEM, 2008. *Garis Panduan Mengenai Ujian Alat Sistem Penentududukan Sejagat (GNSS) yang Menggunakan Perkhidmatan Malaysian RTK GNSS Network*, Pekeliling Ketua Pengarah Ukur dan Pemetaan Malaysia Bilangan 1 Tahun 2008.

JUPEM, 2009a. *Technical Guide to the Coordinate Reference Systems*, Pekeliling Ketua Pengarah Ukur dan Pemetaan Malaysia Bilangan Bilangan 1 Tahun 2009.

JUPEM, 2009b. *Technical Guide to the Coordinate Conversion, Datum Transformation and Map Projection*, Pekeliling Ketua Pengarah Ukur dan Pemetaan Malaysia Bilangan 3 Tahun 2009.

Kampes, B. and Usai, S., 1999. "Doris: the Delft Object-oriented Radar Interferometric Software." In *2nd International Symposium on Operationalization of Remote Sensing*. Enschede, The Netherlands (16–20 August 1999), pp. 1–4.

Kampes, B.M., 2005. *Displacement Parameter Estimation using Permanent Scatterer Interferometry*. PhD Thesis, Delft University of Technology.

Kampes, B.M., 2006. *Radar Interferometry*, Springer Netherlands.

Koh, L.P., Miettinen, J., Liew, S.C. and Ghazoul, J., 2011. "Remotely Sensed Evidence of Tropical Peatland Conversion to Oil Palm." *Proceedings of the National Academy of Sciences of the United States of America*, 108(12), pp.5127–32.

Kornejady, A., Ownegh, M. and Bahremand, A., 2017. "Landslide Susceptibility Assessment Using Maximum Entropy Model with Two Different Data Sampling Methods." *Catena*, 152, pp.144–162.

Kouba, J., 2003. "Measuring Seismic Waves Induced by Large Earthquakes with GPS." *Studia Geophysica et Geodaetica*, 47(4), pp.741–755.

Kouba, J., 2008. "Implementation and Testing of the Gridded Vienna Mapping Function 1 (VMF1)." *Journal of Geodesy*, 82(2008), pp.193–205.

Kouba, J., 2009a. "Testing of Global Pressure / Temperature (GPT) Model and Global Mapping Function (GMF) in GPS Analyses." *Journal of Geodesy*, 83(3–4), pp.199–208.

Kouba, J., 2009b. "A Guide to Using International GNSS Service (IGS) Products." *Geodetic Survey Division Natural Resources Canada Ottawa*, 6, p.34.

Kuehn, F., Albiol, D., Cooksley, G., Duro, J., Granda, J., Haas, S., Hoffmann-Rothe, A. and Murdohardono, D., 2010. "Detection of Land Subsidence in Semarang, Indonesia, Using Stable Points Network (SPN) Technique." *Environmental Earth Sciences*, 60(5), pp.909–921.

Kumaran, S., 2014. *Peat Resource Management in Peninsular Malaysia: Connections between Policy and Practice*. PhD Thesis, Charles Darwin University.

Lagios, E., Papadimitriou, P., Novali, F., Sakkas, V., Fumagalli, A., Vlachou, K. and Del Conte, S., 2012. "Combined Seismicity Pattern Analysis, DGPS and PSInSAR Studies in the Broader Area of Cephalonia (Greece)." *Tectonophysics*, 524–525, pp.43–58.

Lagler, K., Schindelegger, M., Böhm, J., Krásná, H. and Nilsson, T., 2013. "GPT2: Empirical Slant Delay Model for Radio Space Geodetic Techniques." *Geophysical Research Letters*, 40(6), pp.1069–1073.

Lanari, R., Berardino, P., Bonano, M., Casu, F., De Luca, C., Elefante, S., Fusco, A., Manunta, M., Manzo, M., Ojha, C., Pepe, A., Sansosti, E. and Zinno, I., 2015. "Sentinel-1 Results: SBAS-DInSAR Processing Chain Developments and Land Subsidence Analysis." In *2015 IEEE International Geoscience and Remote Sensing Symposium (IGARSS)*. IEEE, pp. 2836–2839.

Lanari, R., Berardino, P., Bonano, M., Casu, F., Manconi, A., Manunta, M., Manzo, M., Pepe, A., Pepe, S., Sansosti, E., Solaro, G., Tizzani, P. and Zeni, G., 2010. "Surface Displacements Associated with the L'Aquila 2009 Mw 6.3 Earthquake (Central Italy): New Evidence from SBAS-DInSAR Time Series Analysis." *Geophysical Research Letters*, 37(20).

Lanari, R., Lundgren, P. and Sansosti, E., 1998. "Dynamic Deformation of Etna Volcano Observed by Satellite Radar Interferometry." *Geophysical Research Letters*, 25(10), pp.1541–1544.

Lanari, R., Mora, O., Manunta, M., Mallorqui, J.J., Berardino, P. and Sansosti, E., 2004. "A Small-Baseline Approach for Investigating Deformations on Full-Resolution Differential SAR Interferograms." *IEEE Transactions on Geoscience and Remote Sensing*, 42(7), pp.1377–1386.

Langley, R.B., 2010. "Innovation: Accuracy versus Precision." *GPS World*. Available at: http://gpsworld.com/gnss-systemalgorithms-methodsinnovation-accuracy-versus-precision-9889/ [Accessed February 24, 2017].

Larson, K.M., 2003. "Using 1-Hz GPS Data to Measure Deformations Caused by the Denali Fault Earthquake." *Science*, 300(5624), pp.1421–1424.

Latif, Z.A., Aman, S.N.A. and Pradhan, B., 2012. "Landslide Susceptibility Mapping using LiDAR Derived Factors and Frequency Ratio Model: Ulu Klang Area, Malaysia." In *2012 IEEE 8th International Colloquium on Signal Processing and its Applications*. IEEE, pp. 378–382.

Latip, A.S.A., Matori, A., Aobpaet, A. and Din, A.H.M., 2015. "Monitoring of Offshore Platform Deformation with Stanford Method of Persistent Scatterer (StaMPS)." In *2015 International Conference on Space Science and Communication (IconSpace)*. IEEE, pp. 79–83.

Lee, M.L., Ng, K.Y., Huang, Y.F. and Li, W.C., 2014. "Rainfall-Induced Landslides in Hulu Kelang Area, Malaysia." *Natural Hazards*, 70(1), pp.353–375.

Leick, A., Rapoport, L. and Tatarnikov, D., 2015. *GPS Satellite Surveying* Fourth Edi., JohnWiley & Sons, Inc., Hoboken, New Jersey.

Leighton, J.M., 2010. *GPS and PSI Integration for Monitoring Urban Land Motion*. PhD Thesis, University of Nottingham.

Li, M., Li, W., Fang, R., Shi, C. and Zhao, Q., 2015. "Real-Time High-Precision Earthquake Monitoring using Single-Frequency GPS Receivers." *GPS Solutions*, 19(1), pp.27–35.

Li, Z., 2005. *Correction of Atmospheric Water Vapour Effects on Repeat-Pass SAR Interferometry Using GPS, MODIS and MERIS Data*. PhD thesis, University of London.

Li, Z., Chen, J. and Baltsavias, E., 2008. *Advances in Photogrammetry, Remote Sensing and Spatial Information Sciences: 2008 ISPRS Congress Book*, Taylor & Francis Group, London, UK.

Li, Z., Fielding, E.J., Cross, P. and Muller, J.-P., 2006a. "Interferometric Synthetic Aperture Radar Atmospheric Correction: GPS Topography-Dependent Turbulence Model." *Journal of Geophysical Research*, 111(B2), p.B02404.

Li, Z., Fielding, E.J., Cross, P. and Preusker, R., 2009. "Advanced InSAR Atmospheric Correction: MERIS / MODIS Combination and Stacked Water Vapour Models." *International Journal of Remote Sensing*, 30(13), pp.3343–3363.

Li, Z., Muller, J.-P. and Cross, P., 2005. "Interferometric Synthetic Aperture Radar (InSAR) Atmospheric Correction: GPS, Moderate Resolution Imaging Spectroradiometer (MODIS), and InSAR Integration." *Journal of Geophysical Research*, 110(B3), p.B03410.

Li, Z., Muller, J. -P., Cross, P., Albert, P., Fischer, J. and Bennartz, R., 2006b. "Assessment of the Potential of MERIS Near-Infrared Water Vapour Products to Correct ASAR Interferometric Measurements." *International Journal of Remote Sensing*, 27(2), pp.349–365.

Li, Z.W., Xu, W.B., Feng, G.C., Hu, J., Wang, C.C., Ding, X.L. and Zhu, J.J., 2012. "Correcting Atmospheric Effects on InSAR with MERIS Water Vapour Data and Elevation-Dependent Interpolation Model." *Geophysical Journal International*, 189(2), pp.898–910.

Liu, P., Li, Z., Hoey, T., Kincal, C., Zhang, J., Zeng, Q. and Muller, J.P., 2012. "Using Advanced InSAR Time Series Techniques to Monitor Landslide Movements in Badong of the Three Gorges Region, China." *International Journal of Applied Earth Observation and Geoinformation*, 21(1), pp.253–264.

López-Quiroz, P., Doin, M.P., Tupin, F., Briole, P. and Nicolas, J.M., 2009. "Time Series Analysis of Mexico City Subsidence Constrained by Radar Interferometry." *Journal of Applied Geophysics*, 69(1), pp.1–15.

Luan, I.O.B., 2010. "Singapore Water Management Policies and Practices." *International Journal of Water Resources Development*, 26(1), pp.65–80.

Lydolph, P.E., 1985. *The Climate of the Earth*, Rowman & Littlefield Publishers.

Mao, A., Harrison, C.G.A. and Dixon, T.H., 1999. "Noise in GPS Coordinate Time Series." *Journal of Geophysical Research: Solid Earth*, 104(B2), pp.2797–2816.

Marfai, M.A. and King, L., 2007. "Monitoring Land Subsidence in Semarang, Indonesia." *Environmental Geology*, 53(3), pp.651–659.

Marini, J.W., 1972. "Correction of Satellite Tracking Data for An Arbitrary Tropospheric Profile." *Radio Sci*, 7(2), pp.223–231.

Markus Rothacer, 1992. *Geodätisch-geophysikalische Arbeiten in der Schweiz*, Schweizerische Geodätische Kommission, Institut für Geodäsie und Photogrammetrie, Eidg. Technische Hochschule Zürich, Zürich.

Martins, T., Oka-Fiori, C., Vieira, B.C. and Montgomery, D.., 2016. "Assessment of Lidar-Derived DTMs for Landslide Susceptibility Mapping: Application in the Brazilian Subtropical Forest." *Landslides and Engineered Slopes. Experience, Theory and Practice*, pp.1389–1392.

Massonnet, D. and Feigl, K.L., 1998. "Radar Interferometry and Its Application to Changes in the Earth's Surface." *Reviews of Geophysics*, 36(4), pp.441–500.

Massonnet, D., Briole, P. and Arnaud, A., 1995. "Deflation of Mount Etna Monitored by Spaceborne Radar Interferometry." *Nature, Vol.375, pp.567-570*.

Massonnet, D., Feigl, K., Rossi, M. and Adragna, F., 1994. "Radar Interferometric Mapping of Deformation in the Year After the Landers Earthquake." *Nature*, 369(6477), pp.227–230.

Massonnet, D., Feigl, K.L., Vadon, H. and Rossi, M., 1996. "Coseismic Deformation Field of the M=6.7 Northridge, California Earthquake of January 17, 1994 Recorded by Two Radar Satellites using Interferometry." *Geophysical Research Letters*, 23(9), pp.969–972.

Massonnet, D., Rossi, M., Carmona, C., Adragna, F., Peltzer, G., Feigi, K. and Rabaute, T., 1993. "The Displacement Field of the Landers Earthquake Mapped by Radar Interferometry." *Nature, Vol. 364, pp. 138-142*.

Matori, A.N., Basith, A. and Harahap, I.S.H., 2012. "Study of Regional Monsoonal Effects on Landslide Hazard Zonation in Cameron Highlands, Malaysia." *Arabian Journal of Geosciences*, 5(5), pp.1069–1084.

McCarthy, D.D., 1996. *IERS Standards 1996*, IERS Technical Note 21, Observatoire de Paris, Paris.

McCauley, J.F., Schaber, G.G., Breed, C.S., Grolier, M.J., Haynes, C. V., Issawi, B., Elachi, C. and Blom, R., 1982. "Subsurface Valleys and Geoarcheology of the Eastern Sahara Revealed by Shuttle Radar." *Science*, 218(4576), pp.1004–1020.

Meijaard, E., Wich, S., Ancrenaz, M. and Marshall, A.J., 2012. "Not by Science Alone: Why Orangutan Conservationists Must Think Outside the Box." *Annals of the New York Academy of Sciences*, 1249(1), pp.29–44.

Meindl, M., Schaer, S., Hugentobler, U. and Beutler, G., 2004. "Tropospheric Gradient Estimation at CODE: Results from Global Solutions." *Journal of the Meteorological Society of Japan*, 82(1B), pp.331–338.

Mendes, V.B., Madeira, J., Brum da Silveira, A., Trota, A., Elosegui, P. and Pagarete, J., 2013. "Present-Day Deformation in São Jorge Island, Azores, from Episodic GPS Measurements (2001–2011)." *Advances in Space Research*, 51(8), pp.1581–1592.

Meng, X., Dodson, A.H. and Roberts, G.W., 2007. "Detecting Bridge Dynamics with GPS and Triaxial Accelerometers." *Engineering Structures*, 29(11), pp.3178–3184.

Metzger, S. and Jónsson, S., 2014. "Plate Boundary Deformation in North Iceland During 1992–2009 Revealed by InSAR Time-Series Analysis and GPS." *Tectonophysics*, 634, pp.127–138.

Metzger, S., Jónsson, S. and Geirsson, H., 2011. "Locking Depth and Slip-Rate of the Húsavík Flatey Fault, North Iceland, Derived from Continuous GPS Data 2006-2010." *Geophysical Journal International*, 187(2), pp.564–576.

Metzger, S., Jonsson, S., Danielsen, G., Hreinsdottir, S., Jouanne, F., Giardini, D. and Villemin, T., 2013. "Present Kinematics of the Tjornes Fracture Zone, North Iceland, from Campaign and Continuous GPS Measurements." *Geophysical Journal International*, 192(2), pp.441–455.

Meyer, F., 2010. "A Review of Ionospheric Effects in Low-Frequency SAR-Signals, Correction Methods, and Performance Requirements." In *2010 IEEE International Geoscience and Remote Sensing Symposium*. IEEE, pp. 29–32.

Meyer, F.J. and Nicoll, J., 2008. "The Impact of the Ionosphere on Interferometric SAR Processing." In *IGARSS 2008 - 2008 IEEE International Geoscience and Remote Sensing Symposium*. IEEE, p. II-391-II-394.

Michel, G.W., Yu, Y.Q., Zhu, S.Y., Reigber, C., Becker, M., Reinhart, E., Simons, W., Ambrosius, B., Vigny, C., Chamot-Rooke, N., Le Pichon, X., Morgan, P. and Matheussen, S., 2001. "Crustal Motion and Block Behaviour in SE-Asia from GPS Measurements." *Earth and Planetary Science Letters*, 187(3–4), pp.239–244.

Miettinen, J. and Liew, S.C., 2010. "Degradation and Development of Peatlands in Peninsular Malaysia and in the Islands of Sumatra and Borneo Since 1990." *Land Degradation & Development*, pp.285–296.

Miettinen, J., Hooijer, A., Tollenaar, D., Page, S. and Malins, C., 2012. "Historical Analysis and Projection of Oil Palm Plantation Expansion on Peatland in Southeast Asia." *Indirect Effects of Biofuel Production*, pp.1–49.

Miettinen, J., Shi, C. and Liew, S.C., 2016. "Land Cover Distribution in the Peatlands of Peninsular Malaysia, Sumatra and Borneo in 2015 with Changes Since 1990." *Global Ecology and Conservation*, pp.67–78.

Milillo, P., Perissin, D., Lundgren, P. and Serio, C., 2015. "COSMO-SkyMed Very Short Repeat-Pass SAR Interferometry over Rural Areas: The VAL D'agri and Potenza Test Cases in Basilicata, Italy." In *2015 IEEE International Geoscience and Remote Sensing Symposium (IGARSS)*. IEEE, pp. 98–101.

Miranda, N., 2015. *Definition of the TOPS SLC Deramping Function for Products Generated by the S-1 IPF*, European Space Agency, COPE-GSEG-EOPG-TN-14-0025, Issue 1, Revision 2, 22 April 2015.

Mohanakumar, K., 2008. *Stratosphere Troposphere Interactions*, Dordrecht: Springer Netherlands.

Monti Guarnieri, A., 2003. "Using Topography Statistics to Help Phase Unwrapping." *IEE Proceedings - Radar, Sonar and Navigation*, 150(3), p.144.

Montillet, J., Szeliga, W.M., Melbourne, T.I., Flake, R.M. and Schrock, G., 2016. "Critical Infrastructure Monitoring with Global Navigation Satellite Systems." *Journal of Surveying Engineering*, (2004), p.4016014.

Morrison, K., Bennett, J.C. and Nolan, M., 2013. "Using DInSAR to Separate Surface and Subsurface Features." *IEEE Transactions on Geoscience and Remote Sensing*, 51(6), pp.3424–3430.

Morrogh-Bernard, H., Husson, S., Page, S.E. and Rieley, J.O., 2003. "Population Status of the Bornean Orang-Utan (Pongo Pygmaeus) in the Sebangau Peat Swamp Forest, Central Kalimantan, Indonesia." *Biological Conservation*, 110(1), pp.141–152.

Mosaic Mapping System Inc., 2001. "A White Paper on LIDAR Mapping." *Mosaic Mapping Systems Inc.*

Mousavi, Z., Walpersdorf, A., Walker, R.T., Tavakoli, F., Pathier, E., Nankali, H., Nilfouroushan, F. and Djamour, Y., 2013. "Global Positioning System Constraints on the Active Tectonics of NE Iran and the South Caspian Region." *Earth and Planetary Science Letters*, 377–378, pp.287–298.

Müller, M.D., Geiger, A., Kahle, H.-G., Veis, G., Billiris, H., Paradissis, D. and Felekis, S., 2013. "Velocity and Deformation Fields in the North Aegean Domain, Greece, and Implications for Fault Kinematics, Derived from GPS Data 1993–2009." *Tectonophysics*, 597–598, pp.34–49.

Munekane, H. and Boehm, J., 2010. "Numerical Simulation of Troposphere-Induced Errors in GPS-Derived Geodetic Time Series Over Japan." *Journal of Geodesy*, 84(7), pp.405–417.

Murakmi, S., Nishigaya, T., Tien, T.L., Sakai, N., Lateh, H.H. and Azizat, N., 2014. "Development of Historical Landslide Database in Peninsular Malaysia." In *2014 IEEE 2nd International Symposium on Telecommunication Technologies (ISTT)*. IEEE, pp. 149–153.

Murakami, S., Tien, T.L., Bte, R., Omar, C., Nishigaya, T., Aziza, N., Roslan, R., Baharuddin, I.N.Z., Lateh, H.H. and Sakai, N., 2014. "Landslides Hazard Map in Malay Peninsula by Using Historical Landslide Database and Related Information." *Journal of Civil Engineering Research*, 4(4(3A)), pp.54–58.

Nee, T.S., Tien, T.L. and Lateh, H., 2015. "A Comparison Between StaMPS Technique with TerraSAR-X Data and Theodolite Surveying on Land Deformation Monitoring (Case study: Gunung Pass)." In *2015 IEEE International Geoscience and Remote Sensing Symposium (IGARSS)*. IEEE, pp. 3544–3547.

New Straits Times, 2010. "Sea Level to Rise 13 cm in a Century." Available at: http://news.asiaone.com/News/AsiaOne+News/Malaysia/Story/A1Story20100723-228502.html [Accessed January 25, 2017].

Nicholls, R.J., 2004. "Coastal Flooding and Wetland Loss in the 21st Century: Changes Under the SRES Climate and Socio-Economic Scenarios." *Global Environmental Change*, 14(1), pp.69–86.

Nicholls, R.J. and Tol, R.S.J., 2006. "Impacts and Responses to Sea-Level Rise: A Global Analysis of the SRES Scenarios Over the Twenty-First Century." *Philosophical transactions. Series A, Mathematical, physical, and engineering sciences*, 364(1841), pp.1073–95.

Niell, A. E., 1996. "Global Mapping Functions for the Atmosphere Delay at Radio Wavelengths." *Journal of Geophysical Research*, 101, p.3227.

Ofeigsson, B.G., Hooper, A., Sigmundsson, F., Sturkell, E. and Grapenthin, R., 2011. "Deep Magma Storage at Hekla Volcano, Iceland, Revealed by InSAR Time Series Analysis." *Journal of Geophysical Research: Solid Earth*, 116(5), pp.1–15.

Ogundare, J.O., 2015. "Deformation Monitoring and Analysis: Geotechnical and Structural Techniques." In *Precision Surveying*. Hoboken, NJ, USA: John Wiley & Sons, Inc, pp. 377–440.

Onn, F. and Zebker, H.A., 2006. "Correction for Interferometric Synthetic Aperture Radar Atmospheric Phase Artifacts using Time Series of Zenith Wet Delay Observations from a GPS Network." *Journal of Geophysical Research*, 111(B9), p.B09102.

Osmanoğlu, B., Dixon, T.H., Wdowinski, S., Cabral-Cano, E. and Jiang, Y., 2011. "Mexico City Subsidence Observed with Persistent Scatterer InSAR." *International Journal of Applied Earth Observation and Geoinformation*, 13(2011), pp.1–12.

Osmanoğlu, B., Sunar, F., Wdowinski, S. and Cabral-Cano, E., 2016. "Time Series Analysis of InSAR Data: Methods and Trends." *ISPRS Journal of Photogrammetry and Remote Sensing*, 115, pp.90–102.

Ostini, L., 2012. *Analysis and Quality Assessment of GNSS-Derived Parameter Time Series*. The University of Bern.

Othman, Z., Wan, A.W.A. and Anuar, A., 2011. "Evaluating the Performance of GPS Survey Methods for Landslide Monitoring at Hillside Residential Area: Static vs Rapid Static." *Proceedings - 2011 IEEE 7th International Colloquium on Signal Processing and Its Applications, CSPA 2011*, pp.453–459.

Ozener, H., Yilmaz, O., Dogru, A., Turgut, B. and Gurkan, O., 2013. "GPS-Derived Velocity Field of the Iznik-Mekece Segment of the North Anatolian Fault Zone." *Journal of Geodynamics*, 67, pp.46–52.

Padfield, R., Waldron, S., Drew, S., Papargyrpoulou, E., Kumaran, S., Page, S., Gilvear, D., Armstrong, A., Evers, S., Williams, P., Zakaria, Z., Chin, S.Y., Balle Hansen, S., Campos-Arceiz, A., Latif, M.T., Sayok, A. and Tham, M.H., 2014. "Research Agendas for the Sustainable Management of Tropical Peatland in Malaysia." *Environmental Conservation*, pp.1–11.

Paillou, P., Reynard, B., Malézieux, J.M., Dejax, J., Heggy, E., Rochette, P., Reimold, W.U., Michel, P., Baratoux, D., Razin, P. and Colin, J.P., 2006. "An Extended Field of Crater-Shaped Structures in the Gilf Kebir Region, Egypt: Observations and Hypotheses About Their Origin." *Journal of African Earth Sciences*, 46(3), pp.281–299.

Parker, D.J., Fink, A., Janicot, S., Ngamini, J.-B., Douglas, M., Afiesimama, E., Agusti-Panareda, A., Beljaars, A., Dide, F., Diedhiou, A., Lebel, T., Polcher, J., Redelsperger, J.-L., Thorncroft, C. and Ato Wilson, G., 2008. "The Amma Radiosonde Program and its Implications for the Future of Atmospheric Monitoring Over Africa." *Bulletin of the American Meteorological Society*, 89(7), pp.1015–1027.

Paul, J., Rajendran, C.P., Lowry, A.R., Andrade, V. and Rajendran, K., 2012. "Andaman Postseismic Deformation Observations: Still Slipping after All These Years?" *Bulletin of the Seismological Society of America*, 102(1), pp.343–351.

Perissin, D. and Wang, T., 2012. "Repeat-Pass SAR Interferometry with Partially Coherent Targets." *IEEE Transactions on Geoscience and Remote Sensing*, 50(1), pp.271–280.

Petrov, L. and Boy, J.-P., 2004. "Study of the Atmospheric Pressure Loading Signal in Very Long Baseline Interferometry Observations." *Journal of Geophysical Research*, 109(B3), pp.1–14.

Phien-wej, N., Giao, P.H. and Nutalaya, P., 2006. "Land Subsidence in Bangkok, Thailand." *Engineering Geology*, 82(4), pp.187–201.

Pinel, V., Hooper, A., De la Cruz-Reyna, S., Reyes-Davila, G., Doin, M.P. and Bascou, P., 2011. "The Challenging Retrieval of the Displacement Field from InSAR Data for Andesitic Stratovolcanoes: Case Study of Popocatepetl and Colima Volcano, Mexico." *Journal of Volcanology and Geothermal Research*, 200(1–2), pp.49–61.

Pour, A.B. and Hashim, M., 2016. "Application of PALSAR-2 Remote Sensing Data for Landslide Hazard Mapping in Kelantan River Basin, Peninsular Malaysia." *International Archives of the Photogrammetry, Remote Sensing and Spatial Information Sciences - ISPRS Archives*, 41(July), pp.413–416.

Pradhan, B., 2010. "Remote Sensing and GIS-Based Landslide Hazard Analysis and Cross-Validation using Multivariate Logistic Regression Model on Three Test Areas in Malaysia." *Advances in Space Research*, 45(10), pp.1244–1256.

Pradhan, B. and Youssef, A.M., 2010. "Manifestation of Remote Sensing Data and GIS on Landslide Hazard Analysis Using Spatial-Based Statistical Models." *Arabian Journal of Geosciences*, 3(3), pp.319–326.

Pradhan, B., Oh, H.-J. and Buchroithner, M., 2010. "Weights-of-Evidence Model Applied to Landslide Susceptibility Mapping in A Tropical Hilly Area." *Geomatics, Natural Hazards and Risk*, 1(3), pp.199–223.

Prats-Iraola, P., Nannini, M., Scheiber, R., De Zan, F., Wollstadt, S., Minati, F., Costantini, M., Bucarelli, A., Borgstromc, S. and Walter, T., 2015. "Investigations with the Sentinel-1 Interferometric Wide Swath Mode." In *FRINGE 2015*. Frascati, Italy, pp. 3–4.

Pritt, M.D., 1996. "Phase Unwrapping by Means of Multigrid Techniques for Interferometric SAR." *IEEE Transactions on Geoscience and Remote Sensing*, 34(3), pp.728–738.

Puysségur, B., Michel, R. and Avouac, J.P., 2007. "Tropospheric Phase Delay in Interferometric Synthetic Aperture Radar Estimated from Meteorological Model and Multispectral Imagery." *Journal of Geophysical Research: Solid Earth*, 112(5).

Qiao, X., Yu, P., Nie, Z., Li, J., Wang, X., Kuzikov, S.I., Wang, Q. and Yang, S., 2017. "The Crustal Deformation Revealed by GPS and InSAR in the Northwest Corner of the Tarim Basin, Northwestern China." *Pure and Applied Geophysics*, 174(3), pp.1405–1423.

Qu, W., Lu, Z., Zhang, Q., Li, Z., Peng, J., Wang, Q., Drummond, J. and Zhang, M., 2014. "Kinematic Model of Crustal Deformation of Fenwei Basin, China Based on GPS Observations." *Journal of Geodynamics*, 75, pp.1–8.

Radzi, A.B.A. and Ismail, P.H.B., 2013. "Trend Analysis of Sea Level Rise for West Coast of Peninsular Malaysia (Lumut)." *International Conference on Emerging Trends in Engineering and Technology (ICETET'2013) Dec. 7-8, 2013 Patong Beach, Phuket (Thailand) Trend*, 3, pp.113–115.

Rahimi, Z., Mohd Shafri, H.Z., Othman, F. and Norman, M., 2017. "Effect of Tropospheric Models on Derived Precipitable Water Vapor over Southeast Asia." *Journal of Atmospheric and Solar-Terrestrial Physics*, 157–158(March 2016), pp.55–66.

Raja, N.B., Çiçek, I., Türkoğlu, N., Aydin, O. and Kawasaki, A., 2017. "Landslide Susceptibility Mapping of the Sera River Basin Using Logistic Regression Model." *Natural Hazards*, 85(3), pp.1323–1346.

Ray, J.R., Cannon, M.E. and Fenton, P.C., 1999. "Mitigation of Static Carrier-Phase Multipath Effects using Multiple Closely Spaced Antennas." *Navigation*, 46(3), pp.193–202.

Ray, R.D. and Ponte, R.M., 2003. "Barometric Tides from ECMWF Operational Analyses." *Annales Geophysicae*, 21(8), pp.1897–1910.

Rebischung, P., Altamimi, Z., Ray, J. and Garayt, B., 2016. "The IGS Contribution to ITRF2014." *Journal of Geodesy*, 90(7), pp.611–630.

Refice, A., Bovenga, F., Wasowski, J. and Guerriero, L., 2000. "Use of InSAR Data for Landslide Monitoring: A Case Study from Southern Italy." In *IGARSS 2000. IEEE 2000 International Geoscience and Remote Sensing Symposium. Taking the Pulse of the Planet: The Role of Remote Sensing in Managing the Environment. Proceedings (Cat. No.00CH37120)*. IEEE, pp. 2504–2506.

Resch, G.M., 1984. "Water Vapor Radiometry in Geodetic Applications." In *Geodetic Refraction*. Berlin, Heidelberg: Springer Berlin Heidelberg, pp. 53–84.

Rodriguez, E. and Martin, J.M., 1992. "Theory and Design of Interferometric Synthetic Aperture Radars." *IEE Proceedings F Radar and Signal Processing*, 139(2), p.147.

Rothacher, M., Springer, T.A., Schaer, S. and Beutler, G., 1998. "Processing Strategies for Regional GPS Networks." In pp. 93–100.

Rott, H. and Nagler, T., 2006. "The Contribution of Radar Interferometry to the Assessment of Landslide Hazards." *Advances in Space Research*, 37(4), pp.710–719.

Saastamoinen, J., 1973. "Contribution to the Theory of Atmospheric Refraction." *Bulletin Geodesique*, (107), pp.13–34.

Samsonov, S. and d'Oreye, N., 2012. "Multidimensional Time-Series Analysis of Ground Deformation from Multiple InSAR Data Sets Applied to Virunga Volcanic Province." *Geophysical Journal International*, 191(3), pp.1095–1108.

Samsonov, S.V., Tiampo, K.F. and Rundle, J.B., 2008. "Application of DInSAR-GPS Optimization for Derivation of Three-Dimensional Surface Motion of the Southern California Region Along the San Andreas Fault." *Computers & Geosciences*, 34(5), pp.503–514.

Sansosti, E., Casu, F., Manzo, M. and Lanari, R., 2010. "Space-Borne Radar Interferometry Techniques for the Generation of Deformation Time Series: An Advanced Tool for Earth's Surface Displacement Analysis." *Geophysical Research Letters*, 37(20), pp.1–9.

Sarkar, M.S.K., Begum, R.A., Pereira, J.J., Jaafar, A.H. and Saari, M.Y., 2014. "Impacts of and Adaptations to Sea Level Rise in Malaysia." *Asian Journal of Water, Environment and Pollution*, 11(2), pp.29–36.

Sato, M., Yamamoto, Y., Nishioka, T., Kodama, K., Mochizuki, N. and Tsunakawa, H., 2016. "Hydrostatic Pressure Effect on Magnetic Hysteresis Parameters of Pseudo-Single-Domain Magnetite." *Geochemistry, Geophysics, Geosystems*, 17(7), pp.2825–2834.

SBAS Ionospheric Working Group, 2010. "Effect of Ionospheric Scintillations on GNSS - A White Paper." *SBAS Ionospheric Working Group (Stanford University)*, pp.1–22.

Scheiber, R. and Moreira, A., 2000. "Coregistration of Interferometric SAR Images using Spectral Diversity." *IEEE Transactions on Geoscience and Remote Sensing*, 38(September), pp.2179–2191.

Schlögel, R., Doubre, C., Malet, J.-P. and Masson, F., 2015. "Landslide Deformation Monitoring with ALOS/PALSAR Imagery: A D-InSAR Geomorphological Interpretation Method." *Geomorphology*, 231, pp.314–330.

Schmid, R., Mader, G. and Herring, T., 2005. "From Relative to Absolute Antenna Phase Center Corrections." *IGS Workshop and Symposium*.

Schmid, R., Steigenberger, P., Gendt, G., Ge, M. and Rothacher, M., 2007. "Generation of a Consistent Absolute Phase-Center Correction Model for GPS Receiver and Satellite Antennas." *Journal of Geodesy*, 81(12), pp.781–798.

Shaaban, A.J., 2008. "Malaysian Experience in Fine Resolution Regional Climate Projection for Vulnerability Assessment and Adaptation in the Wake of Climate Change." In *UNFCCC Expert Meeting on Methods and Tools and on Data and Observations Under the Nairobi Work Programme on Impacts, Vulnerability and Adaptation to Climate Change*. Mexico City.

Shan-Long, K., 1991. *Optimization and Design of Deformation Monitoring Schemes*. PhD Thesis, University of New Brunswick.

Shao, Z., Zhan, W., Zhang, L. and Xu, J., 2016. "Analysis of the Far-Field Co-seismic and Post-seismic Responses Caused by the 2011 M W 9.0 Tohoku-Oki Earthquake." *Pure and Applied Geophysics*, 173(2), pp.411–424.

Shi, J., 2012. *Precise Point Positioning Integer Ambiguity Resolution with Decoupled Clocks*. PhD Thesis, University of Calgary.

Sillard, P. and Boucher, C., 2001. "A Review of Algebraic Constraints in Terrestrial Reference Frame Datum Definition." *Journal of Geodesy*, 75(2–3), pp.63–73.

Smith, E. and Weintraub, S., 1953. "The Constants in the Equation for Atmospheric Refractive Index at Radio Frequencies." *Proceedings of the IRE*, 41(8), pp.1035–1037.

Sowter, A., Bateson, L., Strange, P., Ambrose, K. and Syafiudin, M.F., 2013. "DInSAR Estimation of Land Motion using Intermittent Coherence with Application to the South Derbyshire and Leicestershire Coalfields." *Remote Sensing Letters*, 4(10), pp.979–987.

Sowter, A., Bin Che Amat, M., Cigna, F., Marsh, S., Athab, A. and Alshammari, L., 2016. "Mexico City Land Subsidence in 2014–2015 with Sentinel-1 IW TOPS: Results Using the Intermittent SBAS (ISBAS) Technique." *International Journal of Applied Earth Observation and Geoinformation*, 52, pp.230–242.

Stramondo, S., Tesauro, M., Briole, P., Sansosti, E., Salvi, S., Lanari, R., Anzidei, M., Baldi, P., Fornaro, G., Availone, A., Buongiorno, M.F. and Boschi, E., 1999. "The September 26, 1997 Colfiorito, Italy, Earthquakes: Modeled Coseismic Surface Displacement from SAR Interferometry and GPS." *Geophysical Research Letters*, 26(7), pp.883–886.

Sun, Q., Zhang, L., Ding, X.L., Hu, J., Li, Z.W. and Zhu, J.J., 2015. "Slope Deformation Prior To Zhouqu, China Landslide from InSAR Time Series Analysis." *Remote Sensing of Environment*, 156, pp.45–57.

Tang, F., Chen, Z. and Wu, H., 2012. "Application of GPS / InSAR Fusion Technology in Dynamic Monitoring of Mining Subsidence in Western Mining Areas." In *2012 2nd International Conference on Consumer Electronics, Communications and Networks (CECNet)*. IEEE, pp. 2420–2423.

Tang, P., Chen, F., Zhu, X. and Zhou, W., 2016. "Monitoring Cultural Heritage Sites with Advanced Multi-Temporal InSAR Technique: The Case Study of the Summer Palace." *Remote Sensing*, 8(5), p.432.

Teferle, F.N., 2003. *Strategies for Long-Term Monitoring of Tide Gauges using GPS*. PhD Thesis, University of Nottingham.

Tesmer, V., Boehm, J., Heinkelmann, R. and Schuh, H., 2007. "Effect of Different Tropospheric Mapping Functions on the TRF, CRF and Position Time-Series Estimated from VLBI." *Journal of Geodesy*, 81(6–8), pp.409–421.

Teunissen, P.J.G. and Khodabandeh, A., 2015. "Review and Principles of PPP-RTK Methods." *Journal of Geodesy*, 89(3), pp.217–240.

Thayer, G.D., 1974. "An Improved Equation for the Radio Refractive Index of Air." *Radio Science*, 9(10), pp.803–807.

The Star, 2015. "Six Squatter Houses Buried in Johor Landslide." Available at: http://www.thestar.com.my/news/nation/2015/06/29/squatter-houses-landslide-johor/ [Accessed January 25, 2017].

Tol, R.S.J., 2002a. "Estimates of the Damage Costs of Climate Change - Part I: Benchmark Estimate." *Environmental and Resource Economics*, 21(1), pp.47–73.

Tol, R.S.J., 2002b. "Estimates of the Damage Costs of Climate Change - Part II: Dynamic Estimates." *Environmental and Resource Economics*, 21(2), pp.135–160.

Tong, X. and Schmidt, D., 2016. "Active Movement of the Cascade Landslide Complex in Washington from A Coherence-Based InSAR Time Series Method." *Remote Sensing of Environment*, 186, pp.405–415.

Torres, R., Snoeij, P., Geudtner, D., Bibby, D., Davidson, M., Attema, E., Potin, P., Rommen, B., Floury, N., Brown, M., Traver, I.N., Deghaye, P., Duesmann, B., Rosich, B., Miranda, N., Bruno, C., L'Abbate, M., Croci, R., Pietropaolo, A., et al., 2012. "GMES Sentinel-1 Mission." *Remote Sensing of Environment*, 120(2012), pp.9–24.

Trần, Đ.T., Nguyễn, T.Y., Dương, C.C., Vy, Q.H., Zuchiewicz, W., Nguyễn, Q.C. and Nguyễn, V.N., 2013. "Recent Crustal Movements of Northern Vietnam from GPS Data." *Journal of Geodynamics*, 69, pp.5–10.

Tregoning, P. and van Dam, T., 2005. "Atmospheric Pressure Loading Corrections Applied to GPS Data at the Observation Level." *Geophysical Research Letters*, 32(22), pp.1–4.

Urquhart, L., Nievinski, F.G. and Santos, M.C., 2013. "Assessment of Troposphere Mapping Functions using Three-Dimensional Ray-Tracing." *GPS Solutions*, 18(3), pp.345–354.

USGS, 2016a. "Earthquake Glossary - Ring of Fire." Available at: http://earthquake.usgs.gov/learn/glossary/?termID=150 [Accessed February 23, 2017].

USGS, 2016b. "Historical Earthquakes and Statistics." Available at: https://www2.usgs.gov/faq/categories/9831/3342 [Accessed February 23, 2017].

van den Dool, H.M., Saha, S., Schemm, J. and Huang, J., 1997. "A Temporal Interpolation Method to Obtain Hourly Atmospheric Surface Pressure Tides in Reanalysis 1979-1995." *Journal of Geophysical Research: Atmospheres*, 102(D18), pp.22013–22024.

Van Nee, R.D.J., 1992. "Multipath Effects on GPS Code Phase Measurements." *Navigation*, 39(2), pp.177–190.

Vandam, T.M., Blewitt, G. and Heflin, M.B., 1994. "Atmospheric Pressure Loading Effects on Global Positioning System Coordinate Determinations." *Journal of Geophysical Research: Solid Earth*, 99(B12), pp.23939–23950.

Vernant, P., Nilforoushan, F., Hatzfeld, D., Abbassi, M.R., Vigny, C., Masson, F., Nankali, H., Martinod, J., Ashtiani, A., Bayer, R., Tavakoli, F. and Chéry, J., 2004. "Present-Day Crustal Deformation and Plate Kinematics in the Middle East Constrained by GPS Measurements in Iran and Northern Oman." *Geophysical Journal International*, 157(1), pp.381–398.

Vigny, C., Simons, W.J.F., Abu, S., Bamphenyu, R., Satirapod, C., Choosakul, N., Subarya, C., Socquet, A., Omar, K., Abidin, H.Z. and Ambrosius, B.A.C., 2005. "Insight Into the 2004 Sumatra-Andaman Earthquake from GPS Measurements in Southeast Asia." *Nature*, 436(7048), pp.201–6.

Wadge, G., Webley, P.W., James, I.N., Bingley, R., Dodson, A., Waugh, S., Veneboer, T., Puglisi, G., Mattia, M., Baker, D., Edwards, S.C., Edwards, S.J. and Clarke, P.J., 2002. "Atmospheric Models, GPS and InSAR Measurements of the Tropospheric Water Vapour Field over Mount Etna." *Geophysical Research Letters*, 29(19), p.1905.

Walters, R.J., Elliott, J.R., Li, Z. and Parsons, B., 2013. "Rapid Strain Accumulation on the Ashkabad Fault (Turkmenistan) from Atmosphere-Corrected InSAR." *Journal of Geophysical Research: Solid Earth*, 118(7), pp.3674–3690.

Walters, R.J., Parsons, B. and Wright, T.J., 2014. "Constraining Crustal Velocity Fields with InSAR for Eastern Turkey: Limits to the Block-Like Behavior of Eastern Anatolia." *Journal of Geophysical Research: Solid Earth*, 119(6), pp.5215–5234.

Wan, Y., Shen, Z.-K., Bürgmann, R., Sun, J. and Wang, M., 2017. "Fault Geometry and Slip Distribution of the 2008 Mw 7.9 Wenchuan, China Earthquake, Inferred from GPS and InSAR Measurements." *Geophysical Journal International*, 208(2), pp.748–766.

Wang, C., Ding, X., Shan, X., Zhang, L. and Jiang, M., 2012. "Slip Distribution of the 2011 Tohoku Earthquake Derived from Joint Inversion of GPS, InSAR and Seafloor GPS / Acoustic Measurements." *Journal of Asian Earth Sciences*, 57, pp.128–136.

Wang, T., Perissin, D., Liao, M. and Rocca, F., 2008. "Deformation Monitoring by Long Term D-InSAR Analysis in Three Gorges Area, China." In *IGARSS 2008 - 2008 IEEE International Geoscience and Remote Sensing Symposium*. IEEE, p. IV-5-IV-8.

Wang, T., Perissin, D., Rocca, F. and Liao, M.-S., 2010. "Three Gorges Dam Stability Monitoring with Time-Series InSAR Image Analysis." *Science China Earth Sciences*, 54(5), pp.720–732.

Wanwan Zhang, Yinghai Ke, Huili Gong, Lin Zhu and Beibei Chen, 2016. "Monitoring of Land Surface Deformation in Beijing with Time-Series InSAR Technique Based on Multi_Band InSAR data using RADARSAT-2 and TERRASAR-X." In *2016 4th International Workshop on Earth Observation and Remote Sensing Applications (EORSA)*. IEEE, pp. 260–264.

Wdowinski, S., Bock, Y., Zhang, J., Fang, P. and Genrich, J., 1997. "Southern California Permanent GPS Geodetic Array: Spatial Filtering of Daily Positions for Estimating Coseismic and Postseismic Displacements Induced by the 1992 Landers Earthquake." *Journal of Geophysical Research*, 102(97), pp.57–70.

Wegmüller, U., Werner, C., Strozzi, T., Wiesmann, A., Frey, O. and Santoro, M., 2015. "Sentinel-1 Support in the GAMMA Software." In *Proceedings of the Fringe 2015 Conference, ESA ESRIN, Frascati, Italy*. pp. 23–27.

Wells, D., Beck, N., Delikaraoglou, D., Kleusberg, A., Krakiwsky, E.J., Lachapelle, G., Langley, R.B., Nakiboglu, M., Schwarz, K.-P., Tranquilla, J.M. and Vanicek, P., 1986. *Guide to GPS Positioning*, Canadian GPS Associates, Fredericton, N.B., Canada.

Wen, Y., Li, Z., Xu, C., Ryder, I. and Brgmann, R., 2012. "Postseismic Motion After the 2001 Mw 7.8 Kokoxili Earthquake in Tibet Observed by InSAR Time Series." *Journal of Geophysical Research: Solid Earth*, 117(8), pp.1–15.

Werner, C., Wegmuller, U., Strozzi, T. and Wiesmann, A., 2003. "Interferometric Point Target Analysis for Deformation Mapping." In *IGARSS 2003. 2003 IEEE International Geoscience and Remote Sensing Symposium. Proceedings (IEEE Cat. No.03CH37477)*. IEEE, pp. 4362–4364.

Wicks, C.W., 2002. "Magmatic Activity Beneath the Quiescent Three Sisters Volcanic Center, Central Oregon Cascade Range, USA." *Geophysical Research Letters*, 29(7), pp.2–5.

Williams, S., Bock, Y. and Fang, P., 1998. "Integrated Satellite Interferometry: Tropospheric Noise, GPS Estimates and Implications for Interferometric Synthetic Aperture Radar Products." *Journal of Geophysical Research: Solid Earth*, 103(B11), pp.27051–27067.

Williams, S.D.P., 1995. *Current Motion on Faults of the San Andreas System in Central California Inferred from Recent GPS and Terrestrial Survey Measurements*. PhD Thesis, Durham University.

Woodhouse, I.H., 2005. *An Introduction to Microwave Remote Sensing*, Taylor and Francis, London.

Wösten, J.H.M., Ismail, A.B. and Van Wijk, A.L.M., 1997. "Peat Subsidence and Its Practical Implications: A Case Study in Malaysia." *Geoderma*, 78(1–2), pp.25–36.

Wright, P.A. and Stow, R.J., 1997. "Detection and Measurement of Mining Subsidence by SAR Interferometry." *IEEE Colloquium on Radar Interferometry (Digest No.: 1997/153), pp. 5/1 -5/6*.

Wright, T.J., 2002. "Remote Monitoring of the Earthquake Cycle using Satellite Radar Interferometry." *The Royal Society*, 360(1801), pp.2873–88.

Wright, T.J., Parsons, B.E. and Lu, Z., 2004. "Toward Mapping Surface Deformation in Three Dimensions Using InSAR." *Geophysical Research Letters*, 31(1), p.L01607.

Wu, J.T., Wu, S.C., Hajj, G.A., Bertiger, W.I. and Lichten, S.M., 1991. "Effects of Antenna Orientation on GPS Carrier Phase." In *Proceedings of the AAS/AIAA Astrodynamics Conference*. Durango, CO, United States, pp. 1647–1660.

Xu, Y.S., Ma, L., Du, Y.J. and Shen, S.L., 2012. "Analysis of Urbanisation-Induced Land Subsidence in Shanghai." *Natural Hazards*, 63(2), pp.1255–1267.

Xu, Y.S., Shen, S.L., Ren, D.J. and Wu, H.N., 2016. "Analysis of Factors in Land Subsidence in Shanghai: A View Based on A Strategic Environmental Assessment." *Sustainability (Switzerland)*, 8(6).

Yan, Y., Doin, M.-P., Lopez-Quiroz, P., Tupin, F., Fruneau, B., Pinel, V. and Trouve, E., 2012. "Mexico City Subsidence Measured by InSAR Time Series: Joint Analysis Using PS and SBAS Approaches." *IEEE Journal of Selected Topics in Applied Earth Observations and Remote Sensing*, 5(4), pp.1312–1326.

Yang, C., Zhang, Q., Xu, Q., Zhao, C., Peng, J. and Ji, L., 2016. "Complex Deformation Monitoring over the Linfen–Yuncheng Basin (China) with Time Series InSAR Technology." *Remote Sensing*, 8(4), p.284.

Yang, H., Omidalizarandi, M., Xu, X. and Neumann, I., 2017. "Terrestrial Laser Scanning Technology for Deformation Monitoring and Surface Modeling of Arch Structures." *Composite Structures*, 169, pp.173–179.

Yao, Y., Xu, C., Shi, J., Cao, N., Zhang, B. and Yang, J., 2015. "ITG: A New Global GNSS Tropospheric Correction Model." *Scientific Reports*, 5(10273), pp.1–9.

Yetkin, M. and Inal, C., 2015. "Optimal Design of Deformation Monitoring Networks Using the Global Optimization Methods." In H. Kutterer et al., eds. *The 1st International Workshop on the Quality of Geodetic Observation and Monitoring Systems (QuGOMS'11)*. International Association of Geodesy Symposia. Cham: Springer International Publishing, pp. 27–31.

Yi, T., Li, H. and Gu, M., 2013. "Recent Research and Applications of GPS-Based Monitoring Technology for High-Rise Structures." *Structural Control and Health Monitoring*, 20(5), pp.649–670.

Yigit, C.O., Coskun, M.Z., Yavasoglu, H., Arslan, A. and Kalkan, Y., 2016. "The Potential of GPS Precise Point Positioning Method for Point Displacement Monitoring: A Case Study." *Measurement*, 91, pp.398–404.

Yin, J., Yu, D. and Wilby, R., 2016. "Modelling the Impact of Land Subsidence on Urban Pluvial Flooding: A Case Study of Downtown Shanghai, China." *Science of the Total Environment*, 544(July 2011), pp.744–753.

Zebker, A., Rosen, P.A. and Hensley, S., 1997. "Atmospheric Effects in Interferometric Synthetic Aperture Radar Surface Deformation and Topographic Maps." *Journal of Geophysical Research*, 102, pp.7547–7563.

Zhang, J., Bock, Y., Johnson, H., Fang, P., Williams, S., Genrich, J., Wdowinski, S. and Behr, J., 1997. "Southern California Permanent GPS Geodetic Array: Error Analysis of Daily Position Estimates and Site Velocities." *Journal of Geophysical Research: Solid Earth*, 102(B8), pp.18035–18055.

Zhang, K., Hu, Y., Liu, G., Wu, F. and Deakin, R., 2005. "Deformation Monitoring and Analysis using Victorian Regional CORS Data." *Journal of Global Postioning Sysmtems*, 4(1–2), pp.129–138.

Zhu, B., Li, J., Chu, Z., Tang, W., Wang, B. and Li, D., 2016. "A Robust and Multi-Weighted Approach to Estimating Topographically Correlated Tropospheric Delays in Radar Interferograms." *Sensors*, 16(7), p.1078.

APPENDIX A

List of Publications and Potential Publications from This Research

Publication / Potential Publication	Status
Mexico City Land Subsidence in 2014-2015 with Sentinel-1 IW TOPS: Results using the Intermittent SBAS (ISBAS) Technique	Paper published in the International Journal of Applied Earth Observation and Geoinformation on 13 June 2016
Joint Analysis of GPS and InSAR to Support the Maintenance of Geodetic Infrastructure: A Feasibility Study in Johor, Malaysia	Paper submitted to FIG Congress 2018 (Istanbul, 6 - 11 May 2018)
Intermittent SBAS Ground Motion Analysis in Low Seismicity Areas: Case Studies in the Lancashire and Staffordshire Coalfields, UK	Poster presented at the Royal Astronomical Society - Specialist Discussion Meeting (London, 9 May 2014)
Application of GPS-Derived Troposphere Model from the Malaysia Real-Time Kinematic GNSS Network (MyRTKnet) to Support Atmospheric Modelling in Equatorial Region	Paper in preparation
Assessment of Long-Term Deformation in Johor, Malaysia using Global Positioning System (GPS) and Interferometric Synthetic Aperture Radar (InSAR)	Paper in preparation
Assessment of the Quality of Interferograms using Coefficient of the Interferogram Phase Differences (CIPD)	Join paper with the British Geological Survey in preparation
Implications of Plates Tectonic Motion to Relative Positioning in Johor using Malaysia Real-Time Kinematic GNSS Network (MyRTKnet)	Potential paper
Implementation of Tropospheric Correction and Outlier Rejection to Improve the Intermittent SBAS (ISBAS) Algorithm	Potential paper
Issues and Challenges in the Application of Sentinel-1 for Monitoring Land Changes in Johor, Malaysia	Potential paper

APPENDIX B

Example of Ambiguity Resolution Summary from Bernese Processing using DD

```
================================================================================
PART 6: AMBIGUITY RESOLUTION SUMMARY
================================================================================

================================================================================
 Code-Based Widelane (WL) Ambiguity Resolution (<6000 km)
================================================================================

 File     Sta1 Sta2    Length     Before     After    Res  Sys  Max/RMS L5    Receiver 1           Receiver 2
                        (km)    #Amb (mm)  #Amb (mm)  (%)       (L5 Cycles)
 ------------------------------------------------------------------------------------------------------------------------
 ALKT0010 ALIC KAT1   1043.680    55  0.0    19  0.3  65.5 G    0.145  0.074  LEICA GRX1200GGPRO   LEICA GRX1200+GNSS   #AR_WL
 BAJH0010 BAKO JHJY    949.429    50  0.0    10  0.2  80.0 G    0.148  0.077  LEICA GRX1200+GNSS   TRIMBLE 5700         #AR_WL
 CODV0010 COCO DGAV   2716.504    44  0.0     2  0.2  95.5 G    0.150  0.071  TRIMBLE NETR5        JPS EGGDT            #AR_WL
 COXM0010 COCO XMIS    984.535    52  0.0    11  0.3  78.8 G    0.166  0.092  TRIMBLE NETR5        LEICA GRX1200GGPRO   #AR_WL
 CUJH0010 CUSV JHJY   1393.405    44  0.0     2  0.3  95.5 G    0.180  0.071  TRIMBLE NETRS        TRIMBLE 5700         #AR_WL
 DAKT0010 DARW KAT1    202.319    65  0.0    16  0.1  75.4 G    0.146  0.054  LEICA GRX1200GGPRO   LEICA GRX1200+GNSS   #AR_WL
 GGKT0010 GUUG KAT1   3337.191    54  0.0    12  0.2  77.8 G    0.146  0.077  TRIMBLE NETR5        LEICA GRX1200+GNSS   #AR_WL
 GGTW0010 GUUG TWTF   2765.124    45  0.0     2  0.3  95.6 G    0.150  0.074  TRIMBLE NETR5        ASHTECH Z-XII3T      #AR_WL
 HYII0010 HYDE IISC    497.626    55  0.1    11  0.3  80.0 G    0.136  0.065  LEICA GRX1200GGPRO   ASHTECH UZ-12        #AR_WL
 HYLH0010 HYDE LHAZ   1856.740    55  0.0    15  0.3  72.7 G    0.148  0.073  LEICA GRX1200GGPRO   TPS E_GGD            #AR_WL
 HYPR0010 HYDE PRTS   3128.337    42  0.0     9  0.3  78.6 G    0.143  0.085  LEICA GRX1200GGPRO   TRIMBLE NETR5        #AR_WL
 KAXM0010 KARR XMIS   1682.678    48  0.0     8  0.2  83.3 G    0.131  0.059  TRIMBLE NETR8        LEICA GRX1200GGPRO   #AR_WL
 KAYA0010 KARR YAR2    909.905    45  0.0     2  0.3  95.6 G    0.135  0.062  TRIMBLE NETR8        ASHTECH UZ-12        #AR_WL
 KTXM0010 KAT1 XMIS   2883.353    50  0.0    13  0.1  74.0 G    0.097  0.045  LEICA GRX1200+GNSS   LEICA GRX1200GGPRO   #AR_WL
 NNYA0010 NNOR YAR2    236.453    49  0.0     4  0.2  91.8 G    0.111  0.054  ASHTECH Z-XII3       ASHTECH UZ-12        #AR_WL
 PITW0010 PIMO TWTF   1140.747    50  0.1     1  0.2  98.0 G    0.140  0.055  ASHTECH UZ-12        ASHTECH Z-XII3T      #AR_WL
 SHTW0010 SHAO TWTF    680.806    47  0.0     1  0.2  97.9 G    0.135  0.057  ASHTECH UZ-12        ASHTECH Z-XII3T      #AR_WL
 TRXM0010 TGRH XMIS   1396.151    50  0.0    11  0.3  78.0 G    0.140  0.080  TRIMBLE NETR5        LEICA GRX1200GGPRO   #AR_WL
 ------------------------------------------------------------------------------------------------------------------------
 Tot:  18             1544.721   900  0.0   149  0.2  83.4 G    0.180  0.069                                            #AR_WL

================================================================================
 Code-Based Narrowlane (NL) Ambiguity Resolution (<6000 km)
================================================================================

 File     Sta1 Sta2    Length     Before     After    Res  Sys  Max/RMS L1    Receiver 1           Receiver 2
                        (km)    #Amb (mm)  #Amb (mm)  (%)       (L1 Cycles)
 ------------------------------------------------------------------------------------------------------------------------
 ALKT0010 ALIC KAT1   1043.680    77  1.4    47  1.5  39.0 G    0.120  0.040  LEICA GRX1200GGPRO   LEICA GRX1200+GNSS   #AR_NL
 BAJH0010 BAKO JHJY    949.429    60  1.7    29  1.7  51.7 G    0.135  0.046  LEICA GRX1200+GNSS   TRIMBLE 5700         #AR_NL
 CODV0010 COCO DGAV   2716.504    44  2.1     9  2.1  79.5 G    0.131  0.058  TRIMBLE NETR5        JPS EGGDT            #AR_NL
 COXM0010 COCO XMIS    984.535    52  1.7    15  1.9  71.2 G    0.148  0.068  TRIMBLE NETR5        LEICA GRX1200GGPRO   #AR_NL
 CUJH0010 CUSV JHJY   1393.405    44  1.5     4  1.6  90.9 G    0.140  0.054  TRIMBLE NETRS        TRIMBLE 5700         #AR_NL
 DAKT0010 DARW KAT1    202.319    77  1.5    35  1.5  54.5 G    0.163  0.071  LEICA GRX1200GGPRO   LEICA GRX1200+GNSS   #AR_NL
 GGKT0010 GUUG KAT1   3337.191    56  1.5    20  1.6  64.3 G    0.138  0.069  TRIMBLE NETR5        LEICA GRX1200+GNSS   #AR_NL
 GGTW0010 GUUG TWTF   2765.124    47  1.3     9  1.3  80.9 G    0.145  0.058  TRIMBLE NETR5        ASHTECH Z-XII3T      #AR_NL
 HYII0010 HYDE IISC    497.626    61  1.2    20  1.3  67.2 G    0.131  0.059  LEICA GRX1200GGPRO   ASHTECH UZ-12        #AR_NL
 HYLH0010 HYDE LHAZ   1856.740    56  1.0    17  1.1  69.6 G    0.111  0.044  LEICA GRX1200GGPRO   TPS E_GGD            #AR_NL
 HYPR0010 HYDE PRTS   3128.337    42  1.8    12  1.9  71.4 G    0.147  0.074  LEICA GRX1200GGPRO   TRIMBLE NETR5        #AR_NL
 KAXM0010 KARR XMIS   1682.678    49  1.7    15  1.7  69.4 G    0.141  0.066  TRIMBLE NETR8        LEICA GRX1200GGPRO   #AR_NL
 KAYA0010 KARR YAR2    909.905    46  1.4     5  1.5  89.1 G    0.144  0.045  TRIMBLE NETR8        ASHTECH UZ-12        #AR_NL
 KTXM0010 KAT1 XMIS   2883.353    50  1.7    19  1.7  62.0 G    0.160  0.062  LEICA GRX1200+GNSS   LEICA GRX1200GGPRO   #AR_NL
 NNYA0010 NNOR YAR2    236.453    50  1.1     7  1.2  86.0 G    0.126  0.042  ASHTECH Z-XII3       ASHTECH UZ-12        #AR_NL
 PITW0010 PIMO TWTF   1140.747    50  1.0     3  1.0  94.0 G    0.130  0.042  ASHTECH UZ-12        ASHTECH Z-XII3T      #AR_NL
 SHTW0010 SHAO TWTF    680.806    49  1.0     4  1.0  91.8 G    0.068  0.022  ASHTECH UZ-12        ASHTECH Z-XII3T      #AR_NL
 TRXM0010 TGRH XMIS   1396.151    51  1.9    21  2.0  58.8 G    0.167  0.069  TRIMBLE NETR5        LEICA GRX1200GGPRO   #AR_NL
 ------------------------------------------------------------------------------------------------------------------------
 Tot:  18             1544.721   961  1.5   291  1.6  69.7 G    0.167  0.056                                            #AR_NL

================================================================================
 Phase-Based Widelane (L5) Ambiguity Resolution (<200 km)
================================================================================

 File     Sta1 Sta2    Length     Before     After    Res  Sys  Max/RMS L5    Receiver 1           Receiver 2
                        (km)    #Amb (mm)  #Amb (mm)  (%)       (L5 Cycles)
 ------------------------------------------------------------------------------------------------------------------------
 GAJH0010 GAJA JHJY     76.949    43  3.5     1  3.7  97.7 G    0.123  0.042  TRIMBLE 5700         TRIMBLE 5700         #AR_L5
 JHKU0010 JHJY KUKP     44.321    43  2.4     0  2.7 100.0 G    0.074  0.024  TRIMBLE 5700         TRIMBLE 5700         #AR_L5
 JHTG0010 JHJY TGPG     39.424    43  2.1     1  2.2  97.7 G    0.053  0.018  TRIMBLE 5700         TRIMBLE 5700         #AR_L5
 JHTR0010 JHJY TGRH     62.315    43  3.5     0  3.8 100.0 G    0.097  0.042  TRIMBLE 5700         TRIMBLE NETR5        #AR_L5
 NNPE0010 NNOR PERT     88.485    53  3.6     2  3.9  96.2 G    0.143  0.043  ASHTECH Z-XII3       ASHTECH UZ-12        #AR_L5
 NTSP0010 NTUS SPGR     65.093    46  2.8     9  2.9  80.4 G    0.072  0.028  LEICA GRX1200GGPRO   TRIMBLE NETR5        #AR_L5
 NTSP0010 NTUS SPGR     65.093    47  2.8    20  2.9  57.4  R    0.134  0.060  LEICA GRX1200GGPRO   TRIMBLE NETR5        #AR_L5
 NTSP0010 NTUS SPGR     65.093    93  2.8    29  2.9  68.8 GR    0.134  0.044  LEICA GRX1200GGPRO   TRIMBLE NETR5        #AR_L5
 PRSP0010 PRTS SPGR     53.294    47  2.4     1  2.5  97.9 G    0.094  0.027  TRIMBLE NETR5        TRIMBLE NETR5        #AR_L5
 PRSP0010 PRTS SPGR     53.294    42  2.4    11  2.5  73.8  R    0.130  0.039  TRIMBLE NETR5        TRIMBLE NETR5        #AR_L5
 PRSP0010 PRTS SPGR     53.294    89  2.4    12  2.5  86.5 GR    0.130  0.033  TRIMBLE NETR5        TRIMBLE NETR5        #AR_L5
 SPTR0010 SPGR TGRH     75.731    46  3.3     0  3.6 100.0 G    0.148  0.048  TRIMBLE NETR5        TRIMBLE NETR5        #AR_L5
 SPTR0010 SPGR TGRH     75.731    37  3.3    11  3.6  70.3  R    0.111  0.043  TRIMBLE NETR5        TRIMBLE NETR5        #AR_L5
 SPTR0010 SPGR TGRH     75.731    83  3.3    11  3.6  86.7 GR    0.148  0.046  TRIMBLE NETR5        TRIMBLE NETR5        #AR_L5
 ------------------------------------------------------------------------------------------------------------------------
 Tot:   8               63.202   364  3.0    14  3.2  96.2 G    0.148  0.036                                            #AR_L5
 Tot:   3               64.706   126  2.9    42  3.0  66.7  R    0.134  0.048                                            #AR_L5
 Tot:   8               63.202   490  3.0    56  3.2  88.6 GR    0.148  0.039                                            #AR_L5
```

Phase-Based Narrowlane (L3) Ambiguity Resolution (<200 km)

File	Sta1	Sta2	Length (km)	Before #Amb	Before (mm)	After #Amb	After (mm)	Res (%)	Sys	Max/RMS L1 (L1 Cycles)		Receiver 1	Receiver 2	
GAJH0010	GAJA	JHJY	76.949	43	1.7	3	1.8	93.0	G	0.134	0.046	TRIMBLE 5700	TRIMBLE 5700	#AR_L3
JHKU0010	JHJY	KUKP	44.321	43	2.0	3	2.1	93.0	G	0.135	0.058	TRIMBLE 5700	TRIMBLE 5700	#AR_L3
JHTG0010	JHJY	TGPG	39.424	43	1.8	3	1.8	93.0	G	0.145	0.044	TRIMBLE 5700	TRIMBLE 5700	#AR_L3
JHTR0010	JHJY	TGRH	62.315	43	1.9	2	2.0	95.3	G	0.179	0.073	TRIMBLE 5700	TRIMBLE NETR5	#AR_L3
NNPE0010	NNOR	PERT	88.485	53	1.2	7	1.3	86.8	G	0.144	0.042	ASHTECH Z-XII3	ASHTECH UZ-12	#AR_L3
NTSP0010	NTUS	SPGR	65.093	46	1.8	13	1.8	71.7	G	0.111	0.052	LEICA GRX1200GGPRO	TRIMBLE NETR5	#AR_L3
NTSP0010	NTUS	SPGR	65.093	47	1.8	26	1.8	44.7	R	0.130	0.074	LEICA GRX1200GGPRO	TRIMBLE NETR5	#AR_L3
NTSP0010	NTUS	SPGR	65.093	93	1.8	39	1.8	58.1	GR	0.130	0.061	LEICA GRX1200GGPRO	TRIMBLE NETR5	#AR_L3
PRSP0010	PRTS	SPGR	53.294	47	2.0	3	2.0	93.6	G	0.139	0.062	TRIMBLE NETR5	TRIMBLE NETR5	#AR_L3
PRSP0010	PRTS	SPGR	53.294	42	2.0	14	2.0	66.7	R	0.150	0.073	TRIMBLE NETR5	TRIMBLE NETR5	#AR_L3
PRSP0010	PRTS	SPGR	53.294	89	2.0	17	2.0	80.9	GR	0.150	0.066	TRIMBLE NETR5	TRIMBLE NETR5	#AR_L3
SPTR0010	SPGR	TGRH	75.731	46	1.9	5	2.0	89.1	G	0.144	0.055	TRIMBLE NETR5	TRIMBLE NETR5	#AR_L3
SPTR0010	SPGR	TGRH	75.731	37	1.9	14	2.0	62.2	R	0.112	0.066	TRIMBLE NETR5	TRIMBLE NETR5	#AR_L3
SPTR0010	SPGR	TGRH	75.731	83	1.9	19	2.0	77.1	GR	0.144	0.059	TRIMBLE NETR5	TRIMBLE NETR5	#AR_L3
Tot:	8		63.202	364	1.8	39	1.9	89.3	G	0.179	0.055			#AR_L3
Tot:	3		64.706	126	1.9	54	1.9	57.1	R	0.150	0.071			#AR_L3
Tot:	8		63.202	490	1.8	93	1.9	81.0	GR	0.179	0.058			#AR_L3

Quasi-Ionosphere-Free (QIF) Ambiguity Resolution (<2000 km)

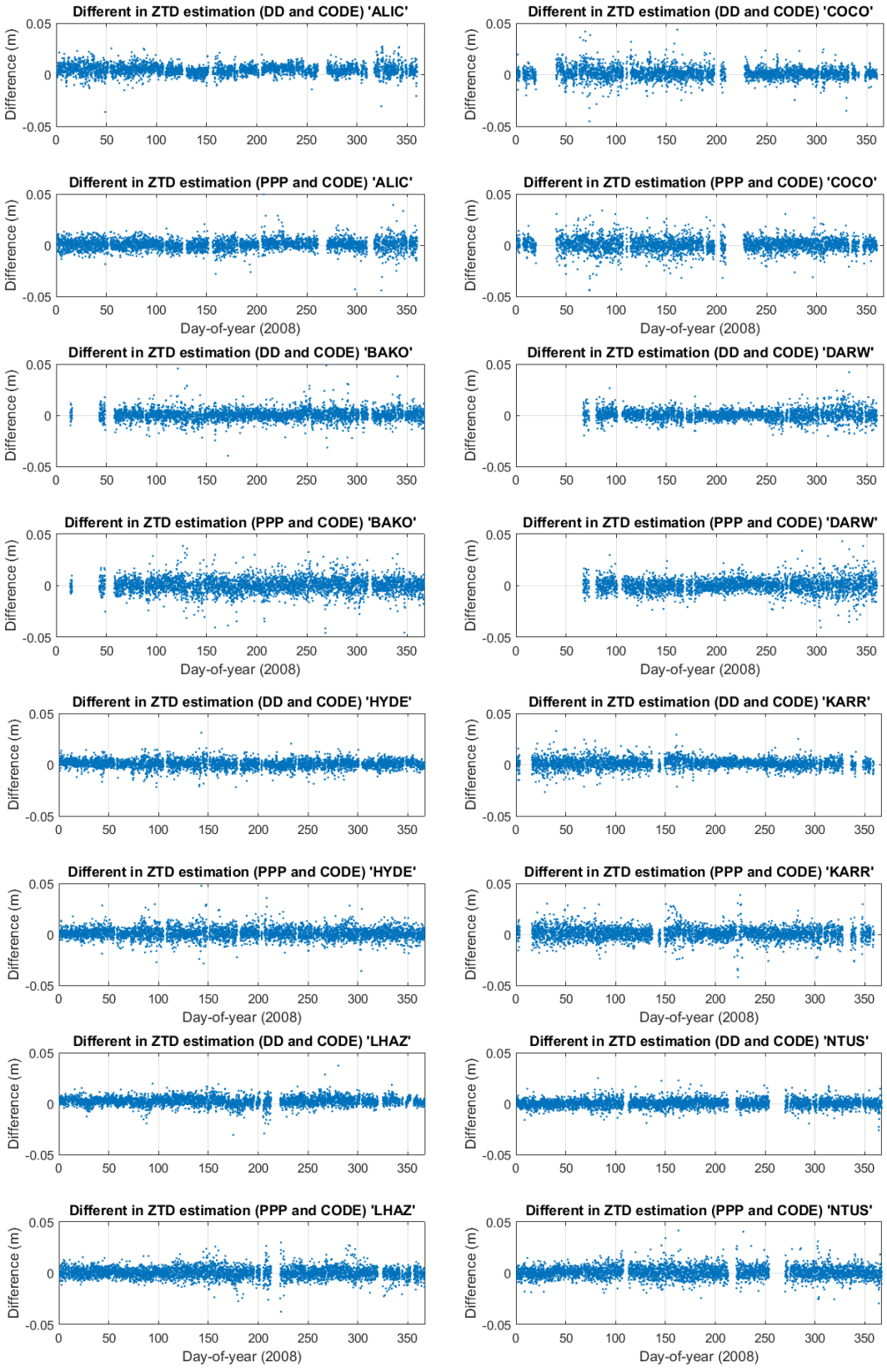
File	Sta1	Sta2	Length (km)	Before #Amb	Before (mm)	After #Amb	After (mm)	Res (%)	Sys	Max/RMS L5 (L5 Cycles)		Max/RMS L3 (L3 Cycles)		Receiver 1	Receiver 2	
ALKT0010	ALIC	KAT1	1043.680	94	2.1	94	2.1	0.0	G	0.000	0.000	0.000	0.000	LEICA GRX1200GGPRO	LEICA GRX1200+GNSS	#AR_QIF
ALKT0010	ALIC	KAT1	1043.680	74	2.1	48	2.1	35.1	R	0.470	0.191	0.100	0.039	LEICA GRX1200GGPRO	LEICA GRX1200+GNSS	#AR_QIF
ALKT0010	ALIC	KAT1	1043.680	168	2.1	142	2.1	15.5	GR	0.470	0.191	0.100	0.039	LEICA GRX1200GGPRO	LEICA GRX1200+GNSS	#AR_QIF
BAJH0010	BAKO	JHJY	949.429	58	2.3	54	2.3	6.9	G	0.454	0.284	0.094	0.047	LEICA GRX1200+GNSS	TRIMBLE 5700	#AR_QIF
COXM0010	COCO	XMIS	984.535	30	2.1	28	2.1	6.7	G	0.324	0.229	0.092	0.065	TRIMBLE NETR5	LEICA GRX1200GGPRO	#AR_QIF
COXM0010	COCO	XMIS	984.535	70	2.1	50	2.1	28.6	R	0.389	0.130	0.080	0.035	TRIMBLE NETR5	LEICA GRX1200GGPRO	#AR_QIF
COXM0010	COCO	XMIS	984.535	100	2.1	78	2.1	22.0	GR	0.389	0.142	0.092	0.039	TRIMBLE NETR5	LEICA GRX1200GGPRO	#AR_QIF
CUJH0010	CUSV	JHJY	1393.405	8	2.1	6	2.1	25.0	G	0.395	0.279	0.088	0.062	TRIMBLE NETRS	TRIMBLE 5700	#AR_QIF
DAKT0010	DARW	KAT1	202.319	72	1.8	72	1.8	0.0	G	0.000	0.000	0.000	0.000	LEICA GRX1200GGPRO	LEICA GRX1200+GNSS	#AR_QIF
DAKT0010	DARW	KAT1	202.319	158	1.8	138	1.8	12.7	R	0.472	0.196	0.083	0.028	LEICA GRX1200GGPRO	LEICA GRX1200+GNSS	#AR_QIF
DAKT0010	DARW	KAT1	202.319	230	1.8	210	1.8	8.7	GR	0.472	0.196	0.083	0.028	LEICA GRX1200GGPRO	LEICA GRX1200+GNSS	#AR_QIF
GAJH0010	GAJA	JHJY	76.949	6	1.9	6	1.9	0.0	G	0.000	0.000	0.000	0.000	TRIMBLE 5700	TRIMBLE 5700	#AR_QIF
HYII0010	HYDE	IISC	497.626	40	2.0	38	2.0	5.0	G	0.079	0.056	0.070	0.049	LEICA GRX1200GGPRO	ASHTECH UZ-12	#AR_QIF
HYLH0010	HYDE	LHAZ	1856.740	36	2.2	36	2.2	0.0	G	0.000	0.000	0.000	0.000	LEICA GRX1200GGPRO	TPS E_GGD	#AR_QIF
HYLH0010	HYDE	LHAZ	1856.740	74	2.2	66	2.2	10.8	R	0.317	0.156	0.091	0.055	LEICA GRX1200GGPRO	TPS E_GGD	#AR_QIF
HYLH0010	HYDE	LHAZ	1856.740	110	2.2	102	2.2	7.3	GR	0.317	0.156	0.091	0.055	LEICA GRX1200GGPRO	TPS E_GGD	#AR_QIF
JHKU0010	JHJY	KUKP	44.321	6	2.3	6	2.3	0.0	G	0.000	0.000	0.000	0.000	TRIMBLE 5700	TRIMBLE 5700	#AR_QIF
JHTG0010	JHJY	TGPG	39.424	6	2.0	6	2.0	0.0	G	0.000	0.000	0.000	0.000	TRIMBLE 5700	TRIMBLE 5700	#AR_QIF
JHTR0010	JHJY	TGRH	62.315	4	2.2	4	2.2	0.0	G	0.000	0.000	0.000	0.000	TRIMBLE 5700	TRIMBLE NETR5	#AR_QIF
KAXM0010	KARR	XMIS	1682.678	30	2.3	30	2.3	0.0	G	0.000	0.000	0.000	0.000	TRIMBLE NETR8	LEICA GRX1200GGPRO	#AR_QIF
KAYA0010	KARR	YAR2	909.905	10	1.7	8	1.7	20.0	G	0.240	0.170	0.003	0.002	TRIMBLE NETR8	ASHTECH UZ-12	#AR_QIF
NNPE0010	NNOR	PERT	88.485	14	1.4	14	1.4	0.0	G	0.000	0.000	0.000	0.000	ASHTECH Z-XII3	ASHTECH UZ-12	#AR_QIF
NNYA0010	NNOR	YAR2	236.453	14	1.3	12	1.3	14.3	G	0.008	0.006	0.048	0.034	ASHTECH Z-XII3	ASHTECH UZ-12	#AR_QIF
NTSP0010	NTUS	SPGR	65.093	26	1.9	26	1.9	0.0	G	0.000	0.000	0.000	0.000	LEICA GRX1200GGPRO	TRIMBLE NETR5	#AR_QIF
NTSP0010	NTUS	SPGR	65.093	52	1.9	52	1.9	0.0	R	0.000	0.000	0.000	0.000	LEICA GRX1200GGPRO	TRIMBLE NETR5	#AR_QIF
NTSP0010	NTUS	SPGR	65.093	78	1.9	78	1.9	0.0	GR	0.000	0.000	0.000	0.000	LEICA GRX1200GGPRO	TRIMBLE NETR5	#AR_QIF
PITW0010	PIMO	TWTF	1140.747	6	2.8	4	2.8	33.3	G	0.216	0.153	0.025	0.018	ASHTECH UZ-12	ASHTECH Z-XII3T	#AR_QIF
PRSP0010	PRTS	SPGR	53.294	6	2.1	6	2.1	0.0	G	0.000	0.000	0.000	0.000	TRIMBLE NETR5	TRIMBLE NETR5	#AR_QIF
PRSP0010	PRTS	SPGR	53.294	28	2.1	28	2.1	0.0	R	0.000	0.000	0.000	0.000	TRIMBLE NETR5	TRIMBLE NETR5	#AR_QIF
PRSP0010	PRTS	SPGR	53.294	34	2.1	34	2.1	0.0	GR	0.000	0.000	0.000	0.000	TRIMBLE NETR5	TRIMBLE NETR5	#AR_QIF
SHTW0010	SHAO	TWTF	680.806	8	2.6	8	2.6	0.0	G	0.000	0.000	0.000	0.000	ASHTECH UZ-12	ASHTECH Z-XII3T	#AR_QIF
SPTR0010	SPGR	TGRH	75.731	10	2.1	10	2.1	0.0	G	0.000	0.000	0.000	0.000	TRIMBLE NETR5	TRIMBLE NETR5	#AR_QIF
SPTR0010	SPGR	TGRH	75.731	28	2.1	28	2.1	0.0	R	0.000	0.000	0.000	0.000	TRIMBLE NETR5	TRIMBLE NETR5	#AR_QIF
SPTR0010	SPGR	TGRH	75.731	38	2.1	38	2.1	0.0	GR	0.000	0.000	0.000	0.000	TRIMBLE NETR5	TRIMBLE NETR5	#AR_QIF
TRXM0010	TGRH	XMIS	1396.151	42	2.3	40	2.3	4.8	G	0.168	0.119	0.014	0.010	TRIMBLE NETR5	LEICA GRX1200GGPRO	#AR_QIF
TRXM0010	TGRH	XMIS	1396.151	92	2.3	84	2.3	8.7	R	0.443	0.216	0.093	0.049	TRIMBLE NETR5	LEICA GRX1200GGPRO	#AR_QIF
TRXM0010	TGRH	XMIS	1396.151	134	2.3	124	2.3	7.5	GR	0.443	0.201	0.093	0.044	TRIMBLE NETR5	LEICA GRX1200GGPRO	#AR_QIF
Tot:	21		641.909	526	2.1	508	2.1	3.4	G	0.454	0.200	0.094	0.043			#AR_QIF
Tot:	8		709.693	576	2.1	494	2.1	14.2	R	0.472	0.179	0.100	0.039			#AR_QIF
Tot:	21		641.909	1102	2.1	1002	2.1	9.1	GR	0.472	0.183	0.100	0.039			#AR_QIF

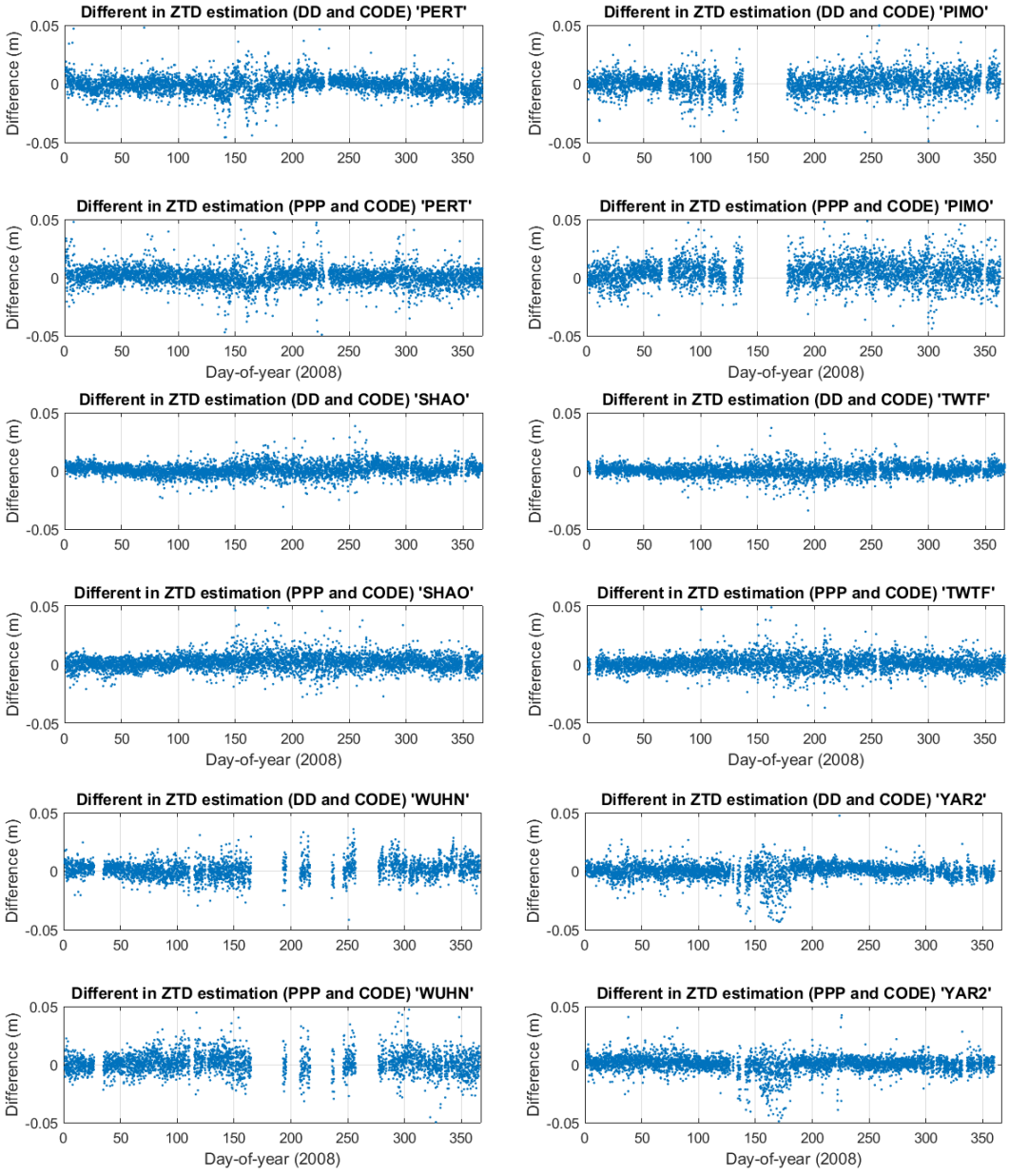
Direct L1/L2 Ambiguity Resolution (<20 km)

File	Sta1	Sta2	Length (km)	Before #Amb	Before (mm)	After #Amb	After (mm)	Res (%)	Sys	Max/RMS L1 (L1 Cycles)		Receiver 1	Receiver 2	
DGDV0010	DGAR	DGAV	0.000	82	0.5	0	0.5	100.0	G	0.005	0.001	ASHTECH UZ-12	JPS EGGDT	#AR_L12
Tot:	1		0.000	82	0.5	0	0.5	100.0	G	0.005	0.001			#AR_L12

APPENDIX C

Comparison between the Estimated ZTDs (PPP and DD) and the Published ZTDs from CODE




Different in ZTD estimation (DD and CODE) 'PERT'
Different in ZTD estimation (DD and CODE) 'PIMO'
Different in ZTD estimation (PPP and CODE) 'PERT'
Different in ZTD estimation (PPP and CODE) 'PIMO'
Different in ZTD estimation (DD and CODE) 'SHAO'
Different in ZTD estimation (DD and CODE) 'TWTF'
Different in ZTD estimation (PPP and CODE) 'SHAO'
Different in ZTD estimation (PPP and CODE) 'TWTF'
Different in ZTD estimation (DD and CODE) 'WUHN'
Different in ZTD estimation (DD and CODE) 'YAR2'
Different in ZTD estimation (PPP and CODE) 'WUHN'
Different in ZTD estimation (PPP and CODE) 'YAR2'
Difference (m)
0.05
0
-0.05
0
50
100
150
200
250
300
350
Day-of-year (2008)

APPENDIX D

Extracted Daily Coordinate Time-Series from PPP Processing (1 August 2007 – 31 October 2007)

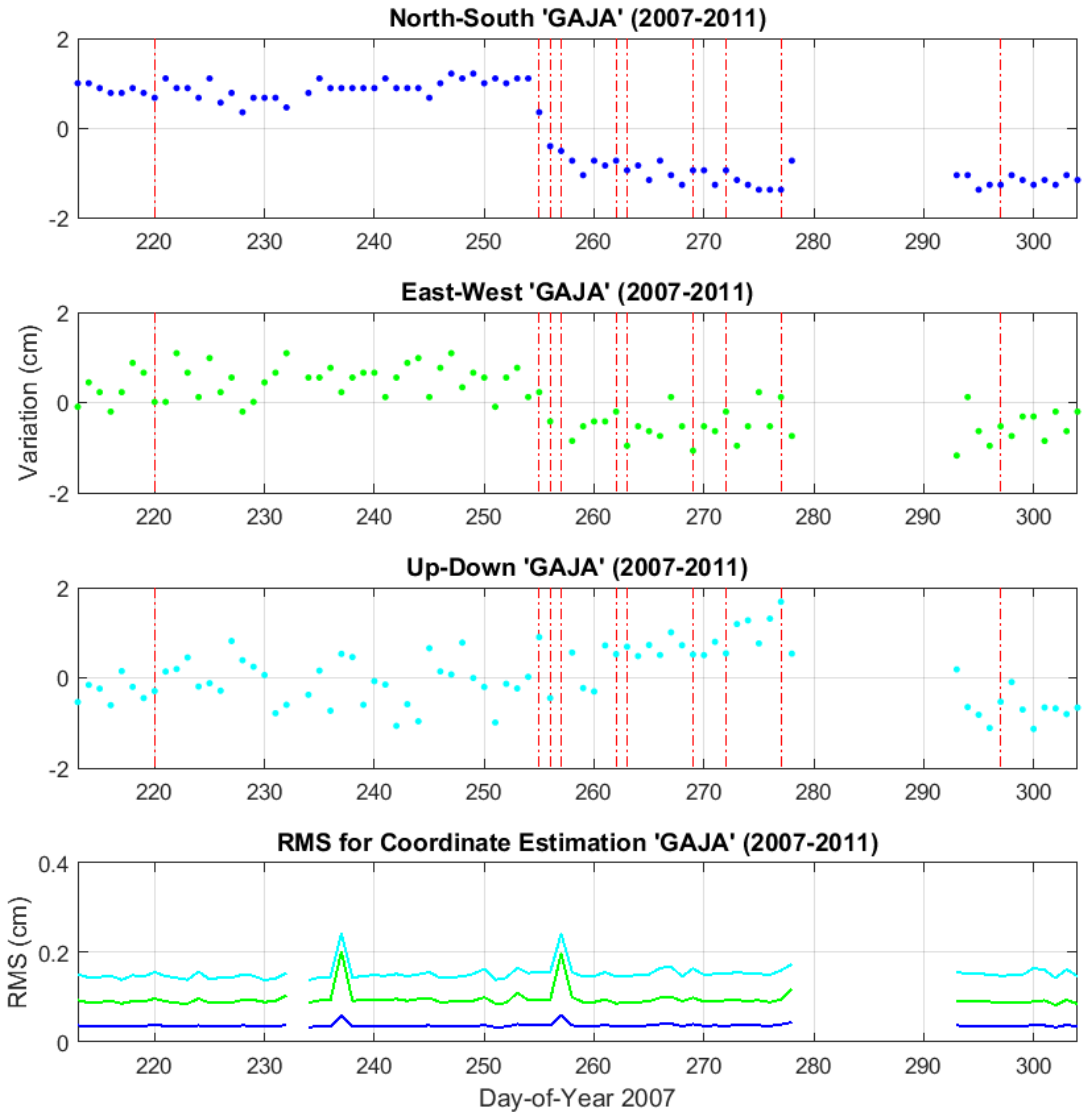


Figure C1: Extracted daily coordinate time-series for station GAJA (1 August 2007 - 31 October 2007) from PPP processing: (*a*) in North-South component, (*b*) in East-West component, (*c*) in Up-Down component, and (*d*) RMS for the estimation in colour coded, i.e. blue for North-South component, green for East-West component, and cyan for Up-Down component. The red dotted lines in the y-axis of figure (*a*), (*b*), and (*c*) represent earthquakes larger than 6Mw.

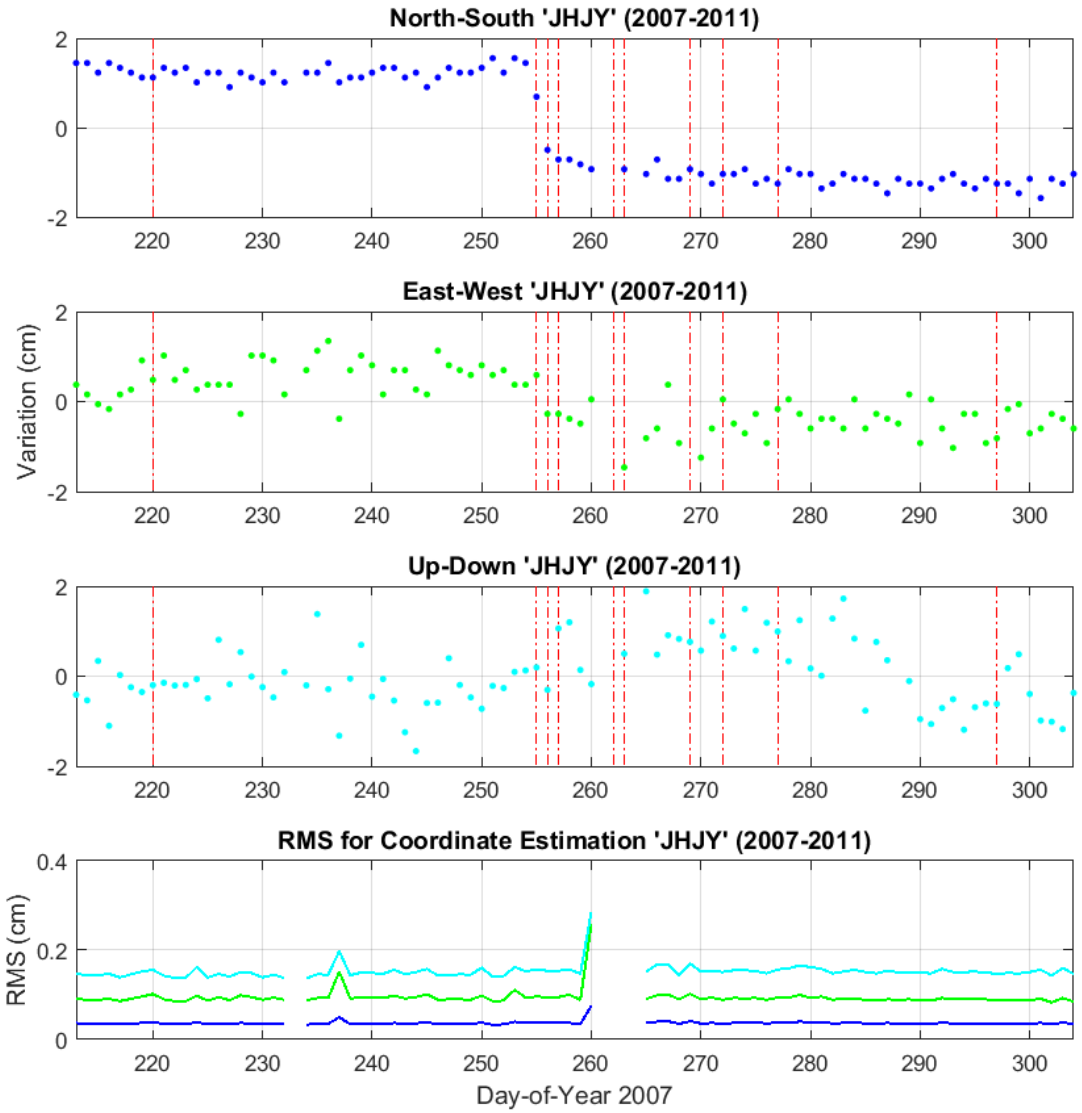


Figure C2: Extracted daily coordinate time-series for station JHJY (1 August 2007 - 31 October 2007) from PPP processing: (*a*) in North-South component, (*b*) in East-West component, (*c*) in Up-Down component, and (*d*) RMS for the estimation in colour coded, i.e. blue for North-South component, green for East-West component, and cyan for Up-Down component. The red dotted lines in the y-axis of figure (*a*), (*b*), and (*c*) represent earthquakes larger than 6Mw.

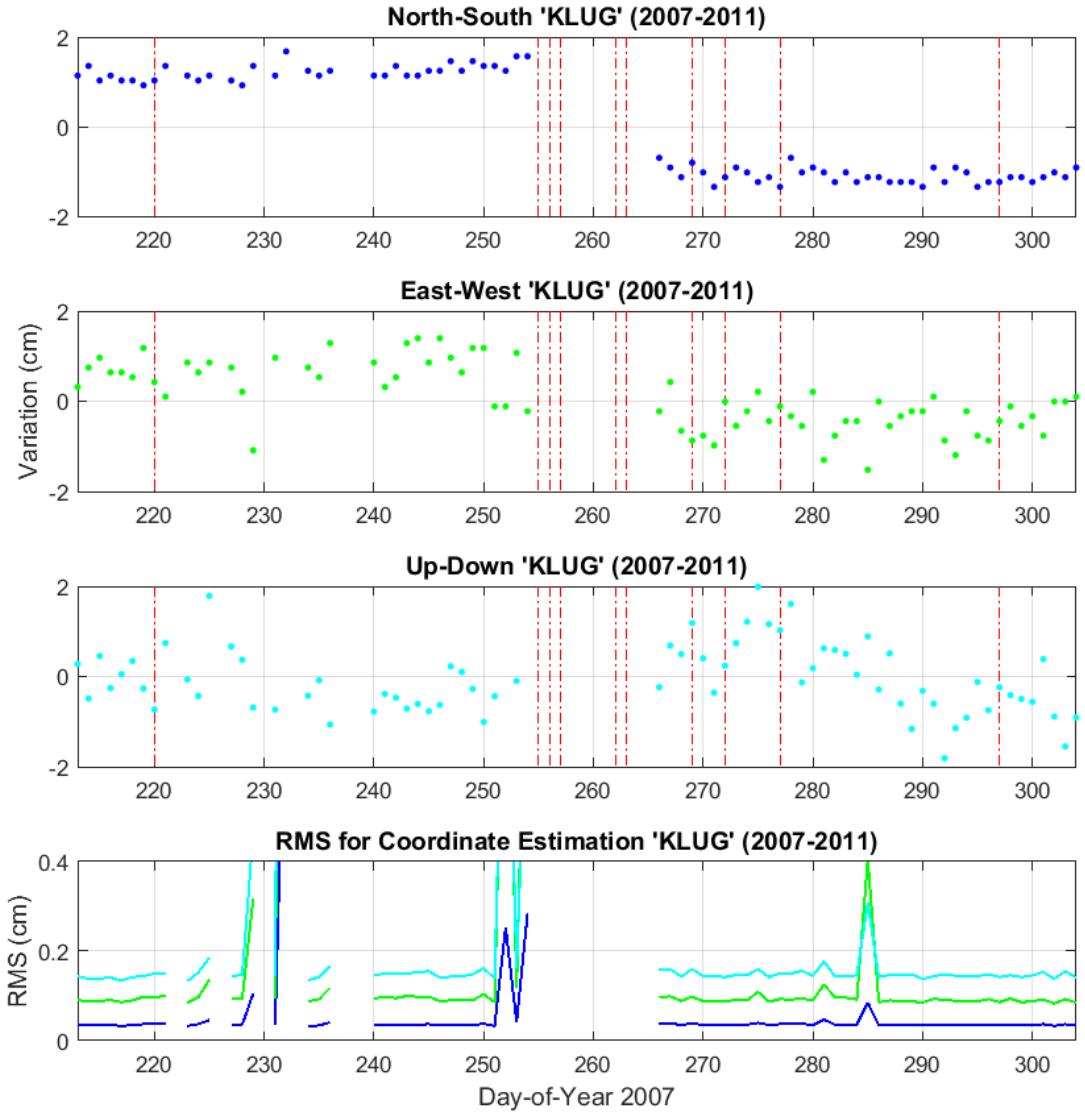


Figure C3: Extracted daily coordinate time-series for station KLUG (1 August 2007 - 31 October 2007) from PPP processing: (*a*) in North-South component, (*b*) in East-West component, (*c*) in Up-Down component, and (*d*) RMS for the estimation in colour coded, i.e. blue for North-South component, green for East-West component, and cyan for Up-Down component. The red dotted lines in the y-axis of figure (*a*), (*b*), and (*c*) represent earthquakes larger than 6Mw.

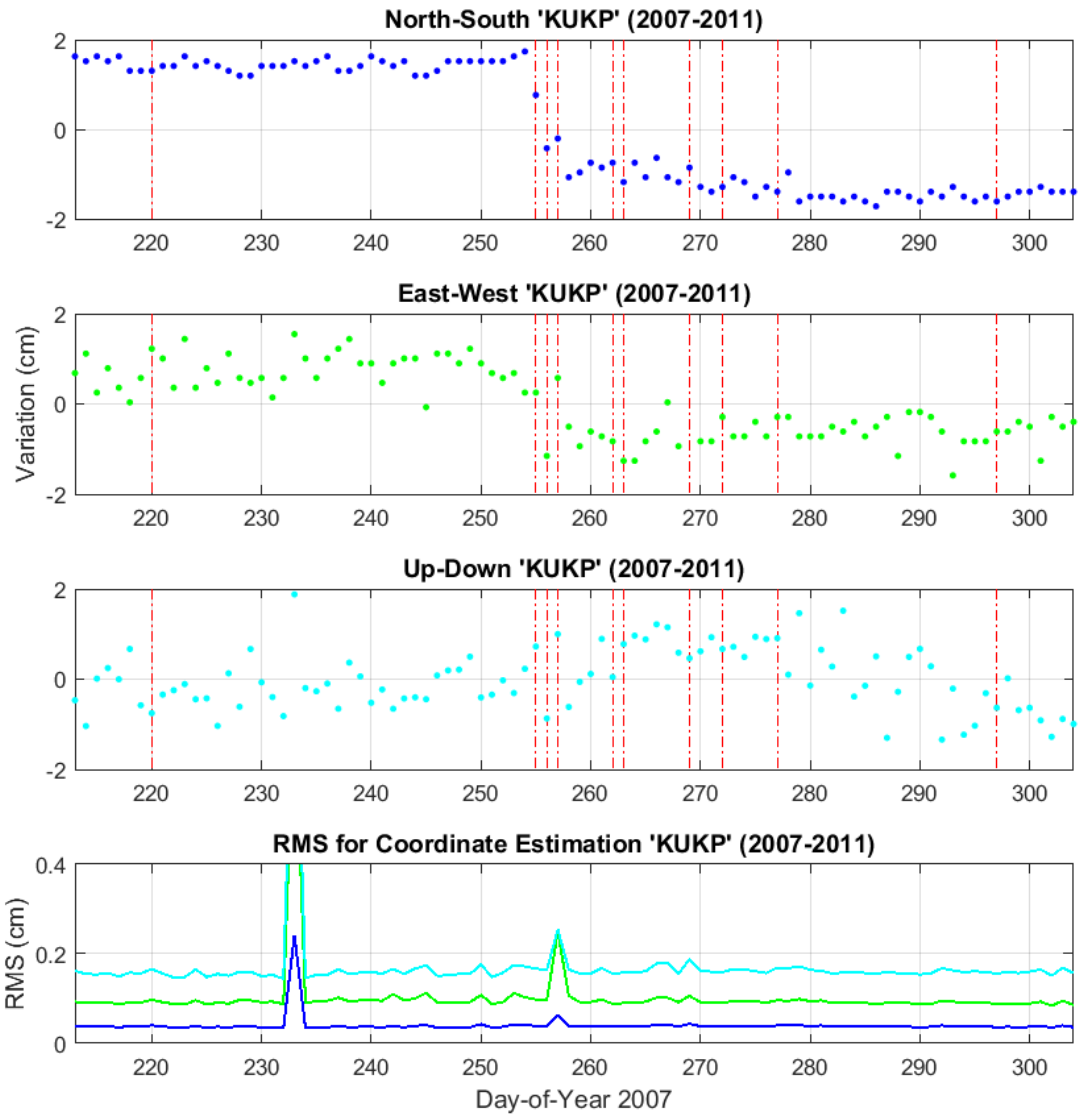


Figure C4: Extracted daily coordinate time-series for station KUKP (1 August 2007 - 31 October 2007) from PPP processing: (*a*) in North-South component, (*b*) in East-West component, (*c*) in Up-Down component, and (*d*) RMS for the estimation in colour coded, i.e. blue for North-South component, green for East-West component, and cyan for Up-Down component. The red dotted lines in the y-axis of figure (*a*), (*b*), and (*c*) represent earthquakes larger than 6Mw.

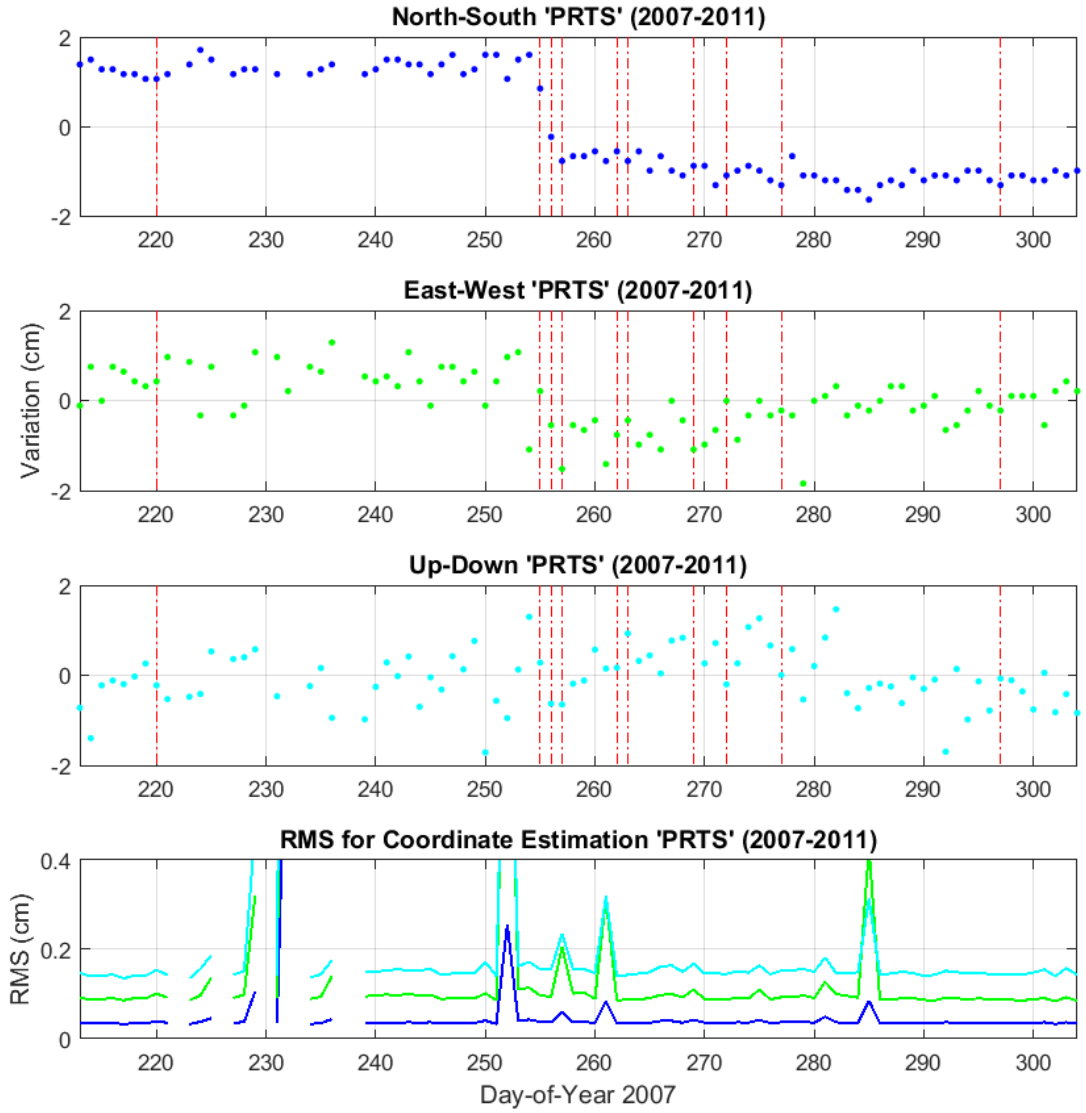


Figure C5: Extracted daily coordinate time-series for station PRTS (1 August 2007 - 31 October 2007) from PPP processing: (*a*) in North-South component, (*b*) in East-West component, (*c*) in Up-Down component, and (*d*) RMS for the estimation in colour coded, i.e. blue for North-South component, green for East-West component, and cyan for Up-Down component. The red dotted lines in the y-axis of figure (*a*), (*b*), and (*c*) represent earthquakes larger than 6Mw.

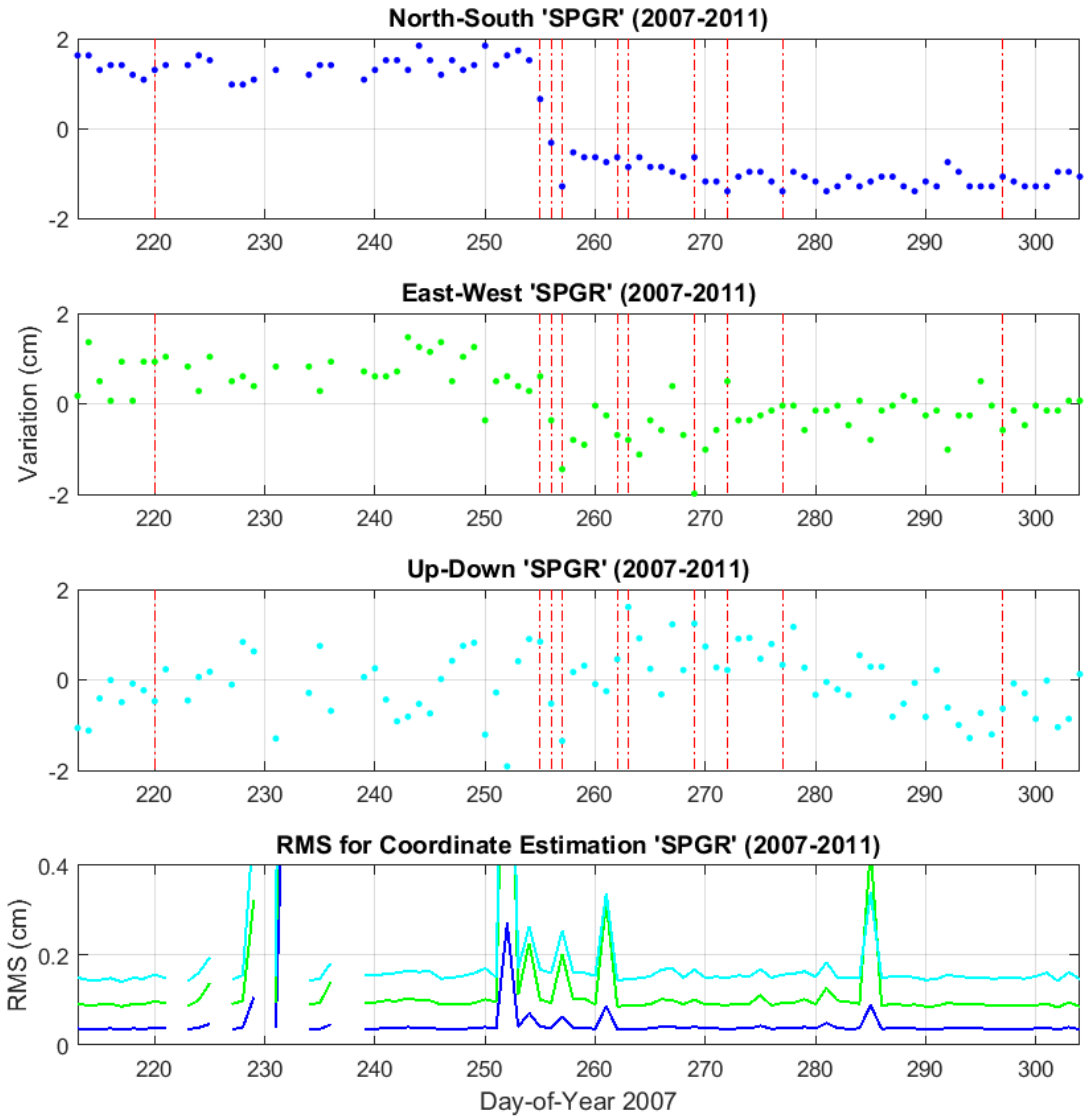


Figure C6: Extracted daily coordinate time-series for station SPGR (1 August 2007 - 31 October 2007) from PPP processing: (*a*) in North-South component, (*b*) in East-West component, (*c*) in Up-Down component, and (*d*) RMS for the estimation in colour coded, i.e. blue for North-South component, green for East-West component, and cyan for Up-Down component. The red dotted lines in the y-axis of figure (*a*), (*b*), and (*c*) represent earthquakes larger than 6Mw.

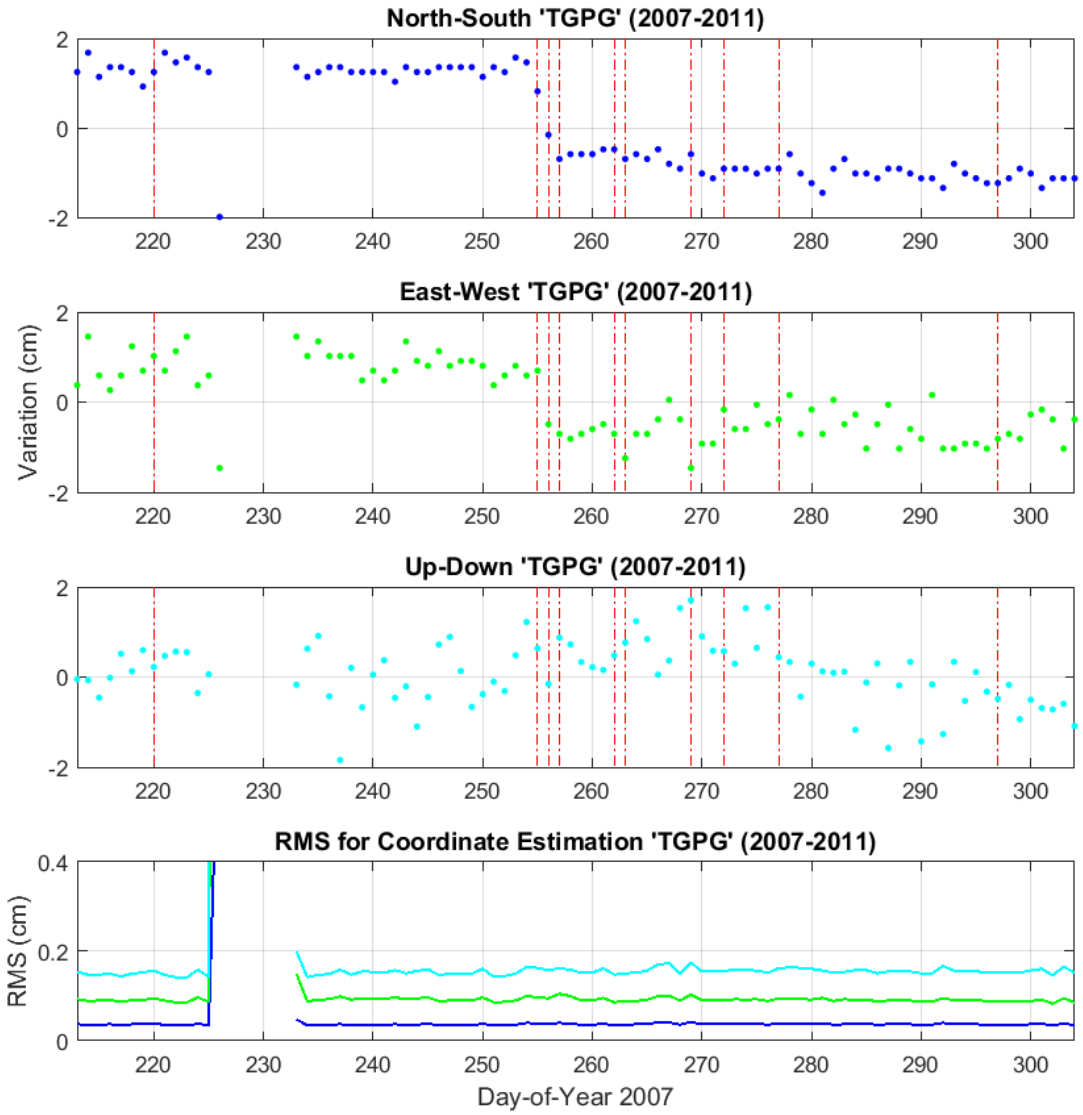


Figure C7: Extracted daily coordinate time-series for station TGPG (1 August 2007 - 31 October 2007) from PPP processing: (*a*) in North-South component, (*b*) in East-West component, (*c*) in Up-Down component, and (*d*) RMS for the estimation in colour coded, i.e. blue for North-South component, green for East-West component, and cyan for Up-Down component. The red dotted lines in the y-axis of figure (*a*), (*b*), and (*c*) represent earthquakes larger than 6Mw.

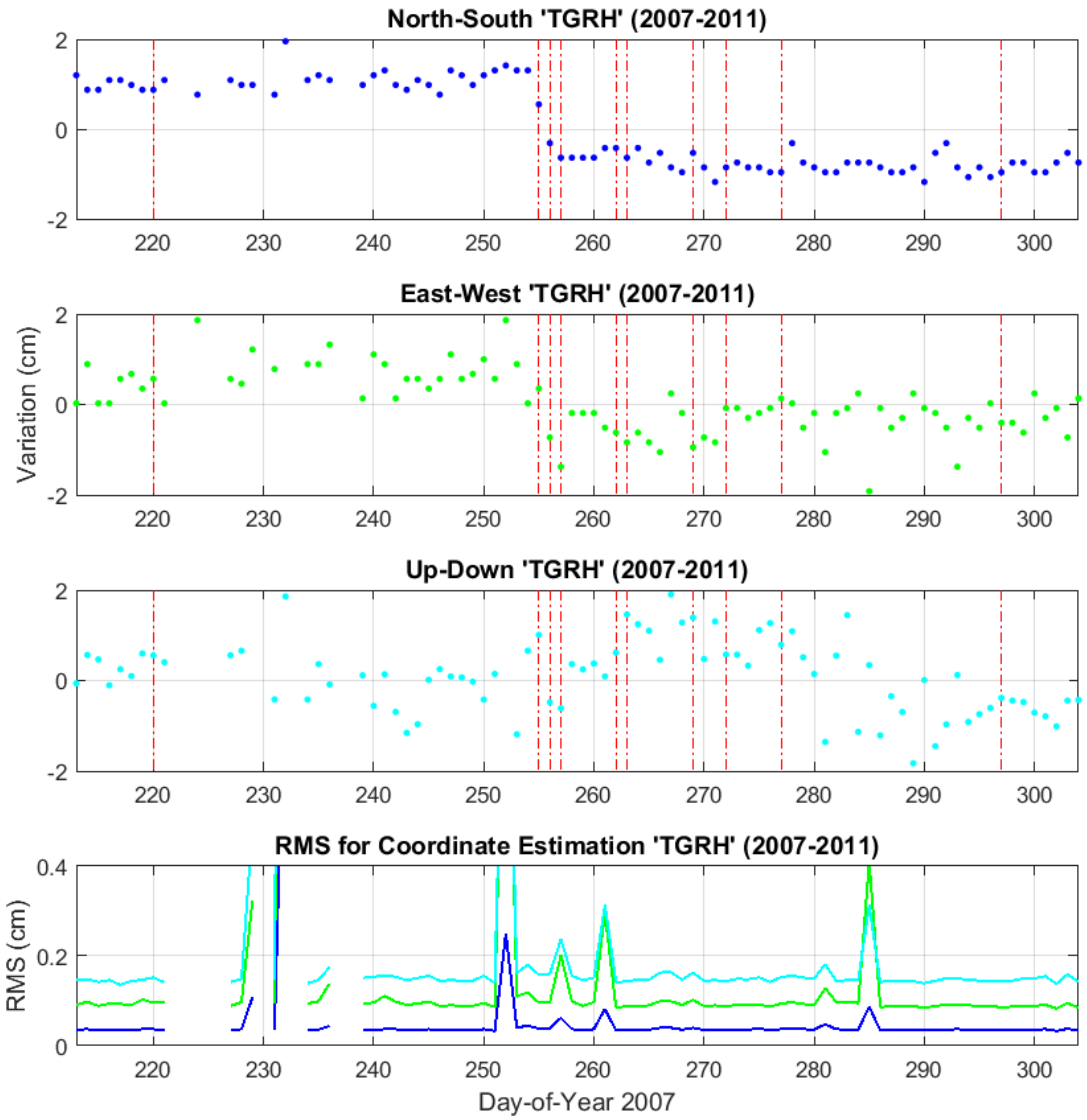


Figure C8: Extracted daily coordinate time-series for station TGRH (1 August 2007 - 31 October 2007) from PPP processing: (*a*) in North-South component, (*b*) in East-West component, (*c*) in Up-Down component, and (*d*) RMS for the estimation in colour coded, i.e. blue for North-South component, green for East-West component, and cyan for Up-Down component. The red dotted lines in the y-axis of figure (*a*), (*b*), and (*c*) represent earthquakes larger than 6Mw.

APPENDIX E

Extracted Daily Coordinate Time-Series from DD Processing (1 August 2007 – 31 October 2007)

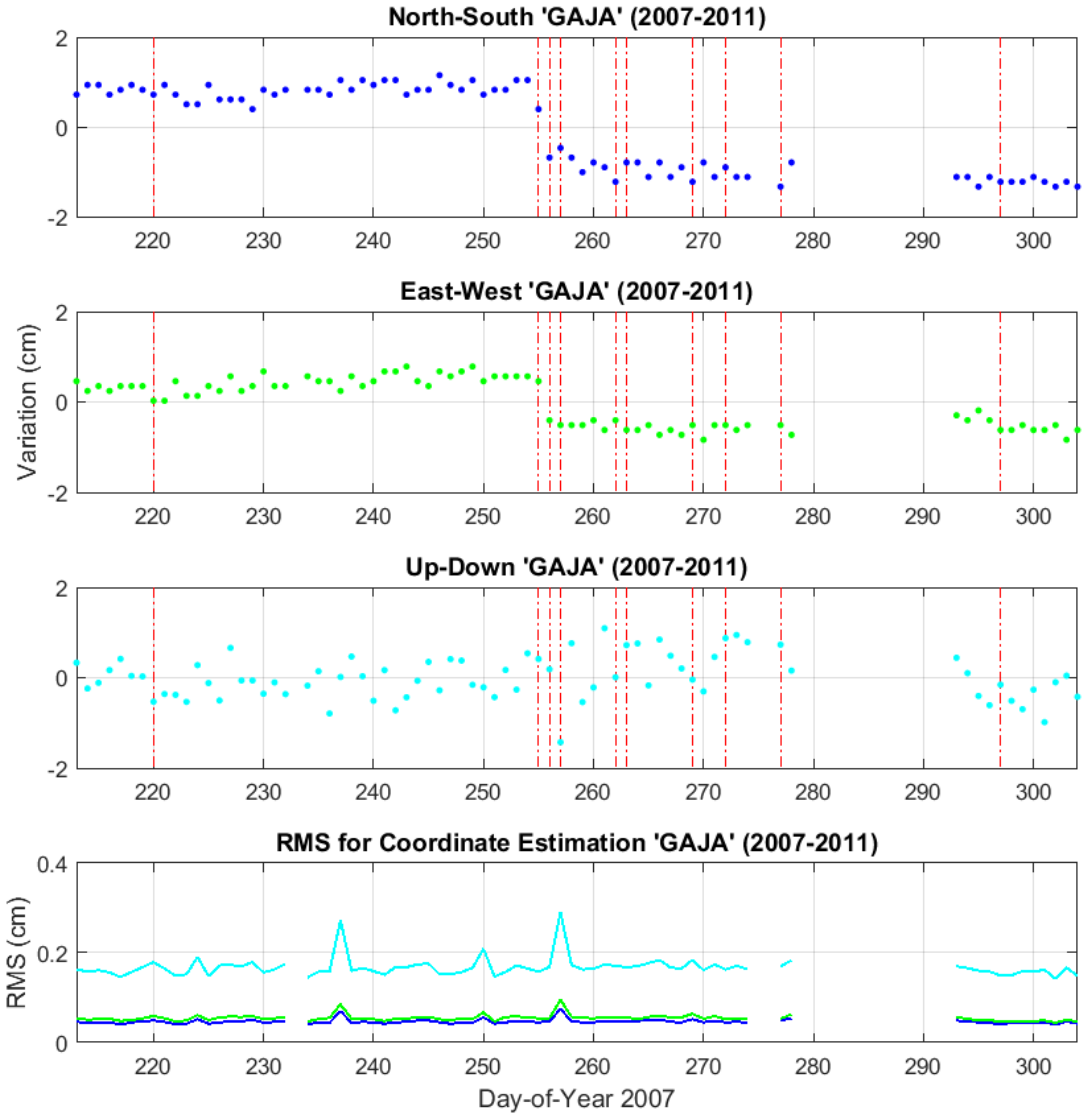


Figure D1: Extracted daily coordinate time-series for station GAJA (1 August 2007 - 31 October 2007) from DD processing: (*a*) in North-South component, (*b*) in East-West component, (*c*) in Up-Down component, and (*d*) RMS for the estimation in colour coded, i.e. blue for North-South component, green for East-West component, and cyan for Up-Down component. The red dotted lines in the y-axis of figure (*a*), (*b*), and (*c*) represent earthquakes larger than 6Mw.

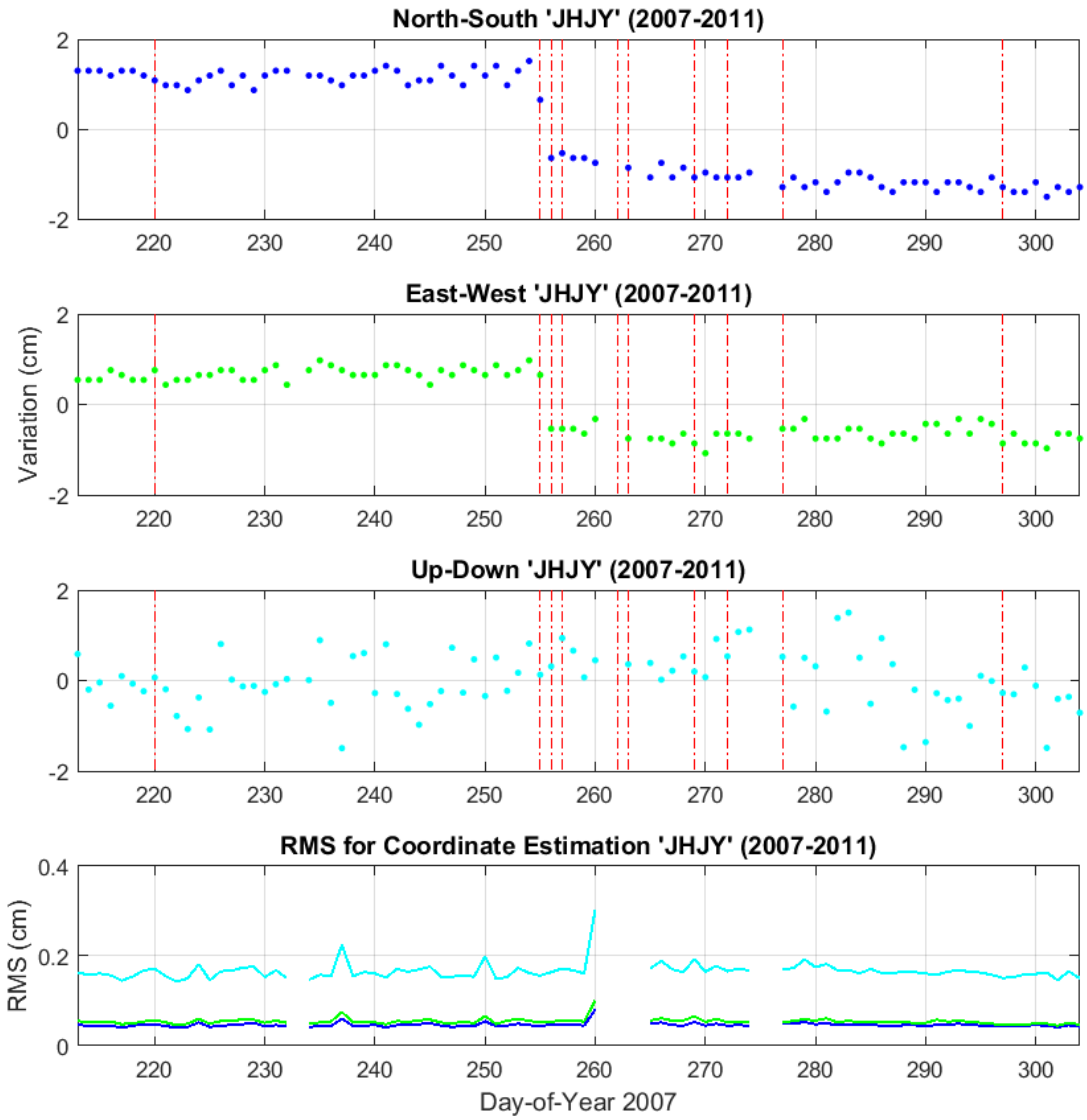


Figure D2: Extracted daily coordinate time-series for station JHJY (1 August 2007 - 31 October 2007) from DD processing: (*a*) in North-South component, (*b*) in East-West component, (*c*) in Up-Down component, and (*d*) RMS for the estimation in colour coded, i.e. blue for North-South component, green for East-West component, and cyan for Up-Down component. The red dotted lines in the y-axis of figure (*a*), (*b*), and (*c*) represent earthquakes larger than 6Mw.

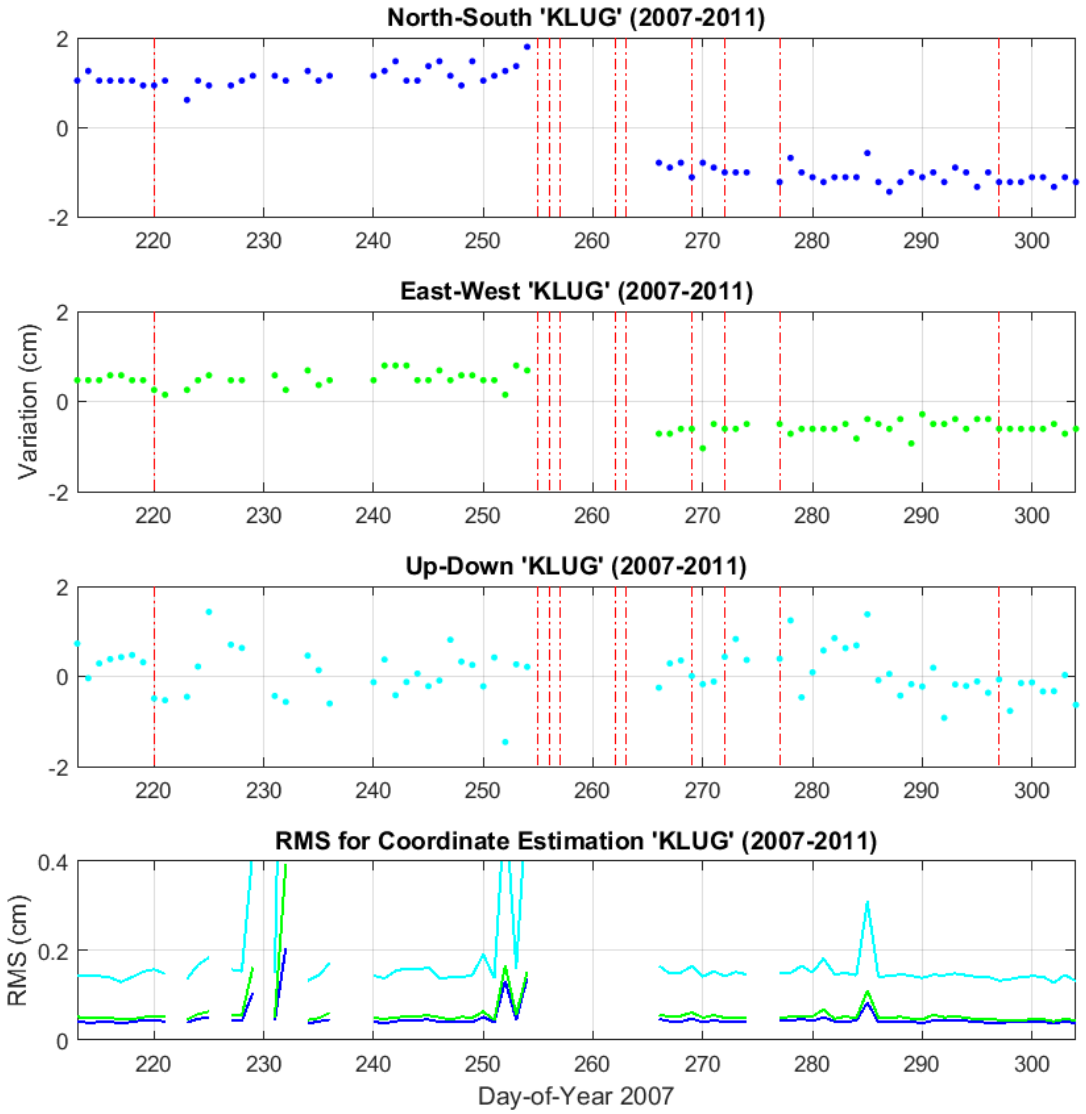


Figure D3: Extracted daily coordinate time-series for station KLUG (1 August 2007 - 31 October 2007) from DD processing: (*a*) in North-South component, (*b*) in East-West component, (*c*) in Up-Down component, and (*d*) RMS for the estimation in colour coded, i.e. blue for North-South component, green for East-West component, and cyan for Up-Down component. The red dotted lines in the y-axis of figure (*a*), (*b*), and (*c*) represent earthquakes larger than 6Mw.

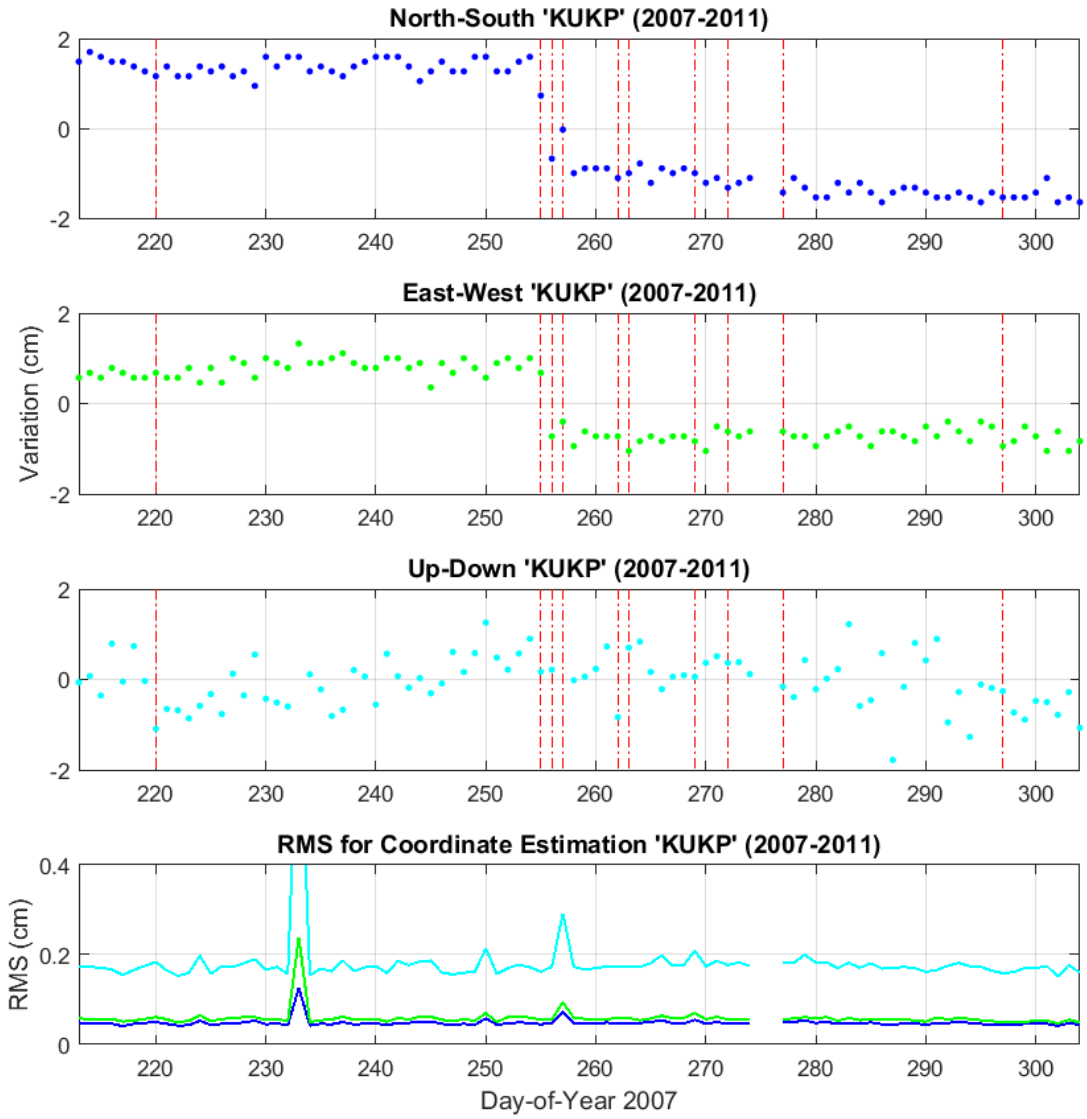


Figure D4: Extracted daily coordinate time-series for station KUKP (1 August 2007 - 31 October 2007) from DD processing: (*a*) in North-South component, (*b*) in East-West component, (*c*) in Up-Down component, and (*d*) RMS for the estimation in colour coded, i.e. blue for North-South component, green for East-West component, and cyan for Up-Down component. The red dotted lines in the y-axis of figure (*a*), (*b*), and (*c*) represent earthquakes larger than 6Mw.

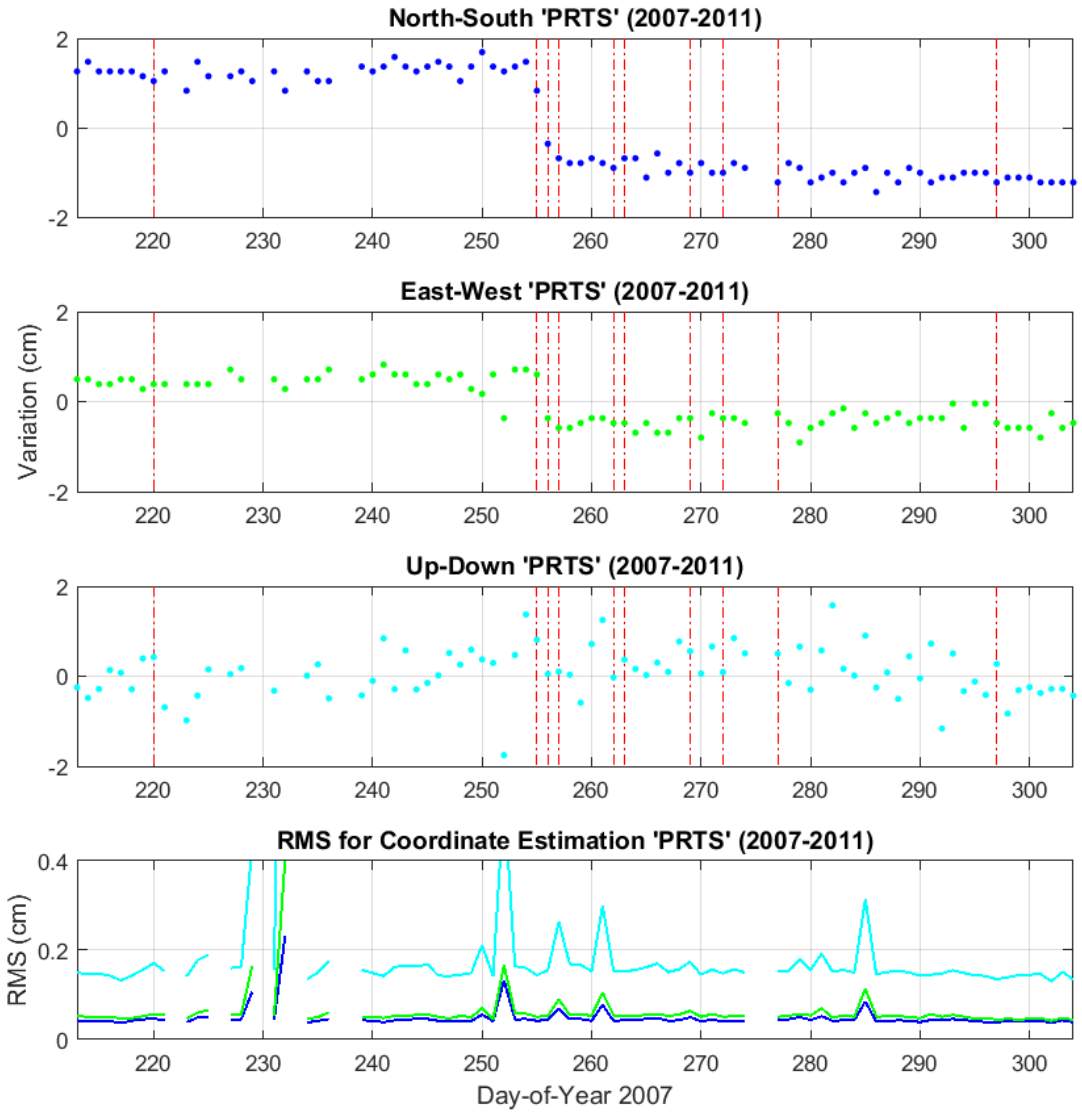


Figure D5: Extracted daily coordinate time-series for station PRTS (1 August 2007 - 31 October 2007) from DD processing: (*a*) in North-South component, (*b*) in East-West component, (*c*) in Up-Down component, and (*d*) RMS for the estimation in colour coded, i.e. blue for North-South component, green for East-West component, and cyan for Up-Down component. The red dotted lines in the y-axis of figure (*a*), (*b*), and (*c*) represent earthquakes larger than 6Mw.

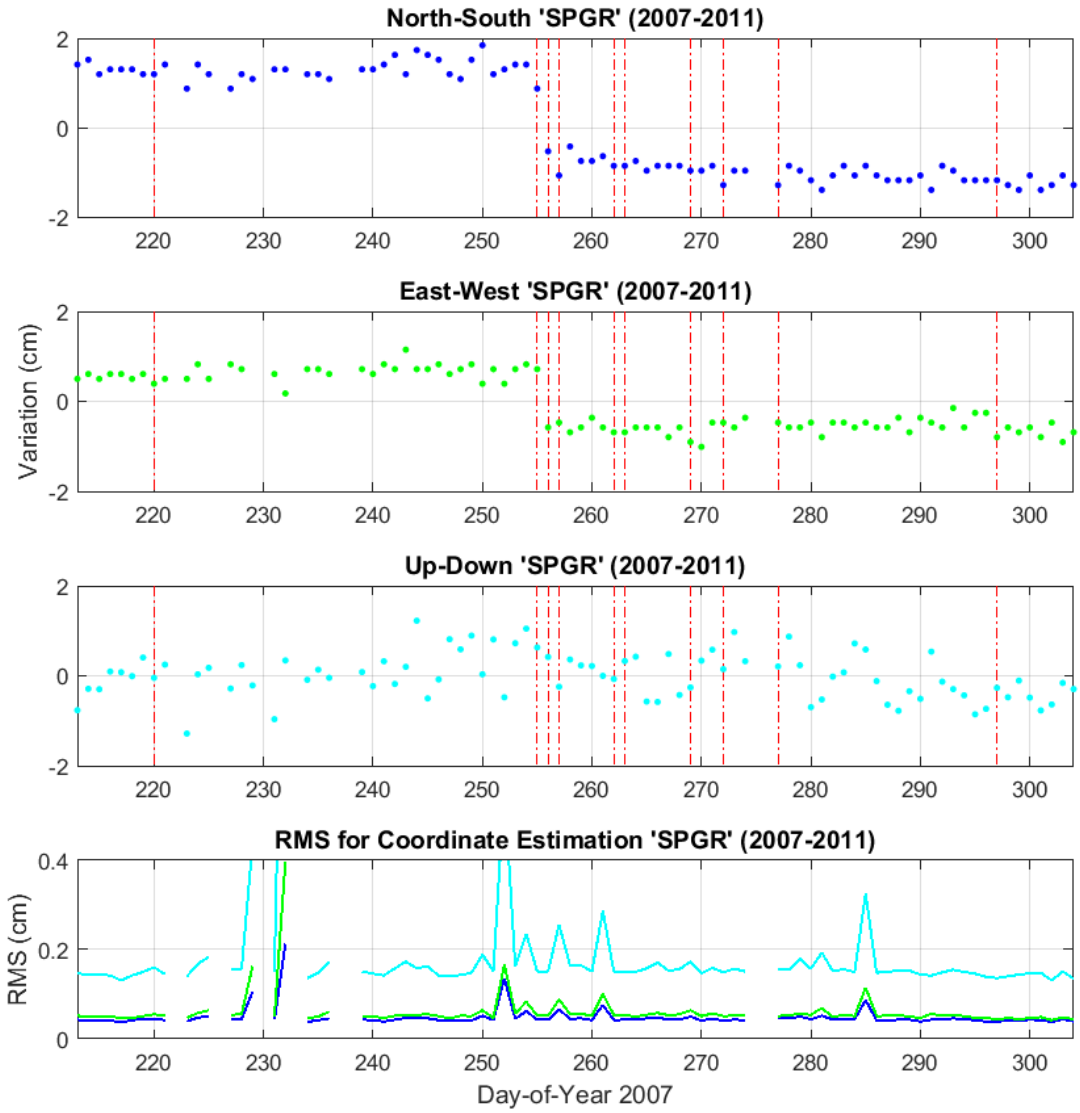


Figure D6: Extracted daily coordinate time-series for station SPGR (1 August 2007 - 31 October 2007) from DD processing: (*a*) in North-South component, (*b*) in East-West component, (*c*) in Up-Down component, and (*d*) RMS for the estimation in colour coded, i.e. blue for North-South component, green for East-West component, and cyan for Up-Down component. The red dotted lines in the y-axis of figure (*a*), (*b*), and (*c*) represent earthquakes larger than 6Mw.

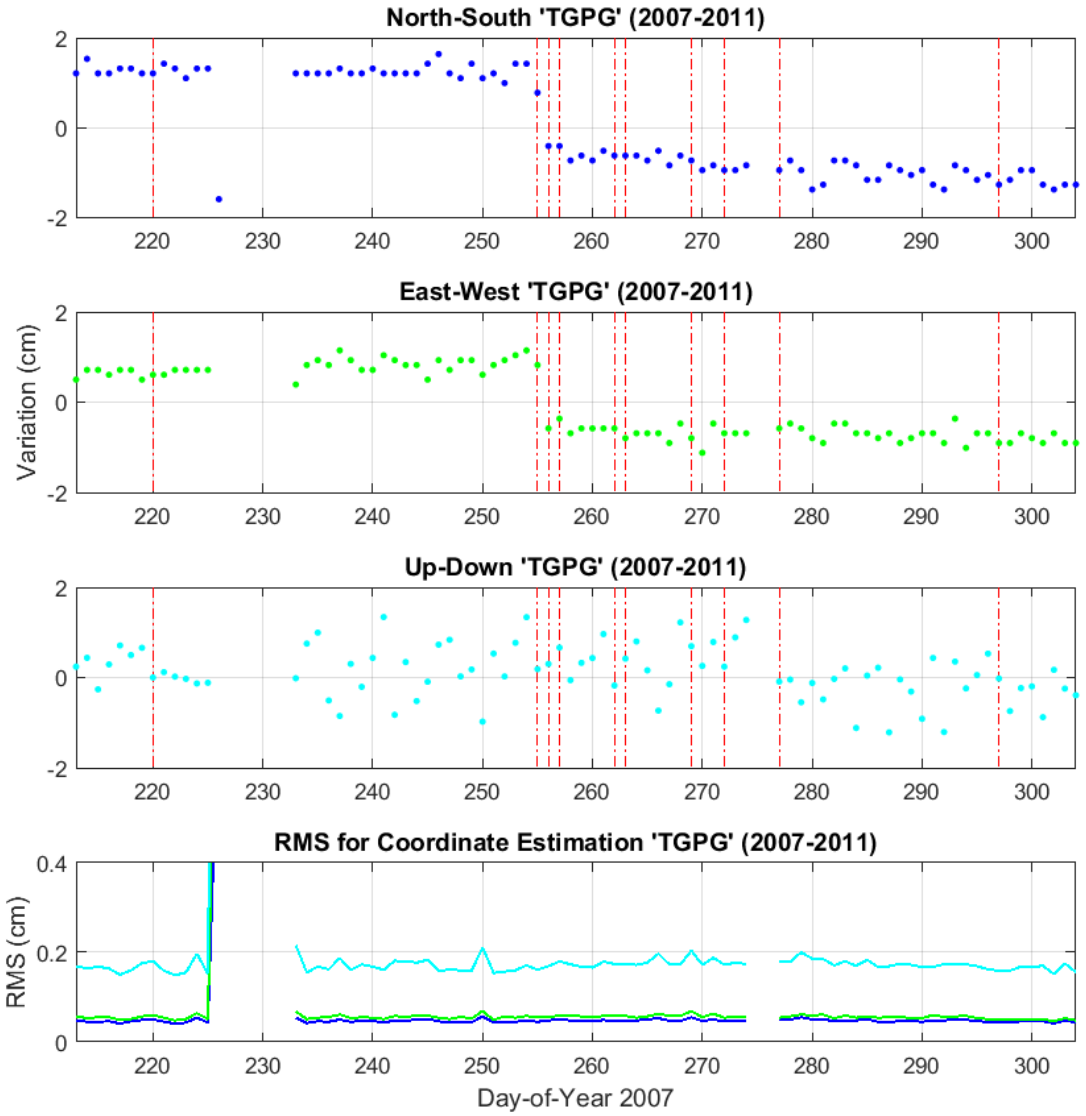


Figure D7: Extracted daily coordinate time-series for station TGPG (1 August 2007 - 31 October 2007) from DD processing: (*a*) in North-South component, (*b*) in East-West component, (*c*) in Up-Down component, and (*d*) RMS for the estimation in colour coded, i.e. blue for North-South component, green for East-West component, and cyan for Up-Down component. The red dotted lines in the y-axis of figure (*a*), (*b*), and (*c*) represent earthquakes larger than 6Mw.

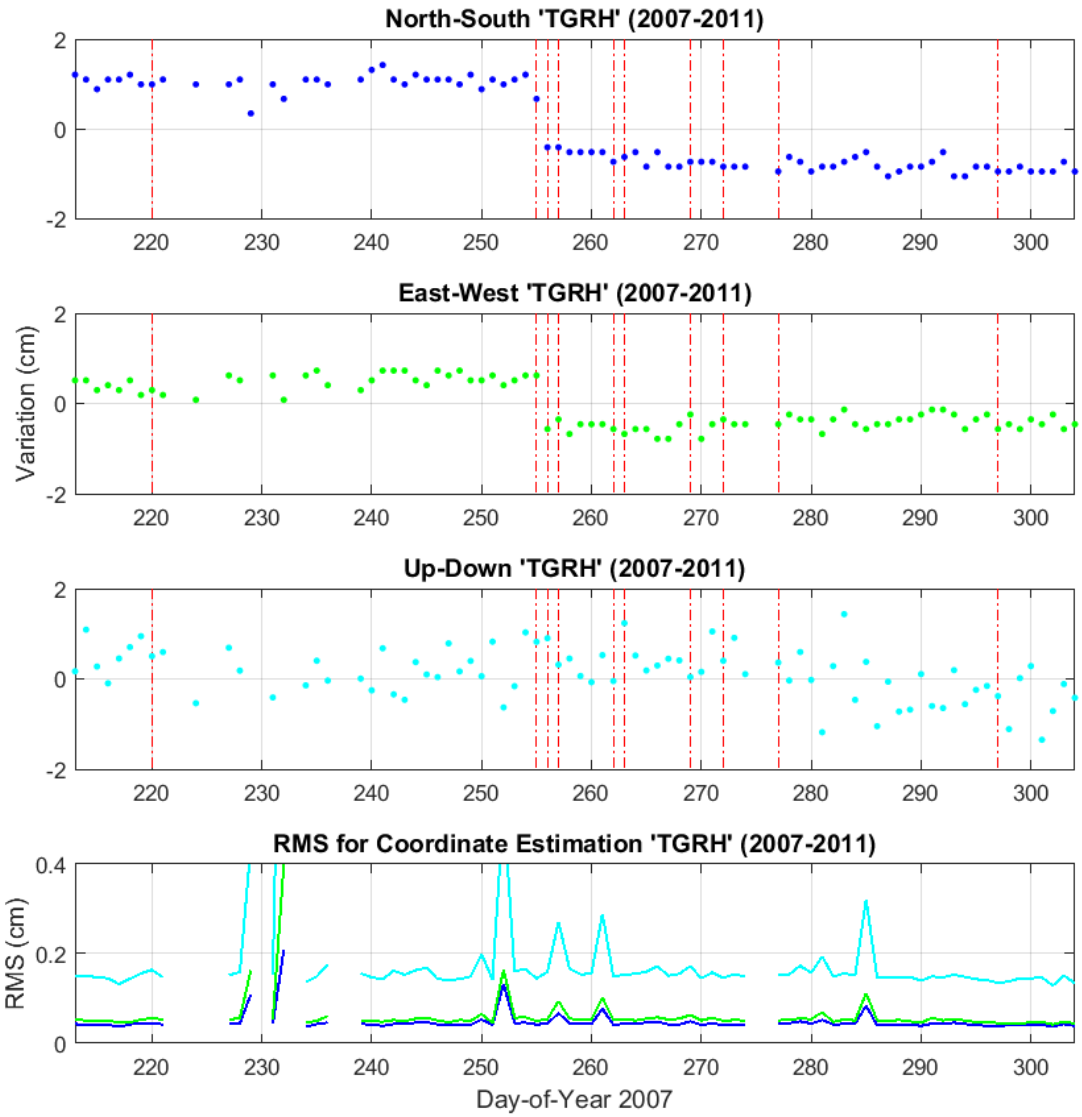


Figure D8: Extracted daily coordinate time-series for station TGRH (1 August 2007 - 31 October 2007) from DD processing: (*a*) in North-South component, (*b*) in East-West component, (*c*) in Up-Down component, and (*d*) RMS for the estimation in colour coded, i.e. blue for North-South component, green for East-West component, and cyan for Up-Down component. The red dotted lines in the y-axis of figure (*a*), (*b*), and (*c*) represent earthquakes larger than 6Mw.